

**MECHANISTIC INVESTIGATIONS OF RHODIUM-  
CATALYZED ALKYNE HYDROTHIOLATION**

by

Matthew James Wathier

B.Sc.H., Queen's University, 2009

A THESIS SUBMITTED IN PARTIAL FULFILLMENT OF  
THE REQUIREMENTS FOR THE DEGREE OF

DOCTOR OF PHILOSOPHY

in

THE FACULTY OF GRADUATE AND POSTDOCTORAL STUDIES  
(Chemistry)

THE UNIVERSITY OF BRITISH COLUMBIA  
(Vancouver)

September, 2016

© Matthew James Wathier, 2016

## Abstract

Herein, thorough mechanistic investigations into alkyne hydrothiolation catalyzed by  $[\text{Tp}^*\text{Rh}^{\text{I}}(\text{PPh}_3)_2]$  ( $\text{Tp}^*$  = tris(3,5-dimethylpyrazolyl)borate) are reported. The mechanism is shown to proceed through an intermediate  $[\text{Tp}^*\text{Rh}^{\text{III}}\text{H}(\text{SR})]$  complex ( $\text{R}$  = alkyl, aryl). Alkyne migratory insertion is shown to occur chemoselectively into the Rh-SR bond, despite the availability of a Rh-H bond, to produce a rhodathiacyclobutene intermediate. The regioselectivity of product formation is revealed to be the result of a competition between 1,2 and 2,1 migratory insertion of the alkyne to produce regioisomeric rhodathiacyclobutene intermediates. Product formation occurs upon reductive elimination, which is associatively induced by coordination of thiol.

Putative off-cycle intermediates  $[\text{Tp}^*\text{RhH}(\text{SR})(\text{PMe}_3)]$  ( $\text{R}$  = alkyl, aryl) have been successfully synthesized from  $[\text{Tp}^*\text{RhH}(\text{CH}_3)(\text{PMe}_3)]$ . The mechanism of formation of the  $[\text{Tp}^*\text{RhH}(\text{SR})(\text{PMe}_3)]$  complexes is proposed to involve the reductive elimination of methane, associatively induced by coordination of thiol. This mechanism is analogous to the mechanism proposed for alkyne hydrothiolation catalyzed by  $[\text{Tp}^*\text{Rh}(\text{PPh}_3)_2]$ . Alkyne hydrothiolation reactions in the presence of  $[\text{Tp}^*\text{RhH}(\text{SR})(\text{PMe}_3)]$  are shown to produce the same product regioisomer as reactions catalyzed by  $[\text{Tp}^*\text{Rh}(\text{PPh}_3)_2]$ .

The synthesis of the vinyl sulfone-containing drug K777, currently in clinical trials for the treatment of Chagas disease, via alkyne hydrothiolation methodology catalyzed by  $[\text{RhCl}(\text{PPh}_3)_3]$ , is reviewed. The methodology proves to be versatile in the synthesis of K777 and related analogues. The analogues are assessed in terms of their reactivity towards Michael addition as a method of predicting pharmacodynamics properties.

The methanolic  $pK_{AS}$  of a series of *para*-substituted aryl thiols are reported and correlated to their predicted aqueous  $pK_A$  values. The Hammett dual parameter correlation to the experimental data reveals that the acidity constants are more dependent on the inductive effects of the *para*-substituent compared to the resonance effect. The dual parameter correlation also allows for the prediction of the methanolic and aqueous acidity constant of any *para*-substituted aryl thiol, as long as the substituent's resonance and induction Hammett constants are known.

## Preface

A version of the review of hydroelementation of carbon-carbon unsaturated bonds catalyzed by metal-scorpionate complexes presented in Chapter 2 has been published in the *European Journal of Inorganic Chemistry*. I was responsible for writing the manuscript, while Dr. Jennifer A. Love was responsible for editing the manuscript.

Doi: 10.1002/ejic.201501272

A version of Chapter 4 has been published in *Organic Letters*. The synthesis of K777 described in 4.2.1 was performed by Erica R. Kiemele. I was responsible for the kinetic assays of Michael addition relating to expected potency in Cruzain inhibition, writing of the manuscript and supporting information.

E. R. Kiemele, M. Wathier, P. Bichler, J. A. Love. *Org. Lett.* **2016**, *18*, 492–495.

In conjunction with Moonhee Lee and Dr. Patrick McGeer, from the Kinsmen Laboratory of Neurological Research, Department of Psychiatry at UBC, and Aurin Biotech, I was responsible for the synthesis of compounds with potential application in the treatment of, among others, Alzheimer's and Parkinson's disease.

M. Lee, M. Wathier, J. A. Love, E. McGeer, P. L. McGeer, *Neurobiology of Aging*, **2015**, *36*, 2748-2756.

## Table of Contents

Abstract .....	ii
Preface.....	iv
Table of Contents .....	v
List of Tables .....	x
List of Figures.....	xi
List of Schemes.....	xvii
List of Abbreviations .....	xx
Acknowledgements.....	xxvi
Dedication.....	xxvii
Chapter 1 Introduction.....	1
1.1 Sulfur-Containing Compounds .....	1
1.2 Synthetic Methods Towards Vinyl-Sulfides.....	3
1.2.1 Alkyne Hydrothiolation .....	4
1.2.2 Transition Metal Catalyzed Alkyne Hydrothiolation .....	6
1.3 Mechanisms of Metal-Catalyzed Hydrothiolation.....	10
1.3.1 Class I Mechanisms .....	10
1.3.2 Class II Mechanisms .....	11
1.3.2.1 Regioselectivity in Class II Mechanisms .....	15
1.4 Insertions into Rhodium-Heteroatom Bonds .....	18
1.4.1 Systems with Direct Evidence for Rhodium-Heteroatom Insertion .....	18
1.4.2 Systems with Indirect Evidence for Rhodium-Heteroatom Insertion.....	22
1.5 Thesis Outline .....	28
Chapter 2 Review of Hydroelementation of Carbon-Carbon Unsaturated Bonds Catalyzed by Metal-Scorpionate Complexes.....	29
2.1 Hydrothiolation of Alkynes .....	32
2.1.1 Alkyne Hydrothiolation Catalyzed by Tris(pyrazolyl)borate Complexes of Rhodium.....	34
2.2 Hydroamination .....	40
2.2.1 Hydroamination with Homoscorpionate Ligands.....	41
2.2.2 Hydroamination with Heteroscorpionate Ligands .....	49
2.3 Hydroalkoxylation of Alkynes.....	56
2.3.1 Cyclization of Alkynoic Acids.....	57

2.4	Hydrophosphinylation of Alkynes .....	61
2.5	Conclusion .....	63
Chapter 3	Substrate-Activity Relationships in Mechanistic Elucidation .....	65
3.1	Introduction.....	65
3.1.1	Linear Free Energy Relationships.....	66
3.1.2	Interpretation of $\rho$ .....	68
3.1.3	Hammett $\sigma^-$ and $\sigma^+$ constants .....	68
3.1.4	Dual substituent parameter LFER.....	69
3.2	Measurement of Aryl Thiol $pK_A$ in Methanolic Solution.....	71
3.2.1	Single and Dual Parameter Hammett Treatment of Aryl Thiol $pK_A$ Values .....	75
3.3	Conclusion .....	81
3.4	Experimental .....	82
3.4.1	Measurements of Acidity Constants of Substituted Aryl Thiols in Methanol .....	82
Chapter 4	Application of Alkyne Hydrothiolation in the Synthesis of K777 .....	83
4.1	Chagas Disease .....	83
4.1.1	Existing Treatments for Chagas Disease .....	83
4.1.2	Treatment of Chagas Disease by Inhibition of Cruzain.....	84
4.2	K777 as Potent Cysteine Protease Inhibitor.....	86
4.2.1	Erica Kiemele's Synthesis of K777 via Rhodium-Catalyzed Alkyne Hydrothiolation .....	90
4.3	Rates of Michael Addition with <i>para</i> -Substituted Vinyl Sulfones.....	93
4.4	Conclusion .....	98
4.5	Experimental .....	99
4.5.1	Measurement of Rate of Addition of 2-phenethanethiol to Vinyl Sulfones .....	99
Chapter 5	Mechanistic Studies of Alkyne Hydrothiolation Catalyzed by $[Tp^*Rh(PPh_3)_2]$ ..	101
5.1	Introduction.....	101
5.2	Results.....	107
5.2.1	Contrast Between $[Tp^*Rh(PPh_3)_2]$ and $[Tp^*Rh(SPh)_2(MeCN)]$ Catalyzed Alkyne Hydrothiolation .....	107
5.2.2	Kinetic Order and Phosphine Dependence .....	109
5.2.3	Deuterium Kinetic Isotope Effects.....	111
5.2.4	Stoichiometric Reactions .....	112
5.2.5	Thiol Substrate-Activity Relationship .....	114
5.2.6	Alkyne Steric Bulk.....	115

5.2.7	Alkyne Substrate-Activity Relationship .....	117
5.2.8	Eyring Data .....	117
5.2.9	DFT Calculations of Alkyne Insertion Products.....	120
5.3	Discussion .....	121
5.3.1	Hydridothiolate vs Bisthiolate Intermediate .....	121
5.3.2	Kinetic Order and PPh <sub>3</sub> Dependence .....	122
5.3.3	Alkyne Steric Effects .....	123
5.3.4	Substrate-Activity Relationships. ....	125
5.3.5	Eyring Data .....	127
5.4	Proposed Mechanism .....	128
5.4.1	Migratory Insertion. ....	129
5.4.2	The Effect of Alkyne Electronics. ....	132
5.4.3	Reductive Elimination as the Rate-Limiting Step. ....	133
5.5	Detailed Mechanism and Assignment of Putative Structures for Hydride Signals ....	138
5.6	Conclusion .....	141
5.7	Experimental .....	142
5.7.1	Hammett Plots and Alkyne Sterics Experiments .....	143
5.7.2	Substrate Order Experiments .....	144
5.7.3	Added Triphenylphosphine Experiment .....	145
5.7.4	Kinetic Isotope Experiments.....	146
5.7.5	Eyring Experiments by Initial Rates in Mixture of C <sub>6</sub> D <sub>6</sub> : DCE.....	146
5.7.6	Eyring Experiments by <i>Pseudo</i> -First Order Rate Constants in d <sub>8</sub> -Toluene.....	147
5.7.7	Stoichiometric Reactions .....	148
5.7.8	Synthesis of 3,5-dimethylphenylacetylene .....	148
5.7.9	Synthesis of 3,5-di- <i>tert</i> -butylbenzalhyde.....	149
5.7.10	Synthesis of 3,5-di- <i>tert</i> -butylphenylacetylene .....	150
5.7.11	Synthesis of 1,3,5-trimethylbenzaldehyde.....	150
5.7.12	Synthesis of 1,3,5-trimethylphenylacetylene.....	151
Chapter 6	Progress Towards the Synthesis of Putative Intermediates in Alkyne Hydrothiolation Catalyzed by [Tp*Rh(PPh <sub>3</sub> ) <sub>2</sub> ] .....	152
6.1	Review of the Synthesis and Reactivity of Trispyrazolylborate Complexes of Rh <sup>III</sup> . .....	154
6.1.1	Synthesis of [Tp*Rh <sup>III</sup> ] Complexes from [Rh <sup>III</sup> Cl <sub>3</sub> ] Derivatives.....	154

6.1.2	Synthesis of $[\text{Tp}^*\text{Rh}^{\text{III}}]$ Complexes from $[\text{Tp}^*\text{Rh}^{\text{I}}]$ Complexes.....	161
6.2	Progress Towards the Synthesis of Rhodathiacyclobutene Intermediates.....	165
6.3	Synthesis of $[\text{Tp}^*\text{RhHCl}(\text{PR}_3)]$ and $[\text{Tp}^*\text{RhH}_2(\text{PR}_3)]$ Complexes.....	172
6.4	Synthesis of Hydridothiolate Complexes $[\text{Tp}^*\text{RhH}(\text{SR})(\text{PMe}_3)]$ .....	178
6.4.1	Mechanistic Implications of the Synthesis of Hydridothiolate Complexes.....	194
6.4.2	Reactivity of $[\text{Tp}^*\text{RhH}(\text{SEt})(\text{PMe}_3)]$ with Alkynes.....	196
6.5	Conclusion .....	202
6.6	Experimental .....	203
6.6.1	Recrystallization of $\text{KTp}^*$ .....	203
6.6.2	Synthesis of $[\text{Tp}^*\text{RhCl}_2(\text{MeOH})]$ .....	204
6.6.3	Synthesis of $[\text{Tp}^*\text{RhCl}_2(\text{PPh}_3)]$ .....	204
6.6.4	Synthesis of $[\text{Tp}^*\text{RhCl}_2(\text{PEt}_3)]$ .....	205
6.6.5	Synthesis of $[\text{Tp}^*\text{RhCl}_2(\text{BnSH})]$ .....	206
6.6.6	Synthesis of $[\text{Tp}^*\text{RhHCl}(\text{PPh}_3)]$ .....	206
6.6.7	Synthesis of $[\text{Tp}^*\text{RhH}_2(\text{PPh}_3)]$ .....	207
6.6.8	Synthesis of $[\text{Tp}^*\text{RhHCl}(\text{PEt}_3)]$ .....	208
6.6.9	Synthesis of $[\text{Tp}^*\text{RhH}(\text{SBn})(\text{PMe}_3)]$ .....	208
6.6.10	Synthesis of $[\text{Tp}^*\text{RhH}(\text{SEt})(\text{PMe}_3)]$ .....	209
6.6.11	Synthesis of $[\text{Tp}^*\text{RhH}(\text{SC}_6\text{F}_5)(\text{PMe}_3)]$ .....	210
6.6.12	Synthesis of $[\text{Tp}^*\text{RhH}(\text{SPh})(\text{PMe}_3)]$ .....	211
Chapter 7	Conclusions and Future Work .....	213
7.1	Future Work .....	216
7.1.1	Mechanistic Studies of Alkyne Hydrothiolation Catalyzed by $[\text{RhCl}(\text{PPh}_3)_3]$ .....	216
7.1.2	Oxidative Addition of H-P(O)R <sub>2</sub> Bonds.....	217
7.1.3	Modification of the Phosphine Ligand of $[\text{Tp}^*\text{RhH}(\text{Me})(\text{PMe}_3)]$ .....	218
7.1.4	Synthesis of New Tris(pyrazolylborate) Ligands. ....	219
7.1.5	Proposal for Modification of the Phosphine Ligands of $[\text{Tp}^*\text{Rh}(\text{PPh}_3)_2]$ .....	226
References	.....	227
Appendix A	. Sample Spectra and Concentration Plots for the Michael Addition of 2-phenethanethiol to Substituted Vinyl Sulfones.....	248
Appendix B	. Sample Spectra and Concentration Plots for Alkyne Hydrothiolation Catalyzed by $[\text{Tp}^*\text{Rh}(\text{PPh}_3)_2]$ .....	260
Appendix C	Characterization of Substituted Aldehydes and Alkynes .....	298
Appendix D	Characterization of $[\text{Tp}^*\text{Rh}^{\text{III}}]$ Complexes.....	303

Appendix E	Synthesis and Characterization of Substituted Pyrazoles .....	333
Appendix F	Preliminary Mechanistic Studies of Alkyne Hydrothiolation Catalyzed by [RhCl(PPh <sub>3</sub> ) <sub>3</sub> ] .....	338

## List of Tables

Table 2.1. Scope of alkyne hydrothiolation catalyzed by [Tp*Rh(PPh <sub>3</sub> ) <sub>2</sub> ] .....	36
Table 2.2. [PhB(S-Ox <sup>iPr,Me2</sup> ) <sub>2</sub> (C <sub>5</sub> H <sub>4</sub> )Zr(NMe <sub>2</sub> ) <sub>2</sub> ] catalyzed cyclization of aminoalkenes .....	52
Table 2.3. Rh <sup>I</sup> catalyzed cyclization of alkynyl benzoic acids .....	61
Table 3.1. Measured pK <sub>A</sub> s for a series of substituted aryl thiols in methanol. ....	73
Table 3.2. Predicted pK <sub>A</sub> (H <sub>2</sub> O) values .....	75
Table 3.3. Dual parameter Hammett correlation values for the ionization of aryl thiols. ....	78
Table 3.4. Predicted pK <sub>A</sub> (MeOH) values based on equations 5A and 5B.....	80
Table 3.5. Predicted pK <sub>A</sub> (H <sub>2</sub> O) values based on equations 6A and 6B.....	80
Table 4.1. Synthesis of a series of <i>para</i> -substituted vinyl sulfones via rhodium-catalyzed alkyne hydrothiolation.....	93
Table 4.2. Relative rates of reaction of 2-phenethanethiol with a series of <i>para</i> -substituted vinyl sulfones. ....	94
Table 5.1. Rates and regioselectivity of vinyl sulfide formation for various <i>para</i> -substituted aryl thiols.....	114
Table 5.2. Hydrothiolation of substituted phenylacetylenes with thiophenol and 4-(trifluoromethoxy)thiophenol .....	116
Table 5.3. Rates and regioselectivity of vinyl sulfide formation for various <i>para</i> -substituted terminal aryl alkynes.....	117
Table 5.4. Calculated partial charges and tabulated <sup>13</sup> C NMR chemical shifts.....	132

## List of Figures

Figure 1.1. Sulfur-containing pharmaceuticals.....	1
Figure 1.2. Sulfur-containing agrochemicals.....	2
Figure 1.3. Vinyl-sulfone containing pharmaceuticals.....	3
Figure 2.1. Select examples of scorpionate ligands.....	30
Figure 2.2. Examples of vinyl sulfone containing drugs.....	33
Figure 2.3. Pyrazoleborate ligands assayed by Love and coworkers.....	35
Figure 2.4. Selected alkaloids.....	41
Figure 2.5. Thunberginol A and (-)-Tetracycline.....	57
Figure 2.6. Tris(pyrazol-1-yl)toluidine ligands, <i>p</i> -tpt and <i>o</i> -tpt, and the tris( <i>N</i> -methylimidazol-2-yl)methanol ligand (tim).....	58
Figure 3.1. Ionization of substituted benzoic acids.....	67
Figure 3.2. Saponification of substituted ethyl benzoate esters.....	68
Figure 3.3. Ionization of protonated quinuclidines.....	71
Figure 3.4. Linear correlation between $pK_A(\text{MeOH})$ and $pK_A(\text{H}_2\text{O})$ .....	74
Figure 3.5. Single parameter Hammett correlations for aryl thiol $pK_A$ values.....	76
Figure 3.6. Dual parameter Hammett correlations for aryl thiol $pK_A$ values. A) $\log(K_x/K_H)(\text{MeOH})$ vs. $\rho^I\sigma^I + \rho^R\sigma^R$ . B) $\log(K_x/K_H)(\text{MeOH})$ vs. $\rho^I\sigma^I + \rho^R\sigma^R$ .....	77
Figure 3.7. Titration curve for titration of PhSH with 0.1 M KOH in methanol.....	82
Figure 4.1. Benzimidazole and Nifurtimox.....	84
Figure 4.2. General structure of vinyl sulfone peptidomimetic drugs and K777.....	87
Figure 4.3. Selection of Michael acceptors assayed by Roush and coworkers.....	95
Figure 4.4. Hammett plot for the reaction of 2'-(phenethyl)thiol with para-substituted vinyl sulfones.....	96
Figure 4.5. $P_1'$ derivatives assayed by Roush and coworkers.....	97
Figure 5.1. Vinyl-sulfone containing pharmaceuticals.....	101
Figure 5.2. Regio- and stereo-isomers in hydrothiolation of terminal alkynes.....	102
Figure 5.3. Initial rate of product formation versus [PhCCH].....	109
Figure 5.4. Initial rate of product formation versus [PhSH].....	110
Figure 5.5. $k_{obs}$ vs added [PPh <sub>3</sub> ].....	111
Figure 5.6. KIE for alkyne hydrothiolation catalyzed by [Tp*Rh(PPh <sub>3</sub> ) <sub>2</sub> ].....	112
Figure 5.7. <sup>1</sup> H NMR and <sup>1</sup> H{ <sup>31</sup> P} NMR spectra at -33°C for reaction between Tp*Rh(PPh <sub>3</sub> ) <sub>2</sub> and PhSH.....	113
Figure 5.8. <sup>1</sup> H{ <sup>31</sup> P} NMR spectrum at -33°C for the addition of PhCCH to a solution of Tp*Rh(PPh <sub>3</sub> ) <sub>2</sub> and PhSH.....	113
Figure 5.9. Normalized product selectivity versus $\sigma^-$ constants for <i>para</i> -substituted arylthiols. Lines are guides only. Data from Table 4.1.....	115
Figure 5.10. Eyring plot by initial rates in 1:1 mix of C <sub>6</sub> D <sub>6</sub> : DCE.....	118
Figure 5.11. Eyring plot in <i>d</i> <sub>8</sub> -toluene by <i>pseudo</i> -first order rate constants ( $k_{obs}$ ).....	118
Figure 5.12. Time-course plots for production of branched product at 14 °C, 5 °C and -5°C....	120
Figure 5.13. Time course plots for the production of the <i>E</i> -linear product at 25 °C, 12 °C, and -5 °C.....	120
Figure 5.14. Calculated energies for 1,2 and 2,1 rhodathiacyclobutenes.....	121
Figure 5.15. Solid state structure of [Tp*RhCl <sub>2</sub> (PPh <sub>3</sub> ) <sub>2</sub> ].....	125

Figure 5.16. Hammett plot for <i>para</i> -substituted aryl thiols. ....	126
Figure 5.17. Rhodathiacyclobutene Intermediate .....	129
Figure 5.18. Hammett plot for <i>para</i> -substituted phenylacetylenes.....	133
Figure 5.19. Energy profile for reductive elimination. ....	134
Figure 5.20. Putative hydride species. ....	141
Figure 6.1. Synthetic targets of type A and B, related to the intermediate hydridothiolate and rhodathiacyclobutene complexes. ....	153
Figure 6.2. X-ray diffraction structures of [Tp*RhCl <sub>2</sub> (pyz)] (A) and <i>mer</i> -[RhCl <sub>3</sub> (pyz) <sub>3</sub> ] (B). ..	166
Figure 6.3. X-ray diffraction solid state structure of [Tp*RhCl <sub>2</sub> (PPh <sub>3</sub> )]. ....	168
Figure 6.4. X-ray diffraction solid state structure of [Tp*RhCl(MeCN) <sub>2</sub> ](BF <sub>4</sub> ). ....	169
Figure 6.5. X-ray diffraction solid state structure of [Tp*RhCl <sub>2</sub> (HSBn)] and variable temperature <sup>1</sup> H NMR spectra of the bound HSBn resonances between 3.6 ppm – 5.4 ppm.....	171
Figure 6.6. Selective <sup>31</sup> P{ <sup>1</sup> H} decoupled spectra for [Tp*RhHCl(PPh <sub>3</sub> )] (left) and [Tp*RhH <sub>2</sub> (PPh <sub>3</sub> )] (right).....	173
Figure 6.7. X-ray diffraction solid state structure of [Tp*RhCl <sub>2</sub> (PEt <sub>3</sub> )]. ....	176
Figure 6.8. X-ray diffraction solid state structure of [Tp*RhCl <sub>3</sub> ](PCy <sub>3</sub> Me). ....	177
Figure 6.9. <sup>1</sup> H NMR spectrum of [Tp*RhH(SBn)(PMe <sub>3</sub> )] in C <sub>6</sub> D <sub>12</sub> . The region between 2.7 and 3.0 ppm is magnified to show the two doublets corresponding to H <sub>A</sub> and H <sub>B</sub> . ....	184
Figure 6.10. 1D selective NOE spectrum for [Tp*RhH(SBn)(PMe <sub>3</sub> )] in C <sub>6</sub> D <sub>6</sub> . NOE interactions are shown as arrows. Protons being irradiated are indicated by red box.....	185
Figure 6.11. 1D selective NOE spectrum for [Tp*RhH(SBn)(PMe <sub>3</sub> )] in C <sub>6</sub> D <sub>6</sub> . NOE interactions are shown as arrows. Protons being irradiated are indicated by red box.....	186
Figure 6.12. Overlaid <sup>1</sup> H- <sup>13</sup> C HSQC (Red) and <sup>1</sup> H- <sup>13</sup> C HMBC (Blue) correlation spectra. Lines indicate the cross-peaks for the [RhSEt] fragment. ....	187
Figure 6.13. <sup>13</sup> C{ <sup>1</sup> H} peaks for the [RhSEt] fragment of [Tp*RhH(SEt)(PMe <sub>3</sub> )]. ....	188
Figure 6.14. 1D TOCSY correlation showing the spin system of the [RhSEt] fragment of [Tp*RhH(SEt)(PMe <sub>3</sub> )]. ....	189
Figure 6.15. 1D selective NOE spectrum for [Tp*RhH(SEt)(PMe <sub>3</sub> )] in C <sub>6</sub> D <sub>6</sub> . NOE interactions are shown as arrows. Protons being irradiated are indicated by red box.....	190
Figure 6.16. 1D selective NOE spectrum for [Tp*RhH(SEt)(PMe <sub>3</sub> )] in C <sub>6</sub> D <sub>6</sub> . NOE interactions are shown as arrows. Protons being irradiated are indicated by red box.....	191
Figure 6.17. 1D selective NOE spectrum for [Tp*RhH(SPh)(PMe <sub>3</sub> )] in C <sub>6</sub> D <sub>6</sub> . NOE interactions are shown as arrows. Proton being irradiated is indicated by red box.....	192
Figure 6.18. 2D HOESY spectrum for [Tp*RhH(SC <sub>6</sub> F <sub>5</sub> )(PMe <sub>3</sub> )] in C <sub>6</sub> D <sub>6</sub> . HOESY interactions are shown as arrows. ....	193
Figure 6.19. Stacked <sup>31</sup> P{ <sup>1</sup> H} NMR spectra of [Tp*RhH(SEt)(PMe <sub>3</sub> )] in C <sub>6</sub> D <sub>6</sub> heated to 60 °C for 12 h.....	197
Figure 6.20. Hydrothiolation of phenylacetylene with EtSH catalyzed by [Tp*Rh(PPh <sub>3</sub> ) <sub>2</sub> ].....	199
Figure 6.21. Background reaction between EtSH and phenylacetylene in C <sub>6</sub> D <sub>6</sub> .....	200
Figure 6.22. Reaction between EtSH and phenylacetylene in C <sub>6</sub> D <sub>6</sub> in the presence of [Tp*RhH(SEt)(PMe <sub>3</sub> )]. ....	201
Figure 7.1. Substituent numbering for typical homoscorpionate trispyrazolylborate ligand. ....	221
Figure 7.2. Proposed Tp <sup>3Me,4Ar,5Me</sup> ligands (left). Solid state structure of [Tp*RhCl <sub>2</sub> (PPh <sub>3</sub> )] (right). ....	222
Figure 7.3. Typical retrosynthetic scheme for substituted trispyrazolylborate ligands. ....	222

Figure A.1. <sup>1</sup> H NMR Spectra for the Addition of 2-phenethanethiol to <i>para</i> -methoxy-substituted vinyl sulfone.....	248
Figure A.2. Time-course plot for disappearance of starting material for the addition of 2-phenethanethiol to <i>para</i> -methoxy-substituted vinyl sulfone. ....	249
Figure A.3. <sup>1</sup> H NMR Spectra for the Addition of 2-phenethanethiol to <i>para</i> -methyl-substituted vinyl sulfone.....	250
Figure A.4. Time-course plot for disappearance of starting material for the addition of 2-phenethanethiol to <i>para</i> -methyl-substituted vinyl sulfone. ....	251
Figure A.5. <sup>1</sup> H NMR spectra for the addition of 2-phenethanethiol to parent vinyl sulfone.....	252
Figure A.6. Time course plots of the disappearance of starting material for the addition of 2-phenethanethiol to parent vinyl sulfone. ....	253
Figure A.7. <sup>1</sup> H NMR spectra for the addition of 2-phenethanethiol to <i>para</i> -chloro-substituted vinyl sulfone.....	254
Figure A.8. Time-course plots for the disappearance of starting material for the addition of 2-phenethanethiol to <i>para</i> -chloro-substituted vinyl sulfone. ....	255
Figure A.9. <sup>1</sup> H NMR spectra for the addition of 2-phenethanethiol to <i>para</i> -bromo-substituted vinyl sulfone.....	256
Figure A.10. Time-course plot for the disappearance of starting material for the addition of 2-phenethanethiol to <i>para</i> -bromo-substituted vinyl sulfone.....	257
Figure A.11. <sup>1</sup> H NMR spectra for the addition of 2-phenethanethiol to <i>para</i> -trifluoromethyl-substituted vinyl sulfone. ....	258
Figure A.12. Time-course plot for the disappearance of starting material for the addition of 2-phenethanethiol to <i>para</i> -trifluoromethyl-substituted vinyl sulfone.....	259
Figure B.1. <sup>1</sup> H NMR spectra for the [Tp*Rh(PPh <sub>3</sub> ) <sub>2</sub> ] catalyzed hydrothiolation of phenylacetylene with <i>para</i> -methoxythiophenol .....	260
Figure B.2. Time-course plot (A) and natural log plot (B) for [Tp*Rh(PPh <sub>3</sub> ) <sub>2</sub> ] catalyzed hydrothiolation of phenylacetylene with <i>para</i> -methoxythiophenol. ....	261
Figure B.3. <sup>1</sup> H NMR spectra for the [Tp*Rh(PPh <sub>3</sub> ) <sub>2</sub> ] catalyzed hydrothiolation of phenylacetylene with <i>para</i> -methylthiophenol .....	262
Figure B.4. Time-course plot (A) and natural log plot (B) for [Tp*Rh(PPh <sub>3</sub> ) <sub>2</sub> ] catalyzed hydrothiolation of phenylacetylene with <i>para</i> -methylthiophenol. ....	263
Figure B.5. <sup>1</sup> H NMR spectra for the [Tp*Rh(PPh <sub>3</sub> ) <sub>2</sub> ] catalyzed hydrothiolation of phenylacetylene with <i>para</i> -(dimethylamino)thiophenol.....	264
Figure B.6. Time-course plot (A) and natural log plot (B) for [Tp*Rh(PPh <sub>3</sub> ) <sub>2</sub> ] catalyzed hydrothiolation of phenylacetylene with <i>para</i> -(dimethylamino)thiophenol.....	265
Figure B.7. <sup>1</sup> H NMR spectra for the [Tp*Rh(PPh <sub>3</sub> ) <sub>2</sub> ] catalyzed hydrothiolation of phenylacetylene with <i>para</i> -(fluoro)thiophenol.....	266
Figure B.8. Time-course plot (A) and natural log plot (B) for [Tp*Rh(PPh <sub>3</sub> ) <sub>2</sub> ] catalyzed hydrothiolation of phenylacetylene with <i>para</i> -(fluoro)thiophenol.....	267
Figure B.9. <sup>1</sup> H NMR spectra for the [Tp*Rh(PPh <sub>3</sub> ) <sub>2</sub> ] catalyzed hydrothiolation of phenylacetylene with thiophenol. ....	268
Figure B.10. Time-course plot (A) and natural log plot (B) for [Tp*Rh(PPh <sub>3</sub> ) <sub>2</sub> ] catalyzed hydrothiolation of phenylacetylene with thiophenol. ....	269
Figure B.11. <sup>1</sup> H NMR spectra for the [Tp*Rh(PPh <sub>3</sub> ) <sub>2</sub> ] catalyzed hydrothiolation of phenylacetylene with <i>para</i> -(methylthio)thiophenol .....	270

Figure B.12. Time-course plot (A) and natural log plot (B) for [Tp*Rh(PPh <sub>3</sub> ) <sub>2</sub> ] catalyzed hydrothiolation of phenylacetylene with <i>para</i> -(methylthio)thiophenol. ....	271
Figure B.13. <sup>1</sup> H NMR spectra for the [Tp*Rh(PPh <sub>3</sub> ) <sub>2</sub> ] catalyzed hydrothiolation of phenylacetylene with <i>para</i> -(chloro)thiophenol.....	272
Figure B.14. Time-course plot (A) and natural log plot (B) for [Tp*Rh(PPh <sub>3</sub> ) <sub>2</sub> ] catalyzed hydrothiolation of phenylacetylene with <i>para</i> -(chloro)thiophenol.....	273
Figure B.15. <sup>1</sup> H NMR spectra for the [Tp*Rh(PPh <sub>3</sub> ) <sub>2</sub> ] catalyzed hydrothiolation of phenylacetylene with <i>para</i> -(bromo)thiophenol .....	274
Figure B.16. Time-course plot (A) and natural log plot (B) for [Tp*Rh(PPh <sub>3</sub> ) <sub>2</sub> ] catalyzed hydrothiolation of phenylacetylene with <i>para</i> -(bromo)thiophenol. ....	275
Figure B.17. <sup>1</sup> H NMR spectra for the [Tp*Rh(PPh <sub>3</sub> ) <sub>2</sub> ] catalyzed hydrothiolation of phenylacetylene with <i>para</i> -(trifluoromethoxy)thiophenol .....	276
Figure B.18. Time-course plot (A) and natural log plot (B) for [Tp*Rh(PPh <sub>3</sub> ) <sub>2</sub> ] catalyzed hydrothiolation of phenylacetylene with <i>para</i> -(trifluoromethoxy)thiophenol. ....	277
Figure B.19. <sup>1</sup> H NMR spectra for the [Tp*Rh(PPh <sub>3</sub> ) <sub>2</sub> ] catalyzed hydrothiolation of <i>para</i> -(methoxy)phenylacetylene with thiophenol.....	278
Figure B.20. Time-course plot (A) and natural log plot (B) for [Tp*Rh(PPh <sub>3</sub> ) <sub>2</sub> ] catalyzed hydrothiolation of <i>para</i> -(methoxy)phenylacetylene with thiophenol.....	279
Figure B.21. <sup>1</sup> H NMR spectra for the [Tp*Rh(PPh <sub>3</sub> ) <sub>2</sub> ] catalyzed hydrothiolation of <i>para</i> -(methyl)phenylacetylene with thiophenol.....	280
Figure B.22. Time-course plot (A) and natural log plot (B) for [Tp*Rh(PPh <sub>3</sub> ) <sub>2</sub> ] catalyzed hydrothiolation of <i>para</i> -(methyl)phenylacetylene with thiophenol.....	281
Figure B.23. <sup>1</sup> H NMR spectra for the [Tp*Rh(PPh <sub>3</sub> ) <sub>2</sub> ] catalyzed hydrothiolation of <i>para</i> -(fluoro)phenylacetylene with thiophenol.....	282
Figure B.24. Time-course plot (A) and natural log plot (B) for [Tp*Rh(PPh <sub>3</sub> ) <sub>2</sub> ] catalyzed hydrothiolation of <i>para</i> -(methyl)phenylacetylene with thiophenol.....	283
Figure B.25. <sup>1</sup> H NMR spectra for the [Tp*Rh(PPh <sub>3</sub> ) <sub>2</sub> ] catalyzed hydrothiolation of <i>para</i> -(chloro)phenylacetylene with thiophenol .....	284
Figure B.26. Time-course plot (A) and natural log plot (B) for [Tp*Rh(PPh <sub>3</sub> ) <sub>2</sub> ] catalyzed hydrothiolation of <i>para</i> -(chloro)phenylacetylene with thiophenol.....	285
Figure B.27. <sup>1</sup> H NMR spectra for the [Tp*Rh(PPh <sub>3</sub> ) <sub>2</sub> ] catalyzed hydrothiolation of <i>para</i> -(bromo)phenylacetylene with thiophenol .....	286
Figure B.28. Time-course plot (A) and natural log plot (B) for [Tp*Rh(PPh <sub>3</sub> ) <sub>2</sub> ] catalyzed hydrothiolation of <i>para</i> -(bromo)phenylacetylene with thiophenol. ....	287
Figure B.29. <sup>1</sup> H NMR spectra for [Tp*Rh(PPh <sub>3</sub> ) <sub>2</sub> ] catalyzed hydrothiolation of 3,5-dimethylphenylacetylene with thiophenol .....	288
Figure B.30. Final product ratio for [Tp*Rh(PPh <sub>3</sub> ) <sub>2</sub> ] catalyzed hydrothiolation of 3,5-dimethylphenylacetylene with thiophenol .....	289
Figure B.31. <sup>1</sup> H NMR spectra for [Tp*Rh(PPh <sub>3</sub> ) <sub>2</sub> ] catalyzed hydrothiolation of 3,5-di( <i>tert</i> -butyl)phenylacetylene with thiophenol.....	290
Figure B.32. Final product ratio for [Tp*Rh(PPh <sub>3</sub> ) <sub>2</sub> ] catalyzed hydrothiolation of 3,5-di( <i>tert</i> -butyl)phenylacetylene with thiophenol.....	291
Figure B.33. <sup>1</sup> H NMR spectra for [Tp*Rh(PPh <sub>3</sub> ) <sub>2</sub> ] catalyzed hydrothiolation of 3,5-di( <i>tert</i> -butyl)phenylacetylene with <i>para</i> -(trifluoromethoxy)thiophenol.....	292

Figure B.34. Final product ratio for [Tp*Rh(PPh <sub>3</sub> ) <sub>2</sub> ] catalyzed hydrothiolation of 3,5-di( <i>tert</i> -butyl)phenylacetylene with <i>para</i> -(trifluoromethoxy)thiophenol.....	293
Figure B.35. Final product ratio for [Tp*Rh(PPh <sub>3</sub> ) <sub>2</sub> ] catalyzed hydrothiolation of mesitylacetylene with thiophenol .....	294
Figure B.36. Final product ratio for [Tp*Rh(PPh <sub>3</sub> ) <sub>2</sub> ] catalyzed hydrothiolation of mesitylacetylene with <i>para</i> -(trifluoromethoxy)thiophenol.....	295
Figure B.37. Final product ratio for [Tp*Rh(PPh <sub>3</sub> ) <sub>2</sub> ] catalyzed hydrothiolation of <i>tert</i> -butylacetylene with thiophenol.....	296
Figure B.38. Product ratio for [Tp*Rh(PPh <sub>3</sub> ) <sub>2</sub> ] catalyzed hydrothiolation of <i>tert</i> -butylacetylene with <i>para</i> -(trifluoromethoxy)thiophenol .....	297
Figure C.1. <sup>1</sup> H NMR spectrum (C <sub>6</sub> D <sub>6</sub> , 300 MHz) of 3,5-dimethylphenylacetylene .....	298
Figure C.2. <sup>1</sup> H NMR spectrum (CDCl <sub>3</sub> , 300 MHz) of 3,5-di( <i>tert</i> -butyl)benzaldehyde. ....	299
Figure C.3. <sup>1</sup> H NMR spectrum (C <sub>6</sub> D <sub>6</sub> , 300 MHz) of 3,5-di( <i>tert</i> -butyl)phenylacetylene.....	300
Figure C.4. <sup>1</sup> H NMR spectrum (C <sub>6</sub> D <sub>6</sub> , 300 MHz) of mesitylaldehyde.....	301
Figure C.5. <sup>1</sup> H NMR spectrum (C <sub>6</sub> D <sub>6</sub> , 300 MHz) of mesitylacetylene. ....	302
Figure D.1. <sup>1</sup> H NMR spectrum (DMSO- <i>d</i> <sub>6</sub> , 300 MHz) of [Tp*RhCl <sub>2</sub> (MeOH)]......	303
Figure D.2. <sup>1</sup> H NMR spectrum (CDCl <sub>3</sub> , 300 MHz) of [Tp*RhCl <sub>2</sub> (PPh <sub>3</sub> )]......	304
Figure D.3. <sup>31</sup> P { <sup>1</sup> H} NMR spectrum (CDCl <sub>3</sub> , 300 MHz) of [Tp*RhCl <sub>2</sub> (PPh <sub>3</sub> )]......	305
Figure D.4. <sup>1</sup> H NMR spectrum (C <sub>6</sub> D <sub>6</sub> , 400 Mhz) of [Tp*RhHCl(PPh <sub>3</sub> )]......	306
Figure D.5. <sup>13</sup> C { <sup>1</sup> H} NMR spectrum (C <sub>6</sub> D <sub>6</sub> , 100 Mhz) of [Tp*RhHCl(PPh <sub>3</sub> )]......	307
Figure D.6. <sup>31</sup> P { <sup>1</sup> H} NMR spectrum (C <sub>6</sub> D <sub>6</sub> , 162 Mhz) of [Tp*RhHCl(PPh <sub>3</sub> )] .....	308
Figure D.7. <sup>1</sup> H NMR spectrum (C <sub>6</sub> D <sub>6</sub> , 400 Mhz) of [Tp*RhH <sub>2</sub> (PPh <sub>3</sub> )] .....	309
Figure D.8. <sup>13</sup> C { <sup>1</sup> H} NMR spectrum (C <sub>6</sub> D <sub>6</sub> , 100 Mhz) of [Tp*RhH <sub>2</sub> (PPh <sub>3</sub> )] .....	310
Figure D.9. <sup>31</sup> P { <sup>1</sup> H} NMR spectrum (C <sub>6</sub> D <sub>6</sub> , 162 Mhz) of [Tp*RhH <sub>2</sub> (PPh <sub>3</sub> )] .....	311
Figure D.10. <sup>1</sup> H NMR spectrum (CD <sub>2</sub> Cl <sub>2</sub> , 300 Mhz) of [Tp*RhCl <sub>2</sub> (BnSH)]......	312
Figure D.11. <sup>13</sup> C { <sup>1</sup> H} NMR spectrum (CD <sub>2</sub> Cl <sub>2</sub> , 100 Mhz) of [Tp*RhCl <sub>2</sub> (BnSH)] .....	313
Figure D.12. <sup>1</sup> H NMR spectrum (CD <sub>2</sub> Cl <sub>2</sub> , 300 Mhz) of [Tp*RhCl <sub>2</sub> (PEt <sub>3</sub> )] .....	314
Figure D.13. <sup>13</sup> C { <sup>1</sup> H} NMR spectrum (C <sub>6</sub> D <sub>6</sub> , 100 Mhz) of [Tp*RhCl <sub>2</sub> (PEt <sub>3</sub> )]......	315
Figure D.14. <sup>31</sup> P { <sup>1</sup> H} NMR spectrum (CD <sub>2</sub> Cl <sub>2</sub> , 122 Mhz) of [Tp*RhCl <sub>2</sub> (PEt <sub>3</sub> )] .....	316
Figure D.15. <sup>1</sup> H NMR spectrum (C <sub>6</sub> D <sub>6</sub> , 400 Mhz) of [Tp*RhHCl(PEt <sub>3</sub> )] .....	317
Figure D.16. <sup>13</sup> C { <sup>1</sup> H} NMR spectrum (C <sub>6</sub> D <sub>6</sub> , 100 Mhz) of [Tp*RhHCl(PEt <sub>3</sub> )] .....	318
Figure D.17. <sup>31</sup> P { <sup>1</sup> H} NMR spectrum (C <sub>6</sub> D <sub>6</sub> , 162 Mhz) of [Tp*RhHCl(PEt <sub>3</sub> )]......	319
Figure D.18. <sup>1</sup> H NMR spectrum (C <sub>6</sub> D <sub>6</sub> , 400 Mhz) of [Tp*RhH(SBn)(PMe <sub>3</sub> )]......	320
Figure D.19. <sup>13</sup> C { <sup>1</sup> H} NMR spectrum (C <sub>6</sub> D <sub>6</sub> , 100 Mhz) of [Tp*RhH(SBn)(PMe <sub>3</sub> )]......	321
Figure D.20. <sup>31</sup> P { <sup>1</sup> H} NMR spectrum (C <sub>6</sub> D <sub>12</sub> , 162 Mhz) of [Tp*RhH(SBn)(PMe <sub>3</sub> )]......	322
Figure D.21. <sup>1</sup> H NMR spectrum (C <sub>6</sub> D <sub>6</sub> , 400 Mhz) of [Tp*RhH(SET)(PMe <sub>3</sub> )]......	323
Figure D.22. <sup>13</sup> C { <sup>1</sup> H} NMR spectrum (C <sub>6</sub> D <sub>6</sub> , 101 Mhz) of [Tp*RhH(SET)(PMe <sub>3</sub> )]......	324
Figure D.23. <sup>31</sup> P { <sup>1</sup> H} NMR spectrum (C <sub>6</sub> D <sub>12</sub> , 162 Mhz) of [Tp*RhH(SET)(PMe <sub>3</sub> )]......	325
Figure D.24. <sup>1</sup> H NMR spectrum (C <sub>6</sub> D <sub>12</sub> , 400 Mhz) of [Tp*RhH(SC <sub>6</sub> F <sub>5</sub> )(PMe <sub>3</sub> )]......	326
Figure D.25. <sup>13</sup> C { <sup>1</sup> H} NMR spectrum (C <sub>6</sub> D <sub>6</sub> , 101 Mhz) of [Tp*RhH(SC <sub>6</sub> F <sub>5</sub> )(PMe <sub>3</sub> )]......	327
Figure D.26. <sup>19</sup> F NMR spectrum (C <sub>6</sub> D <sub>6</sub> , 282 Mhz) of [Tp*RhH(SC <sub>6</sub> F <sub>5</sub> )(PMe <sub>3</sub> )] .....	328
Figure D.27. <sup>31</sup> P { <sup>1</sup> H} NMR spectrum (C <sub>6</sub> D <sub>12</sub> , 162 Mhz) of [Tp*RhH(SC <sub>6</sub> F <sub>5</sub> )(PMe <sub>3</sub> )]......	329
Figure D.28. <sup>1</sup> H NMR spectrum (C <sub>6</sub> D <sub>6</sub> , 400 Mhz) of [Tp*RhH(SPh)(PMe <sub>3</sub> )] .....	330
Figure D.29. <sup>13</sup> C { <sup>1</sup> H} NMR spectrum (C <sub>6</sub> D <sub>6</sub> , 101 Mhz) of [Tp*RhH(SPh)(PMe <sub>3</sub> )] .....	331
Figure D.30. <sup>31</sup> P { <sup>1</sup> H} NMR spectrum (C <sub>6</sub> D <sub>6</sub> , 162 Mhz) of [Tp*RhH(SPh)(PMe <sub>3</sub> )]......	332

Figure E.1. $^1\text{H}$ NMR spectrum ( $\text{CDCl}_3$ , 300 Mhz) of 4-mesityl-1,3,5-trimethylpyrazole .....	334
Figure E.2. $^1\text{H}$ NMR spectrum ( $\text{CDCl}_3$ , 400 Mhz) of 4-mesityl-3,5-dimethylpyrazole .....	335
Figure E.3. $^1\text{H}$ NMR spectrum ( $\text{CDCl}_3$ , 300 Mhz) of 1-boc-4-bromo-3,5-dimethylpyrazole....	336
Figure E.4. $^1\text{H}$ NMR spectrum ( $\text{CDCl}_3$ , 300 Mhz) of 1-benzyl-4-bromo-3,5-dimethylpyrazole	337
Figure F.1. Kinetic profile for the hydrothiolation of phenylacetylene with thiophenol catalyzed by $[\text{RhCl}(\text{PPh}_3)_3]$ . 275 mM PhSH, 250 mM PhCCH, 7.50 mM $[\text{RhCl}(\text{PPh}_3)_3]$ , $\text{CDCl}_3$ , 15 $^\circ\text{C}$ ..	339
Figure F.2. Time-course plots for the production of the <i>E</i> -linear vinyl sulfide products with substituted aryl thiols for the hydrothiolation of phenylacetylene catalyzed by $[\text{RhCl}(\text{PPh}_3)_3]$ .	340

## List of Schemes

Scheme 1.1. Alkyne hydrothiolation .....	4
Scheme 1.2. Free radical alkyne hydrothiolation.....	5
Scheme 1.3. Radical initiated alkyne hydrothiolation towards the synthesis of Rigosertib. ....	6
Scheme 1.4. Alkyne bischalcogenation .....	7
Scheme 1.5. Vinyl sulfide isomerization .....	7
Scheme 1.6. Rhodium-catalyzed hydrothiolation with alkane thiols .....	9
Scheme 1.7. Class I mechanisms .....	11
Scheme 1.8. Hydridothiolate mechanism .....	12
Scheme 1.9. Formation of metal-thiolate complexes $L_n[M^m](SR)_y$ .....	13
Scheme 1.10. Dithiolate mechanism.....	14
Scheme 1.11. Dithiolate intermediate with $Tp^*Rh(coe)(MeCN)$ .....	15
Scheme 1.12. 1,2 vs 2,1 alkyne insertion in dithiolate mechanism .....	16
Scheme 1.13. 1,2 vs 2,1 insertion for hydridothiolate intermediate .....	17
Scheme 1.14. Coordination restriction for alkyne hydrothiolation catalyzed by $[Rh(IPr)(Cl)(\eta^2-CH_2=CH_2)(Pyridine)]$ .....	18
Scheme 1.15. Insertion of alkynes into rhodium-oxygen bond of $Cp^*$ ligated rhodium ( $P,O$ )-chelating phosphane complex. ....	19
Scheme 1.16. Rh-O insertion of acetonitrile and acetone with rhodaoxetanes. ....	20
Scheme 1.17. Rhodaoxetane ring expansion with activated alkynes.....	21
Scheme 1.18. Rhodathiacyclobutene formation with $Tp^*Rh(SPh_2)(MeCN)$ .....	22
Scheme 1.19. Mechanism for imine formation from rhodium-amido complexes.....	23
Scheme 1.20. Rhodium-oxygen bond insertion in $[Rh(PEt_3)_2(\kappa^1-\eta^2-OCR_2CH_RCH=CH_2)]$ .....	25
Scheme 1.21. Computed energy for insertion of ethylene into Rh-X bonds. ....	26
Scheme 2.1. Hydroelementation of alkynes and alkenes.....	32
Scheme 2.2. Hydrothiolation of phenylacetylene with benzylthiol catalyzed by $Tp^*Rh(PPh_3)_2$ . 34	
Scheme 2.3. Alkynyl C-H activation by $Tp^*Rh(PPh_3)_2$ .....	37
Scheme 2.4. Hydrothiolation of an unsymmetrically substituted internal alkyne with Benzylthiol catalyzed by $Tp^*Rh(PPh_3)_2$ .....	38
Scheme 2.5. Rhodathiacyclobutene formed from $[Tp^*Rh(SPh)_2(MeCN)]$ and phenylacetylene 39	
Scheme 2.6. Rhodathiacyclobutene diastereomers due to sulfur inversion.....	39
Scheme 2.7. Hydrothiolation of $p$ -MeOC <sub>6</sub> H <sub>4</sub> CCH catalyzed by $[Tp^*Rh(SPh)_2(MeCN)]$ . ....	40
Scheme 2.8. $[TpRh(C_2H_4)_2]/PPh_3$ catalyzed intermolecular hydroamination .....	42
Scheme 2.9. Synthesis of tris(oxazolonyl)borato ligands.....	43
Scheme 2.10. Zirconium complexes of $To^M$ .....	44
Scheme 2.11. Yttrium amide complexes of $To^M$ .....	45
Scheme 2.12. Intramolecular olefin insertion into metal-amide bonds. ....	46
Scheme 2.13. Observed magnesium amidoalkene and pyrrolide complexes. ....	47
Scheme 2.14. Proposed mechanism for $To^M$ Mg-mediated aminoalkene hydroamination. ....	48
Scheme 2.15. Enantioselective cyclizations of aminoalkenes catalyzed by $[To^TMgMe]$ and $[To^TCaC(SiHMe_2)_3]$ .....	49
Scheme 2.16. Heteroscorpionate complexes of Zr and Hf. ....	50
Scheme 2.17. $[\{PhB(S-Ox^{iPr,Me_2})_2(C_5H_4)\}Zr(NMe_2)_2]$ catalyzed desymmetrization of aminoalkenes.....	54

Scheme 2.18. Synthesis of [ZrCl <sub>3</sub> (bpzcp)] .....	55
Scheme 2.19. [Lu(bpztcp)(CH <sub>2</sub> SiMe <sub>3</sub> ) <sub>2</sub> ] catalyzed bicyclization of aminodialkenes. ....	56
Scheme 2.20. Catalytic cyclization of 4-pentynoic acid.....	60
Scheme 2.21. Alkyne hydrophosphinylation catalyzed by Tp <sup>*</sup> Rh(PPh <sub>3</sub> ) <sub>2</sub> .....	62
Scheme 4.1. Amide hydrolysis by cysteine proteases. ....	85
Scheme 4.2. Irreversible inhibition of cysteine proteases.....	86
Scheme 4.3. Palmer's synthesis of K777.....	88
Scheme 4.4. Comparison of HWE olefination versus alkyne hydrothiolation strategies for the synthesis of vinyl sulfones.....	89
Scheme 4.5. Diastereoselective synthesis of homophenylalanine stereocenter. Synthesis by Erica Kiemele. ....	90
Scheme 4.6. Synthesis of di-Boc protected propargyl amine 7. Synthesis performed by Erica Kiemele.....	91
Scheme 4.7. Rhodium-catalyzed alkyne hydrothiolation of propargyl amines. Reactions performed by Erica Kiemele and Paul Bichler. ....	92
Scheme 5.1. External nucleophilic attack on activated alkynes. ....	103
Scheme 5.2. Four pathways for migratory insertion in a metal-hydrido-thiolate intermediate. ..	104
Scheme 5.3. Generation of metal-thiolate complexes (top). Catalytic cycle involving intermediate metal-thiolate complex (bottom).....	105
Scheme 5.4. Coordination of alkyne trans to the hydride for [RhX(IPr)(pyr)(η <sup>2</sup> -olefin)]-catalyzed alkyne hydrothiolation. ....	106
Scheme 5.5. Stoichiometric reactions for branched product formation with [Tp <sup>*</sup> Rh(SR) <sub>2</sub> (MeCN)]-catalyzed alkyne hydrothiolation (ref. 155). ....	108
Scheme 5.6. Possible insertion pathways for MesCCH with [Rh(H)(SR)] species.....	123
Scheme 5.7. General proposed mechanism .....	128
Scheme 5.8. 1,2 vs 2,1 Migratory Insertion with HS-EDG and HS-EWG.....	131
Scheme 5.9. Associatively induced reductive elimination for [Tp <sup>*</sup> RhH(Ph)(CNCH <sub>2</sub> CMe <sub>3</sub> )]...	136
Scheme 5.10. Reductive elimination. ....	137
Scheme 5.11. Detailed mechanism. ....	139
Scheme 6.1. Simplified proposed mechanism for [Tp <sup>*</sup> Rh(PPh <sub>3</sub> ) <sub>2</sub> ] catalyzed alkyne hydrothiolation.....	152
Scheme 6.2. Synthesis of [Tp <sup>*</sup> RhCl <sub>2</sub> (L)] and [Tp <sup>*</sup> RhCl <sub>2</sub> (X)] <sup>-</sup> (NR <sub>4</sub> <sup>+</sup> ) derivatives. ....	155
Scheme 6.3. Chloride substitution reactions of [Tp <sup>*</sup> RhCl <sub>2</sub> (MeOH)].....	156
Scheme 6.4. Synthesis of alkyl and vinyl complexes [Tp <sup>*</sup> RhCl(R)(CNCH <sub>2</sub> CMe <sub>3</sub> )].....	157
Scheme 6.5. Synthesis of [Tp <sup>*</sup> RhH <sub>2</sub> (H <sub>2</sub> )]. ....	158
Scheme 6.6. Synthesis of [Tp <sup>3R,4R,5R</sup> RhCl <sub>2</sub> (L)] and ligand decomposition products. ....	159
Scheme 6.7. Synthesis of anionic [Tp <sup>3R,4R,5R</sup> RhCl <sub>3</sub> ][PPh <sub>4</sub> ] complexes. ....	160
Scheme 6.8. Synthesis of mono and dihydride complexes.....	161
Scheme 6.9. Generation of [Tp <sup>*</sup> RhH(R)(CO)] complexes by photoirradiation of [Tp <sup>*</sup> Rh(CO) <sub>2</sub> ]. ....	162
Scheme 6.10. C-H activation by [Tp <sup>*</sup> Rh <sup>I</sup> (L)] species.....	163
Scheme 6.11. Oxidative addition of B-H, Si-H and C-F bonds by [Tp <sup>*</sup> Rh <sup>I</sup> (PMe <sub>3</sub> )], generated by reductive elimination of CH <sub>4</sub> from [Tp <sup>*</sup> Rh <sup>III</sup> H(CH <sub>3</sub> )(PMe <sub>3</sub> )] or H <sub>2</sub> from [Tp <sup>*</sup> Rh <sup>III</sup> (H) <sub>2</sub> (PMe <sub>3</sub> )]. ....	164
Scheme 6.12. Synthesis of [Tp <sup>*</sup> RhHCl(PPh <sub>3</sub> )] and [Tp <sup>*</sup> RhH <sub>2</sub> (PPh <sub>3</sub> )] .....	173

Scheme 6.13. Formation of ortho-metallated product from [Tp*RhHCl(PPh <sub>3</sub> )].	175
Scheme 6.14. Synthesis of alkoxy hydride complexes [Tp*RhH(OR)(PMe <sub>3</sub> )].	179
Scheme 6.15. Synthesis of [Tp*RhCl(Me)(PMe <sub>3</sub> )].	179
Scheme 6.16. Synthesis of [Tp*RhH(Me)(PMe <sub>3</sub> )] and side products.	180
Scheme 6.17. Reaction of [Tp*RhCl(Me)(PMe <sub>3</sub> )] with [Cp <sub>2</sub> ZrHCl] and [Cp <sub>2</sub> ZrH <sub>2</sub> ]. Product ratios based on integration of diagnostic <sup>1</sup> H NMR signals.	181
Scheme 6.18. Synthesis of hydridothiolate complexes [Tp*RhH(SR)(PMe <sub>3</sub> )].	183
Scheme 6.19. Associatively induced reductive elimination of methane from [Tp*RhH(Me)(L)].	194
Scheme 6.20. Proteolytic cleavage mechanism (top). Treatment of [Tp*RhCl(Me)(PMe <sub>3</sub> )] with BnSH (bottom).	195
Scheme 6.21. Parallel between the proposed mechanisms of [Tp*RhH(SR)(PMe <sub>3</sub> )] complex formation and alkyne hydrothiolation catalyzed by [Tp*Rh(PPh <sub>3</sub> ) <sub>2</sub> ].	196
Scheme 7.1. Alkyne hydrophosphinylation catalyzed by [Tp*Rh(PPh <sub>3</sub> ) <sub>2</sub> ] (top). Proposed synthesis and reactivity of [Tp*RhH(P(O)R <sub>2</sub> )(PMe <sub>3</sub> )] complexes (bottom).	218
Scheme 7.2. Origin of product regioselectivity in alkyne hydrothiolation reactions catalyzed by [Tp*Rh(PPh <sub>3</sub> ) <sub>2</sub> ].	219
Scheme 7.3. Synthesis of 4-mesityl-3,5-dimethylpyrazole.	223
Scheme 7.4. Proposed methods for successful synthesis of <i>N</i> -protected 4-aryl-3,5-dimethylpyrazoles.	224
Scheme 7.5. Synthesis of novel 4-aryl-3,5-dimethylpyrazole containing ligands.	225

## List of Abbreviations

©	Copyright
1D	One dimensional
2D	Two dimensional
Å	Angstrom, 10 <sup>-10</sup> meters
acac	acetylacetonate
Ar	Aryl group
bim	Bis(imidazolyl)methane
Bn	Benzyl group
Boc	tert-Butylcarbonate
Bp*	Bis(3,5-dimethylpyrazolyl)borate
Bpin	Pinacolborane
bpm	Bis(pyrazol-1-yl)methane
bpzcp	2,2-bis(3,5-dimethylpyrazol-1-yl)-1,1-diphenylethylcyclopentadienyl
bpztcp	2,2-bis(3,5-dimethylpyrazol-1-yl)-1-tert-butylethylcyclopentadienyl
cat.	Catalytic
Cbz	Carboxybenzyl
CG	CpSiMe <sub>2</sub> N- <sup>t</sup> Bu
CGC	Cp''SiMe <sub>2</sub> NCMe <sub>3</sub>
cod	1,4-cyclooctadiene
coe	Cyclooctene
COSY	Correlation Spectroscopy

Cp	Cyclopentadienyl
Cp*	Pentamethylcyclopentadienyl
Cp''	Tetramethylcyclopentadienyl
d	Doublet (NMR spectroscopy)
DCE	1,2-dichloroethane
DCM	Dichloromethane
E	Element
Et	Ethyl group
g	Grams
h	Hours
hfac	hexafluoroacetylacetonate
HMBC	Heteronuclear Multiple Bond Coherence
HOESY	Heteronuclear Overhauser Effect Spectroscopy
HSQC	Heteronuclear Single Quantum Correlation
HWE	Horner-Wadsworth-Emmons Olefination
Hz	Hertz
<sup>i</sup> Pr	Isopropyl group
IPr	1,3-Bis(2,6-diisopropylphenyl)-1,3-dihydro-2H-imidazol-2-ylidene
J	Coupling constant (NMR spectroscopy)
L	Liter
L.G.	Leaving group
m	Multiplet (NMR spectroscopy)
M	Molar, moles/liter

m/z	Mass to charge ratio (Mass spectrometry)
Me	Methyl group
MeCN	Acetonitrile
Mes	Mesityl
mg	Milligrams
MHz	Megahertz
min	Minutes
mL	Milliliter
mM	Millimolar, millimoles/liter
mmol	Millimoles
mol	Moles
N.R.	No reaction
n/a	Not applicable
nbd	Norboradiene
n/d	Not determined
NHC	N-heterocyclic carbene
NMR	Nuclear Magnetic Resonance
NOE	Nuclear Overhauser Effect
NOESY	Nuclear Overhauser Effect Spectroscopy
Nu	Nucleophile
<i>o</i>	Ortho
OAc	Acetate
°	Degree

OTf	Trifluoromethanesulfonate
Ox	Oxazolinyll
Ox <sup>iPr,Me2</sup>	3-isopropyl-4,4-dimethyloxazolinyll
Ox <sup>Me2</sup>	4,4-dimethyloxazolinyll
Ox <sup>tBu</sup>	4-tert-butyl-oxazolinyll
<i>p</i>	Para
PCy <sub>3</sub>	Tricyclohexylphosphine
pdt	Product
PEt <sub>3</sub>	Triethylphosphine
PG	Protecting group
Ph	Phenyl group
Ph <sub>2</sub> Box	Bis(oxazonlinato)diphenylmethane
PMe <sub>3</sub>	Trimethylphosphine
P(O)Me <sub>3</sub>	Trimethylphosphine oxide
P(O)Ph <sub>3</sub>	Triphenylphosphine oxide
PPh <sub>3</sub>	Triphenylphosphine
ppm	Parts per million
ppt	Parts per trillion
pyr	Pyridine
Pyz	3,5-dimethylpyrazole
q	Quartet (NMR spectroscopy)
R	Organic group
RPKA	Reaction progress kinetic analysis

rt	Room temperature
sec	Seconds
s	singlet (NMR spectroscopy)
SIPr	1,3-Bis(2,6-diisopropylphenyl)imidazolidene
t	Triplet (NMR spectroscopy)
<sup>t</sup> Bu	<i>tert</i> -Butyl
Temp	Temperature
THF	Tetrahydrofuran
tim	Tris(N-methylimidazol-2-yl)methanol
TMB	Trimethoxybenzene
TMS	Trimethylsilyl
TOCSY	Total Correlated Spectroscopy
Tol	Toluene
To <sup>M</sup>	Tris(4,4-dimethyl-2-oxazoliny)phenylborate
To <sup>P</sup>	Tris(4 <i>S</i> -isopropyl-2-oxazoliny)phenylborate
To <sup>T</sup>	Tris(4- <i>S-tert</i> -butyl-2-oxazoliny)phenylborate
Tp	Tris(pyrazolyl)borate
Tpm	Tris(pyrazolyl)methane
Tp*	Tris(3,5-dimethylpyrazolyl)borate
TPA	Tris(2-pyridylmethyl)amine
tpt	Tris(pyrazol-1-yl)toluidine
UBC	University of British Columbia
UV	Ultraviolet

WHO	World Health Organization
$\delta$	Delta, chemical shift (NMR spectroscopy)
$\eta$	eta
$\kappa$	Kappa
$\mu$	mu, micro ( $10^{-6}$ )
$\mu\text{L}$	Microliter

## Acknowledgements

I thank the University of British Columbia, NSERC (Discovery grant, Research Tools and Instrumentation grants) and the Canada Foundation for Innovation for supporting this work.

I would like to thank my supervisor, Dr. Jennifer Love, who never stopped believing in me.

I offer my gratitude to the faculty, staff, and coworkers in the chemistry department of UBC, without many of whom this research would not have been possible. Special thanks to Dr. Maria Ezhova for helping me with my every NMR need.

I would thank Dr. Shrinwantu Pal, for being a friend and a mentor.

I would like to thank Dr. Jennifer A. Love and Dr. Parisa Mehrkhodavandi, Weiling Chiu, Eric Bowes and Addison Desnoyer for helping edit and revise my thesis.

I would like to personally thank Dr. Kajin Lee, for her love and support over the more difficult times in my degree, and for teaching me many of the laboratory techniques I needed.

I would like to thank my parents, grandparents, and extended family. Without their love and support, both emotionally and financially, I would have never made it this far.

I would like to thank Domino's Pizza, for providing me with the bare minimum of nutrients to sustain human life.

And finally I would like to thank Elham Saeedy, for her love, support, and admiration.

## **Dedication**

*In Loving Memory of Rhéal Wathier*

## Chapter 1 Introduction

### 1.1 Sulfur-Containing Compounds

Sulfur is found universally in nature. For example, the amino acids methionine and cysteine both contain sulfur and play major roles in protein structure and activity. Interestingly, despite their often pungent odor, sulfur-containing compounds are important components of several flavors in the ppm to ppt range. For example, 2-furfurylthiol, 3-mercapto-3-methylbutylformate and 3-methyl-2-butene-1-thiol are partly responsible for the roasted flavor of coffee and meat. (*R*)-2-(4-methylcyclohex-3-enyl)propane-2-thiol is responsible for the characteristic taste of grapefruit, while some 39 thiol-containing compounds have been identified in aged cheddar.<sup>1</sup> Additionally, sulfur is commonly found in natural and pharmaceutical products, agrochemicals, and bioactive molecules. Compounds such as griseoviridin – a streptogramin antibiotic and macrocyclic molecule characterized by a vinyl sulfide linkage – and Singulair – a leukotriene receptor antagonist used in the treatment of asthma and seasonal allergy symptoms – are two examples of popular sulfur-containing pharmaceuticals (Figure 1.1).

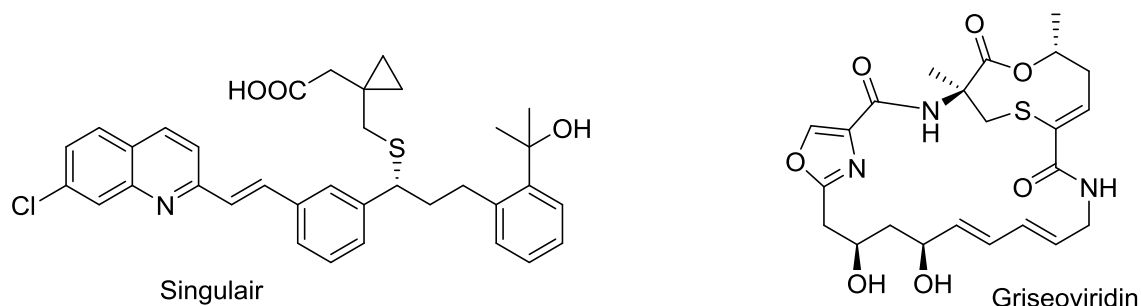


**Figure 1.1. Sulfur-containing pharmaceuticals**

Elemental sulfur is one of the oldest known pesticides and so it should come as no surprise that sulfur containing compounds are found extensively in agrochemical applications. Select examples of their use as such include Malathion, an insecticide, Thiodicarb, an insecticide and molluscicide, and Thiocarbamate, an herbicide (Figure 1.2). Notably, Malathion has found application in regional programs to control mosquito populations associated with West Nile Virus because of its low toxicity to humans, birds and mammals compared to other organophosphate insecticides.

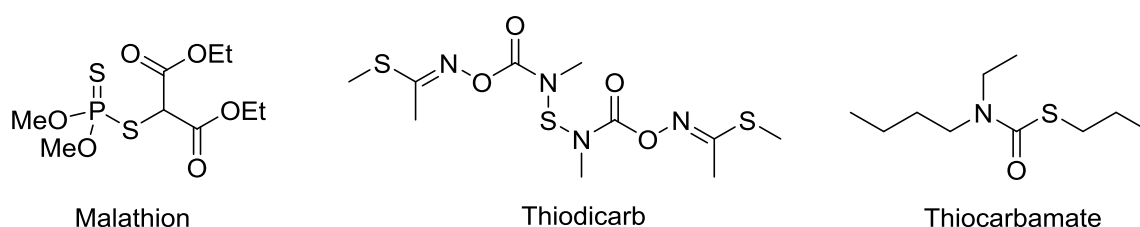


**Figure 1.2. Sulfur-containing agrochemicals**

Moreover, sulfur-containing compounds continue to find importance in the development of new pharmaceuticals. Recently, two very promising compounds, Rigosertib and K777, have entered clinical trials (Figure 1.3). Rigosertib kills a wide variety of human tumor cell lines at subnanomolar concentrations without affecting the growth of normal cells.<sup>2</sup> K777 is currently entering clinical trials for treatment of Chagas disease, the leading cause of heart disease in Latin America.<sup>3</sup> Both drugs contain a vinyl sulfone moiety that is the key to their mechanism of action. Such vinyl sulfones can be easily obtained from vinyl sulfides by simple oxidation.

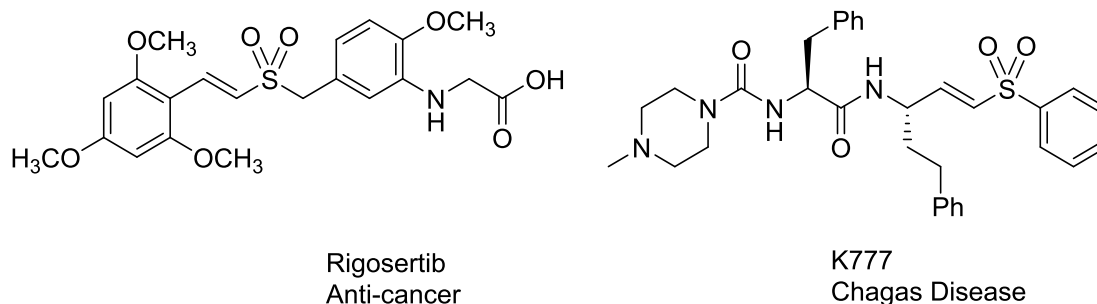


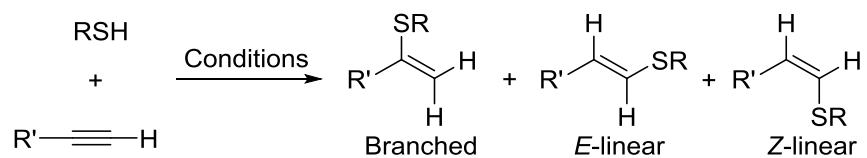
**Figure 1.3. Vinyl-sulfone containing pharmaceuticals**

## 1.2 Synthetic Methods Towards Vinyl-Sulfides

Vinyl sulfides are important not only as synthetic targets but also as intermediates and starting materials in several total syntheses including (+)-Laurencin,<sup>4</sup> Lapidilectine B,<sup>5</sup> and (-)-Coriolin.<sup>6</sup> Vinyl sulfides and their oxidized derivatives can be used as enolate equivalents, Michael acceptors and masked carbonyls. They are particularly useful synthons due to their ability to survive a variety of reaction conditions before their selective manipulation.<sup>7</sup> They have even been shown to be effective as the electrophilic partner in Kumada cross-coupling reactions.<sup>8</sup> Several synthetic methods towards vinyl sulfides have been reported, including elimination from thio-ketals/-acetals,<sup>9</sup> nucleophilic substitution of vinyl-halides,<sup>10</sup> and Wittig reactions.<sup>11</sup> These methods, however, require the preparation of starting materials and are limited by the restrictions imposed by these preparations. Alkyne hydrothiolation, on the other hand, is a 100% atom economic method for the generation of vinyl sulfides from commercially available alkynes and thiols. Alkyne hydrothiolation can be achieved under nucleophilic, radical, or, more recently, transition metal catalyzed conditions as discussed below.

### 1.2.1 Alkyne Hydrothiolation

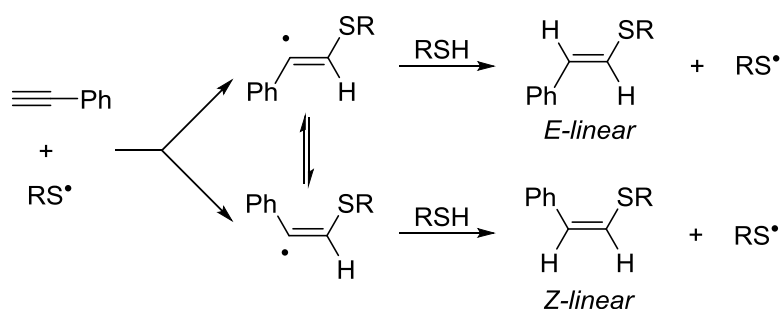
Alkyne hydrothiolation is a 100% atom economic method for the preparation of a wide variety of vinyl sulfides from commercially available starting materials. Three isomers can arise from alkyne hydrothiolation, depending on the reaction conditions and the nature of R and R' (Scheme 1.1). Nucleophilic addition of a thiol to an unsaturated compound is the oldest method for generating vinyl sulfides, first reported over 100 years ago.<sup>12</sup> Most methods produce a mixture of the three isomers with low selectivity. Recent advances have allowed for the formation of the *Z*-linear isomer selectively with catalytic amounts of cesium carbonate.<sup>13</sup> Nucleophilic methods are currently the only route to selectively form this isomer. Although the use of catalytic amounts of base is a notable breakthrough in nucleophilic alkyne hydrothiolation, most methods utilize a stoichiometric amount of base as well as elevated reaction temperatures. Additionally, issues of chemoselectivity arise in nucleophilic methods due to the potency of thiolate nucleophiles.



**Scheme 1.1. Alkyne hydrothiolation**

The first example of alkyne hydrothiolation under radical conditions was reported in 1949.<sup>14</sup> The reaction of aryl thiols occurs at room temperature without initiation however aliphatic thiols require initiation by UV irradiation or by radical initiator. Radical alkyne hydrothiolation proceeds via a typical radical chain reaction (Scheme 1.2). Following initiation, the thiyl radical adds to the less substituted end of the alkyne to produce the more substituted

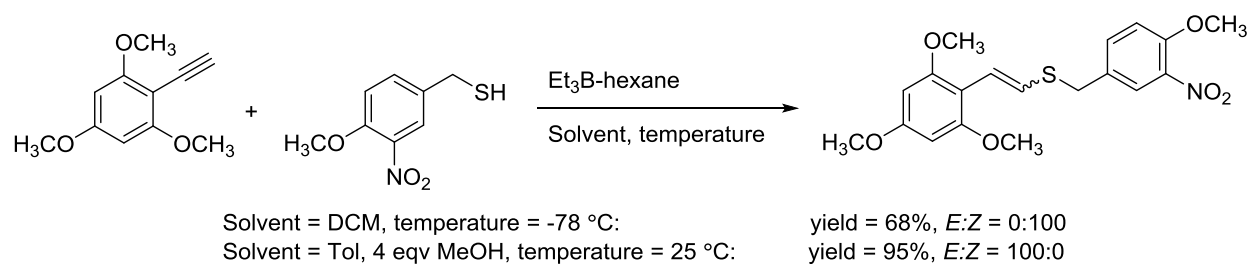
vinyl radical. Isomerization of this intermediate can give either the *E*- or *Z*-linear isomers; however, the selectivity is low because the barrier to inversion is around 2 kcal/mol.<sup>15</sup> Although free radical hydrothiolation has the advantage of completely eliminating the branched isomer, radical reactions have low chemoselectivity with respect to alkenes versus alkynes. Therefore it is difficult to prevent over-addition of the thiol. Due to the limitations of nucleophilic and radical mechanisms, there has been an increase in the exploration of transition-metal-catalyzed alkyne hydrothiolation.



**Scheme 1.2. Free radical alkyne hydrothiolation**

Despite the challenges of radical alkyne hydrothiolation, recent advances in radical alkyne hydrothiolation have allowed for its application in total synthesis. Reddy *et al* reported the synthesis of Rigosertib by radical alkyne hydrothiolation.<sup>16</sup> However, it should be noted that the substrates possess limited functional groups, avoiding potential chemoselectivity issues. The authors found radical conditions initiated by  $\text{Et}_3\text{B}$  to result in the best yields. However the reactions were found to generate the inactive *Z* isomer. Solvent, temperature and additives were found to play a significant role in yield and diastereoselectivity. Low temperature ( $-78\text{ }^\circ\text{C}$ ) reactions in DCM gave complete selectivity for the *Z* isomer, while addition of four equivalents

of methanol to reactions in benzene or toluene at room temperature gave complete selectivity for the desired E isomer (Scheme 1.3).

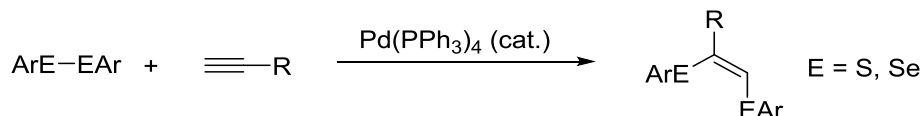


**Scheme 1.3. Radical initiated alkyne hydrothiolation towards the synthesis of Rigoseritib.**

## 1.2.2 Transition Metal Catalyzed Alkyne Hydrothiolation

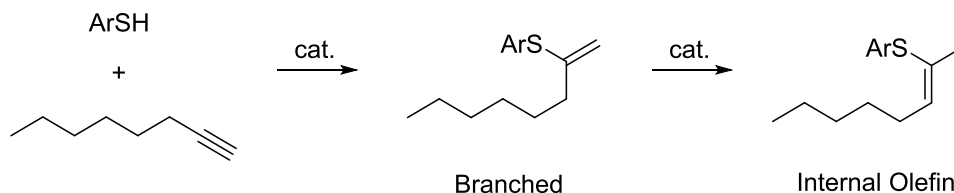
Although transition metals have long been used to catalyze the formation of carbon-element bonds, development of methodology for the formation of carbon-sulfur bonds has been delayed due to the ability of sulfur-containing compounds to act as catalyst poisons. Sulfur forms strong bonds with many late transition metals, frequently resulting in S-bridged dimeric and oligomeric species. Consequently, it was not until 1976 when the first report of transition metal catalyzed hydrothiolation emerged, using a molybdenum catalyst.<sup>17</sup>

Despite this earlier report, metal catalyzed addition of chalcogenides to unsaturated carbon-carbon bonds did not receive much attention until after 1991, when Ogawa and coworkers reported that several transition-metal catalysts, particularly Pd(PPh<sub>3</sub>)<sub>4</sub>, were capable of adding aryl dichalcogenides to terminal alkynes stereospecifically, forming the *Z* isomer exclusively (Scheme 1.4).<sup>18</sup>



#### Scheme 1.4. Alkyne bischalcogenation

This initial development led to the discovery by the same research group of several transition-metal complexes capable of adding aryl thiols across alkynes.<sup>19</sup> The authors found that a mixture of five possible isomers arose in the reaction of 1-octyne, the major product depending on the particular metal complex employed. While Pd(OAc)<sub>2</sub> was found to give the branched product selectively, Pd(PPh<sub>3</sub>)<sub>4</sub>, Pt(PPh<sub>3</sub>)<sub>4</sub>, and Ni(PPh<sub>3</sub>)<sub>2</sub>Cl<sub>2</sub> were found to give an isomerized internal olefin as the major product. The branched isomer was believed to be formed initially, which then isomerized to the internal alkene in the presence of the catalyst (Scheme 1.5). Wilkinson's complex [RhCl(PPh<sub>3</sub>)<sub>3</sub>] however was found to give the *E*-linear product selectively.



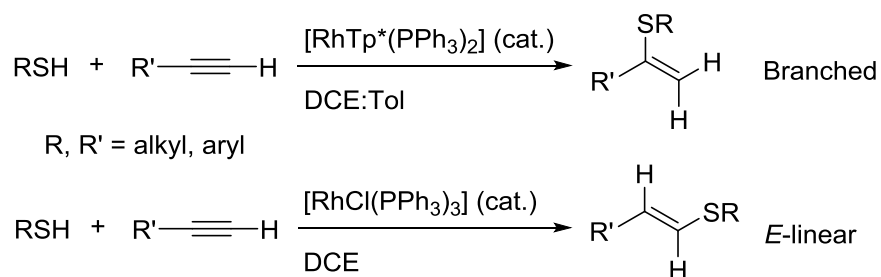
#### Scheme 1.5. Vinyl sulfide isomerization

Following the report by Ogawa in 1992, the area of metal-catalyzed hydrothiolation saw a surge of interest, becoming a major area of research for several groups. Transition metal catalyzed alkyne hydrothiolation is of interest due to increased yield, increased or complementary selectivity, and milder reaction conditions compared to traditional nucleophilic

or radical conditions.<sup>20</sup> Subsequently, several transition and rare earth metal catalysts have emerged for alkyne hydrothiolation, notably Pd,<sup>19</sup> Pt,<sup>19</sup> Rh,<sup>19,23,26,27,28</sup> Ir,<sup>23</sup> Ni,<sup>19,24</sup> Zr,<sup>29</sup> and several lanthanide and actinide complexes.<sup>30</sup> Beletskaya *et al* have recently reviewed the application of transition metal catalysts in hydroelementation reactions,<sup>21</sup> while Marks *et al* have recently reviewed the application of lanthanide and actinide catalysts in hydroelementation reactions.<sup>22</sup>

In 2003, Messerle and coworkers examined several rhodium and iridium catalysts with bidentate N,N and N,P donor ligands and found them to give the linear isomer as the major product with good to excellent *E/Z* selectivity. However, there were limited examples of alkynes and thiophenol was the only thiol employed.<sup>23</sup> Beletskaya and coworkers reported several homogeneous and heterogeneous nickel chloride catalysts, notably Ni(IMES)Cl,<sup>24</sup> were capable of forming the branched isomer selectively. Again, examples were limited to aryl thiols and only a handful of alkynes. These results, combined with those previously reported, led to the belief that only aryl thiols were viable substrates for metal-catalyzed hydrothiolation, and that rhodium and iridium provided the linear isomers, while other metals such as Pd and Ni produced the branched isomer. Although the bischalcogenation strategy was extended to include alkane disulfides in 2001,<sup>25</sup> alkyl thiols were reported unreactive in catalytic hydrothiolation.<sup>19,20,23,24</sup> Given that a number of synthetic targets, including Rigosertib, that could potentially be derived from alkyne hydrothiolation using an alkyl thiol, this presented a significant limitation in scope. Moreover, the reported scope of aryl thiols rarely exceeded simple thiophenol. Expansion of the methodology to include tolerance of a wide variety of functional groups as well as alkyl thiols remained a highly desired goal in metal-catalyzed hydrothiolation.

Despite these preconceptions, the Love group demonstrated for the first time in 2005 that alkane thiols could be used in hydrothiolation reactions with both terminal and internal alkynes using  $[\text{Tp}^*\text{Rh}(\text{PPh}_3)_2]$  (Scheme 1.6).<sup>26</sup> Of additional significance, the branched isomer was produced in high yield and with excellent selectivity, a novelty for rhodium catalysts. This result highlights that the choice of anionic ligand has a large role in product selectivity. In 2007, the Love group reported that Wilkinson's catalyst, contrary to the initial report by Ogawa, was also effective with alkane thiols, producing the *E*-linear isomer in high yield and excellent selectivity.<sup>27</sup> The substrate scope reported by the Love group for both catalysts greatly exceeds any other report to date. These significant discoveries dispelled the prejudice against aliphatic thiols in metal-catalyzed hydrothiolation. Both catalysts have been shown to be tolerant of a wide variety of functional groups, making this methodology the most applicable to complex total syntheses.



**Scheme 1.6. Rhodium-catalyzed hydrothiolation with alkane thiols**

Subsequent to our initial report of metal-catalyzed hydrothiolation using alkane thiols, other examples of metal catalyzed alkyne hydrothiolation with alkyl thiols emerged. The Mizobe group published in 2006 that the related complex  $[\text{Tp}^*\text{Rh}(\text{SPh})_2(\text{MeCN})]$  is also an active catalyst for hydrothiolation with aliphatic thiols.<sup>28</sup> In 2010, the Marks group has shown that the

zirconium complex  $[\text{CGCZrMe}_2]^{29}$  and the samarium and thallium complexes  $[\text{Cp}^*_2\text{SmCH}(\text{TMS})_2]$  and  $[\text{Me}_2\text{SiCp}''_2\text{Th}(\text{CH}_2\text{TMS})_2]^{30}$  are active catalysts for hydrothiolation with alkane thiols. Although the number of examples in both reports was very limited, the authors did examine the mechanism of hydrothiolation, as will be discussed in the next section.

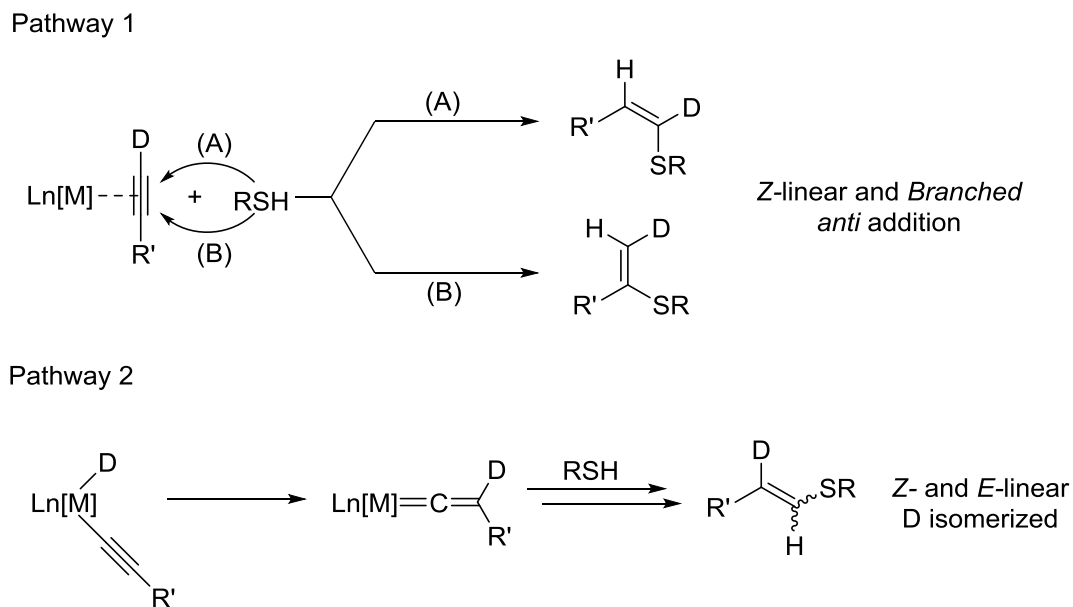
### 1.3 Mechanisms of Metal-Catalyzed Hydrothiolation

Since the discovery of metal-catalyzed alkyne hydro-elementation reactions, several mechanisms have been put forth. These can be classified into two groups. Class I mechanisms involve activation of the alkyne as entry point into the catalytic cycle, followed by attack of an external nucleophilic thiol. Class I mechanisms will be discussed in Section 1.3.1. Class II mechanisms involve activation of the thiol as entry point into the catalytic cycle, with the alkyne entering the catalytic cycle in a later step. Class II mechanisms will be discussed in detail in Section 1.3.2.

#### 1.3.1 Class I Mechanisms

As mentioned above, Class I mechanisms involve activation of the alkyne as entry point into the catalytic cycle. This may occur in one of two ways (Scheme 1.7). Pathway 1 involves simple coordination of the alkyne as the activation step. The activated alkyne is then attacked by external thiol nucleophile, and protonation of the resulting metal-carbon bond yields the product of hydrothiolation. Pathway 2 involves activation of the alkynyl C-H bond and isomerization to form a metal vinylidene. This species is again attacked by external nucleophile to yield the product of hydrothiolation. While pathway 1 was initially thought to be a possibility in

Markovnikov-selective reactions, both Class I mechanisms have been largely excluded in alkyne hydrothiolation due to the observations that thiol addition is *syn* and that any *Z*-linear isomer observed is due to the background radical reaction and could be suppressed with radical inhibitors or shielding from light.<sup>19,26,27</sup>

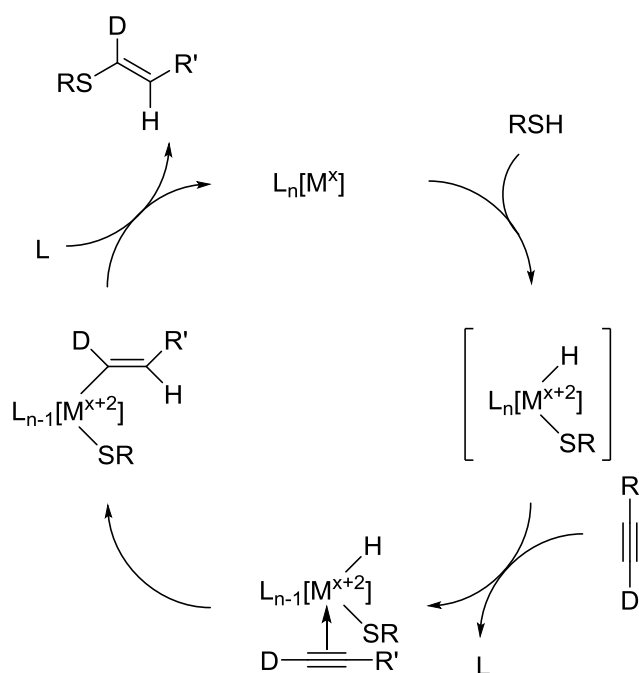


**Scheme 1.7. Class I mechanisms**

### 1.3.2 Class II Mechanisms

Class II mechanisms involve activation of the thiol as entry point into the catalytic cycle. There are two mechanisms belonging to this class. The first proceeds through a hydridothiolate intermediate and is generally accepted, albeit with scant evidence, for catalysts forming the *E*-linear isomer as the major product (Scheme 1.8).<sup>19b,20,27</sup> The mechanism involves oxidative addition of the thiol to the metal center, followed by coordination and migratory insertion of the

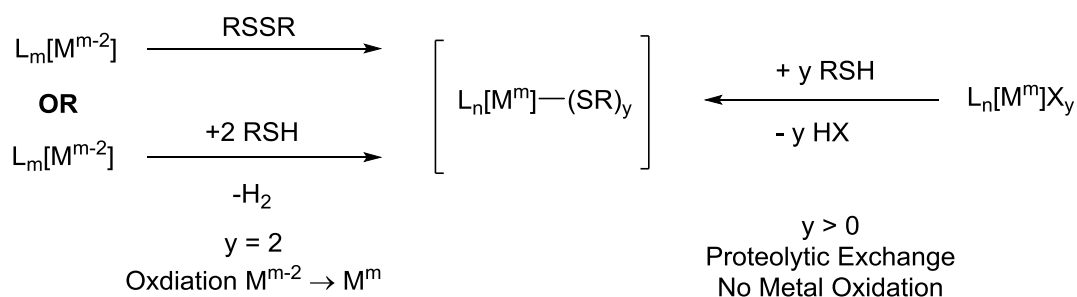
alkyne into the M-H bond. Alkyne insertion occurs into the more reactive M-H bond in the direction that reduces overall steric constraint (i.e., the metal-carbon bond is formed at the less substituted carbon of the alkyne).<sup>153</sup> The product is released by reductive elimination of the alkenyl and thiolate ligands and the cycle continues. It is worth noting that ligand dissociation is often required for alkyne coordination and that this may occur before or after oxidative addition.



**Scheme 1.8. Hydridothiolate mechanism**

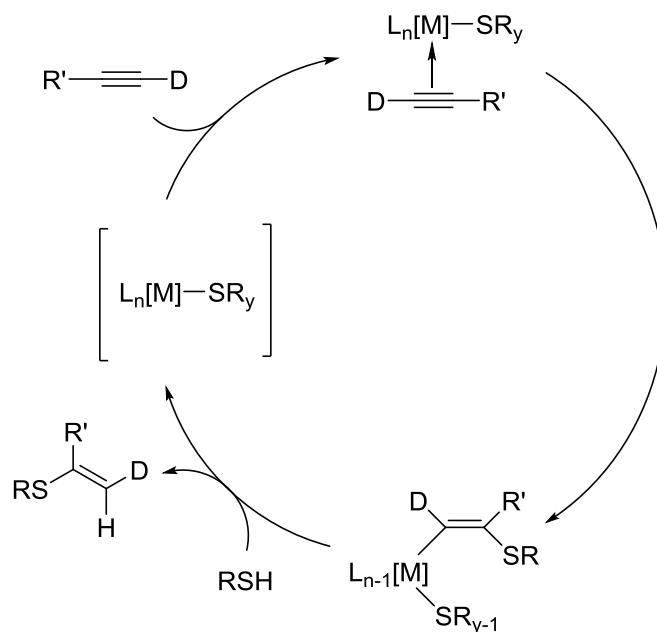
The second Class II mechanism involves the formation of a metal-thiolate intermediate and is the generally accepted mechanism for catalysts forming the branched isomer as the major product.<sup>19a,20,24,28,29,30</sup> The metal-thiolate intermediate is formed by one of three distinct pathways (Scheme 1.10). It can be formed by protonation and exchange of ligands on the precatalyst for thiolate ligands, releasing equivalents of protonated ligand. In this pathway the oxidation state of

the metal is unchanged upon entry into the cycle. This pathway is believed to be operable with  $\text{Pd}(\text{OAc})_2$ <sup>19,20</sup> as well as the zirconium, lanthanide and actinide systems developed by the Marks group.<sup>29,30</sup> Alternatively, the dithiolate can be formed by oxidative addition of one equivalent of thiol followed by protonation and exchange of the hydride ligand for a second thiolate ligand with concomitant formation of dihydrogen. Finally, the dithiolate can also be formed directly via the oxidative addition of disulfides.<sup>28</sup> Both the second and third pathways result in an oxidation of the metal center by +2.



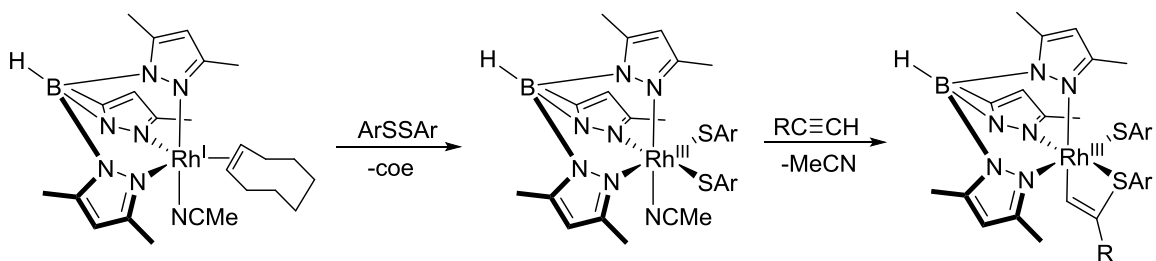
**Scheme 1.9. Formation of metal-thiolate complexes  $\text{L}_n[\text{M}^m](\text{SR})_y$ .**

Once the metal-thiolate complex is formed, alkyne coordination and migratory insertion gives the alkenyl-thiolate intermediate, the regiochemistry of which is again dictated by sterics (Scheme 1.10). The final step is protonolysis of the Rh-C bond, releasing the vinyl sulfide product, and reforming the metal-thiolate complex.



**Scheme 1.10. Dithiolate mechanism**

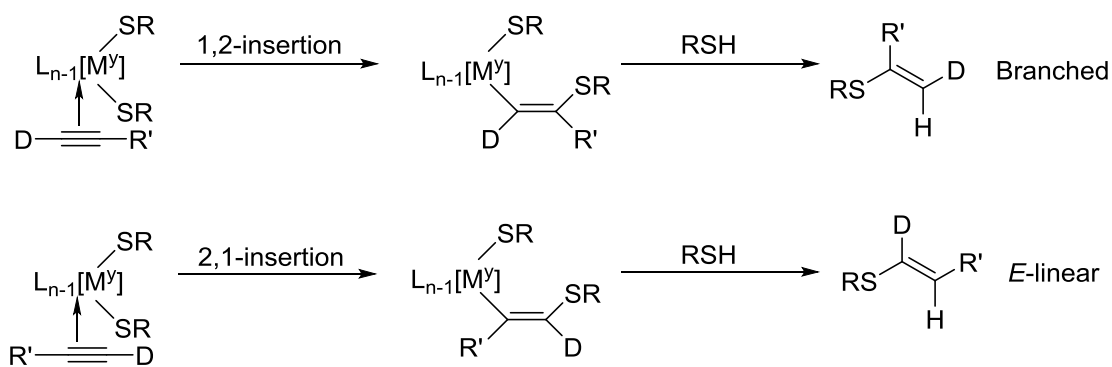
Stoichiometric reactions using  $\text{Tp}^*\text{Rh}(\text{coe})(\text{MeCN})$  have shown that adding one equivalent of thiol results in a mixture of hydridothiolate and dithiolate species. Addition of a second equivalent of thiol results in the formation of the dithiolate complex with evolution of dihydrogen observable by both  $^1\text{H}$  NMR spectroscopy and bubbling of the solution. Crystals of both the dithiolate complex and the alkenyl-thiolate intermediate have been isolated and characterized and found to be active in hydrothiolation (Scheme 1.11).



**Scheme 1.11. Dithiolate intermediate with Tp\*Rh(coe)(MeCN)**

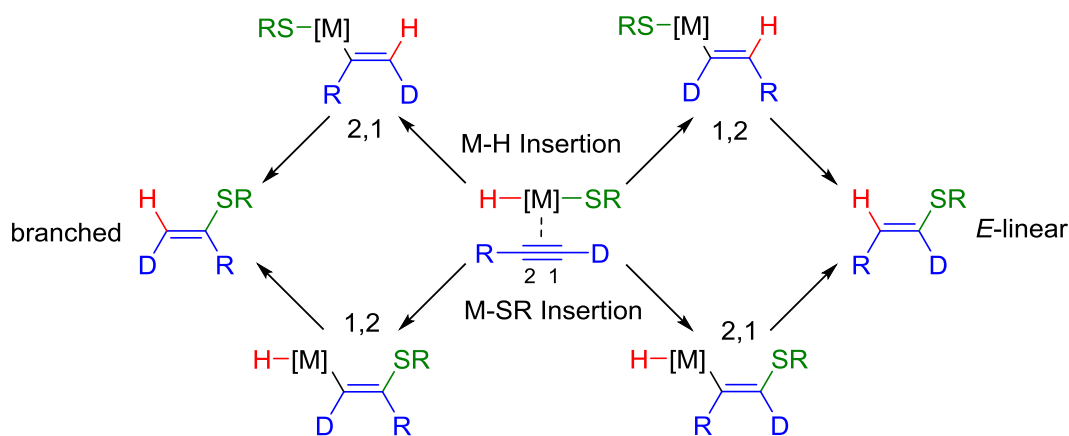
### 1.3.2.1 Regioselectivity in Class II Mechanisms

A closer inspection of class II mechanisms reveals additional pathways. Although the bis-thiolate mechanism contains a single reactive metal-element bond, there are two possible modes for insertion of the alkyne. Reactions shown to proceed through a bis-thiolate mechanism are not 100% selective, and this is due to the directionality of alkyne insertion. 1,2-insertion, where the less substituted carbon becomes bonded to the metal and the more substituted carbon bonds to the nucleophilic sulfur atom, results in formation of the branched isomer. 2,1-insertion of the alkyne results in formation of the *E*-linear product (Scheme 1.12). Because 1,2-insertion is preferred for both steric and electronic reasons, reactions proceeding through the generation of intermediate metal-thiolate complexes produce the branched regioisomer as the major product.



**Scheme 1.12. 1,2 vs 2,1 alkyne insertion in dithiolate mechanism**

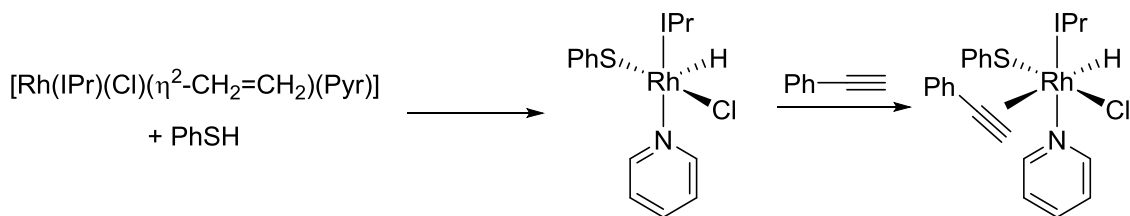
For class II mechanisms involving a hydridothiolate intermediate, there are four possible modes for insertion. Mechanisms involving the generation of an intermediate metal-hydridothiolate are proposed to proceed through chemoselective insertion of the alkyne into the metal-hydride bond. 1,2 migratory insertion of the alkyne into the metal-hydride bond, as depicted in Scheme 1.8, is favored for steric and electronic reasons and results in formation of the *E*-linear product as the major product. 2,1-insertion into the metal-hydride bond would generate the branched product. However the alkyne may also insert into the metal-thiolate bond, again with the possibility of 1,2- or 2,1-insertion (Scheme 1.13). Thus four potential pathways exist for the formation of either isomer. Only one may be active, or all four may be active simultaneously, rendering full mechanistic investigations of mechanisms involving hydridothiolate intermediates challenging.



**Scheme 1.13. 1,2 vs 2,1 insertion for hydridothiolate intermediate**

Another variation in the source of selectivity was revealed by the work of Castarlenas and coworkers.  $[\text{Rh}(\text{IPr})(\mu\text{-Cl})(\eta^2\text{-olefin})]_2$  (olefin = cyclooctene or ethylene) complexes were found to give the *E*-linear product as the major isomer for hydrothiolation reactions between thiophenol and phenylacetylene.<sup>31</sup> However, a switch in regioselectivity was observed when either the dimeric rhodium complexes were used in the presence of 10 equivalents of pyridine, or when the monomeric pyridine complex  $[\text{Rh}(\text{IPr})(\text{Cl})(\eta^2\text{-CH}_2\text{=CH}_2)(\text{Pyridine})]$  were employed. The authors attributed this change in selectivity to precoordination of the pyridine to a rhodium hydrido thiolate complex (Scheme 1.14). The pyridine ligand restricts coordination of the incoming alkyne, and the high *trans* influence of the hydride ligand directs coordination of the alkyne *cis* to the thiolate ligand. As a result, the alkyne is only able to insert into the metal-thiolate bond. 1,2-insertion of the alkyne and subsequent reductive elimination generates the branched regioisomer as the major product. In the absence of coordinated pyridine, the alkyne is able to coordinate and insert into the metal-hydride bond, thus generating the *E*-linear product as the

major isomer via a 1,2-insertion pathway. This is an elegant solution to the problem of migratory insertion pathways for metal-hydrido-thiolate complexes presented above.



**Scheme 1.14. Coordination restriction for alkyne hydrothiolation catalyzed by  $[\text{Rh}(\text{IPr})(\text{Cl})(\eta^2\text{-CH}_2=\text{CH}_2)(\text{Pyridine})]$ .**

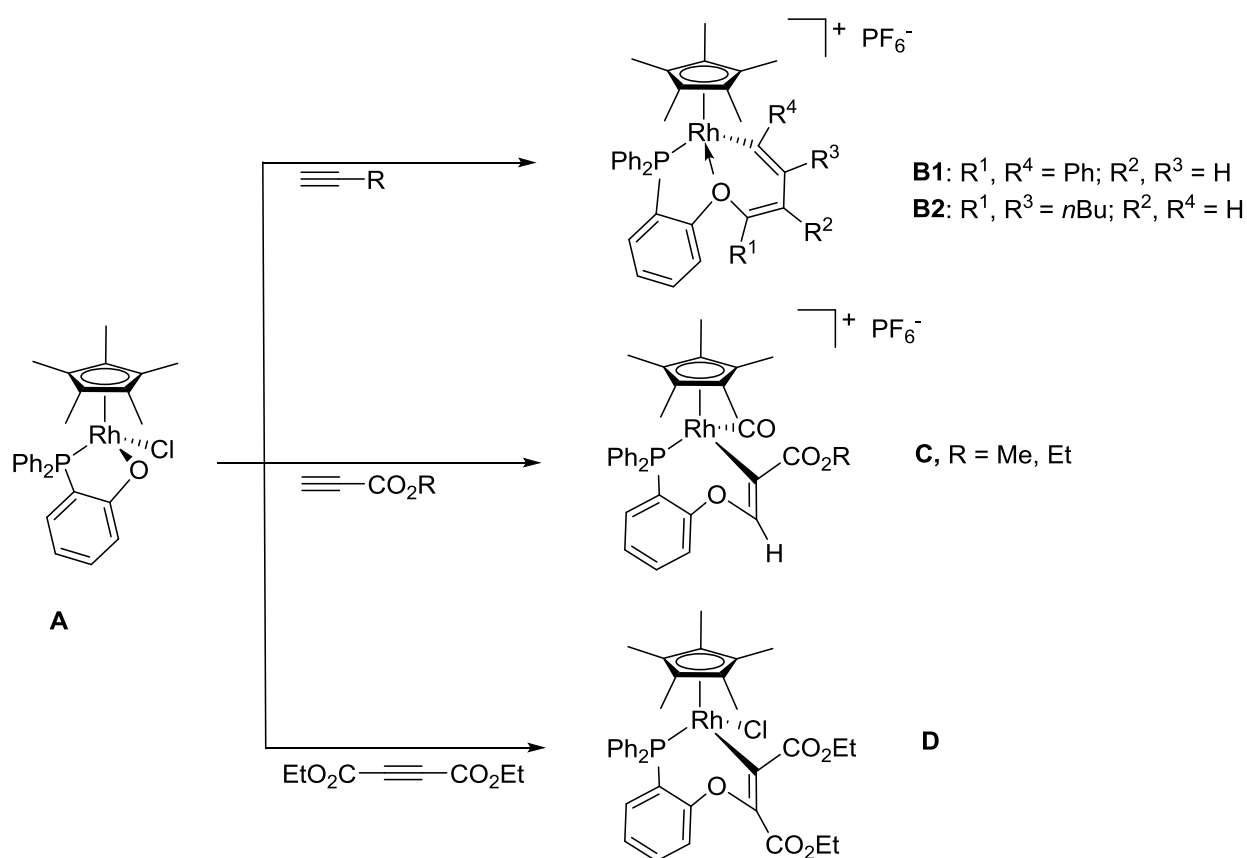
## 1.4 Insertions into Rhodium-Heteroatom Bonds

An important consideration when examining the mechanism of rhodium-catalyzed hydroelementation reactions is the feasibility of insertion of alkenes and alkynes into rhodium-heteroatom bonds. In this section we will review recent literature regarding insertion into rhodium heteroatom bonds.

### 1.4.1 Systems with Direct Evidence for Rhodium-Heteroatom Insertion

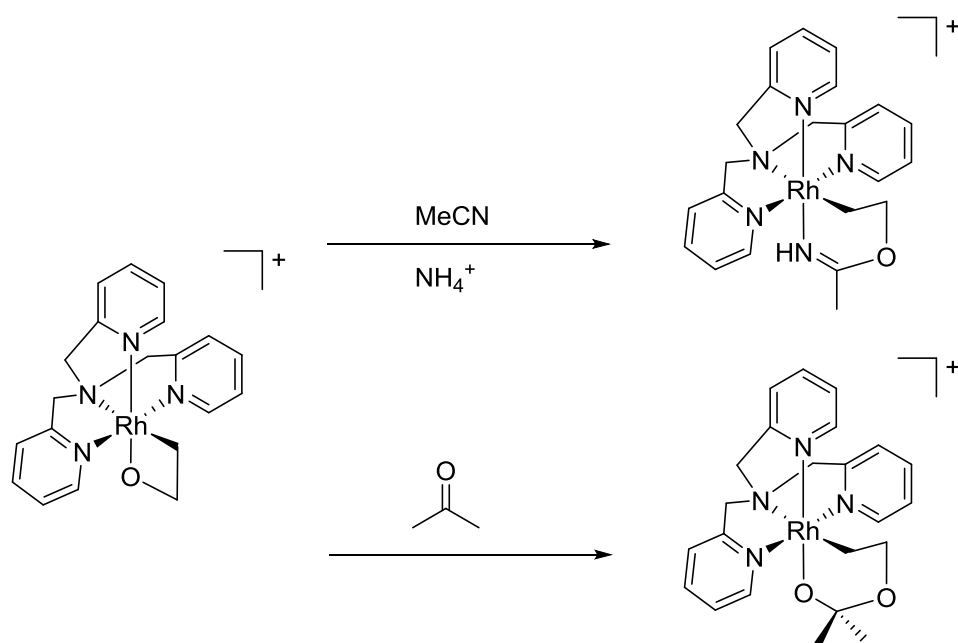
First, systems with direct evidence for rhodium-heteroatom insertion will be discussed. Typically the condition for direct evidence involves crystallographic evidence for products or intermediate products following substrate insertion. The earliest direct example of insertion of an unsaturated carbon-carbon into a rhodium-heteroatom bond is that of Yamamoto *et al* in 2000.<sup>32</sup> In their initial report, the authors examine the reactivity of complex **A** with unactivated and activated internal and terminal alkynes. Symmetrically substituted activated alkyne proceeded to

the corresponding Rh-O insertion product **B** (Scheme 1.15). However, unsymmetrically substituted activated alkynes proceeded with additional CO extrusion of another equivalent of substrate to generate cationic complexes **C**, and unactivated terminal alkynes underwent double insertion and displacement of the chloride ligand, generating cationic complexes **D**. While phenylacetylene underwent head-to-head double insertion, 1-hexyne underwent head-to-tail double insertion. All complexes were characterized crystallographically.



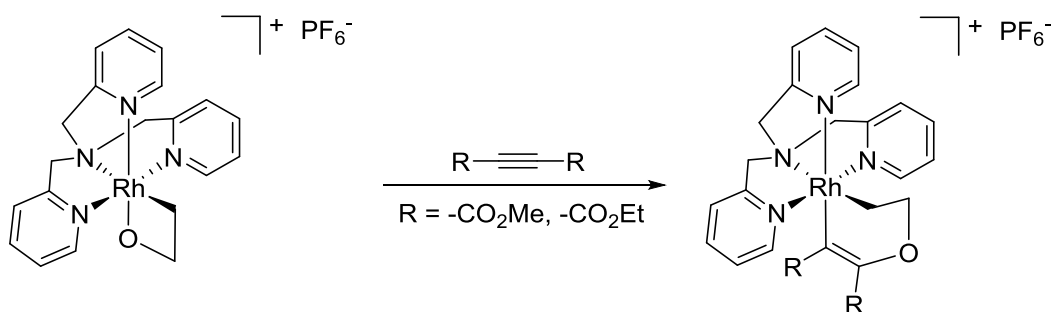
**Scheme 1.15.** Insertion of alkynes into rhodium-oxygen bond of Cp\* ligated rhodium (*P,O*)-chelating phosphane complex.

Subsequent to this report, the only other direct example of insertion into a rhodium-oxygen bond is that of TPA-substituted rhodaoxetanes (TPA = tris(2-pyridylmethyl)amine). de Bruin and coworkers had previously reported the synthesis<sup>33</sup> and reactivity of rhodaoxetanes towards acid.<sup>34</sup> de Bruin and coworkers reported the insertion of acetonitrile and acetone into the Rh-O bond of these rhodaoxetanes (Scheme 1.16). The acid-induced insertion of acetonitrile into the Rh-O bond of the rhodaoxetane cannot be considered a direct insertion, since the mechanism involves protonation and ring-opening of the rhodaoxetane. Furthermore, the rhodaoxetane is stable in neat acetonitrile. Without any rigorous mechanistic studies, however, the insertion of acetone could be considered a direct Rh-O insertion.



**Scheme 1.16. Rh-O insertion of acetonitrile and acetone with rhodaoxetanes.**

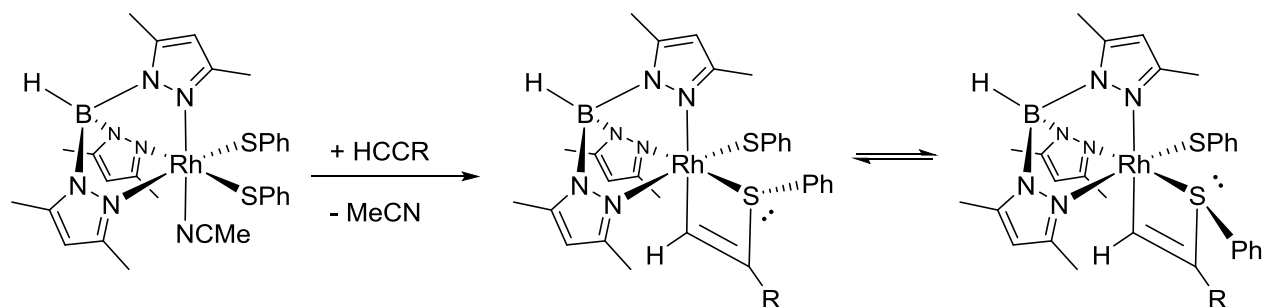
Addison Desnoyer, a current graduate student in the Love lab, expanded on previous work by Alexander Dauth<sup>35</sup> and found that the rhodaoxetanes underwent insertion reactions with CS<sub>2</sub>, aldehydes, and activated disubstituted alkynes (Scheme 1.17). It is notable that the alkyne inserts into the rhodium-oxygen bond and not the rhodium-carbon bond. The final complex was characterized by x-ray crystallographic methods.



**Scheme 1.17. Rhodaoxetane ring expansion with activated alkynes.**

As mentioned above, Mizobe and coworkers were able to isolate and characterize the rhodathiacyclobutene product of alkyne insertion into the Rh-S bond of a dithiolate complex. Interestingly, the resulting rhodathiacyclobutene was observed to give two sets of signals in the <sup>1</sup>H NMR spectra. Due to the similar chemical shifts and coupling constants for the C-H of the rhodathiacyclobutene ring, the two sets of signals were assigned to structures **A** and **B**. Due to the high barrier to inversion of sulfur (38-41 kcal/mol for chiral sulfoxides),<sup>36</sup> the sulfur atom is a stereogenic, resulting in two diastereoisomers in solution (Scheme 1.18). There is the possibility that a rapid equilibrium in solution between the 1,2-insertion product and the 2,1-insertion product is responsible for these two sets of signals. However, the similar chemical shifts and

rhodium coupling constants for the vinyl C-H of the two rhodathiacyclobutene species makes this unlikely.



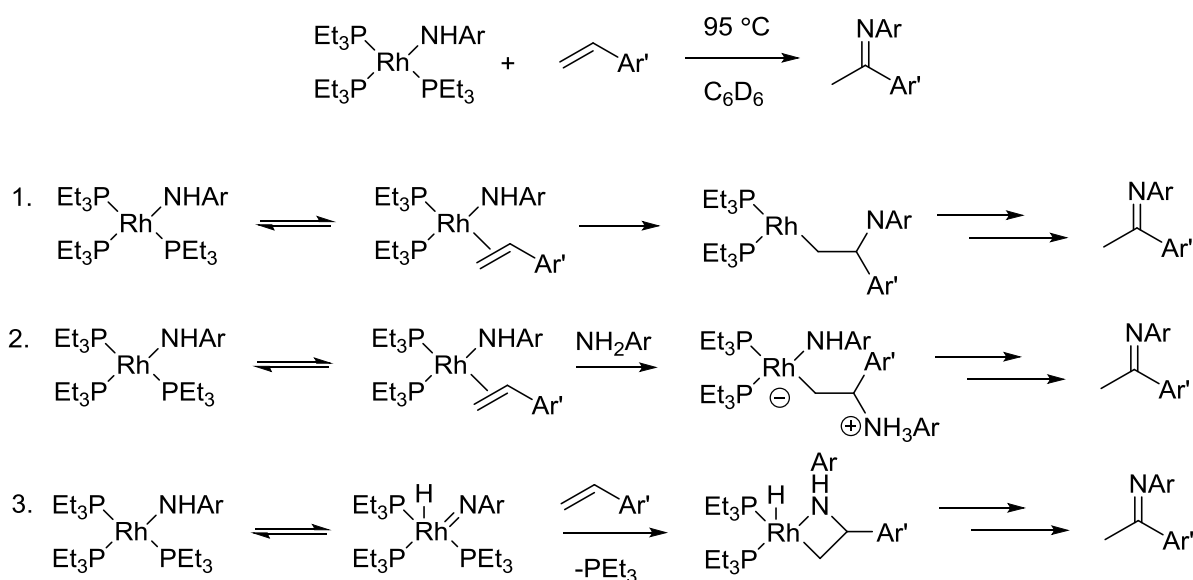
**Scheme 1.18. Rhodathiacyclobutene formation with  $Tp^*Rh(SPh_2)(MeCN)$**

#### 1.4.2 Systems with Indirect Evidence for Rhodium-Heteroatom Insertion

Frequently, the putative products of insertion into a rhodium-heteroatom bond cannot be isolated, or are unstable, or intermediates on a longer reaction pathway. In these cases, a good understanding of the mechanistic pathway is necessary to show that product formation proceeds via insertion into the metal-heteroatom bond and not some other mechanism (e.g., class I mechanisms, *vide supra*). For indirect evidence for the insertion of carbon-carbon unsaturated moieties into rhodium-heteroatom bonds, we turn to the work of Hartwig and coworkers.

In 2005, the Hartwig group reported the formation of imines via the reaction of isolated rhodium-amido species and a variety of olefins.<sup>37</sup> The authors examined four potential mechanisms for imine formation (Scheme 1.19). The first involves Rh-N insertion of a coordinated olefin. The second involves external nucleophilic attack of a coordinated olefin. The third involves isomerization of the amido to a rhodium-hydride species which could undergo

[2+2] cycloaddition. Finally the fourth involves a dimeric rhodium intermediate which was immediately excluded due to the observation that the reaction rate is first order in rhodium-amido complex, contrary to the predicted second-order dependence for a dimeric pathway. In each mechanism,  $\beta$ -hydrogen elimination subsequent to carbon-nitrogen bond formation, and isomerization of the resulting enamine to the imine, would complete the mechanistic pathway.

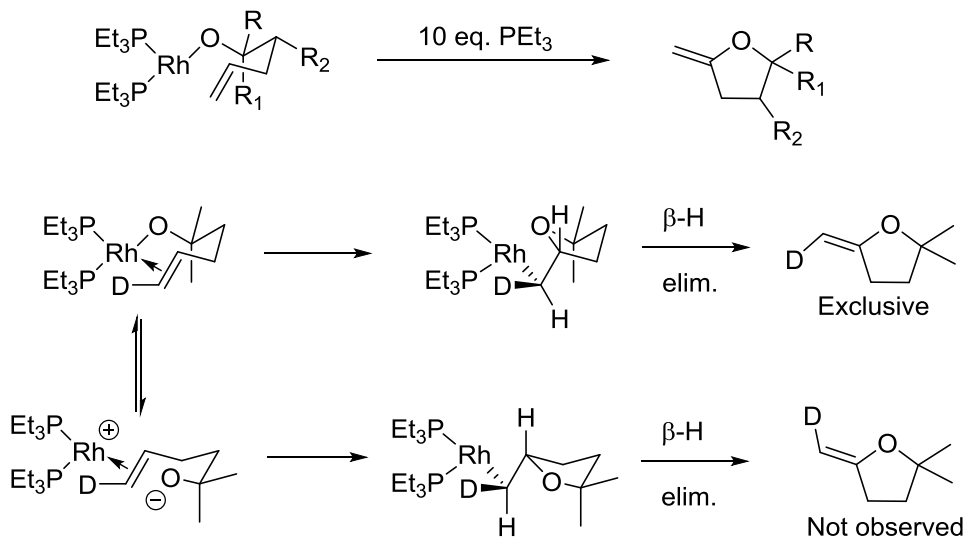


**Scheme 1.19. Mechanism for imine formation from rhodium-amido complexes.**

The authors began by determining if  $\beta$ -hydrogen elimination were the rate determining step through kinetic isotope effect experiments. Reactions with styrene and styrene- $d_8$  gave experimentally identical reaction rates. Thus it was determined that the rate-determining step occurred prior to  $\beta$ -hydrogen elimination and further mechanistic experiments would reveal which of the three remaining pathways were operative. In order to differentiate the remaining three pathways, the authors examined the kinetic orders of substrates and added phosphine. The

reaction was found to be inverse-first order in phosphine, suggesting that reversible phosphine dissociation occurs prior to the rate-determining step. The reaction was found to be first order in olefin and independent of added amine concentration. This observation excluded pathway 2, as rate-limiting external nucleophilic attack of amine onto a coordinated olefin is expected to be first order in amine concentration. The final pathway involving spontaneous formation of a rhodium-hydride from the amido complex was ruled due to the observations that: 1) no kinetic isotope effect was observed for reaction of the N-deuterated analogous complexes; 2) some secondary amines, which are unable to undergo isomerization to the Rh-H complex shown in pathway 3, were also substrates for the reaction. Thus the only pathway consistent with all experimental observations was that involving direct insertion of the coordinated olefin into the rhodium-nitrogen bond.

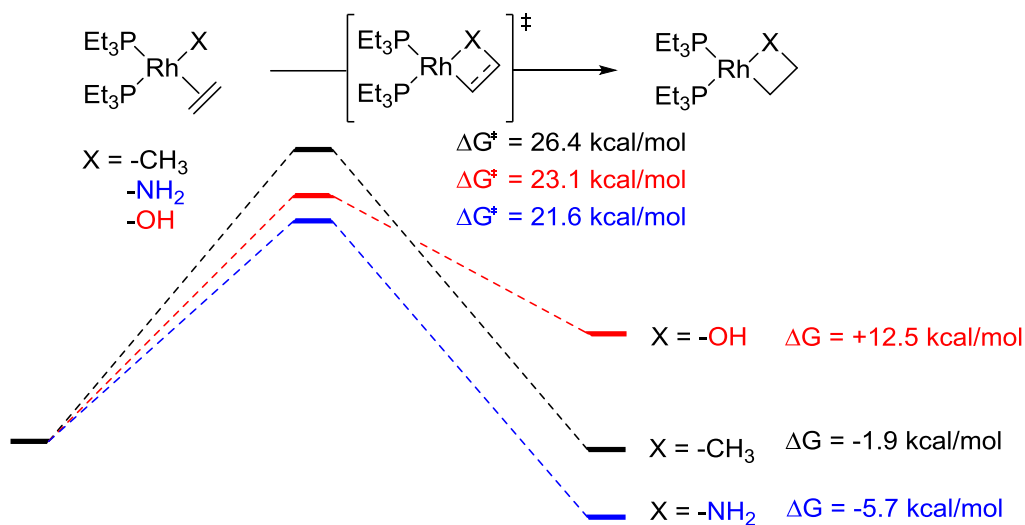
In 2006, the Hartwig group reported indirect experimental evidence for the insertion of a coordinated olefin into a rhodium-oxygen bond.<sup>38</sup> In the presence of excess phosphine, rhodium complexes bearing an alkoxo ligand and intramolecularly-coordinated olefin resulted in the formation of substituted 5-methylenetetrahydrofuran derivatives (Scheme 1.20). In comparison to the intermolecular rhodium-amido reaction discussed above, the intramolecular nature of this reaction greatly simplified the possible mechanistic pathways. Product formation might either proceed via direct insertion of the olefin into the rhodium-oxygen bond, or by dissociation of the alkoxo ligand and nucleophilic attack of the alkoxide onto the coordinated olefin. Thus, deuterium labeling of the olefin determined that product formation proceeded exclusively via insertion of the olefin into the rhodium-oxygen bond (Scheme 1.20).



**Scheme 1.20. Rhodium-oxygen bond insertion in  $[\text{Rh}(\text{PEt}_3)_2(\kappa^1\text{-}\eta^2\text{-OCR}_2\text{CHRCH}=\text{CH}_2)]$**

Following these two reports of rhodium-nitrogen and rhodium-oxygen bond insertion, the Hartwig group used computational methods to compare the energetics for insertion of olefins into Rh-X bonds, where X = O, N, C.<sup>39</sup> The authors examined the relative rates for ethylene insertion for model complexes  $[\text{Rh}(\text{PMe}_3)_2(\text{CH}_2=\text{CH}_2)(\text{X})]$ , where X = -CH<sub>3</sub>, -NH<sub>2</sub>, and -OH (Scheme 1.21). The computed barriers for C-X bond formation follow the trend of C-C > C-O > C-N. In each case, the initial product involves some form of Rh-X interaction: a  $\gamma$ -agostic interaction for X = -CH<sub>3</sub>, and dative Rh-X bonds for X = -NH<sub>2</sub>, and -OH similar to the dative Rh-S bond observed by Mizobe and coworkers (*vide supra*). The Rh-X interaction was found to play a large role in stabilizing the transition state for migratory insertion, and so it follows that the computed energies of the barrier to insertion follow the trend X = -CH<sub>3</sub> > -OH > -NH<sub>2</sub>. Insertion into the Rh-N bond has the lowest activation energy and is the most exothermic, while insertion into the Rh-C bond has the highest activation barrier and is only slightly exothermic.

Insertion into the rhodium-oxygen bond, although intermediate in activation energy, was found to be overall endergonic.



**Scheme 1.21. Computed energy for insertion of ethylene into Rh-X bonds.**

Since ethylene and the  $-\text{NH}_2$  and  $-\text{OH}$  must rotate approximately  $90^\circ$  from their ground state configurations to the transition state geometries, the authors attempted to simulate the reorganizational energy required for bond formation by calculating the relative energies of the corresponding rotamers. The differences in energy between the transition state and the rotamers with atoms in the correct orientations are as follows: 14.8 kcal/mol for  $\text{X} = -\text{CH}_3$ ; 10.8 kcal/mol for  $\text{X} = -\text{OH}$ ; and 6.3 kcal/mol for  $\text{X} = -\text{NH}_2$ . Since bond rotation and bond formation likely occur simultaneously, these results, while not a direct measurement of the reorganizational energy in the transition states, indicate that a significant portion of the transition state energy is due to reorganization of the ligands.

Finally the authors examined the 1,2- vs 2,1-insertion of propene into the same series of model complexes. The calculated barrier for 1,2-insertion was found to be lower for all three complexes compared to 2,1-insertion. 1,2-insertion has generally been found to be the dominant pathway due to both steric and electronic effects.<sup>40</sup> While the barrier to 1,2-insertion into the Rh–C bond was found to be nearly identical for that of ethylene, the calculated barriers were found to be significantly lower for X = –NH<sub>2</sub> and –OH for propene 1,2-insertion compared to ethylene insertion. Additionally, the  $\Delta\Delta G^\ddagger$  for 1,2- vs 2,1-insertion was found to be much larger for Rh–N and Rh–O insertion compared to Rh–C insertion. This mirrors experimental observations of low 1,2 vs 2,1 preference for insertion into late transition metal-alkyl bonds compared to exclusive formation of 1,2-insertion products for late transition metal-amide or –alkoxide bonds. The authors propose that these differences result from increased ionic character of the nascent C–X bond and accompanying increase in partial positive charge of the carbon, which is stabilized by increased substitution.

While the results contained in this section are only for Rh(I) d<sup>8</sup> metal complexes, it nonetheless highlights the importance of understanding the mechanism of hydroelementation of carbon-carbon unsaturated bonds. As discussed in section 1.3.2., the regioselectivity of product formation via a hydridothiolate intermediate metal complex can be the result of insertion into the metal-hydride or metal-heteroatom bond, or 1,2- vs 2,1-insertion, or a combination of all four pathways. The logical design of new ligands and catalyst complexes for hydroelementation reactions must take into account the subtleties of the competing mechanistic pathways in order to increase selectivity or reaction rate.

## 1.5 Thesis Outline

The outline for the thesis is as follows:

In chapter 2, we review the application of scorpionate metal complexes in the hydroelementation of alkenes and alkynes, where element = O, N, S and P. In chapter 3, we review the Hammett single and dual parameter treatment for analysis of substituent effects in equilibrium and reaction rates. We use dual parameter Hammett correlation for the prediction of aqueous and methanolic  $pK_{AS}$  for *para*-substituted aryl thiols. In chapter 4 we review the application of alkyne hydrothiolation catalyzed by  $[RhCl(PPh_3)_3]$  in the synthesis of K777, an inhibitor of enzyme Cruzain for the treatment of Chagas disease. We analyze a series of vinyl sulfones in terms of their rates of Michael addition as a method of predicting their efficacy in inhibiting Cruzain. In chapter 5, we examine the mechanism of alkyne hydrothiolation catalyzed by  $[Tp^*Rh(PPh_3)_2]$ . In chapter 6, we report the synthesis of hydridothiolate complexes  $[Tp^*RhH(SR)(PR_3)]$ , putative intermediates in the catalytic cycle of alkyne hydrothiolation catalyzed by  $[Tp^*Rh(PPh_3)_2]$ . Chapters 5 and 6 consist of the bulk of work performed during this PhD. Chapter 7 are conclusions and presents projects for future work. Some work was necessarily excluded from the thesis, namely the preliminary investigations into the mechanism of alkyne hydrothiolation catalyzed by  $[RhCl(PPh_3)_3]$  – some of which is included in the appendix – and much of the research performed while working with Aurin Biotech, which is protected under a non-disclosure agreement.

## Chapter 2 Review of Hydroelementation of Carbon-Carbon Unsaturated Bonds Catalyzed by Metal-Scorpionate Complexes

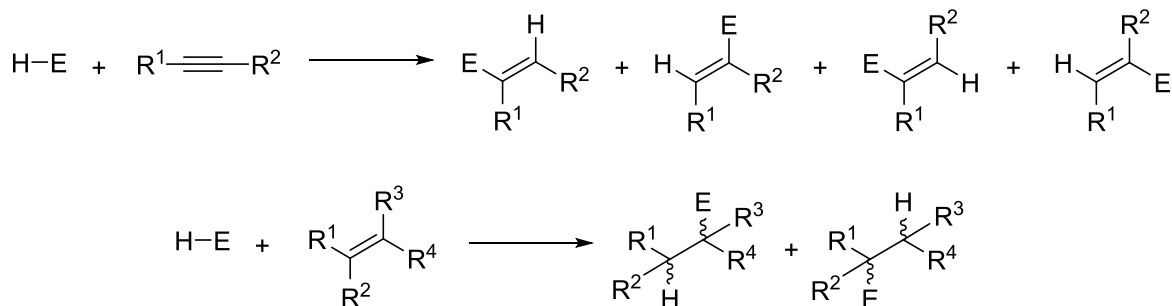
Since the introduction of poly(pyrazole)borate ligands by Trofimenko in 1966,<sup>41</sup> scorpionate ligands have found wide use in coordination chemistry. Tridentate tris(pyrazole)borate and bidentate bis(pyrazole)borate ligands are the most common scorpionate ligands employed, and have been ligated to nearly every metal and metalloid on the periodic table.<sup>42,43,44</sup> Following Trofimenko's seminal work with poly(pyrazole)borates, the field has expanded greatly. Tris(pyrazole)methane substitutes the anionic central borate atom for a neutral carbon atom, generating neutral analogues. The donor atom is typically nitrogen, including, but not limited to, imidazole,<sup>45</sup> oxazole,<sup>46</sup> and triazole rings,<sup>47</sup> although the field has grown to include imidazole-2-thione<sup>48</sup> and 3-mercapto-1,2,4-triazole rings<sup>49</sup> bearing a sulfur donor atom, and tripodal phosphine ligands, a field unto itself.

Tridentate scorpionate ligands have been frequently compared to cyclopentadienyl (Cp) ligands due to their similar charge, facial (*fac*) coordination mode, electron donation and occupation of coordination sites. Scorpionate ligands are divided into 2 classes: homoscorpionate, where all three donor arms are identical (i.e.  $L_1 = L_2$ ), and heteroscorpionates, where two donor arms are identical and the third arm is different (i.e.  $L_1 \neq L_2$ ) (Figure 2.1). The field of heteroscorpionate ligands has developed considerably in recent years, with several variations in donor arms, including carbenes,<sup>50</sup> acetoxy,<sup>51</sup> amine,<sup>52</sup> amidinate,<sup>53</sup> and thiol donors.<sup>54</sup> The definition of scorpionate requires that the ligand: 1) be tridentate; 2) coordinate *fac* to the metal centre; 3) contain a central atom bearing the three donor arms which cannot



Traditional nucleophilic and radical hydroelementation methodologies often require harsh reagents and elevated temperatures, which typically makes them unsuitable for late-stage total synthesis applications. Thus transition-metal-catalyzed hydroelementation has become an increasingly attractive alternative to traditional methods. Transition-metal-catalyzed reactions also offer much more flexibility in tuning regio-, stereo-, and chemoselectivity properties. Hydroelementation reactions are atom economic, producing no by-products, and thus classified as green chemistry. The transition-metal-catalyzed addition of heteroatom-hydrogen bonds to alkynes has recently been reviewed;<sup>63</sup> however this review was published prior to recent reports of transition-metal scorpionate complexes in hydroelementation reactions. The use of palladium in transformations of alkynes, including hydroelementation reactions, has been reviewed recently.<sup>64</sup> Sequential hydroelement addition to carbon-carbon unsaturated bonds has also been recently reviewed.<sup>65</sup>

Despite the potential utility of hydroelementation reactions, product regio- and stereoselectivity becomes an inherent challenge for generating synthetically useful protocols. Addition of H-E to an unsymmetrically substituted alkyne can generate one of four potential products (Scheme 2.1). These products differ in terms of the diastereoselectivity of addition (syn vs anti), and the regioselectivity of addition (loosely termed Markovnikov and anti-Markovnikov). In hydroamination, secondary amines yield the corresponding enamines while primary amines isomerize to the corresponding imines. Addition to alkenes adds the further challenge of chirality control to methodology and catalyst design.



**Scheme 2.1. Hydroelementation of alkynes and alkenes**

Hydroelementation of alkenes and alkynes have numerous potential applications for the synthesis of a variety of biologically active compounds. Herein we will review recent advances in the use of scorpionate ligands in hydroamination, hydroalkoxylation, hydrophosphinylation, and hydrothiolation reactions. We will focus on solid phase and solution phase coordination mode and fluxionality of scorpionate complexes, and examine their catalytic activity in hydroelementation reactions. In each section, a brief overview of the field and its relevance in synthetic applications will be discussed.

## 2.1 Hydrothiolation of Alkynes

Transition-metal-catalyzed alkyne hydrothiolation is of recent interest due to the utility of vinyl sulfides and their oxidized counterpart's vinyl sulfones. Vinyl sulfides and vinyl sulfones are versatile intermediates in total synthesis, whilst vinyl sulfones are reactive Michael acceptors.<sup>66</sup> As such, vinyl sulfones have been incorporated into a variety of drugs aimed at enzyme inhibition through irreversible reaction between catalytic residues within the active site

and the vinyl sulfone moiety.<sup>67</sup> Vinyl sulfones can be easily obtained from vinyl sulfides through simple oxidation.<sup>68</sup>

Many advances have been made in metal-free nucleophilic and radical hydrothiolation reactions over the years,<sup>69</sup> however the highly reactive nature of sulfur nucleophiles and radicals makes chemoselectivity difficult to achieve. Radical alkyne hydrothiolation has been successfully applied to the synthesis of Rigosertib,<sup>70</sup> while transition-metal-catalyzed alkyne hydrothiolation has been successfully applied to the total synthesis of K777, a cysteine protease inhibitor (Figure 2.2).<sup>71</sup>

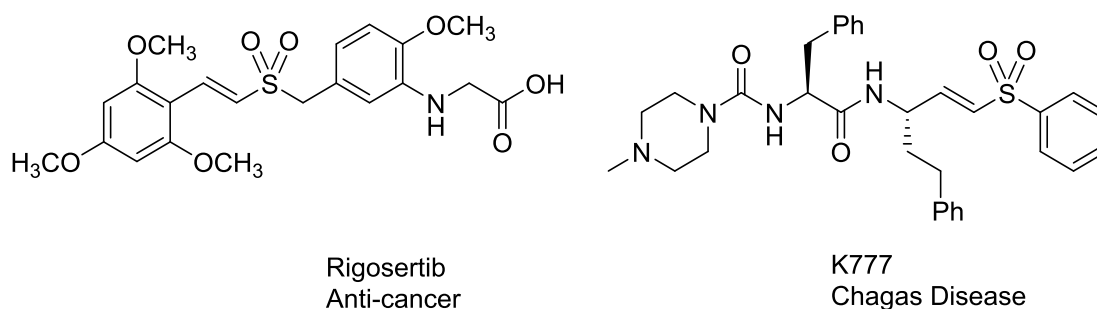


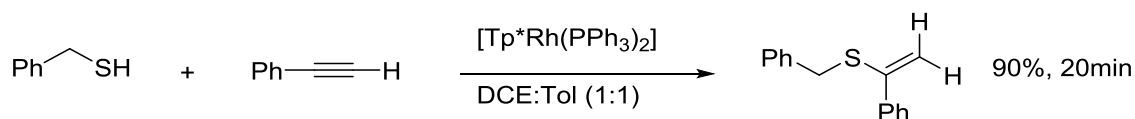
**Figure 2.2. Examples of vinyl sulfone containing drugs**

It was not until the seminal work by Ogawa and co-workers in 1992 that transition-metals were shown to be effective catalysts for alkyne hydrothiolation with aryl thiols.<sup>72</sup> However, catalysts capable of employing aliphatic thiols remained elusive until 2005, when Love and co-workers reported that the scorpionate complex  $[\text{Tp}^*\text{Rh}(\text{PPh}_3)_2]$  was active for alkyne hydrothiolation with both aliphatic and aromatic thiols. Strategies towards C-S bond formation, including hydrothiolation, have recently been reviewed.<sup>73</sup> Marks *et al* have also recently

reviewed the application of organo-f-element catalysts in hydrothiolation and hydroalkoxylation.<sup>74</sup>

### 2.1.1 Alkyne Hydrothiolation Catalyzed by Tris(pyrazolyl)borate Complexes of Rhodium

Love and co-workers found  $[\text{Tp}^*\text{Rh}(\text{PPh}_3)_2]$  to be a highly active catalyst for the hydrothiolation of both internal and terminal alkynes with both aliphatic and aromatic thiols. The test reaction between phenylacetylene and benzylthiol produced the vinyl sulfide product in 20 min and 90% isolated yield. Surprisingly, the branched isomer was found to be the sole isomer generated (Scheme 2.2). This was the first example of transition metal-catalyzed alkyne hydrothiolation with aliphatic thiols.



**Scheme 2.2. Hydrothiolation of phenylacetylene with benzylthiol catalyzed by  $\text{Tp}^*\text{Rh}(\text{PPh}_3)_2$ .**

Having established that rhodium complexes bearing tris(pyrazolyl)borate ligands were effective catalysts for alkyne hydrothiolation, the Love group examined a series of substituted tris(pyrazolyl)borate ligands, as well as  $[\text{Bp}^*\text{Rh}(\text{PPh}_3)_2]$ .<sup>75</sup> Solid state structures of the resulting rhodium poly(pyrazolyl)borate bisphosphine complexes revealed that the scorpionate ligands adopted a bidentate  $\kappa^2$  coordination mode. For tris(pyrazolyl)borate complexes, the third

pyrazole arm was located either towards the square planar rhodium center for pyrazoles with substitution at the 5-position, or away from the rhodium center for pyrazoles without such substitution. Low temperature  $^1\text{H}$  NMR spectra were also consistent with  $\kappa^2$  coordination of the tridentate homoscorpionate ligands.

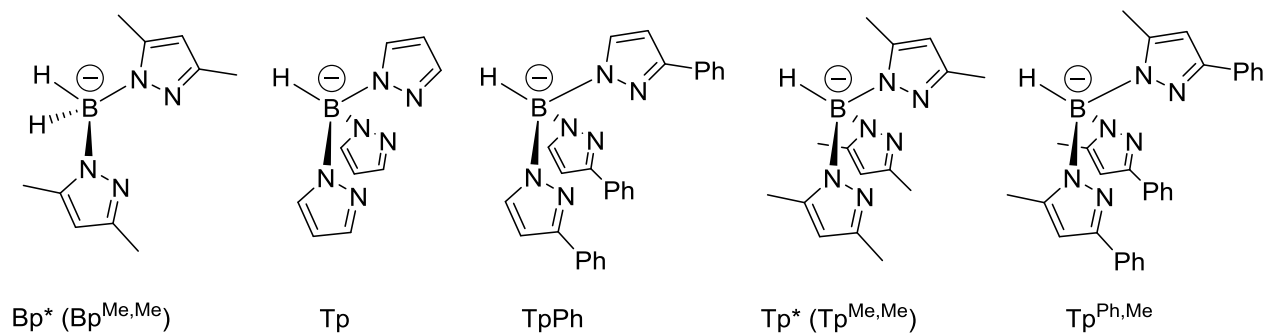


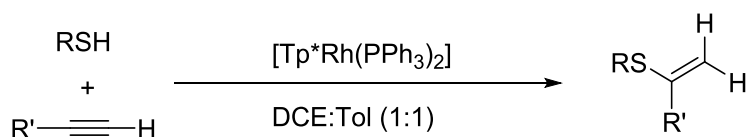
**Figure 2.3. Pyrazoleborate ligands assayed by Love and coworkers.**

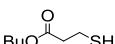
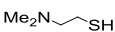
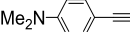
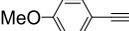
Using the hydrothiolation of phenylacetylene and benzylthiol as a benchmark reaction, substituted tris(pyrazolyl)borate rhodium complexes were found to be more active and selective than unsubstituted  $[\text{TpRh}(\text{PPh}_3)_2]$  or bidentate  $[\text{Bp}^*\text{Rh}(\text{PPh}_3)_2]$ . Thus, it was concluded that both the presence of a third pyrazole arm and substitution of the pyrazole were crucial to both the yield and selectivity of the reaction. Across the board,  $[\text{Tp}^*\text{Rh}(\text{PPh}_3)_2]$  was found to be the highest yielding and most selective catalyst examined.

The authors subsequently decided to examine the full substrate scope of alkyne hydrothiolation.<sup>76</sup> The reaction was found to be remarkably tolerant to functional groups; nitriles, ethers, esters, alkyl chlorides, and even unprotected amines were all well tolerated under the reaction conditions, although free carboxylic acids were not. Selected examples are presented in

Table 2.1. The authors also found that the more acidic thiols thiophenol and 2,2,2-trifluoroethanethiol were equally active substrates, although with lower selectivity for the branched product.

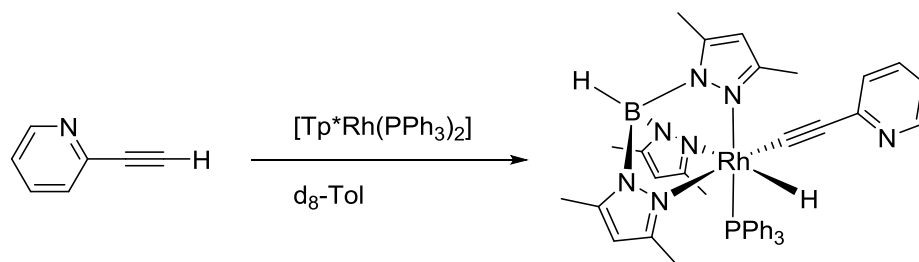
**Table 2.1. Scope of alkyne hydrothiolation catalyzed by [Tp\*Rh(PPh<sub>3</sub>)<sub>2</sub>]**



R' = -Ph			R = -Bn		
Entry	Thiol	Yield	Entry	Alkyne	Yield
1	BnSH	90%	9		85%
2	PrSH	87%	10		88%
3		78%	11		90%
4		70%	12		33%
5		75%	13		81%
6		80%	14		63%
7		65%	15		90%
8		0%	16		93%

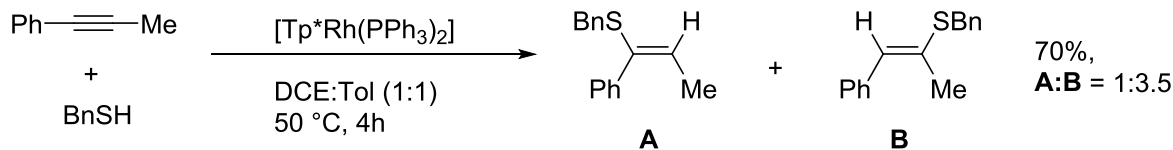
Electron deficient aryl acetylenes were found to react in lower yields, while 2-pyridylacetylene was found to be unreactive. The authors suspected that coordination of the

nitrogen might preclude catalysis. Consistent with this hypothesis, the reaction between 2-pyridylacetylene and  $[\text{Tp}^*\text{Rh}(\text{PPh}_3)_2]$  was found to result in alkynyl C-H activation (Scheme 2.3). This product was characterized in both solution and solid phase and was observed to form during the attempted catalytic reactions.



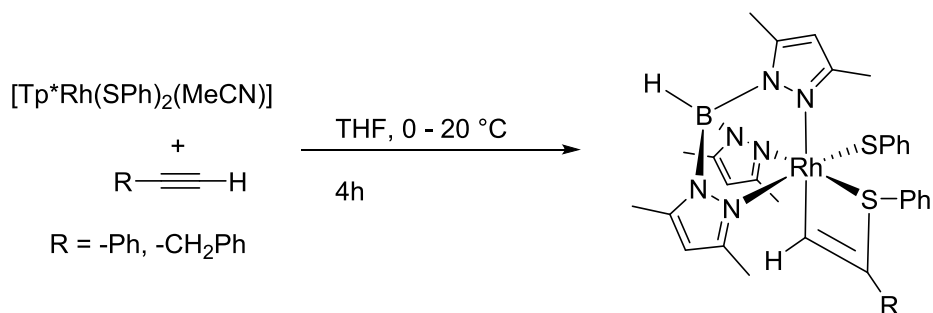
**Scheme 2.3. Alkynyl C-H activation by  $\text{Tp}^*\text{Rh}(\text{PPh}_3)_2$**

Internal alkynes were also reactive substrates, generating the product of *syn* addition, albeit at elevated temperatures. For example, 3-hexyne reacted to give the vinyl sulfide product in 32% yield, however cyclotrimerization was observed under the reaction conditions to generate hexaethylbenzene in 20% yield. Unsymmetrically substituted internal alkynes proceeded with modest regioselectivity in favor of the less hindered isomer (Scheme 2.4). Despite these few limitations,  $[\text{Tp}^*\text{Rh}(\text{PPh}_3)_2]$  catalyzed alkyne hydrothiolation has the largest substrate scope reported to date.<sup>77</sup>



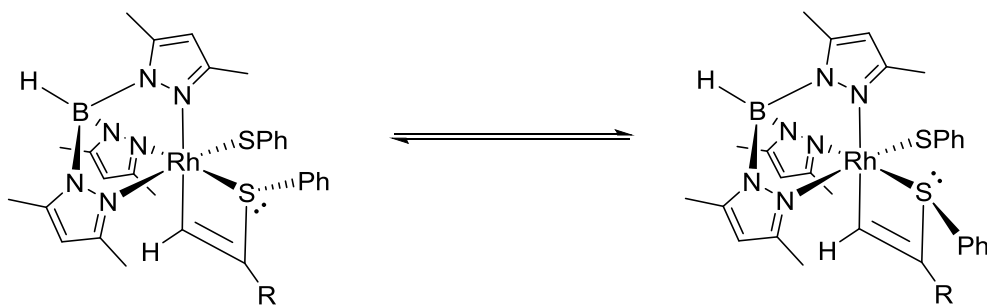
**Scheme 2.4. Hydrothiolation of an unsymmetrically substituted internal alkyne with Benzylthiol catalyzed by  $\text{Tp}^*\text{Rh}(\text{PPh}_3)_2$ .**

Shortly after the initial report of alkyne hydrothiolation catalyzed by a rhodium tris(pyrazolyl)borate complex by Love in 2005, the Mizobe group published that the related complexes  $[\text{Tp}^*\text{Rh}(\text{coe})(\text{MeCN})]$  and  $[\text{Tp}^*\text{Rh}(\text{SPh})_2(\text{MeCN})]$  were active catalysts for the hydrothiolation of alkyl and aryl alkynes with thiophenol.<sup>78</sup> Oxidative addition of disulfides to  $[\text{Tp}^*\text{Rh}(\text{coe})(\text{MeCN})]$  generates the bithiolate complexes in which the MeCN is labile and useful for further substitution. Substitution of MeCN for  $\text{XyNC}$  on  $[\text{Tp}^*\text{Rh}(\text{SPh})_2(\text{MeCN})]$  generates  $[\text{Tp}^*\text{Rh}(\text{SPh})_2(\text{XyNC})]$ .  $[\text{Tp}^*\text{Rh}(p\text{-MeC}_6\text{H}_4\text{S})_2(\text{MeCN})]$ <sup>79</sup> and  $[\text{Tp}^*\text{Rh}(\text{SPh})_2(\text{XyNC})]$  were both characterized in the solid state and show to adopt a distorted octahedral structure in which the  $\text{Tp}^*$  is bound in a  $\kappa^3$  coordination mode. The MeCN ligand could also be displaced by a variety of terminal acetylenes, resulting in a rhodathiacyclobutene structure which was also characterized in the solid state (Scheme 2.5).



**Scheme 2.5. Rhodathiacyclobutene formed from  $[\text{Tp}^*\text{Rh}(\text{SPh})_2(\text{MeCN})]$  and phenylacetylene**

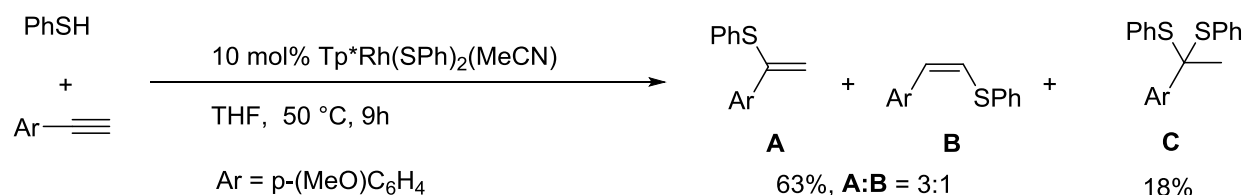
In the solution state, two species were observed by  $^1\text{H}$  NMR spectroscopy. The chemical shift and Rh-H coupling constant of the hydrogen directly bound to the rhodathiacyclobutene moiety were similar for both species. Therefore the authors concluded that inversion of the configuration of the sulfur atom within the rhodathiacyclobutene resulted in two diastereomers in solution (Scheme 2.6).



**Scheme 2.6. Rhodathiacyclobutene diastereomers due to sulfur inversion.**

The rhodathiacyclobutenes were found to be unstable in solution, decomposing to the branched vinyl sulfide  $\text{R}(\text{PhS})\text{C}=\text{CH}_2$  and an uncharacterized Rh species. Subsequently, both

[Tp\*Rh(coe)(MeCN)] and [Tp\*Rh(SPh)<sub>2</sub>(MeCN)] were found catalyze hydrothiolation of 3-phenylpropyne and 1-octyne by thiophenol regioselectively at 50 °C to generate the branched vinyl sulfide in 92% and 58% yield, respectively. [Tp\*Rh(coe)(MeCN)] was found to be less effective for the hydrothiolation of the aryl alkyne *p*-MeOC<sub>6</sub>H<sub>4</sub>CCH, while [Tp\*Rh(SPh)<sub>2</sub>(MeCN)] was found to give a mixture of isomers (Scheme 2.7). Notably, while [Tp\*Rh(PPh<sub>3</sub>)<sub>2</sub>] was found to give a small amount of the *E*-linear product as a minor isomer in less selective reactions, [Tp\*Rh(SPh)<sub>2</sub>(MeCN)] was found to give the *Z*-linear isomer **B** and thioketal product **C**.



**Scheme 2.7. Hydrothiolation of *p*-MeOC<sub>6</sub>H<sub>4</sub>CCH catalyzed by [Tp\*Rh(SPh)<sub>2</sub>(MeCN)].**

## 2.2 Hydroamination

In the past two decades, hydroamination has emerged as an excellent strategy for the synthesis of nitrogen-containing heterocycles, due to the availability of starting materials, the atom economic nature of hydroelementation reactions, and the variety of catalysts available with broad substrate scope. Several reviews have been written on hydroamination in recent years,<sup>80</sup> including reviews focused on the application of metal-free and late transition-metal catalysts,<sup>81</sup> earth abundant metal catalysts,<sup>82</sup> group 4 metal catalysts,<sup>83</sup> and lanthanide catalysts.<sup>84</sup> Hydroamination of alkenes and alkynes are particularly challenging, especially intermolecular

reactions, due to the near thermoneutral nature of such processes, coupled with high activation barriers.<sup>85</sup> Consequently, much of the research into metal-catalyzed hydroamination has been on the cyclization of aminoalkenes and aminoalkynes in order to reduce the entropic cost.<sup>86</sup>

Hydroamination of alkynes yields either imines or enamines, which are useful reagents for a wide variety of organic transformations. Hydroamination of olefins yields alkaloids, which are present in a wide variety of biologically and pharmaceutically active compounds (Figure 2.4). These compounds typically contain several stereocenters; thus catalysts capable of high stereoselectivity and functional group tolerance have the potential to be highly effective in synthetic applications. Herein we will discuss the application of scorpionate complexes to inter- and intra-molecular hydroamination of alkenes and alkynes.

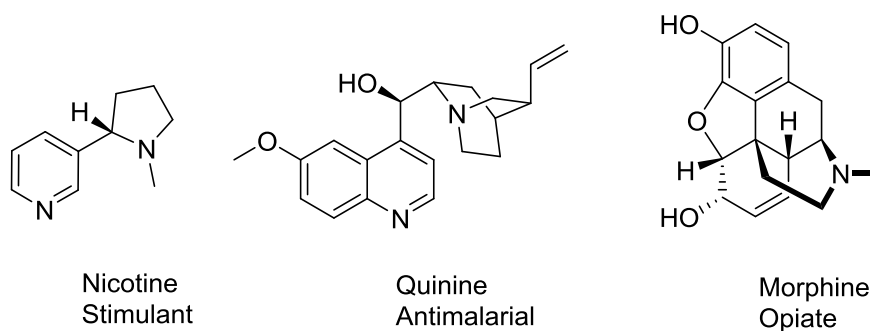
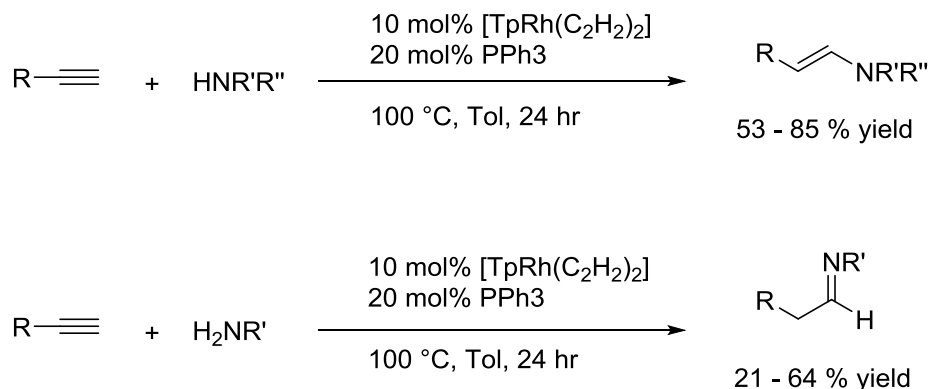


**Figure 2.4. Selected alkaloids**

### 2.2.1 Hydroamination with Homoscorpionate Ligands

The first use of a tridentate scorpionate ligand in metal-catalyzed olefin hydroamination was reported by Fukumoto *et al* in 2007.<sup>87</sup> The authors report the use of  $[\text{TpRh}(\text{C}_2\text{H}_4)_2]$  in the presence of  $\text{PPh}_3$  to catalyze the intermolecular hydroamination of alkynes. Both primary and secondary amines were viable substrates, generating the corresponding imines and enamines

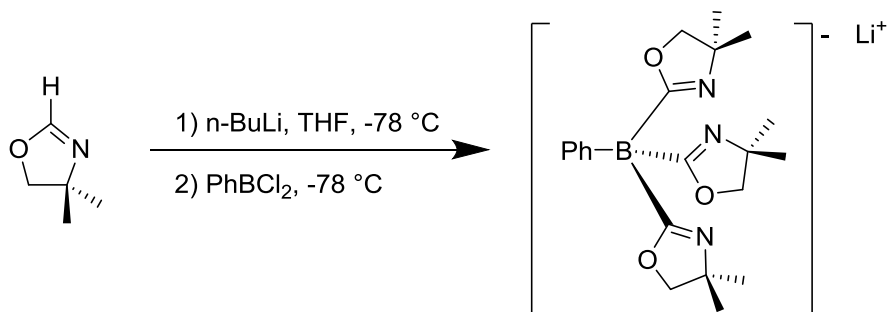
resulting from anti-Markovnikov addition (Scheme 2.8). Anti-Markovnikov selectivity with both primary and secondary amines is notable, since mechanistic constraints (e.g., formation of a metal-imido species) typically restrict reactions to one or the other.<sup>88</sup> Treatment of [RhCl(PPh<sub>3</sub>)<sub>3</sub>] with KTp in situ generated nearly identical reactivity, however internal alkynes were unreactive substrates. Tris(pyrazolyl)borate complexes of rhodium are well known to activate the C-H bond of terminal alkynes.<sup>67,89</sup> Therefore, it is likely the reaction proceeds through a rhodium vinylidene species. This explains the reactivity with both primary and secondary amines as well as the lack of reactivity with internal alkynes. The catalyst system was tolerant of siloxy, ester and cyano functionality but surprisingly primary amines were unreactive towards benzylic or aromatic alkynes.



**Scheme 2.8.** [TpRh(C<sub>2</sub>H<sub>4</sub>)<sub>2</sub>]/PPh<sub>3</sub> catalyzed intermolecular hydroamination

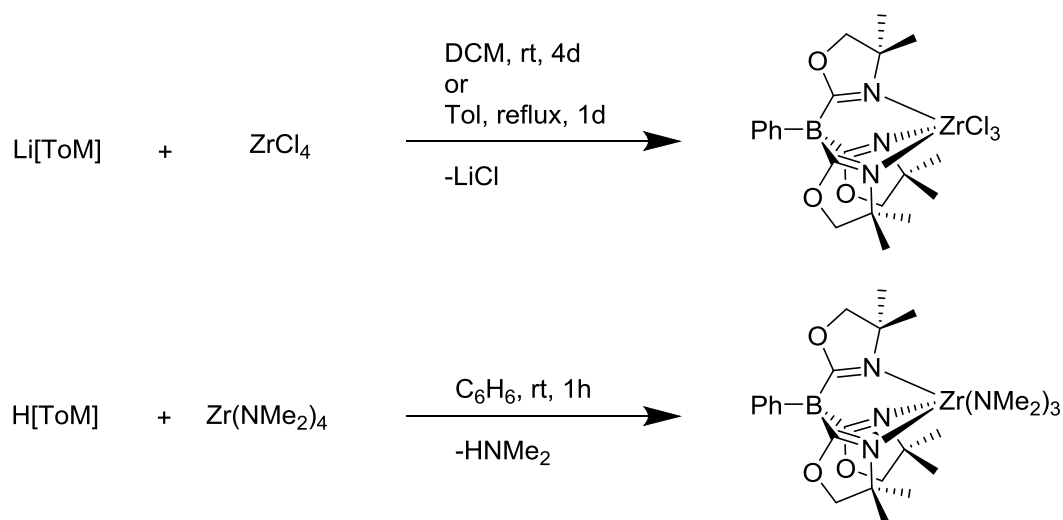
Beginning in 2009,<sup>90</sup> the Sadow group has published several reports of the use of oxazolanyl borate scorpionate ligands in hydroamination reactions. They had previously described a facile synthesis of the first tris(oxazolanyl)borate ligand and zirconium complexes

thereof in 2008 (Scheme 2.9).<sup>91</sup> Careful control of stoichiometry is required to avoid potential side reactions.



**Scheme 2.9. Synthesis of tris(oxazolinyl)borato ligands**

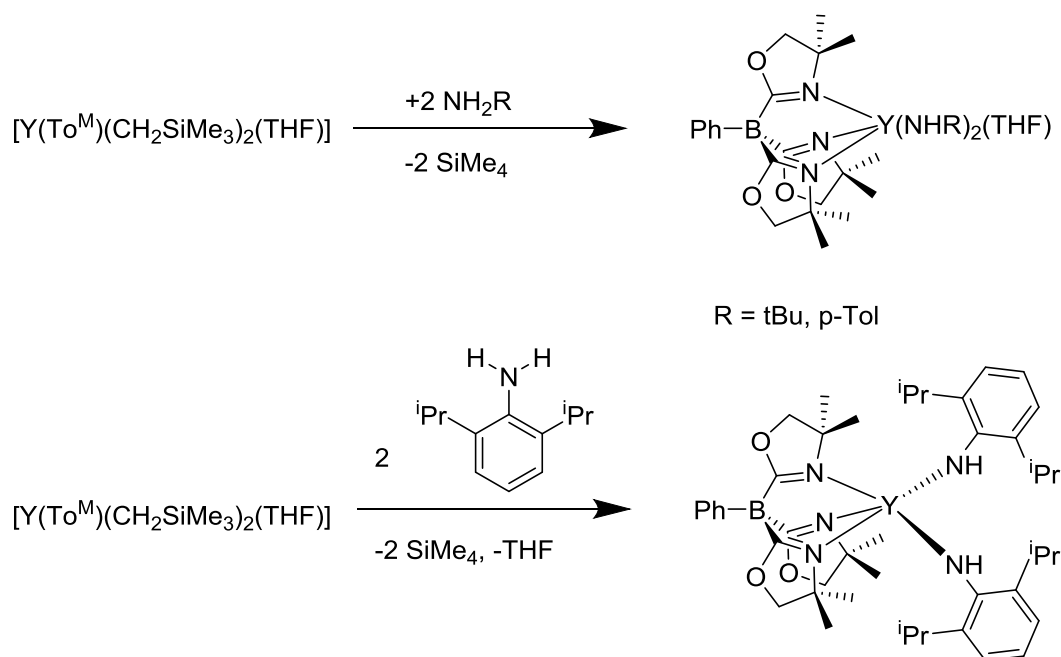
The resulting lithium salt was shown to react with  $\text{ZrCl}_4$  to form  $[\text{Zr}(\kappa^3\text{-To}^{\text{M}})\text{Cl}_3]$  via salt metathesis. The acidic proligand,  $\text{H}[\text{To}^{\text{M}}]$ , prepared from  $\text{Li}[\text{To}^{\text{M}}]$  by silica gel flash chromatography, was found to react with  $\text{Zr}(\text{NMe}_2)_4$  via amine elimination to produce the  $\text{C}_{3v}$  symmetric complex  $[\text{Zr}(\kappa^3\text{-To}^{\text{M}})(\text{NMe}_2)_3]$  (Scheme 2.10). Both complexes exhibit a single C=N IR stretching frequency and a single set of  $^1\text{H}$  NMR resonances, consistent with a  $\text{C}_{3v}$  symmetric complex and  $\kappa^3$  coordination mode of the ligand. Characterization of  $[\text{Zr}(\kappa^3\text{-To}^{\text{M}})\text{Cl}_2(\text{O}-t\text{Bu})]$ , synthesized via salt metathesis from  $[\text{Zr}(\kappa^3\text{-To}^{\text{M}})\text{Cl}_3]$  and  $\text{KO}-t\text{Bu}$ , in the solid state confirmed  $\kappa^3$  coordination mode of the ligand.



### Scheme 2.10. Zirconium complexes of $\text{To}^{\text{M}}$

In 2009, Sadow and co-workers reported the synthesis of a series of yttrium complexes of  $\text{To}^{\text{M}}$ . Proligand  $\text{H[To}^{\text{M}}]$  was reacted with  $[\text{Y}(\text{CH}_2\text{SiMe}_3)_3(\text{THF})_2]$  in THF to yield  $[\text{Y}(\kappa^3\text{-To}^{\text{M}})(\text{CH}_2\text{SiMe}_3)_2(\text{THF})]$ . Again, crystallographic evidence confirmed the  $\kappa^3$  N,N,N tridentate fac coordination mode of the  $\text{To}^{\text{M}}$  ligand. Surprisingly, the  $^1\text{H}$  NMR spectrum of  $[\text{Y}(\kappa^3\text{-To}^{\text{M}})(\text{CH}_2\text{SiMe}_3)_2(\text{THF})]$  revealed a single set of resonances for the  $\text{To}^{\text{M}}$  ligand consistent with a  $\text{C}_{3v}$  symmetric structure in solution. The authors were able to establish that this was due to rapid dissociative exchange of the bound THF ligand and not oxazoline arm dissociation.

The reaction of  $[\text{Y}(\kappa^3\text{-To}^{\text{M}})(\text{CH}_2\text{SiMe}_3)_3(\text{THF})]$  with triphenylphosphine oxide in benzene yielded the corresponding complex  $[\text{Y}(\kappa^3\text{-To}^{\text{M}})(\text{CH}_2\text{SiMe}_3)_3(\text{OPPh}_3)]$ . Protonolysis of the alkyl fragments with primary amines generated the corresponding bis-amide six-coordinate complexes for  $^t\text{BuNH}_2$  and  $p\text{-TolNH}_2$ . In comparison, the bulkier 2,6-diisopropylaniline yielded the five-coordinate complex lacking a bound THF (Scheme 2.11).

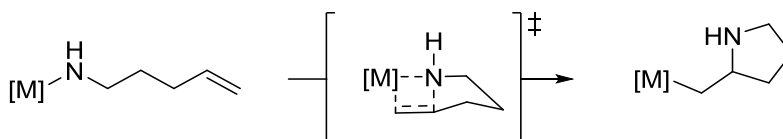


**Scheme 2.11. Yttrium amide complexes of To<sup>M</sup>**

With a series of yttrium To<sup>M</sup> complexes in hand, Sadow and co-workers investigated their activity in intramolecular olefin hydroamination. The authors report that [Y(To<sup>M</sup>)(CH<sub>2</sub>SiMe<sub>3</sub>)<sub>2</sub>(THF)], [Y(To<sup>M</sup>)(CH<sub>2</sub>SiMe<sub>3</sub>)<sub>2</sub>(OPPH<sub>3</sub>)], and [Y(To<sup>M</sup>)(NH-2,6-*i*-Pr-C<sub>6</sub>H<sub>3</sub>)<sub>2</sub>] are all modestly active catalysts for the hydroamination of geminal di-substituted amino olefins for both primary and secondary amines with turnover rates in the range of 1.9 to 9 h<sup>-1</sup>. Aminoalkenes lacking gem di-substitution produced only trace amounts of product. Despite their lower activities compared to their bidentate Ph<sub>2</sub>Box counterparts (Ph<sub>2</sub>Box = bis(oxazoninato)diphenylmethane),<sup>92</sup> the authors were encouraged to find that the coordinatively unsaturated compound [Y(To<sup>M</sup>)(NH-2,6-*i*-Pr-C<sub>6</sub>H<sub>3</sub>)<sub>2</sub>] showed the highest activity. The authors attributed this enhanced reactivity to greater concentration of five-coordinate species in solution, suggesting that bulkier tris(oxazoliny)borato ligands may enhance reactivity.

Subsequently, the Sadow group reported in 2010 the synthesis and hydroamination reactivity of the four-coordinate magnesium complex  $[\text{To}^{\text{M}}\text{MgMe}]$ .<sup>93</sup> Synthesized from  $\text{MgMe}_2(\text{O}_2\text{C}_4\text{H}_8)_2$ , the  $\text{To}^{\text{M}}$  ligand was again shown to bind in a  $\kappa^3$  coordination mode. There was no fluxionality observed in the solution phase, even when heated to 150 °C, and no exchange processes were observed upon addition of THF or dioxane, suggesting that the  $\text{To}^{\text{M}}$  ligand retains a rigid  $\kappa^3$  coordination mode and that there is no vacant coordination site. Despite these observations,  $[\text{To}^{\text{M}}\text{MgMe}]$  was found to be a competent catalyst for the cyclization of gem di-substituted aminoalkenes at 50 °C in benzene. Once again, substrates lacking geminal di-substitution were non-reactive.

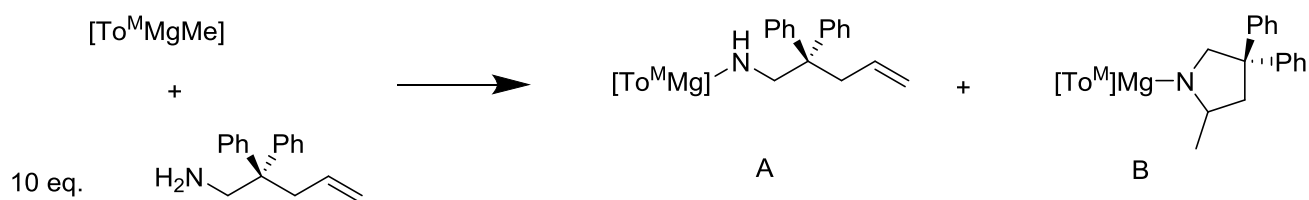
Typically, metal catalyzed intramolecular hydroamination is characterized by an empirical rate law which is zero-order in substrate (i.e.  $-\text{d}[\text{substrate}]/\text{dt} = k_{\text{obs}}[\text{catalyst}]^1[\text{substrate}]^0$ ). This result is commonly attributed to rate-limiting intramolecular insertion of the olefin into the metal-nitrogen bond (Scheme 2.12).<sup>94</sup>



**Scheme 2.12. Intramolecular olefin insertion into metal-amide bonds.**

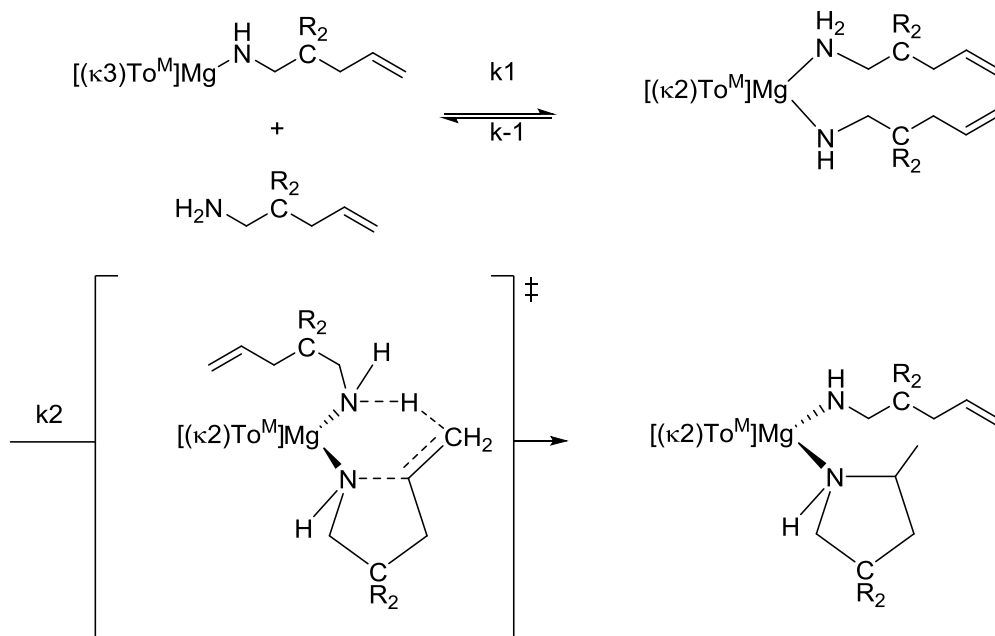
Intrigued by the hydroamination reactivity of  $[\text{To}^{\text{M}}\text{MgMe}]$  despite the lack of open coordination sites, Sadow *et al* proceeded to investigate the mechanism of  $[\text{To}^{\text{M}}\text{MgMe}]$ -catalyzed intramolecular hydroamination. Kinetic experiments revealed a large primary kinetic isotope effect and first order dependence on substrate concentration. Two  $\text{To}^{\text{M}}\text{Mg}$  containing

species were observed during catalytic reactions, synthesized independently and characterized as compounds **A** and **B** (Scheme 2.13). Remarkably, despite catalysis occurring readily at 50 °C, no product or cyclization was observed when compound **A** was heated to 100 °C. Compound **A** was, however, readily converted to compound **B** upon addition of a small amount (0.01 eq.) of the aminoalkene.



**Scheme 2.13. Observed magnesium amidoalkene and pyrrolide complexes.**

Examining the homoleptic  $[(\text{To}^{\text{M}})_2\text{Mg}]$  complex, in which both  $\text{To}^{\text{M}}$  ligands are coordinated in a bidentate  $\kappa^2$  mode, the authors found that the rate of dissociative exchange of the oxazoline arms is significantly faster than rate of product formation in the catalytic system. Consequently, the authors proposed a six-centered transition state involving concerted C-N and C-H bond formation (Scheme 2.14). However it should be noted that a computational study has revealed that the mechanism for  $[\text{To}^{\text{M}}\text{MgMe}]$ -catalyzed hydroamination actually consists of a reversible insertion, followed by rate-limiting protonolysis.<sup>95</sup>

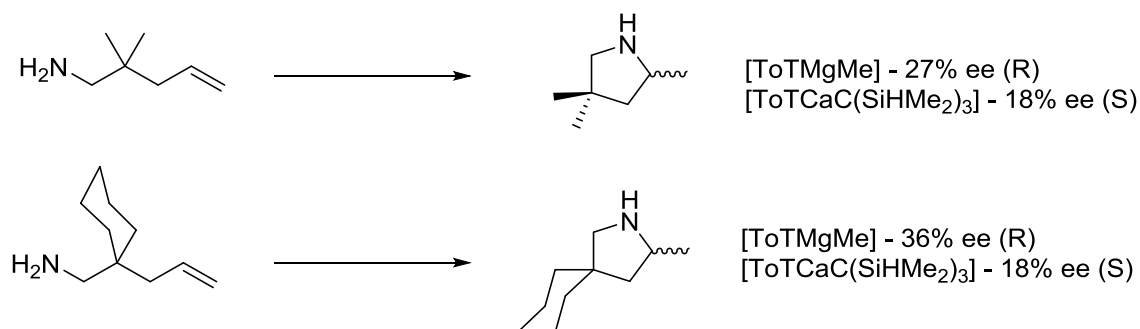


**Scheme 2.14. Proposed mechanism for  $To^M$  Mg-mediated aminoalkene hydroamination.**

The Sadow group then proceeded to investigate optically active analogues of the  $To^M$  ligand. In 2011, they reported the synthesis and Mg and Ca complexes of optically active tris(4*S*-isopropyl-2-oxazolinyl)phenylborate ( $To^P$ ) and tris(4-*S*-*tert*-butyl-2-oxazolinyl)phenylborate ( $To^T$ ).<sup>96</sup>  $[To^T MgMe]$ , synthesized from  $H[To^T]$  and  $MgMe_2(O_2C_4H_8)_2$ , exhibits similar characteristics to  $[To^M MgMe]$ . The three oxazoline rings are equivalent, based on  $^1H$  NMR spectroscopy, indicating pseudo  $C_3$  symmetry (due to free rotation of the B- $C_{phenyl}$  bond). A single C=N stretching frequency in the IR spectrum and a single  $^{15}N$  resonance in the  $^1H$ - $^{15}N$  HMBC spectrum are consistent with  $\kappa^3$  coordination of the  $To^T$  ligand, confirmed by solid state structure. Analogous to  $[To^M MgMe]$ , no changes in the  $^1H$  NMR spectrum of  $[To^T MgMe]$  were observed after heating to 120 °C for 5 days. Interestingly, the related four-coordinate  $[To^T CaC(SiHMe_2)_3]$  complex was found to be stabilized by  $\beta$ -agostic Si-H

interactions observed by both  $^{15}\text{N}$  NMR and IR spectroscopy. No evidence of an uncoordinated oxazoline arm was observed for  $[\text{To}^{\text{T}}\text{CaC}(\text{SiHMe}_2)_3]$ .

Although both  $[\text{To}^{\text{T}}\text{MgMe}]$  and  $[\text{To}^{\text{T}}\text{CaC}(\text{SiHMe}_2)_3]$  were found to be active catalysts for the cyclization of 2,2-diphenyl-1-amino-pent-4-ene, both complexes yielded a racemic mixture. More encouraging were the cyclizations of 2,2-dimethyl-1-amino-pent-4-ene and C-(1-allyl-cyclohexyl)-methylamine. Interestingly, the Mg complex was found to give R enantiomers while the Ca complex gave rise to the S enantiomers (Scheme 2.15).



**Scheme 2.15. Enantioselective cyclizations of aminoalkenes catalyzed by  $[\text{To}^{\text{T}}\text{MgMe}]$  and  $[\text{To}^{\text{T}}\text{CaC}(\text{SiHMe}_2)_3]$**

## 2.2.2 Hydroamination with Heteroscorpionate Ligands

First reported by the Sadow group in 2010,<sup>97</sup> metal complexes of heteroscorpionate borate ligands containing two oxazole rings and a cyclopentadienyl ring were found to be highly effective catalysts for hydroamination/cyclization of aminoalkenes and aminoalkynes. In their initial report, the authors describe the synthesis and characterization of zirconium and hafnium complexes of the achiral  $\text{PhB}(\text{C}_5\text{H}_4)(\text{Ox}^{\text{Me}_2})_2$  ligand (Scheme 2.16). Synthesized from the

corresponding  $M(\text{NMe}_2)_4$  complexes, both  $[\{\text{PhB}(\text{C}_5\text{H}_4)(\text{Ox}^{\text{Me}_2})_2\}M(\text{NMe}_2)_2]$  ( $M = \text{Zr}, \text{Hf}$ ) exhibit a single set of diastereotopic oxazoline resonances in the  $^1\text{H}$  NMR spectrum and a single  $\text{C}=\text{N}$  stretching frequency for amorphous solids in the IR spectrum, suggesting both oxazoline arms are coordinated to the metal center or rapid exchange between bound and unbound oxazoline arms. No fluxionality was observed over the temperature range from 190 K to 300 K. The solid state structure of  $[\text{PhB}(\text{C}_5\text{H}_4)(\text{Ox}^{\text{Me}_2})_2\text{Zr}(\text{NMe}_2)_2]$  was not reported until 2013.<sup>98</sup> Both this complex and the THF adduct crystallize with a single oxazoline arm bound to the metal center. It is worthwhile noting that crystalline  $[\text{PhB}(\text{C}_5\text{H}_4)(\text{Ox}^{\text{Me}_2})_2\text{Zr}(\text{NMe}_2)_2]$  exhibited two  $\text{C}=\text{N}$  stretching frequencies in the IR, similar to its THF adduct.  $[\text{PhB}(\text{C}_5\text{H}_4)(\text{Ox}^{\text{Me}_2})_2\text{Zr}(\text{NMe}_2)_2]$  was reported to catalyze the cyclization for primary aminoalkenes at room temperature, uncommon for group 4 catalysts. Secondary amines were found to be unreactive.



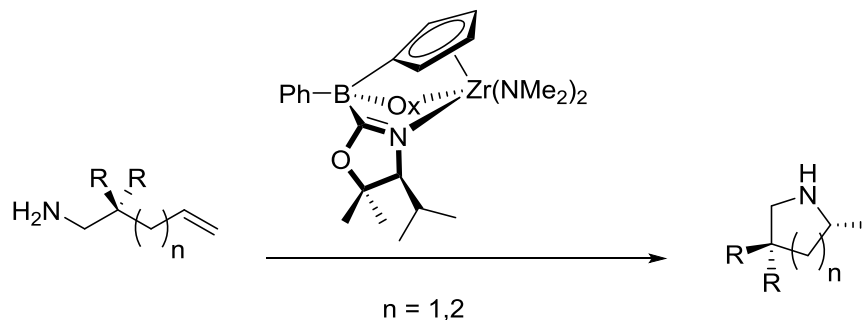
**Scheme 2.16. Heteroscorpionate complexes of Zr and Hf.**

Having shown that heteroscorpionate zirconium complexes are highly effective catalysts for the cyclization of aminoalkenes, the Sadow group then turned their attention to optically active heteroscorpionate ligands. In 2011, the Sadow group reported that the optically active complex  $[\{\text{PhB}(\text{S-Ox}^{\text{iPr,Me}_2})_2(\text{C}_5\text{H}_4)\}\text{Zr}(\text{NMe}_2)_2]$  catalyzed the cyclizations of a variety of aminoalkenes at room temperature in both high conversion and high enantioselectivity (Table 2.2).<sup>99</sup> Notably, aminoalkenes lacking geminal disubstitution were also active substrates.

Secondary amines were once again found to be unreactive unless a small amount of primary amine was added.

Intrigued by the high reactivity even at low temperature and the lack of reactivity of secondary amines, the authors set out to determine the mechanism of  $[\{\text{PhB}(\text{S-Ox}^{\text{iPr,Me}_2})_2(\text{C}_5\text{H}_4)\}\text{Zr}(\text{NMe}_2)_2]$  catalyzed hydroamination. Similar to the results obtained for  $\text{To}^{\text{M}}\text{MgMe}$  catalyzed hydroamination, the authors discovered a large kinetic isotope effect and first order dependence on aminoalkene concentration. Interestingly, stereoselectivity was found to increase upon isotopic substitution (i.e. ee% was found to be higher for  $\text{ND}_2\text{R}$  compared to  $\text{NH}_2\text{R}$ ). This suggested that N-H bond cleavage was involved in both the turn-over limiting and stereochemistry determining step(s). The data was determined to be inconsistent with 1,2-insertion of the olefin into a Zr-N bond. Instead, a similar mechanism to that shown in Scheme 2.14 was proposed.

**Table 2.2.**  $[\text{PhB}(\text{S-Ox}^{\text{iPr,Me}_2})_2(\text{C}_5\text{H}_4)\text{Zr}(\text{NMe}_2)_2]$  catalyzed cyclization of aminoalkenes



Entry	aminoalkene	Time (h)	Conversion (%)	ee (%)
1		1.25	>95	93
2		1.25	>95	90
3		4	88	92
4		7	89	89
5		5	24	n/a
6		40	48	31
7		30	65	46

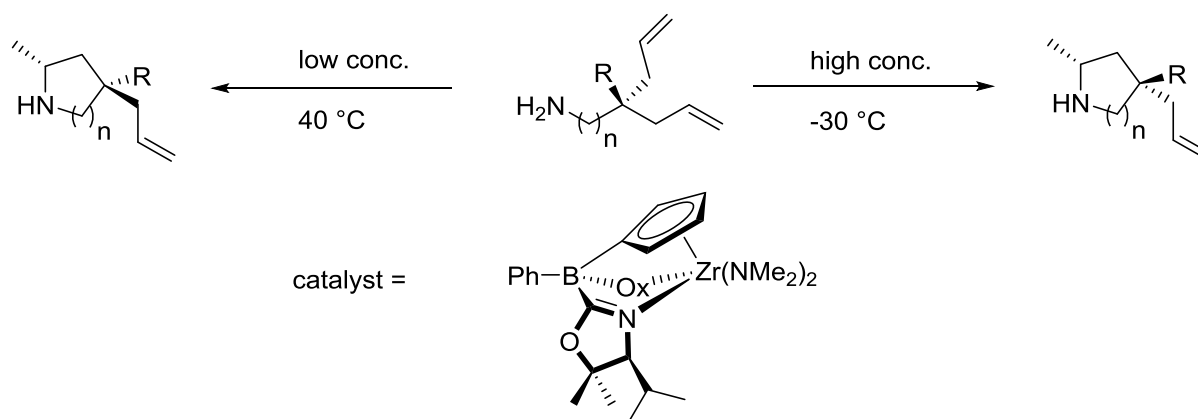
In the same year, the Sadow group examined the related yttrium complex  $[\{\text{PhB}(\text{S-Ox}^{\text{iPr,Me}_2})_2(\text{C}_5\text{H}_4)\}\text{Y}(\text{CH}_2\text{SiMe}_3)]$  and zirconium and yttrium complexes of the heteroscorpionate ligand  $\{\text{PhB}(\text{S-Ox}^{\text{tBu}})_2\}$  lacking the geminal dimethyl substitution on the oxazoline rings.<sup>100</sup> While  $[\{\text{PhB}(\text{S-Ox}^{\text{iPr,Me}_2})_2(\text{C}_5\text{H}_4)\}\text{Y}(\text{CH}_2\text{SiMe}_3)]$  was found to give low conversions,  $[\{\text{PhB}(\text{S-Ox}^{\text{tBu}})_2\}\text{Y}(\text{CH}_2\text{SiMe}_3)]$  was found to give very high conversions (95-100%) within minutes at

room temperature in high enantiomeric excess ranging from 89-96%. The yttrium complexes were found to give the opposite enantiomer compared to the zirconium complexes. Kinetic analysis revealed many similarities between the yttrium and zirconium systems (first-order dependence on substrate, large primary KIEs, enzyme-like rate laws). The only difference between the two systems – other than yielding opposite absolute configurations – was that ee% was found to decrease upon N-deuteration for  $[\{\text{PhB}(\text{S-Ox}^{\text{tBu}})_2\}\text{Y}(\text{CH}_2\text{SiMe}_3)]$  catalyzed hydroamination. Nevertheless, due to the numerous similarities between the two systems, a similar mechanism of concerted C-N and C-H bond formation was proposed for yttrium.

In 2013, the Sadow group expanded their heteroscorpionate ligand set to include complexes of titanium and hafnium.<sup>98</sup> In general, the zirconium complexes were found to be much more reactive than their hafnium or titanium counterparts, while titanium complexes were found to give much lower ee's than the zirconium and hafnium complexes. In contrast to the yttrium system described above,  $\{\text{PhB}(\text{Ox}^{\text{iPr,Me}_2})_2(\text{C}_5\text{H}_4)\}$  complexes of Zr, Hf and Ti consistently gave higher ee's than the *tert*-Bu substituted oxazoline ligand.

In order to determine the effect of having two oxazoline arms, the authors synthesized the corresponding bidentate complex lacking a second oxazoline arm. In stark contrast to their tridentate counterparts, no hydroamination activity was observed for this complex even after heating at 120 °C for four days. The authors also found that the mono-amide complex  $[\{\text{PhB}(\text{S-Ox}^{\text{iPr,Me}_2})_2(\text{C}_5\text{H}_4)\}\text{Zr}(\text{NMe}_2)\text{Cl}]$  was not active for hydroamination. This is in contrast to the related systems reported by Marks and co-workers, where the mixed  $[\{\text{CG}\}\text{Zr}(\text{NMe}_2)\text{Cl}]$  (CG =  $\text{Me}_2\text{Si}(\text{C}_5\text{H}_4)\text{N-}^t\text{Bu}$ ) was found to be more reactive than its diamide counterpart.<sup>101</sup> Also in contrast to the results obtained by Sadow and coworkers, Marks and co-workers found strong evidence supporting a M-N alkene/alkyne insertion mechanism.

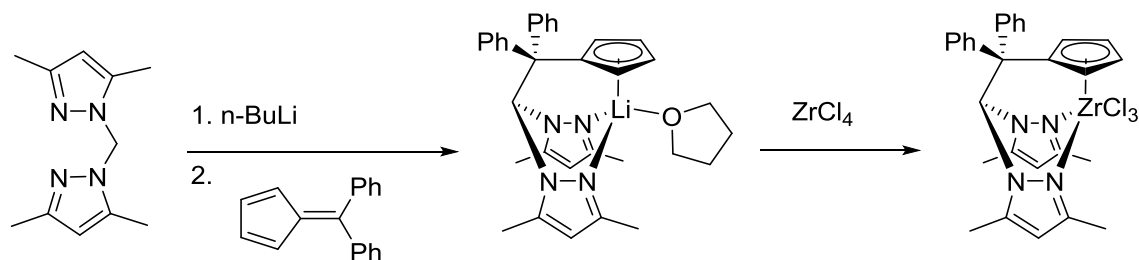
Finally, the Sadow group recently reported that the  $[\{\text{PhB}(\text{S-Ox}^{\text{iPr,Me}_2})_2(\text{C}_5\text{H}_4)\}\text{Zr}(\text{NMe}_2)_2]$  complex was highly effective for the catalytic desymmetrization of aminodialkenes and aminodialkynes.<sup>102</sup> Remarkably, *cis* or *trans* products could be obtained in high ee's (92 – 99%) and good d.r.'s (up to 43 : 1 for N-deutero substrates) with the same complex by varying the temperature and concentration of the reaction (Scheme 2.17). And since the *R* enantiomer of the heteroscorpionate ligand reverses the absolute configuration of the stereocenter adjacent to the nitrogen, all four stereoisomeric products can be accessed readily. Thus two stereocenters can be set with high fidelity from a single achiral starting material.



**Scheme 2.17.**  $[\{\text{PhB}(\text{S-Ox}^{\text{iPr,Me}_2})_2(\text{C}_5\text{H}_4)\}\text{Zr}(\text{NMe}_2)_2]$  catalyzed desymmetrization of aminoalkenes.

While the Sadow group thoroughly explored Group 3 and Group 4 heteroscorpionate complexes in hydroamination, Otero *et al* expanded the utility of heteroscorpionate complexes in hydroamination to lutetium.<sup>103</sup> The group had previously reported the synthesis of the heteroscorpionate 2,2-bis(3,5-dimethylpyrazol-1-yl)-1,1-diphenylethylcyclopentadienyl (bpzcp)

ligand (Scheme 2.18) in THF.<sup>104</sup> Reaction of the resulting lithium salt with ZrCl<sub>4</sub> yielded [(bpzcp)ZrCl<sub>3</sub>] complex via salt metathesis. The <sup>1</sup>H NMR spectra of [(bpzcp)ZrCl<sub>3</sub>] were consistent with  $\kappa^3$  coordination of the heteroscorpionate ligand, and this binding mode was confirmed in the solid state structure.

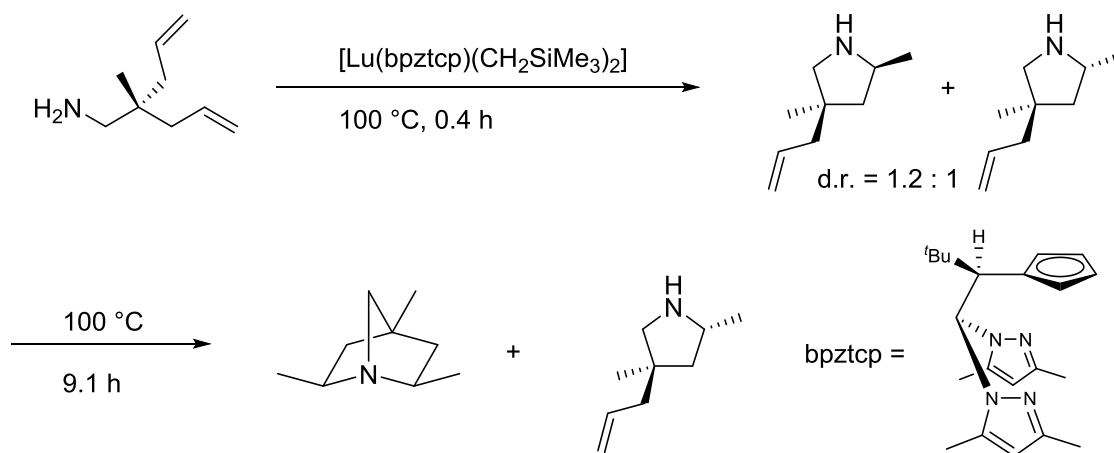


**Scheme 2.18. Synthesis of [ZrCl<sub>3</sub>(bpzcp)]**

The mono *tert*-butyl substituted analogue 2,2-bis(3,5-dimethylpyrazol-1-yl)- 1-*tert*-butylethylcyclopentadienyl (bpztcp) was synthesized in similar fashion. Surprisingly, enantiomerically enriched [Lu(bpztcp)(CH<sub>2</sub>SiMe<sub>3</sub>)<sub>2</sub>(THF)] was obtained by spontaneous resolution and preferential crystallization, although the authors were not able to ascertain the value of enantiomeric excess. <sup>1</sup>H NMR spectra of both compounds were consistent with  $\kappa^3$ -NN- $\eta^5$ -Cp coordination mode of the heteroscorpionate ligands, further confirmed through solid state structure analysis.

Both [Lu(bpzcp)(CH<sub>2</sub>SiMe<sub>3</sub>)<sub>2</sub>] and [Lu(bpztcp)(CH<sub>2</sub>SiMe<sub>3</sub>)<sub>2</sub>] and enantiomerically enriched [Lu(bpztcp)(CH<sub>2</sub>SiMe<sub>3</sub>)<sub>2</sub>] were found to be efficient catalysts for the hydroamination/cyclization of aminopentenes at room temperature in 90-99% conversion. The racemic complexes gave racemic products as expected, while enantiomerically enriched

[Lu(bpztcp)(CH<sub>2</sub>SiMe<sub>3</sub>)<sub>2</sub>] yielded the corresponding pyrrolidines in up to 66% ee. Although the ee's are considerably lower than those of Sadow's zirconium heteroscorpionate complexes, the yields and turn-over frequencies are comparable. Although no bicyclic products were detected in the [{PhB(S-Ox<sup>iPr,Me2</sup>)<sub>2</sub>(C<sub>5</sub>H<sub>4</sub>)}Zr(NMe<sub>2</sub>)<sub>2</sub>] catalyzed cyclization of aminodialkenes and aminodialkynes, extended reaction times in the [Lu(bpztcp)(CH<sub>2</sub>SiMe<sub>3</sub>)<sub>2</sub>] catalyzed hydroamination of aminodialkenes yielded a mixture of the pyrrolidine minor diastereomer and the bicyclic product with high diastereoselectivity for the *exo,exo* product (Scheme 2.19).



**Scheme 2.19.** [Lu(bpztcp)(CH<sub>2</sub>SiMe<sub>3</sub>)<sub>2</sub>] catalyzed bicyclization of aminodialkenes.

### 2.3 Hydroalkoxylation of Alkynes

The addition of alcohols to alkynes generates enol ethers and oxygen-containing heterocycles, while the cyclization of alkynyl benzoic acids generates isocoumarin and phthalide compounds. These molecules, notably phthalides, are important classes of compounds with wide-ranging biological activities, and have also been used as synthons in the total synthesis of complex natural products (e.g. (-)-tetracycline) (Figure 2.5).<sup>105</sup> Weak bases and strong acids can

catalyze hydroalkoxylation, and has been used in the synthesis of Thunberginol A.<sup>106</sup> Regioselectivity in intramolecular reactions can be achieved, however diastereoselectivity is a challenge. Intermolecular reactions are more challenging still. Thus transition-metal complexes capable of achieving high selectivity have become a desirable alternative to traditional methods. The applications of gold catalysts<sup>107</sup> and organo-f-element catalysts<sup>74</sup> for the hydroalkoxylation of alkynes have recently been reviewed.

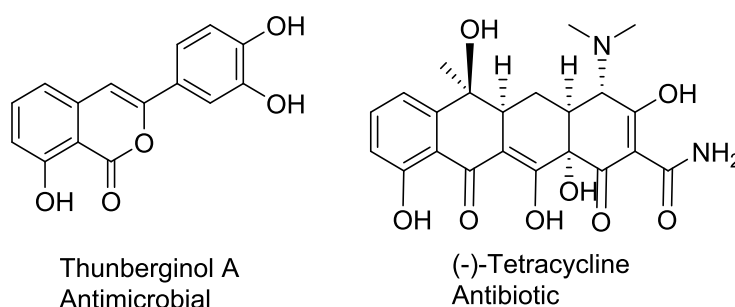


**Figure 2.5. Thunberginol A and (-)-Tetracycline**

### 2.3.1 Cyclization of Alkynoic Acids

Messerle and co-workers first reported the cyclization of alkynoic acids in 2011.<sup>108</sup> In this initial report, neutral tris(pyrazol-1-yl)toluidine (tpt) and tris(*N*-methylimidazol-2-yl)methanol (tim) ligands were examined (Figure 2.6). A series of six cationic complexes,  $[\text{Rh}(p\text{-tpt})(\text{L}_2)](\text{B}_{\text{Ar}}^{\text{F}})$  and  $[\text{Rh}(o\text{-tpt})(\text{L}_2)](\text{B}_{\text{Ar}}^{\text{F}})$  ( $\text{L} = \text{COD}, \text{NBD}, \text{CO}$ ), were synthesized from the corresponding  $[\text{Rh}(\text{L}_2)](\text{B}_{\text{Ar}}^{\text{F}})$  complexes in yields ranging from 58-98%.  $[\text{Rh}(\text{tim})(\text{L}_2)](\text{B}_{\text{Ar}}^{\text{F}})$  complexes ( $\text{L}_2 = \text{COD}, \text{CO}$ ) were also synthesized in the same manner in 70% and 57% yield respectively.

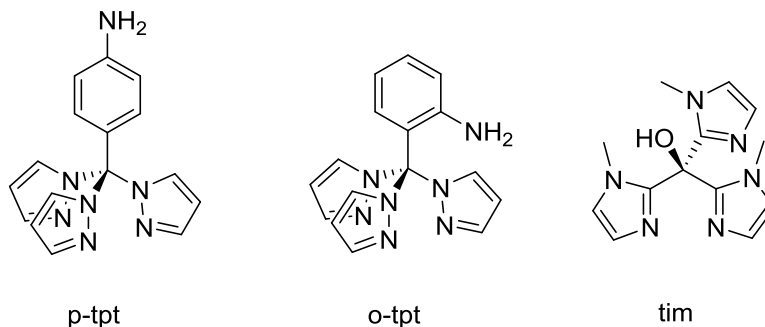


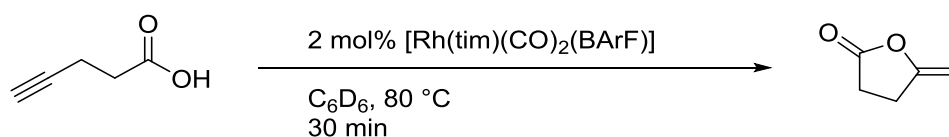
**Figure 2.6. Tris(pyrazol-1-yl)toluidine ligands, *p*-tpt and *o*-tpt, and the tris(*N*-methylimidazol-2-yl)methanol ligand (tim).**

The solid state structures of all structures examined were found to adopt distorted square planar structures in which the scorpionate ligands were coordinated in a  $\kappa^2$  binding mode. Unlike the analogous tris(3,5-dimethylpyrazol-1-yl)methane complexes of Rh<sup>I</sup> reported by Hallet *et al*<sup>109</sup> and Adams *et al*,<sup>110</sup> in which the smaller NBD and CO ligands induced a  $\kappa^3$  binding mode, the coordination mode of the tpt and tim scorpionate ligands were unaffected by the choice of ancillary ligand. The geometry of the scorpionate ligand however was found to be dependent on the ancillary ligand. The third pyrazole arm was positioned away from the Rh center in the solid state for both [Rh(*p*-tpt)(NBD)](B<sub>Ar</sub><sup>F</sup>) and [Rh(*p*-tpt)(COD)](B<sub>Ar</sub><sup>F</sup>), with the phenyl ring positioned above the Rh center, whereas the pyrazole ring was positioned over the Rh center in [Rh(*p*-tpt)(CO)<sub>2</sub>](B<sub>Ar</sub><sup>F</sup>). [Rh(*o*-tpt)(COD)](B<sub>Ar</sub><sup>F</sup>) crystallized as two geometric isomers, one with the third unbound pyrazole positioned above the Rh center and one with the phenyl ring above the rhodium center. The [Rh(*o*-tpt)(CO)<sub>2</sub>](B<sub>Ar</sub><sup>F</sup>) complex however crystallized exclusively with the pyrazole arm positioned above the Rh center.

Low temperature  $^1\text{H}$  NMR spectra of all three complexes of  $[\text{Rh}^{\text{I}}(p\text{-tpt})(\text{L}_2)](\text{B}_{\text{Ar}}^{\text{F}})$  showed two equivalent pyrazole rings and a third one in a different chemical environment, consistent with the  $\kappa^2$  binding mode observed in the solid state. The resonances were found to broaden upon warming to room temperature, suggesting either exchange processes between  $\kappa^2$  and  $\kappa^3$  modes or rotation of the toluidine ring. Low temperature  $^1\text{H}$  NMR spectroscopy of  $[\text{Rh}(o\text{-tpt})(\text{COD})](\text{B}_{\text{Ar}}^{\text{F}})$ , on the other hand, showed three distinct chemical environments for the three pyrazole rings, as well as a minor isomer. NOESY cross peaks suggested exchange between the major and minor isomers, while  $^1\text{H}$ - $^{13}\text{C}$  HMBC correlation revealed only a small (0.7 ppm) difference in chemical shift of the bridging carbon between the two isomers. It was thus concluded that the two isomers were due to restricted rotation of the toluidine substituent about bond between the bridging carbon and the aryl carbon.  $[\text{Rh}(\text{tim})(\text{L}_2)](\text{B}_{\text{Ar}}^{\text{F}})$  ( $\text{L} = \text{COD}, \text{CO}$ ) also crystallized with the ligand in a  $\kappa^2$  coordination mode with the third imidazole ring positioned away from the RH center. However the  $^1\text{H}$  NMR spectra for both complexes shows a single set of resonances for all three imidazolyl rings. Cooling the solution to  $-90\text{ }^\circ\text{C}$  did not resolve the resonances due to the ligand, suggesting rapid interconversion between  $\kappa^2$  and  $\kappa^3$  binding modes.

Having established the solid phase and solution phase structures for a series of complexes, the authors then evaluated their catalytic activity for the cyclization of 4-pentynoic acid.  $[\text{Rh}(\text{tim})(\text{CO})_2](\text{B}_{\text{Ar}}^{\text{F}})$  was found to be the most active of the series, requiring only 30 min at  $80\text{ }^\circ\text{C}$  for complete conversion (Scheme 2.20).  $[\text{Rh}(p\text{-tpt})(\text{CO})_2](\text{B}_{\text{Ar}}^{\text{F}})$  reacted significantly faster than the  $[\text{Rh}(o\text{-tpt})(\text{CO})_2](\text{B}_{\text{Ar}}^{\text{F}})$  suggesting the position of the amine has a large impact on reactivity. To determine the effect of a third unbound donor on reactivity,  $[\text{Rh}(\text{bim})(\text{CO})_2](\text{B}_{\text{Ar}}^{\text{F}})$ , bearing the bidentate bis(imidazolyl)methane (bim) ligand, was also examined and found to react slightly faster than the tridentate complex. In fact,  $[\text{Rh}(\text{bim})(\text{CO})_2](\text{B}_{\text{Ar}}^{\text{F}})$  was found to be the

most active catalyst for the cyclization of 5-hexynoic acid reported in the literature. The difference in reactivity between the various complexes tested was attributed to steric interference by the third uncoordinated ligand arms.



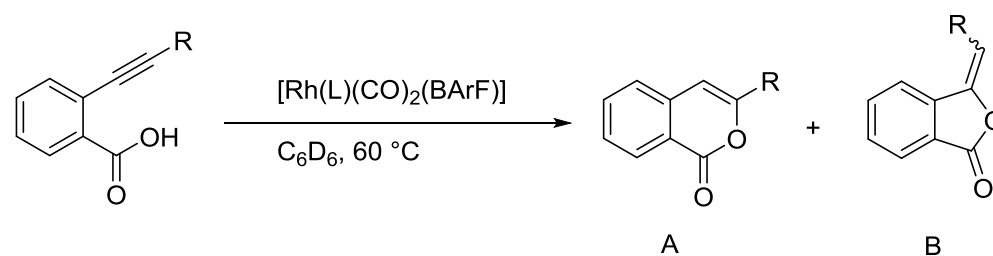
**Scheme 2.20. Catalytic cyclization of 4-pentynoic acid.**

Subsequent to their initial report regarding the cyclization of aliphatic alkyne acids, Messerle and co-workers examined the cyclization of 2-alkynyl benzoic acids.<sup>111</sup> Specifically, the authors examined both bidentate and tridentate complexes of Rh<sup>I</sup> in terms of their selectivity for formation of either the six-membered ring isocoumarin derivatives (**A**) or the five-membered ring phthalide derivatives (**B**). The authors evaluated cationic Rh<sup>I</sup> complexes of general formula [Rh(L)(CO)<sub>2</sub>](B<sub>Ar</sub><sup>F</sup>), where L = *p*-tpt, tpm, and bim and bpm (bis(pyrazol-1-yl)methane) (Table 2.3).

The authors found that the *endo* vs *exo* selectivity was greatly influenced by the substitution of the alkyne. Unsubstituted alkynes favored the five-membered *exo* product **B** whereas substituted alkynes favored the *endo* product **A**. In all cases the bidentate analogues were found to react faster than their tridentate counterparts. However, the tridentate ligands offered comparable (entries 7 & 8, 4 & 5) or even significantly enhanced (entries 1 & 2) selectivity. The only exception being indicated in entry 6, in which the tridentate tim ligand resulted in poorer selectivity than its bidentate counterpart. The authors examined a series of aryl

substituted alkynes with both electron donating and electron withdrawing substituents in the para position. They found no correlation between the *endo* vs *exo* selectivity and the electronic influence of the para substituent, suggesting that steric effects play a much larger role in product selectivity than do electronic effects. It is thus unsurprising that the bulkier tridentate scorpionate ligands might have such an effect on product distribution.

**Table 2.3. Rh<sup>I</sup> catalyzed cyclization of alkynyl benzoic acids**



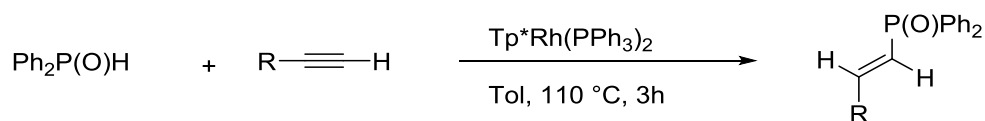
Entry	R	L	Reaction Time (h)	A : B
1	-H	bim	0.42	0.31 : 1
2	-H	tim	0.67	0.01 : 1
3	-Ph	bim	0.2	1 : 0.11
4	-Ph	bpm	0.15	1 : 0.04
5	-Ph	p-tpt	1.25	1 : 0.05
6	-Ph	tim	1.28	1 : 0.5
7	-C <sub>5</sub> H <sub>11</sub>	bim	0.27	1 : 0
8	-C <sub>5</sub> H <sub>11</sub>	tim	1.28	1 : 0

## 2.4 Hydrophosphinylation of Alkynes

The products of alkyne hydrophosphinylation, vinylphosphine oxides, are valuable reagents for a variety of organic transformations and precursors to a wide range of phosphine ligands.<sup>112</sup> Hydrophosphinylation is comparatively rare among transition-metal-catalyzed

reactions. The field is largely dominated by palladium catalysts,<sup>64</sup> however nickel catalysts have also been reported.<sup>113</sup> The application of organolanthanide catalysts has also been reviewed.<sup>82</sup> Montchamp *et al* have recently reviewed of hydrophosphinylation via radical and transition-metal-catalyzed reactions,<sup>114</sup> and Wang *et al* have reviewed the metal-catalyzed addition of phosphorus nucleophiles.<sup>115</sup>

The single example of hydrophosphinylation catalyzed by a metal complex bearing a scorpionate ligand is that of Love and co-workers in 2006.<sup>116</sup> The Love group had previously reported that the tris(pyrazolyl)borate complex [Tp\*Rh(PPh<sub>3</sub>)<sub>2</sub>] was an active catalysts for alkyne hydrothiolation selective for the branched vinyl sulfide isomer (*vide supra*).<sup>117</sup> Expecting similar reactivity with [Tp\*Rh(PPh<sub>3</sub>)<sub>2</sub>] in hydrophosphinylation, the authors were surprised to find that the catalyst was selective for formation of linear isomers (Scheme 2.21). Isolated yields of the linear vinylphosphine oxide range from 41-51% for aliphatic alkynes but lower for aryl alkynes. The internal alkyne 3-hexyne was also found to react, yielding the product of *syn* addition in 61% isolated yield.



**Scheme 2.21. Alkyne hydrophosphinylation catalyzed by Tp\*Rh(PPh<sub>3</sub>)<sub>2</sub>**

The authors also found that the cyclooctadiene complex [Tp\*Rh(cod)] was also an active catalyst for alkyne hydrophosphinylation, albeit in lower yields. Both complexes were active at

room temperature, giving comparable yields when reaction times were increased to 18 h. However neither complex was found to be as active as Wilkinson's complex,  $[\text{RhCl}(\text{PPh}_3)_3]$ .

## 2.5 Conclusion

Numerous advances in hydroelementation of alkenes and alkynes have been made thanks to scorpionate ligand complexes. The first example of transition-metal-catalyzed hydrothiolation of alkynes came thanks to a rhodium scorpionate complex reported by Love and co-workers. Although several other examples of transition-metal-catalyzed alkyne hydrothiolation with aliphatic thiols emerged after this initial report,  $[\text{Tp}^*\text{Rh}(\text{PPh}_3)_2]$  remains the leader in reported substrate scope. The second generation heteroscorpionate ligands reported by Sadow and co-workers allowed for room temperature hydroamination to proceed with excellent enantioselectivity. More striking is their recent report of desymmetrization of aminodialkenes and alkynes, which allows not only for two stereocenters to be installed selectively from an achiral starting material, but the resulting compounds contain functional groups for further reactivity and potential application in synthetic methodology.

A defining feature of scorpionate complexes is their ability to bind in either a  $\text{K}2$  or  $\text{K}3$  coordination mode. Such flexibility allows for control of available coordination sites with the potential for increasing selectivity and blocking potential side reactions. In their report on alkyne hydrothiolation, the Love group found tris(pyrazolyl)borate ligands to yield much higher selectivity than their bis(pyrazolyl)borate counterparts. This increase in selectivity was attributed to the availability of a third donor atom, which restricts substrate binding and increase selectivity for the major product. Sadow's heteroscorpionate ligands contained a tightly bound Cp ring and fluxional oxazole arms. This second generation of scorpionate ligands proved to be much more

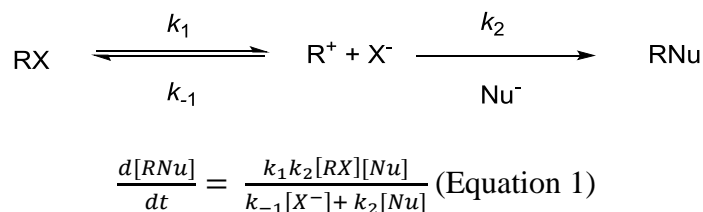
effective than their more rigid homoscorpionate predecessors. However tridentate ligands are not always more effective than their bidentate analogues.

As synthetic protocols evolve, so does the library of homoscorpionate and heteroscorpionate ligands. Because of their modular synthesis and diversity in charge, donor atoms, and substitution, scorpionate ligands will continue to find increasing use in catalytic transformations.

## Chapter 3 Substrate-Activity Relationships in Mechanistic Elucidation

### 3.1 Introduction

Several methods exist for the elucidation of mechanisms of reaction. One such method involves determining the order in each reactant. For example,  $S_N2$  reactions show first order kinetic dependence on both nucleophile and electrophile, whereas  $S_N1$  reactions, to a first approximation, show first order kinetic dependence on only the electrophile. Thus, determining the order in each reactant for substitution reactions can reveal whether the reaction proceeds via direct nucleophilic displacement, or through the generation of an intermediate carbocation. However, only rigorous mechanistic investigations can reveal subtleties in the mechanism. For example, although  $S_N1$  reactions are usually independent of the nature and concentration of the nucleophile, low concentrations of nucleophile or particularly weak nucleophiles do show kinetic dependence on the nucleophile. This is because the true kinetic expression for an  $S_N1$  reaction is given by equation 1, derived by application of the steady state approximation to  $[R^+]$ .



Under common conditions for substitution with a strong nucleophile,  $k_2$  and  $[\text{Nu}]$  are large. In this case where  $k_2[\text{Nu}] \gg k_{-1}[\text{X}^-]$ , the latter term can be ignored and the equation simplifies to the familiar equation for  $S_N1$  substitution,  $\frac{d[\text{RNu}]}{dt} = k_1[\text{RX}]$ . However, when  $[\text{Nu}]$  is low, or  $k_2$  is small (weak nucleophile),  $S_N1$  substitutions show kinetic dependence on both the

electrophile and the nucleophile in accordance with Equation 1. Equation 1 also presumes that the addition of the nucleophile is irreversible, which is not always the case. Even in the simple case of substitution reactions, determining the kinetic order in each reactant is not sufficient for a complete understanding of the underlying mechanism.

In addition to determining the kinetic order in each reactant and catalyst, if present, a variety of other methods must be explored in order to completely elucidate the mechanism of a given transformation. These include, but are not limited to, isotopic labeling experiments, kinetic isotope effects, temperature dependence, isolation or independent synthesis of putative intermediates, and examining the stereochemical outcome of the reaction (if applicable). Another popular method is to examine the relationship between the electronic nature of the reactant(s) and either rate or equilibrium constants. Such relationships are generally referred to as linear free energy relationships (LFER). The purpose of this section of the thesis is to review Hammett LFER and examine its application in understanding the effect of electronics on the acidity and reactivity of aryl thiols. Furthermore, we report to measurement of the methanolic acidity constants of a large series of *para*-substituted aryl thiols and develop empirical relationships for the accurate prediction of aryl thiol  $pK_{AS}$  for virtually any *para*-substituent.

### 3.1.1 Linear Free Energy Relationships

A common method for analyzing the effects of varying the electronic nature of nucleophiles and electrophiles on reactivity is by correlation to Hammett parameters.<sup>118</sup> Hammett constants were first measured by examining the effect of changes in the acidity of substituted benzoic acids (Figure 3.1).<sup>119</sup> Hammett found that the relationship  $\log(K_X) - \log(K_H) = \rho\sigma$  is linear, where  $\sigma$  is a substituent constant for substituent X, and  $\rho$  is a constant for a given reaction

series. For the ionization of substituted benzoic acids in water at 25 °C,  $\rho$  is set to 1 by definition, and  $\sigma = 0$  for  $X = H$ . Thus, the measurement of the  $pK_A$  of a given substituted benzoic acid allows for the determination of the corresponding Hammett  $\sigma$  parameter for a given substituent.

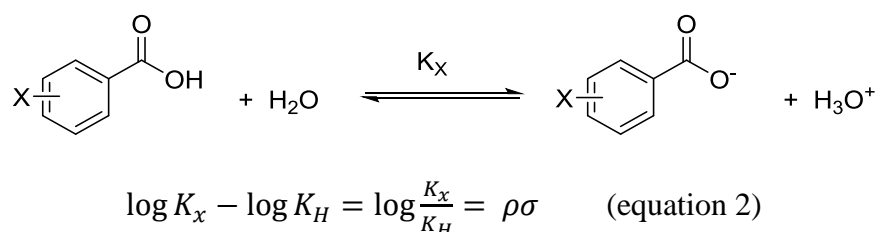


**Figure 3.1. Ionization of substituted benzoic acids.**

While this relationship is ultimately empirical in nature, it is grounded sufficiently in physical properties to be broadly applicable. The broad applicability of the Hammett LFER is due to the logarithmic relationship between Gibb's free energy,  $\Delta G^\circ$ , and  $K$  (i.e.  $\Delta G^\circ = -RT\ln(K)$ ). Equation 2 can therefore be interpreted as arising from the difference in free energies of ionization for  $X$  vs.  $H$ . Hence, these structure-activity relationships were named linear free energy relationships. Because the relationship between reaction rate  $k$  and Gibbs free energy of activation  $\Delta G^\ddagger$  is also logarithmic (i.e.  $\Delta G^\ddagger = -RT(\ln(k) - \ln(k_B T/h))$ ), the Hammett relationship can also be applied to data for reaction rates. For example, the rate of saponification of substituted ethyl benzoate esters in 60% aqueous acetone follows a Hammett relationship with  $\rho = 2.364$ .<sup>120</sup> Subsequent to Hammett's initial proposal, hundreds of reactions have been fit to the Hammett equation.<sup>121</sup>

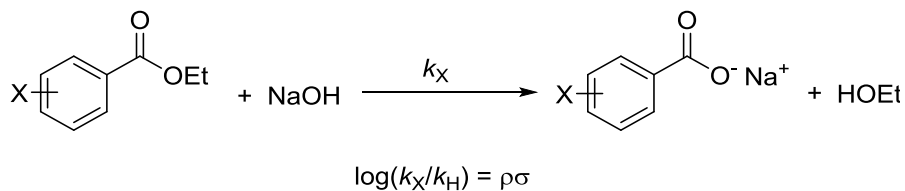


**Figure 3.2. Saponification of substituted ethyl benzoate esters.**

### 3.1.2 Interpretation of $\rho$

The value of  $\rho$  depends on several factors, including solvent, temperature, and the reaction series being investigated. The magnitude of  $\rho$  indicates how sensitive the reaction series is to changes in the electronic nature of the substrate. If  $|\rho| > 1$ , the reaction is more sensitive to changes in the electronic nature of the substrate compared to the ionization of benzoic acid. If  $|\rho| < 1$ , the reaction is less sensitive to changes in the electronic nature of the substrate compared to benzoic acid. If  $\rho$  is positive, then the reaction is generating negative charge. If  $\rho$  is negative, then the reaction is generating positive charge. If  $\rho \approx 0$ , the reaction can be said to be independent of the electronic nature of the substrate. The value of  $\rho$  is therefore a strong indicator of the fundamental reaction mechanism.

### 3.1.3 Hammett $\sigma^-$ and $\sigma^+$ constants

The basic Hammett  $\sigma$  constants, derived from the ionization of benzoic acids, reflect the relative stability for generation of negative charge where said charge is unable to be stabilized by resonance delocalization into the aromatic ring. For the determination of Hammett  $\sigma$  constants in which the negative charge can be stabilized by resonance interaction with the aromatic ring, a similar relationship was developed for a series of *para*-substituted phenols. In this case, the notation is changed to  $\sigma^-$  parameters, to indicate that anionic charge is stabilized through

resonance. A similar set of parameters were developed for resonance interaction with positive charge, denoted  $\sigma^+$  constants. Since their introduction, Hammett  $\sigma$ ,  $\sigma^-$ , and  $\sigma^+$  constants have been determined for hundreds of *para*-substituents.<sup>122</sup>

### 3.1.4 Dual substituent parameter LFER

Hammett  $\sigma$ ,  $\sigma^-$ , and  $\sigma^+$  constants are ultimately a combination of two substituent effects: induction and resonance. In some cases, it is desirable or necessary to separate the effects of resonance and induction. Resonance and inductive effects can act in concert but often are opposite. For example, fluorine is the most electronegative element and consequently is a strong inductively withdrawing group. However, fluorine is also a great resonance donor, undergoing hybridization and delocalization of its lone pairs with  $\pi$  systems. Therefore, while fluorine's  $\sigma$  constant is 0.06 (i.e. an electron withdrawing group), fluorine's  $\sigma^-$  and  $\sigma^+$  constants are -0.03 and -0.07, respectively (i.e. an electron *donating* group). In order to address the issue of resonance versus induction, a dual substituent parameter equation was developed (Equation 3),<sup>123</sup> where  $\sigma^I$  is the contribution of induction and  $\sigma^R$  is the contribution of resonance to the substituent parameter. The  $\rho^I$  and  $\rho^R$  coefficients represent the sensitivity of the reaction series to changes in the inductive and resonance contributions of the substituents.  $\sigma^I$  parameters, sometimes denoted F, are constant across all reaction and substrate types, whereas  $\sigma^R$  constants depend on whether or not charge from the reaction center can be stabilized by resonance delocalization, similar to Hammett  $\sigma$ ,  $\sigma^-$ , and  $\sigma^+$  constants. In these cases, the  $\sigma^R$  parameters are denoted by  $R^0$ ,  $R^-$  and  $R^+$ .

$$\rho\sigma = \rho^I\sigma^I + \rho^R\sigma^R \quad (\text{Equation 3})$$

Several methods have been employed in order to separate resonance and inductive substituents effects in order to determine  $\sigma^I$  and  $\sigma^R$  parameters.  $\sigma^I$  can be derived by comparing  $\sigma$  values for *para*-substituted benzoic acids, denoted  $\sigma^P$ , to those of *meta*-substituted benzoic acids, denoted  $\sigma^m$ . In the fluorine example, the  $\sigma^P$  constant for fluorine is 0.06, a weak withdrawing group. In comparison, the  $\sigma^m$  constant is 0.34, a moderate electron withdrawing group, due to loss of the resonance component. Because the  $\sigma^m$  parameter is largely the result of the inductive effect of the substituent,  $\sigma^I$  parameters can be obtained following some mathematical manipulation of  $\sigma^m$  and  $\sigma^P$  parameters.<sup>124</sup> Taft used the  $\sigma^m$  and  $\sigma^P$  parameters measured by  $^{19}\text{F}$  NMR chemical shifts of substituted fluorebenzenes<sup>125</sup> for the determination of  $\sigma^I$  and  $\sigma^R$  parameters.<sup>126</sup> Grob *et al* used the ionization of substituted quinuclidines to determine  $\sigma^I$  (Figure 3.3).<sup>127</sup> Returning to the example of fluorine, the dual nature of the fluorine substituent is revealed by comparison of its  $\sigma^I$  and  $\sigma^R$  parameters. The  $\sigma^I$  constant for fluorine is 0.45, indicative of its strong inductively electron withdrawing effects. In comparison, the  $\sigma^R$  constant for fluorine is -0.52, a strong resonance *donating* group. Calculated  $\sigma^I$  constants are virtually identical, regardless of the method or reaction series examined.<sup>128</sup> It follows logically that  $\sigma^I$  constants can be applied to any reaction series, independent of the resonance interactions. For the ionization of substituted benzoic acids,  $\rho = \rho^I = \rho^R = 1$  by definition, and so  $\sigma^R$  values can be calculated. The parameter  $\lambda = \rho^R/\rho^I$  is an indicator of whether a reaction series is more sensitive to inductive effects or resonance effects. The reaction series is more sensitive to resonance effects when  $\lambda > 1$ , and more sensitive to inductive effects when  $\lambda < 1$ .

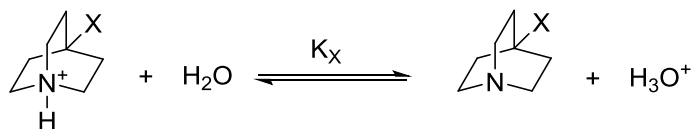


**Figure 3.3. Ionization of protonated quinuclidines.**

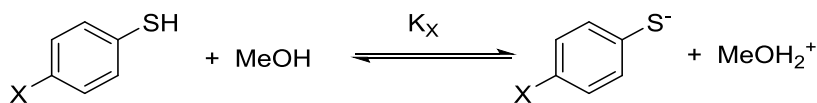
### 3.2 Measurement of Aryl Thiol $\text{pK}_A$ in Methanolic Solution

Given our interest in elucidating the mechanism of reactions involving thiols, we wanted to understand certain fundamental properties of thiols, such as the relationship between the electronic nature of substituted thiols and their acidity and nucleophilicity. In order to understand such fundamental properties, we must first examine the correlation between the acidity of thiols and the Hammett parameters. Unfortunately, the acidity constants for substituted thiols are largely underreported, due to the poor solubility of thiols in aqueous media. Therefore, we elected to measure the acidity constants for a series of *para*-substituted aryl thiols in order to both fill a gap in the literature and to better understand these fundamental properties. Methanol was chosen to be an appropriate solvent for the measurement of aryl thiol  $\text{pK}_A$  due to the high solubility of aryl thiols in methanolic solution, and methanol's high dielectric constant and ability to undergo similar proton transfer events to  $\text{H}_2\text{O}$ . Since the proton transfer equilibrium in methanol is different from that in water, a correction factor for this difference must be applied in order to calculate their effective  $\text{pK}_A$  in aqueous media. Bosch<sup>129</sup> and others<sup>130</sup> have found that the relationship between  $\text{pK}_A$  values measured in water and  $\text{pK}_A$  values measured in other solvents to be essentially linear (equation 4). Equation 4 is a derivation of the Hammett equation, linking the ionization of a series of compounds in two different solvents. The effect of solvent on the resolution of acid strengths in a given solvent compared to the resolution in water (i.e. the

effect of solvent on  $\rho$ ) is accounted for by the slope of the linearly fitted equation,  $a$ . The y-intercept  $b$  accounts for changes in solvation of the ions and is related to, among other things, the hydrogen bond donor/acceptor ability of the solvent and its dielectric constant. Therefore, predicting the  $pK_A$  values in one solvent or another is a straightforward interpolation or extrapolation from the fitted equation.

$$pK_A(\text{MeOH}) = a * pK_A(\text{H}_2\text{O}) + b \quad (\text{Equation 4})$$

The methanolic  $pK_A$  values for a series of *para*-substituted benzenethiols were measured by titration of a solution of the corresponding aryl thiol in methanol with a methanolic solution of KOH by volunteer undergraduate student Shaima Kamoonah. The pH of the solution was measured and plotted against the volume of KOH solution added. The  $pK_A(\text{MeOH})$  value was taken to be the pH value of the solution at the half-equivalence point in accordance with the Henderson–Hasselbalch equation. The titration curves demonstrated the standard curvature for titration of a weak acid with a strong base (see experimental). The results obtained by volunteer undergraduate student Shaima Kammoonah are reported in Table 3.1 as the average of a minimum of three replicates, and the standard deviation of the measured  $pK_A(\text{MeOH})$  values is reported.

**Table 3.1. Measured pK<sub>A</sub>s for a series of substituted aryl thiols in methanol.**

[X]	pK <sub>A</sub> (MeOH) <sup>a</sup>	Standard Deviation <sup>b</sup>	pK <sub>A</sub> (H <sub>2</sub> O) <sup>c</sup>
-OCH <sub>3</sub>	11.34	0.049	6.78
-CH <sub>3</sub>	11.23	0.043	6.61*
-H (parent)	10.98	0.178	6.47*
-SCH <sub>3</sub>	10.61	0.086	
-NHC(O)CH <sub>3</sub>	10.58	0.075	
-F	10.53	0.041	6.10
-Br	9.98	0.044	5.91*
-Cl	9.95	0.102	5.91*
-OCF <sub>3</sub>	9.92	0.096	
-CF <sub>3</sub>	9.56	0.050	
-C(O)OCH <sub>2</sub> CH <sub>3</sub>	9.47	0.107	
-NO <sub>2</sub>	8.25	0.013	4.51*

<sup>a</sup>Measurements performed by volunteer student Shaima Kammoonah. <sup>b</sup>Minimum of three replicates. <sup>c</sup>Literature values.<sup>131</sup> Numbers marked with an asterisk are those for which multiple values have been reported. The number included in the table is the average of those reported values.

The results reported in Table 3.1 follow the expected trend. Aryl thiols bearing electron donating groups, such as -OCH<sub>3</sub> and -CH<sub>3</sub>, have higher measured pK<sub>A</sub>s than thiols bearing electron withdrawing groups, such as -CF<sub>3</sub> and -NO<sub>2</sub>. The available literature data for the aqueous pK<sub>A</sub> values for the series of compounds have been included. Substrates for which several pK<sub>A</sub> values have been reported have had their reported values averaged. These averaged values have been marked with an asterisk. The standard deviation for these averaged values is ~0.2 pK<sub>A</sub> units. While the literature data for the aqueous pK<sub>A</sub> values of aryl thiols is limited, there are sufficient data points to encompass the series of aryl thiols examined herein. Figure 3.4 shows the correlation between pK<sub>A</sub>(MeOH) and pK<sub>A</sub>(H<sub>2</sub>O). Linear regression analysis gives the slope  $a = 1.377 \pm 0.035$  and the y-intercept  $b = 2.036 \pm 0.177$  and an adjusted R<sup>2</sup> of 0.996.

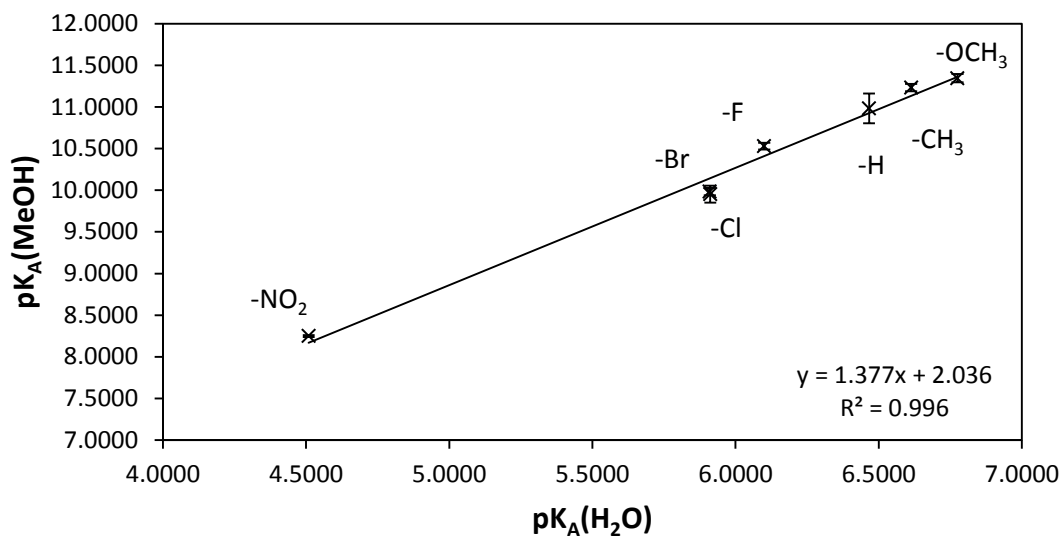


**Figure 3.4. Linear correlation between  $pK_A(\text{MeOH})$  and  $pK_A(\text{H}_2\text{O})$ .**

The results show a good linear correlation between  $pK_A(\text{MeOH})$  and  $pK_A(\text{H}_2\text{O})$ . The linear correlation allows for interpolation and extrapolation of the predicted  $pK_A(\text{H}_2\text{O})$  values for which the measurement is either unavailable or unattainable, due to the aforementioned low solubility of aryl thiols in aqueous solution. These values are reported in Table 3.2, along with the  $pK_A(\text{H}_2\text{O})$  values reported in the literature from Table 3.1. The predicted values show good agreement with those reported in the literature.

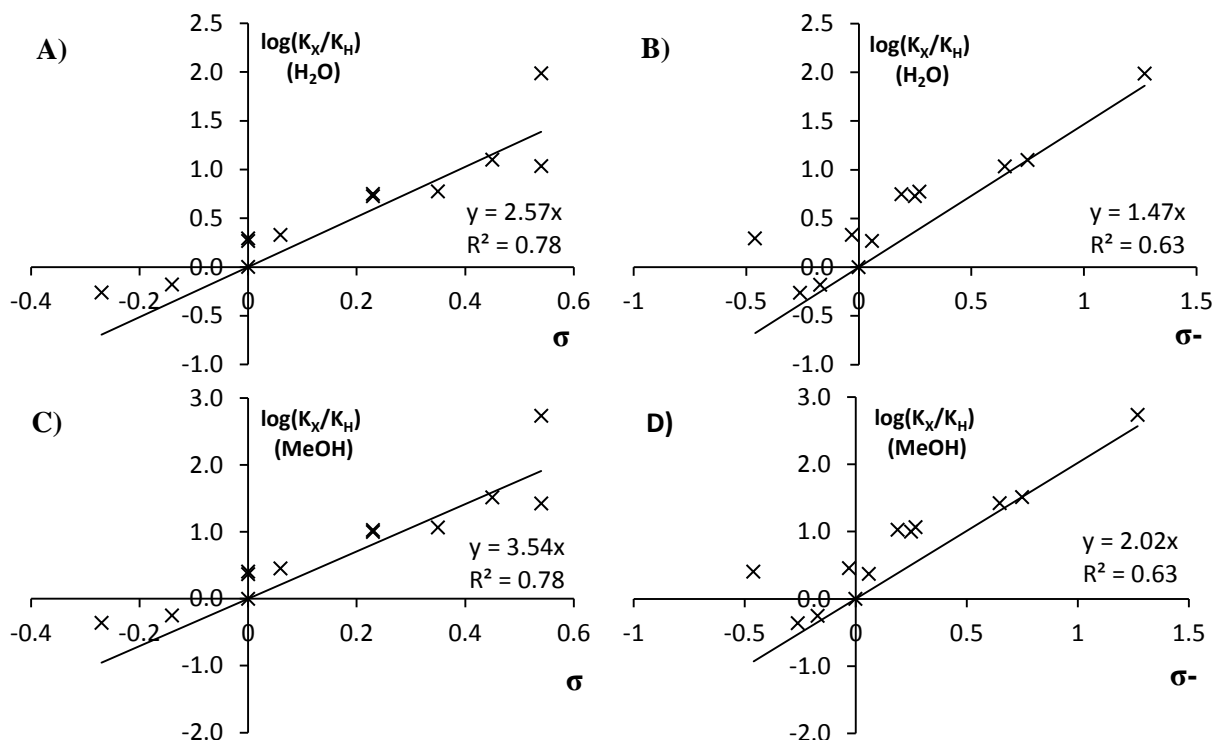
**Table 3.2. Predicted pK<sub>A</sub>(H<sub>2</sub>O) values**

[X]	pK <sub>A</sub> (H <sub>2</sub> O)(Predicted) <sup>a</sup>	error <sup>b</sup>	pK <sub>A</sub> (H <sub>2</sub> O)(Lit.) <sup>c</sup>	Standard Deviation <sup>d</sup>
-OCH <sub>3</sub>	6.76	0.22	6.78	
-CH <sub>3</sub>	6.68	0.21	6.61*	0.18
-H (parent)	6.50	0.25	6.47*	0.20
-SCH <sub>3</sub>	6.23	0.21		
-NHC(O)CH <sub>3</sub>	6.20	0.21		
-F	6.17	0.20	6.10	
-Br	5.77	0.20	5.91*	0.16
-Cl	5.75	0.21	5.91*	0.22
-OCF <sub>3</sub>	5.72	0.21		
-CF <sub>3</sub>	5.46	0.19		
-C(O)OCH <sub>2</sub> CH <sub>3</sub>	5.40	0.20		
-NO <sub>2</sub>	4.51	0.17	4.51*	0.14

<sup>a</sup>Calculated based on the linear relationship reported in Figure 3.4. <sup>b</sup>Propagated error based on the errors in slope and y-intercept of the linear regression analysis and the standard deviation of the measured pK<sub>A</sub>(MeOH) values. <sup>c</sup>Literature values. Numbers marked with an asterisk are those for which multiple values have been reported. The number included in the table is the average of those reported values. <sup>d</sup>Standard deviation of the reported literature values, where applicable.

### 3.2.1 Single and Dual Parameter Hammett Treatment of Aryl Thiol pK<sub>A</sub> Values

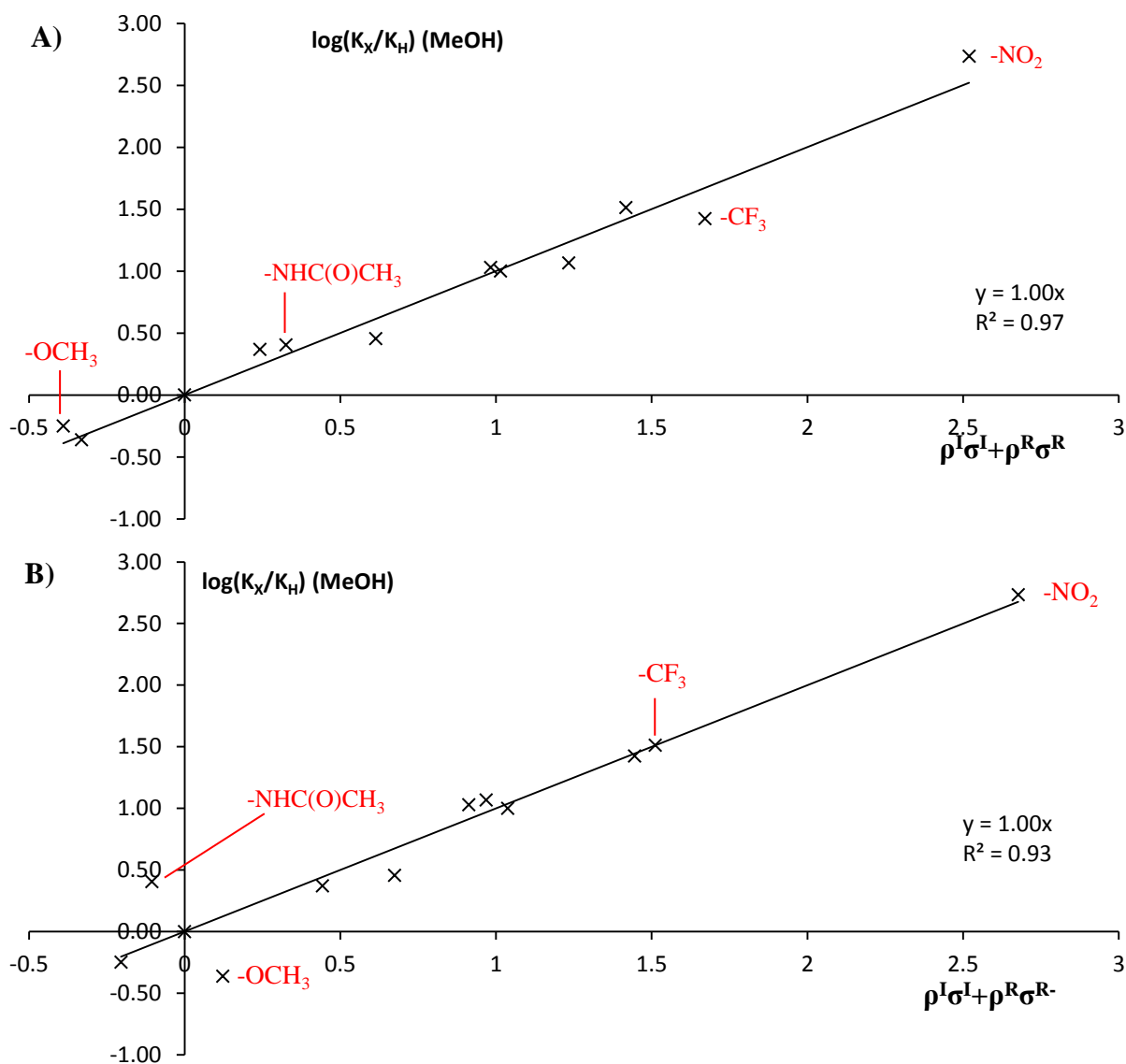
In order to better understand the effects of varying the *para*-substituent on the ionization of aryl thiols, we constructed a series of single and dual parameter Hammett relationships for both the measured pK<sub>A</sub>(MeOH) values and the predicted pK<sub>A</sub>(H<sub>2</sub>O) values. The predicted pK<sub>A</sub>(H<sub>2</sub>O) values show identical correlations as those for the measured pK<sub>A</sub>(MeOH) values. Consistent with equation 4, the only difference between constructing Hammett plots for pK<sub>A</sub>(MeOH) values and pK<sub>A</sub>(H<sub>2</sub>O) values is that  $\rho^{\text{MeOH}}/\rho^{\text{H}_2\text{O}} = a = 1.377$ . The single parameter Hammett correlations are shown in Figures 3.5 A-D.



**Figures 3.5. Single parameter Hammett correlations for aryl thiol pK<sub>A</sub> values.**

The correlations shown in Figures 3.5 A-D are poor. This is due to the weak resonance interaction between the thiolate anion and the  $\pi$  system of the benzene ring. Unlike the ionization of benzoic acids, for which the anionic charge cannot delocalize into the aromatic ring, the anionic charge of the thiolate anion can be stabilized by resonance. However, because the valence electrons of the thiolate anion are less likely to hybridize and engage in resonance with the aromatic system, this resonance interaction is expected to be poor compared to the resonance interaction of phenolate anions. Consequently, while some dependence on the resonance parameter for each substituent is to be expected, the resolution of acidic strength of the series of aryl thiols is expected to be largely dependent on the inductive capacity of the para substituent. In order to better understand the resonance and inductive effects, we constructed dual parameter

Hammett relationships using both  $\sigma^R$  and  $\sigma^{R-}$ .  $\rho^I$  and  $\rho^R$  parameters were determined by non-linear regression. Because the aforementioned relationship between  $\rho^{\text{MeOH}}/\rho^{\text{H}_2\text{O}} = a = 1.377$  holds true for both  $\rho^I$  and  $\rho^R$ , only the plots for  $\log(K_x/K_H)(\text{MeOH})$  are shown Figures 3.6 A-B.



**Figures 3.6. Dual parameter Hammett correlations for aryl thiol  $pK_A$  values. A)  $\log(K_x/K_H)(\text{MeOH})$  vs.  $\rho^I \sigma^I + \rho^R \sigma^R$ . B)  $\log(K_x/K_H)(\text{MeOH})$  vs.  $\rho^I \sigma^I + \rho^R \sigma^R$ .**

**Table 3.3. Dual parameter Hammett correlation values for the ionization of aryl thiols.**

Solvent	correlation	$\rho^I$	$\rho^R$	$\lambda$
MeOH	$\rho^I\sigma^I + \rho^R\sigma^{R-}$	$3.40 \pm 0.13$	$2.36 \pm 0.18$	0.692
	$\rho^I\sigma^I + \rho^R\sigma^{R-}$	$2.88 \pm 0.19$	$1.30 \pm 0.18$	0.450
H <sub>2</sub> O	$\rho^I\sigma^I + \rho^R\sigma^{R-}$	$2.47 \pm 0.09$	$1.71 \pm 0.13$	0.692
	$\rho^I\sigma^I + \rho^R\sigma^{R-}$	$2.09 \pm 0.14$	$0.94 \pm 0.13$	0.450

The dual parameter Hammett correlations offer significant improvement in the goodness of fit. The resultant  $\rho^I$ ,  $\rho^R$ , and corresponding  $\lambda$  values are listed in Table 3.3 for both the  $\log(K_X/K_H)(\text{MeOH})$  and  $\log(K_X/K_H)(\text{H}_2\text{O})$  correlations. As expected, the ionization of aryl thiols is more strongly related to the inductive effect of the *para* substituent than the resonance effects, as indicated by the  $\lambda$  values of 0.692 and 0.450 for either correlation. Some of the outliers have been labeled in Figures 3.6 A and B. The strong withdrawing groups  $-\text{NO}_2$  and  $-\text{CF}_3$  are better modeled by correlation to  $\sigma^{R-}$  than to  $\sigma^R$  parameters.  $\sigma^R$  parameters, derived from the ionization of benzoic acids, do not account for delocalization of the charge into the  $\pi$  systems of the aromatic ring and the *para* substituent. Therefore, these substrates are better modeled by the  $\sigma^{R-}$  parameters. Conversely, the strong resonance donators  $-\text{F}$ ,  $-\text{NHC}(\text{O})\text{CH}_3$  and  $-\text{OCH}_3$  are better modeled by correlation to the  $\sigma^R$  parameters than to the  $\sigma^{R-}$  parameters. Strong resonance donators destabilize the phenolate anions to a much greater extent than the thiolate anions, which are less dependent on resonance interactions. Therefore, strong resonance donators are better modeled by the  $\sigma^R$  parameters.

While Equation 3 allows for prediction of methanolic or aqueous acidity constants when one or the other is known, the dual parameter Hammett treatment allows for prediction of either acidity constant for which neither value is known. As mentioned previously,  $\sigma^I$ ,  $\sigma^R$  and  $\sigma^{R-}$  parameters have been determined for hundreds of substituents. Based on these known values and

the correlations reported in Table 3.3, the  $pK_A$  for a given *para*-substituted aryl thiol in either water or methanol can be predicted with a fair degree of certainty. For strong resonance donors better modeled by correlation to  $\sigma^R$  parameters, equations 5A and 6A should be employed. Conversely, for strongly electron withdrawing groups, equations 5B and 6B should be employed.

$$pK_A(\text{MeOH}) = 10.98 - 3.41 * \sigma^I - 2.36 * \sigma^R \quad (\text{Equation 5A})$$

$$pK_A(\text{MeOH}) = 10.98 - 2.88 * \sigma^I - 1.30 * \sigma^{R-} \quad (\text{Equation 5B})$$

$$pK_A(\text{H}_2\text{O}) = 6.50 - 2.47 * \sigma^I - 1.71 * \sigma^R \quad (\text{Equation 6A})$$

$$pK_A(\text{H}_2\text{O}) = 6.50 - 2.09 * \sigma^I - 0.94 * \sigma^{R-} \quad (\text{Equation 6B})$$

Using equations 5 and 6, we calculated the aqueous and methanolic acidity constants for the series of aryl thiols examined herein. The predicted  $pK_A(\text{MeOH})$  values are reported in Table 3.4, and the predicted  $pK_A(\text{H}_2\text{O})$  values are reported in Table 3.5. The difference between the experimentally determined values and those calculated by the above equations are included. Those predicted values with large differences ( $> 0.2$   $pK_A$  units) between the measured and predicted values are bolded.

**Table 3.4. Predicted pK<sub>A</sub>(MeOH) values based on equations 5A and 5B.**

[X]	pK <sub>A</sub> (MeOH) <sup>a</sup>	Std. Dev. <sup>b</sup>	Eqn. 5A	Δ <sup>c</sup>	Eqn. 5B	Δ <sup>d</sup>
-OCH <sub>3</sub>	11.34	0.05	11.31	0.03	10.86	<b><u>0.48</u></b>
-CH <sub>3</sub>	11.23	0.04	11.37	-0.14	11.19	0.05
-H (parent)	10.98	0.18	10.98	0.00	10.98	0.00
-SCH <sub>3</sub>	10.61	0.09	10.74	-0.12	10.54	0.08
-NHC(O)CH <sub>3</sub>	10.58	0.07	10.65	-0.08	11.09	<b><u>-0.51</u></b>
-F	10.53	0.04	10.37	0.16	10.31	<b><u>0.22</u></b>
-Br	9.98	0.04	9.96	0.02	9.94	0.04
-Cl	9.95	0.10	10.00	-0.04	10.07	-0.12
-OCF <sub>3</sub>	9.92	0.10	9.74	0.17	10.01	-0.10
-CF <sub>3</sub>	9.56	0.05	9.31	<b><u>0.25</u></b>	9.53	0.03
-C(O)OCH <sub>2</sub> CH <sub>3</sub>	9.47	0.11	9.56	-0.09	9.47	0.00
-NO <sub>2</sub>	8.25	0.01	8.46	<b><u>-0.21</u></b>	8.30	-0.05

<sup>a</sup>Experimentally determined value (Table 3.1). <sup>b</sup>Standard deviation of the experimentally determined pK<sub>A</sub> values. <sup>c</sup>Column 2 – column 4. <sup>d</sup>Column 2 – column 6.

**Table 3.5. Predicted pK<sub>A</sub>(H<sub>2</sub>O) values based on equations 6A and 6B.**

[X]	pK <sub>A</sub> (H <sub>2</sub> O)(Lit.) <sup>a</sup>	Eqn. 4	Eqn. 6A	Δ <sup>b</sup>	Eqn. 6B	Δ <sup>c</sup>
-OCH <sub>3</sub>	6.775	6.76	6.74	0.03	6.41	<b><u>0.36</u></b>
-CH <sub>3</sub>	6.613*	6.68	6.78	-0.17	6.65	-0.04
-H (parent)	6.466*	6.50	6.50	-0.03	6.50	-0.03
-SCH <sub>3</sub>		6.23	6.33		6.18	
-NHC(O)CH <sub>3</sub>		6.20	6.26		6.58	
-F	6.1	6.17	6.06	0.04	6.01	0.09
-Br	5.91*	5.77	5.76	0.15	5.75	0.16
-Cl	5.911*	5.75	5.79	0.12	5.84	0.07
-OCF <sub>3</sub>		5.72	5.61		5.80	
-CF <sub>3</sub>		5.46	5.29		5.45	
-C(O)OCH <sub>2</sub> CH <sub>3</sub>		5.40	5.47		5.40	
-NO <sub>2</sub>	4.5088*	4.51	4.67	-0.16	4.56	-0.05

<sup>a</sup>Literature reported values. Numbers marked with an asterisk are those for which multiple values have been reported. The number included in the table is the average of those reported values. <sup>b</sup>Column 2 – column 4. <sup>c</sup>Column 2 – column 6.

### 3.3 Conclusion

In this chapter, we review the application of Hammett single and dual parameter substituent correlations in mechanistic analysis. Hammett correlations reveal the physical relationship between the electronic effects of a substituent and the resultant changes in free energies of equilibrium or reaction rate.

We reported the measurement of the acidity constants of a variety of *para*-substituted aryl thiols in methanol. The linear correlation between acidity constants in methanol and those in aqueous media allows for the prediction of aqueous aryl thiol acidity constants for which data was either previously unknown or unattainable due to the poor solubility of aryl thiols in water. Hammett single and dual parameter treatments were applied to the resulting acidity constants. The dual parameter treatment provided a much better correlation, and revealed a much higher dependence on the inductive effects of the *para*-substituents compared to the resonance effects. The dual parameter correlation allows for the prediction of acidity constants in either water or methanol based on known  $\sigma^I$ ,  $\sigma^R$ , and  $\sigma^{R-}$  parameters with a good degree of accuracy.

Due to sulfur's ability to be a weak resonance donor, strong electron withdrawing groups were found to give better correlation to  $\sigma^{R-}$  parameters whereas strong resonance donating groups were found to give better correlation to  $\sigma^R$  parameters. Ideally, a new series of resonance parameters for sulfur should be elucidated. These new parameters, which we will denote  $\sigma^{RS-}$ , would give a better assessment of the resonance interaction of electron accepting and electron donating groups. However, there is insufficient data reported herein to calculate such parameters and is a matter for future work.

### 3.4 Experimental

#### 3.4.1 Measurements of Acidity Constants of Substituted Aryl Thiols in Methanol

Methanolic solutions of substituted aryl thiols were prepared and titrated with a 0.1 M solution of KOH in methanol. The pH of the solution was measured with a pH electrode and monitored after each addition of KOH solution. The titration curves of pH versus volume of KOH solution added showed standard curvature of titration of a weak acid with a strong base (Figure 3.7). The  $pK_A$  of the aryl thiol was taken to be the pH of the solution at half-equivalence point according to the Henderson-Hasselbalch equation. The initial concentration of aryl thiol solution varied over a 25 – 100 mM range. The measured  $pK_A$  is independent of the initial concentration of aryl thiol. Measurements were performed in triplicate.

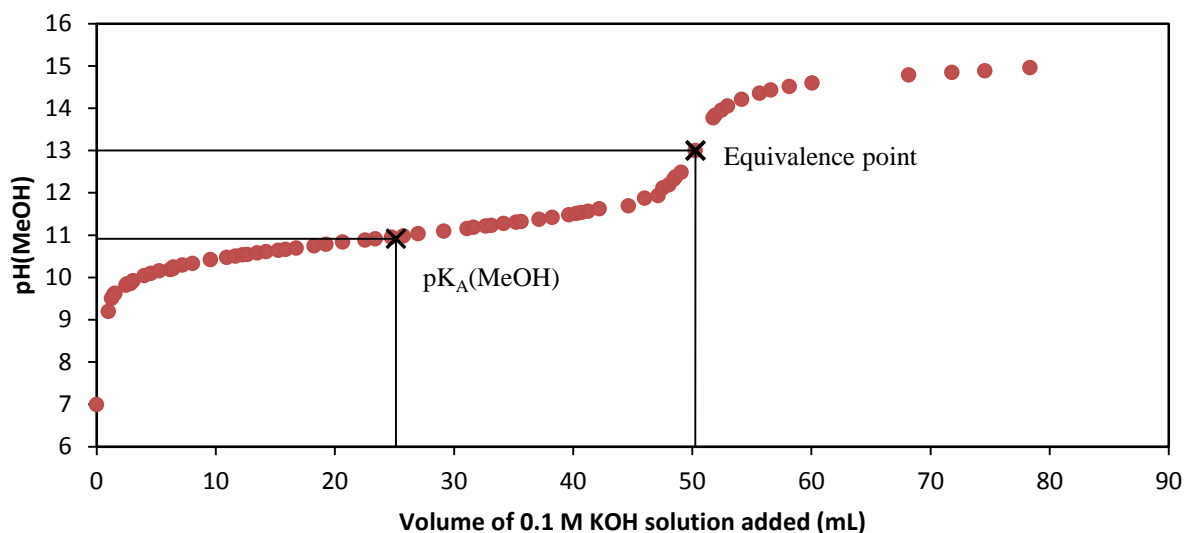


**Figure 3.7. Titration curve for titration of PhSH with 0.1 M KOH in methanol.**

## **Chapter 4 Application of Alkyne Hydrothiolation in the Synthesis of K777**

### **4.1 Chagas Disease**

Chagas disease is one of the leading causes of heart disease in Latin America and is considered by the World Health Organization (WHO) as a neglected global disease.<sup>132</sup> Chagas disease is due to infection by protozoa *Trypanosoma cruzi* (T. cruzi) and is largely transmitted through insect bites.<sup>133</sup> The disease is particularly problematic in poor areas lacking proper health infrastructure and quality housing. Because those infected are generally poor people living in rural areas of Latin America, there has been little interest in research and development into treatments from large pharmaceutical companies.<sup>134</sup> However, due to immigration, cases of people infected with Chagas disease have begun to appear more frequently in developed countries, with an estimated >300,000 cases in the United States alone.<sup>135</sup> This factor, in combination with its classification as a globally neglected disease by the WHO, has resulted in increased funding for research into Chagas disease at both the federal and university levels.

#### **4.1.1 Existing Treatments for Chagas Disease**

There are currently two drugs available for treatment of Chagas disease: benznidazole and nifurtimox. Both drugs contain an aromatic nitro group (Figure 4.1) which is likely responsible for their activity.<sup>136</sup> The drugs are thought to act by reacting with DNA and are typically only effective during the early stages of the disease. Due to their putative mechanism of action, both drugs are wrought with side effects. Nifurtimox affects the central nervous system, potentially causing seizures, while benznidazole can cause inflammation, bone marrow suppression, and peripheral neuropathy.<sup>137</sup> Both drugs are considered mutagenic and

carcinogenic.<sup>138</sup> Lengthy dosage times (60-120 days), increasing drug resistance, and toxicity, all contribute to the need for better treatments.<sup>139</sup>

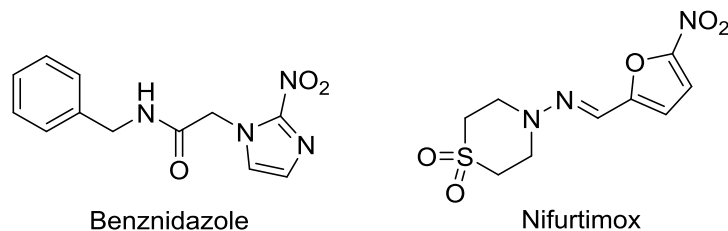


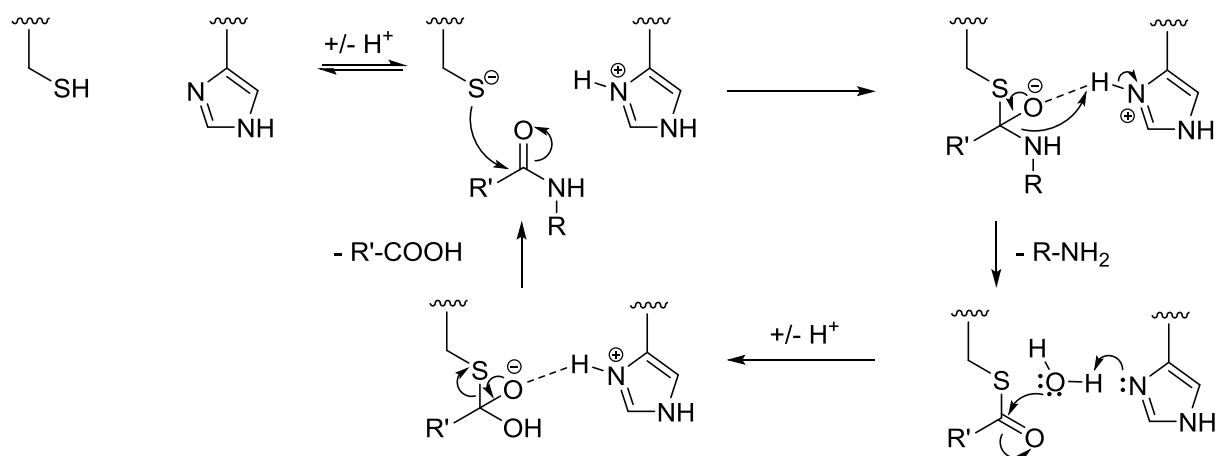
**Figure 4.1. Benznidazole and Nifurtimox.**

#### 4.1.2 Treatment of Chagas Disease by Inhibition of Cruzain

One popular target for the treatment of Chagas' disease is inhibition of the enzyme Cruzain, a cysteine protease essential to life for the pathogen.<sup>140</sup> Proteases cleave peptides by hydrolyzing a peptide linkage and are usually specific to a certain amino acid sequence.<sup>141</sup> The enzymes contain a recognition site which selectively binds to a specific sequence of peptides. Proteases are often essential for life in several viral pathogens, as many of the viral proteins are derived from a single precursor protein which is cleaved at specific points by a protease, which is also derived from the same precursor protein. Hence protease inhibition can be an extremely effective method of treatment.

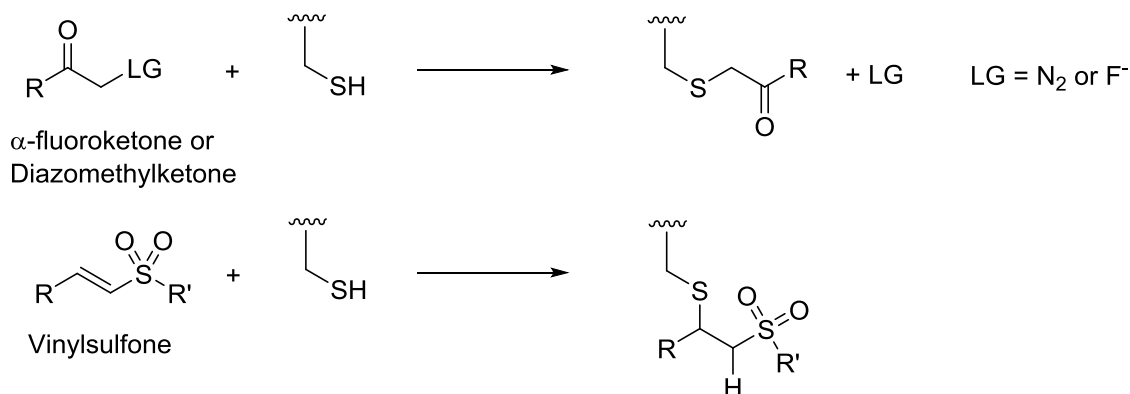
Cysteine proteases function by cleaving peptides through the generation of intermediate thioesters with a cysteine residue found in the active site. The active site also typically contains a histidine residue which acts as a base to activate the cysteine sulfur nucleophile, as a conjugate

acid to assist departure of the amine leaving group, and as an oxyanion hole to stabilize the tetrahedral intermediates (Scheme 4.1).



**Scheme 4.1. Amide hydrolysis by cysteine proteases.**

Cysteine protease inhibitors can be reversible or irreversible. Reversible inhibitors include peptidomimetic aldehyde, cyano, and  $\alpha$ -ketocarbonyl compounds.<sup>142</sup> These compounds form reversible covalent intermediates with the cysteine residue and are therefore less potent than their irreversible counterparts. Irreversible inhibitors include  $\alpha$ -fluoroketones, diazomethylketones and vinyl sulfones, however research into  $\alpha$ -fluoroketones was halted once it was discovered that they metabolized into highly toxic fluoroacetate.<sup>143</sup>  $\alpha$ -fluoroketones and diazomethylketones react with the cysteine residue in the active site to displace the halide or lose nitrogen gas, while vinyl sulfones act as Michael acceptors (Scheme 4.2). In both cases, the enzyme is irreversibly inhibited due to the formation of a stable covalent bond. In all cases the R group is a peptide or peptide-like fragment which can be tailored to increase the specificity of the drug to the desired target enzyme.



**Scheme 4.2. Irreversible inhibition of cysteine proteases.**

#### 4.2 K777 as Potent Cysteine Protease Inhibitor

Vinyl sulfones offer the advantage over  $\alpha$ -fluoroketones and diazomethylketones in that they are much more stable both in solution (or blood) and unreactive towards other proteases such as serine and aspartyl proteases.<sup>144</sup> The drugs are peptidomimetic, containing a short peptide sequence designed to mimic the peptide recognition sequence of the target protease. Palmer and coworkers began investigating vinyl sulfone peptidomimetics in 1995 with the general structure shown in Figure 4.2.<sup>145</sup> The structure contains two peptide linkages and two amino acid derivatives ( $\text{R}^2$  and  $\text{R}^3$ ) which can be tailored to increase specificity and enzyme affinity, while the  $\text{P}_3$  region ( $\text{R}^1$  substituent) is typically tailored to increase bioavailability.<sup>146</sup> Finally, the vinyl sulfone ( $\text{R}^4$ ) can be substituted to increase binding affinity, the rate of enzyme inhibition, and stability towards decomposition and cleavage.

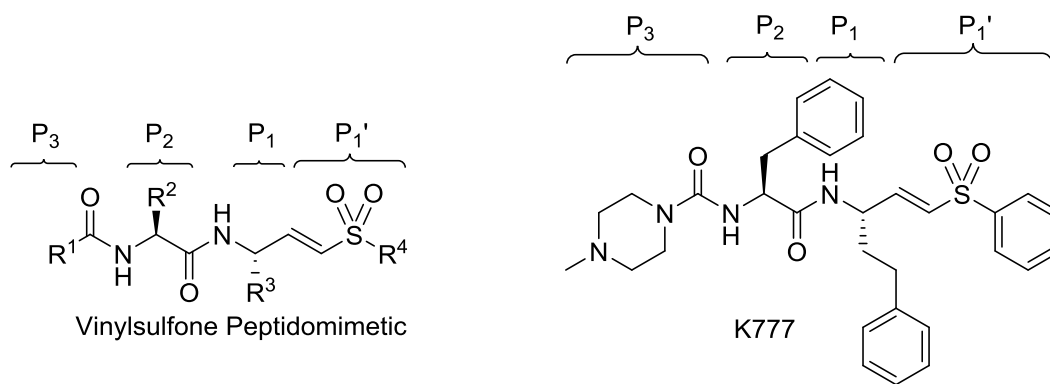
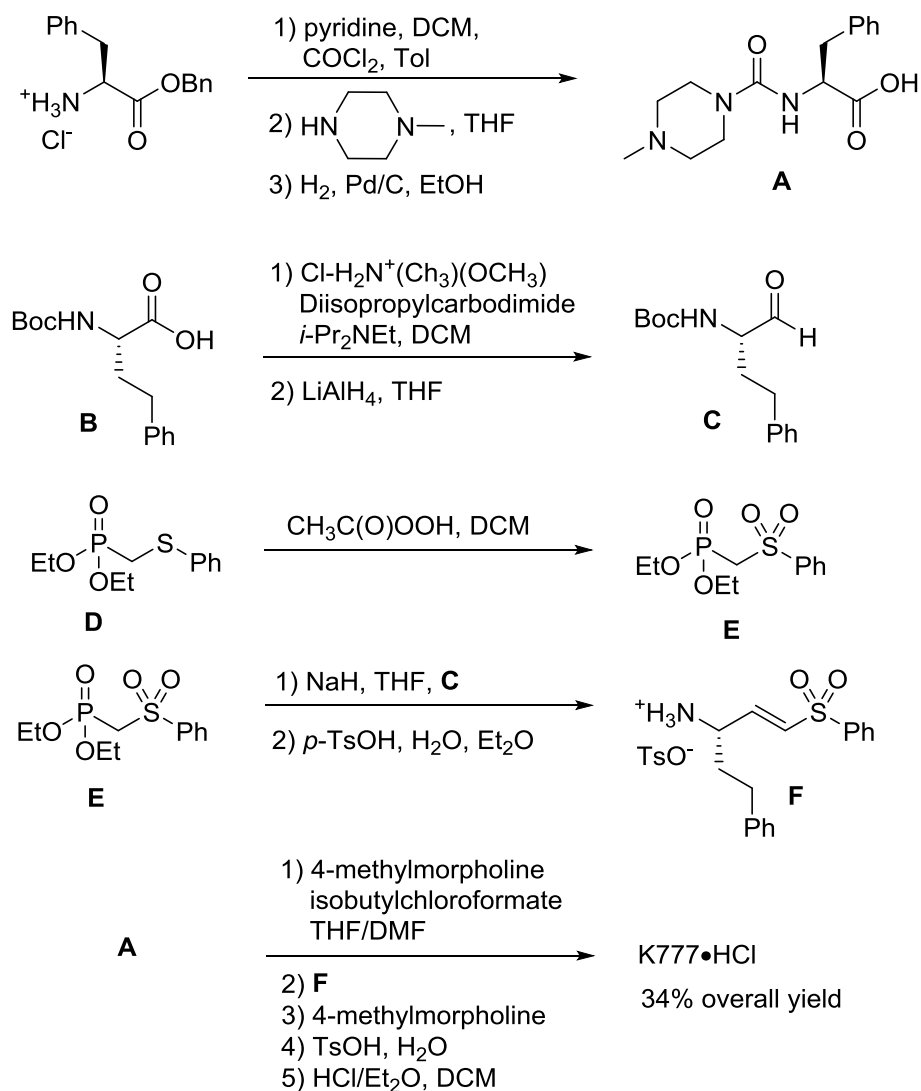


**Figure 4.2. General structure of vinyl sulfone peptidomimetic drugs and K777**

Several variations in the  $R^1$ ,  $R^2$  and  $R^3$  domains have been examined and K777 has been found to be the most promising for treatment of Chagas disease. K777 has already been tested in primates, dogs and mice and shown very promising results well within the guidelines set out by the WHO. Its first synthesis was reported by Palmer *et al* in 1995 (Scheme 4.3). While the  $P_3$  and  $P_2$  portions are readily synthesized from cheap and available starting materials, the original syntheses of the  $P_1$  and  $P_1'$  fragments had two major drawbacks: 1) the use of homophenylalanine as a starting material (Scheme 4.3, **B**) and 2) the need for Horner-Wadsworth-Emmons (HWE) olefination to generate the  $P_1'$  fragment (Scheme 4.3, conversion **E**  $\rightarrow$  **F**).

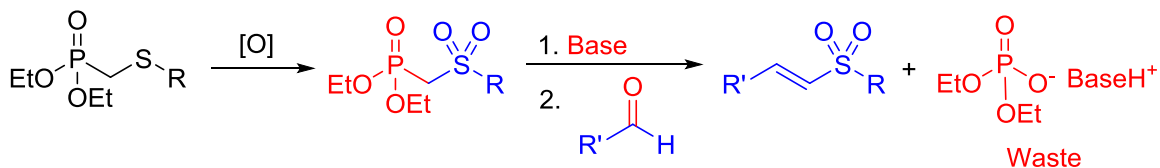


**Scheme 4.3. Palmer's synthesis of K777**

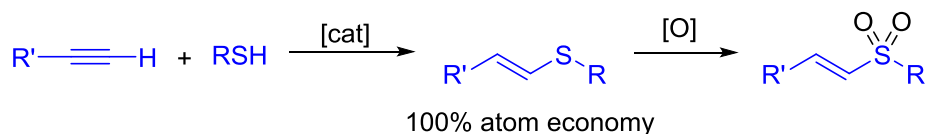
Homophenylalanine (Scheme 4.3, **B**) is an expensive unnatural amino acid, which significantly increases the cost of synthesis. Despite the fact that the P<sub>1</sub>' fragment is the functionally responsible for the drug's activity, variations in the P<sub>1</sub>' fragment have not been thoroughly investigated due to the necessity of independently synthesizing each HWE reagent. Furthermore, HWE olefination has poor atom economy. Therefore, while HWE olefination is

effective for synthesizing the desired  $P_1'$  fragment, it limits diversification of the strategy employed by Palmer. As shown in Scheme 4.3, several steps are required to reach the desired vinyl sulfone beginning from the expensive homophenylalanine starting material. Additionally, variations in the  $P_1'$  fragment are limited by the availability of substituted  $\alpha$ -mercaptophosphonate esters (Scheme 4.3, **D**). In order to address these concerns, we set out to synthesize K777 using the rhodium-catalyzed alkyne hydrothiolation methodology developed in our lab. Alkyne hydrothiolation has the advantage over HWE olefination in that it is an atom economic process and the methodology developed in our lab has broad substrate scope (Scheme 4.4). This strategy allows for the synthesis of a broad range of  $P_1'$  derivatives of K777 from cheap and readily available starting materials.

1. HWE strategy for synthesis of vinyl sulfones



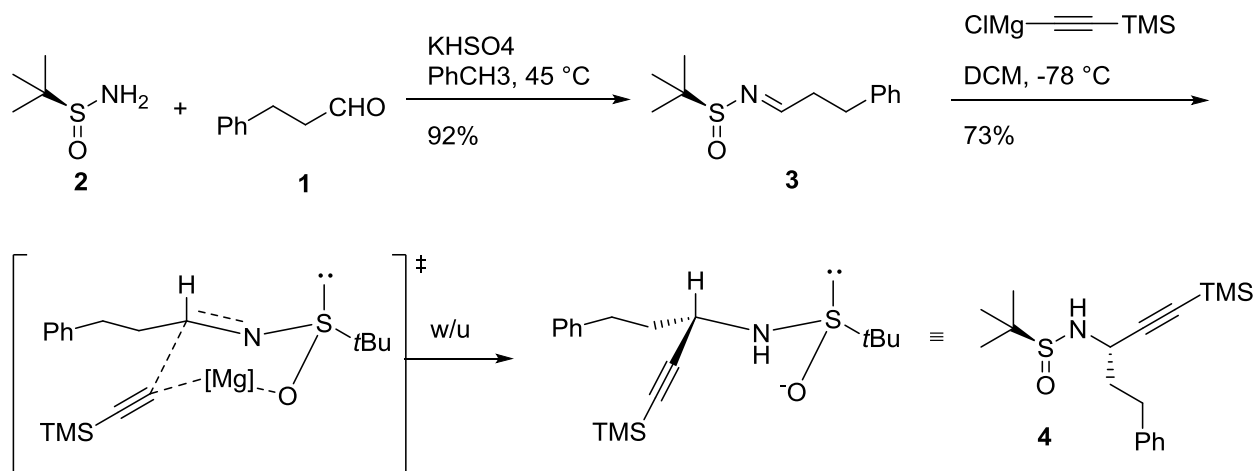
2. Alkyne hydrothiolation strategy for synthesis of vinyl sulfones



**Scheme 4.4. Comparison of HWE olefination versus alkyne hydrothiolation strategies for the synthesis of vinyl sulfones.**

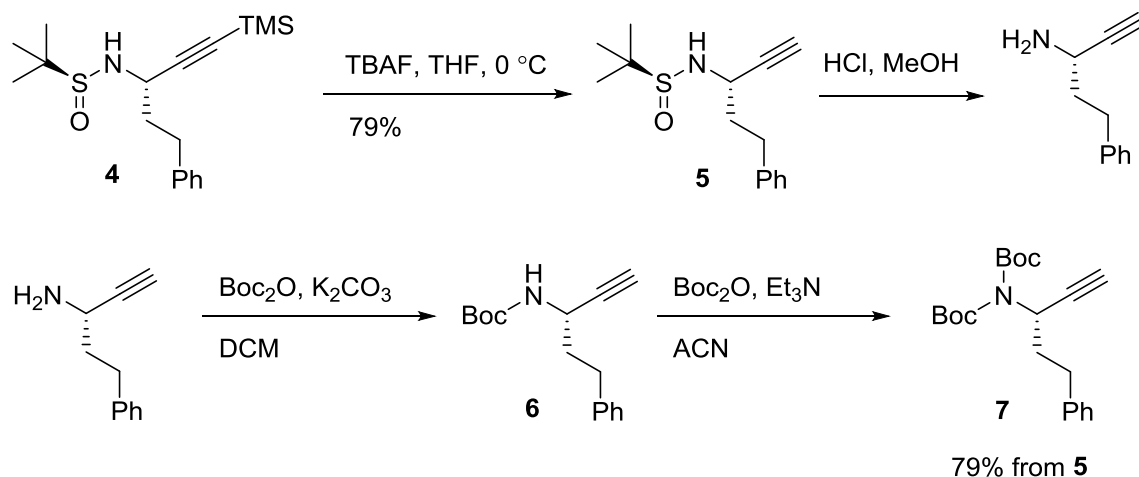
#### 4.2.1 Erica Kiemele's Synthesis of K777 via Rhodium-Catalyzed Alkyne Hydrothiolation

The synthesis of K777 via alkyne hydrothiolation was performed by Erica Kiemele, a previous master's student in the Love group. The synthesis follows a similar method for generation of the **A** fragment, with the substitution of triphosgene instead of phosgene.<sup>147</sup> Triphosgene is less toxic than phosgene and, in principle, only requires 0.33 equivalents relative to the amines to be coupled. The synthesis of the **A** fragment is otherwise identical. The synthesis of the **F** fragment began from cheap and readily available hydrocinnamaldehyde (**1**). In order to generate the homophenylalanine stereocenter, Ellman's auxiliary (**2**) was incorporated in order to direct addition of the acetylene Grignard reagent (Scheme 4.5). The addition of the Grignard reagent follows a *pseudo*-chair transition state in which the sterically bulky substituents are in equatorial positions.<sup>148</sup>



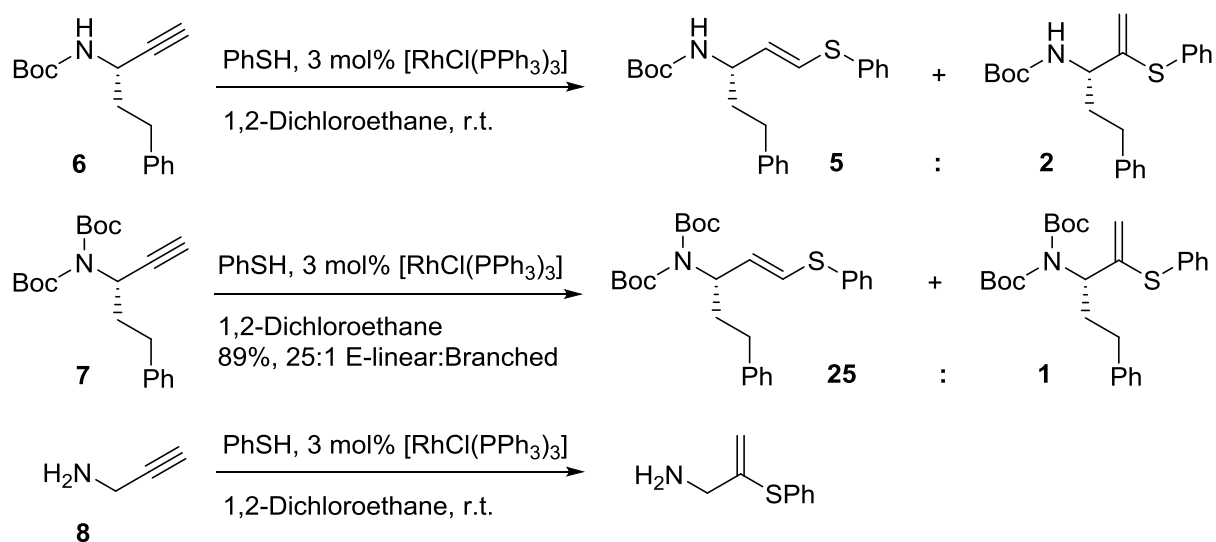
**Scheme 4.5. Diastereoselective synthesis of homophenylalanine stereocenter. Synthesis by Erica Kiemele.**

Deprotection of the TMS protected amine **4** yields the desired enantiomerically enriched terminal alkyne substrate for rhodium-catalyzed alkyne hydrothiolation. The Ellman's auxiliary can then be cleaved and recycled.<sup>149</sup>



**Scheme 4.6. Synthesis of di-Boc protected propargyl amine 7. Synthesis performed by Erica Kiemele.**

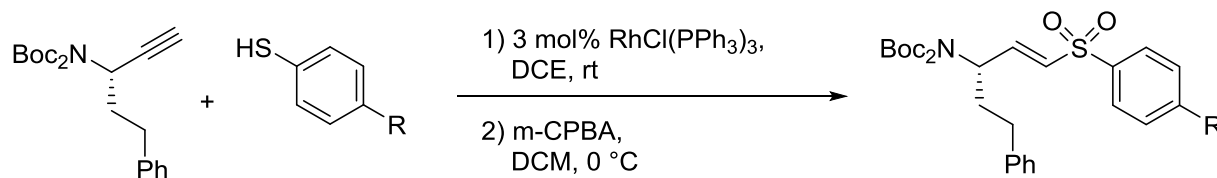
It was found that the nitrogen required double Boc protection in order to undergo alkyne hydrothiolation with high regioselectivity; mono-Boc protected propargyl amine **6** underwent hydrothiolation with poor regioselectivity (5:2) for the branched product (Scheme 4.7). Unprotected propargyl amine **8** was found to produce the branched regioisomer exclusively. The reversal of regioselectivity from *E*-linear to branched for the hydrothiolation of propargyl amines catalyzed by  $[\text{RhCl}(\text{PPh}_3)_3]$  can be attributed to pre-coordination of the nitrogen prior to migratory insertion. Pre-coordination causes the alkyne to insert with opposite regioselectivity. Double Boc protection of the propargyl amine prevents pre-coordination. The enhanced regioselectivity may also be a result of the increased steric bulk of the alkyne.



**Scheme 4.7. Rhodium-catalyzed alkyne hydrothiolation of propargyl amines. Reactions performed by Erica Kiemele and Paul Bichler.**

Subsequent chemoselective oxidation of the vinyl sulfide with *m*-CPBA generated the desired vinyl sulfones in high yield. With a general method for generating the desired vinyl sulfide in high regioselectivity, a series of aryl substituted vinyl sulfones were synthesized from the corresponding aryl thiols (Table 4.1). Enantiomeric excess for the vinyl sulfones were measured by HPLC using a chiral reverse phase column. The methodology was found to be generally applicable and high yielding. Notably, both chloro- and bromo-substituted aryl vinyl sulfones could be generated without any detectable cleavage of the carbon-halide bonds. This methodology can be extended to virtually any aryl or alkyl thiol. The substituted vinyl sulfones were then converted to the corresponding K777 derivatives by simple peptide coupling.

**Table 4.1. Synthesis of a series of *para*-substituted vinyl sulfones via rhodium-catalyzed alkyne hydrothiolation.**



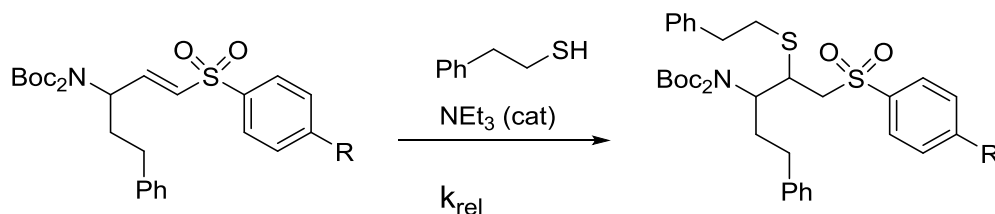
Entry	R	Vinyl sulfide Yield <sup>a</sup>	E-linear: Branched <sup>b</sup>	Vinyl sulfone Yield <sup>c</sup>	ee% <sup>c</sup>
1	H	89%	25:1	80%	96
2	OCH <sub>3</sub>	52%	50:1	81%	92
3	CH <sub>3</sub>	81%	50:1	79%	98
4	Cl	88%	50:1	68%	99
5	Br	80%	50:1	79%	90
6	CF <sub>3</sub>	84%	50:1	61%	98

Synthesis by Erica Kiemele. <sup>a</sup>Isolated yields after step 1. <sup>b</sup>Determined by integration of diagnostic <sup>1</sup>H NMR signals. <sup>c</sup>Isolated yields after step 2. <sup>c</sup>Determined by chiral HPLC separation. Performed by Diana Yu.

### 4.3 Rates of Michael Addition with *para*-Substituted Vinyl Sulfones

With a series of *para*-substituted vinyl sulfones in hand, we then sought to understand the effect of varying the substitution of the Michael accepting reactivity of the vinyl sulfones. Following the work of Roush and coworkers,<sup>150</sup> we simulated the reaction of the vinyl sulfone with the cysteine residue of the enzyme active site by reacting the vinyl sulfones with 2-phenethanethiol with triethylamine as an activator. Pseudo first order rate constants for the reaction of the series of *para*-substituted vinyl sulfones and 2<sup>o</sup>-(phenethyl)thiol in methanolic solution were measured and the data is presented in Table 4.2.

**Table 4.2. Relative rates of reaction of 2-phenethanethiol with a series of *para*-substituted vinyl sulfones.**



Entry	R	$\sigma^a$	$k_{\text{obs}} (\times 10^{-5} \text{ s}^{-1})^b$	$k_{\text{rel}}^c$	$t_{1/2} (\text{min})^d$
1	OCH <sub>3</sub>	-0.27	3.21 ± 0.27	0.34	360
2	CH <sub>3</sub>	-0.17	5.00 ± 0.11	0.52	231
3	H	0	9.53 ± 0.60	1	121
4	Cl	0.23	33.3 ± 1.6	3.49	35
5	Br	0.23	12.9 ± 0.68	1.35	90
6	CF <sub>3</sub>	0.54	156 ± 13	16.4	7

Racemic vinyl sulfones were used as substrates. <sup>a</sup>From Reference 118. <sup>b</sup>*Pseudo*-first order rate constant for disappearance of vinyl sulfone. Rate constants were determined by the slope of the natural log of concentration of the vinyl sulfone over time. Concentration of the vinyl sulfone was measured by integration of diagnostic <sup>1</sup>H NMR signals relative to trimethoxybenzene as internal standard. Reactions were performed in triplicate. See Appendix A. <sup>c</sup> $k_{\text{obs}}^{\text{R}}/k_{\text{obs}}^{\text{H}}$ . <sup>d</sup> $\ln(2)/k_{\text{obs}}$ .

In polar, protic solvents such as methanol, addition of thiols to Michael acceptors involves two steps: nucleophilic attack to generate an enolate ion, followed by protonation.<sup>151</sup> Relative rates are highly dependent on the electrophilicity of the  $\beta$ -carbon and stabilization of the emerging enolate.<sup>152</sup> Due to the poor overlap of  $sp^3$  and d orbitals between the  $\alpha$ -carbanion and sulfur, the stability of the carbanion intermediate is attributed to induction and  $\sigma$  effects of antibonding orbitals of the sulfur atom.<sup>153</sup> Consequently, Roush and coworkers found vinyl sulfonate ester **A** to be the most reactive Michael acceptor, reacting 25 times faster than vinyl sulfone **B** and 176 times faster than the  $\alpha$ - $\beta$ -unsaturated ester **C** (Figure 4.3).

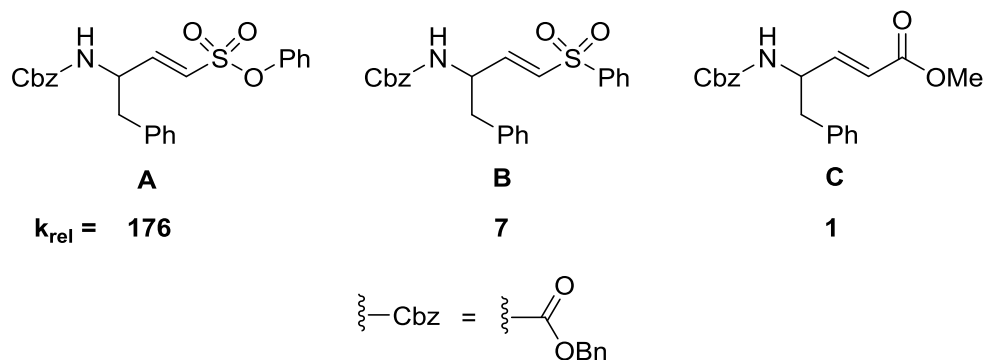


**Figure 4.3. Selection of Michael acceptors assayed by Roush and coworkers.**

Unsurprisingly, vinyl sulfones with electron-withdrawing substituents reacted much faster than those bearing electron-donating substituents. *Para*-trifluoromethyl ( $\sigma = 0.54$ ) reacted 16 times faster than compound the parent vinyl sulfone ( $R = H$ ), and 49 times faster than *para*-methoxy ( $\sigma = -0.27$ ). Comparison of half-lives is much more dramatic: whereas the half-life for compound the *para*-methoxy substituted vinyl sulfone is 6 h at room temperature, the half-life for the *para*-trifluoromethyl substituted vinyl sulfone is a mere 7 min. Such a drastic change in reactivity with the simple incorporation of a trifluoromethyl group on the aryl ring allows for significant changes in the pharmacodynamic properties of the drug without affecting the synthetic strategy. The broad scope of the alkyne hydrothiolation methodology, combined with the generality of peptide coupling strategies, allows for a wide variety of peptidomimetic vinyl sulfone inhibitors to be easily synthesized from readily available starting materials.

Measuring the rates of reaction for series of *para*-substituted compounds allowed us to generate a Hammett plot for the reaction of 2'-(phenethyl)thiol with vinyl sulfones (Figure 4.4). A Hammett plot is an empirical relationship between the electronic nature of the *para* substituent and the observed rate of reactions (*vide infra*). The high positive  $\rho$  value of 2.0 is consistent with

rate-limiting nucleophilic attack of the thiol. It is unclear at this time why the *para*-bromo substituted vinyl sulfone is slower than expected ( $R^2$  without including this data is 0.99).

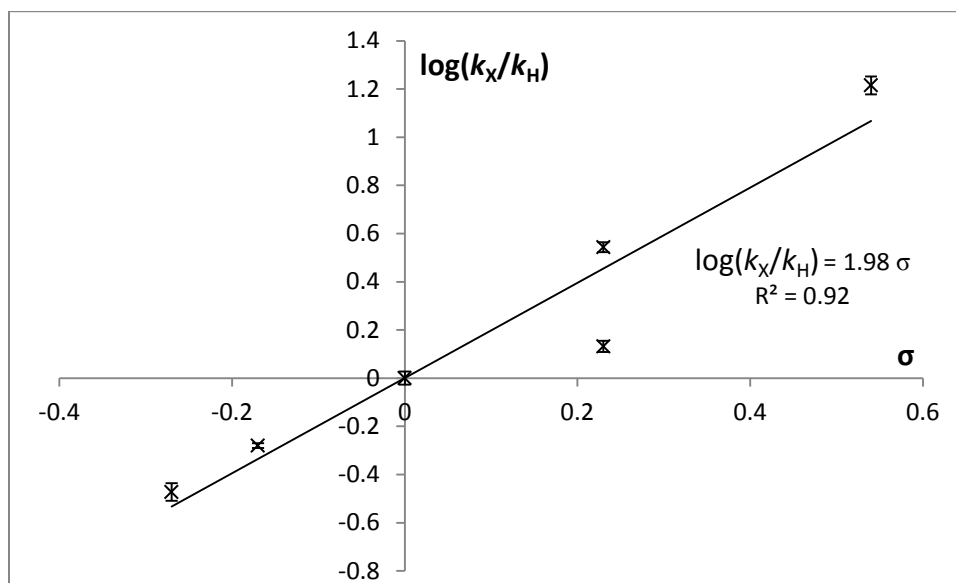


**Figure 4.4. Hammett plot for the reaction of 2'-(phenethyl)thiol with *para*-substituted vinyl sulfones.**

It should be noted that the barrier to nucleophilic attack of the cysteine residue in the active site is likely lower than that in methanolic solution due to activation by other active site residues (e.g. activation of the vinyl sulfone by hydrogen bonding to the sulfone oxygens). However, protonation of the resultant carbanion intermediate in aqueous solution is likely rapid; therefore, nucleophilic attack would still be rate-limiting. Thus differences in solution phase kinetics should be a good indication of the differences in the rate of inhibition. Inhibition is also dependent on the binding constant for the association of the inhibitor to the enzyme active site ( $K_I$ ). Thus a complete picture of the differences in reactivity requires the additional measurement of binding constants. For example, the enzyme active site must be able to accommodate the

additional steric bulk at the *para* carbon. Roush and coworkers evaluated several K777 derivatives in terms of their second order inhibition constants ( $k_{\text{inact}}/K_{\text{I}}$ ).<sup>154</sup> The analogues investigated include the sulfonate ester and the benzyl and phenethyl sulfones (Figure 4.5). Sulfonamides were found to be poor inhibitors of Cruzain. The results indicate that the P<sub>1</sub>' fragment has a significant effect on *in vitro* potency.

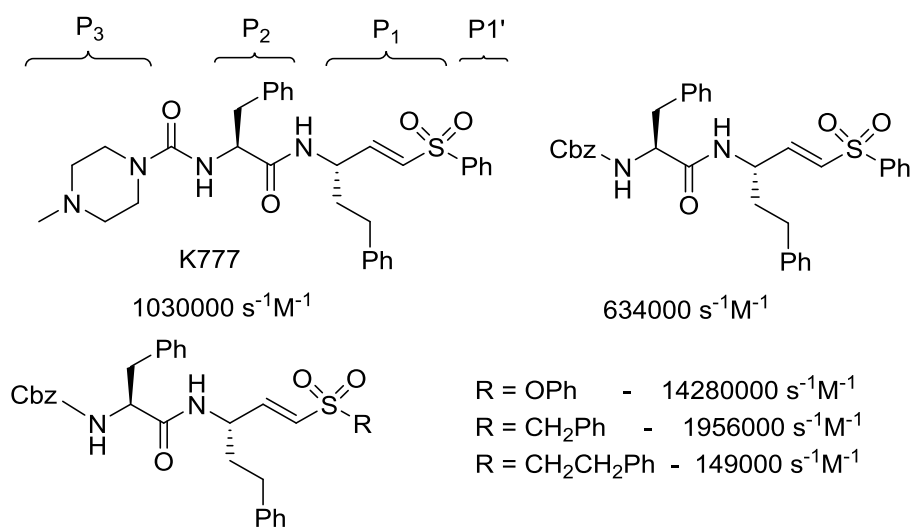


**Figure 4.5. P<sub>1</sub>' derivatives assayed by Roush and coworkers.**

The Cbz protected K777 P<sub>3</sub> derivatives have slightly weaker inhibition constants compared to K777. Nevertheless, comparison of P<sub>1</sub>' derivatives of the Cbz substituted compounds provides insight into the effects of varying the reactivity of the vinyl sulfone. The highest reactivity was observed with the sulfonate ester (R = OPh). The benzyl substituted vinyl sulfone had higher reactivity compared to the phenyl substituted parent compound; however the ethylphenyl substituted vinyl sulfone showed the weakest reactivity. The authors attributed the higher reactivity of the benzyl substituted vinyl sulfone to an increase binding affinity ( $K_{\text{I}}$ ), while

the high reactivity of the vinyl sulfonate ester is almost certainly due to increased electrophilicity of the vinyl sulfone and stabilization of the carbanion intermediate due to S-O  $\sigma^*$  interaction. The comparison between the benzyl and phenoxy substituted vinyl sulfones reveals that enhancement in the rate of inhibition ( $k_i$ ) can have a large impact in the overall efficacy of the molecule with respect to Cruzain inhibition. The large increase in second order inactivation constants from the benzyl to the phenoxy vinyl sulfone is mimicked Roush's solution phase analysis of the Michael reactivity of vinyl sulfones (*vide supra*). This lends validation to the Roush's assay and the potential implications of inhibitory activity of cysteine protease inhibitors. These results demonstrate that the variations in the P<sub>1</sub>' unit can have large effects on the rate of enzyme inactivation. Furthermore, the enhanced reactivity shown with the benzyl and phenethyl substituted derivatives indicate that the enzyme active site can accommodate an additional carbon unit (e.g., *para*-CF<sub>3</sub>) but not more. While the sulfonate ester shows the highest reactivity, sulfonate esters are unstable towards hydrolysis in aqueous solutions and therefore this derivative is unlikely to be a viable drug candidate.

#### 4.4 Conclusion

In this Chapter, we review the application of alkyne hydrothiolation catalyzed by [RhCl(PPh<sub>3</sub>)<sub>3</sub>] in Erica Kiemle's total synthesis of K777. The methodology proved to be very effective in the synthesis of K777 and derivatives thereof. The synthetic sequence solved two problems with Palmer's previously reported synthesis of K777. First, an enantioselective synthesis of the propargyl amine circumvented the use of homophenylalanine, an expensive unnatural amino acid. Second, hydrothiolation of the protected propargyl amine, catalyzed by [RhCl(PPh<sub>3</sub>)<sub>3</sub>], allowed for a series of K777 derivatives to be easily synthesized from readily

available starting materials. In contrast, the Horner-Wadsworth-Emmons olefination procedure employed by Palmer requires independent synthesis of each ylide reagent.

In order to model the expected changes in the rate of inhibition of Cruzain by different derivatives of K777, we examined the rate of Michael reaction between substituted vinyl sulfones and 2-phenethanethiol in methanolic solution. This model system has been shown to be an effective predictor of inhibition rates. Vinyl sulfones substituted with electron withdrawing reacted much faster than those substituted with electron donating groups. The large difference in reactivity towards Michael addition for vinyl sulfone derivatives allows for potential fine-tuning of the pharmacodynamics properties of the peptidomimetic vinyl sulfone drugs. The rate data allowed for construction of a Hammett correlation for *para*-substituted vinyl sulfones. The data was found to be consistent with rate-limiting nucleophilic attack of the thiol on the vinyl sulfone.

## **4.5 Experimental**

### **4.5.1 Measurement of Rate of Addition of 2-phenethanethiol to Vinyl Sulfones**

CD<sub>3</sub>OD was dried over Mg and Iodine and distilled under nitrogen. 2-Phenethanethiol was purified by vacuum distillation under nitrogen and dried over activated 4 Å molecular sieves. Triethylamine was dried over CaH<sub>2</sub> and distilled under nitrogen. 1,3,5-Trimethoxybenzene was purified by sublimation prior to use. Vinyl sulfone substrates were purified by column chromatography and dried under high vacuum prior to use. Kinetic measurements were performed using quantitative methods using 1,3,5-Trimethoxybenzene as an internal standard. Reactions were performed under nitrogen in screw-cap NMR tubes (total volume = 700 µL). Initial concentrations of reagents are as follows: trimethylamine 10.0 mM, 2-

phenethanethiol 78.0 mM, vinyl sulfone substrate 10.0 mM. The concentration of the vinyl sulfone was measured by  $^1\text{H}$  NMR via integration of the diagnostic vinyl sulfone peaks, relative to trimethoxybenzene as internal standard. Natural log of the concentration of the vinyl sulfone over time was used to determine the *pseudo*-first-order rate constants, which were linear for >5 half-lives. Reactions were performed in triplicate.  $^1\text{H}$  NMR spectra of the reactions and corresponding concentration versus time plots can be found in the Appendix.

# Chapter 5 Mechanistic Studies of Alkyne Hydrothiolation Catalyzed by $[\text{Tp}^*\text{Rh}(\text{PPh}_3)_2]$

## 5.1 Introduction

Vinyl sulfides, as well as their oxidized counterparts vinyl sulfoxides and vinyl sulfones, are useful synthetic intermediates and have been employed as key intermediates in many total syntheses.<sup>155</sup> Vinyl sulfoxides,<sup>156</sup> sulfides and sulfones are also important structural motifs in several existing pharmaceuticals and those under development. For example, Griseoviridin, a streptogramin antibiotic, is characterized by a macrocyclic vinyl sulfide linkage. K777, a drug to treat the globally neglected Chagas disease,<sup>157</sup> and Rigosertib, a potent anti-tumor agent,<sup>158</sup> both in clinical trials, are characterized by a vinyl-sulfone “warhead” responsible for their mechanism of action (Figure 5.1). Vinyl sulfones can be easily obtained from vinyl sulfides by simple oxidation.<sup>159</sup>

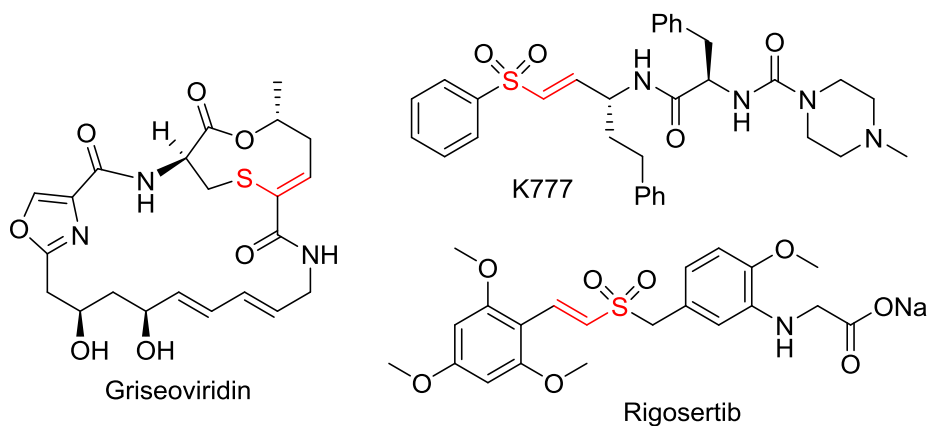


**Figure 5.1. Vinyl-sulfone containing pharmaceuticals.**

An efficient method for the preparation of vinyl sulfides is alkyne hydrothiolation – the addition of a thiol RS-H bond across an alkyne  $\text{RC}\equiv\text{CH}$  to produce a vinyl sulfide (Figure 5.2). Compared to other methods, alkyne hydrothiolation has the advantage of being a 100% atom economical approach, in that all starting material atoms are incorporated into the desired product, and that starting materials are readily accessible and typically commercially available. Nucleophilic and radical conditions for alkyne hydrothiolation have been known for decades;<sup>160</sup> however, transition-metal catalyzed alkyne hydrothiolation has only emerged in the last two decades due to the longstanding belief that thiols are potent catalyst poisons.<sup>161</sup> Three potential isomers may arise in alkyne hydrothiolation (Figure 5.2). Thus controlling both regio- and diastereoselectivity is paramount to rendering alkyne hydrothiolation a useful synthetic procedure.

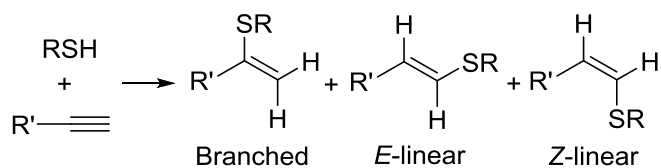
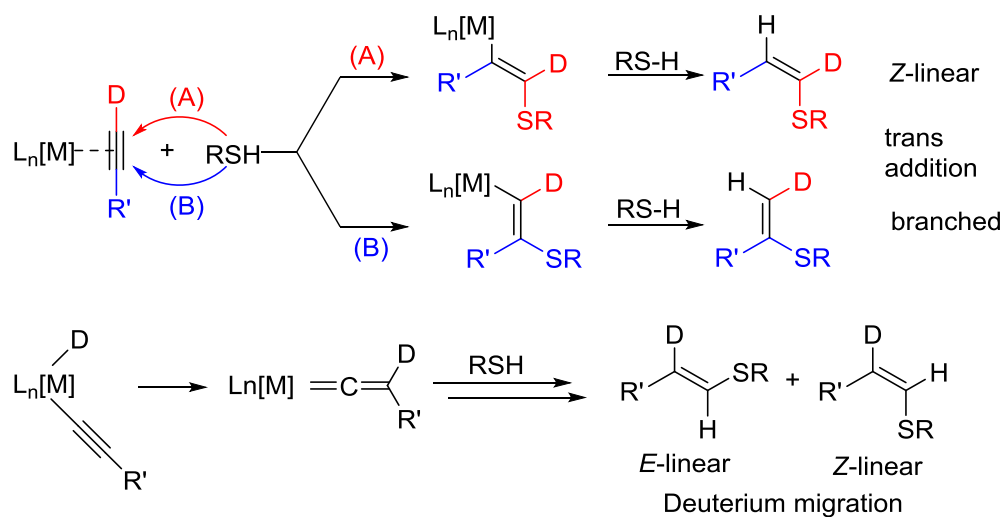


**Figure 5.2. Regio- and stereo-isomers in hydrothiolation of terminal alkynes.**

Alkyne hydrothiolation catalyzed by transition metal complexes can proceed through one of two entry points into the catalytic cycle: activation of the alkyne, or activation of the thiol. There are two potential mechanisms involving activation of the alkyne as an entry point to the catalyst: 1) activation of the alkyne through coordination to the metal center, followed by nucleophilic attack of the thiol, 2) activation of the terminal C-H of an alkyne to form a metal-vinylidene, which then undergoes external nucleophilic attack of the thiol (Scheme 5.1).

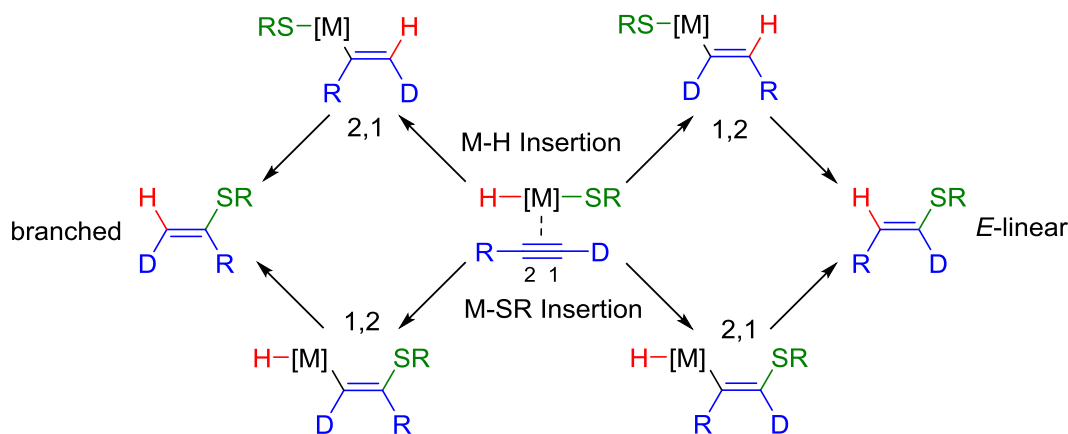
Mechanisms involving activation of the alkyne have been largely discounted by two observations: 1) addition of the thiol is syn and 2) *Z*-linear products are the result of background radical reactions that can be suppressed by shielding from light or addition of radical scavengers. While C-H activation of terminal alkynes has been observed for several rhodium complexes,<sup>162</sup> two additional observations exclude this mechanism: 1) no migration of deuterium label from the terminal carbon of the alkyne to the internal position is observed and 2) terminal alkynes are also viable substrates in metal-catalyzed alkyne hydrothiolation reactions. Consequently, alkyne hydrothiolation catalyzed by transition metal complexes has been proposed to proceed via activation of the S-H bond in the majority of systems.<sup>163</sup>



**Scheme 5.1. External nucleophilic attack on activated alkynes.**

Syn addition of the thiol results in control of diastereoselectivity (*E*- vs *Z*-linear isomers), however, control of regioselectivity (linear vs. branched) remains a challenge largely due to the mechanism of reaction. Oxidative addition of the thiol to the metal center produces a metal-

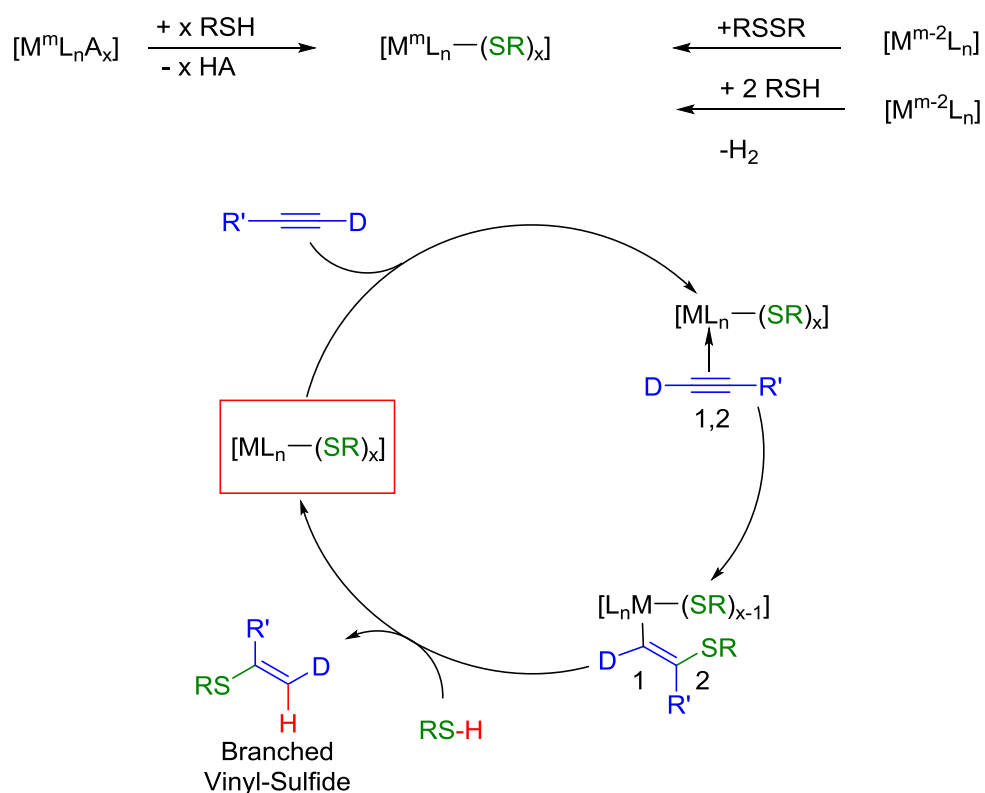
hydridothiolate complex  $[L_n[M](H)(SR)]$ . Consequently, there are four distinct pathways for alkyne insertion (Scheme 5.2). The alkyne may undergo 1,2 or 2,1 migratory insertion into either the M-H bond or the M-SR bond. In principle, all four pathways may be operating simultaneously, making an accurate description of mechanisms involving intermediate metal-hydridothiolate complexes difficult to characterize or control. Subsequent to oxidative addition and alkyne insertion, reductive elimination releases free vinyl sulfide product and completes the catalytic cycle. The hydride is typically more reactive than the thiolate, and 1,2 migratory insertion is generally favored due to steric and electronic interactions.<sup>164</sup> Consequently, alkyne hydrothiolation proceeding via the generation of an intermediate metal-hydridothiolate complex favors formation of *E*-linear vinyl sulfides.



**Scheme 5.2. Four pathways for migratory insertion in a metal-hydridothiolate intermediate.**

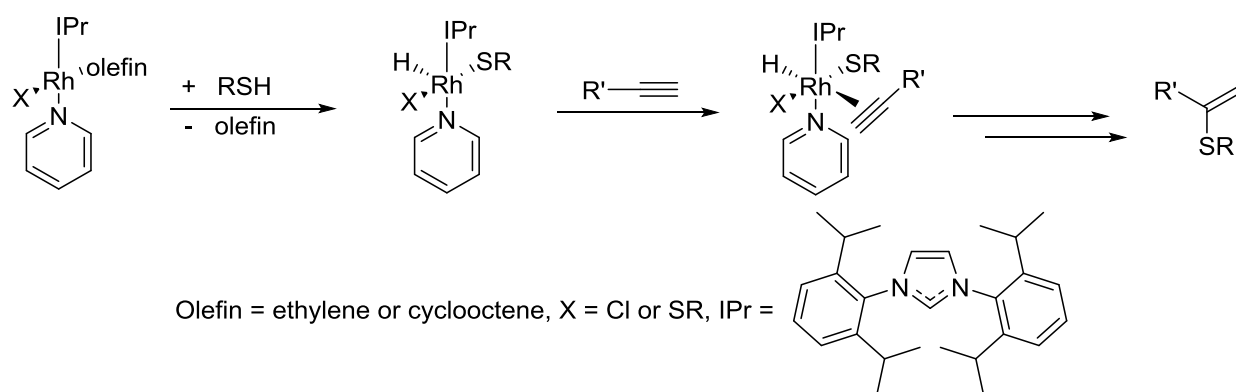
The most common strategy for formation of the branched regioisomer as the major product involves forming metal-thiolate complexes lacking any hydride moiety  $[L_n[M](SR)_x]$

(Scheme 5.3). The metal-thiolate complex can be accessed through one of three pathways: 1) protonation of acid-labile ligands on the precatalyst,<sup>165</sup> 2) oxidative addition of disulfides,<sup>166</sup> or 3) addition of 2 equivalents of thiol with concomitant release of dihydrogen.<sup>155</sup> Regioselectivity arises from 1,2 vs 2,1 migratory insertion of the alkyne into the metal-sulfur bond, with 1,2 alkyne migratory insertion again favored for steric and electronic reasons. Thus, the branched vinyl-sulfide is formed as the major product. Protonolysis of the vinylic carbon releases the vinyl sulfide product and regenerates the metal-thiolate intermediate.



**Scheme 5.3. Generation of metal-thiolate complexes (top). Catalytic cycle involving intermediate metal-thiolate complex (bottom).**

Another strategy involves forcing alkyne migratory insertion into the M-SR bond in a metal-hydrido-thiolate complex. This strategy was successfully and elegantly exploited by Castarlenas and coworkers. A switch in regioselectivity from *E*-linear to branched was observed when mononuclear rhodium N-heterocyclic carbene (NHC) complexes were employed in the presence of pyridine.<sup>167</sup> The authors attributed this change in selectivity to selective binding of the alkyne trans to the hydride, thereby forcing migratory insertion into the metal-thiolate bond (Scheme 5.4). In the absence of pyridine, the *E*-linear isomer is the major product, presumably due to preferential insertion into the Rh-H bond.



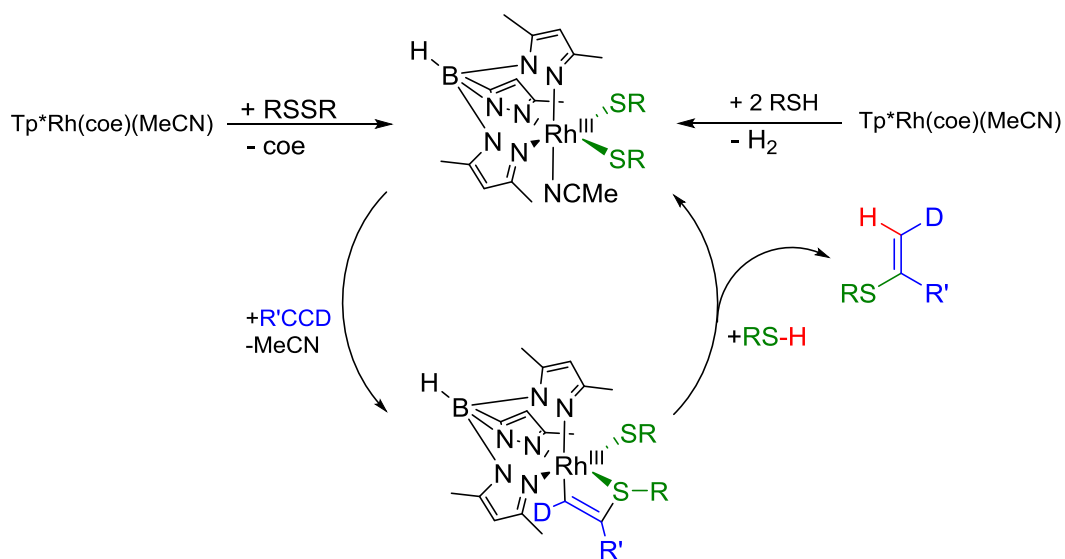
**Scheme 5.4. Coordination of alkyne trans to the hydride for [RhX(IPr)(pyr)( $\eta^2$ -olefin)]-catalyzed alkyne hydrothiolation.**

In this chapter, we explore the mechanism of [Tp\**Rh*(PPh<sub>3</sub>)<sub>2</sub>] catalyzed alkyne hydrothiolation through a series of kinetic investigations and substrate-activity relationships. [Tp\**Rh*(PPh<sub>3</sub>)<sub>2</sub>] was the first catalyst shown to be efficient in catalyzing alkyne hydrothiolation with aliphatic thiols and the first example of reversal in product regioselectivity by substitution of the anionic ligand. The results suggest a mechanism that is unique to [Tp\**Rh*(PPh<sub>3</sub>)<sub>2</sub>].

## 5.2 Results

### 5.2.1 Contrast Between $[\text{Tp}^*\text{Rh}(\text{PPh}_3)_2]$ and $[\text{Tp}^*\text{Rh}(\text{SPH})_2(\text{MeCN})]$ Catalyzed Alkyne Hydrothiolation

Prior to any rigorous mechanistic investigation, several observations led us to believe that alkyne hydrothiolation catalyzed by  $[\text{Tp}^*\text{Rh}(\text{PPh}_3)_2]$  did not involve an intermediate metal bithiolate complex. Mizobe and coworkers observed that  $[\text{Tp}^*\text{Rh}(\text{coe})(\text{MeCN})]$  forms  $[\text{Tp}^*\text{Rh}(\text{SR})_2(\text{MeCN})]$  upon reaction with disulfides (RSSR) by oxidative addition and loss of the cyclooctene ligand.<sup>168</sup> The same dithiolate complex was found to form upon treatment of  $[\text{Tp}^*\text{Rh}(\text{coe})(\text{MeCN})]$  with excess RSH, along with release of dihydrogen. The resulting  $[\text{Tp}^*\text{Rh}(\text{SR})_2(\text{MeCN})]$  was found to undergo insertion of alkynes to generate a rhodathiacyclobutene structure, which was characterized by x-ray crystallography.<sup>155</sup> Addition of thiol to the resulting rhodathiacyclobutene structure was found to form the branched product and regenerate the bithiolate complex (Scheme 5.5).



**Scheme 5.5. Stoichiometric reactions for branched product formation with  $[\text{Tp}^*\text{Rh}(\text{SR})_2(\text{MeCN})]$ -catalyzed alkyne hydrothiolation (ref. 155).**

Contrary to the related complex  $[\text{Tp}^*\text{Rh}(\text{coe})(\text{MeCN})]$  employed by Mizobe and coworkers,  $[\text{Tp}^*\text{Rh}(\text{PPh}_3)_2]$  was found to be unreactive towards disulfides.<sup>169</sup> Furthermore, when  $[\text{Tp}^*\text{Rh}(\text{PPh}_3)_2]$  was treated with excess thiol, no release of dihydrogen was observed, a necessary by-product of metal-bisthiolate complex formation. Additionally, thioketal products, from addition of two equivalents of thiol to the alkyne, were observed for  $[\text{Tp}^*\text{Rh}(\text{SPh})_2(\text{MeCN})]$ -catalyzed reactions, but never observed for  $[\text{Tp}^*\text{Rh}(\text{PPh}_3)_2]$  catalyzed reactions. Finally, added triphenylphosphine was found to accelerate the rate of product formation, suggesting that, unlike the ancillary  $\text{coe}$  and  $\text{MeCN}$  ligands in the Mizobe system, phosphine is involved in the overall mechanism.

## 5.2.2 Kinetic Order and Phosphine Dependence

Kinetic order experiments were conducted to determine the relationship between substrate, catalyst, and phosphine concentration and reaction rate. Reaction rates were determined by either initial rates or by determining the *pseudo*-first order observed rate constant ( $k_{\text{obs}}$ ). Both measurements were made to determine what, if any, difference existed between the initial phase of the reaction and the overall reaction progress. While most reactions were performed at 12 °C, initial rate measurements were performed at 8 °C in order to obtain sufficient data points within the initial linear phase of the reaction. The reaction was found to be first order in catalyst, first order in alkyne (Figure 5.3) and first order in thiol up to 1.5 equivalents of thiol to alkyne (Figure 5.4).<sup>169,170</sup> Above a 1.5:1 ratio of thiol : alkyne, significant substrate inhibition was observed. Order in catalyst in C<sub>6</sub>D<sub>6</sub> had been previously reported by Shiva Shoai.<sup>170</sup> Catalyst order experiments were repeated by Chris Tehennepe in a 50:50 mixture of C<sub>6</sub>D<sub>6</sub> : DCE.<sup>169</sup> Both experiments showed a first order dependence on catalyst concentration. These results give an overall empirical rate law as described in equation 1.

$$\frac{d[P]}{dt} = k[\text{PhSH}]^1[\text{PhCCH}]^1[\text{RhTp}^*(\text{PPh}_3)_2]^1 \text{ (eqn. 1)}$$

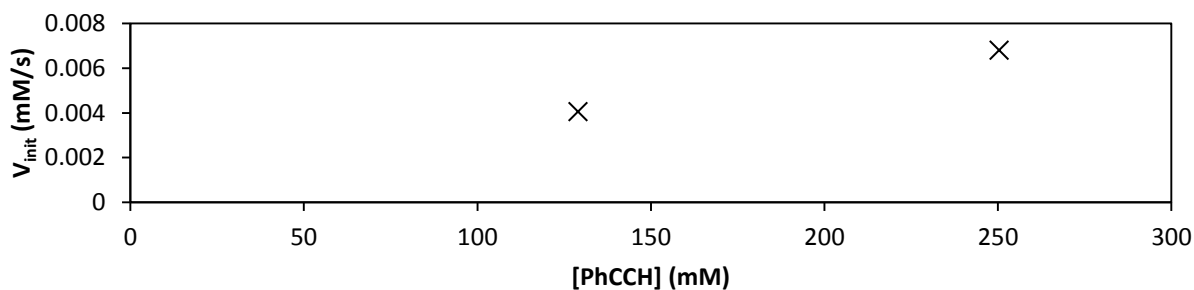


**Figure 5.3. Initial rate of product formation versus [PhCCH].**

Experiments performed by Chris Tehennepe.<sup>170</sup> Conditions: 8.95 mM [Tp<sup>\*</sup>Rh(PPh<sub>3</sub>)<sub>2</sub>], 275 mM [PhSH]. Solvent: 50:50 C<sub>6</sub>D<sub>6</sub> : DCE. Temperature: 8 °C. Initial rates of product formation were measured by integration of the diagnostic vinyl sulfide peaks relative to trimethoxybenzene as internal standard.

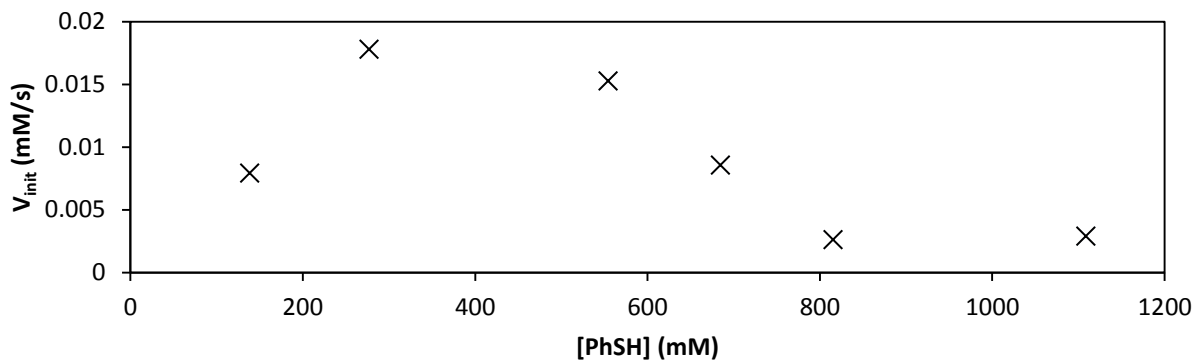


**Figure 5.4. Initial rate of product formation versus [PhSH].**

Experiments performed by Chris Tehennepe.<sup>159</sup> Conditions: 8.95 mM  $[\text{Tp}^*\text{Rh}(\text{PPh}_3)_2]$ , 250 mM  $[\text{PhCCH}]$ . Solvent: 50:50  $\text{C}_6\text{D}_6$  : DCE. Temperature: 8 °C. Initial rates of product formation were measured by integration of the diagnostic vinyl sulfide peaks relative to trimethoxybenzene as internal standard.

The empirical rate law derived from Figure 5.3 and 5.4 is necessarily incomplete and its interpretation should be considered with a significant degree of skepticism. This is due to two factors. First, Figure 5.3 only contains two data points. Second, any attempts to linearize concentration dependencies, especially by initial rate measurements, necessarily hides complex subtleties in the rate law by essentially ignoring the contribution from the denominator. A more rigorous method for kinetic analysis is Reaction Progress Kinetic Analysis (RPKA) and the “same excess, different excess” methodology popularized by Donna Blackmond.<sup>171</sup> RPKA analysis of alkyne hydrothiolation catalyzed by  $[\text{Tp}^*\text{Rh}(\text{PPh}_3)_2]$  is a matter for future work.

Perhaps more interesting is the relationship between the rate of product formation and the concentration of added phosphine (Figure 5.5). Above 50 mM added  $\text{PPh}_3$ , expected *pseudo*-inverse-first order dependence on added  $\text{PPh}_3$  is observed. However, low concentrations of added phosphine increased the rate of product formation. No effect on the regioselectivity of the reaction was observed in the presence of added  $\text{PPh}_3$ .

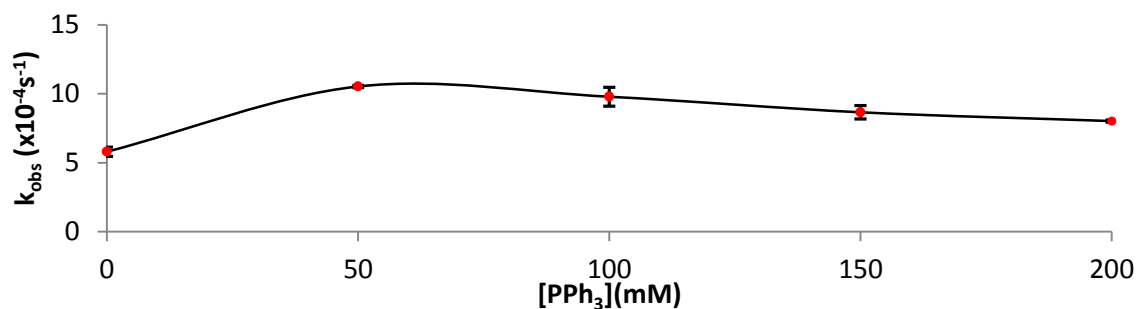


**Figure 5.5.**  $k_{obs}$  vs added [PPh<sub>3</sub>].

Line is guide only. Conditions: 8.95 mM [Tp\*Rh(PPh<sub>3</sub>)<sub>2</sub>], 275 mM [PhSH], 250 mM [PhCCH]. Solvent: C<sub>6</sub>D<sub>6</sub>. Temperature: 12 °C. *Pseudo*-first order rate constants for product formation were determined by natural log plots of the integration of the diagnostic vinyl sulfide peaks relative to trimethoxybenzene as internal standard.

### 5.2.3 Deuterium Kinetic Isotope Effects

We hypothesized that employing a deuterated thiol might reveal the presence of an intermediate rhodium-hydrido-thiolate complex. Inverse deuterium kinetic isotope (KIE) effects are common for systems in which reductive elimination of a hydride and a carbon fragment from the metal center is rate-limiting.<sup>172</sup> Reductive elimination of alkanes and arenes has been found to give inverse KIEs in several systems, most notably for reductive elimination from [Tp\*Rh(CNCH<sub>2</sub>Me<sub>3</sub>)(H)(R)] complexes (R = alkyl, aryl).<sup>173</sup> Indeed, significant inverse kinetic isotope effects were observed for deuterated thiols, while no kinetic isotope effect was observed for deuterated alkyne (Figure 5.6). For the hydrothiolation of phenylacetylene using 4-CF<sub>3</sub>OPhSH, the KIE is within error of that for PhSH.

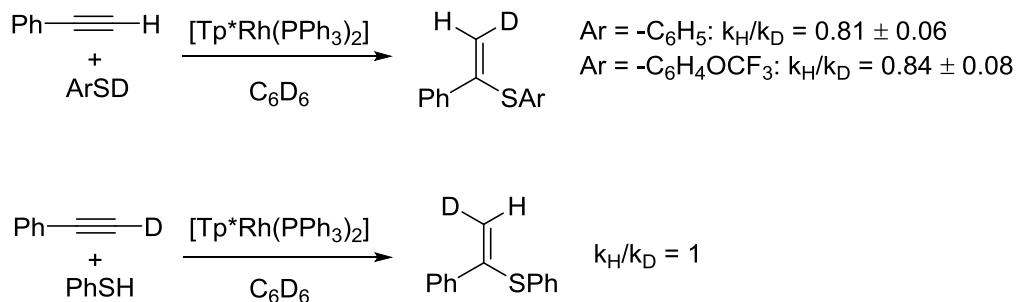


**Figure 5.6. KIE for alkyne hydrothiolation catalyzed by  $[\text{Tp}^*\text{Rh}(\text{PPh}_3)_2]$ .**

### 5.2.4 Stoichiometric Reactions

In addition to the observed kinetic isotope effect, hydride signals in stoichiometric reactions between  $[\text{Tp}^*\text{Rh}(\text{PPh}_3)_2]$  and thiophenol can be observed by  $^1\text{H}$  NMR spectroscopy at  $-33^\circ\text{C}$ . A total of four hydride signals are observed at low temperature upon addition of one equivalent of thiophenol to a solution of  $[\text{Tp}^*\text{Rh}(\text{PPh}_3)_2]$  in  $d_8$ -toluene (Figure 5.7). The hydride  $^1\text{H}$  NMR signals are split into doublets due to coupling to the rhodium nucleus, and again (when applicable) by coupling to the phosphorus nucleus or nuclei. The solution remained unchanged even upon standing at room temperature for two days. Unfortunately, these species are formed in very low concentration, precluding all but the most basic NMR characterization.

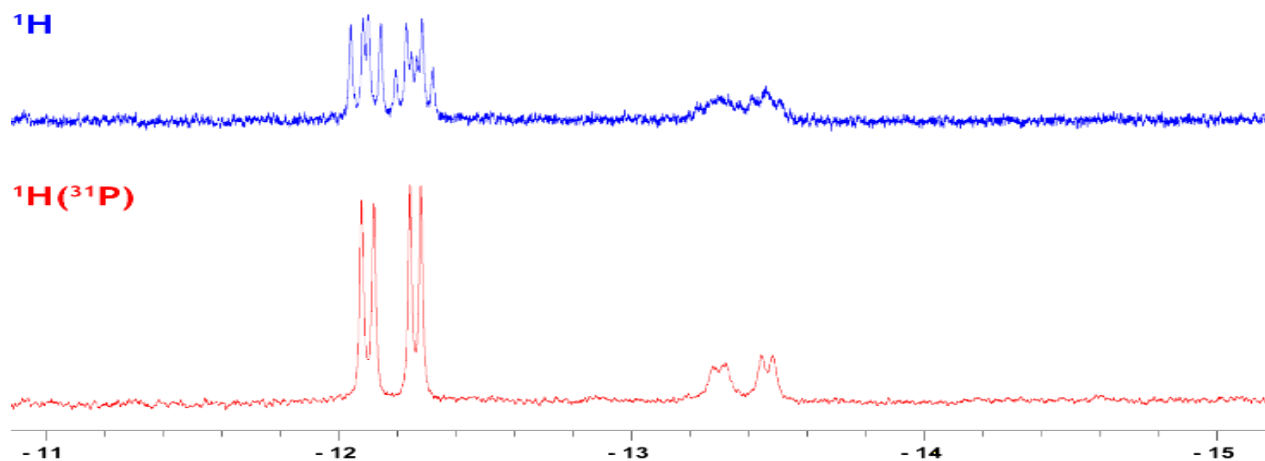


**Figure 5.7.**  $^1\text{H}$  NMR and  $^1\text{H}\{^{31}\text{P}\}$  NMR spectra at  $-33^\circ\text{C}$  for reaction between  $\text{Tp}^*\text{Rh}(\text{PPh}_3)_2$  and  $\text{PhSH}$ .

Addition of one equivalent of phenylacetylene to the solution of  $[\text{Tp}^*\text{Rh}(\text{PPh}_3)_2]$  and  $\text{PhSH}$  results in the appearance of several new hydride signals along with the observance of product formation (Figure 5.8). Without phosphorus decoupling, the new hydride signals are not resolved enough to observe.

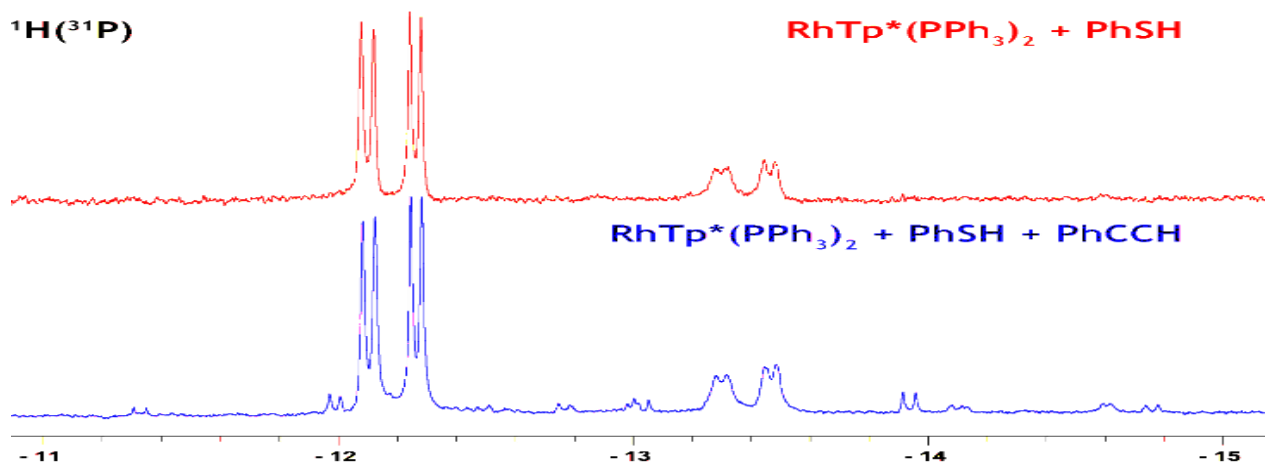


**Figure 5.8.**  $^1\text{H}\{^{31}\text{P}\}$  NMR spectrum at  $-33^\circ\text{C}$  for the addition of  $\text{PhCCH}$  to a solution of  $\text{Tp}^*\text{Rh}(\text{PPh}_3)_2$  and  $\text{PhSH}$ .

## 5.2.5 Thiol Substrate-Activity Relationship

We hypothesized that alkyne migratory insertion into either the Rh-H or Rh-SR bond would be strongly dependent on the electronic nature of the thiol. In order to assess the effect of varying the electronic nature of the thiolate on the rate and selectivity of the reaction, we examined a series of *para*-substituted aryl thiols bearing electron-donating and electron-withdrawing substituents. The results are outlined in Table 5.1, where  $k_{\text{norm}} = k_{\text{obs}}/[\text{Tp}^*\text{Rh}(\text{PPh}_3)_2]$

**Table 5.1. Rates and regioselectivity of vinyl sulfide formation for various *para*-substituted aryl thiols**

Substituent	$\sigma^{-a}$	$k_{\text{norm}}(\times 10^{-2} \text{ s}^{-1} \text{ M}^{-1})^b$	B : E-lin <sup>c</sup>
-OCH <sub>3</sub>	-0.26	8.97 ± 0.88	88 : 12
-CH <sub>3</sub>	-0.17	7.27 ± 0.21	86 : 14
-N(CH <sub>3</sub> ) <sub>2</sub>	-0.12	7.77 ± 0.27	95 : 5
-F	-0.03	4.54 ± 0.049	62 : 38
-H	0	4.75 ± 0.12	70 : 30
-SCH <sub>3</sub>	0.06	3.72 ± 0.33	59 : 41
-Cl	0.19	2.89 ± 0.35	57 : 43
-Br	0.25	2.49 ± 0.56	39 : 61
-OCF <sub>3</sub>	0.27	2.81 ± 0.43	34 : 66

<sup>a</sup> $\sigma^{-}$  values from Taft.<sup>174</sup> <sup>b</sup> $k_{\text{obs}}/[\text{Tp}^*\text{Rh}(\text{PPh}_3)_2]$ . <sup>c</sup>Measured by the relative integration of the diagnostic vinyl sulfide signals. Conditions: 8.95 mM  $[\text{Tp}^*\text{Rh}(\text{PPh}_3)_2]$ , 275  $[\text{ArSH}]$ , 250 mM  $[\text{PhCCH}]$ . Solvent:  $\text{C}_6\text{D}_6$ . Temperature: 12 °C. *Pseudo*-first order rate constants ( $k_{\text{obs}}$ ) for product formation were determined by natural log plots of the integration of the diagnostic vinyl sulfide peaks over time, relative to trimethoxybenzene as internal standard.

The results show a strong dependence on the electronic nature for both the rate and the regioselectivity of thiol addition. Aryl thiols bearing electron donating groups (e.g., methoxy) in

the para position react much more rapidly than those with electron-withdrawing groups (e.g., trifluoromethoxy). Aryl thiols with strongly electron-withdrawing groups in the para position (e.g. trifluoromethyl, nitro) gave less than 5% conversion over the course of two weeks. A smooth reversal of regioselectivity is also observed; electron-rich thiols favor formation of the branched isomer, while electron-poor thiols favor *E*-linear product formation (Figure 5.9).

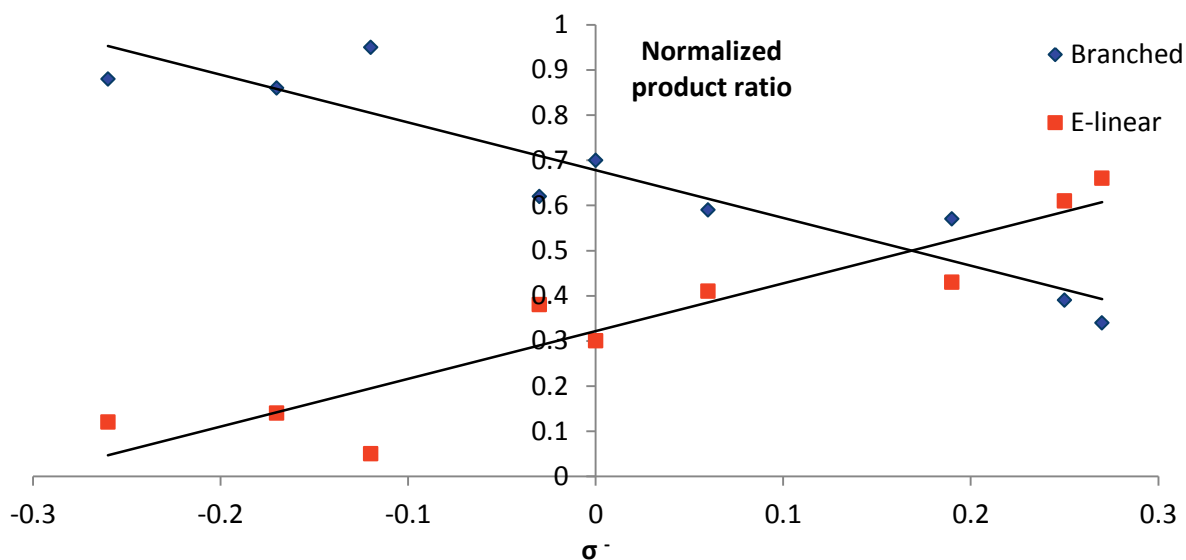


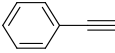
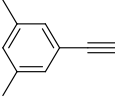
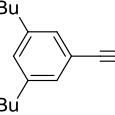
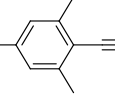
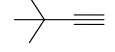
**Figure 5.9.** Normalized product selectivity versus  $\sigma^-$  constants for *para*-substituted arylthiols. Lines are guides only. Data from Table 4.1.

### 5.2.6 Alkyne Steric Bulk

In order to address the directionality of alkyne migratory insertion, we turned our attention to the steric bulk of the alkyne. We hypothesized that terminal alkynes with bulkier substituents would be expected to increase 1,2 migratory insertion due to increased steric interactions. Consequently, increased selectivity for the branched vinyl sulfide would be expected if migratory insertion of the alkyne into the Rh-SR bond was occurring. Conversely,

increased selectivity for the *E*-linear isomer would be expected if migratory insertion into the Rh-H bond were occurring. The results of these experiments are outlined in Table 5.2. There was no change in rate or selectivity for 3,5-dimethylphenylacetylene, while 3,5-di-*tert*-butylphenylacetylene resulted in a 10% decrease in the rate of product formation. The [Tp\*Rh(PPh<sub>3</sub>)<sub>2</sub>]-catalyzed hydrothiolation of MesCCH required gentle heating to 40 °C for reaction to occur. The effect of increased steric bulk is dramatic for sterically demanding alkynes: complete selectivity for the branched isomer was observed with MesCCH, even with an electron-deficient thiol.

**Table 5.2. Hydrothiolation of substituted phenylacetylenes**

Alkyne	Thiol	Branched : <i>E</i> -linear <sup>a</sup>
	PhSH 4-(CF <sub>3</sub> O)PhSH	70 : 30 34 : 66
	PhSH 4-(CF <sub>3</sub> O)PhSH	70 : 30 n/d <sup>d</sup>
	PhSH 4-(CF <sub>3</sub> O)PhSH	>95 : 5 <sup>b</sup> 50 : 50
	PhSH 4-(CF <sub>3</sub> O)PhSH	>95 : 5 <sup>b, c</sup> >95 : 5 <sup>b, c</sup>
	PhSH 4-(CF <sub>3</sub> O)PhSH	>95 : 5 <sup>e</sup> >95 : 5 <sup>e</sup>

Conditions: 8.95 mM [Tp\*Rh(PPh<sub>3</sub>)<sub>2</sub>], 275 [ArSH], 250 mM [PhCCH]. Solvent: C<sub>6</sub>D<sub>6</sub>. Temperature: 12 °C. <sup>a</sup>Measured by the relative integration of the diagnostic vinyl sulfide signals. <sup>b</sup>No *E*-linear vinyl sulfide was observed by <sup>1</sup>H NMR. <sup>c</sup>Samples were heated to 40°C. <sup>d</sup>Not determined. <sup>e</sup>Some *E*-linear were observed due to background radical reaction. Samples were heated to 45°C. Increased catalyst loading to 10 mol%.

### 5.2.7 Alkyne Substrate-Activity Relationship

A similar study of the effects of para substitution for terminal aryl alkynes was also undertaken. In stark contrast to the effects of varying the electronic nature of the thiol, both the rate and regioselectivity of product formation were found to be independent of alkyne electronics for most alkynes studied (Table 5.3). Strongly electron-deficient alkynes such as *p*-CF<sub>3</sub>PhCCH and *p*-NO<sub>2</sub>PhCCH, however, resulted in less than 5% conversion over the course of 2 weeks.

**Table 5.3. Rates and regioselectivity of vinyl sulfide formation for various *para*-substituted terminal aryl alkynes**

Substituent	$\sigma^+$ (a)	$k_{\text{norm}}(10^{-2}\text{s}^{-1}\text{M}^{-1})^{(b)}$	Branched : E-linear
-OCH <sub>3</sub>	-0.78	4.47 ± 0.97	77 : 23
-CH <sub>3</sub>	-0.31	5.43 ± 0.24	70 : 30
-F	-0.07	5.62 ± 0.14	74 : 26
-H	0	4.75 ± 0.18	70 : 30
-Cl	0.11	5.52 ± 0.23	77 : 23
-Br	0.15	4.36 ± 0.64	74 : 26

<sup>a</sup> $\sigma^+$  values from Taft.<sup>161</sup> <sup>b</sup> $k_{\text{obs}}/[\text{Tp}^*\text{Rh}(\text{PPh}_3)_2]$ . Conditions: 8.95 mM [Tp\*Rh(PPh<sub>3</sub>)<sub>2</sub>], 275 mM [PhSH], 250 mM [ArCCH]. Solvent: C<sub>6</sub>D<sub>6</sub>. Temperature: 12 °C. *Pseudo*-first order rate constants ( $k_{\text{obs}}$ ) for product formation were determined by natural log plots of the integration of the diagnostic vinyl sulfide peaks over time, relative to trimethoxybenzene as internal standard.

### 5.2.8 Eyring Data

Enthalpies and entropies of activation were calculated in both toluene and a mixture of benzene and 1,2-dichloroethane (DCE) to determine what, if any, the effect of solvent or solvent mixtures might have on the mechanism or rate-limiting step. The data in Figure 5.10 were measured by initial rates in a 1:1 mixture of C<sub>6</sub>D<sub>6</sub> : DCE by undergraduate student Chris Tehennepe, and the data in Figure 5.11 were determined by measuring *pseudo*-first-order rates constants, normalized in catalyst concentration, in *d*<sub>8</sub>-toluene.

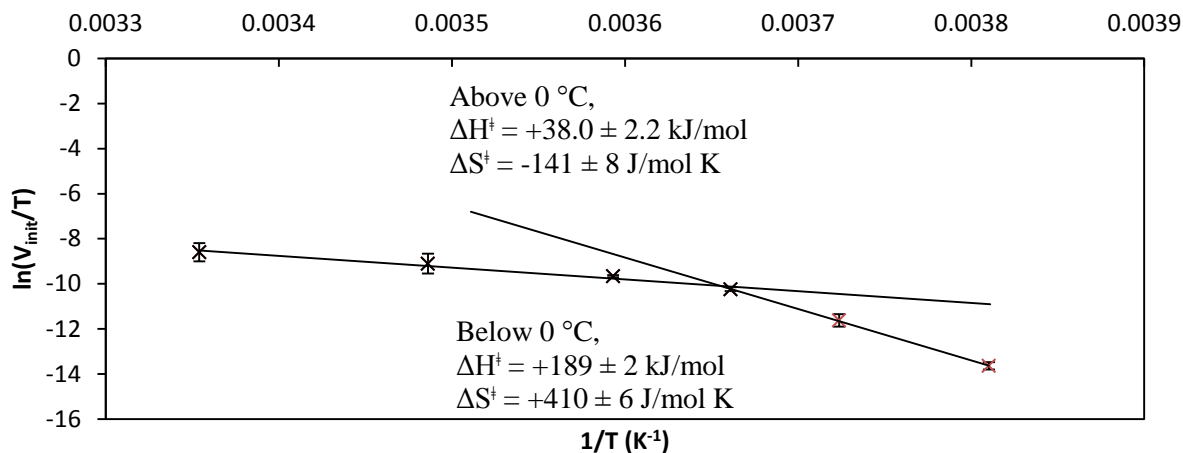


**Figure 5.10. Eyring plot by initial rates in 1:1 mix of C<sub>6</sub>D<sub>6</sub> : DCE.**

Experiments performed by Chris Tehennepe.<sup>159</sup> Conditions: 8.95 mM [Tp\*Rh(PPh<sub>3</sub>)<sub>2</sub>], 275 mM [PhSH], 250 mM [PhCCH]. Solvent: 50:50 C<sub>6</sub>D<sub>6</sub> : DCE. Initial rates of product formation were measured by the slope of product concentration over time. Product concentration was determined by <sup>1</sup>H NMR via integration of the diagnostic vinyl sulfide peaks, relative to trimethoxybenzene as internal standard.

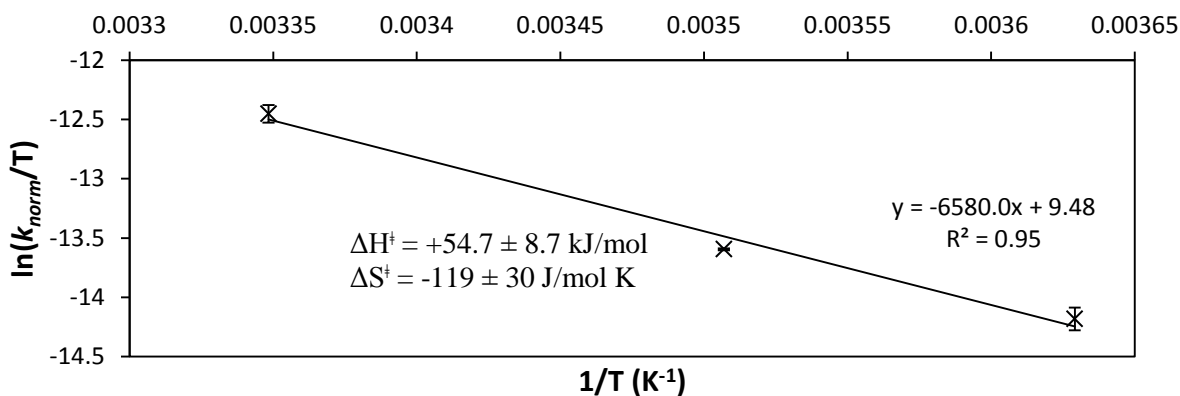


**Figure 5.11. Eyring plot in *d*<sub>8</sub>-toluene by *pseudo*-first order rate constants (*k*<sub>obs</sub>).**

Conditions: 8.95 mM [Tp\*Rh(PPh<sub>3</sub>)<sub>2</sub>], 275 mM [PhSH], 250 mM [PhCCH]. Solvent: C<sub>7</sub>D<sub>8</sub>. *Pseudo*-first order rate constants (*k*<sub>obs</sub>) for product formation were determined by natural log plots of the concentration of the vinyl sulfide over time. Product concentration was determined by <sup>1</sup>H NMR via integration of the diagnostic vinyl sulfide peaks, relative to trimethoxybenzene as internal standard.

Eyring parameters for product formation above 0 °C were calculated to be  $\Delta H^\ddagger = +38.0 \pm 2.2$  kJ/mol and  $\Delta S^\ddagger = -141 \pm 8$  J/mol K by initial rates in a mixture of C<sub>6</sub>D<sub>6</sub> and DCE, and  $\Delta H^\ddagger = +54.7 \pm 8.7$  kJ/mol and  $\Delta S^\ddagger = -119 \pm 30$  J/mol K by *pseudo*-first order rate constants in *d*<sub>8</sub>-toluene, using weighted linear regression analysis. No changes in product selectivity were observed over the temperature range examined, including the region after the observed break in reactivity.

Unfortunately, above 25 °C the reaction was too fast to monitor by NMR spectroscopy and below 0 °C product formation was no longer *pseudo*-first order in *d*<sub>8</sub>-toluene. Instead, the reaction showed near linear or zeroth-order product formation (Figure 5.12). Time course plots of the *E*-linear product also exhibit the same change in reactivity as those for the formation of the branched product at low temperatures (Figure 5.13). This change in reactivity is further exemplified in Figure 5.10 by an apparent break or curvature below 0 °C, where significantly reduced initial rates are observed. The Eyring parameters calculated after the apparent break from Figure 5.10 are  $\Delta H^\ddagger = +189 \pm 2$  kJ/mol and  $\Delta S^\ddagger = +410 \pm 6$  J/mol K. Below -15 °C, product formation essentially ceases, and no meaningful kinetic data can be acquired. Due to these experimental limitations, the temperature range over which data could be collected was limited.

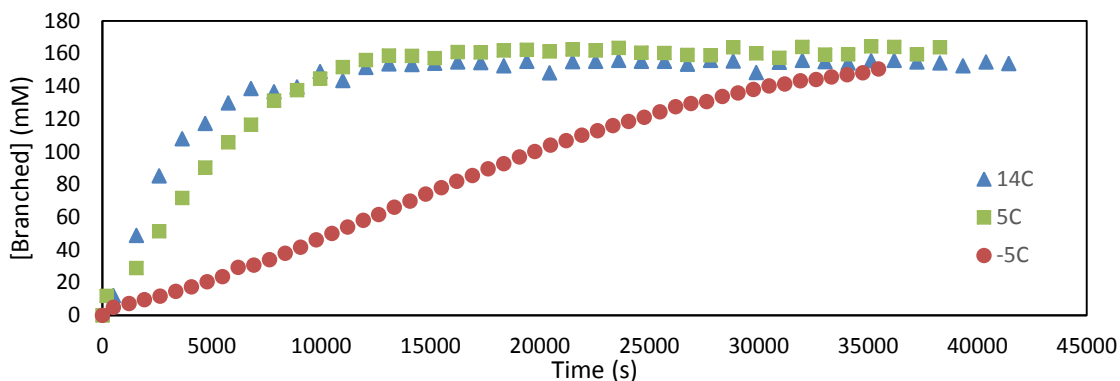


**Figure 5.12.** Time-course plots for production of branched product at 14 °C, 5 °C and -5°C

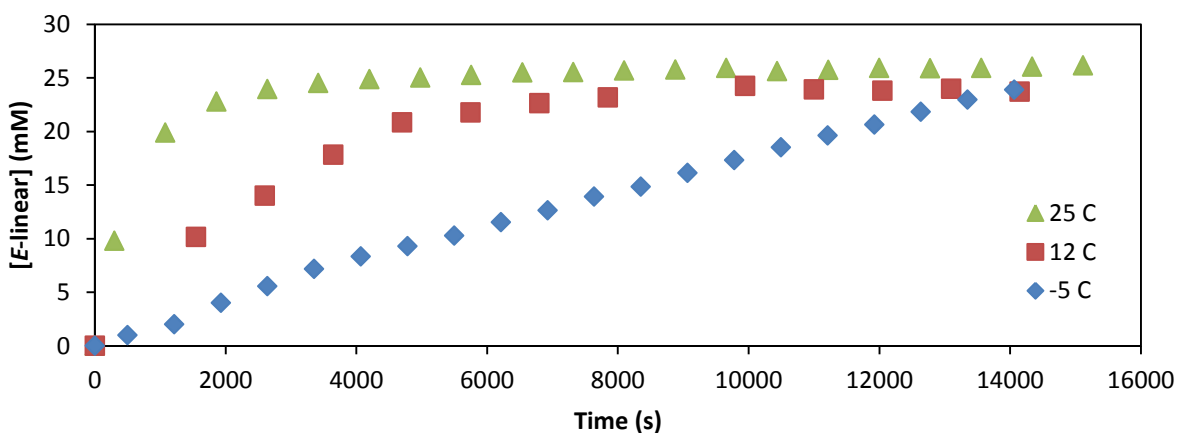


**Figure 5.13.** Time course plots for the production of the *E*-linear product at 25 °C, 12 °C, and -5 °C.

### 5.2.9 DFT Calculations of Alkyne Insertion Products

In collaboration with Dr. Shrinwantu Pal, some preliminary DFT calculations were undertaken to understand the effects of sterics on alkyne insertion. Structures for the insertion products of 1-propyne with putative hydrido thiolate intermediates were calculated at the BP86/6-31G(d,p) level of theory (Figure 5.14). The results indicate that the methyl substituents of the Tp\* ligand have a significant impact on the relative energies of the two

rhodathiacyclobutenes resulting from 1,2 versus 2,1 insertion. This is consistent with the results of preparative scale reactions, in which the [Tp\*Rh(PPh<sub>3</sub>)<sub>2</sub>] was found to give better selectivity for the branched product compared to [TpRh(PPh<sub>3</sub>)<sub>2</sub>].

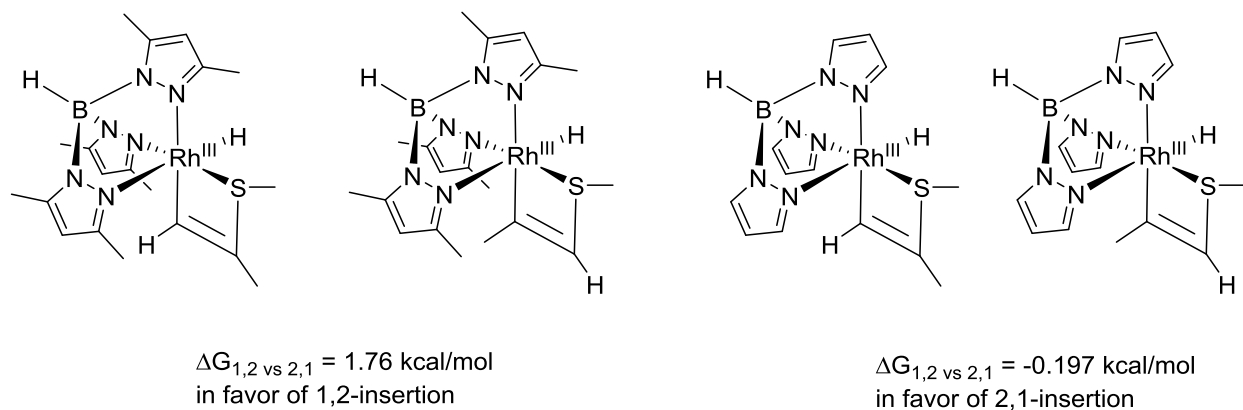


**Figure 5.14. Calculated energies for 1,2 and 2,1 rhodathiacyclobutenes.**

## 5.3 Discussion

### 5.3.1 Hydridothiolate vs Bisthiolate Intermediate

As discussed in the introduction, there are two generally accepted mechanisms for transition-metal-catalyzed alkyne hydrothiolation. The first involves a hydridothiolate intermediate, and the second involves a thiolate or polythiolate intermediate. In the case of [Tp\*Rh(SPh)<sub>2</sub>(MeCN)]-catalyzed alkyne hydrothiolation, the latter mechanism was shown to be viable through stoichiometric reactions. However, several observations for [Tp\*Rh(PPh<sub>3</sub>)<sub>2</sub>]-catalyzed alkyne hydrothiolation were inconsistent with a bisthiolate mechanism, as discussed above.

Consistent with our hypothesis of a hydridothiolate intermediate, inverse KIE were observed for both PhSH and (*p*-CF<sub>3</sub>O)PhSH. The only step in a bisthiolate mechanism involving activation of the RS-H bond is protonation of the alkenyl ligand to release product. If this step was rate-limiting, a normal ( $k_H/k_D > 1$ ) kinetic isotope effect would be expected.<sup>175</sup> Additionally, more electron deficient (i.e. more acidic) thiols would be expected to react more rapidly, when in fact the opposite is observed in [Tp\*Rh(PPh<sub>3</sub>)<sub>2</sub>]-catalyzed alkyne hydrothiolation. These results, in addition to the qualitative observations listed above, are inconsistent with a bisthiolate mechanism.

### 5.3.2 Kinetic Order and PPh<sub>3</sub> Dependence

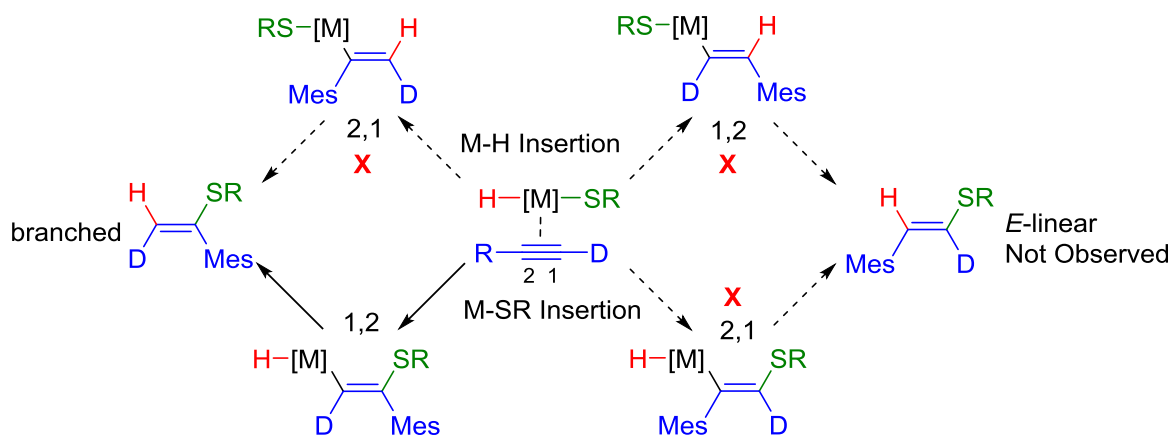
First-order dependence on catalyst concentration reveals that the active catalyst is monomeric in rhodium, ruling out any potential dimeric or  $\mu$ -thiolate bridged species. First-order dependence on thiol and alkyne concentration reveals that both species enter the catalytic cycle prior to the rate-limiting step. The substrate inhibition observed at high concentrations of thiophenol suggests competitive inhibition, likely with alkyne coordination.

The effects of added PPh<sub>3</sub> are more complex. The *pseudo*-inverse first-order dependence observed at higher concentrations of added PPh<sub>3</sub> is consistent with competitive inhibition, likely with alkyne coordination, prior to the rate-limiting step. However the initial increase in the rate of product formation may be due to several effects. Phosphine coordination may be required for generation of the active species, or added phosphine may prevent the formation of inactive, off-cycle species. Alternatively, phosphine coordination may be required in the rate-limiting step. The effects of added phosphine will be discussed in more detail below. The lack of any changes

in regioselectivity with added phosphine suggests that the observed reversal in regioselectivity does not involve changes in the speciation of the active catalyst.

### 5.3.3 Alkyne Steric Effects

The results of alkyne steric bulk on product selectivity is strongly indicative of selectivity arising from 1,2- vs 2,1-migratory insertion. Since the *E*-linear product is not observed for MesCCH, this rules out both 1,2-insertion into the Rh-H bond and 2,1-insertion into the Rh-S bond as possible pathways (Scheme 5.6). More importantly, it effectively rules out migratory insertion into the Rh-H bond. Given the relative sizes of H, S and Rh, increased selectivity for the *E*-linear isomer via 1,2 migratory insertion of the alkyne into the Rh-H bond would be expected for MesCCH. However the opposite regioselectivity is observed, suggesting selective insertion into the Rh-SR bond.



**Scheme 5.6. Possible insertion pathways for MesCCH with  $[\text{Rh}(\text{H})(\text{SR})]$  species.**

Of the remaining two pathways, 1,2-insertion into the Rh-SR bond is much more likely for two reasons: 1) significantly reduced steric interactions, 2) stabilization of the resulting

insertion product by a dative  $S \rightarrow Rh$  interaction. We presume that migratory insertion into the Rh-SR bond would result in a rhodathiacyclobutene structure with a dative interaction similar to the structure isolated by Mizobe and coworkers (Scheme 5.5, *vide supra*). In examining the insertion of ethylene and propene into Rh-X bonds, Hartwig and coworkers calculated that the initial products of insertion into Rh-X bonds ( $X = O, N$ ) contained dative  $O \rightarrow M$  and  $N \rightarrow Rh$  bonds.<sup>176</sup> These interactions significantly increased the overall stability of the insertion product.

In Figure 5.15 we show the solid state structure of  $[Tp^*RhCl_2(PPh_3)_2]$ .<sup>177</sup> While this solid state structure is known, it nevertheless lends a strong argument to the expected steric interactions for 2,1-insertion pathways. Firstly, for successful 2,1-insertion, the aryl moiety would have to be positioned between two pyrazole rings of the  $Tp^*$  ligand during binding and insertion. The phenyl ring of  $PPh_3$  in the solid state structure satisfies this condition, indicating that 2,1-insertion is indeed possible. Second, the measured distances between the ortho (2.5 Å) and meta (4.7 Å) hydrogens of the  $PPh_3$  phenyl ring and the pyrazole rings are strongly correlated with the observed changes in selectivity. While meta substitution would result in some steric interaction with the 5-methyl substituents on the pyrazole ring, there is sufficient space to accommodate a *tert*-butyl substituent, since this substituent would lie parallel to the ligand system. This is consistent with the increased, but not 100%, branched selectivity observed for 3,5-di-*tert*-butylphenylacetylene. In contrast, the distance of 2.5 Å between the ortho hydrogen and the pyrazole rings cannot accommodate even a methyl substituent. This would prevent any 2,1-insertion pathways for *ortho*-substituted aryl alkynes, consistent with the proposed insertion pathway for MesCCH in Scheme 5.6.

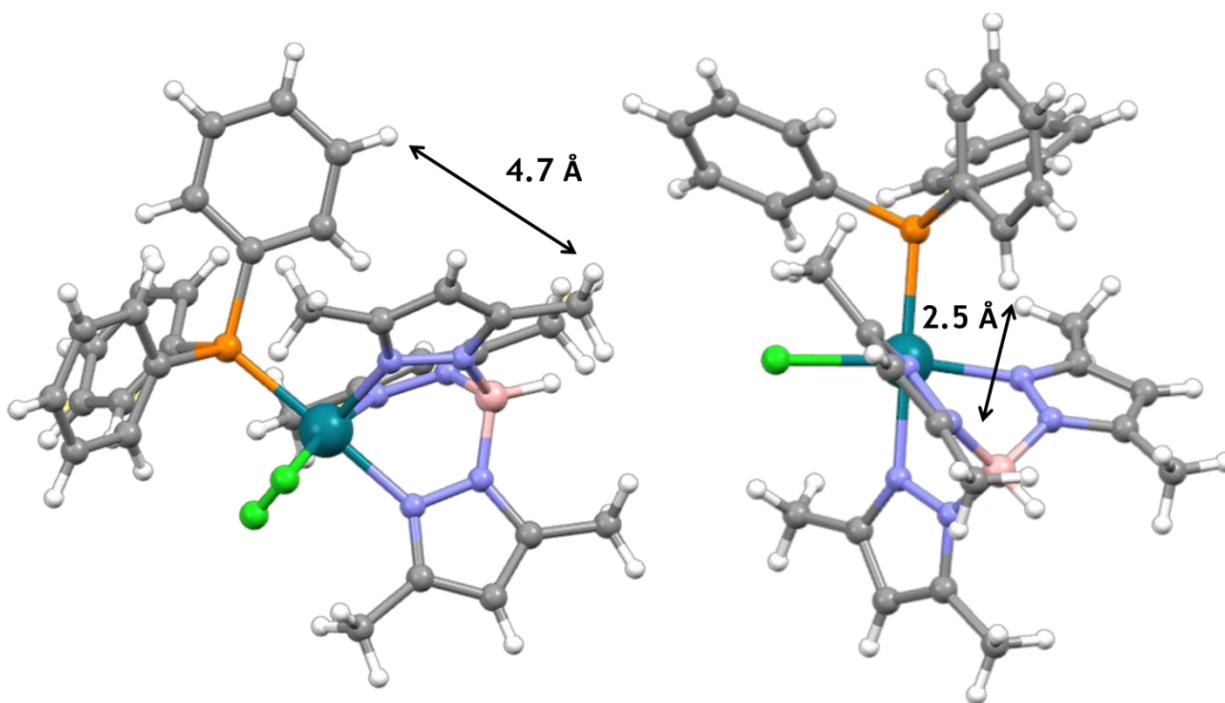


**Figure 5.15.** Solid state structure of [Tp\*RhCl<sub>2</sub>(PPh<sub>3</sub>)<sub>2</sub>].

#### 5.3.4 Substrate-Activity Relationships.

As expected, the rate and regioselectivity of alkyne hydrothiolation catalyzed by [Tp\*Rh(PPh<sub>3</sub>)<sub>2</sub>] is strongly dependent on the electronic nature of the thiol. In order to better understand the effects of thiol electronics on the rate of reaction, a Hammett plot for the series of *para*-substituted aryl thiols was constructed (Figure 5.16). The data is best fitted to a single parameter correlation to Hammett  $\sigma$ - constants. No improvement in goodness of fit was observed upon fitting to any dual parameter correlation.

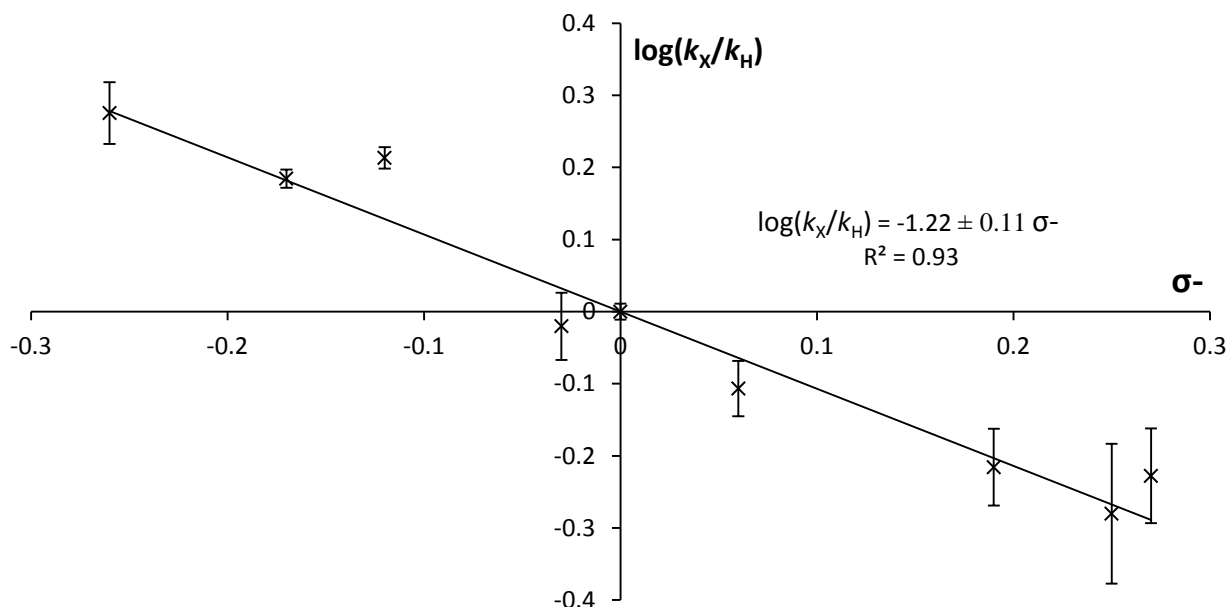


**Figure 5.16. Hammett plot for *para*-substituted aryl thiols.**

The negative  $\rho$  value of  $-1.22 \pm 0.11$  can be interpreted in one of two ways. In a classical sense, the negative  $\rho$  value is indicative of a buildup of positive charge in the rate-limiting step, stabilized by increased electron donation from sulfur atom. However it can also be interpreted as being the result of more favorable interactions between the sulfur and the rhodium during the rate-limiting step.

Importantly, the linear relationship in the Hammett plot, combined with the similar KIE for both PhSD and 4-(CF<sub>3</sub>O)PhSD, suggest that the observed reversal of selectivity is not due to change in mechanism or rate-limiting step, but rather that both regioisomers are formed through a similar mechanism and/or common intermediate. This is further evidenced by the virtually identical Eyring parameters for the formation of both regioisomers, and their similar change in reactivity at low temperatures. The complete lack of any change in rate of product formation or

regioselectivity for variation in alkyne electronics is certainly unexpected. This is discussed in greater detail below.

### 5.3.5 Eyring Data

The data presented in Figure 5.10 and Figure 5.11 reveal similar Eyring parameters for alkyne hydrothiolation catalyzed by  $[\text{Tp}^*\text{Rh}(\text{PPh}_3)_2]$  in both 1:1  $\text{C}_6\text{D}_6$ :DCE and  $d_8$ -toluene, suggesting that neither the mechanism nor the rate-limiting step is affected to any significant degree by changes in solvent. This data is important for two reasons. First, the data suggests that the Eyring data obtained in  $d_8$ -toluene is applicable to the overall mechanistic studies presented herein, which were performed in  $\text{C}_6\text{D}_6$ . Second, the data suggests that the mechanistic data presented in this chapter is applicable to the preparative scale reactions, which are performed in a 1:1 mixture of DCE : toluene.

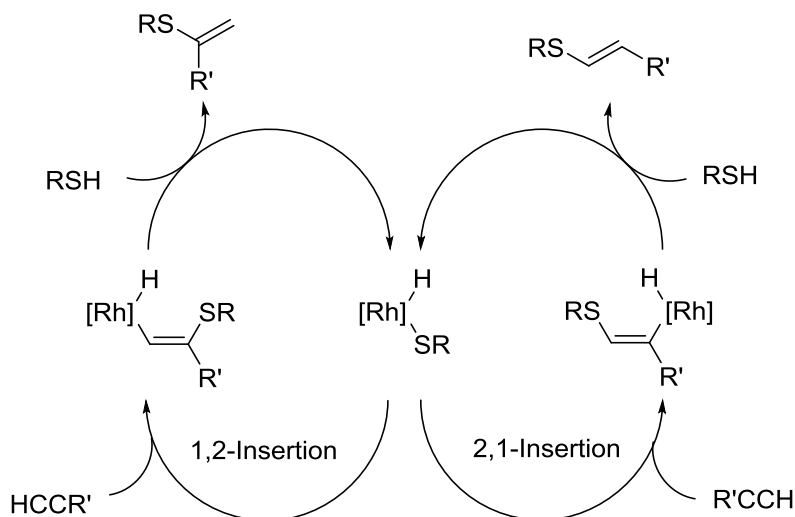
The positive enthalpies of activation shown in Figure 5.10 and Figure 5.11 suggest that significant bond reorganization is occurring in the rate-limiting step, while the negative entropies of activation suggest that the transition state for the rate-limiting step is highly organised or associative in nature.

The observed break in reactivity below 0 °C is either due to a change in mechanism or a change in rate-limiting step. At this point it is unclear which change is responsible for the observed break in kinetic profile. However, since there is no observed change in product selectivity, we hypothesize that the break is due to a change in rate-limiting step. Because of the entropic cost of dissociative events, it is reasonable to expect that this step would become rate-limiting at lower temperatures. This is consistent with the observed large positive entropy of activation at low temperatures.

The identical Eyring parameters for the formation of both the branched and *E*-linear products offer further proof that the two products form through a common mechanism. Additionally, the identical changes in reactivity at lower temperatures suggest that both products are derived from a common intermediate.

#### 5.4 Proposed Mechanism

Based on the kinetic data and substrate-activity relationships, we propose the following general mechanism outlined in Scheme 5.7. Initial oxidative addition of the thiol results in the formation of an intermediate metal-hydrido-thiolate complex. Subsequent to oxidative addition, alkyne undergoes 1,2 or 2,1 migratory insertion into the M-SR bond selectively. Finally, rate-limiting reductive elimination releases free vinyl sulfide and completes the catalytic cycle. It is likely that reductive elimination is also rate-limiting for *E*-linear product formation. This is, in our opinion, a valid assumption, given the similar rates of formation, Eyring parameters, KIE and electronic dependence. We will now examine each step individually.



**Scheme 5.7. General proposed mechanism**

### 5.4.1 Migratory Insertion.

It is proposed that 1,2 vs 2,1 migratory insertion into the Rh-S bond selectively is the source of branched vs *E*-linear product formation. This proposal involves a common intermediate and mechanism for both regioisomers, consistent with the experimental data. The initial product of migratory insertion is proposed to be a rhodathiacyclobutene structure involving a dative S→Rh interaction (Figure 5.17), similar to the complex isolated by Mizobe and coworkers. It is proposed that the stabilization afforded by the dative interaction is responsible for the selective insertion of the alkyne into the Rh-S bond instead of the Rh-H bond.

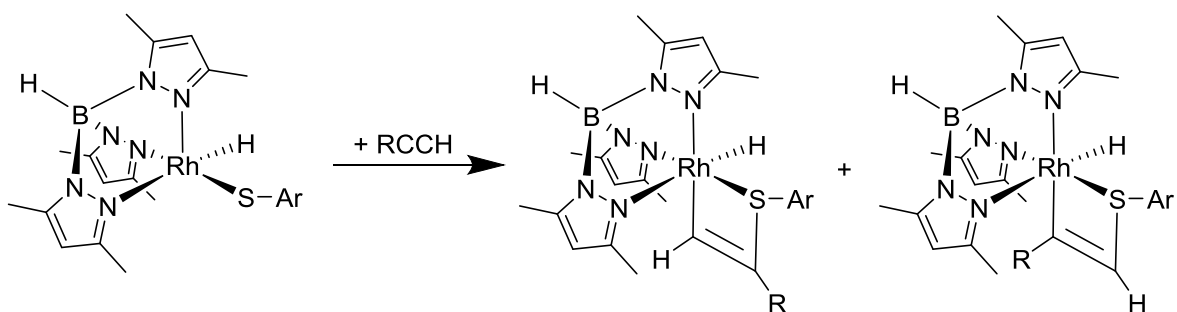
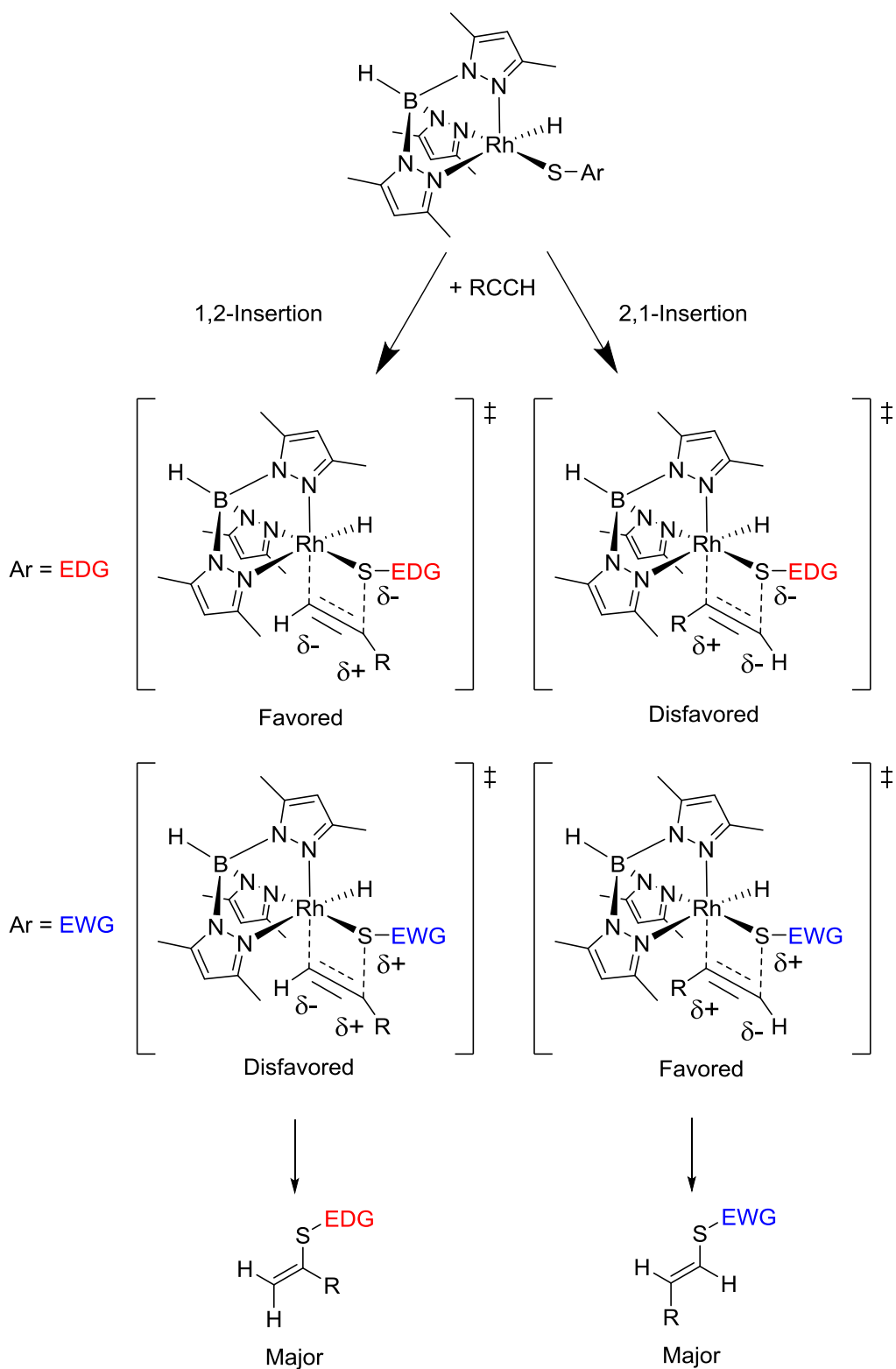


**Figure 5.17. Rhodathiacyclobutene Intermediate**

1,2-Migratory insertions are generally preferred for late transition-metal complexes due to a combination of sterics and electronics. The Hartwig group, in a study of the migratory insertion of olefins into Rh-X bonds ( $X = C, N, O$ ), calculated that 1,2-migratory insertion is favored to a greater extent (i.e. the  $\Delta\Delta G^\ddagger$  is larger) for more electronegative X atoms due to the greater partial positive charge being generated on the more substituted carbon. The preliminary DFT calculations show that there is very little electronic preference for 1,2- vs 2,1-insertion products, since the Tp-substituted rhodathiacyclobutenes have very similar calculated energies.

For Tp\*-substituted rhodathiacyclobutenes, the steric interaction between methyl substituents of the pyrazoles and the R group deriving from the alkyne result in a 1.76 kcal/mol preference for the 1,2-insertion product. These preliminary DFT calculations are consistent with the directionality of insertion be largely dependent on the steric bulk of the alkyne. When considering the electronic nature of the alkyne, migratory insertion results in two possible transition states, wherein electron rich thiolates interact favorably with the more substituted carbon, but electron poor thiolates interact more favorably with the terminal end of the alkyne (Scheme 5.8).

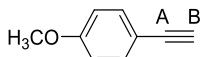
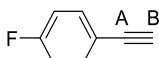
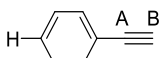
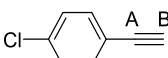
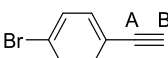


**Scheme 5.8. 1,2 vs 2,1 Migratory Insertion with HS-EDG and HS-EWG.**

### 5.4.2 The Effect of Alkyne Electronics.

The lack of any change in selectivity with variations in alkyne electronics seems at first contrary to the proposed mechanism. However, DFT calculations and  $^{13}\text{C}$  NMR chemical shifts reveal that there are only small differences in partial charges of the two alkyne carbons for the series of *para* substituted phenylacetylenes examined in this report (Table 5.4). As a result, the inherent polarity of the alkyne remains essentially unchanged and *para* substitution has little effect on the observed selectivity. Messerle and coworkers also observed that changes in the magnitude of the polarization of the alkyne triple bond had no discernable effect on rhodium catalyzed hydroalkoxylation of alkynes.<sup>178</sup>

**Table 5.4. Calculated partial charges and tabulated  $^{13}\text{C}$  NMR chemical shifts.**

Alkyne	Partial Charge (a.u.) <sup>a</sup>		$^{13}\text{C}$ NMR Chemical Shift <sup>b</sup>	
	A	B	A	B
	-0.034	-0.216	84.04	76.49
	$\Delta = 0.182$		$\Delta = 7.55$	
	-0.033	-0.218	84.17	77.24
	$\Delta = 0.185$		$\Delta = 6.93$	
	-0.037	-0.212	82.80	77.49
	$\Delta = 0.175$		$\Delta = 5.31$	
	-0.034	-0.213	83.91	77.85
	$\Delta = 0.179$		$\Delta = 6.06$	
	-0.038	-0.204	82.71	78.72
	$\Delta = 0.166$		$\Delta = 3.99$	
	-0.038	-0.204	82.71	78.84
	$\Delta = 0.166$		$\Delta = 3.87$	

<sup>a</sup>Method: BP86/6-31G(d,p). NBO (NPA). <sup>b</sup>In ppm. Solvent:  $\text{C}_6\text{D}_6$

The electronic nature of the alkyne also has no effect on the rate of reaction. The Hammett plot for *para*-substituted phenylacetylenes is shown in Figure 5.18. Using a standard

linear fit, the slope is essentially 0. Using linear regression, the  $\rho$  value is calculated to be  $-0.18 \pm 0.17$  with an adjusted  $R^2$  of 0.02. The results indicate that the electronic nature of the alkyne has no effect on the rate-limiting step of alkyne hydrothiolation catalyzed by  $[\text{Tp}^*\text{Rh}(\text{PPh}_3)_2]$ .

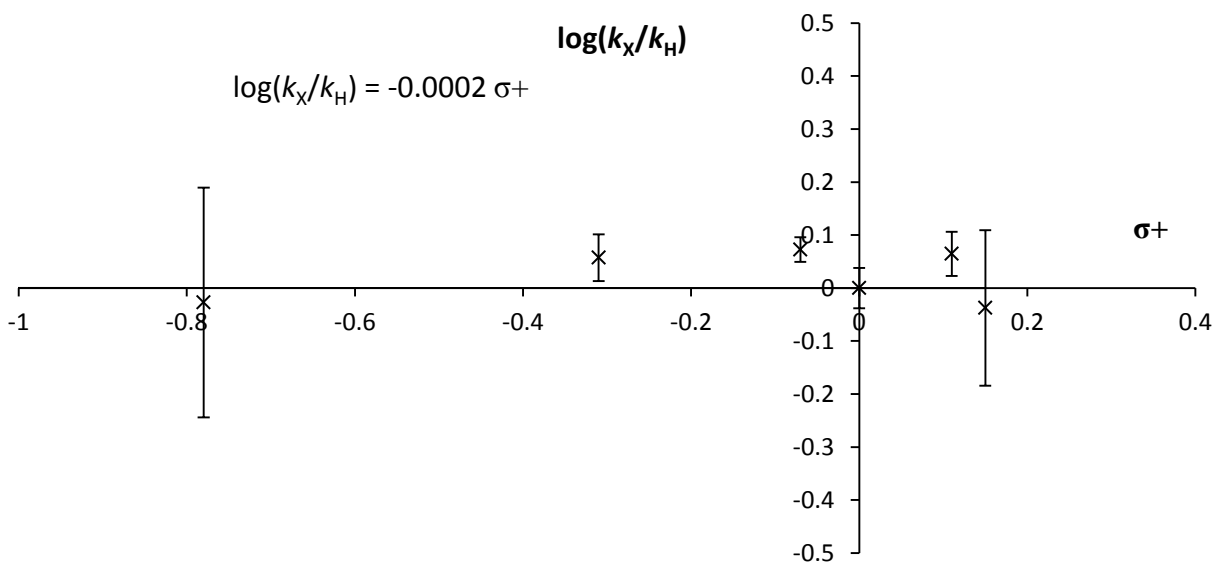


**Figure 5.18. Hammett plot for *para*-substituted phenylacetylenes.**

### 5.4.3 Reductive Elimination as the Rate-Limiting Step.

Inverse KIE's are common for reductive elimination of a hydride and a carbon fragment from metal centers.<sup>179</sup> Jones and coworkers have extensively investigated the reductive elimination from  $\text{Tp}^*$ -substituted  $\text{Rh}^{\text{III}}$  complexes and have measured inverse KIEs for reductive elimination from several  $[\text{Tp}^*\text{Rh}(\text{L})(\text{H})(\text{R})]$  complexes ( $\text{R} = \text{alkyl, phenyl}$ ).<sup>180</sup> Jones and others have shown that reductive elimination is a two-step process involving a  $\sigma$ -complex for reductive elimination of alkyl fragments, or an  $\eta^2$ - $\pi$ -complex for reductive elimination of phenyl or alkenyl fragments.<sup>181</sup> Inverse KIEs for reductive elimination are ultimately the result of an inverse

*equilibrium* isotope effect (i.e.  $K_H/K_D < 1$ ), applied to the rate-limiting step (Figure 5.19).<sup>182</sup> In either for the forward (reductive coupling), or reverse (oxidative cleavage), there is a normal KIE (i.e.  $k_H/k_D > 1$ ). However, since there is a much large difference in zero point energy for H vs. D in the product compared to the reactant, there is an overall inverse *EIE*. Since  $K_{\text{eqm}} = k_{\text{forward}}/k_{\text{reverse}}$ , the inverse equilibrium isotope effect can also be regarded as  $K_{\text{eqm}}^{H/D} = (k_{\text{rc}}^H/k_{\text{rc}}^D)/(k_{\text{oc}}^H/k_{\text{oc}}^D)$ . Thus the inverse EIE arises from a difference in the magnitude of normal KIEs in the forward and reverse reaction (i.e.  $k_{\text{rc}}^H/k_{\text{rc}}^D < k_{\text{oc}}^H/k_{\text{oc}}^D$ ).

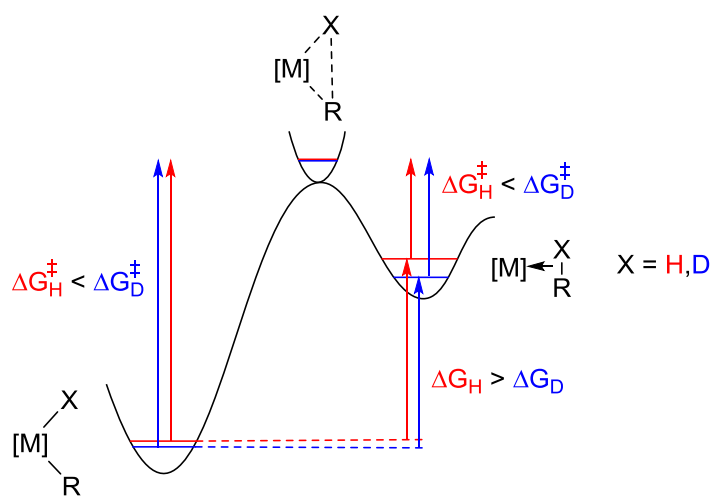
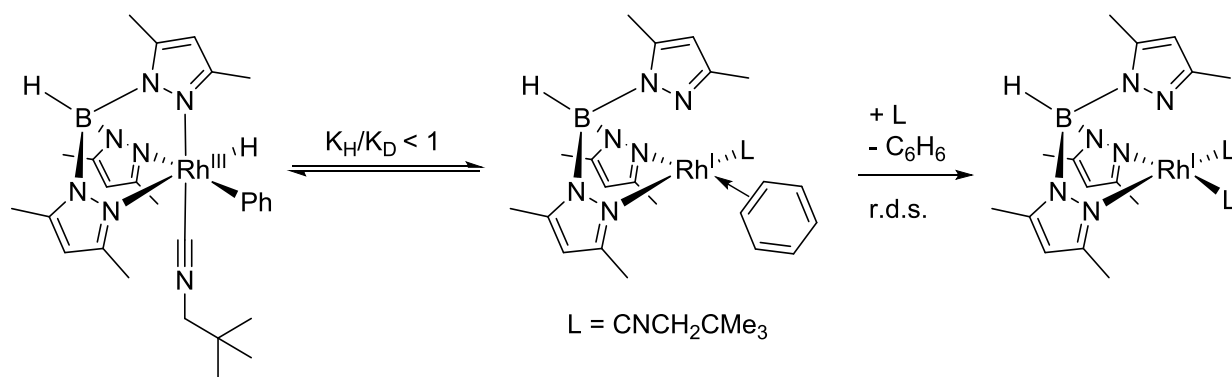


**Figure 5.19. Energy profile for reductive elimination.**

A complete analysis of this equilibrium process requires measurement of both the forward and reverse kinetic isotope effects. Such an analysis also reveals whether the transition state has a difference in zero point energy for  $X = \text{H}$  vs  $\text{D}$  approaching zero, as shown in Figure 5.19, or if the difference in zero point energy is mid-way between the reactant and product.<sup>183</sup> In the latter case, the KIE for oxidative cleavage remains normal, but the KIE for reductive

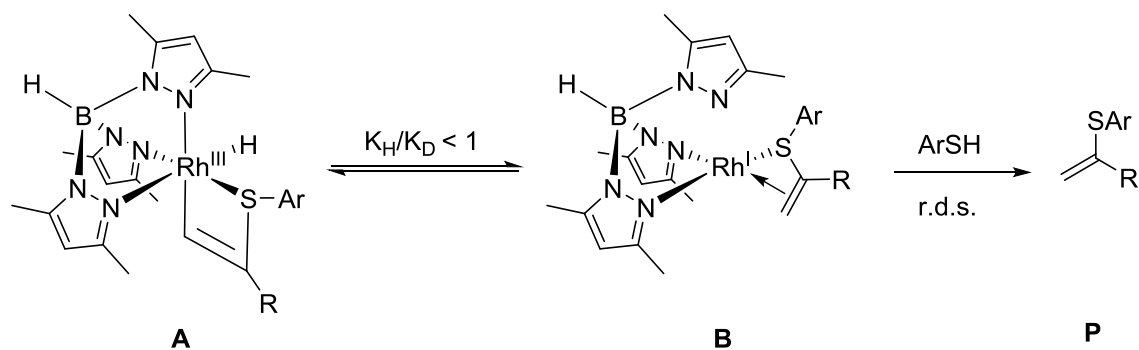
coupling is *inverse* (i.e.  $k_{rc}^H/k_{rc}^D < 1$ ). For either transition state scenario, the EIE remains inverse. Such measurements are possible in systems where isotopic scrambling can be observed.<sup>184</sup> However, in the present system, no isotopic scrambling for reductive elimination of vinyl sulfides is possible. Therefore, for the sake of simplicity, we will only consider that reductive elimination gives rise to an inverse EIE.

Most pertinent to the present system at hand is Jones and Hessell's study of reductive elimination from  $[Tp^*Rh(H)(Ph)(CNCH_2CMe_3)]$ .<sup>185</sup> In this system, the authors measured an inverse KIE of  $0.85 \pm 0.02$  for the reductive elimination of benzene. This value is nearly identical to those measured in the present system, where  $k_H/k_D = 0.81$  for two different thiols. Given that aromatic C-H bonds and vinylic C-H bonds have nearly identical bond dissociation energies (113 kcal/mol and 111 kcal/mol, respectively), it is not surprising that reductive elimination of aromatic and vinylic fragments would give rise to similar KIEs. Additionally, the authors found that the reductive elimination of benzene is *associatively induced*. The rate of reductive elimination was found to increase in the presence of added donor ligand  $CNCH_2CMe_3$ . The authors determined the entropy of activation  $\Delta S^\ddagger = -36 \pm 3$  eu, indicating that the rate-limiting step is associative in nature. They were also able to observe isotopic scrambling prior to reductive elimination. Consistent with the mechanistic data, the authors proposed a mechanism involving reversible reductive coupling to generate an  $\eta^2$ -benzene complex, followed by rate-limiting associatively induced dissociation of the bound benzene (Scheme 5.9).



**Scheme 5.9.** Associatively induced reductive elimination for [Tp\*RhH(Ph)(CNCH<sub>2</sub>CMe<sub>3</sub>)].

For alkyne hydrothiolation reactions catalyzed by [Tp\*Rh(PPh<sub>3</sub>)<sub>2</sub>], reductive elimination from the putative rhodathiacyclobutene intermediate would generate a structure containing a bound vinyl sulfide as shown in Scheme 5.10. It should be noted that [Tp\*Rh(PPh<sub>3</sub>)<sub>2</sub>] has been shown to undergo orthometallation of the phenyl ring of triphenylphosphine,<sup>186</sup> a process analogous to the reverse of reductive elimination shown in Scheme 5.10. Intermediates **A** and **B** remain in equilibrium until association of a donor ligand. Similar to the [Tp\*RhH(Ph)(CNCH<sub>2</sub>CMe<sub>3</sub>)] system, an increase in the rate of product formation for [Tp\*Rh(PPh<sub>3</sub>)<sub>2</sub>] catalyzed alkyne hydrothiolation was observed with low concentrations of added PPh<sub>3</sub>. It is proposed that this is due to association of PPh<sub>3</sub> to the reductively coupled species **B**, halting the reversibility of the **A** ⇌ **B** equilibrium and inducing dissociation of the product. However, the concentration of free PPh<sub>3</sub> in the reaction mixture is quite low (ca. 0.5 mM). The thiol concentration, on the other hand, is high ([RSH]<sub>initial</sub> = 275 mM). Therefore, it is proposed that it is the RSH which binds to the reductively coupled species **B** in order to induce dissociation of the product in the catalytic cycle. The fate of the rhodium species upon associatively induced reductive elimination will be discussed in the next section.



**Scheme 5.10. Reductive elimination.**

In this proposed mechanism, the rate-limiting step is association of the thiol to the reductively coupled species **B** in order to induce product dissociation. This step is associative in nature, consistent with the measured negative entropy of activation. Furthermore, the rate of product formation is defined by the equation  $\frac{d[P]}{dt} = k[\mathbf{B}][\text{ArSH}]$ . When measuring the substrate-dependency by initial rates, the concentration of ArSH is constant, and so the equation for the rate of product formation simplifies to  $\frac{d[P]}{dt} = k'[\mathbf{B}]$ . The formation of **B** is first order in thiol, alkyne and catalyst, consistent with the experimental results. When measuring the rate of product formation for the full catalytic reaction, we observed *pseudo*-first order kinetics (i.e. the natural log of product concentration over time is linear). During the course of the reaction, there is a steady-state concentration of **B** (i.e.  $[\mathbf{B}]$  is constant). Therefore, the equation for product formation simplifies to  $\frac{d[P]}{dt} = k'[\text{ArSH}]$ , which is *pseudo*-first order in thiol concentration. Finally, association of the thiol to the metal center results in the generation of positive charge on the sulfur, consistent with the negative  $\rho$  value of -1.07 for the Hammett plot of substituted aryl

thiols. This step is essentially independent of the electronic nature of the R group deriving from the alkyne, consistent with the  $\rho$  value of 0 for *para*-substituted alkynes.

From Scheme 5.10, it is clear that the sulfur atom is participating strongly in the reductive elimination step. Jones and coworkers found that the rate of reductive elimination from  $[\text{Tp}^*\text{RhL}(\text{R})(\text{H})]$  complexes was strongly dependent on the strength of the Rh-C bond.<sup>187</sup> They found that more electron deficient substituents on the carbon fragment resulted in a stronger Rh-C bond. A similar stabilizing effect could retard the rate of vinyl sulfide reductive elimination with electron-deficient substituents on the sulfur. While this may have a small influence on the equilibrium  $\text{A} \rightleftharpoons \text{B}$ , this effect is unlikely to result in the large dependence on the electronic nature of the thiol observed herein.

## 5.5 Detailed Mechanism and Assignment of Putative Structures for Hydride Signals

Now that we have examined each step in detail, we are in position to propose a more detailed mechanism and assign putative structures for the hydride species observed in Figure 5.7 and Figure 5.8. The stoichiometric reaction between  $[\text{Tp}^*\text{Rh}(\text{PPh}_3)_2]$  and PhSH results in the formation of four hydride signals. Comparison of  $^1\text{H}$  NMR and  $^1\text{H}\{^{31}\text{P}\}$  NMR spectra and  $^1\text{H}$ - $^{31}\text{P}$  HMBC experiments reveal that two of these hydride species are coupled to single rhodium-bound phosphorus nucleus, while one hydride signal is coupled to two equivalent rhodium-bound phosphorus nuclei, and the last is not coupled to phosphorus. These species are proposed to be  $[\kappa^3\text{-Tp}^*\text{RhH}(\text{SPh})(\text{PPh}_3)]$ ,  $[\kappa^2\text{-Tp}^*\text{RhH}(\text{SPh})(\text{PPh}_3)(\text{HSPh})]$ ,  $[\kappa^2\text{-Tp}^*\text{RhH}(\text{SR})(\text{PPh}_3)_2]$ , and  $[\kappa^3\text{-Tp}^*\text{RhH}(\text{SR})(\text{HSPh})]$ , respectively, where the  $\kappa^2$ -species are intermediate on the pathway to



This detailed mechanism incorporates every detail of the experimental results, including hapticity of the Tp\* ligand and inhibition by thiol and PPh<sub>3</sub>. Notably, the detailed mechanism proposes that oxidative addition of the thiol occurs *prior* to product dissociation. Below -5°C, a distinct change in reactivity is observed: a change in product formation from *pseudo*-first order to zeroth order is observed, coupled with a positive entropy of activation. These observations are consistent with a change in rate-limiting step from association of the thiol to dissociation of the product. In examining the proposed detailed catalytic cycle, only product dissociation is dissociative in nature, excluding thiol and PPh<sub>3</sub> competitive inhibition. Given the propensity of [Tp\*Rh(L)] species to undergo oxidative addition (See Chapter 6.1.2 and references therein), it is likely that the bound thiol undergoes rapid oxidative addition following rate-limiting association. Furthermore, oxidative addition of the thiol prior to product dissociation is consistent with the observed hydride signals for the stoichiometric reaction between PhSH, [Tp\*Rh(PPh<sub>3</sub>)<sub>2</sub>] and PhCCH. Upon addition of PhCCH to a solution of PhSH and [Tp\*Rh(PPh<sub>3</sub>)<sub>2</sub>], eight new hydride signals are observed, each in an approximately 2:1 ratio (n.b. [Tp\*Rh(PPh<sub>3</sub>)<sub>2</sub>] catalyzed alkyne hydrothiolation produces a 7 : 3 ratio of branched and *E*-linear products). Consistent with these observations, the putative structures of these eight new hydride signals are shown in Figure 5.20. For each structure, the three-coordinate sulfur atom is chiral. This causes the hydride to be diastereotopic, resulting in a total of eight hydride species.

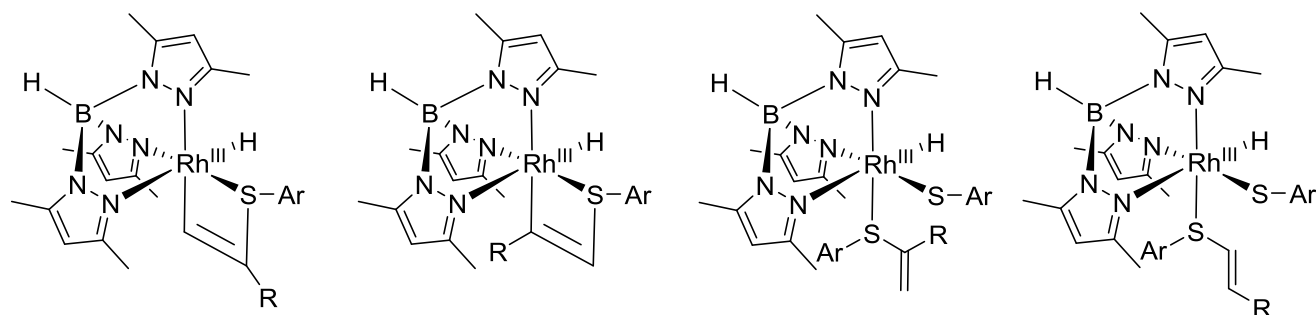


**Figure 5.20. Putative hydride species.**

## 5.6 Conclusion

Herein we have reported the results of several kinetic experiments and substrate-activity relationships pertaining to alkyne hydrothiolation catalyzed by  $[\text{Tp}^*\text{Rh}(\text{PPh}_3)_2]$ . This complex was the first reported example wherein a reversal in regioselectivity of thiol addition could be induced by switching the anionic ligand. Despite the structural similarities between  $[\text{Tp}^*\text{Rh}(\text{PPh}_3)_2]$  and  $[\text{Tp}^*\text{Rh}(\text{coe})(\text{MeCN})]$ , several observations led us to conclude that  $[\text{Tp}^*\text{Rh}(\text{PPh}_3)_2]$  did not operate by the same mechanism.

In conjunction with the differences in reactivity towards disulfides and the lack of dihydrogen formation when treated with excess thiol, the inverse KIE and observed hydride signals are strong evidence for formation of an intermediate metal-hydridothiolate complex. The selectivity and rate of product formation were found to be strongly dependent on the electronic nature of the thiol and the steric bulk of the alkyne, but independent of the electronic nature of the alkyne. The results suggest the regioselectivity arises from 1,2 vs 2,1 migratory insertion of the alkyne into the Rh-SR bond preferentially, despite the presence of an available Rh-H bond. Such selectivity is unique to  $[\text{Tp}^*\text{Rh}(\text{PPh}_3)_2]$  catalyzed alkyne hydrothiolation.

A reversal of regioselectivity was observed with electron-deficient thiols. The presence of similar inverse KIEs for both PhSD and 4-(CF<sub>3</sub>O)PhSD and linear Hammett plot suggest that the observed reversal of selectivity for *para*-substituted aryl thiols is not due to a change in mechanism or rate-limiting step.

The virtually identical Eyring parameters and similar change in reactivity at low temperatures for both regioisomers suggest that they form from a common intermediate and proceed through similar rate-limiting steps. The data is consistent with an equilibrium between the rhodathiacyclobutene and reductively coupled product prior to associatively induced dissociation of the product as a rate-limiting step. The equilibrium between the rhodathiacyclobutene and reductive elimination product is affected by an equilibrium isotope effect. Turnover is achieved upon coordination of thiol to the reductively coupled species. This step is associative in nature, consistent with negative entropy of activation.

## 5.7 Experimental

C<sub>6</sub>D<sub>6</sub> and C<sub>7</sub>D<sub>8</sub> were dried over sodium/benzophenone, distilled under vacuum and then degassed by three freeze-pump-thaw cycles. DCE was dried over CaH, distilled and then degassed by three freeze-pump-thaw cycles. Solid thiols, alkynes and trimethoxybenzene were purified by vacuum sublimation. Triphenylphosphine was recrystallized from refluxing ethanol, crushed and dried under high vacuum. Stock solutions of solid reagents were then made in the dried, degassed NMR solvents. Exact concentrations of substrate solutions were measured by aliquoting the stock solutions with a known amount of internal standard prior to use. Liquid thiols were freeze-pump-thawed three times in a vacuum distillation setup, before distilling into a Schlenk flask containing activated 4 Å molecular sieves. Liquid alkynes were dried over CaH

before vacuum distillation, and then degassed by three freeze-pump-thaw cycles. Stock solutions of  $[\text{Tp}^*\text{Rh}(\text{PPh}_3)_2]$  were prepared by weighing out  $[\text{Tp}^*\text{Rh}(\text{PPh}_3)_2]$  and trimethoxybenzene (internal standard) in a glovebox, followed by quantitative transfer to a volumetric flask using the appropriate dried, degassed NMR solvent.

Kinetic experiments were performed by transferring the stock solutions of catalyst and internal standard to a screw-cap NMR tube using a microliter pipette. These solutions were then diluted with an appropriate volume of dried, degassed NMR solvent such that the final volume of solvent is equal to 600  $\mu\text{L}$ . To this NMR tube was then added the appropriate volume of dried, degassed thiol and alkyne using a microliter syringe. Reactions were monitored by  $^1\text{H}$  NMR spectroscopy using the appropriate quantitative NMR methods, and concentrations were calculated relative to the integration of the internal standard. Observed pseudo-first order rate constants for product formation were calculated by taking the slope of the natural log of product concentration over time. Errors represent the standard deviation of a minimum of three replicates and are propagated according to the standard methods of error propagation. Errors in slope and y-intercept in linear correlations incorporate these standard deviations and/or propagated errors.

### **5.7.1 Hammett Plots and Alkyne Sterics Experiments**

To a screw cap NMR tube inside a glove box, an appropriate volume of catalyst stock solution containing trimethoxybenzene (internal standard) was added and diluted with dried, degassed  $\text{C}_6\text{D}_6$  such that concentration of catalyst in solution be 8.95 mM and the final solution volume be equal to 600  $\mu\text{L}$ . To this solution was then added an appropriate volume of thiol or thiol stock solution such that the initial concentration of thiol be 275 mM. To this solution was then added an appropriate volume of alkyne or alkyne stock solution such that the initial concentration of be 250 mM. The NMR tube was then inverted several times to ensure thorough

mixing. The reaction was then monitored by  $^1\text{H}$  NMR at 12 °C using the appropriate 90° pulse sequence and delay times equal five times the longest T1 relaxation time. Spectra were recorded every five times the NMR experiment time. Concentrations of branched and *E*-linear product (when possible) were measured by integration of the diagnostic vinylic C-H resonances relative to the integration of the internal standard peaks. *Pseudo*-first order rate constants ( $k_{\text{obs}}$ ) were measured according to the equation  $\ln\left(\frac{([P]_{\infty}-[P]_t)}{[P]_{\infty}}\right) = -k_{\text{obs}}t$ , where  $[P]_{\infty}$  is the final concentration of product and  $[P]_t$  is the concentration of product at time  $t$ . Plots of  $\ln\left(\frac{([P]_{\infty}-[P]_t)}{[P]_{\infty}}\right)$  versus time were linear for five half-lives.

### 5.7.2 Substrate Order Experiments

Stock solutions of catalyst and trimethoxybenzene (internal standard) were prepared in a 50:50 mixture of  $\text{C}_6\text{D}_6$  : DCE. An appropriate volume of catalyst stock solution was added to a screw cap NMR tube and diluted with an appropriate volume of a 50:50 mixture of  $\text{C}_6\text{D}_6$ :DCE such that the catalyst concentration be 8.95 mM and the final solution volume be equal to 600  $\mu\text{L}$ . For thiol order experiments, the initial concentration of phenylacetylene was held constant at 250 mM, while the initial concentration of thiol was varied over range of 138 mM to 1.11 mM. For alkyne order experiments, the initial concentration of thiol was held constant at 275 mM while the initial concentration of alkyne was varied over the range of 129 mM to 250 mM. The NMR tube was then inverted several times to ensure thorough mixing. The reaction was then monitored by  $^1\text{H}$  NMR at 8.0 °C using the appropriate 90° pulse sequence with solvent suppression and delay times equal five times the longest T1 relaxation time. Spectra were recorded every five times the NMR experiment time. The concentration of branched product was measured by integration of the diagnostic vinylic C-H resonances relative to the integration of

the internal standard peaks. The initial rate of the reaction was measured as the slope of product concentration versus time. Plots of concentration versus time were linear for at least five data points.

### 5.7.3 Added Triphenylphosphine Experiment

To a screw cap NMR tube inside a glove box, an appropriate volume of catalyst stock solution containing trimethoxybenzene (internal standard) in  $C_6D_6$  was added. To this solution was then added an appropriate volume of a stock solution of known concentration of triphenylphosphine in  $C_6D_6$ . This mixture was then diluted with dried, degassed  $C_6D_6$  such that concentration of catalyst in solution be 8.95 mM and the final solution volume be equal to 600  $\mu$ L. To this solution was then added an appropriate volume of thiol or thiol stock solution such that the initial concentration of thiol be 275 mM. To this solution was then added an appropriate volume of alkyne or alkyne stock solution such that the initial concentration of be 250 mM. The NMR tube was then inverted several times to ensure thorough mixing. The reaction was then monitored by  $^1H$  NMR at 12  $^{\circ}C$  using the appropriate  $90^{\circ}$  pulse sequence and delay times equal five times the longest T1 relaxation time. Spectra were recorded every five times the NMR experiment time. Concentrations of branched and *E*-linear product (when possible) were measured by integration of the diagnostic vinylic C-H resonances relative to the integration of the internal standard peaks. *Pseudo*-first order rate constants ( $k_{obs}$ ) were measured according to the equation  $\ln\left(\frac{([P]_{\infty}-[P]_t)}{[P]_{\infty}}\right) = -k_{obs}t$ , where  $[P]_{\infty}$  is the final concentration of product and  $[P]_t$  is the concentration of product at time t. Plots of  $\ln\left(\frac{([P]_{\infty}-[P]_t)}{[P]_{\infty}}\right)$  versus time were linear for five half-lives.

#### 5.7.4 Kinetic Isotope Experiments.

Deuterated PhSD and *p*-(CF<sub>3</sub>O)PhSD were prepared by dissolving the thiol in a mixture of D<sub>2</sub>O and NaOD, stirring for 1hr under N<sub>2</sub> atmosphere, quenching with DCI/D<sub>2</sub>O solution and extracting with Et<sub>2</sub>O, all using deuterium washed glassware. This process was repeated three times. The final extraction was washed using a saturated NaCl/D<sub>2</sub>O solution followed by drying over anhydrous Na<sub>2</sub>SO<sub>4</sub>, and the solvent removed under high vacuum. The deuterated thiol was then distilled under vacuum and stored under N<sub>2</sub> using deuterium washed glassware. 99 % D incorporation was measured by integration of the residual RS-H signal relative to the aromatic resonances. Experiments were carried out under the same conditions as the Hammett experiments, using deuterium washed screw cap NMR tubes. Reaction rates were measured by observed rate constant  $k_{\text{obs}}$ .

#### 5.7.5 Eyring Experiments by Initial Rates in Mixture of C<sub>6</sub>D<sub>6</sub> : DCE

Stock solutions of catalyst and trimethoxybenzene (internal standard) were prepared in a 50:50 mixture of C<sub>6</sub>D<sub>6</sub> : DCE. An appropriate volume of catalyst stock solution was added to a screw cap NMR tube and diluted with an appropriate volume of a 50:50 mixture of C<sub>6</sub>D<sub>6</sub> : DCE such that the catalyst concentration be 8.95 mM and the final solution volume be equal to 600  $\mu$ L. To this solution was then added an appropriate volume of dried, degassed thiophenol, such that the initial concentration of thiol be equal to 275 mM. To this solution was then added an appropriate volume of dried, degassed phenylacetylene, such that the initial concentration of alkyne be equal to 275 mM. The NMR tube was then inverted several times to ensure thorough mixing. The sample was then placed in the spectrometer, which was pre-equilibrated to the appropriate temperature. Experiments were performed over the range of -5 °C to 25 °C. The

reaction was then monitored by  $^1\text{H}$  NMR using the appropriate  $90^\circ$  pulse sequence with solvent suppression and delay times equal five times the longest T1 relaxation time. Spectra were recorded every five times the NMR experiment time. The concentration of branched was measured by integration of the diagnostic vinylic C-H resonances relative to the integration of the internal standard peaks. The initial rate of the reaction was measured as the slope of product concentration versus time. Plots of concentration versus time were linear for at least five data points.

#### 5.7.6 Eyring Experiments by *Pseudo-First Order Rate Constants in $\text{d}_8$ -Toluene*

To a screw cap NMR tube inside a glove box, an appropriate volume of catalyst stock solution containing trimethoxybenzene (internal standard) in  $\text{C}_7\text{D}_8$  was added. This mixture was then diluted with dried, degassed  $\text{C}_7\text{D}_8$  such that concentration of catalyst in solution be 8.95 mM and the final solution volume be equal to 600  $\mu\text{L}$ . To this solution was then added an appropriate volume of thiophenol such that the initial concentration of thiol be 275 mM. To this solution was then added an appropriate volume of phenylacetylene such that the initial concentration of be 250 mM. The NMR tube was then inverted several times to ensure thorough mixing. The sample was then placed in a spectrometer pre-equilibrated to the appropriate temperature. Experiments were performed over a temperature range of  $-5^\circ\text{C}$  to  $25^\circ\text{C}$ . The reaction was then monitored by  $^1\text{H}$  NMR using the appropriate  $90^\circ$  pulse sequence and delay times equal five times the longest T1 relaxation time. Spectra were recorded every five times the NMR experiment time. Concentrations of branched and *E*-linear product were measured by integration of the diagnostic vinylic C-H resonances relative to the integration of the internal standard peaks. *Pseudo*-first order rate constants ( $k_{\text{obs}}$ ) were measured according to the equation

$\ln\left(\frac{([P]_{\infty}-[P]_t)}{[P]_{\infty}}\right) = -k_{obs}t$ , where  $[P]_{\infty}$  is the final concentration of product and  $[P]_t$  is the concentration of product at time t. Plots of  $\ln\left(\frac{([P]_{\infty}-[P]_t)}{[P]_{\infty}}\right)$  versus time were linear for five half-lives.

### 5.7.7 Stoichiometric Reactions

In a glove box,  $[\text{Tp}^*\text{Rh}(\text{PPh}_3)_2]$  (26.2 mg, 0.0283 mmol) was weighed out and dissolved in a minimal amount of  $\text{C}_7\text{D}_8$ . This solution was then transferred to a screw cap NMR tube. To this solution was then added thiophenol (2.9  $\mu\text{L}$ , 0.0284 mmol), and the NMR tube was inverted several times to ensure thorough mixing, during which time the solution changed from orange to red. The solution was then frozen in liquid nitrogen and transported to the NMR lab. The solution was then gently thawed and placed in a spectrometer pre-equilibrated to  $-33\text{ }^{\circ}\text{C}$ . The mixture was characterized by  $^1\text{H}$  NMR,  $^1\text{H}\{^{31}\text{P}\}$  NMR,  $^{31}\text{P}\{^1\text{H}\}$  NMR, and  $^1\text{H}\text{-}^{31}\text{P}$  HMBC experiments. No change in the spectra was observed upon warming to  $-5\text{ }^{\circ}\text{C}$ , and nor was any change in the spectra observed upon standing at room temperature for two days. The sample was then removed from the spectrometer, and phenylacetylene (3.1  $\mu\text{L}$ , 0.0282 mmol) was added. The sample was inverted several times to ensure thorough mixing, then placed in the spectrometer pre-equilibrated to  $-33\text{ }^{\circ}\text{C}$ . The mixture was then characterized by  $^1\text{H}$  NMR and  $^1\text{H}\{^{31}\text{P}\}$  NMR.

### 5.7.8 Synthesis of 3,5-dimethylphenylacetylene

3,5-dimethylbenzaldehyde (2.0 mL, 14.9 mmol, 1.0 equiv.) was dissolved in 125 mL of dry DCM under  $\text{N}_2$  atmosphere in a Schlenk flask. The solution was cooled to  $0\text{ }^{\circ}\text{C}$  in an ice bath, and  $\text{CBr}_4$  (12.61 g, 38.0 mmol, 2.55 equiv.) and  $\text{PPh}_3$  (9.91 g, 37.8 mmol, 2.54 equiv.) were added to the solution. The solution was stirred at  $0\text{ }^{\circ}\text{C}$  for 2 h, then  $0\text{ }^{\circ}\text{C}$  to room temperature overnight. The intermediate dibromo alkene was isolated by column chromatography using

petroleum ether as eluent. The dibromo alkene (3.37 g, 11.6 mmol, 1.0 equiv.) was then dissolved in 50 mL dry THF in a Schlenk flask under N<sub>2</sub> atmosphere. The solution was cooled to -77 °C using a dry ice/acetone bath, and BuLi (1.0 M in hexane, 35.0 mL, 35.0 mmol, 3.0 equiv.) was added dropwise. The solution was stirred at -77 °C for 1 h, then -77 °C to room temperature overnight. The reaction mixture was then poured into 150 mL of ice water and extracted into diethyl ether. The organic layer was washed with 2 50 mL portions of water and then dried over anhydrous MgSO<sub>4</sub>. The solvent was removed by rotary evaporation and the product dried under reduced pressure. The product was then distilled under vacuum to yield 3,5-dimethylphenylacetylene as a colorless liquid. <sup>1</sup>H NMR (C<sub>6</sub>D<sub>6</sub>, 300 MHz) δ = 7.24 (s, 2H), 6.74 (s, 1H), 2.85 (s, 1H), 2.05 (s, 6H).

#### 5.7.9 Synthesis of 3,5-di-*tert*-butylbenzalhyde.

1-Bromo-3,5-di-*tert*-butylbenzene (2.04 g, 7.57 mmol, 1.0 equiv.) was dissolved in dry THF in a Schlenk flask under N<sub>2</sub> atmosphere. The solution was cooled to -77 °C and BuLi (1.0 M in hexane, 9.0 mL, 14.4 mmol, 1.9 equiv.) was added dropwise. The solution was stirred at -77 °C for 20 min, and dry DMF (2.0 mL, 25.9 mmol, 3.4 equiv.) was added dropwise. The solution was stirred at -77 °C for 30 min then -77 °C to room temperature for 1 h. The reaction mixture was then quenched by addition of methanol. The solvent was removed by rotary evaporation and the product extracted with Et<sub>2</sub>O and acidified water. The combined organic layers were dried over anhydrous MgSO<sub>4</sub> and the solvent removed by rotary evaporation. The product was then dried under reduced pressure to give 3,5-di-*tert*-butylbenzalhyde as a white solid in quantitative yield. <sup>1</sup>H NMR (CDCl<sub>3</sub>, 300 MHz) δ = 10.04 (s, 1H), 7.75 (s, 1H), 7.74 (s, 2H), 1.40 (s, 18H).

#### 5.7.10 Synthesis of 3,5-di-*tert*-butylphenylacetylene

3,5-di-*tert*-butylbenzaldehyde (569 mg, 2.61 mmol, 1.0 equiv.) was dissolved in dry DCM in a Schlenk flask under N<sub>2</sub> atmosphere. The solution was cooled to 0 °C in an ice bath, and CBr<sub>4</sub> (1.77 g, 5.34 mmol, 2.0 equiv.) and PPh<sub>3</sub> (2.81 g, 10.7 mmol, 4.1 equiv.) were added to the solution. The solution was stirred at 0 °C for 2 h, then 0 °C to room temperature overnight. The intermediate dibromo alkene was isolated by column chromatography using petroleum ether as eluent. The dibromo alkene (760 mg, 2.03 mmol, 1.0 equiv.) was then dissolved in dry THF in a Schlenk flask under N<sub>2</sub> atmosphere, and cooled to -77 °C in a dry ice/acetone bath. BuLi (1.6 M in hexane, 5.0 mL, 8.0 mmol, 3.9 equiv.) was then added dropwise. The solution was stirred at -77 °C for 2 h, then -77 °C to room temperature overnight. The solution was then quenched with methanol, the solvent removed by rotary evaporation and the product extracted with benzene. The product was then purified by column chromatography using 3:1 hexanes : THF as eluent to yield 3,5-di-*tert*-butylphenylacetylene as a yellow solid. <sup>1</sup>H NMR (C<sub>6</sub>D<sub>6</sub>, 300 MHz) δ = 7.66 (d, 2H), 7.56 (t, 1H), 2.88 (s, 1H), 1.26 (s, 18H).

#### 5.7.11 Synthesis of 1,3,5-trimethylbenzaldehyde.

Mesitylbromide (10.0 mL, 65.3 mmol, 1.0 equiv.) was dissolved in 150 mL dry DCM in a Schlenk flask under N<sub>2</sub> atmosphere. The solution was cooled to -77 °C in a dry ice/acetone bath and BuLi (1.6 M in hexane, 50.0 mL, 80.0 mmol, 1.23 equiv.) was added to the solution dropwise. The solution was stirred at -77 °C for 30 min. Dry DMF (7.0 mL, 90.1 mmol, 1.4 equiv.) was then added dropwise and the solution stirred at -77 °C for 30 min and then -77 °C to room temperature for 1 h. The solution was then quenched with methanol and the solvent removed by rotary evaporation. The product was then extracted with diethyl ether and acidified

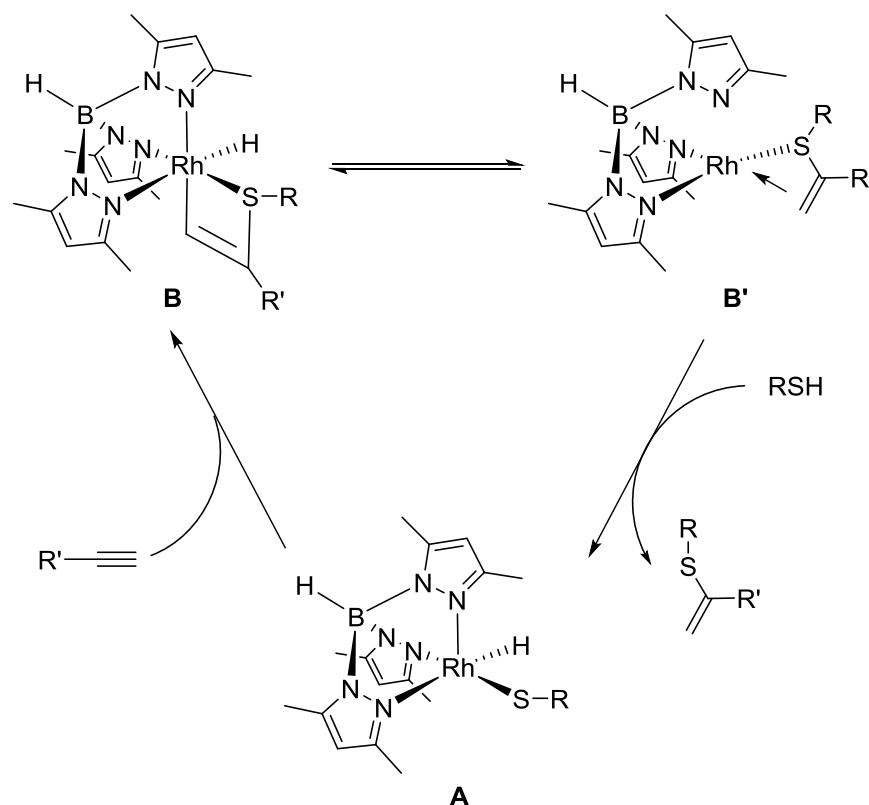
water. The combined organic layers were then dried over anhydrous  $\text{MgSO}_4$  and the solvent removed by rotary evaporation. The product was then dried under reduced pressure to give 1,3,5-trimethylbenzaldehyde as a yellow liquid in quantitative yield.  $^1\text{H}$  NMR ( $\text{C}_6\text{D}_6$ , 300 MHz)  $\delta$  = 10.40 (s, 1H), 6.53 (s, 2H), 2.36 (s, 6H), 1.95 (s, 3H).

#### 5.7.12 Synthesis of 1,3,5-trimethylphenylacetylene

1,3,5-trimethylbenzaldehyde (7.50 g, 50.6 mmol, 1.0 equiv.) was dissolved in dry DCM in a Schlenk flask under  $\text{N}_2$  atmosphere. The solution was cooled to 0 °C in an ice bath, and  $\text{CBr}_4$  (34.0 g, 102.5 mmol, 2.0 equiv.) and  $\text{PPh}_3$  (54.0 g, 206 mmol, 4.0 equiv.) were added. The solution was then stirred at 0 °C to room temperature overnight. The intermediate dibromo alkene was purified by column chromatography using petroleum ether as eluent. The resulting dibromo alkene (2.31 g, 7.60 mmol, 1.0 equiv.) was then dissolved in dry THF in a Schlenk flask under  $\text{N}_2$  atmosphere. The solution was cooled to -77 °C and BuLi (1.6 M in hexane, 12.0 mL, 19.2 mmol, 2.5 equiv.) was added dropwise. The solution was stirred at -77 °C for 2 h, then -77 °C to room temperature overnight. Methanol was then added to the solution, and the solvent removed by rotary evaporation. The product was extracted with benzene, and the combined organic layers were dried over anhydrous  $\text{MgSO}_4$ . The solvent was then removed by rotary evaporation, and the product dried under reduced pressure. The product was then distilled under vacuum to give 1,3,5-trimethylphenylacetylene as a colorless liquid.  $^1\text{H}$  NMR ( $\text{C}_6\text{D}_6$ , 300 MHz)  $\delta$  = 6.66 (s, 2H), 3.17 (s, 1H), 2.41 (s, 6H), 2.04 (s, 3H).

## Chapter 6 Progress Towards the Synthesis of Putative Intermediates in Alkyne Hydrothiolation Catalyzed by $[\text{Tp}^*\text{Rh}(\text{PPh}_3)_2]$

In Chapter 5, the mechanism for alkyne hydrothiolation catalyzed by  $[\text{Tp}^*\text{Rh}(\text{PPh}_3)_2]$  was proposed to involve generation of an intermediate hydridothiolate complex **A** (Scheme 6.1). This hydridothiolate complex was then proposed to undergo chemoselective alkyne migratory insertion into the Rh-SR bond, generating a rhodathiacyclobutene **B**. A simplified scheme of the proposed mechanism is shown in Scheme 6.1.



**Scheme 6.1.** Simplified proposed mechanism for  $[\text{Tp}^*\text{Rh}(\text{PPh}_3)_2]$  catalyzed alkyne hydrothiolation.

While the mechanistic data was convincing, the identification of the hydride signals present in stoichiometric reactions and evidence showing that they are involved in the catalytic cycle remained elusive. In order to identify these hydride signals and prove that the proposed intermediates are viable in the catalytic cycle, we set out to independently synthesize these and related structures. Two synthetic targets were identified, where structures of type **A** are related to putative intermediate hydridothiolate complexes, and structures of type **B** are related to putative rhodathiacyclobutene complexes (Figure 6.1). The purpose of synthesizing these structures is two-fold: first, to assess their viability in undergoing the transformations in the proposed mechanism for [Tp\*Rh(PPh<sub>3</sub>)<sub>2</sub>]-catalyzed alkyne hydrothiolation; and second, to examine the impact of R and R' on these fundamental transformations under stoichiometric conditions.

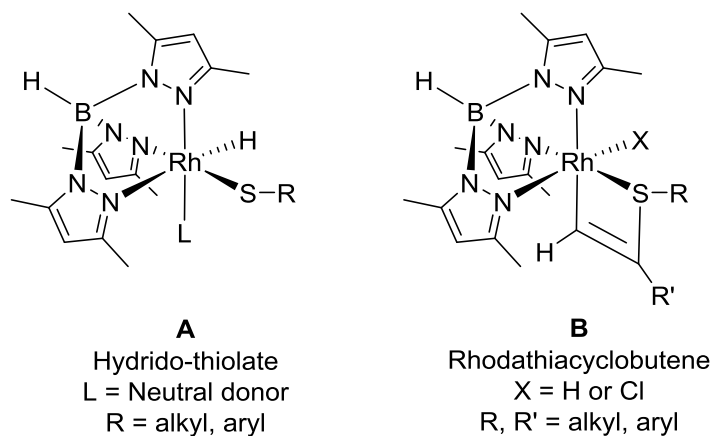
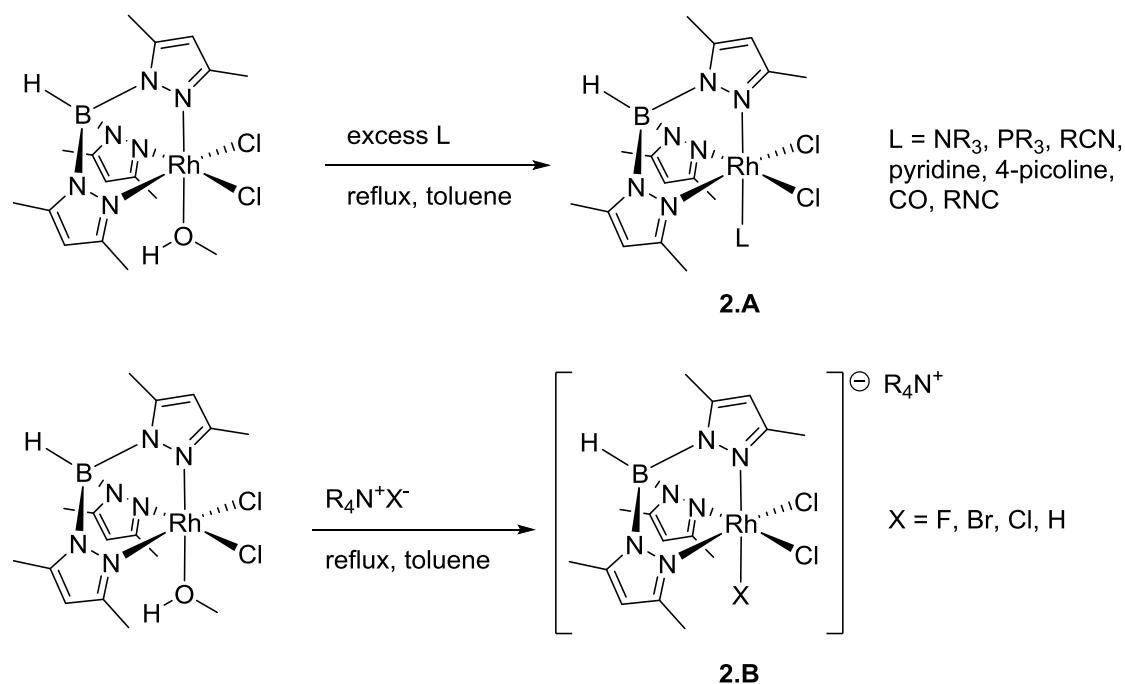


**Figure 6.1. Synthetic targets of type A and B, related to the intermediate hydridothiolate and rhodathiacyclobutene complexes.**

## 6.1 Review of the Synthesis and Reactivity of Trispyrazolylborate Complexes of Rh<sup>III</sup>

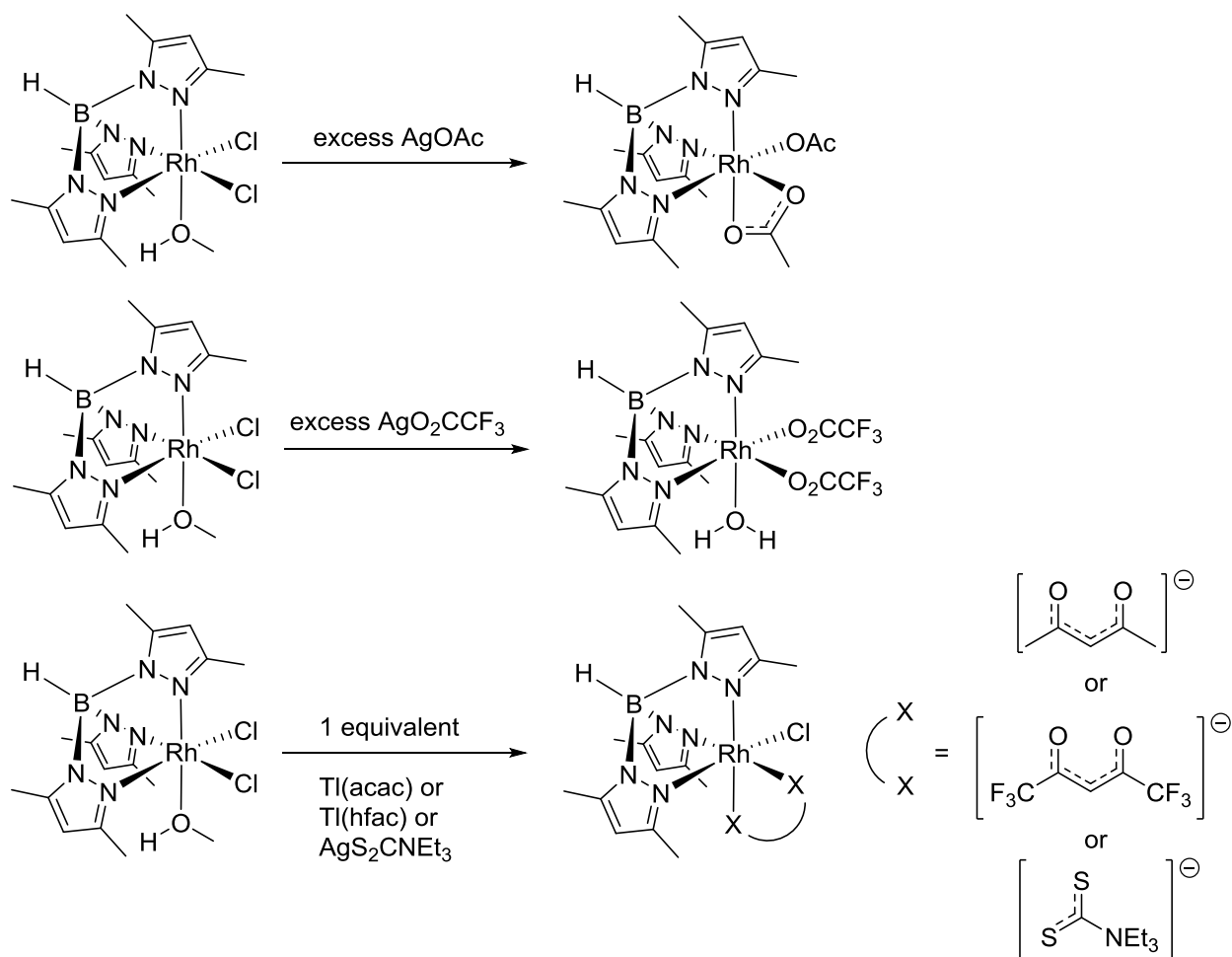
### 6.1.1 Synthesis of [Tp\*Rh<sup>III</sup>] Complexes from [Rh<sup>III</sup>Cl<sub>3</sub>] Derivatives.

The first report examining the synthesis and reactivity of [Tp\*Rh<sup>III</sup>] complexes is that of Powell *et al.*<sup>188</sup> Complexation of the Tp\* ligand to Rh<sup>III</sup> was achieved by refluxing KTp\* and [RhCl<sub>3</sub>•xH<sub>2</sub>O] in methanol, forming the neutral  $\kappa^3$  complex, [Tp\*RhCl<sub>2</sub>(MeOH)]. Using [Tp\*RhCl<sub>2</sub>(MeOH)] as a starting material, the authors synthesized a series of [Tp\*RhCl<sub>2</sub>(L)] complexes (Scheme 6.2, **2.A**), where L is a neutral donor ligand, by refluxing [Tp\*RhCl<sub>2</sub>(MeOH)] in dry toluene with an excess of the donor ligand L (Scheme 6.2). The exception was [Tp\*RhCl<sub>2</sub>(MeCN)], which was prepared by refluxing [Tp\*RhCl<sub>2</sub>(MeOH)] in dry acetonitrile. The authors also prepared a series of anionic complexes of type (NR<sub>4</sub>)[Tp\*RhCl<sub>2</sub>(X)] (X = F, Cl, Br) by refluxing [Tp\*RhCl<sub>2</sub>(MeOH)] in toluene with an equimolar amount of (R<sub>4</sub>N)X (Scheme 6.2, **2.B**). (NEt<sub>3</sub>H)[Tp\*RhCl<sub>2</sub>(H)] was prepared by refluxing [Tp\*RhCl<sub>2</sub>(MeOH)] in the presence of excess Et<sub>3</sub>N while bubbling H<sub>2</sub> through the solution.



**Scheme 6.2. Synthesis of  $[\text{Tp}^*\text{RhCl}_2(\text{L})]$  and  $[\text{Tp}^*\text{RhCl}_2(\text{X})]^- (\text{NR}_4^+)$  derivatives.**

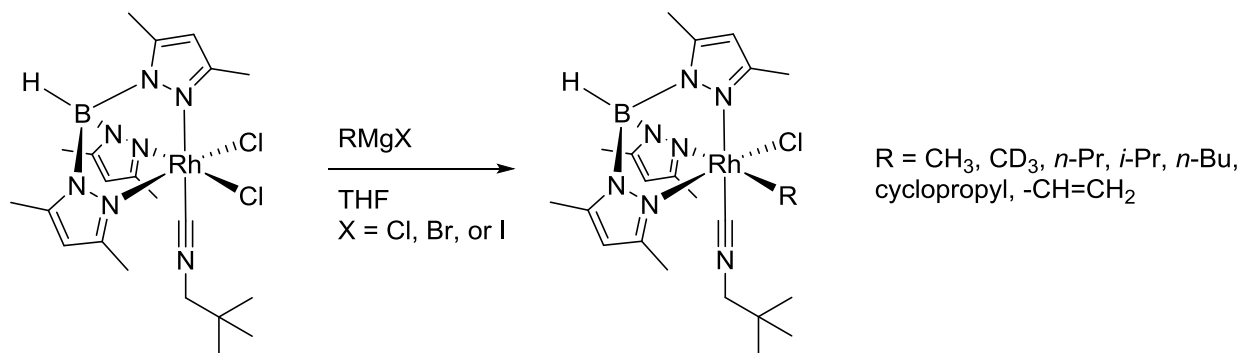
Finally, Powell and coworkers examined substitution of the chloride ligands with a variety of AgX and TlX salts (Scheme 6.3). Reactions of  $[\text{Tp}^*\text{RhCl}_2(\text{MeOH})]$  with excess AgX resulted in double substitution of the Cl ligands for X ligands. For  $\text{X} = \text{CH}_3\text{CO}_2^-$ , the complex  $[\text{Tp}^*\text{Rh}(\kappa^2\text{-OAc})(\kappa^1\text{-OAc})]$  was isolated, whereas when  $\text{X} = \text{CF}_3\text{CO}_2^-$ , the resulting complex readily reacted with adventitious water to form  $[\text{Tp}^*\text{Rh}(\text{CF}_3\text{CO}_2)_2(\text{H}_2\text{O})]$ . Treatment of  $[\text{Tp}^*\text{RhCl}_2(\text{MeOH})]$  with one equivalent of Tl(acac), Tl(hfac) or  $\text{AgS}_2\text{CNEt}_3$  yielded products of single chloride substitution. In each case, MeOH was displaced, resulting in bidentate coordination of the anionic ligand. All assignments were made on the basis of  $^1\text{H}$  NMR chemical shifts and integrations.



**Scheme 6.3. Chloride substitution reactions of  $[\text{Tp}^*\text{RhCl}_2(\text{MeOH})]$ .**

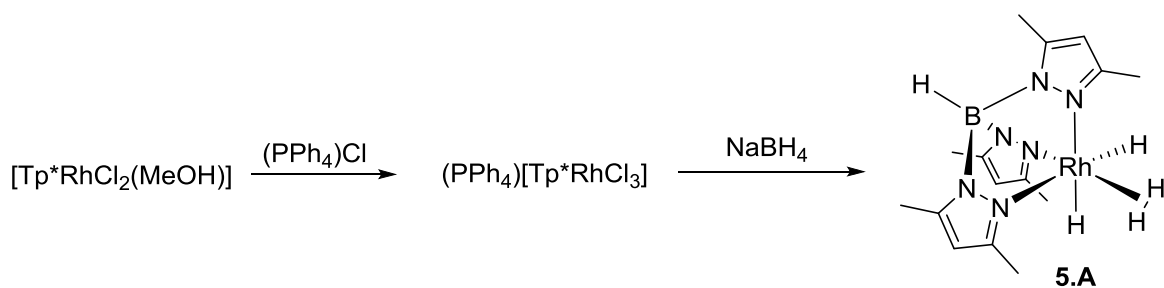
Jones and coworkers reported the synthesis of a series of asymmetrically substituted complexes of type  $[\text{Tp}^*\text{RhCl}(\text{R})(\text{CNCH}_2\text{CMe}_3)]$  ( $\text{R} = \text{alkyl, vinyl}$ ).<sup>189</sup> The authors used the neopentylisocyanide derivative  $[\text{Tp}^*\text{RhCl}_2(\text{CNCH}_2\text{CMe}_3)]$  as the starting material, which was prepared by refluxing  $[\text{Tp}^*\text{RhCl}_2(\text{MeCN})]$  in benzene with excess  $\text{CNCH}_2\text{CMe}_3$ . The authors reported that the successful synthesis of  $[\text{Tp}^*\text{RhCl}_2(\text{MeCN})]$  from  $\text{KTp}^*$  and  $[\text{RhCl}_3(\text{MeCN})_3]$  required highly pure  $\text{KTp}^*$ . Otherwise,  $[\text{Tp}^*\text{RhCl}_2(\text{pyz})]$  is formed ( $\text{pyz} = 3,5\text{-dimethylpyrazole}$ ). The desired  $[\text{Tp}^*\text{RhCl}(\text{R})(\text{CNCH}_2\text{CMe}_3)]$  complexes were formed by reaction of one equivalent

of the appropriate Grignard reagent,  $\text{RMgX}$  ( $\text{X} = \text{Cl}, \text{Br}, \text{or I}$ ), with  $[\text{Tp}^*\text{RhCl}_2(\text{CNCH}_2\text{CMe}_3)]$  (Scheme 6.4). In cases where  $\text{X} = \text{Br}$  or  $\text{I}$ , a mixture of  $[\text{Tp}^*\text{RhCl}(\text{R})(\text{CNCH}_2\text{CMe}_3)]$  and  $[\text{Tp}^*\text{Rh}(\text{X})(\text{R})(\text{CNCH}_2\text{CMe}_3)]$  was initially formed. Reaction of this mixture with an excess of  $\text{AgOTf}$  followed by excess  $n\text{-Bu}_4\text{N}^+\text{Cl}^-$  produced the desired rhodium chloride species.



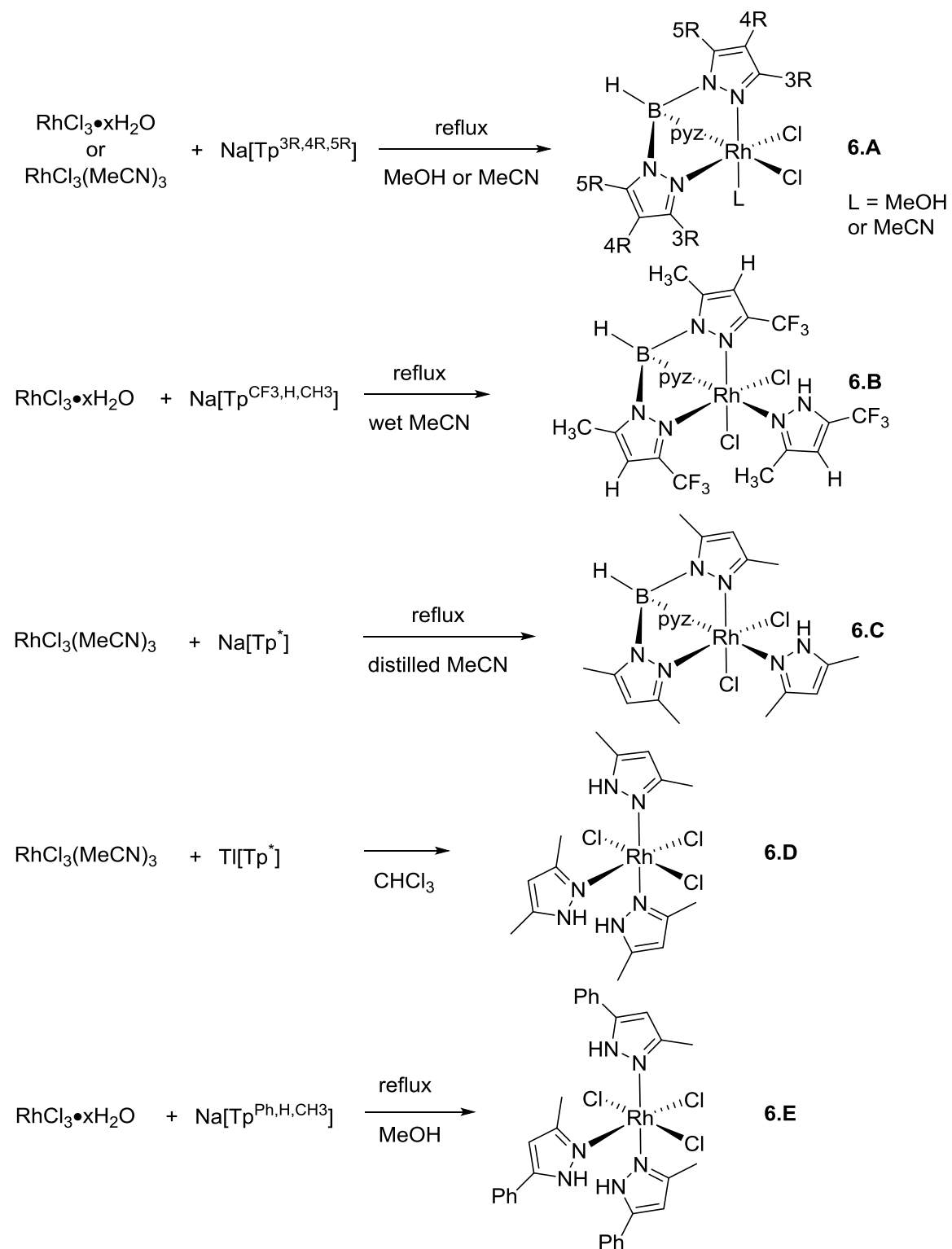
**Scheme 6.4. Synthesis of alkyl and vinyl complexes  $[\text{Tp}^*\text{RhCl}(\text{R})(\text{CNCH}_2\text{CMe}_3)]$ .**

In 1990, Venanzi and coworkers reported the synthesis of the rhodium-hydrido complex  $[\text{Tp}^*\text{RhH}_2(\text{H}_2)]$  containing coordinated molecular hydrogen.<sup>190</sup>  $[\text{Tp}^*\text{RhCl}_2(\text{MeOH})]$  was reacted with  $(\text{PPh}_4)\text{Cl}$  in order to generate the anionic  $(\text{PPh}_4)[\text{Tp}^*\text{RhCl}_3]$  complex.  $(\text{PPh}_4)[\text{Tp}^*\text{RhCl}_3]$  was then reacted with  $\text{NaBH}_4$ , which resulted in formation of a complex containing four dynamically equivalent hydrides (Scheme 6.5, **5.A**). The complex was characterized by 2D ( $^1\text{H}$ - $^{103}\text{Rh}$ )-NMR experiments, and, on the basis of  $T_1$  relaxation times, was determined to contain coordinated molecular hydrogen.



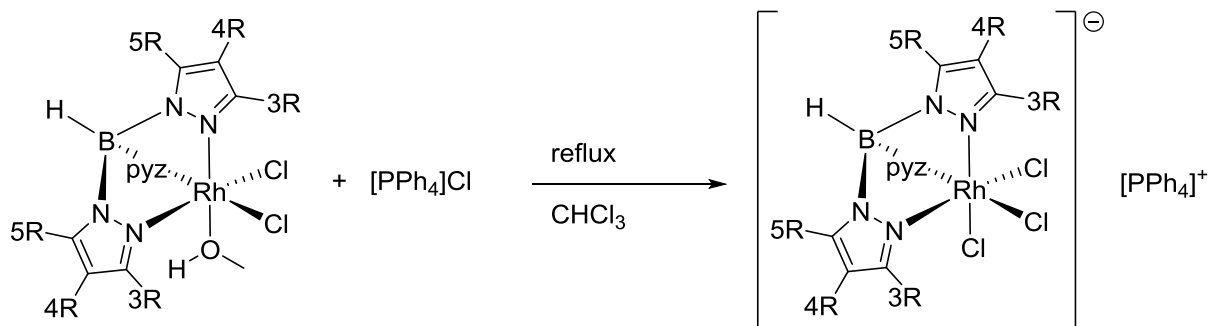
**Scheme 6.5. Synthesis of  $[\text{Tp}^*\text{RhH}_2(\text{H}_2)]$ .**

Expanding upon the work of Powell *et al*, Venanzi and coworkers explored the synthesis a series of  $[\text{Tp}^{3\text{R},4\text{R},5\text{R}}\text{RhCl}_2(\text{L})]$  complexes, where  $3\text{R} = \text{CH}_3, \text{CF}_3, \textit{i}\text{Pr}$ ,  $4\text{R} = \text{H}, \text{Cl}, \text{Br}, \text{CH}_3$ , and  $5\text{R} = \text{H}, \text{CH}_3$ , while  $\text{L} = \text{MeOH}, \text{MeCN}$  or  $\text{pyz}^{3\text{R},4\text{R},5\text{R}}$  (Scheme 6.6, **6.A**).<sup>191</sup> The authors found that the reaction of  $[\text{RhCl}_3 \cdot x\text{H}_2\text{O}]$  with  $\text{Na}[\text{Tp}^{\text{CF}_3,\text{H},\text{CH}_3}]$  in wet MeCN or the reaction of  $[\text{RhCl}_3(\text{MeCN})_3]$  with  $\text{NaTp}^*$  in freshly distilled MeCN resulted in the formation of ligand decomposition products  $[\text{Tp}^{\text{CF}_3,\text{H},\text{CH}_3}\text{RhCl}_2(\text{pyz}^{\text{CF}_3,\text{H},\text{CH}_3})]$  and  $[\text{Tp}^*\text{RhCl}_2(\text{pyz}^{\text{CH}_3,\text{H},\text{CH}_3})]$ , respectively (Scheme 6.6, **6.B** and **6.C**).  $[\text{Tp}^{\text{CF}_3,\text{H},\text{CH}_3}\text{RhCl}_2(\text{MeCN})]$  was instead synthesized from  $[\text{RhCl}_3(\text{MeCN})_3]$  in distilled MeCN, while  $[\text{Tp}^*\text{RhCl}_2(\text{MeCN})]$  was synthesized according to the procedure of Powell and coworkers.  $[\text{Tp}^{\text{CF}_3,\text{H},\text{CH}_3}\text{RhCl}_2(\text{pyz}^{\text{CF}_3,\text{H},\text{CH}_3})]$  was likely formed due to the presence of water in the reaction mixture, while  $[\text{Tp}^*\text{RhCl}_2(\text{pyz}^{\text{CH}_3,\text{H},\text{CH}_3})]$  was likely formed due to the use of impure  $\text{NaTp}^*$ , as suggested by Jones and coworkers. The reaction between  $[\text{RhCl}_3(\text{MeCN})_3]$  and  $\text{Ti}[\text{Tp}^*]$  in  $\text{CHCl}_3$  produced *mer*- $[\text{RhCl}_3(\text{pyz}^{\text{CH}_3,\text{H},\text{CH}_3})]$  (Scheme 6.6, **6.D**), the result of complete ligand decomposition, as did the reaction of  $[\text{RhCl}_3 \cdot x\text{H}_2\text{O}]$  with  $\text{Na}[\text{Tp}^{\text{Ph},\text{H},\text{Me}}]$  in MeOH, which produced *mer*- $[\text{RhCl}_3(\text{pyz}^{\text{Ph},\text{H},\text{Me}})]$  (Scheme 6.6, **6.E**).



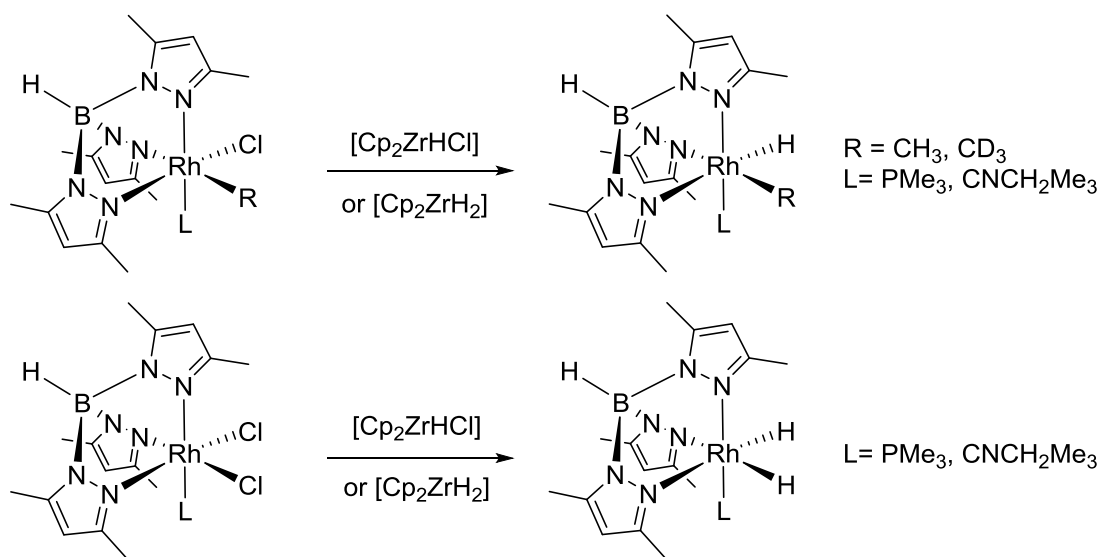
Scheme 6.6. Synthesis of  $[\text{Tp}^{3\text{R},4\text{R},5\text{R}}\text{RhCl}_2(\text{L})]$  and ligand decomposition products.

The authors used the resulting methanol complexes (**6.A**) to generate the corresponding anionic  $(\text{PPh}_4)[\text{Tp}^{3\text{R},4\text{R},5\text{R}}\text{RhCl}_3]$  complexes by refluxing in chloroform with  $(\text{PPh}_4)\text{Cl}$  (Scheme 6.7). The ultimate goal was to access new substituted  $[\text{Tp}^{3\text{R},4\text{R},5\text{R}}\text{RhH}_2(\text{H}_2)]$  species, which have yet to be reported.



**Scheme 6.7. Synthesis of anionic  $[\text{Tp}^{3\text{R},4\text{R},5\text{R}}\text{RhCl}_3][\text{PPh}_4]$  complexes.**

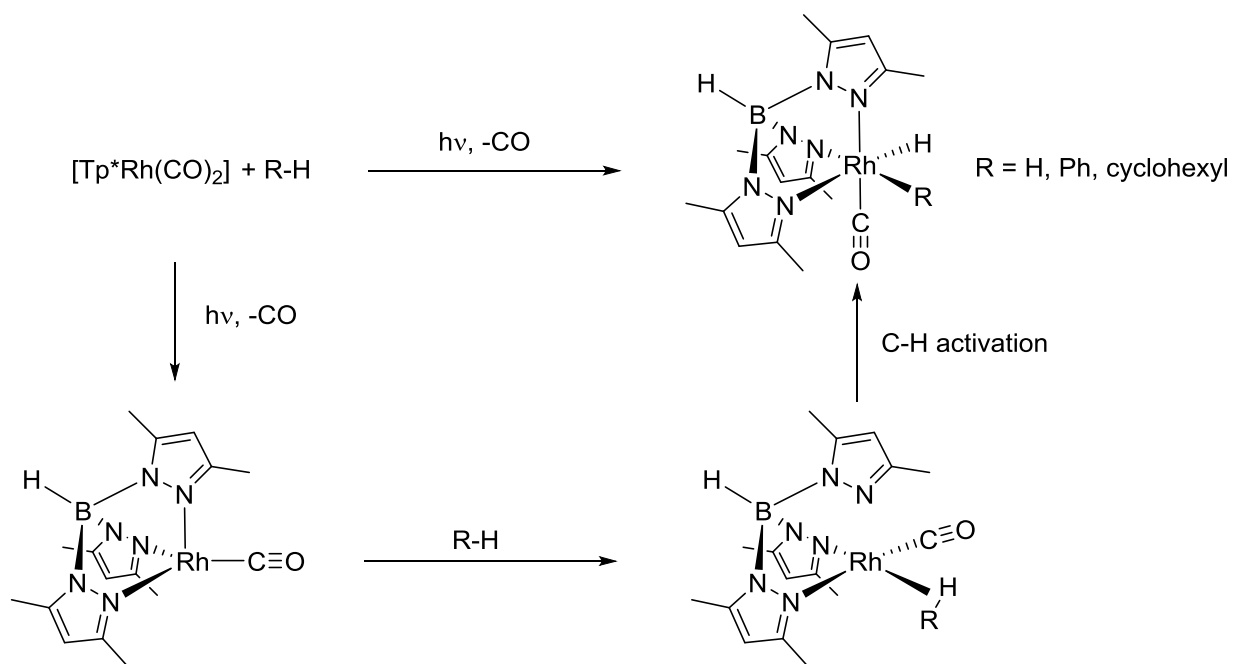
Following up on their synthesis of alkyl and vinyl chloride complexes of rhodium, Jones and coworkers synthesized the corresponding hydride species  $[\text{Tp}^*\text{RhH}(\text{R})(\text{L})]$  by reaction of  $[\text{Tp}^*\text{RhH}(\text{R})(\text{L})]$  with  $[\text{Cp}_2\text{ZrHCl}]$  or  $[\text{Cp}_2\text{ZrH}_2]$ .<sup>192</sup> The dihydride complex  $[\text{Tp}^*\text{RhH}_2(\text{L})]$  was also synthesized by reaction of  $[\text{Tp}^*\text{RhCl}_2(\text{L})]$  with excess  $[\text{Cp}_2\text{ZrHCl}]$  or  $[\text{Cp}_2\text{ZrH}_2]$  (Scheme 6.8).<sup>193</sup>  $[\text{Tp}^*\text{RhH}(\text{Me})(\text{L})]$  complexes were found to be thermally unstable, reductively eliminating methane and subsequently undergoing C-H, C-F, Si-H, and B-H bond activations. While  $[\text{Tp}^*\text{RhH}_2(\text{L})]$  is thermally stable, it underwent dihydrogen reductive elimination upon exposure to UV light, and demonstrated similar bond activations. The formation of  $[\text{Tp}^*\text{Rh}^{\text{III}}]$  complexes from  $[\text{Tp}^*\text{Rh}^{\text{I}}]$  will be discussed further in the next section.



**Scheme 6.8.** Synthesis of mono and dihydride complexes.

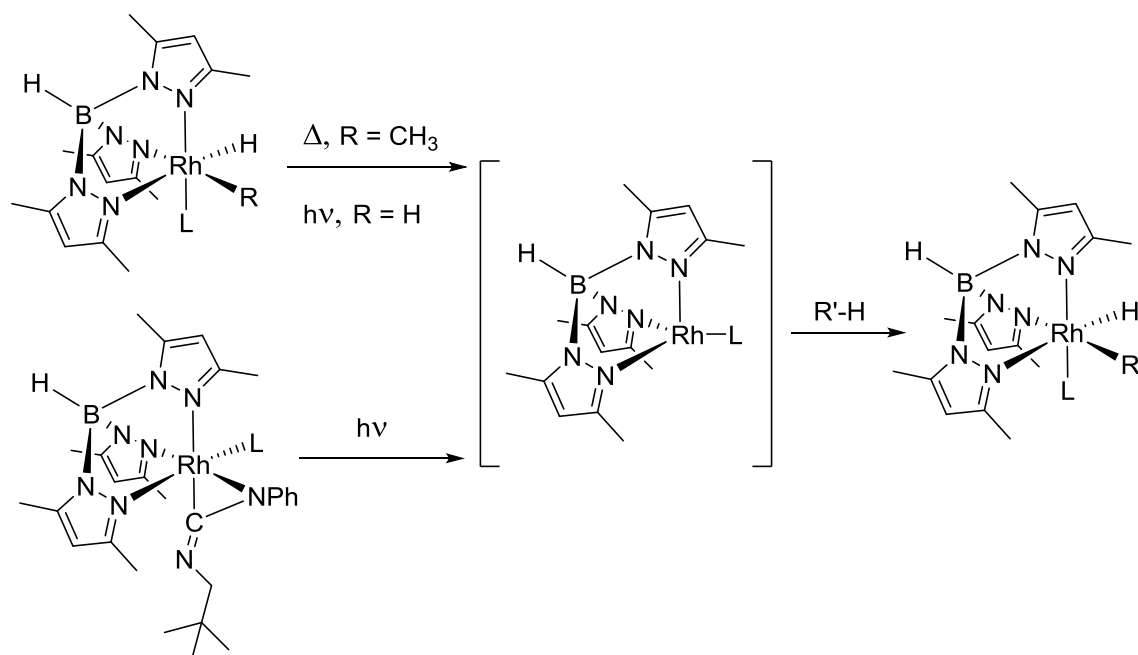
### 6.1.2 Synthesis of [Tp\*Rh<sup>III</sup>] Complexes from [Tp\*Rh<sup>I</sup>] Complexes.

The generation of [Tp\*Rh<sup>III</sup>] complexes from [Tp\*Rh<sup>I</sup>] complexes involves the formation of a coordinatively unsaturated [Tp\*Rh<sup>I</sup>(L)] species, which was first demonstrated by Graham and coworkers in 1987.<sup>194</sup> [Tp\*Rh(CO)<sub>2</sub>] was found to activate the C-H bonds of benzene, cyclohexane and methane upon loss of a CO ligand (Scheme 6.9). Dissociation of the CO ligand was achieved by UV irradiation, but was also found to occur with ambient daylight. The cyclohexyl derivative was found to be highly labile and easily converted to the phenyl and methyl derivatives upon exposure to benzene or methane. The mechanism of C-H activation has been explored by several groups.<sup>195</sup> Subsequent to light-induced dissociation of the CO ligand from [κ<sup>2</sup>-Tp\*Rh(CO)<sub>2</sub>], a [κ<sup>3</sup>-Tp\*Rh(CO)] complex is formed. The alkane then forms a C-H σ-bond with the metal complex prior to C-H activation, ultimately generating the [κ<sup>3</sup>-Tp\*RhH(R)(CO)] complex.



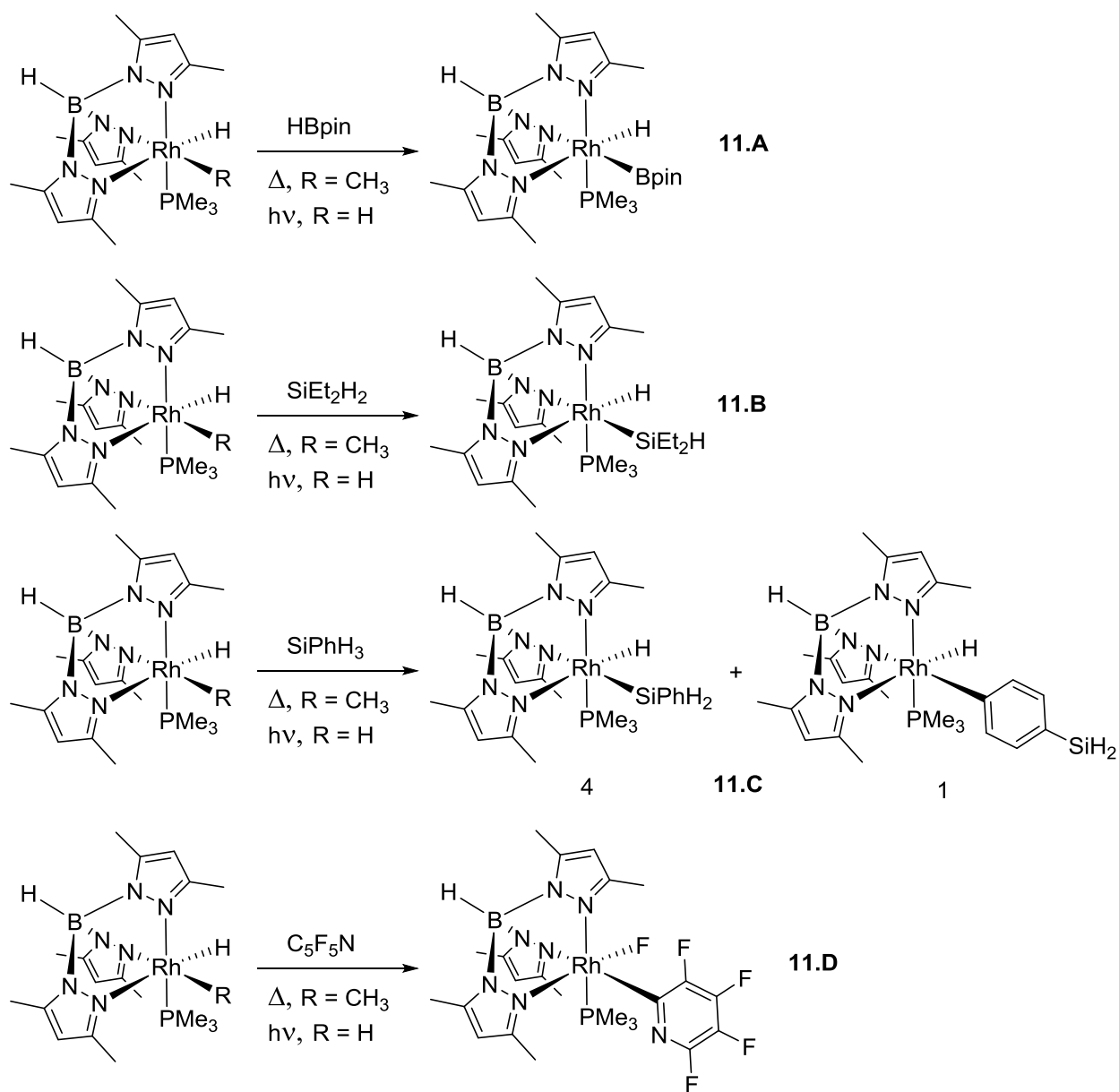
**Scheme 6.9. Generation of  $[\text{Tp}^*\text{RhH}(\text{R})(\text{CO})]$  complexes by photoirradiation of  $[\text{Tp}^*\text{Rh}(\text{CO})_2]$ .**

Jones and coworkers have extensively studied oxidative addition of a variety of bonds to  $[\kappa^3\text{-Tp}^*\text{Rh}^{\text{I}}(\text{L})]$  ( $\text{L} = \text{CNCH}_2\text{CMe}_3, \text{PMe}_3$ ). The  $[\kappa^3\text{-Tp}^*\text{Rh}^{\text{I}}(\text{L})]$  complexes were generated by thermally-induced reductive elimination of methane from  $[\kappa^3\text{-Tp}^*\text{Rh}^{\text{III}}(\text{H})(\text{CH}_3)(\text{L})]$ , light-induced reductive elimination of dihydrogen from  $[\kappa^3\text{-Tp}^*\text{Rh}^{\text{III}}(\text{H})_2(\text{L})]$ <sup>196</sup> or light-induced dissociation of  $\text{PhNCNCH}_2\text{CMe}_3$  from  $[\text{Tp}^*\text{Rh}(\text{PhNCNCH}_2\text{CMe}_3)(\text{CNCH}_2\text{CMe}_3)]$ .<sup>197</sup> The resulting  $[\kappa^3\text{-Tp}^*\text{Rh}^{\text{I}}(\text{L})]$  species were shown to activate a variety of  $\text{C}_{\text{sp}^2}\text{-H}$  and  $\text{C}_{\text{sp}^3}\text{-H}$  bonds with a preference for primary C-H bonds in alkanes and aromatic C-H bonds (Scheme 6.10).



**Scheme 6.10.** C-H activation by  $[\text{Tp}^*\text{Rh}^{\text{I}}(\text{L})]$  species.

In 2015, Jones and coworkers showed that coordinatively unsaturated  $[\text{Tp}^*\text{Rh}^{\text{I}}(\text{PMe}_3)]$  was also capable of activating B-H, Si-H, and C-F bonds.<sup>198</sup> Photoirradiation of  $[\text{Tp}^*\text{RhH}_2(\text{PMe}_3)]$  in neat HBpin or heating  $[\text{Tp}^*\text{RhH}(\text{CH}_3)(\text{PMe}_3)]$  in neat HBpin resulted in selective formation of  $[\text{Tp}^*\text{RhH}(\text{Bpin})(\text{PMe}_3)]$  (i.e. no C-H activation of the pinacol backbone was observed) (Scheme 6.11, **11.A**). Similarly, reactions in neat  $\text{SiEt}_2\text{H}_2$  produced  $[\text{Tp}^*\text{RhH}(\text{SiEt}_2\text{H})(\text{PMe}_3)]$  (Scheme 6.11, **11.B**), while reactions in neat  $\text{PhSiH}_3$  produced a 1 : 4 ratio of C-H to Si-H activation products (Scheme 6.11, **11.C**). Reactions in neat pentafluoropyridine resulted in the C-F activation product  $[\text{Tp}^*\text{RhF}(\text{C}_5\text{F}_4\text{N})(\text{PMe}_3)]$  (Scheme 6.11, **11.D**), whereas the reaction with 2,3,5,6-tetrafluoropyridine resulted in a mixture of C-F and C-H activation products.



**Scheme 6.11.** Oxidative addition of B-H, Si-H and C-F bonds by  $[\text{Tp}^*\text{Rh}^{\text{I}}(\text{PMe}_3)]$ , generated by reductive elimination of  $\text{CH}_4$  from  $[\text{Tp}^*\text{Rh}^{\text{III}}\text{H}(\text{CH}_3)(\text{PMe}_3)]$  or  $\text{H}_2$  from  $[\text{Tp}^*\text{Rh}^{\text{III}}(\text{H})_2(\text{PMe}_3)]$ .

## 6.2 Progress Towards the Synthesis of Rhodathiacyclobutene Intermediates

We hypothesized that the successful synthesis of a rhodathiacyclobutene might be achieved by reacting an appropriate 5-coordinate  $[\text{Tp}^*\text{RhCl}(\text{SR})]$  complex, generated *in situ*, or an isolable 6-coordinate  $[\text{Tp}^*\text{RhCl}(\text{SR})(\text{L})]$  complex, if L was sufficiently labile in solution. The synthesis of putative rhodathiacyclobutene intermediates began with the salt metathesis of a suitable  $\text{Rh}^{\text{III}}$  precursor and  $\text{KTp}^*$ . However, using commercially available  $\text{KTp}^*$  (Strem Chemicals) with either  $\text{RhCl}_3 \cdot x\text{H}_2\text{O}$ ,  $\text{RhCl}_3(\text{MeCN})_3$ , or anhydrous  $\text{RhCl}_3$ , in a variety of solvents, resulted in the isolation of the two ligand decomposition products,  $[\text{Tp}^*\text{RhCl}_2(\text{pyz})]$  (**A**) and *mer*- $[\text{RhCl}_3(\text{pyz})_3]$  ( $\text{pyz} = 3,5\text{-dimethylpyrazol}$ ) (**B**). The X-ray diffraction solid state structures of these two complexes are shown in Figure 6.2. Consistent with Jones' report that the purity of the  $\text{KTp}^*$  has a significant impact on the formation of these ligand decomposition products, reaction of  $\text{RhCl}_3(\text{MeCN})_3$  with recrystallized  $\text{KTp}^*$  in anhydrous MeCN resulted in the isolation of a 2:1 mixture of  $[\text{Tp}^*\text{RhCl}_2(\text{MeCN})] : [\text{Tp}^*\text{RhCl}_2(\text{pyz})]$ . The ratio could be further improved to 9:1 by using doubly-recrystallized  $\text{KTp}^*$  and performing the reaction at  $0^\circ\text{C}$ . However, because the recrystallization of  $\text{KTp}^*$  gave a low yield of 33-50% per recrystallization, this avenue was deemed unsuitable for further studies.

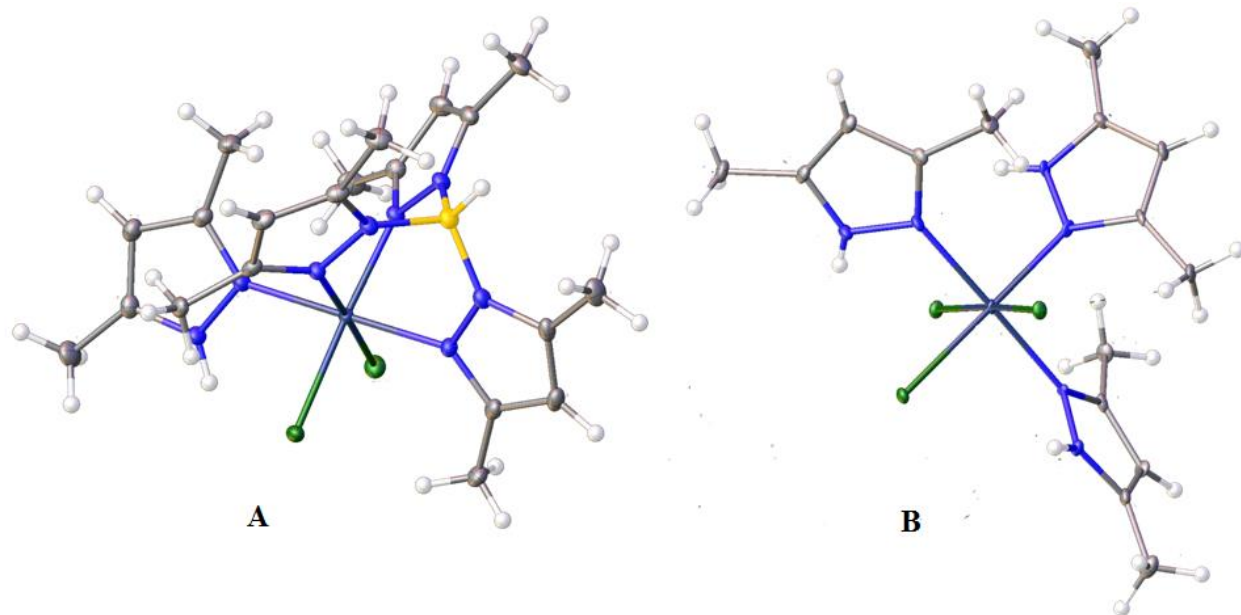


**Figure 6.2. X-ray diffraction structures of [Tp\*RhCl<sub>2</sub>(pyz)] (A) and *mer*-[RhCl<sub>3</sub>(py)<sub>3</sub>] (B).**

Revisiting the work of Powell and coworkers, the salt metathesis of RhCl<sub>3</sub>•xH<sub>2</sub>O with purified KTP\* in methanol resulted solely in decomposition products. It was determined that KTP\* methanolizes rapidly even at room temperature in methanol-*d*<sub>4</sub>. At 60°C, the ligand is completely decomposed within 15 minutes. Nevertheless, performing the same reaction with methanol which had been purified by passage over activated alumina resulted in isolation of [Tp\*RhCl<sub>2</sub>(MeOH)] in 50-60% yield after recrystallization from a concentrated methanolic solution at -20°C. While it is not completely clear what the effect of using purified methanol might be, methanol obtained from passage over activated alumina is known to be slightly basic, and borohydrides are significantly more stable in basic media than in neutral or acidic media. The increased proteolytic stability of the borohydride ligand in the slightly basic methanol purified by passage over activated alumina seems a likely reason for the success of the salt

metathesis reaction. Strangely, these additional precautions are only necessary for KTp\* purchased from Strem Chemicals. KTp\* purchased from Sigma Aldrich can be used as received in regular methanol, and only a small amount (< 5%) of the ligand decomposition product *mer*-RhCl<sub>3</sub>(pyz)<sub>3</sub> was observed.

As shown by Powell and coworkers, the [Tp\*RhCl<sub>2</sub>(MeOH)] is a versatile precursor for the synthesis of a variety of [Tp\*RhCl<sub>2</sub>(L)] complexes. Given that we were interested in assigning the hydride signals observed in stoichiometric reactions, we first made the [Tp\*RhCl<sub>2</sub>(PPh<sub>3</sub>)] complex by refluxing [Tp\*RhCl<sub>2</sub>(MeOH)] in dry toluene with excess PPh<sub>3</sub>. The reaction proceeds quantitatively, and upon recrystallization from a DCM solution layered with hexanes at -20°C, gives [Tp\*RhCl<sub>2</sub>(PPh<sub>3</sub>)] in 70-80% crystalline yield. The X-ray diffraction solid state structure of [Tp\*RhCl<sub>2</sub>(PPh<sub>3</sub>)] is shown in Figure 6.3. The Rh-P bond distance is 2.367 Å and displays a distorted octahedral geometry due to the steric bulk of the PPh<sub>3</sub> ligand, with N<sub>axial</sub>-Rh-Cl<sub>2</sub> bond angles of 86.49° and 90.41°. The three Rh-N bonds are similar, with a Rh-N<sub>axial</sub> bond length of 2.125 Å, and Rh-N<sub>equatorial</sub> bond lengths of 2.078 Å and 2.112 Å.

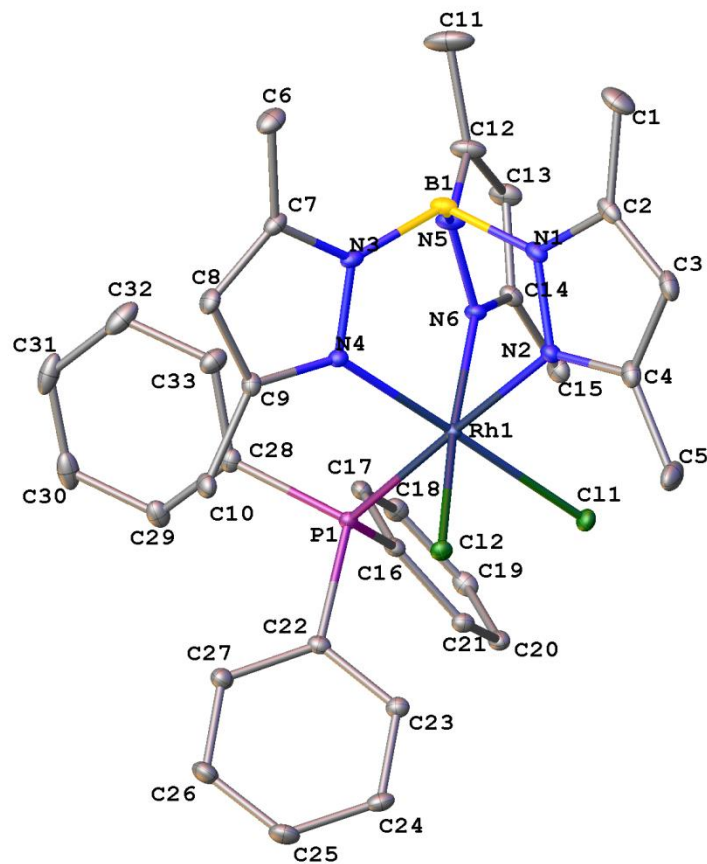


**Figure 6.3. X-ray diffraction solid state structure of [Tp\*RhCl<sub>2</sub>(PPh<sub>3</sub>)].**

Exhaustive screening of suitable reaction conditions for the substitution of a single chloride for a thiolate ligand, using either [Tp\*RhCl<sub>2</sub>(PPh<sub>3</sub>)] or [Tp\*RhCl<sub>2</sub>(MeOH)], invariably resulted in the formation of a complex and intractable mixture of products. The most selective conditions for abstraction of a single chloride anion was determined to be reaction of [Tp\*RhCl<sub>2</sub>(PPh<sub>3</sub>)] with AgBF<sub>4</sub> in a mixture of MeCN/DCM. Crystals of the resulting intermediate complex, [Tp\*RhCl(MeCN)<sub>2</sub>](BF<sub>4</sub>), were isolated after two weeks from a mixture of DCM/hexanes, and the X-ray diffraction solid state structure is shown in Figure 6.4. Unsurprisingly, performing the reaction in acetonitrile resulted in displacement of the PPh<sub>3</sub>

ligand for MeCN. Despite the successful abstraction of a single chloride from the rhodium center, the reaction of  $[\text{Tp}^*\text{RhCl}(\text{MeCN})_2](\text{BF}_4)$  with one equivalent of NaSTol (NaSTol = 4-methylbenzenethiolate) in THF resulted in a mixture of products. Additionally, mass spectrometric analysis of the product mixture revealed a peak at  $m/z = 605$  (ESI positive), corresponding to the  $[\text{Tp}^*\text{Rh}(\text{STol})(\text{MeCN})_2]^+$  cation, indicating that the substitution of the remaining chloride ligand had occurred among other reactions.

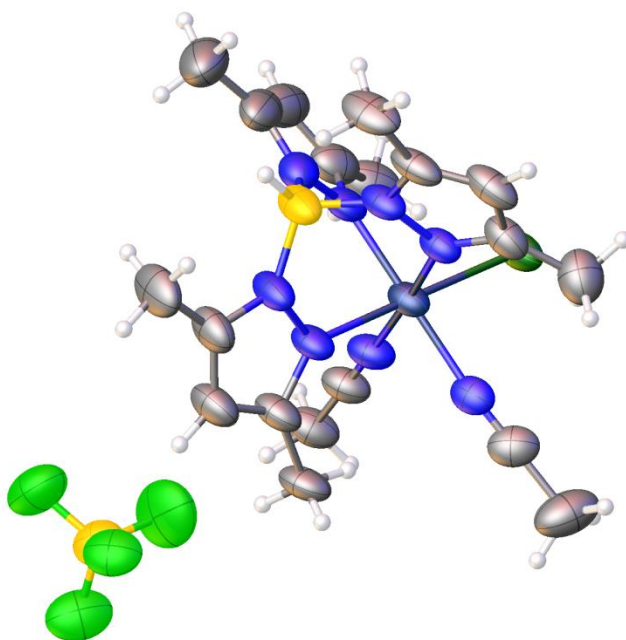


**Figure 6.4.** X-ray diffraction solid state structure of  $[\text{Tp}^*\text{RhCl}(\text{MeCN})_2](\text{BF}_4)$ .

The complexity of the product mixtures obtained when attempting thiolate salt metathesis with  $[\text{Tp}^*\text{RhCl}_2(\text{L})]$  complexes is likely due to several factors. Firstly, there is negligible chemoselectivity for the direct salt metathesis of a single chloride ligand. Additionally, anionic complexes can also be formed. Therefore, a mixture of three neutral complexes

$[\text{Tp}^*\text{RhCl}(\text{SR})(\text{L})]$ ,  $[\text{Tp}^*\text{Rh}(\text{SR})_2(\text{L})]$ , and unreacted  $[\text{Tp}^*\text{RhCl}_2(\text{L})]$ , and three anionic complexes,  $[\text{Tp}^*\text{RhCl}_2(\text{SR})]^-$ ,  $[\text{Tp}^*\text{RhCl}(\text{SR})_2]^-$ ,  $[\text{Tp}^*\text{Rh}(\text{SR})_3]^-$ , can form. The  $[\text{Tp}^*\text{RhCl}_2(\text{PPh}_3)]$  complex presents an additional complication – orthometallation of the  $\text{PPh}_3$  ligand (vide infra).

It was postulated that the selectivity for substitution of a single chloride might be enhanced by first binding a thiol ( $\text{HSR}$ ) or a thiolate ( $\text{SR}^-$ ) to the rhodium center, then inducing salt elimination. To this end,  $\text{Na}[\text{Tp}^*\text{RhCl}_2(\text{SBn})]$  was synthesized by stirring  $[\text{Tp}^*\text{RhCl}_2(\text{MeOH})]$  with one equivalent of  $\text{NaSBn}$  in dry THF. The neutral analogue,  $[\text{Tp}^*\text{RhCl}_2(\text{HSBn})]$ , was synthesized by refluxing  $[\text{Tp}^*\text{RhCl}_2(\text{MeOH})]$  in dry  $\text{C}_6\text{H}_6$  with 1.5 equivalents of  $\text{HSBn}$  for 1 hour. Recrystallization from a DCM solution layered with hexanes at  $-20^\circ\text{C}$  resulted in isolation of  $[\text{Tp}^*\text{RhCl}_2(\text{HSBn})]$  in 67% crystalline yield, and its solid state structure is shown in Figure 6.5. It should be noted that refluxing  $[\text{Tp}^*\text{RhCl}_2(\text{MeOH})]$  with  $\text{HSBn}$  in toluene for 3 hours resulted in the formation of the ligand decomposition product  $[\text{Tp}^*\text{RhCl}_2(\text{pyz})]$  exclusively.

Due to the three-coordinate sulfur atom in  $[\text{Tp}^*\text{RhCl}_2(\text{HSBn})]$  being stereogenic, the methylene protons of this complex are diastereotopic. At room temperature in  $\text{DCM-}d_2$ , the methylene resonance appears as a broad singlet at 4.30 ppm. Variable temperature  $^1\text{H}$  NMR allows for decoalescence of the broad singlet into two doublets at  $-84^\circ\text{C}$ , as well as the appearance of the virtual triplet corresponding to the S-H proton (Figure 6.5). The coalescence temperature is  $-22^\circ\text{C}$ , which gives a calculated  $\Delta G^\ddagger$  of 49.2 kJ/mol. The Rh-S bond length of 2.328 Å is slightly shorter than the Rh-P bond length of in  $[\text{Tp}^*\text{RhCl}_2(\text{PPh}_3)]$  and possesses a

greater octahedral geometry, with  $N_{\text{axial}}\text{-Rh-Cl}_2$  bond angles of  $90.40^\circ$  and  $91.80^\circ$ . All three Rh-N bond lengths are significantly shorter than those in  $[\text{Tp}^*\text{RhCl}_2(\text{PPh}_3)]$ , with a Rh- $N_{\text{axial}}$  bond length of  $2.070 \text{ \AA}$  and Rh- $N_{\text{equatorial}}$  bond lengths of  $2.069 \text{ \AA}$  and  $2.072 \text{ \AA}$ .

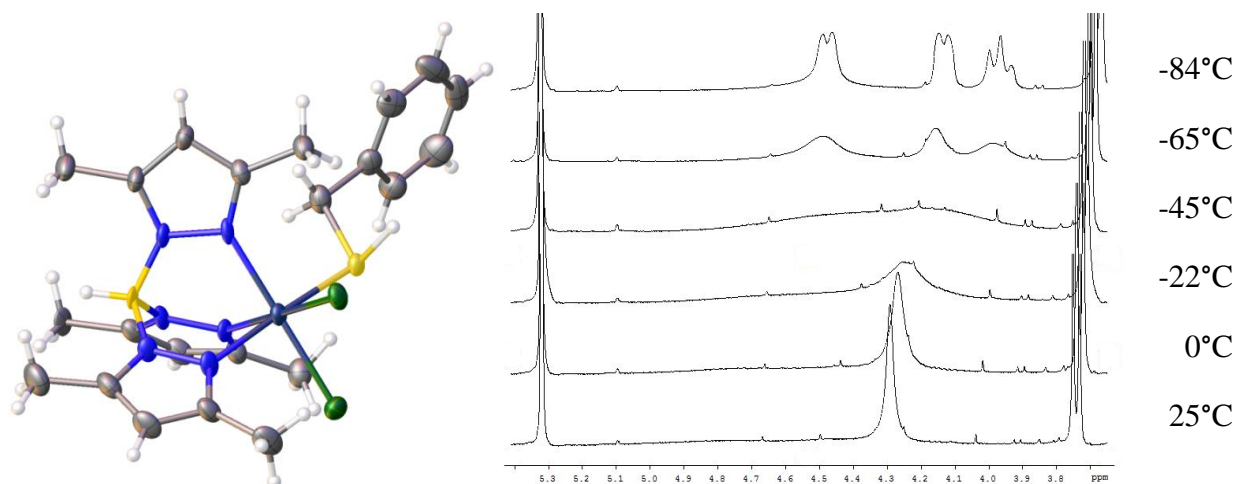


**Figure 6.5. X-ray diffraction solid state structure of  $[\text{Tp}^*\text{RhCl}_2(\text{HSBn})]$  and variable temperature  $^1\text{H}$  NMR spectra of the bound HSBn resonances between 3.6 ppm – 5.4 ppm.**

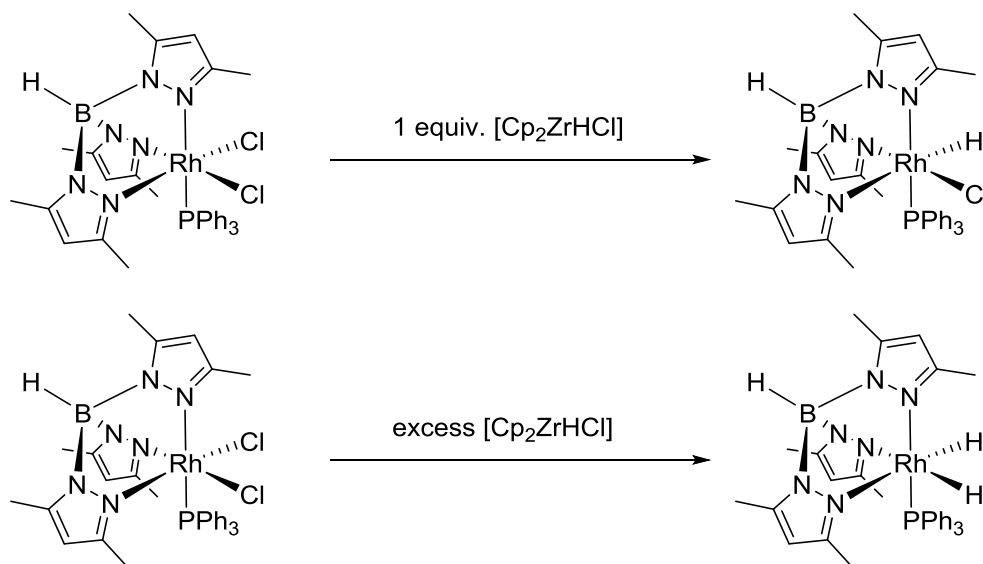
Treatment of a solution of  $[\text{Tp}^*\text{RhCl}_2(\text{HSBn})]$  in benzene with KHMDS resulted in immediate formation of a white precipitate. The precipitate was filtered off, and following removal of the volatiles and dissolving in  $\text{C}_6\text{D}_6$ , addition of MeCN revealed the product to be  $[\text{Tp}^*\text{RhCl}_2(\text{MeCN})]$  by comparison to literature reported NMR characterization.<sup>199</sup> Unfortunately, it appears that upon deprotonation of the HSBn, precipitation of KSBn occurred instead of desired salt elimination of KCl. This may be due to a proximity effect, in that the deprotonation is occurring in close proximity to the sulfur, and thus KSBn forms before salt

metathesis might occur. Alternatively, this may be due to the bound thiol dissociating in solution, and thus deprotonation occurs on free HSBn and not the HSBn bound to the rhodium center. The anionic complex  $\text{Na}[\text{Tp}^*\text{RhCl}_2(\text{SBn})]$  displayed similar reactivity. Heating a solution of  $\text{Na}[\text{Tp}^*\text{RhCl}_2(\text{SBn})]$  in  $d_8$ -toluene resulted in the formation of a white precipitate. Treatment of the resulting solution with MeCN revealed that the major product was, again,  $[\text{Tp}^*\text{RhCl}_2(\text{MeCN})]$ .

### 6.3 Synthesis of $[\text{Tp}^*\text{RhHCl}(\text{PR}_3)]$ and $[\text{Tp}^*\text{RhH}_2(\text{PR}_3)]$ Complexes.

Given the lack of success with substitution of a single chloride in  $[\text{Tp}^*\text{RhCl}_2(\text{L})]$  complexes, we were eager to test if a mono-hydride complex could be generated. Gratifyingly, reaction of  $[\text{Tp}^*\text{RhCl}_2(\text{PPh}_3)]$  with one equivalent of  $[\text{Cp}_2\text{ZrHCl}]$  in benzene resulted in the formation of the mono-hydride complex  $[\text{Tp}^*\text{RhHCl}(\text{PPh}_3)]$  in 90% isolated yield following purification by column chromatography. Treatment of  $[\text{Tp}^*\text{RhCl}_2(\text{PPh}_3)]$  with excess  $[\text{Cp}_2\text{ZrHCl}]$  resulted in the formation of the di-hydride complex  $[\text{Tp}^*\text{RhH}_2(\text{PPh}_3)]$  (Scheme 6.12). The mono-hydride complex exhibits a 1:1:1 integration pattern in the  $^1\text{H}$  NMR spectrum for the three inequivalent pyrazole rings of the  $\text{Tp}^*$  ligand, while the dihydride complex exhibits a 2:1 integration ratio. Relative to the ligand resonances, the hydride signals correctly integrate to 1 and 2 protons, respectively, and exhibit the expected doublet of doublet splitting pattern due to coupling to the rhodium and phosphorus nuclei. Further evidence comes from selective decoupling experiments. Because of the large difference in chemical shift between the hydride signal and the aromatic C-H protons of the  $\text{PPh}_3$  ligand, selective decoupling of the aromatic protons revealed the expected doublet of doublet in the  $^{31}\text{P}\{^1\text{H}\}$  NMR spectrum for the  $[\text{Tp}^*\text{RhHCl}(\text{PPh}_3)]$  complex, and a doublet of triplet for the  $[\text{Tp}^*\text{RhH}_2(\text{PPh}_3)]$  (Figure 6.6).

These hydride complexes are air stable and relatively moisture stable, and can be isolated by silica gel chromatography, although yields can be improved by first drying the silica in an oven.



**Scheme 6.12. Synthesis of [Tp\*RhHCl(PPh<sub>3</sub>)] and [Tp\*RhH<sub>2</sub>(PPh<sub>3</sub>)]**

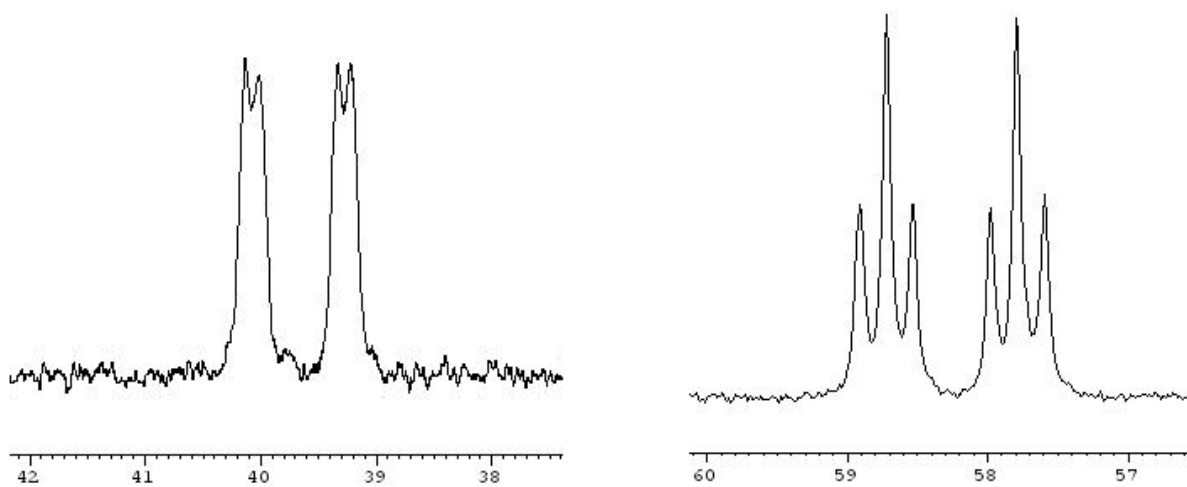
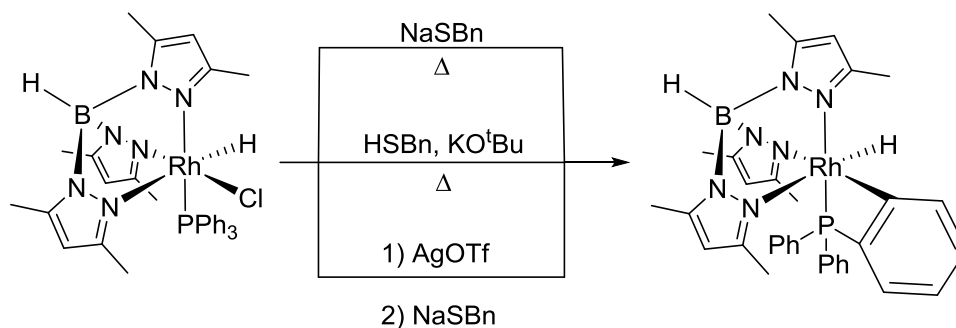


**Figure 6.6. Selective <sup>31</sup>P{<sup>1</sup>H} decoupled spectra for [Tp\*RhHCl(PPh<sub>3</sub>)] (left) and [Tp\*RhH<sub>2</sub>(PPh<sub>3</sub>)] (right).**

Next, we were hopeful that the  $[\text{Tp}^*\text{RhH}_2(\text{PPh}_3)]$  complex might exhibit some similar reactivity as that of Jones's  $[\text{Tp}^*\text{RhH}_2(\text{PMe}_3)]$  complex upon photoirradiation. To this end,  $[\text{Tp}^*\text{RhH}_2(\text{PPh}_3)]$  was dissolved in neat PhSH without shielding from ambient light. An immediate color change from colorless to bright red was observed. However, the  $^1\text{H}$  NMR spectrum revealed a complex mixture of products. While the complexity of the resultant reaction mixture might indicate a competition for C-H vs. S-H activation, it was soon revealed that the  $\text{PPh}_3$  ligand is incompatible with this type of chemistry due to the propensity to undergo orthometallation of the phenyl rings (*vide infra*).

Given the lack of success with photoirradiation of  $[\text{Tp}^*\text{RhH}_2(\text{PPh}_3)]$  to generate the desired  $[\text{Tp}^*\text{RhH}(\text{SR})(\text{PPh}_3)]$  complex, we focused our attention on the  $[\text{Tp}^*\text{RhHCl}(\text{PPh}_3)]$  complex. Since there is only one chloride ligand, it was speculated that the appropriate choice of reaction conditions would allow for clean substitution of the chloride for a thiolate ligand. Three reaction conditions were assayed: 1) heating a  $\text{C}_6\text{D}_6$  solution of  $[\text{Tp}^*\text{RhHCl}(\text{PPh}_3)]$  with one equivalent of NaSBn, 2) heating a  $\text{C}_6\text{D}_6$  solution of  $[\text{Tp}^*\text{RhHCl}(\text{PPh}_3)]$  with one equivalent of HSBn and one equivalent of  $\text{KO}^t\text{Bu}$ , and 3) treatment of  $[\text{Tp}^*\text{RhHCl}(\text{PPh}_3)]$  with AgOTf followed by NaSBn. In each case, a single new product was observed quantitatively. However, by comparison to literature characterization, this product was determined to be that of orthometallation of the  $\text{PPh}_3$  ligand in each case, and not the desired hydridothiolate complex (Scheme 6.13). Attempts to protonolyze the Rh-C bond with HSBn in order to convert this orthometallated complex to the desired hydridothiolate complex resulted in the formation of a complex mixture of products and the complete disappearance of any hydride signals.



**Scheme 6.13. Formation of ortho-metallated product from [Tp\*RhHCl(PPh<sub>3</sub>)].**

It was clear at this juncture that we would be unable to characterize the observed hydride species in stoichiometric reactions between [Tp\*Rh(PPh<sub>3</sub>)<sub>2</sub>] and RSH by independent synthesis. While unfortunate, we were nevertheless eager to show that a hydridothiolate complex was capable of entering the catalytic cycle. We were hopeful that an appropriate choice of L-type ligand would allow for the isolation of a [Tp\*RhH(SR)(L)] complex. [Tp\*RhCl<sub>2</sub>(MeCN)] did not react with [Cp<sub>2</sub>ZrHCl] to produce a Rh-H complex, instead producing a mixture of products with no observable hydride signal. Instead, [Tp\*RhCl<sub>2</sub>(PEt<sub>3</sub>)] was synthesized by refluxing [Tp\*RhCl<sub>2</sub>(MeOH)] in benzene in the presence of excess PEt<sub>3</sub>. The crude reaction mixture showed quantitative conversion to the desired [Tp\*RhCl<sub>2</sub>(PEt<sub>3</sub>)], and recrystallization from a DCM solution layered with hexanes at -20°C resulted in isolation of [Tp\*RhCl<sub>2</sub>(PEt<sub>3</sub>)] in 50% yield. Its X-ray diffraction solid state structure is shown in Figure 6.7. Compared to [Tp\*RhCl<sub>2</sub>(PPh<sub>3</sub>)], [Tp\*RhCl<sub>2</sub>(PEt<sub>3</sub>)] has a much shorter Rh-P bond length at 2.309 Å and the octahedral geometry is less distorted, with N<sub>axial</sub>-Rh-Cl<sub>2</sub> bond angles of 90.41° and 90.83°. The Rh-N bond lengths are slightly longer, with a Rh-N<sub>axial</sub> bond length of 2.141 Å, and Rh-N<sub>equatorial</sub>

bond lengths of 2.102 Å and 2.110 Å. All three  $[\text{Tp}^*\text{RhCl}_2(\text{L})]$  ( $\text{L} = \text{PPh}_3, \text{PEt}_3, \text{BnSH}$ ) have virtually identical Rh-Cl bond lengths in the range of 2.330 Å to 2.340 Å.

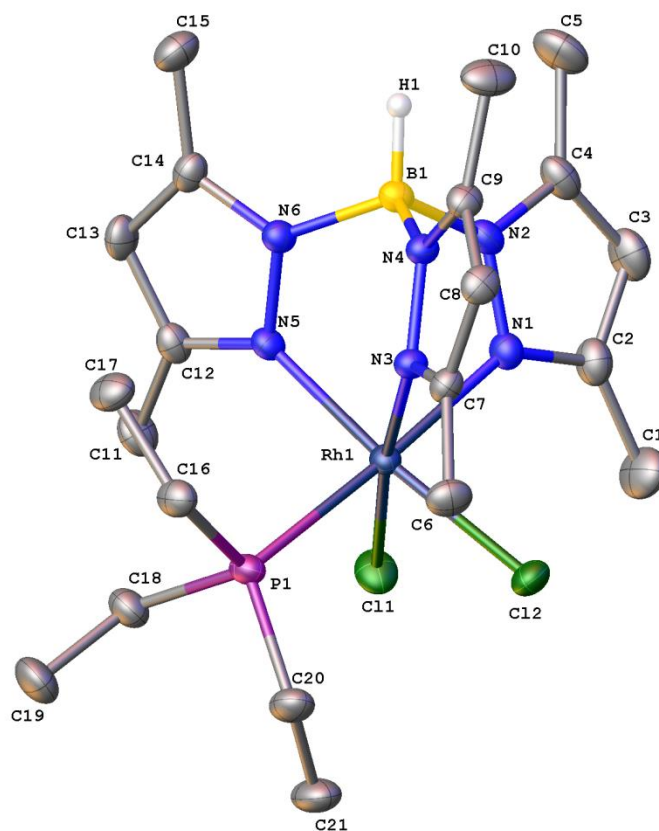


**Figure 6.7. X-ray diffraction solid state structure of  $[\text{Tp}^*\text{RhCl}_2(\text{PEt}_3)]$ .**

Strangely, a similar reaction between  $[\text{Tp}^*\text{RhCl}_2(\text{MeOH})]$  and  $\text{PCy}_3$  resulted instead in isolation of the anionic complex  $(\text{PCy}_3\text{Me})[\text{Tp}^*\text{RhCl}_3]$  in 15% crystalline yield, which can be attributed to the steric bulk of  $\text{PCy}_3$ . Instead, the rhodium scavenges residual KCl from the initial synthesis of  $[\text{Tp}^*\text{RhCl}_2(\text{MeOH})]$ . The methyl fragment on the phosphorus cation is presumably derived from methanol. Its X-ray diffraction solid state structure is shown in Figure 6.8.

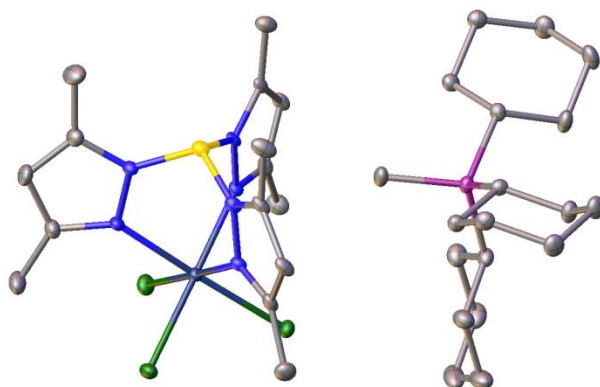


**Figure 6.8. X-ray diffraction solid state structure of  $[\text{Tp}^*\text{RhCl}_3](\text{PCy}_3\text{Me})$ .**

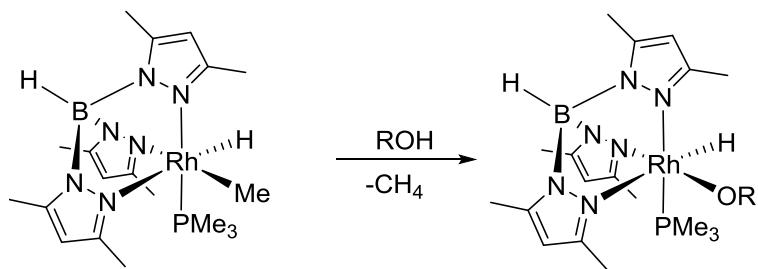
Similar to  $[\text{Tp}^*\text{RhCl}_2(\text{PEt}_3)]$ ,  $[\text{Tp}^*\text{RhCl}_2(\text{PEt}_3)]$  reacted with one equivalent of  $[\text{Cp}_2\text{ZrHCl}]$  to generate the desired  $[\text{Tp}^*\text{RhHCl}(\text{PEt}_3)]$  complex. However, unlike  $[\text{Tp}^*\text{RhHCl}(\text{PPh}_3)]$ ,  $[\text{Tp}^*\text{RhHCl}(\text{PEt}_3)]$  is moisture and thermally sensitive. Interestingly, because the asymmetric Rh center in  $[\text{Tp}^*\text{RhHCl}(\text{PEt}_3)]$  is stereogenic, the  $\text{CH}_2$  protons of the  $\text{PEt}_3$  ligand are diastereotopic, resulting in two multiplets integrating to three protons each.

Salt metathesis reactions with either  $\text{NaSR}$  or  $\text{HSR}$  and  $\text{KO}^t\text{Bu}$  necessarily proceed via a dissociative mechanism. Thus, heating of a solution of  $[\text{Tp}^*\text{RhHCl}(\text{PEt}_3)]$  would be required in order to induce salt metathesis to the desired hydrido-thiolate complex. Due to the thermal sensitivity of  $[\text{Tp}^*\text{RhHCl}(\text{PEt}_3)]$ , these avenues were considered to be unlikely to proceed cleanly. Instead, halide abstraction with  $\text{AgBF}_4$ , followed by addition of  $\text{NaSBn}$  was attempted. Unfortunately, this reaction sequence resulted in the generation of five new hydride signals. Integration of the hydride signals relative to all the pyrazole aromatic C-H signals reveals a 1:3 integration ratio, suggesting that all resulting rhodium hydride species retain the complexed  $\text{Tp}^*$  ligand. One of these hydride signals is a doublet of a triplet, indicative of the formation of the

cationic complex  $[\text{Tp}^*\text{RhH}(\text{PEt}_3)_2](\text{BF}_4)$ . The formation of this cationic complex, in turn, suggests that one of the observed hydride signals in the product mixture might be the anionic complex  $\text{Na}[\text{Tp}^*\text{RhH}(\text{SBn})_2]$ . Additionally, a signal in the  $^{31}\text{P}\{^1\text{H}\}$  NMR is observed at -39 ppm, which was shown to correlate to one of the hydride signals by  $^1\text{H}$ - $^{31}\text{P}$  HMBC experiments. This unusual chemical shift is similar to that of the ortho-metallated  $[\text{Tp}^*\text{RhH}(o\text{-C}_6\text{H}_4\text{PPh}_2)]$  complex and is presumably due to intramolecular C-H activation of the  $\text{PEt}_3$  ligand to produce a cyclometallated product. One of the observed hydride signals might be the desired  $[\text{Tp}^*\text{RhH}(\text{SBn})(\text{PEt}_3)]$  complex, while the final hydride signal remains unassigned.

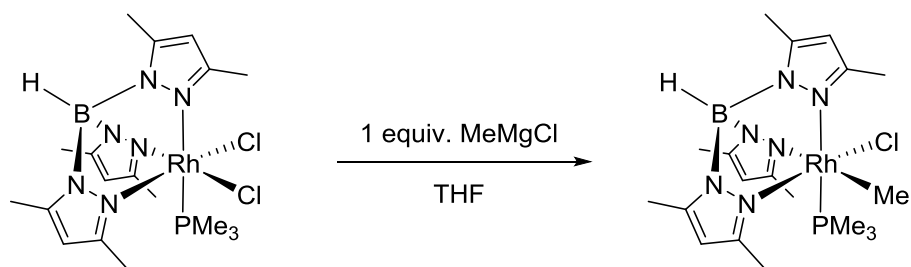
#### 6.4 Synthesis of Hydridothiolate Complexes $[\text{Tp}^*\text{RhH}(\text{SR})(\text{PMe}_3)]$

As discussed previously, Jones and coworkers have had considerable success examining reductive elimination from and oxidative addition to  $[\text{Tp}^*\text{Rh}]$  complexes bearing  $\text{PMe}_3$  as a neutral donor ligand.<sup>200</sup> Recently, Jones and coworkers have successfully synthesized  $[\text{Tp}^*\text{RhH}(\text{OR})(\text{PMe}_3)]$  (R = alkyl) complexes via oxidative addition of alcohols (ROH) to the  $[\text{Tp}^*\text{Rh}^{\text{I}}(\text{PMe}_3)]$  fragment generated upon reductive elimination of methane from  $[\text{Tp}^*\text{Rh}^{\text{III}}\text{H}(\text{Me})(\text{PMe}_3)]$  (Scheme 6.14).<sup>201</sup> The successful synthesis of alkoxy hydride complexes suggests that similar reactivity might be observed with thiols.



**Scheme 6.14. Synthesis of alkoxy hydride complexes [Tp\*RhH(OR)(PMe<sub>3</sub>)]**

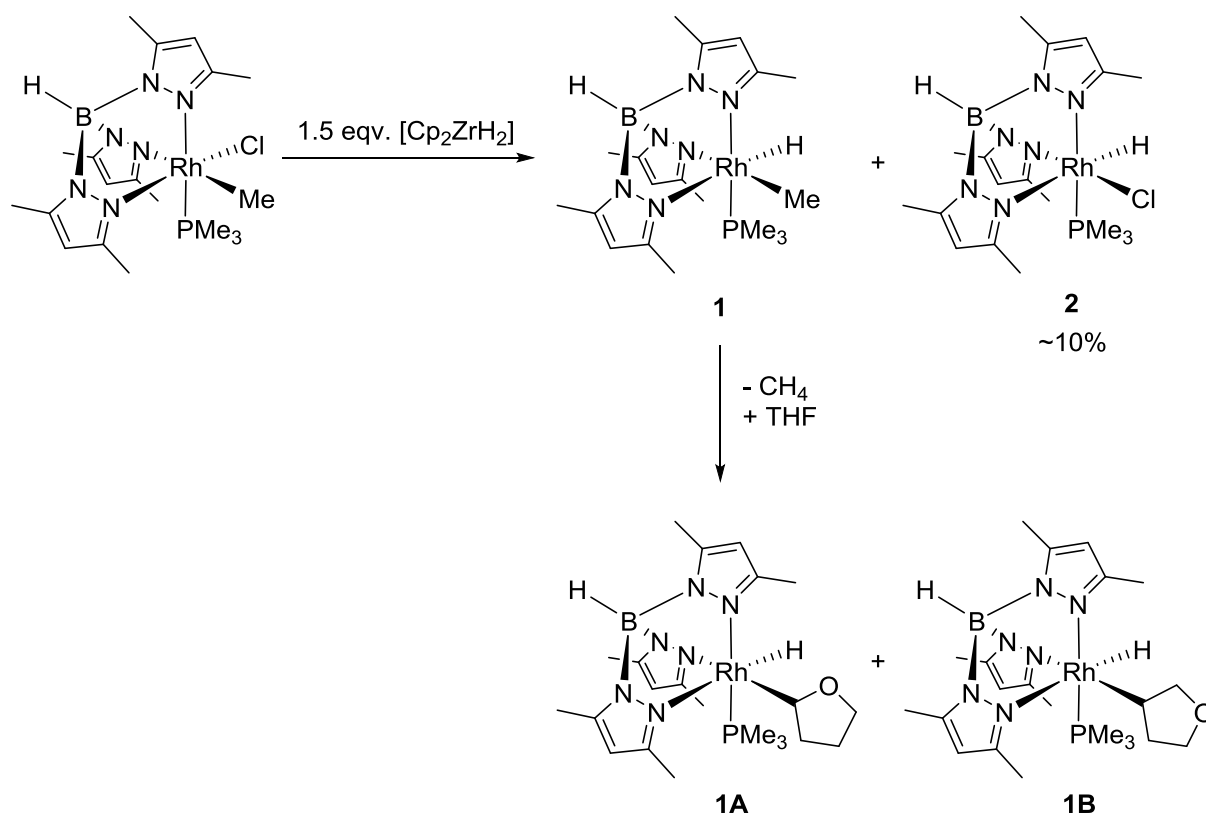
Towards this end, the rhodium methyl complex [Tp\*RhCl(Me)(PMe<sub>3</sub>)] complex was synthesized as previously reported.<sup>202</sup> Treatment of [Tp\*RhCl<sub>2</sub>(PMe<sub>3</sub>)] with one equivalent of MeMgCl in THF results in the quantitative formation of [Tp\*RhCl(Me)(PMe<sub>3</sub>)] (Scheme 6.15). The complex was then purified by recrystallization from a DCM solution of [Tp\*RhCl(Me)(PMe<sub>3</sub>)] layered with hexanes and cooled to -20 °C.



**Scheme 6.15. Synthesis of [Tp\*RhCl(Me)(PMe<sub>3</sub>)].**

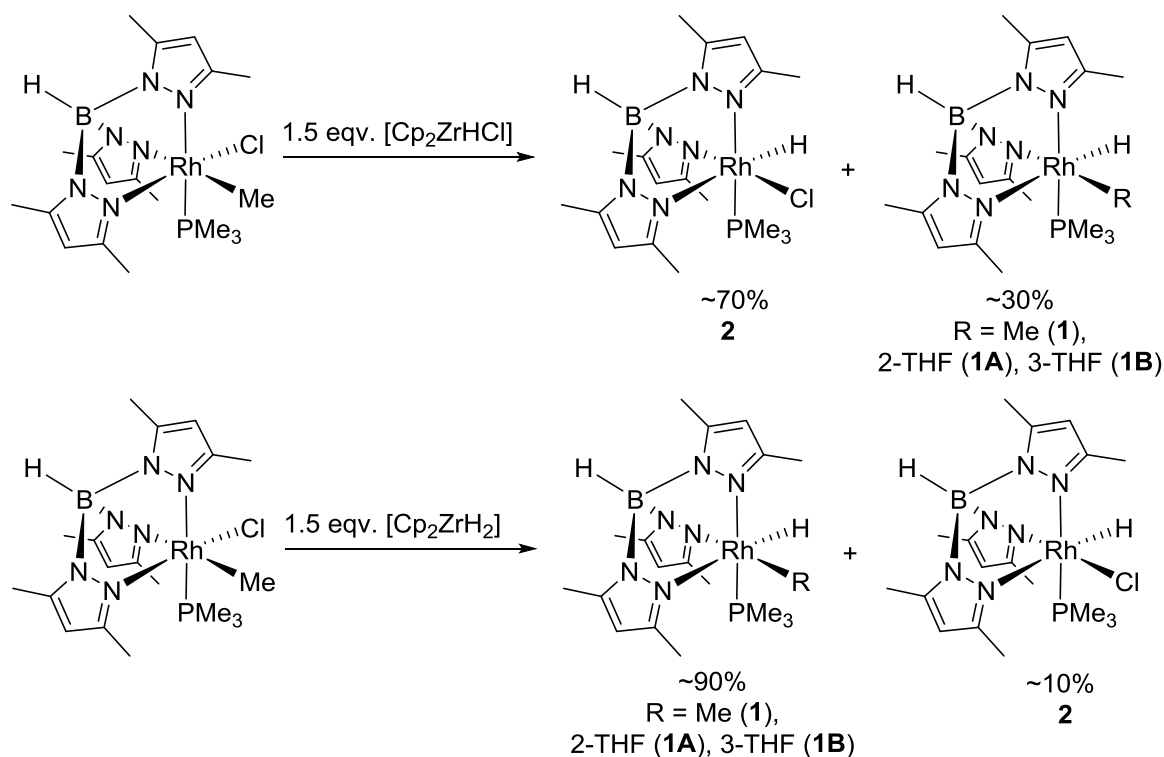
The next step requires conversion of the chloride to the hydride. Jones and coworkers achieved this conversion by reaction of [Tp\*RhCl(Me)(PMe<sub>3</sub>)] with a slight excess of [Cp<sub>2</sub>ZrH<sub>2</sub>] in THF.<sup>203</sup> The resulting [Tp\*RhH(Me)(PMe<sub>3</sub>)] (**1**) complex is thermally unstable, and undergoes reductive elimination of methane and activation of solvent to produce two

regioisomeric products of THF C-H activation (Scheme 6.16, **1A**, **1B**). The quantity of THF C-H activation products generated are dependent on the temperature at which the reaction is performed. Additionally, a small amount (~10%) of  $[\text{Tp}^*\text{RhHCl}(\text{PMe}_3)]$  (**2**) is formed during the reaction, as well as a small amount (~1%) of  $[\text{Tp}^*\text{RhH}_2(\text{PMe}_3)]$ , presumably arising from reaction of  $[\text{Tp}^*\text{RhHCl}(\text{PMe}_3)]$  with excess  $[\text{Cp}_2\text{ZrH}_2]$ . All five complexes have been characterized by the Jones group and can be assigned by their diagnostic rhodium hydride  $^1\text{H}$  NMR signals and  $^{31}\text{P}\{^1\text{H}\}$  NMR signals.



**Scheme 6.16.** Synthesis of  $[\text{Tp}^*\text{RhH}(\text{Me})(\text{PMe}_3)]$  and side products.

When  $[\text{Tp}^*\text{RhCl}(\text{Me})(\text{PMe}_3)]$  was treated with a small excess of  $[\text{Cp}_2\text{ZrHCl}]$ , the major product (~70%) was found to be  $[\text{Tp}^*\text{RhHCl}(\text{PMe}_3)]$ . Repeating the work of Jones and coworkers, treatment of  $[\text{Tp}^*\text{RhCl}(\text{Me})(\text{PMe}_3)]$  with  $[\text{Cp}_2\text{ZrH}_2]$  resulted in the formation of only ~10%  $[\text{Tp}^*\text{RhHCl}(\text{PMe}_3)]$ . The major products were  $[\text{Tp}^*\text{RhH}(\text{Me})(\text{PMe}_3)]$  and the THF C-H activation products (Scheme 6.17).

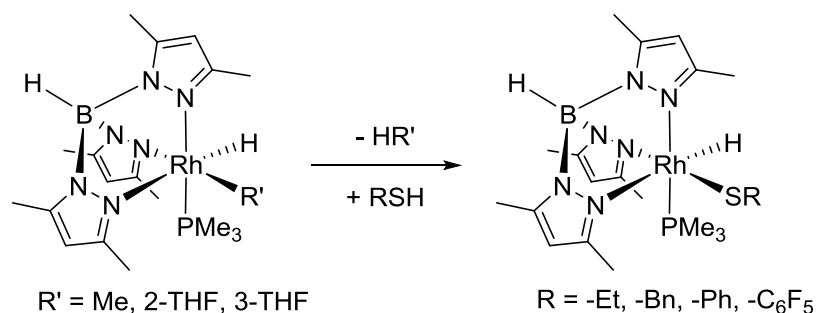


**Scheme 6.17.** Reaction of  $[\text{Tp}^*\text{RhCl}(\text{Me})(\text{PMe}_3)]$  with  $[\text{Cp}_2\text{ZrHCl}]$  and  $[\text{Cp}_2\text{ZrH}_2]$ . Product ratios based on integration of diagnostic  $^1\text{H}$  NMR signals.

Fortuitously, Jones found that complexes **1A** and **1B** react similarly to complex **1**, reductively eliminating THF and undergoing subsequent bond activation. Complex **2** is

unreactive under conditions of thermal hydrocarbon reductive elimination and subsequent bond activation.

Consistent with our hypothesis,  $[\text{Tp}^*\text{RhH}(\text{Me})(\text{PMe}_3)]$  and associated THF products were found to react with thiols to generate hydridothiolate complexes  $[\text{Tp}^*\text{RhH}(\text{SR})(\text{PMe}_3)]$  (Scheme 6.18). To date, four hydridothiolate complexes have been synthesized and characterized by  $^1\text{H}$  NMR,  $^{13}\text{C}\{^1\text{H}\}$  NMR,  $^{31}\text{P}\{^1\text{H}\}$  NMR,  $^{19}\text{F}$  NMR for the  $-\text{SC}_6\text{F}_5$  derivative and a variety of 2D NMR techniques. The reactions were performed in either  $\text{C}_6\text{D}_{12}$ ,  $\text{C}_6\text{D}_6$  or pentanes. In  $\text{C}_6\text{D}_6$ , no competitive C-D activation was observed. When  $\text{BnSH}$ ,  $\text{EtSH}$  and  $\text{PhSH}$  were employed, no competitive C-H activation of the thiol substrate was observed, nor was competitive C-H activation of pentanes observed. When  $\text{C}_6\text{F}_5\text{SH}$  was used as a substrate, no competitive C-F activation was observed. The reactions are complete within 8 hours at room temperature, and within 3 hours when the reactions were heated to  $45\text{ }^\circ\text{C}$  and form quantitatively from the corresponding  $[\text{Tp}^*\text{RhH}(\text{R})(\text{PMe}_3)]$  complexes.  $[\text{Tp}^*\text{RhHCl}(\text{PMe}_3)]$  remains unreactive under the reaction conditions, as does the small amount of  $[\text{Tp}^*\text{RhH}_2(\text{PMe}_3)]$  complex present.  $[\text{Tp}^*\text{RhH}(\text{Me})(\text{PMe}_3)]$  reacts much more rapidly to produce the hydridothiolate complexes compared to the THF activation products. The complexes are stable for several days in  $\text{C}_6\text{D}_6$ , with no observable conversion to  $[\text{Tp}^*\text{RhD}(\text{C}_6\text{D}_5)(\text{PMe}_3)]$ .



**Scheme 6.18. Synthesis of hydrido-thiolate complexes [Tp\**RhH*(SR)(PMe<sub>3</sub>)].**

Interestingly, due to the inequivalency of the three pyrazole rings, the two  $-\text{CH}_2$  protons of [Tp\**RhH*(SEt)(PMe<sub>3</sub>)] and [Tp\**RhH*(SBn)(PMe<sub>3</sub>)] are diastereotopic. For [Tp\**RhH*(SBn)(PMe<sub>3</sub>)], the methylene protons appear as two doublets, likely due to geminal coupling (Figure 6.9). The rotation about the Rh-SBn bond is restricted due to the two adjacent pyrazole methyl groups, as revealed by 1D selective NOE experiments. When irradiating the pyrazole methyl *trans* to the PMe<sub>3</sub> ligand, strong NOE interaction is observed with H<sub>A</sub> and weak NOE interaction with H<sub>B</sub> (Figure 6.10). When irradiating the methyl of the pyrazole *trans* to the Rh-H, a strong NOE interaction is observed with H<sub>B</sub> and a weak NOE interaction with H<sub>A</sub> (Figure 6.11).

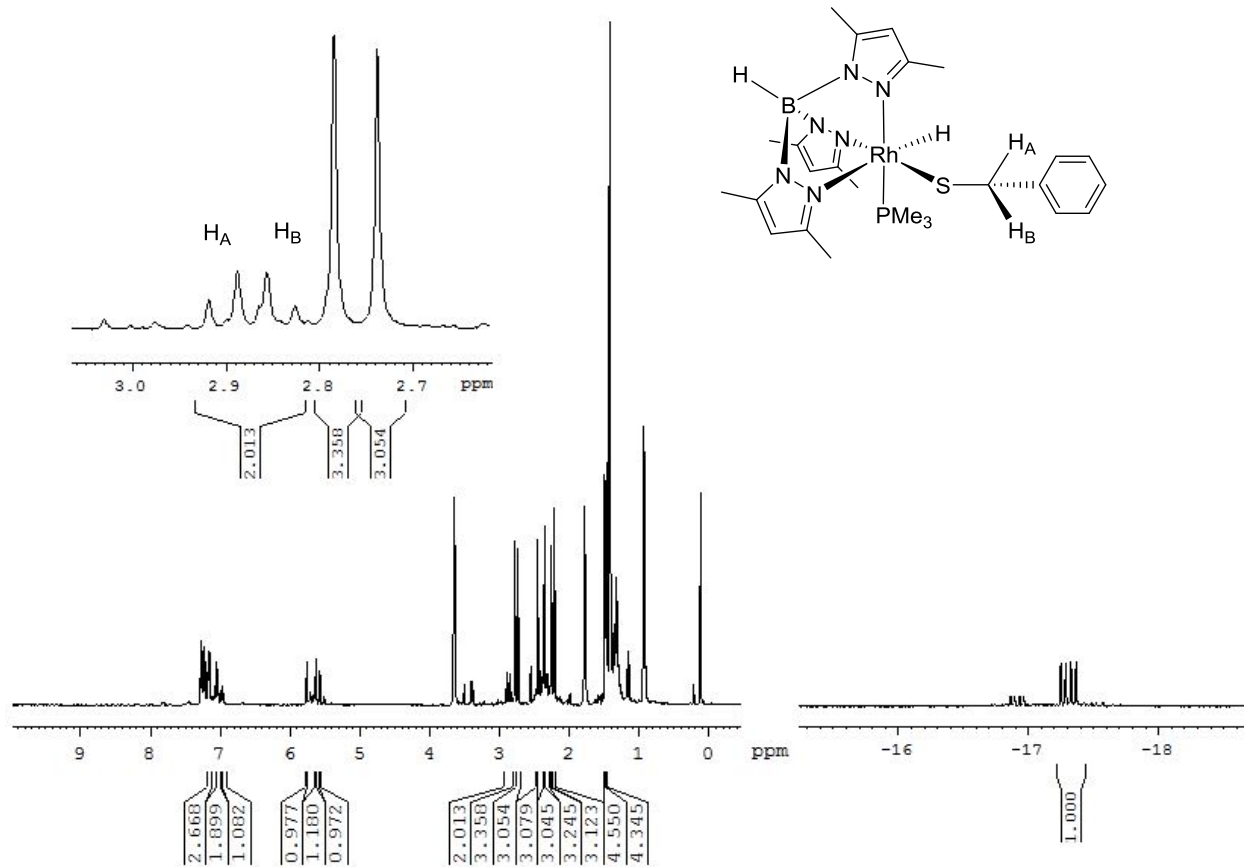


**Figure 6.9.**  $^1\text{H}$  NMR spectrum of  $[\text{Tp}^*\text{RhH}(\text{SBn})(\text{PMe}_3)]$  in  $\text{C}_6\text{D}_{12}$ . The region between 2.7 and 3.0 ppm is magnified to show the two doublets corresponding to  $\text{H}_\text{A}$  and  $\text{H}_\text{B}$ .

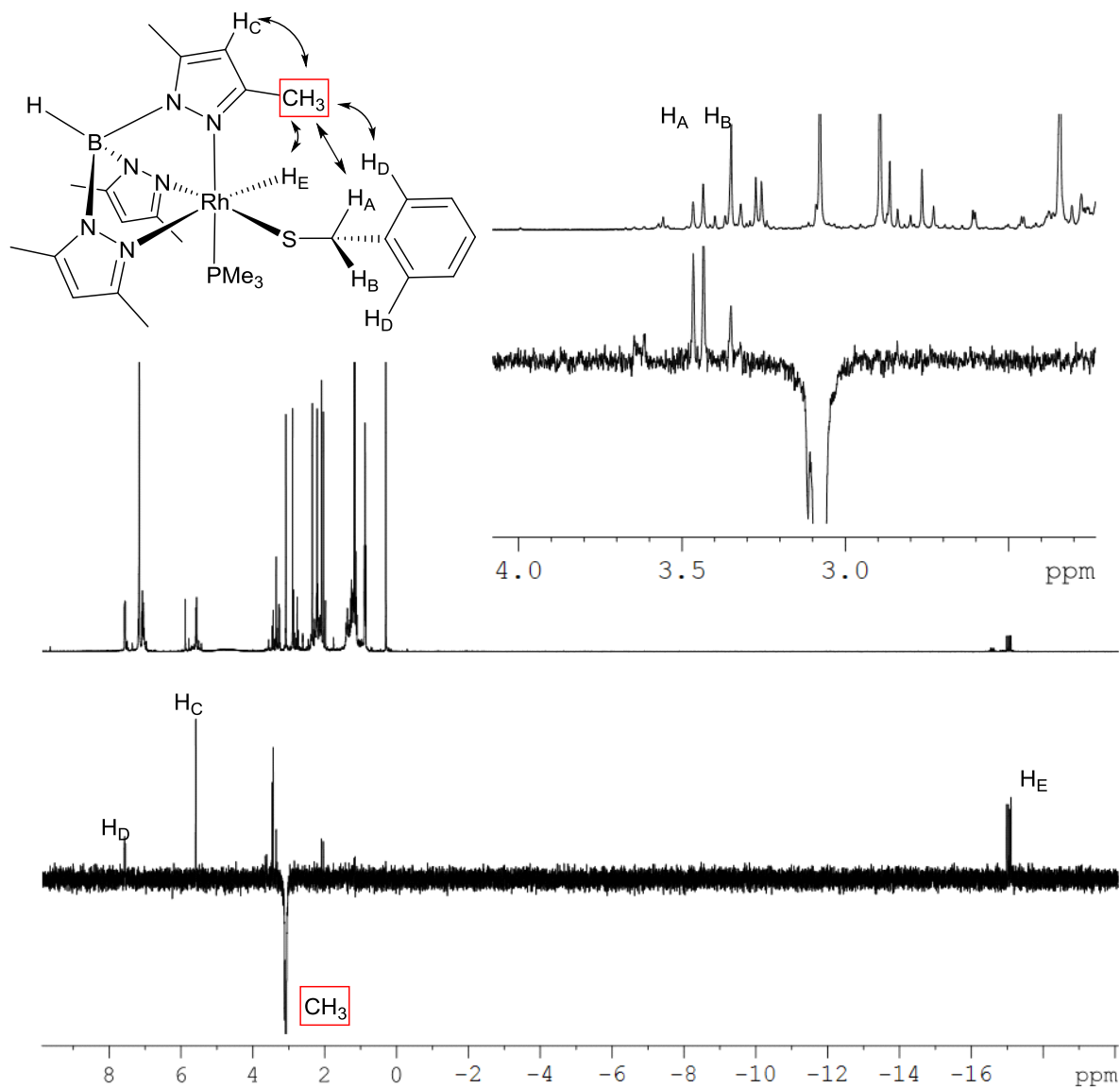


**Figure 6.10.** 1D selective NOE spectrum for  $[\text{Tp}^*\text{RhH}(\text{SBn})(\text{PMe}_3)]$  in  $\text{C}_6\text{D}_6$ . NOE interactions are shown as arrows. Protons being irradiated are indicated by red box.

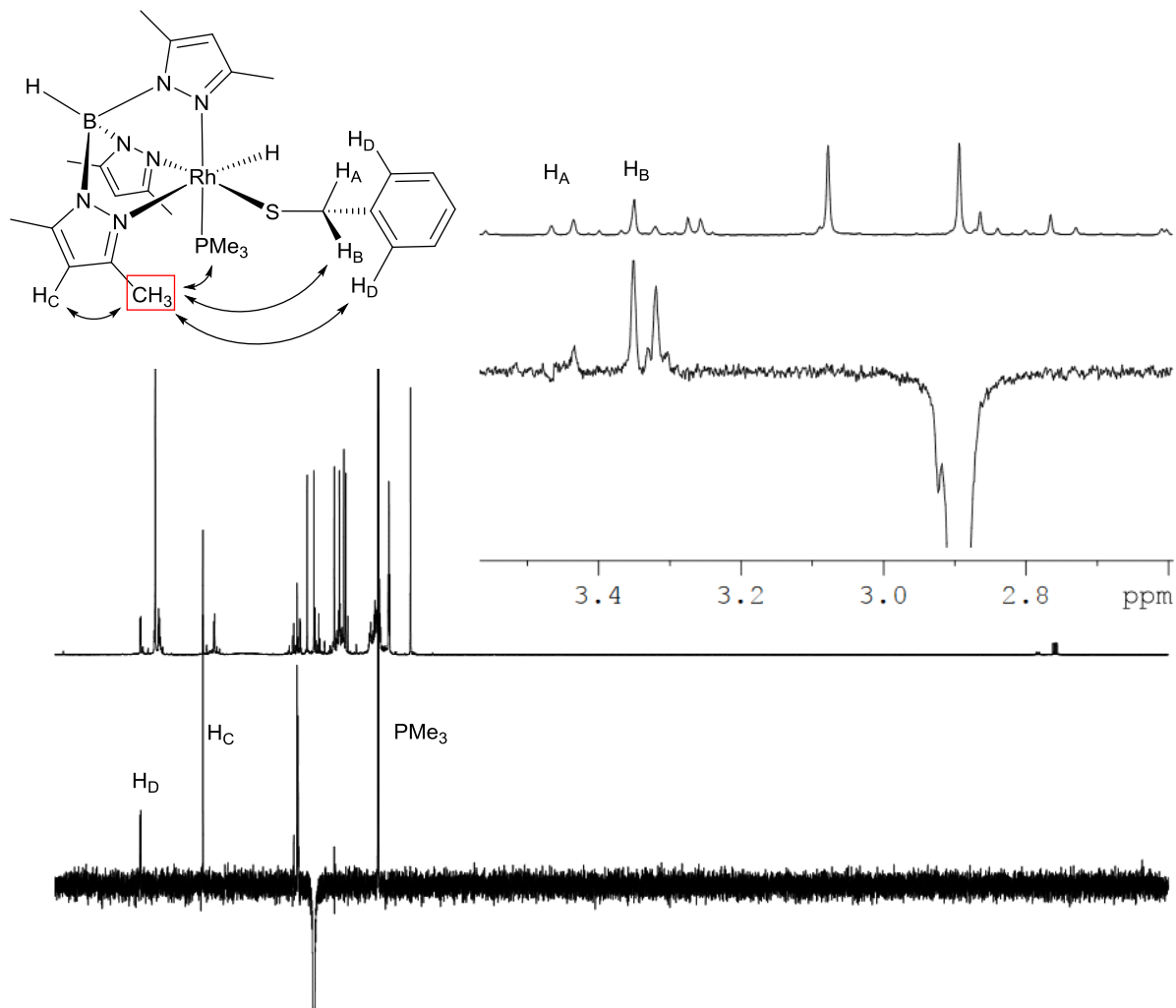


**Figure 6.11. 1D selective NOE spectrum for  $[\text{Tp}^*\text{RhH}(\text{SBn})(\text{PMe}_3)]$  in  $\text{C}_6\text{D}_6$ . NOE interactions are shown as arrows. Protons being irradiated are indicated by red box.**

In the case of  $[\text{Tp}^*\text{RhH}(\text{SEt})(\text{PMe}_3)]$ , the diastereotopic methylene signals are unfortunately obstructed by the pyrazole methyl resonances of the product and the  $[\text{Tp}^*\text{RhHCl}(\text{PMe}_3)]$  impurity. Their chemical shift and multiplicity were instead determined by HMBC, COSY, and 1D TOCSY experiments. Figure 6.12 shows the overlay of  $^1\text{H}$ - $^{13}\text{C}$  HSQC

and HMBC experiments showing the correlation between the CH<sub>3</sub> of the [RhSEt] fragment and the methylene fragment. The <sup>1</sup>H-<sup>13</sup>C HSQC peak for C<sub>A</sub> indicates correlation to two inequivalent protons, H<sub>A</sub> and H<sub>B</sub>, while the <sup>1</sup>H-<sup>13</sup>C HMBC cross peak with the resonance for the H<sub>C</sub> protons show that C<sub>A</sub> is indeed the methylene carbon of the [RhSEt] fragment. The magnified image of the <sup>13</sup>C{<sup>1</sup>H} peak indicates that the peak corresponding to C<sub>A</sub> is a doublet (J = 3 Hz), likely due to coupling to rhodium (Figure 6.13). C<sub>B</sub> also appears to be a doublet, however it is not sufficiently resolved to be conclusive.

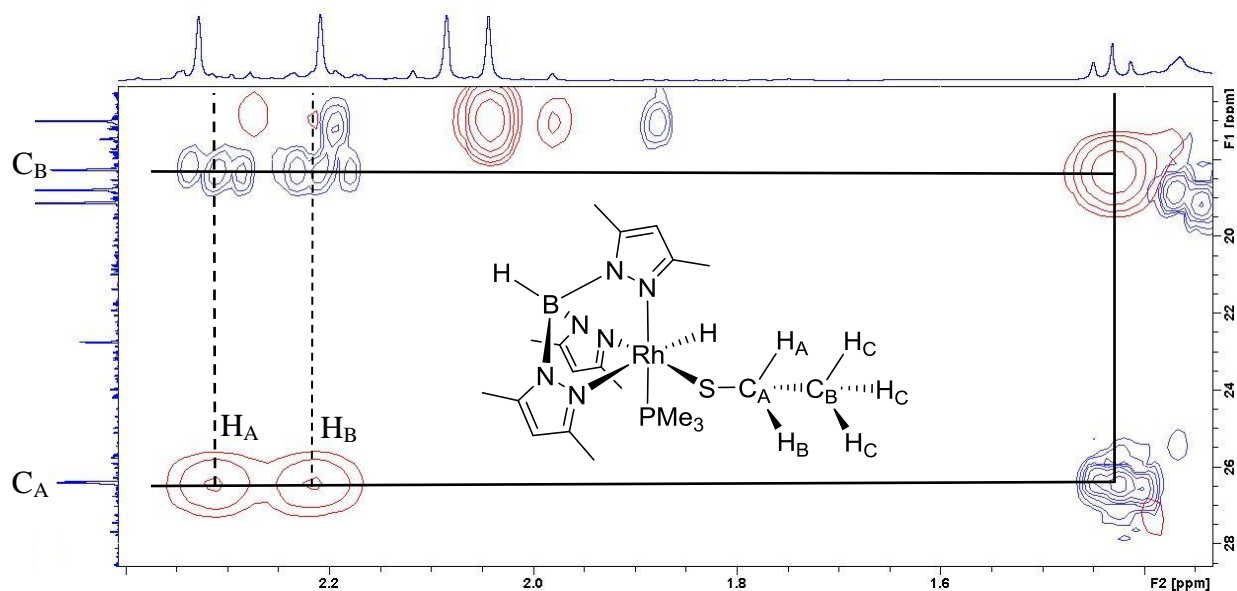


**Figure 6.12. Overlaid <sup>1</sup>H-<sup>13</sup>C HSQC (Red) and <sup>1</sup>H-<sup>13</sup>C HMBC (Blue) correlation spectra. Lines indicate the cross-peaks for the [RhSEt] fragment.**

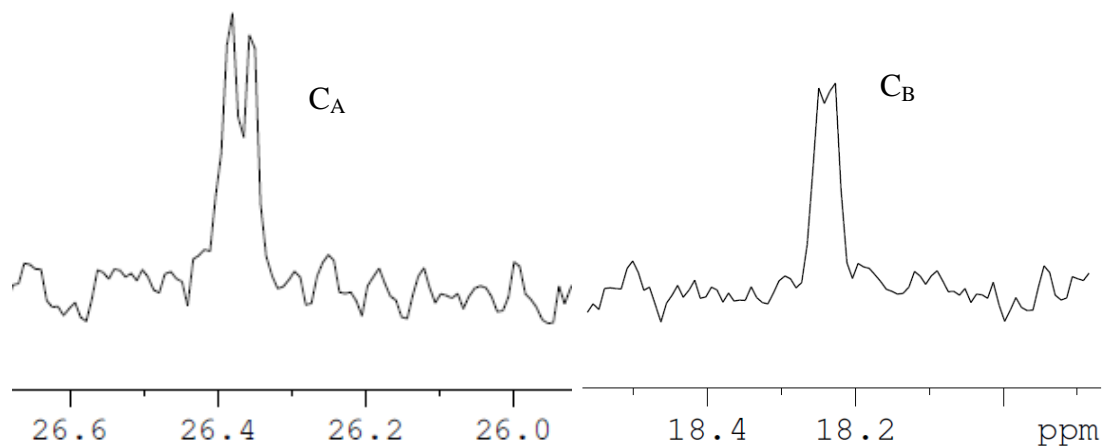


**Figure 6.13.**  $^{13}\text{C}\{^1\text{H}\}$  peaks for the [RhSEt] fragment of  $[\text{Tp}^*\text{RhH}(\text{SEt})(\text{PMe}_3)]$ .

Several experiments were performed in order to more clearly observe the splitting patterns of the diastereotopic methylene signals of the [RhSEt] fragment. By analogy to  $[\text{Tp}^*\text{RhH}(\text{SBn})(\text{PMe}_3)]$ , the methylene protons should be split into doublets – likely due to geminal coupling – and split again into a doublet of a quartet by coupling to the  $\text{CH}_3$  of the [RhSEt] fragment, for a total of eight peaks. The clearest indication of such a splitting pattern was obtained from 1D TOCSY experiments. Selective irradiation the  $\text{CH}_3$  of the [RhSEt] fragment reveals multiplets corresponding to the two diastereotopic methylene signals. Both multiplets exhibit a total of eight peaks (Figure 6.14).

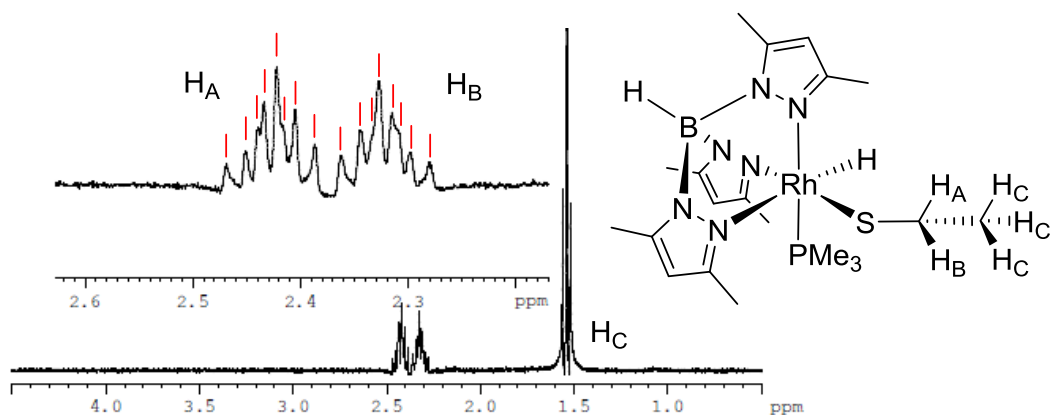


**Figure 6.14. 1D TOCSY correlation showing the spin system of the [RhSEt] fragment of [Tp\*RhH(SEt)(PMe<sub>3</sub>)].**

Similar to [Tp\*RhH(SBn)(PMe<sub>3</sub>)], the diastereotopic methylene group of the [RhSEt] fragment shows strong and weak NOE interactions with the inequivalent pyrazole rings. When irradiating the pyrazole methyl *trans* to the PMe<sub>3</sub> ligand, a strong NOE interaction is observed with H<sub>A</sub> and a weak interaction with H<sub>B</sub> (Figure 6.15). Conversely, when irradiating the pyrazole methyl *trans* to the hydride, a strong NOE interaction is observed with H<sub>B</sub> and a weak interaction is observed with H<sub>A</sub> (Figure 6.16).

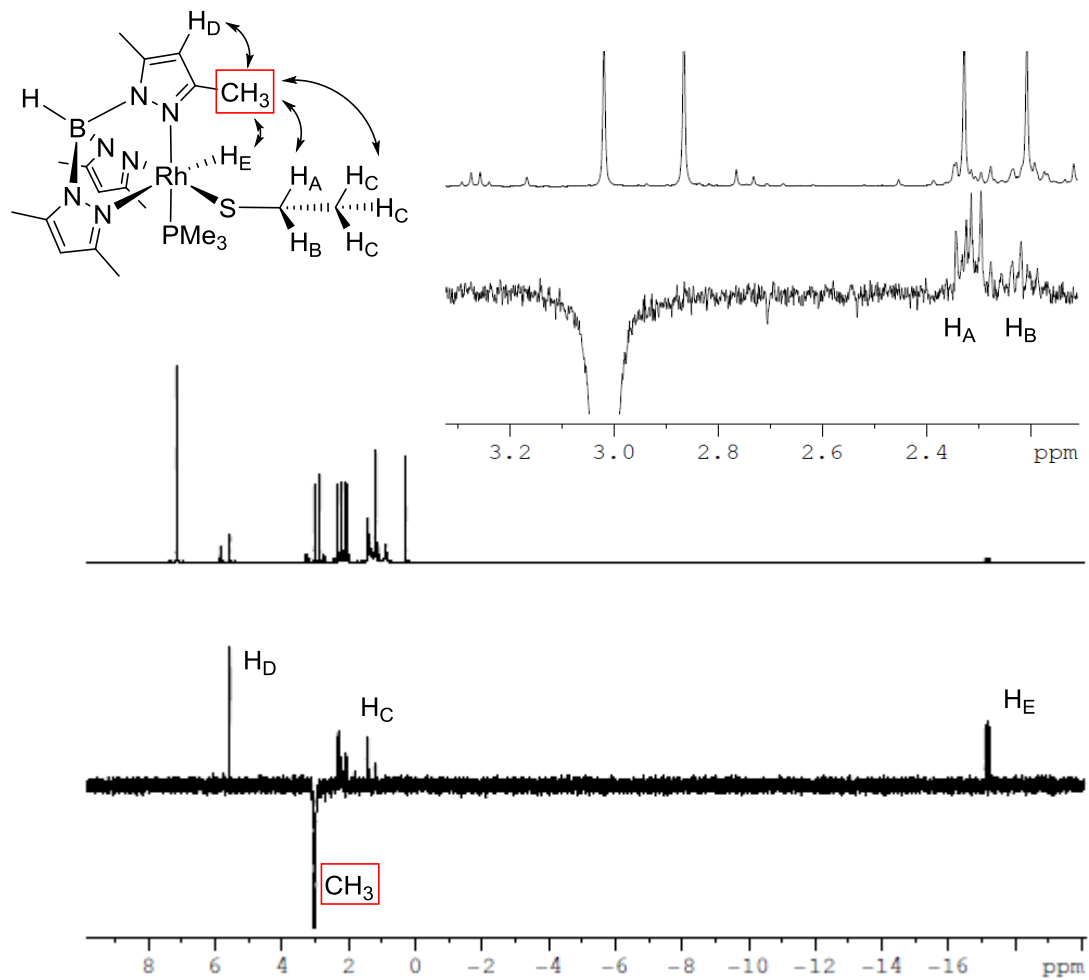


**Figure 6.15.** 1D selective NOE spectrum for  $[\text{Tp}^*\text{RhH}(\text{SEt})(\text{PMe}_3)]$  in  $\text{C}_6\text{D}_6$ . NOE interactions are shown as arrows. Protons being irradiated are indicated by red box.

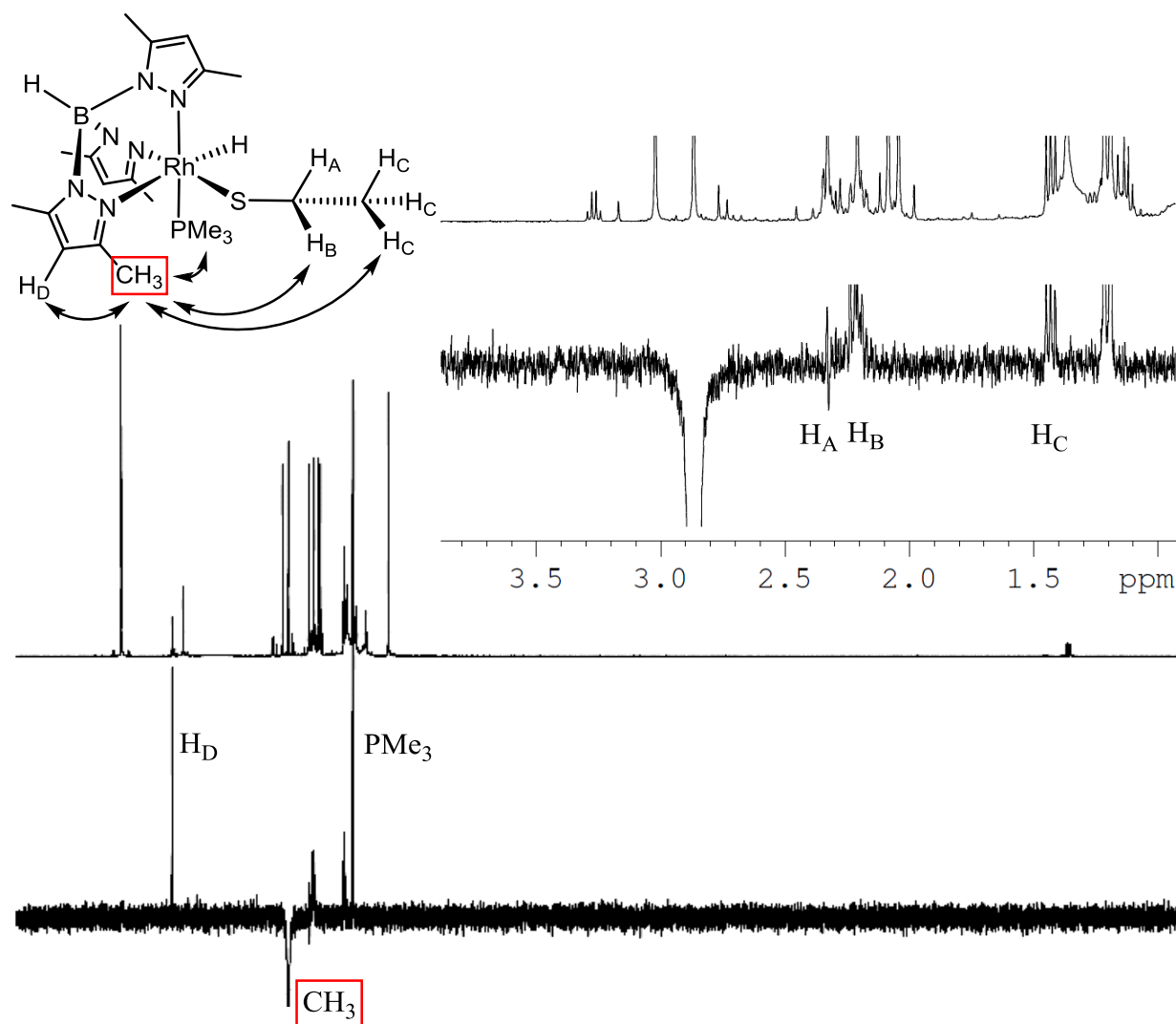


**Figure 6.16.** 1D selective NOE spectrum for  $[\text{Tp}^*\text{RhH}(\text{SET})(\text{PMe}_3)]$  in  $\text{C}_6\text{D}_6$ . NOE interactions are shown as arrows. Protons being irradiated are indicated by red box.

Neither  $[\text{Tp}^*\text{RhH}(\text{SBn})(\text{PMe}_3)]$  nor  $[\text{Tp}^*\text{RhH}(\text{SBn})(\text{PMe}_3)]$  show any NOE contact between the hydride resonance and the resonances of the RhSR fragment. Conversely, both  $[\text{Tp}^*\text{RhH}(\text{SPh})(\text{PMe}_3)]$  and  $[\text{Tp}^*\text{RhH}(\text{SC}_6\text{F}_5)(\text{PMe}_3)]$  do exhibit NOE interaction between the hydride and the RhSR fragment. Irradiation of the hydride resonance of  $[\text{Tp}^*\text{RhH}(\text{SPh})(\text{PMe}_3)]$

shows a strong NOE contact to the ortho protons of the phenyl ring of the [RhSPh] fragment (Figure 6.17). 2D  $^1\text{H}$ - $^{19}\text{F}$  HOESY experiments reveal cross peaks for interaction between the ortho fluorines of the  $\text{RhSC}_6\text{F}_5$  fragment and the hydride resonance, as well as the pyrazole methyl resonances *cis* to the  $\text{SC}_6\text{F}_5$  and the  $\text{PMe}_3$  methyl resonances (Figure 6.18).

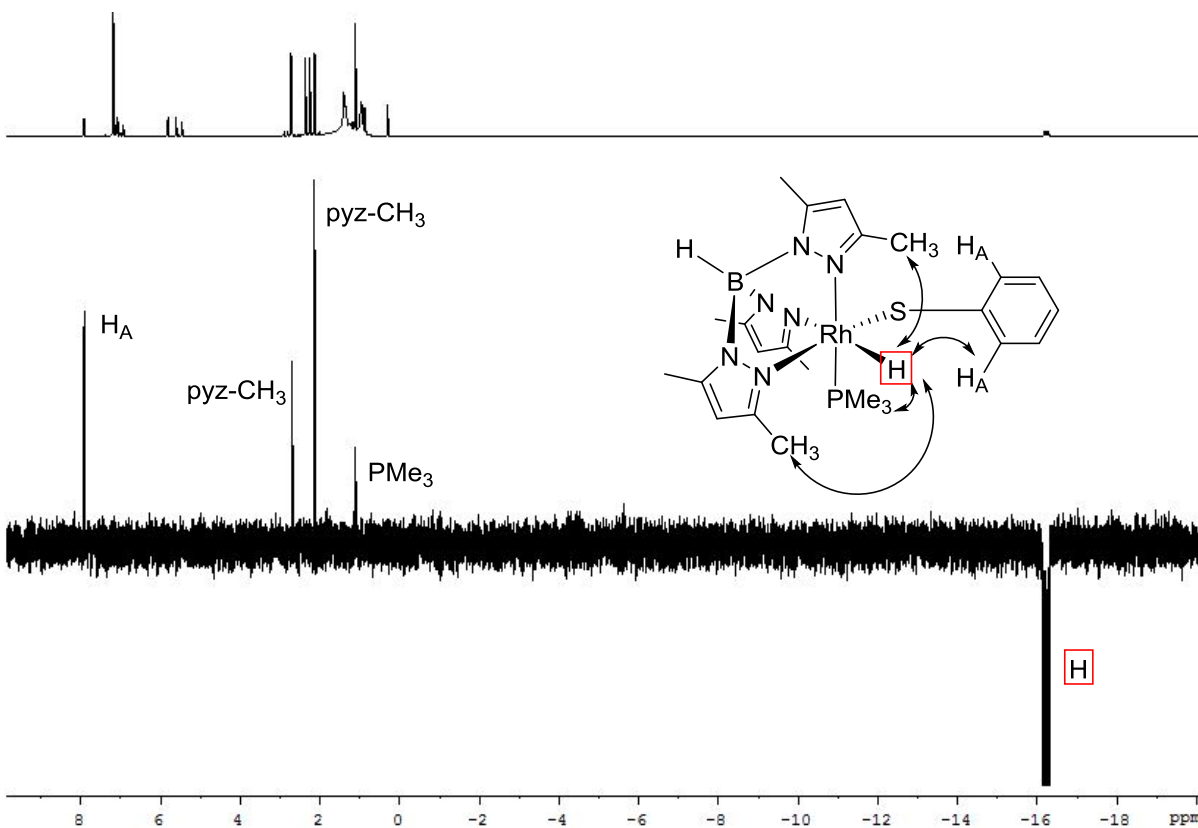


**Figure 6.17.** 1D selective NOE spectrum for  $[\text{Tp}^*\text{RhH}(\text{SPh})(\text{PMe}_3)]$  in  $\text{C}_6\text{D}_6$ . NOE interactions are shown as arrows. Proton being irradiated is indicated by red box.

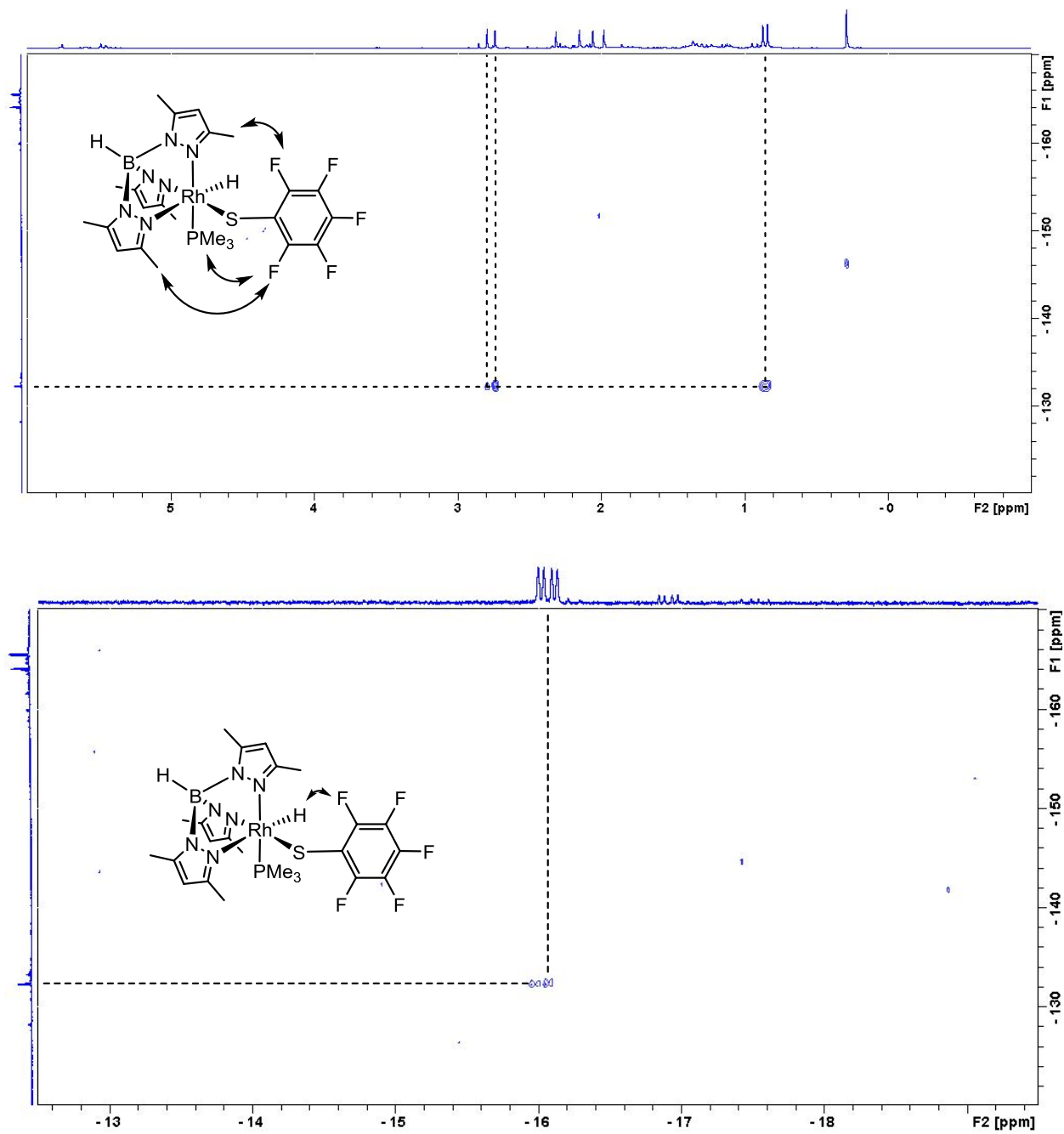
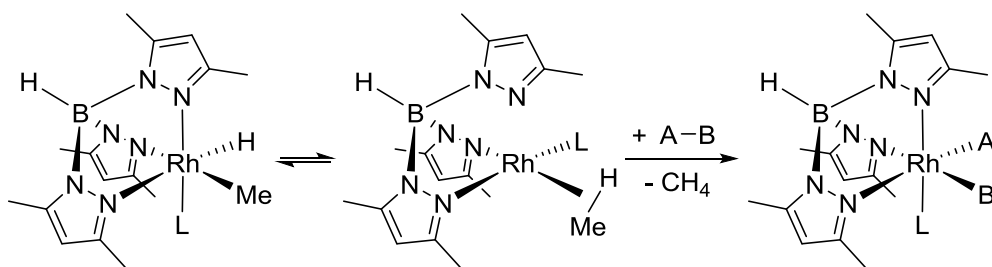


**Figure 6.18.** 2D HOESY spectrum for  $[\text{Tp}^*\text{RhH}(\text{SC}_6\text{F}_5)(\text{PMe}_3)]$  in  $\text{C}_6\text{D}_6$ . HOESY interactions are shown as arrows.

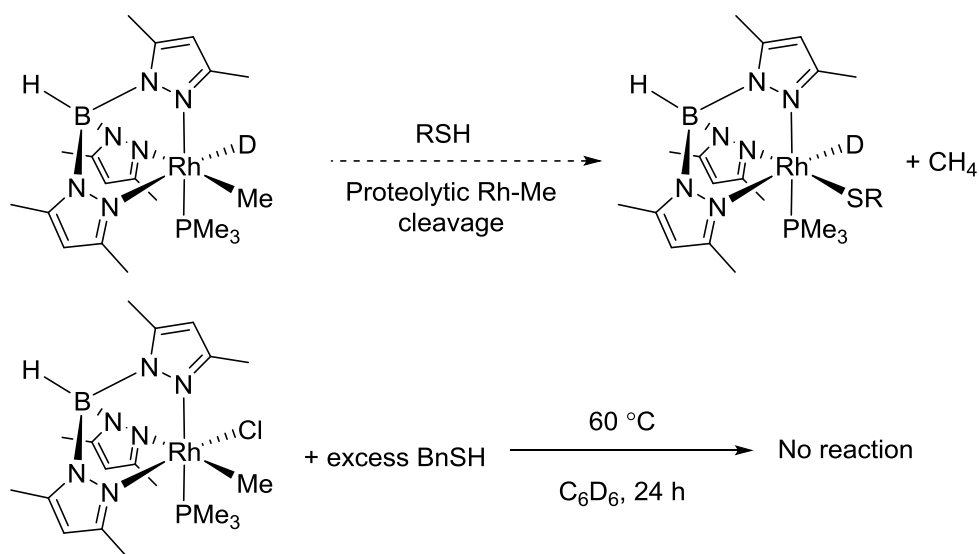
### 6.4.1 Mechanistic Implications of the Synthesis of Hydridothiolate Complexes

The successful synthesis of rhodium hydridothiolate complexes  $[\text{Tp}^*\text{RhH}(\text{SR})(\text{PMe}_3)]$  has implications relative to the proposed mechanism of alkyne hydrothiolation catalyzed by  $[\text{Tp}^*\text{Rh}(\text{PPh}_3)_2]$ . Jones and coworkers have previously shown that the reductive elimination of methane and subsequent bond activation proceeds via an associative mechanism (Scheme 6.19).<sup>204</sup> Reductive coupling of hydride and the alkyl fragment of  $[\text{Tp}^*\text{RhH}(\text{R})(\text{L})]$  ( $\text{L} = \text{PMe}_3, \text{NCCH}_2(\text{CH}_3)_3$ ) occurs reversibly prior to association of a substrate. This has been shown both through isotopic labeling experiments and skeletal rearrangement experiments.<sup>205</sup> This reversible equilibrium gives rise to an inverse equilibrium isotope effect and consequently an inverse kinetic isotope effect upon displacement of the reductively coupled fragment. Bond activation of the incoming substrate occurs subsequent to associative displacement of the reductively coupled fragment. Associative mechanisms have also been shown for Si-H, B-H and C-F bond activations for reductive elimination of methane from  $[\text{Tp}^*\text{RhH}(\text{Me})(\text{PMe}_3)]$ . In contrast, the reductive elimination of THF is independent of substrate concentration.<sup>206</sup>



**Scheme 6.19. Associatively induced reductive elimination of methane from  $[\text{Tp}^*\text{RhH}(\text{Me})(\text{L})]$ .**

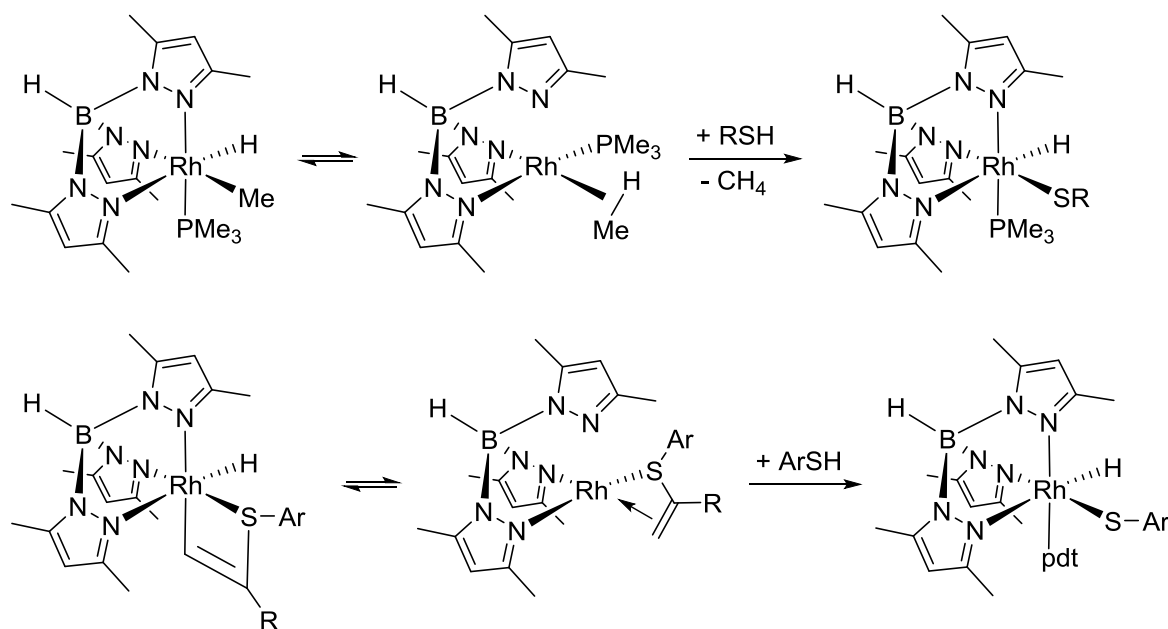
The successful synthesis of rhodium hydrido-thiolate complexes from  $[\text{Tp}^*\text{RhH}(\text{Me})(\text{PMe}_3)]$  and associated THF activation products likely proceeds via a similar associative mechanism. While a mechanism involving proteolytic cleavage of the Rh-R bond could be envisioned, it is important to note that  $[\text{Tp}^*\text{RhCl}(\text{Me})(\text{PMe}_3)]$  does not react with BnSH, even when treated with excess BnSH and heated to 60 °C for 24 h (Scheme 6.20).



**Scheme 6.20. Proteolytic cleavage mechanism (top). Treatment of  $[\text{Tp}^*\text{RhCl}(\text{Me})(\text{PMe}_3)]$  with BnSH (bottom).**

The proposed mechanism for the conversion of  $[\text{Tp}^*\text{RhH}(\text{Me})(\text{PMe}_3)]$  to the corresponding hydrothiolation complexes is shown in Scheme 6.21. Also shown is the parallel to the proposed mechanism for alkyne hydrothiolation catalyzed by  $[\text{Tp}^*\text{Rh}(\text{PPh}_3)_2]$ . While the proteolytic mechanism cannot be conclusively ruled out – this could only be achieved by deuterium labeling experiments – the parallels between the two systems are clear. The major

difference between the two systems is that the L type ligand in the case of alkyne hydrothiolation catalyzed by  $[\text{Tp}^*\text{Rh}(\text{PPh}_3)_2]$  is the vinyl sulfide product itself. The reactions were found to be highly selective for S-H bond activation. This high selectivity for S-H activation is attributable to the high nucleophilicity of the thiols and the weaker S-H bond compared to C-H bonds. The kinetic dependence on the thiol employed is also consistent with an associative mechanism.



**Scheme 6.21. Parallel between the proposed mechanisms of  $[\text{Tp}^*\text{RhH}(\text{SR})(\text{PMe}_3)]$  complex formation and alkyne hydrothiolation catalyzed by  $[\text{Tp}^*\text{Rh}(\text{PPh}_3)_2]$**

#### 6.4.2 Reactivity of $[\text{Tp}^*\text{RhH}(\text{SEt})(\text{PMe}_3)]$ with Alkynes

With a series of  $[\text{Tp}^*\text{RhH}(\text{SR})(\text{PMe}_3)]$  complexes in hand, we were eager to test the reactivity of these hydrido-thiolate complexes with alkynes. Unfortunately, the  $\text{PMe}_3$  ligand is a significantly stronger donor ligand compared to  $\text{PPh}_3$ . Consequently, the rhodium hydrido-thiolate

complexes synthesized herein do not exhibit any dissociation of the phosphine ligand at room temperature. When  $[\text{Tp}^*\text{RhH}(\text{SEt})(\text{PMe}_3)]$  was heated to  $60\text{ }^\circ\text{C}$  for several hours, we observed formation of  $\text{P}(\text{O})\text{Me}_3$ , which suggests that, at these higher temperatures,  $\text{PMe}_3$  does indeed dissociate (Figure 6.19). This presumably generates the 5-coordinate  $[\text{Tp}^*\text{RhH}(\text{SR})]$  fragment, however we were unable to characterize its presence in solution, nor were we able to characterize the putative rhodathiacyclobutene by addition of phenylacetylene to this same solution.

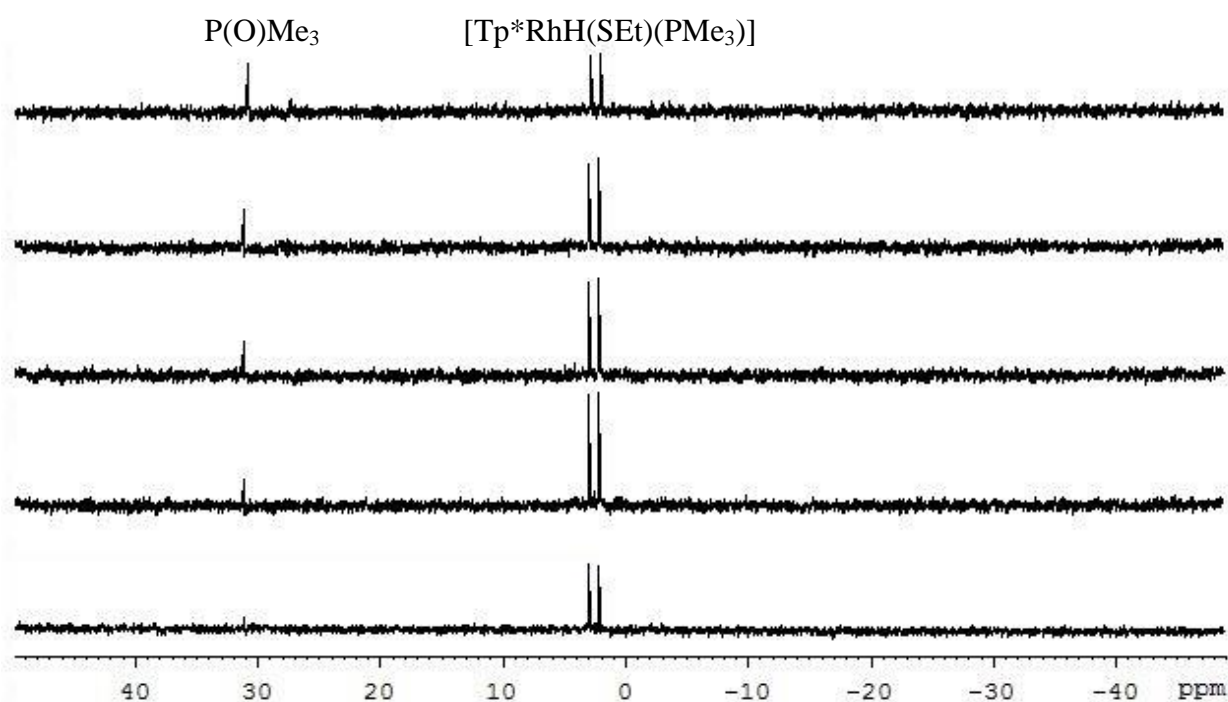


**Figure 6.19.** Stacked  $^{31}\text{P}\{^1\text{H}\}$  NMR spectra of  $[\text{Tp}^*\text{RhH}(\text{SEt})(\text{PMe}_3)]$  in  $\text{C}_6\text{D}_6$  heated to  $60\text{ }^\circ\text{C}$  for 12 h.

Nevertheless, we were eager to determine if the hydridothiolate complexes could catalyze the formation of branched vinyl sulfide product. We therefore compared the hydrothiolation of phenylacetylene with EtSH catalyzed by  $[\text{Tp}^*\text{Rh}(\text{PPh}_3)_2]$ , the background hydrothiolation of

phenylacetylene with EtSH in benzene heated to 60 °C, and the hydrothiolation of phenylacetylene with EtSH in the presence of [Tp\*RhH(SEt)(PMe<sub>3</sub>)] in benzene heated to 60 °C. The hydrothiolation catalyzed by [Tp\*Rh(PPh<sub>3</sub>)<sub>2</sub>] produces exclusively the branched regioisomer (Figure 6.20). The background reaction produces a ~5:1 mixture of the *Z*-linear and *E*-linear regioisomers (Figure 6.21). No branched regioisomer is observed in the background reaction. In the presence of [Tp\*RhH(SEt)(PMe<sub>3</sub>)], a mixture of all three regioisomers are observed (Figure 6.22). The *Z*-linear and *E*-linear isomers form in a ratio of 5:1, identical to the background reaction. One branched peak is over-integrated due to overlap with ligand resonances. The formation of the branched regioisomer can only be attributed to the presence of [Tp\*RhH(SEt)(PMe<sub>3</sub>)] in solution. Similar reactivity is observed for the hydrothiolation of phenylacetylene with PhSH in the presence of [Tp\*RhH(SPh)(PMe<sub>3</sub>)], wherein the branched product is observed, in addition to the *E*-linear and *Z*-linear isomers due to the background reaction.

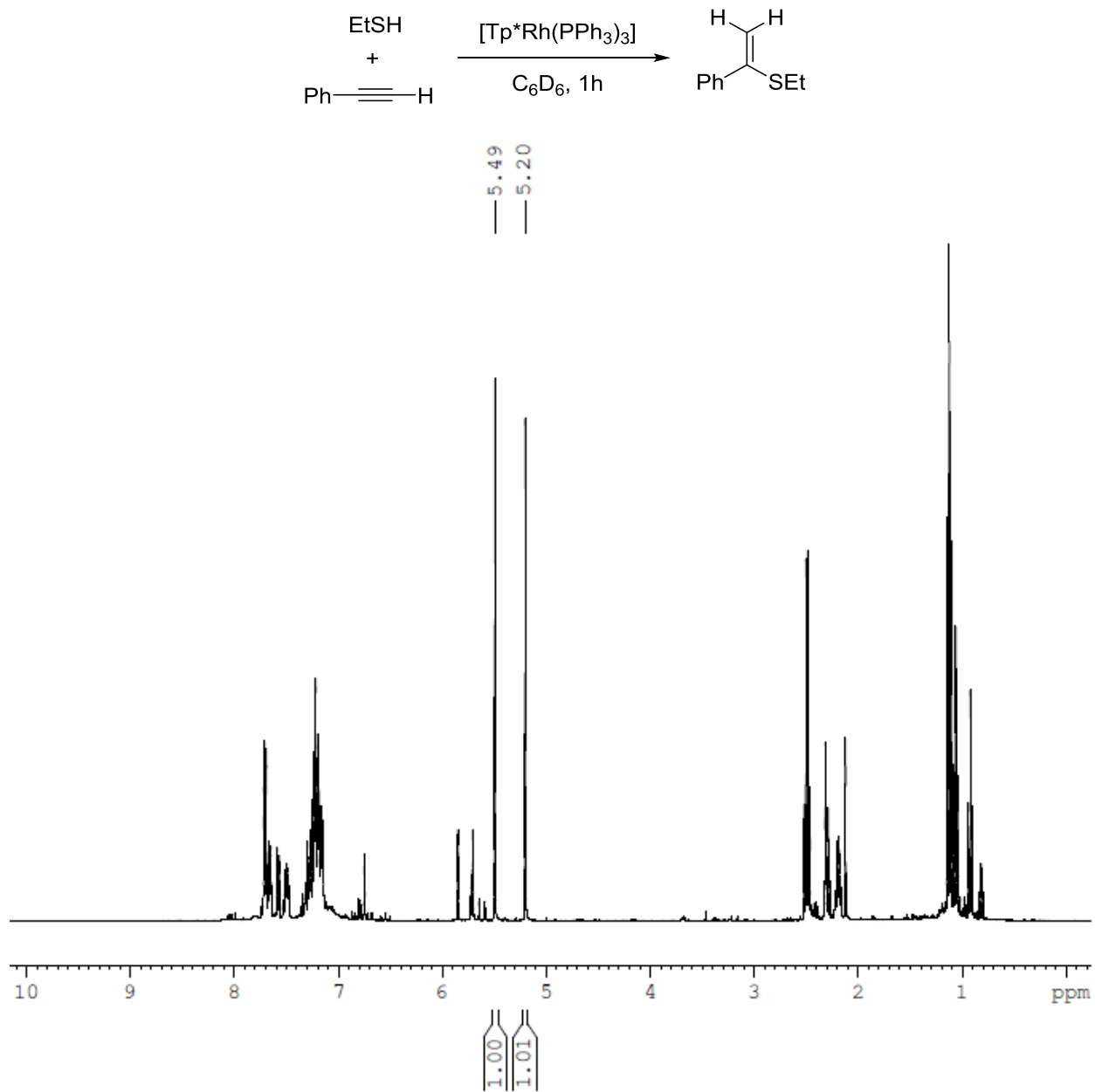


**Figure 6.20.** Hydrothiolation of phenylacetylene with EtSH catalyzed by  $[\text{Tp}^*\text{Rh}(\text{PPh}_3)_2]$ .

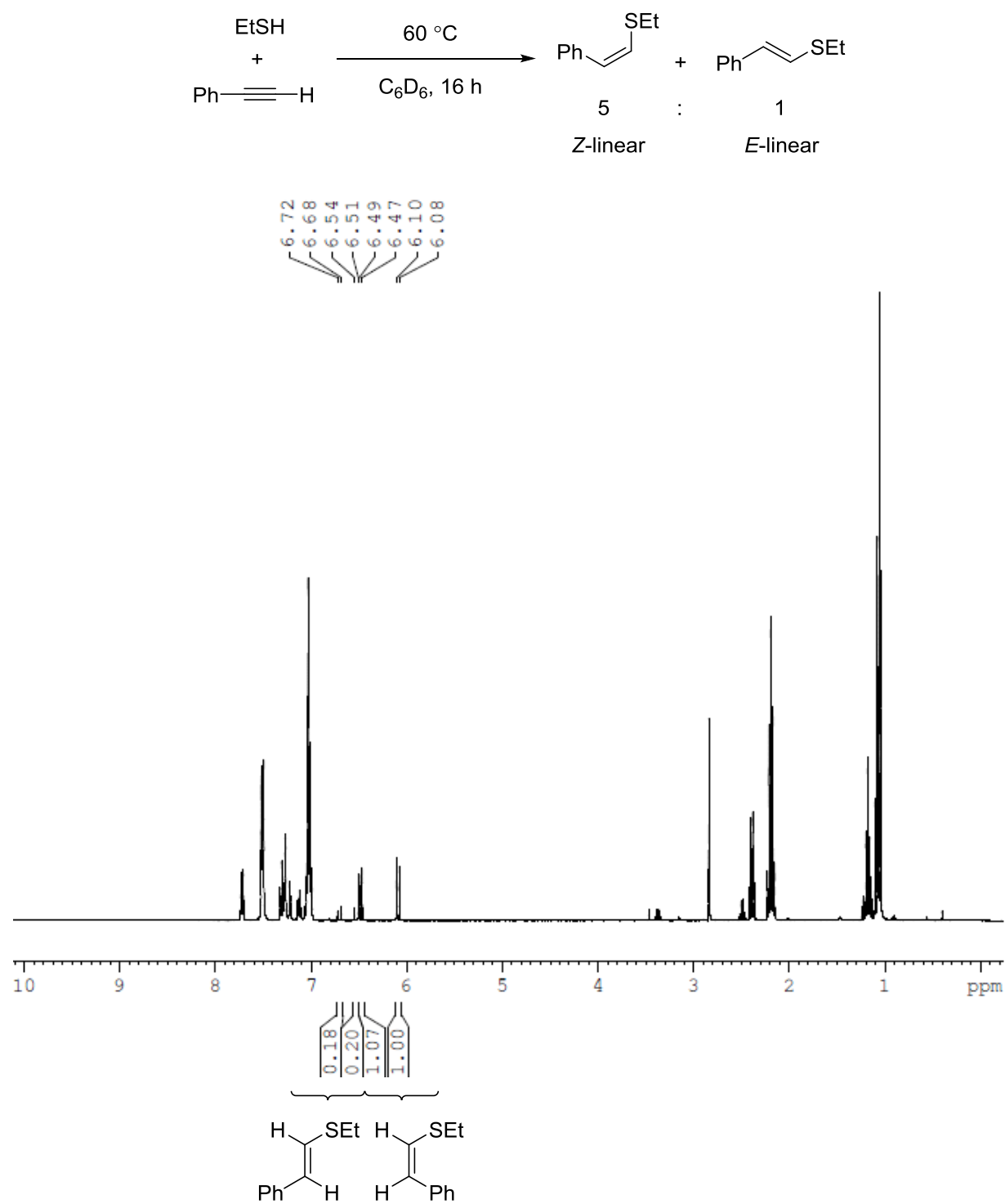


**Figure 6.21.** Background reaction between EtSH and phenylacetylene in  $\text{C}_6\text{D}_6$ .

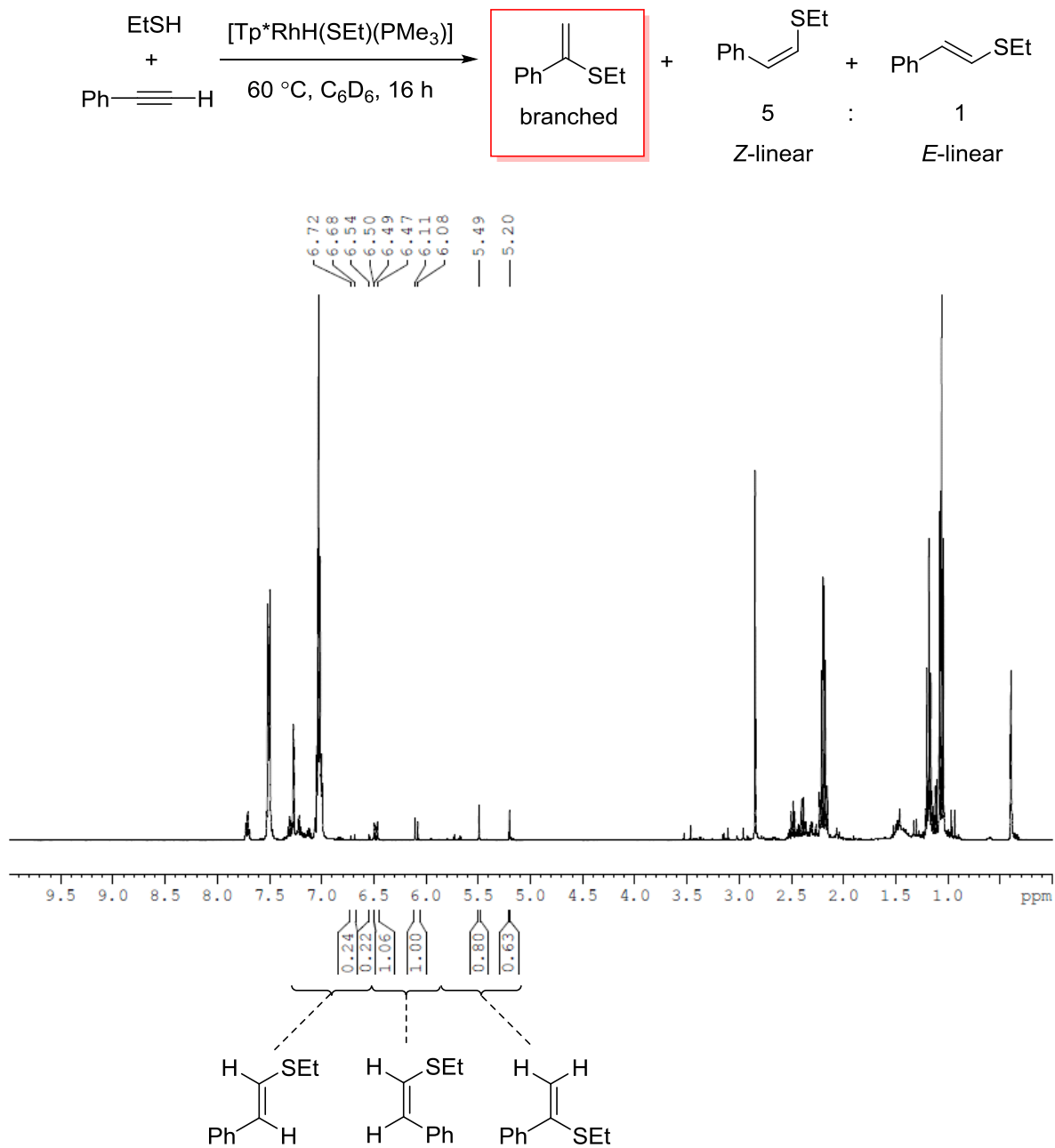


**Figure 6.22.** Reaction between EtSH and phenylacetylene in  $\text{C}_6\text{D}_6$  in the presence of  $[\text{Tp}^*\text{RhH}(\text{SEt})(\text{PMe}_3)]$ .

## 6.5 Conclusion

The desired hydridothiolate complexes  $[\text{Tp}^*\text{RhH}(\text{SR})(\text{PMe}_3)]$  were ultimately synthesized via the reductive elimination of methane from  $[\text{Tp}^*\text{RhH}(\text{Me})(\text{PMe}_3)]$ . Four  $[\text{Tp}^*\text{RhH}(\text{SR})(\text{PMe}_3)]$  complexes have been synthesized to date, where  $-\text{SR} = -\text{SEt}$ ,  $-\text{SBn}$ ,  $-\text{SPh}$ , and  $-\text{SC}_6\text{F}_5$ . The reactions are 100% selective for S-H bond activation and show no competitive C-H activation or C-F activation. The high selectivity for S-H bond activation is attributable to the comparatively weak S-H bond and high nucleophilicity of the thiol.

Due to the high coordination ability of the  $\text{PMe}_3$  ligand, however, the corresponding rhodathiacyclobutene structures could not be characterized in solution. Nevertheless, preliminary results of the reactivity of  $[\text{Tp}^*\text{RhH}(\text{SEt})(\text{PMe}_3)]$  towards alkynes have been reported. The reaction between EtSH and phenylacetylene in the presence of  $[\text{Tp}^*\text{RhH}(\text{SEt})(\text{PMe}_3)]$  was found to result in formation of the branched vinyl sulfide regioisomer. While far from conclusive, this observation is consistent with the proposal that the key intermediate in alkyne hydrothiolation catalyzed by  $[\text{Tp}^*\text{Rh}(\text{PPh}_3)_2]$  is indeed a hydridothiolate complex.

Several decomposition pathways relevant to alkyne hydrothiolation catalyzed by  $[\text{Tp}^*\text{Rh}(\text{PPh}_3)_2]$  were observed. A major problem is the orthometallation of the  $\text{PPh}_3$  ligand. Indeed, this decomposition product is observed to form during catalytic reactions. Additional  $\text{PPh}_3$  was found to increase the rate of product formation. It was proposed that this was due to associatively induced reductive elimination by coordination of  $\text{PPh}_3$  to the reductively coupled species, forming  $[\text{Tp}^*\text{Rh}^{\text{I}}(\text{PPh}_3)(\text{pdt})]$ , where pdt refers to bound vinyl sulfide product. However, product dissociation from this species would necessarily result in the formation of  $[\text{Tp}^*\text{Rh}^{\text{I}}(\text{PPh}_3)]$ , which would then undergo orthometallation to generate the inactive complex

[Tp\*RhH(*o*-C<sub>6</sub>H<sub>4</sub>PPh<sub>2</sub>)]. Indeed, catalytic turnover decreases when PPh<sub>3</sub> is added, despite the increased rate of product formation.

When [Tp\*RhCl<sub>2</sub>(MeOH)] was exposed to BnSH at elevated temperatures, the product of ligand decomposition [Tp\*RhCl<sub>2</sub>(pyz)] (pyz = 3,5-dimethylpyrazole) was observed, suggesting that the Tp\* ligand might be decomposing during catalytic reactions. This ligand decomposition pathway is likely to be more significant in the presence of more acidic (i.e. more electron deficient) thiols. Indeed, catalytic turnover numbers are observed to decrease with increasingly electron deficient aryl thiols. A decrease in the turnover numbers for electron deficient thiols may also be attributed to a relative shift towards in the PPh<sub>3</sub> associatively induced reductive elimination pathway, resulting in the greater formation of the PPh<sub>3</sub> orthometallated product.

## 6.6 Experimental

### 6.6.1 Recrystallization of KTp\*

Following a similar procedure to that of Jones and coworkers,<sup>187</sup> 1.3g of KTp\* was washed with three 25 mL portions of CHCl<sub>3</sub>. The washed KTp\* was allowed to air dry and was then transferred to a large Erlenmeyer flask with a stir bar and a ground glass joint. 100 mL of anisole was added, a condenser attached, and the solution heated to reflux. Anisole was added in 5 mL portions until the solution became clear (total volume ca. 150 mL). The mixture was then hot filtered into a preheated vacuum flask, and immediately transferred to a preheated 500 mL Erlenmeyer flask. The flask was stoppered and placed in a -20°C freezer overnight. After 24 h, the solution was filtered, and the microcrystalline KTp\* was washed with three 50 mL portions of ice cold hexanes. The solid was then transferred to a Schlenk flask with an inverted glass joint

of ice-cold hexanes and dried on high vacuum overnight. The yield after recrystallization varied between 33 – 55 % depending on the initial amount of KTp\* used. It was found that working with less initial KTp\* resulted in lower yields of the crystalline material.

### 6.6.2 Synthesis of [Tp\*RhCl<sub>2</sub>(MeOH)]

Re-crystallized KTp\*, 193 mg (0.573 mmol, 1.0 equiv.), and [RhCl<sub>3</sub>•xH<sub>2</sub>O], 152 mg (0.575 mmol of Rh, 1.0 equiv.), were weighed out in air. The [RhCl<sub>3</sub>•xH<sub>2</sub>O] was then transferred to a Schlenk flask, which had been dried in an oven and back-filled with nitrogen three times. 40 mL of dry methanol was then cannula-transferred into the Schlenk flask. The mixture was then stirred with partial heating until all of the [RhCl<sub>3</sub>•xH<sub>2</sub>O] had dissolved. At this point, the crystalline KTp\* was added to the solution, resulting in an immediate color change from red to orange. An oven-dried condenser was then attached, and the system purged with nitrogen for 20 seconds. The solution was heated to reflux for 1.5 h. After cooling, the reaction mixture was eluted through a Celite™ column to remove metallic rhodium, resulting in a clear orange solution. The volume of solvent was reduced by rotary evaporation until white precipitate or crystals (KCl) began to develop. KCl was filtered by passage through a pipette with a glass microfiber plug. The solution was then placed in a -20°C freezer overnight. After 24 h, orange crystals were filtered off and dried under high vacuum to give [Tp\*RhCl<sub>2</sub>(MeOH)] (171 mg, 59%). The characterization matched literature data. The complex is stable for a few hours in wet DMSO, however it readily converts to the aqua complex when dissolved in wet DCM or CHCl<sub>3</sub>.

### 6.6.3 Synthesis of [Tp\*RhCl<sub>2</sub>(PPh<sub>3</sub>)]

In a glove box, [Tp\*RhCl<sub>2</sub>(MeOH)] (199 mg, 0.396 mmol, 1.0 equiv.), and recrystallized PPh<sub>3</sub> (156 mg, 0.595 mmol, 1.5 equiv.), were combined in a Schlenk flask with 40 mL of dry

toluene. The flask was then moved to a Schlenk line, an oven-dried condenser was attached, and the system purged with nitrogen for 20 seconds. The mixture was heated to reflux for 3 h, and then the solvent was removed on high vacuum. The crude product was redissolved in DCM and filtered through a pipette fitted with a glass microfiber plug. The solvent reduced by rotary evaporation and hexanes were layered on top of the DCM solution. The mixture was then placed in a freezer at -20°C overnight. After 24 h, the golden-orange crystals were filtered off and washed with three 25 mL portions of hexanes, and dried under high vacuum, yielding [Tp\*RhCl<sub>2</sub>(PPh<sub>3</sub>)] (210 mg) in 72% yield. Its characterization matched literature data.

#### 6.6.4 Synthesis of [Tp\*RhCl<sub>2</sub>(PEt<sub>3</sub>)]

In a glove box, [Tp\*RhCl<sub>2</sub>(MeOH)] (171 mg, 0.339 mmol, 1.0 equiv.), and PEt<sub>3</sub> (75.0 μL, 0.509 mmol, 1.5 equiv.), were combined in a Schlenk flask with 40 mL of dry C<sub>6</sub>H<sub>6</sub>. The flask was then moved to a Schlenk line, an oven-dried condenser was attached, and the system purged with nitrogen for 20 seconds. The mixture was heated to reflux for 1.5 h, and then the solvent was removed on high vacuum. The crude product was redissolved in DCM, filtered through a pipette fitted with a glass microfiber plug, and the solvent reduced by rotary evaporation. The solution was layered with hexanes and the mixture was then placed in a freezer at -20°C overnight. After 24 h, the orange crystals were filtered off and washed with three 25 mL portions of hexanes, and dried under high vacuum, yielding [Tp\*RhCl<sub>2</sub>(PEt<sub>3</sub>)] (100.0 mg) in 50% yield. <sup>1</sup>H NMR (CD<sub>2</sub>Cl<sub>2</sub>, 300 MHz) δ = 5.83 (s, 2H), 5.80 (s, 1H), 2.66 (s, 3H), 2.59 (s, 6H), 2.40 (s, 6H), 2.31 (s, 3H), 2.17-2.06 (dq, *J* = 7.48 Hz, 10.14 Hz, 6H), 0.91-0.81 (dt, *J* = 7.48 Hz, 15.81 Hz, 9H). <sup>13</sup>C{<sup>1</sup>H} NMR (CD<sub>2</sub>Cl<sub>2</sub>, 100 MHz) δ = 155.5, 153.6, 146.1, 144.0, 110.9, 108.2,

17.6, 16.2 (d,  $J = 30$  Hz), 14.6, 13.3, 12.7, 6.82 (d,  $J = 5$  Hz).  $^{31}\text{P}\{^1\text{H}\}$  ( $\text{CD}_2\text{Cl}_2$ , 121.5 MHz)  $\delta = 23.6$  (d,  $J = 104$  Hz).

### 6.6.5 Synthesis of $[\text{Tp}^*\text{RhCl}_2(\text{BnSH})]$

In a glove box,  $[\text{Tp}^*\text{RhCl}_2(\text{MeOH})]$  (146 mg, 0.290 mmol, 1.0 equiv.), was transferred to a Schlenk flask with 40 mL of dry  $\text{C}_6\text{H}_6$ . The flask was then moved to a Schlenk line, and distilled BnSH (100.0  $\mu\text{L}$ , 0.851 mmol, 3.0 equiv.) was added via microliter syringe. An oven-dried condenser was attached, and the system purged with nitrogen for 20 seconds. The mixture was heated to reflux for 1.5 h, and then the solvent was removed on high vacuum. The crude product was redissolved in DCM, filtered through a pipette fitted with a glass microfiber plug, and the solvent reduced by rotary evaporation. The solution was layered with hexanes and the mixture was then placed in a freezer at  $-20^\circ\text{C}$  overnight. After 24 h, the orange crystals were filtered off and washed with three 25 mL portions of hexanes, and dried under high vacuum, yielding  $[\text{Tp}^*\text{RhCl}_2(\text{BnSH})]$  (118 mg) in 68% yield.  $^1\text{H}$  NMR ( $\text{CD}_2\text{Cl}_2$ , 300 MHz)  $\delta = 7.41$ - $7.36$  (m, 5H), 5.90 (s, 1H), 5.89 (s, 2H), 4.22 (b, s, 2H), 2.71 (s, 3H), 2.70 (s, 6H), 2.40 (s, 9H).  $^{13}\text{C}\{^1\text{H}\}$  NMR ( $\text{CD}_2\text{Cl}_2$ , 100 MHz)  $\delta = 155.3$ , 153.9, 145.9, 145.1, 136.4, 129.8, 129.0, 128.9, 109.9, 109.3, 34.4, 15.5, 15.4, 13.0, 12.8.

### 6.6.6 Synthesis of $[\text{Tp}^*\text{RhHCl}(\text{PPh}_3)]$

In a glove box,  $[\text{Tp}^*\text{RhCl}_2(\text{PPh}_3)]$  (84.1 mg, 0.115 mmol, 1.0 equiv.) and  $[\text{Cp}_2\text{ZrHCl}]$  (31.6 mg, 0.123 mmol, 1.05 equiv.) were dissolved in dry benzene. A stir bar was added, and the vial wrapped in black tape to shield from light. The mixture was then stirred at room temperature for 24 h. After 24 h, the volume of the solution was reduced by rotary evaporation and the mixture was loaded onto a silica gel column (silica should be dried in an oven beforehand). The

product was then eluted with a 4:1 mixture of hexanes : THF, the solvent removed by rotary evaporation, and the product dried under high vacuum to give [Tp\*RhHCl(PPh<sub>3</sub>)] as a pale yellow solid (77.9 mg, 97%). <sup>1</sup>H NMR (C<sub>6</sub>D<sub>6</sub>, 400 MHz) δ = 7.87 (m, 6 H), 6.96-6.89 (m, 9H), 5.69 (s, 1H), 5.47 (s, 1H), 4.92 (s, 1H), 3.07 (s, 3H), 2.46 (s, 3H), 2.19 (s, 3H), 2.10 (s, 3H), 1.69 (s, 3H), 1.55 (s, 3H), -14.32 (dd, J = 8.65, 20.51 Hz). <sup>13</sup>C{<sup>1</sup>H} NMR (C<sub>6</sub>D<sub>6</sub>, 100 MHz) δ = 155.6, 152.1, 151.5, 144.9, 144.3, 143.2, 135.9 (d, J = 10 Hz), 130.0 (d, J = 2 Hz), 128.1 (d, J = 24 Hz), 108.2, 106.9, 106.6 (d, J = 4 Hz), 16.9, 16.1, 12.9, 12.9, 12.7, 12.1. <sup>31</sup>P{<sup>1</sup>H} NMR (C<sub>6</sub>D<sub>6</sub>, 162 MHz) δ = 39.7 (d, J = 129 Hz).

### 6.6.7 Synthesis of [Tp\*RhH<sub>2</sub>(PPh<sub>3</sub>)]

In a glove box, [Tp\*RhCl<sub>2</sub>(PPh<sub>3</sub>)] (96.9 mg, 0.132 mmol, 1.0 equiv.) and [Cp<sub>2</sub>ZrHCl] (138.8 mg, 0.538 mmol, 4.0 equiv.) were dissolved in dry benzene. A stir bar was added, and the vial wrapped in tape to shield from light. The mixture was then stirred at room temperature for 24 h. After 24 h, the volume of the solution was reduced by rotary evaporation, and the mixture was loaded onto a silica gel column. The product was then eluted with a 4:1 mixture of hexanes:THF, the solvent removed by rotary evaporation, and the product dried on high vacuum to give [Tp\*RhH<sub>2</sub>(PPh<sub>3</sub>)] as a white solid (46.3 mg, 53%). It was later determined that the yield could be significantly improved by drying the silica in an oven prior to use. <sup>1</sup>H NMR (C<sub>6</sub>D<sub>6</sub>, 300 MHz) δ = 7.82-7.79 (m, 6H), 6.91-6.89 (m, 9H), 5.63 (s, 1H), 5.56 (s, 2H), 2.55 (s, 3H), 2.31 (s, 6H), 2.17 (s, 3H), 1.54 (s, 6H), -16.59 (dd, J = 16.5, 31.0 Hz). <sup>31</sup>P{<sup>1</sup>H} NMR (C<sub>6</sub>D<sub>6</sub>, 121.5 MHz) δ = 57.3 (d, J = 152 Hz). <sup>13</sup>C{<sup>1</sup>H} (C<sub>6</sub>D<sub>6</sub>, 100 MHz) δ = 151.2, 149.8, 143.9, 142.9, 137.9 (d, J = 46 Hz), 135.0 (d, J = 11 Hz), 129.7 (d, J = 2 Hz), 128.1 (d, J = 24 Hz), 106.2, 105.3, 17.4, 15.2, 13.3, 12.8.

### 6.6.8 Synthesis of [Tp\*RhHCl(PEt<sub>3</sub>)]

In a glove box, [Tp\*RhCl<sub>2</sub>(PEt<sub>3</sub>)] (31.2 mg, 0.0530 mmol, 1.0 equiv.) and [Cp<sub>2</sub>ZrHCl] (15.0 mg, 0.0582 mmol, 1.1 equiv.) were dissolved in dry benzene, resulting in a cloudy orange solution. A stir bar was added, and the vial wrapped in tape to shield from light. The mixture was then stirred at room temperature for 24 h. After 24 h, the clear, pale yellow solution was transferred to a Schlenk flask, oven dried alumina was added to the solution, and the solvent removed on high vac. The alumina was then dry-loaded onto an alumina column (using oven-dried alumina), and the product was then eluted with a 9:1 mixture of hexanes:THF. The isolated fractions were then transferred to a Schlenk flask and the solvent removed on high vacuum to give [Tp\*RhHCl(PEt<sub>3</sub>)] (26.8 mg) in 51% yield as a pale yellow solid. <sup>1</sup>H NMR (C<sub>6</sub>D<sub>6</sub>, 400 MHz) δ = 5.77 (s, 1H), 5.48 (s, 1H), 5.45 (s, 1H), 2.89 (s, 3H), 2.77 (s, 3H), 2.37 (s, 3H), 2.21 (s, 3H), 2.08 (s, 3H), 2.02 (s, 3H), 1.87-1.76 (m, 3H), 1.63-1.53 (m, 3H), 0.79 (9H, dt, J = 15.28, 7.62 Hz), -16.44 (1H, dd, J = 11.22, 26.21 Hz). <sup>13</sup>C{<sup>1</sup>H} NMR (C<sub>6</sub>D<sub>6</sub>, 100 MHz) δ = 153.6, 151.7 (d, J = 4 Hz), 151.5, 146.0, 144.0, 142.9 (d, J = 3 Hz), 108.1, 107.5, 106.3 (d, J = 4 Hz), 17.3 (d, J = 30 Hz), 17.0, 15.7, 15.6, 13.2, 12.9, 12.6, 7.1 (d, J = 3 Hz). <sup>31</sup>P{<sup>1</sup>H} NMR (C<sub>6</sub>D<sub>6</sub>, 162 MHz) δ = 29.84 (d, J = 122 Hz).

### 6.6.9 Synthesis of [Tp\*RhH(SBn)(PMe<sub>3</sub>)]

In a glove box, [Tp\*RhCl(Me)(PMe<sub>3</sub>)] (10.5 mg, 0.0199 mmol, 1.0 equiv.) and [Cp<sub>2</sub>ZrH<sub>2</sub>] (6.7 mg, 0.030 mmol, 1.5 equiv.) were weighed out and dissolved in 3 mL of dry THF in a vial. To this vial was added a stir bar, and the vial was wrapped in electrical tape to shield from light. The reaction was stirred for 50 min at room temperature, during which time the solution changed from a pale yellow to colorless. The volatiles were removed under reduced

pressure to yield an off-white solid. The solid was extracted with pentanes and eluted through a silica-packed pipette using 5:1 pentanes : THF as an eluent (10 mL). The volatiles were removed under reduced pressure, and the white solid was redissolved in dry  $C_6D_{12}$  and transferred to a screw cap NMR tube. To this NMR tube was then added dry, degassed BnSH (2.5  $\mu$ L , 0.021 mmol, 1.1 equiv.) using a microliter syringe. The solution was heated at 40  $^{\circ}$ C for 8 h, during which time the solution changed from colorless to yellow. Once the reaction was complete, the volatiles were removed under reduced pressure and the yellow solid was redissolved in dry  $C_6D_6$ . [Tp\*RhH(SBn)(PMe<sub>3</sub>)] was then characterized by NMR spectroscopy. <sup>1</sup>H NMR ( $C_6D_6$ , 400 MHz)  $\delta$  = 7.56 (d, 2H, J = 7.7 Hz), 7.09-7.05 (m, 3H), 5.88 (s, 1H), 5.59 (s, 1H), 5.56 (s, 1H), 3.45 (d, 1H, J = 12.4 Hz), 3.26 (d, 1H, J = 11.9 Hz), 3.08 (s, 3H), 2.89 (s, 3H), 2.34 (s, 3H), 2.21 (s, 3H), 2.09 (s, 3H), 2.04 (s, 3H), 1.16 (d, 9H, J = 10.0 Hz), -17.04 (dd, 1H, J = 15.7, 31.0 Hz). <sup>13</sup>C{<sup>1</sup>H} NMR ( $C_6D_{12}$ , 100 MHz)  $\delta$  = 151.5, 150.9, 149.1, 144.4, 144.2, 144.0, 142.8, 128.5, 127.0, 124.5, 106.5, 105.9, 105.2 (d, J = 4 Hz), 35.7 (d, J = 3 Hz), 18.7 (d, J = 33 Hz), 16.3, 14.7, 14.3, 12.4, 12.3, 12.2. <sup>31</sup>P{<sup>1</sup>H} NMR ( $C_6D_{12}$ , 162 MHz)  $\delta$  = 2.8 (d, J = 132 Hz).

#### 6.6.10 Synthesis of [Tp\*RhH(SET)(PMe<sub>3</sub>)]

In a glove box, [Tp\*RhCl(Me)(PMe<sub>3</sub>)] (11.7 mg, 0.0222 mmol, 1.0 equiv.) and [Cp<sub>2</sub>ZrH<sub>2</sub>] (7.5 mg, 0.034 mmol, 1.5 equiv.) were weighed out and dissolved in 3 mL of dry THF in a vial. To this vial was added a stir bar, and the vial was wrapped in electrical tape to shield from light. The reaction was stirred for 50 min at room temperature, during which time the solution changed from a pale yellow to colorless. The volatiles were removed under reduced pressure to yield an off-white solid. The solid was extracted with pentanes and eluted through a silica-packed pipette using 5:1 pentanes : THF as an eluent (10 mL). The volatiles were removed under reduced pressure, and the white solid was redissolved in dry  $C_6D_{12}$ , filtered through a

pipette packed with glass microfiber and transferred to a screw cap NMR tube. To this NMR tube was then added EtSH (20.0  $\mu\text{L}$ , 0.28 mmol, 12.5 equiv.) using a microliter syringe. The solution was then heated to 40  $^{\circ}\text{C}$  for 2.5 h. Once the reaction was complete, the volatiles were then removed under reduced pressure, and the yellow solid was redissolved in dry  $\text{C}_6\text{D}_6$ .  $[\text{Tp}^*\text{RhH}(\text{SEt})(\text{PMe}_3)]$  was then characterized by NMR spectroscopy.  $^1\text{H}$  NMR ( $\text{C}_6\text{D}_6$ , 400 MHz)  $\delta$  = 5.85 (s, 1H), 5.57 (s, 2H), 3.02 (s, 3H), 2.87 (s, 3H), 2.49-2.38 (m, 1H), 2.38-2.27 (m, 1H), 2.33 (s, 3H), 2.21 (s, 3H), 2.08 (s, 3H), 2.04 (s, 3H), 1.43 (t, 3H, 7.5 Hz), 1.20 (d, 9H,  $J$  = 9.8 Hz), -17.16 (dd, 1H,  $J$  = 15.8, 31.2 Hz).  $^{31}\text{P}\{^1\text{H}\}$  NMR( $\text{C}_6\text{D}_{12}$ , 162 MHz)  $\delta$  = 3.5 (d,  $J$  = 133 Hz).  $^{13}\text{C}\{^1\text{H}\}$  NMR ( $\text{C}_6\text{D}_6$ , 100 MHz)  $\delta$  = 152.4, 151.6, 150.1, 145.2, 143.9, 143.2 (d,  $J$  = 4 Hz), 107.2, 106.7, 106.0 (d,  $J$  = 4 Hz), 26.4 (d,  $J$  = 3 Hz), 18.9 (d,  $J$  = 34 Hz), 18.2 (d,  $J$  = 2 Hz), 17.0, 15.2, 15.1, 13.1, 13.0, 12.8.

#### 6.6.11 Synthesis of $[\text{Tp}^*\text{RhH}(\text{SC}_6\text{F}_5)(\text{PMe}_3)]$

In a glove box,  $[\text{Tp}^*\text{RhCl}(\text{Me})(\text{PMe}_3)]$  (12.8 mg, 0.0243 mmol, 1.0 equiv.) and  $[\text{Cp}_2\text{ZrH}_2]$  (8.3 mg, 0.037 mmol, 1.5 equiv.) were weighed out and dissolved in 3 mL of dry THF in a vial. To this vial was added a stir bar, and the vial was wrapped in electrical tape to shield from light. The reaction was stirred for 50 min at room temperature, during which time the solution changed from a pale yellow to colorless. The volatiles were removed under reduced pressure to yield an off-white solid. The solid was extracted with pentanes and eluted through a silica-packed pipette using 5:1 pentanes : THF as an eluent (10 mL). The volatiles were removed under reduced pressure, and the white solid was redissolved in dry  $\text{C}_6\text{D}_{12}$ , filtered through a pipette packed with glass microfiber and transferred to a screw cap NMR tube. To this NMR tube was then added dry, degassed  $\text{C}_6\text{F}_5\text{SH}$  (3.2  $\mu\text{L}$ , 0.024, 1.0 equiv.) using a microliter syringe and an immediate color change from colorless to orange was observed. The solution was then

heated at 40 °C for 2.5 h. Once the reaction was complete, the volatiles were removed under reduced pressure and the orange solid was redissolved in dry C<sub>6</sub>D<sub>6</sub>. [Tp\**RhH*(SC<sub>6</sub>F<sub>5</sub>)(PMe<sub>3</sub>)] was then characterized by NMR spectroscopy. <sup>1</sup>H NMR (C<sub>6</sub>D<sub>12</sub>, 400 MHz) δ = 5.76 (s, 1H), 5.67 (s, 1H), 5.52 (s, 1H), 2.70 (s, 3H), 2.44 (s, 3H), 2.42 (s, 3H), 2.35 (s, 3H), 2.28 (s, 3H), 2.22 (s, 3H), 1.22 (d, 9H, J = 10.2 Hz), -16.08 (dd, 1H, J = 11.9, 28.2 Hz). <sup>31</sup>P{<sup>1</sup>H} (C<sub>6</sub>D<sub>12</sub>, 162 MHz) δ = 3.6 (d, J = 127 MHz). <sup>19</sup>F NMR (C<sub>6</sub>D<sub>6</sub>, 282 MHz) δ = -132.4 (dd, 2F, J = 6.0, 27.2 Hz), -164.2 (t, 1F, J = 21.1 Hz), -165.5 (m, 2F). <sup>13</sup>C{<sup>1</sup>H} NMR (C<sub>6</sub>D<sub>6</sub>, 100 MHz) δ = 152.7, 151.6 (d, J = 4 Hz), 150.6, 145.8, 144.1, 143.3 (d, J = 3 Hz), 108.0, 107.0, 106.6 (d, J = 4 Hz), 17.9 (d, J = 33 Hz), 16.8, 15.6, 14.1, 13.0, 12.8, 12.7.

#### 6.6.12 Synthesis of [Tp\**RhH*(SPh)(PMe<sub>3</sub>)]

In a glove box, [Tp\**RhCl*(Me)(PMe<sub>3</sub>)] (10.8 mg, 0.0205 mmol, 1.0 equiv.) and [Cp<sub>2</sub>ZrH<sub>2</sub>] (6.9 mg, 0.031 mmol, 1.5 equiv.) were weighed out and dissolved in 3 mL of dry THF in a vial. To this vial was added a stir bar, and the vial was wrapped in electrical tape to shield from light. The reaction was stirred for 50 min at room temperature, during which time the solution changed from a pale yellow to colorless. The volatiles were removed under reduced pressure to yield an off-white solid. The solid was extracted with pentanes and eluted through a silica-packed pipette using 5:1 pentanes : THF as an eluent (10 mL). The volatiles were removed under reduced pressure, and the white solid was redissolved in pentanes, filtered through a pipette packed with glass microfiber and transferred to a Schlenk flask fitted with a stir bar. To this Schlenk flask was then added dry, degassed PhSH (2.0 μL, 0.020 mmol, 1.0 equiv.) using a microliter syringe. An immediate color change from colorless to orange was observed. The solution was then heated to 45 °C for 2 h. The volatiles were removed under reduced pressure. In a glove box, the orange solid was redissolved in dry pentanes, filtered through a pipette packed

with glass microfiber, and the volatiles removed under reduced pressure. [Tp\*RhH(SPh)(PMe<sub>3</sub>)] was then characterized by NMR spectroscopy. <sup>1</sup>H NMR (C<sub>6</sub>D<sub>6</sub>, 400 MHz) δ = 7.89 (d, 2H, J = 7.7 Hz), 7.06 (t, 2H, J = 7.7 Hz), 6.90 (t, 1H, J = 7.0 Hz), 5.78 (s, 1H), 5.58 (s, 1H), 5.43 (s, 1H), 2.69 (s, 3H), 2.66 (s, 3H), 2.33 (s, 3H), 2.21 (s, 3H), 2.10 (s, 3H), 2.08 (s, 3H), 1.08 (d, 9H, J = 10.3 Hz), -16.23 (dd, 1H, J = 14.5, 29.5 Hz). <sup>31</sup>P{<sup>1</sup>H} NMR (C<sub>6</sub>D<sub>6</sub>, 162 MHz) δ = 2.8 (d, J = 127 Hz). <sup>13</sup>C{<sup>1</sup>H} NMR (C<sub>6</sub>D<sub>6</sub>, 100 MHz) δ = 158.7, 153.2, 152.0 (d, J = 4 Hz), 150.4, 148.4 (d, J = 2 Hz), 145.4, 144.3, 143.1 (d, J = 3 Hz), 130.8 (d, J = 2 Hz), 127.3, 121.4, 107.7, 107.0, 106.4 (d, J = 4 Hz), 18.4 (d, J = 34 Hz), 17.1, 17.1, 15.6, 13.1, 13.1, 12.9.

## Chapter 7 Conclusions and Future Work

In Chapter 1, alkyne hydrothiolation catalyzed by transition metal complexes and their associated mechanisms was reviewed. Alkyne hydrothiolation catalyzed by transition metal complexes is an efficient and useful method for the preparation of vinyl sulfides from readily available starting materials. The methodology is 100% atom economic, in that all substrate atoms are incorporated into the product.  $[\text{Tp}^*\text{Rh}(\text{PPh}_3)_2]$  was the first complex to show alkyne hydrothiolation activity with alkyl thiols, greatly expanding the scope of the methodology.<sup>207</sup> Shortly thereafter,  $[\text{RhCl}(\text{PPh}_3)_3]$  was also found to catalyze the hydrothiolation of alkynes with alkyl thiols.<sup>208</sup> Both complexes exhibit a high tolerance to a variety of functional groups. Additionally, these two complexes exhibit opposite regioselectivity for addition of the thiol to the alkyne, allowing either the *E*-linear or branched vinyl sulfide to be synthesized with high fidelity. Insertion into Rh-X bonds (X = N, O, S) was also reviewed.

In Chapter 2, the application of transition metal scorpionate complexes in alkene and alkyne hydroelementation reactions was reviewed. Scorpionate complexes have been proven to be effective in the hydroamination, hydroalkoxylation, hydrophosphinylation and hydrothiolation of alkynes and the hydroamination of alkenes.

In Chapter 3, the Hammett single and dual parameter linear free energy relationships were reviewed. The methanolic acidity constants for a variety of *para*-substituted aryl thiols were reported. The linear relationship between methanolic and aqueous acidity constants allows for the prediction of aqueous acidity constants for a wide variety of *para*-substituted aryl thiols from their corresponding methanolic  $\text{pK}_\text{A}$  values. Application of the Hammett dual parameter linear free energy relationship to either aqueous or methanolic acidity constants allows for the

accurate prediction of either methanolic or aqueous  $pK_A$  based on known induction and resonance parameters.

In Chapter 4, as proof of the utility of alkyne hydrothiolation reactions catalyzed by transition metal complexes in total synthesis, Erica Kiemele's synthesis of the peptidomimetic drug K777 was reviewed. The synthesis solves two problems with the previously reported synthesis. First, it bypasses the use of the expensive unnatural amino acid homophenylalanine by employing an enantioselective synthesis of a propargyl amine using Elman's auxiliary. Second, it allows for a wide variety of K777 derivatives to be easily synthesized from readily available thiols by employing alkyne hydrothiolation catalyzed by  $[RhCl(PPh_3)_3]$  methodology to synthesize the desired vinyl sulfones. The methodology was proven to be highly effective for the synthesis of the desired *E*-linear vinyl sulfide, and was used to synthesize a series of aryl-substituted vinyl sulfones. In order to assess the potential variation in inhibitory properties, the rate of Michael addition to the series of *para*-substituted aryl vinyl sulfones was studied. The series of aryl-substituted vinyl sulfones exhibited a large difference in rate of Michael addition with 2-phenethanethiol, allowing the pharmacokinetic properties of the drug to be fine-tuned. Moreover, the general applicability of the alkyne hydrothiolation methodology and broad substrate scope allows for a wide variety of related peptidomimetic vinyl sulfone containing drugs to be synthesized from readily available starting materials.

In Chapter 5, a series of kinetic and mechanistic studies were undertaken to determine the mechanism of alkyne hydrothiolation catalyzed by  $[Tp^*Rh(PPh_3)_2]$ . The ultimate goal was to determine the source of the change in regioselectivity from producing the *E*-linear vinyl sulfide as the major product, as exhibited by other rhodium catalysts, to the branched vinyl sulfide. Two mechanisms have been proposed and generally accepted for alkyne hydrothiolation reactions: the

first involves generation of a metal thiolate or poly-thiolate complex  $[L_nM-(SR)_x]$ ,<sup>209</sup> and the second involves generation of a metal hydridothiolate complex  $[L_nM(H)(SR)]$ .<sup>210</sup> Mechanisms involving generation of a metal thiolate complex produce the branched vinyl sulfide as the major product, whereas mechanisms involving generation of a metal hydridothiolate complex generally produce the *E*-linear vinyl sulfide as the major product. The mechanism for alkyne hydrothiolation catalyzed by  $[Tp^*Rh(PPh_3)_2]$  was shown to proceed through an intermediate rhodium hydridothiolate complex  $[Tp^*Rh(H)(SR)]$ , despite producing the branched regioisomer as the major product. The source of the switch in regioselectivity from *E*-linear to branched vinyl sulfide was determined to be the result of chemoselective migratory insertion of the alkyne into the Rh-SR bond, despite the availability of a Rh-H bond. Such a mechanism is unique to alkyne hydrothiolation catalyzed by  $[Tp^*Rh(PPh_3)_2]$ . The rate-limiting step of alkyne hydrothiolation catalyzed by  $[Tp^*Rh(PPh_3)_2]$  was found to be reductive elimination, associatively induced by coordination of thiol to the reductively coupled species. As far as we are aware, this is the first example of associatively induced reductive elimination in a living catalytic cycle.

In Chapter 6, we reported the synthesis of several rhodium hydride complexes. In order to prove the intermediacy of a hydridothiolate complex in alkyne hydrothiolation catalyzed by  $[Tp^*Rh(PPh_3)_2]$ , we attempted to synthesize the putative intermediate hydridothiolate and rhodathiacyclobutene complexes. After much effort, we found that thiols RSH reacted with  $[Tp^*RhH(Me)(PMe_3)]$  to form hydridothiolate complexes  $[Tp^*RhH(SR)(PMe_3)]$ . The mechanism of formation of the  $[Tp^*RhH(SR)(PMe_3)]$  was proposed to involve associative displacement of the reductively coupled methane by the thiol and subsequent oxidative addition of the thiol. The complete selectivity for S-H bond activation was attributed to the high nucleophilicity of the thiol and the comparatively weak S-H bond. Alkyne hydrothiolation

reactions in the presence of the independently synthesized  $[\text{Tp}^*\text{RhH}(\text{SR})(\text{PMe}_3)]$  complexes were shown to produce product ratios similar to alkyne hydrothiolation reactions catalyzed by  $[\text{Tp}^*\text{Rh}(\text{PPh}_3)_2]$ .

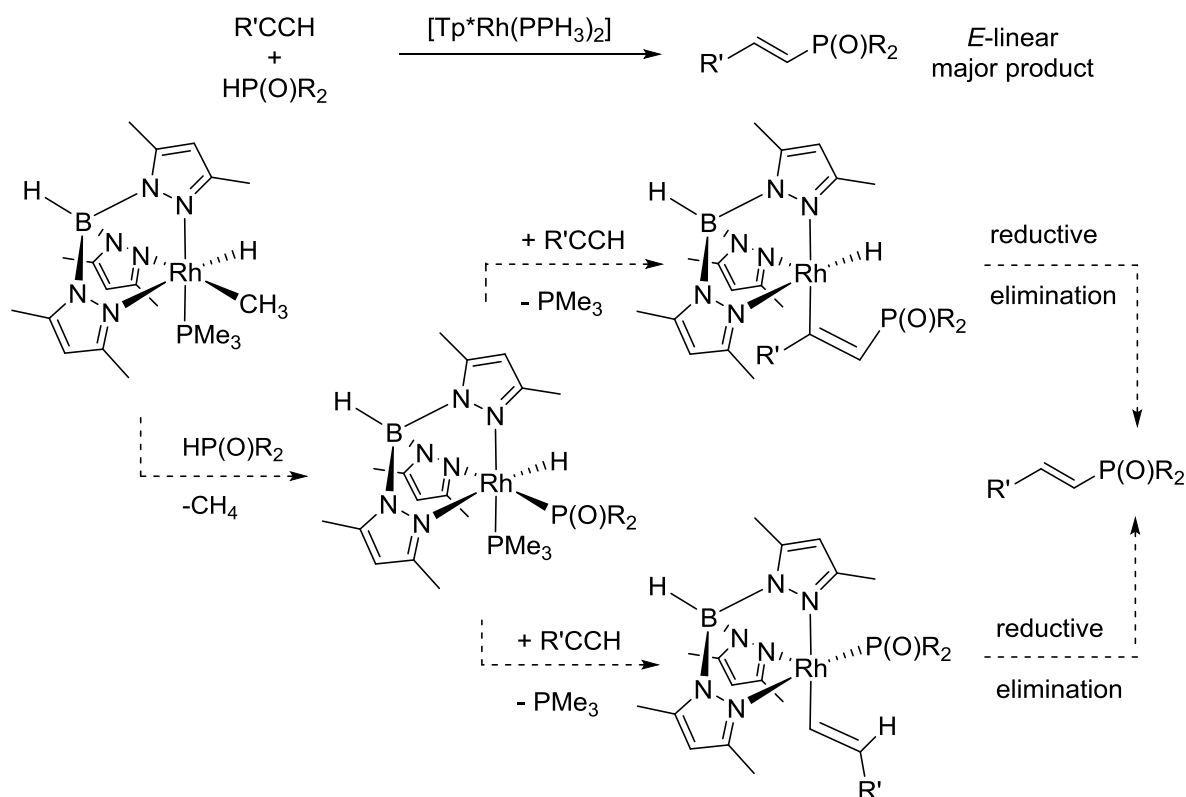
## 7.1 Future Work

### 7.1.1 Mechanistic Studies of Alkyne Hydrothiolation Catalyzed by $[\text{RhCl}(\text{PPh}_3)_3]$

The ultimate goal of mechanistic studies of alkyne hydrothiolation catalyzed by either  $[\text{Tp}^*\text{Rh}(\text{PPh}_3)_2]$  or  $[\text{RhCl}(\text{PPh}_3)_3]$  is to understand the effects governing the chemoselectivity of alkyne insertion. The question such experiments should strive to solve is why the intermediate  $[\text{Tp}^*\text{Rh}(\text{H})(\text{SR})]$  undergoes chemoselective migratory insertion into the Rh-SR bond when other rhodium complexes appear to undergo exclusive migratory insertion into the Rh-H bond. Understanding the underlying forces governing the chemoselectivity of M-H versus M-SR insertion is likely to lend more general insight into to all transition metal catalyzed hydroelementation reactions. Therefore, a similar systematic investigation of the mechanism of alkyne hydrothiolation catalyzed by  $[\text{RhCl}(\text{PPh}_3)_3]$  should be undertaken. Preliminary results reported in Appendix F suggest a mechanism which is far more complex than the simplified mechanism proposed by Ogawa *et al.*<sup>211</sup> Induction periods for product formation were observed, followed by saturation kinetics. Additionally, the mechanism governing the regioselectivity of the thiol addition differs significantly from that of alkyne hydrothiolation catalyzed by  $[\text{Tp}^*\text{Rh}(\text{PPh}_3)_2]$ . Notably, the regioselectivity of the reaction is completely independent of the electronic nature of the thiol employed.

### 7.1.2 Oxidative Addition of H-P(O)R<sub>2</sub> Bonds.

[Tp\*Rh(PPh<sub>3</sub>)<sub>2</sub>] has also been shown to catalyze the hydrophosphinylation of alkynes.<sup>212</sup> Contrary to alkyne hydrothiolation, alkyne hydrophosphinylation catalyzed by [Tp\*Rh(PPh<sub>3</sub>)<sub>2</sub>] produces the *E*-linear regioisomer as the major product. Presumably the mechanism involves oxidative addition of the P-H bond to the metal center to generate an intermediate [Tp\*RhH(P(O)R<sub>2</sub>)] complex. Therefore, a study of the oxidative addition of HP(O)R<sub>2</sub> (R = alkyl, aryl) to the [Tp\*Rh<sup>I</sup>(PMe<sub>3</sub>)] complex generated by reductive elimination of CH<sub>4</sub> from [Tp\*Rh<sup>III</sup>H(Me)(PMe<sub>3</sub>)] should be undertaken. Ideally, this would allow for the isolation of [Tp\*RhH(P(O)R<sub>2</sub>)(PMe<sub>3</sub>)] complexes. A similar study of the chemoselectivity of migratory insertion of alkynes could then be undertaken to determine if migratory insertion into the Rh-H bond or the Rh-P(O)R<sub>2</sub> bond were occurring (Scheme 7.1). A study of the effects of steric bulk of the alkyne in hydrophosphinylation reactions catalyzed by [Tp\*Rh(PPh<sub>3</sub>)<sub>2</sub>] should also be undertaken.



**Scheme 7.1.** Alkyne hydrophosphinylation catalyzed by  $[\text{Tp}^*\text{Rh}(\text{PPh}_3)_2]$  (top). Proposed synthesis and reactivity of  $[\text{Tp}^*\text{RhH}(\text{P}(\text{O})\text{R}_2)(\text{PMe}_3)]$  complexes (bottom).

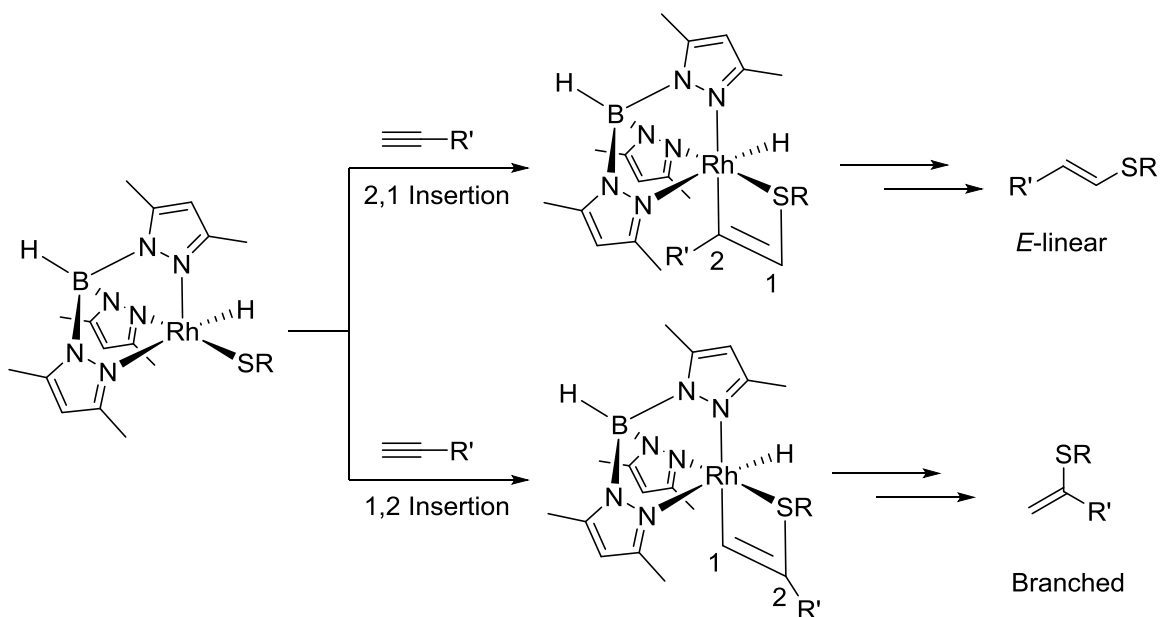
### 7.1.3 Modification of the Phosphine Ligand of $[\text{Tp}^*\text{RhH}(\text{Me})(\text{PMe}_3)]$

A drawback to the successful synthesis of  $[\text{Tp}^*\text{RhH}(\text{SR})(\text{PMe}_3)]$  complexes is the high coordination ability of the  $\text{PMe}_3$  ligand. Consequently, reactivity of the hydridothiolate complexes was only observed when reaction mixtures were heated to 60 °C. At these temperatures, and due to the high inhibition by  $\text{PMe}_3$ , the background reactions are competitive with putative catalytic cycles. The choice of an appropriate phosphine ligand  $\text{PR}_3$ , which does not undergo intramolecular activation of R groups, would allow for insertion chemistry to be

studied on not only the hydrido-thiolate complexes but all of the X-Y bond activation products of  $[\text{Tp}^*\text{RhH}(\text{Me})(\text{PR}_3)]$ , essentially building catalytic cycles from the ground up.

#### 7.1.4 Synthesis of New Tris(pyrazolylborate) Ligands.

In Chapter 5, we proposed that regioselectivity for the formation of branched versus *E*-linear vinyl sulfides in alkyne hydrothiolation reactions catalyzed by  $[\text{Tp}^*\text{Rh}(\text{PPh}_3)_2]$  arises from 1,2 versus 2,1 migratory insertion of the alkyne into the Rh-SR bond (Scheme 7.2). The regioselectivity of the reaction was found to be dependent on both the electronic nature of the thiolate and the steric bulk of the substituent  $\text{R}'$  deriving from the alkyne. A reversal of selectivity from branched to *E*-linear regioisomers was observed when electron deficient thiols were employed. However, when alkynes with large  $\text{R}'$  groups were employed, high selectivity for the branched isomer was observed, regardless of the electronic nature of the thiol employed.



**Scheme 7.2.** Origin of product regioselectivity in alkyne hydrothiolation reactions catalyzed by  $[\text{Tp}^*\text{Rh}(\text{PPh}_3)_2]$ .

Ultimately, for a catalytic process to be synthetically useful, it must generate the desired product in high yield. Producing a mixture of vinyl sulfide regioisomers, which are difficult to separate, reduces the general applicability and substrate scope for alkyne hydrothiolation catalyzed by [Tp\*Rh(PPh<sub>3</sub>)<sub>2</sub>]. Therefore, a new catalyst must be developed to address the issue of regioselectivity of alkyne insertion.

Ultimately, not much can be changed to alter the underlying electronic preference for 1,2 versus 2,1 insertion of the alkyne, especially when it is strongly influenced by the electronic nature of the thiolate. However, much can be done to change the steric preference for 1,2 versus 2,1 insertion by changing the substituents on the pyrazole rings of the ligand. The 3R substituent of the trispyrazolylborate ligand, numbered according to IUPAC nomenclature, is likely too far removed to have a significant impact on the regioselectivity of insertion (Figure 7.1). The 5R substituent, on the other hand, is likely to have a large impact on the steric preference for 1,2 versus 2,1 insertion. However, the 5R substituent will also impact the accessibility of  $\kappa^3$  coordination. In a study of different pyrazolylborate complexes of rhodium, the bidentate [Bp\*Rh(PPh<sub>3</sub>)<sub>2</sub>] was found result in lower selectivity for the branched vinyl sulfide regioisomer compared to its tridentate [Tp\*Rh(PPh<sub>3</sub>)<sub>2</sub>] counterpart.<sup>213</sup> It was therefore proposed that the third pyrazolyl arm, and access to a potential  $\kappa^3$  binding mode, was required for high regioselectivity. Substitution at the 5R position may also be too proximal to the metal center, possibility inhibiting catalytic reactivity altogether.

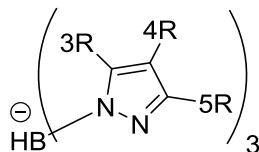


**Figure 7.1. Substituent numbering for typical homoscorpionate trispyrazolylborate ligand.**

Trispyrazolylborate ligands have a relatively large void between the coordinated pyrazole rings. For example, the distance between the 5-methyl substituents is between 5.1 and 6.1 Å, and the distance between the 4-H substituents is between 7.5 and 8.3 Å for [Tp\*RhCl<sub>2</sub>(PPh<sub>3</sub>)] (Figure 7.2). It is this void which allows for alkynes to undergo 2,1 migratory insertion. New ligands must therefore be sufficiently sterically bulky to prevent 2,1 alkyne insertion without affecting accessibility to  $\kappa^3$  binding modes or overly crowd the metal center. A likely candidate which would satisfy these requirements is aryl substitution at the 4R position of a 3,5-dimethylpyrazolylborate (Figure 7.2). Steric interaction between the methyl substituents of the pyrazole rings and the ortho substituents of the aryl ring on the 4R position of the pyrazole ring would cause the aryl ring to rotate near perpendicular to the pyrazole ring. This would fill the void between the pyrazole rings, thereby sterically hindering 2,1 insertion of the alkyne. Variation of the R<sup>1</sup> and R<sup>2</sup> would allow for control over how much steric bulk can be positioned between the pyrazolyl groups without hindering the accessibility of the  $\kappa^3$  binding mode or crowding the metal center. The R<sup>1</sup> and R<sup>2</sup> substituents would be simply alkyl groups such as methyl, ethyl, and iso-propyl. Variation of the R<sup>3</sup> substituent could be used to fine-tune the electronic properties of the ligand.

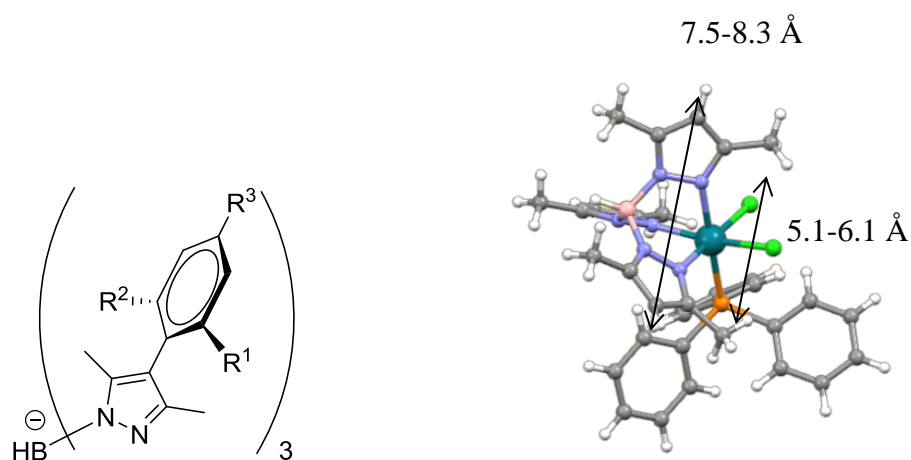


**Figure 7.2.** Proposed  $\text{Tp}^{3\text{Me},4\text{Ar},5\text{Me}}$  ligands (left). Solid state structure of  $[\text{Tp}^*\text{RhCl}_2(\text{PPh}_3)]$  (right).

While many variations of the trispyrazolylborate ligand and their corresponding metal complexes have been synthesized over the years, substitution of the 4R position is less diverse than substitution of the 3R or 5R positions.<sup>214</sup> Those with substitution at the 4R position are typically limited to Br or Cl, or aliphatic substituents. This limitation is largely due to the standard method of synthesizing substituted pyrazoles from 2,4-diketones (Figure 7.3). Therefore, aliphatic and halogenated species are readily accessible; however, no 4-aryl pyrazolylborate ligands have ever been synthesized because no direct method for the synthesis of the corresponding 2,4-diketone exists.

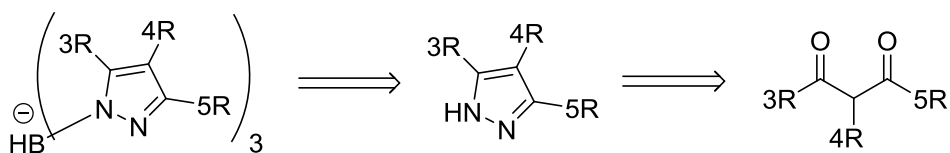
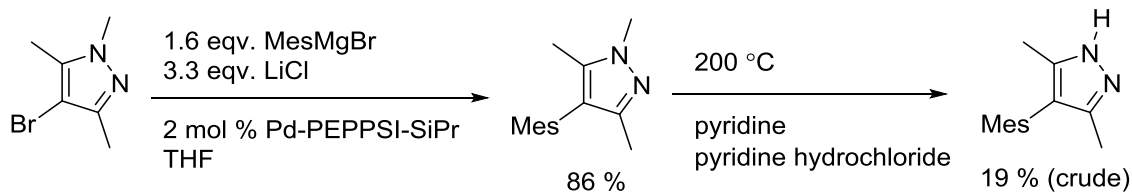


**Figure 7.3.** Typical retrosynthetic scheme for substituted trispyrazolylborate ligands.

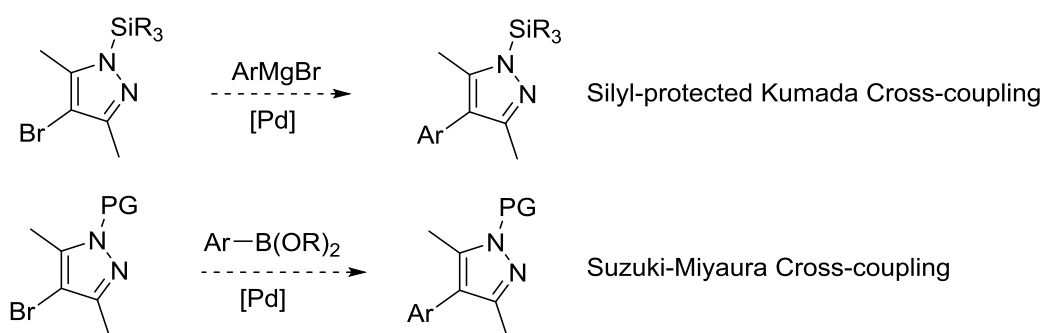
It was only recently that methods for the synthesis of tri- and tetra-*ortho*-substituted biaryls via cross-coupling methods have emerged. Relevant to the proposed ligand system herein, several Pd-catalyzed Suzuki-Matsumura and Kumada cross-coupling methods for the synthesis of 4-aryl-1,3,5-trimethylpyrazoles have been reported.<sup>215</sup> Consistent with these reports, 4-mesityl-1,3,5-trimethylpyrazole was synthesized by the cross-coupling of 4-bromo-1,3,5-trimethylpyrazole with mesitylmagnesium bromide, catalyzed by commercially available Pd-PEPPSI-SiPr, in 86% yield. However, in order to synthesize the desired trispyrazolylborate ligand, the *N*-methyl substituent must be removed. The *N*-demethylation of 4-mesityl-1,3,5-trimethylpyrazole proved to be problematic. A single report of *N*-demethylation of pyrazoles from 1975 requires excessive heating of *N*-methylpyrazoles in a mixture of pyridine and pyridine hydrochloride for extended periods of time.<sup>216</sup> Following this procedure, 4-mesityl-1,3,5-trimethylpyrazole was heated at 200 °C in a mixture of pyridine and pyridine hydrochloride (Scheme 7.3). The reaction was followed by mass spectrometry, and determined to take >96 hours to complete. During this time, significant quantities of black tar formed. The crude yield varied from 8% to 19%. Unfortunately, the crude mixture contained several impurities that could not be removed. Given the low yield of the *N*-demethylation procedure and the number of impurities, this method was deemed unsuitable for further study.



**Scheme 7.3. Synthesis of 4-mesityl-3,5-dimethylpyrazole.**

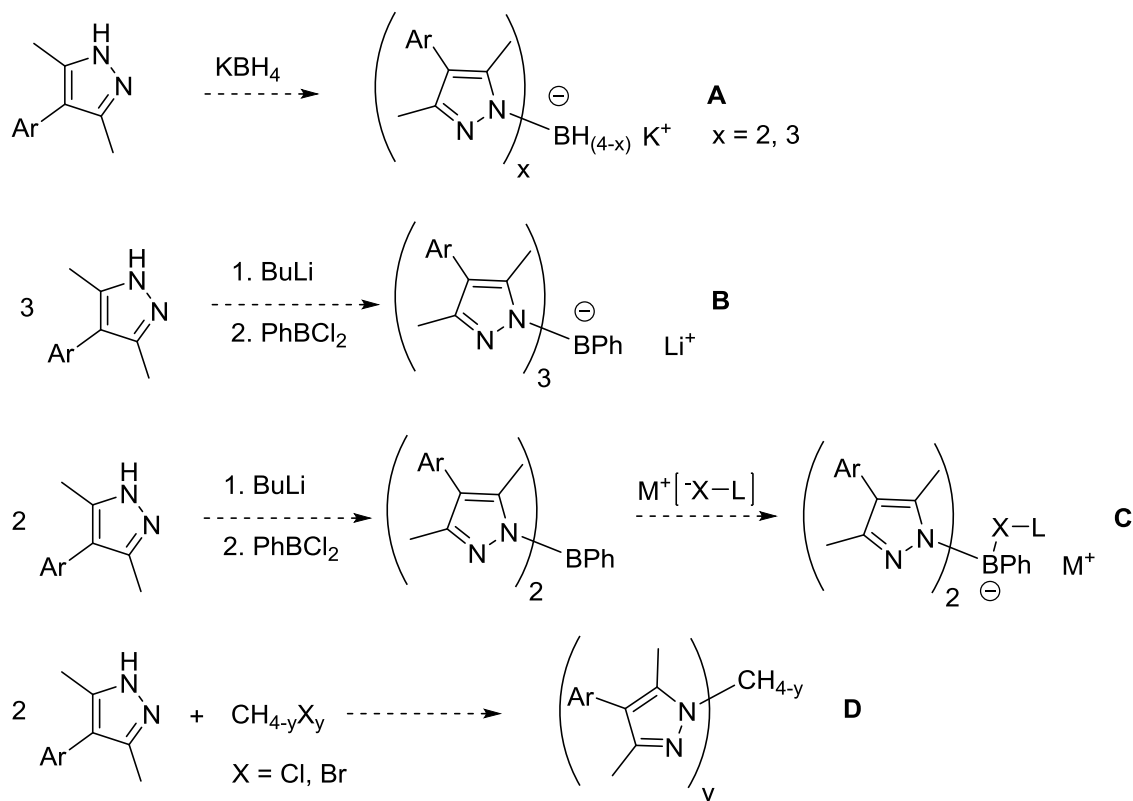
Instead, we postulated that an appropriately *N*-protected 4-bromo-3,5-dimethylpyrazole would provide a more efficient avenue to 4-aryl-substituted trispyrazolylborates. Towards this end, 1-Boc-4-bromo-3,5-dimethylpyrazole (Boc = *tert*-butylcarbamate) and 1-benzyl-4-bromo-3,5-dimethylpyrazole were synthesized by the appropriate methods from 4-bromo-3,5-dimethylpyrazole. Unfortunately, neither of these protecting groups was compatible with the Kumada cross-coupling conditions. The Boc-protected pyrazole gave a mixture of products resulting from attack of the Grignard reagent at the carbonyl of the Boc protecting group. Addition of the Grignard reagent to a solution of the benzyl-protected pyrazole resulted in deprotonation of the benzylic carbon and no cross-coupling was observed.

Given the lack of success with the Pd-catalyzed Kumada couplings with *N*-benzyl and *N*-Boc protected pyrazoles and the difficulty in deprotecting *N*-methyl cross-coupling products, two avenues are proposed for further research into these novel 4-aryl-3,5-dimethylpyrazolylborate ligands. First, silyl protecting groups may be more stable under the Kumada cross coupling conditions. Second, Pd-catalyzed Suzuki-Miyaura cross-coupling conditions may give a broader range of compatible protecting groups (Scheme 7.4).



**Scheme 7.4. Proposed methods for successful synthesis of *N*-protected 4-aryl-3,5-dimethylpyrazoles.**

The successful synthesis of appropriately *N*-protected 4-aryl-3,5-dimethylpyrazoles opens the door for an entirely new class of scorpionate ligands. Bidentate and tridentate pyrazolylborates can be made from sodium or potassium borohydride (Scheme 7.5, **A**).<sup>217</sup> The method of Sadow *et al*, employing PhBCl<sub>2</sub>,<sup>218</sup> allows access to phenyl substituted homoscorpionate and heteroscorpionate ligands (Scheme 7.5, **B**, **C**). Neutral analogues bis(pyrazolyl)methane and tris(pyrazolyl)methane (Scheme 7.5, **D**) and their corresponding heteroscorpionate ligands can also be readily synthesized. For tridentate ligands, their  $\kappa^2 - \kappa^3$  coordination flexibility can be assessed by variable temperature NMR experiments and by synthesizing complexes which must necessarily adopt one coordination mode or the other.



**Scheme 7.5.** Synthesis of novel 4-aryl-3,5-dimethylpyrazole containing ligands.

### 7.1.5 Proposal for Modification of the Phosphine Ligands of [Tp\*Rh(PPh<sub>3</sub>)<sub>2</sub>]

Experimental results in Chapter 6 and previous reports<sup>219</sup> reveal that orthometallation of the PPh<sub>3</sub> ligand is detrimental. Formation of the inactive orthometallated product [Tp\*RhH(*o*-C<sub>6</sub>H<sub>4</sub>PPh<sub>2</sub>)] was observed to form during catalytic reactions and results in reduced turnover numbers. Therefore, new catalysts for alkyne hydrothiolation should avoid the use of PPh<sub>3</sub> as a neutral donor ligand. However, experimental results in Chapter 5 reveal that low concentrations of added PPh<sub>3</sub> accelerate the rate of product formation, but that excess added PPh<sub>3</sub> ultimately inhibits product formation. On the one hand, association of phosphine to the intermediate hydridothiolate complex [Tp\*RhH(SR)] inhibits alkyne coordination. On the other hand, association of phosphine to the reductively coupled species induces product dissociation, and thus increasing the rate of product formation. It is difficult to predict *a priori* which pathway would dominate when designing new catalysts. Nevertheless, variations in the L ligand of [Tp\*Rh(L)<sub>2</sub>] complexes active in alkyne hydrothiolation would allow for an interesting study. The inhibitory equilibrium [Tp\*RhH(SR)]  $\rightleftharpoons$  [Tp\*RhH(SR)(L)] would give information about the relative affinity of the L ligand for the [Tp\*Rh<sup>III</sup>] complexes. The rate enhancement for product formation in the presence of added L ligand would give information about the relative kinetic affinity of the L ligand for [Tp\*Rh<sup>I</sup>] complexes. Ultimately, variations in the L ligand of [Tp\*Rh<sup>I</sup>(L)<sub>2</sub>] complexes active in alkyne hydrothiolation would allow for fine tuning of the overall catalytic activity.

## References

- <sup>1</sup> Joseph Patrick Kleinhenz. PhD. Dissertation, The Ohio State University, 2003
- <sup>2</sup> M. V. Ramana Reddy, P. Venkatapuram, M. R. Mallireddigari, V. R. Pallela, S. C. Cosenza, K. A. Robell, B. Akula, B. S. Hoffman, E. P. Reddy. *J. Med. Chem.* **2011**, *54*, 6254-6276.
- <sup>3</sup> Jacobsen, W.; Christians, U.; Benet, L. Z. *Drug Metab. Dispos.* **2000**, *28*, 1343-1351.
- <sup>4</sup> Bratz, M. ; Bullock, W.H. ; Overman, L. E. ; Takemoto, T. *J. Am. Chem. Soc.* **1995**, *117*, 5958-5966.
- <sup>5</sup> a) Pearson, W. H. ; Lee, I. Y. ; Mi, Y. ; Stoy, P. *J. Am. Chem. Soc.* **2001**, *123*, 6724-6725.  
b) Pearson, W. H. ; Lee, I. Y. ; Mi, Y. ; Stoy, P. *J. Org. Chem.* **2004**, *69*, 9109-9122.
- <sup>6</sup> Mizuno, H. ; Domon, K. ; Masuya, K. ; Tanino, K. ; Kuwajima, I. *J. Org. Chem.* **1999**, *64*, 2648-2656.
- <sup>7</sup> a) Parham, W. E.; Motter, R. F. *J. Am. Chem. Soc.* **1959**, *81*, 2146.  
b) Wenkert, E.; Ferreira, T. W.; Michelotti, E. L. *J. Am. Chem. Soc., Chem. Commun.* **1979**, 637. c) Trost, B. M.; Lavoie, A. C. *J. Am. Chem. Soc.* **1983**, *105*, 5075.
- <sup>8</sup> Sabarre, A.; Love, J. A. *Org. Lett.* **2008**, *10*, 3941.
- <sup>9</sup> a) Cohen, T.; Herman, G.; Falck, J. R.; Mura, A. *J. Org. Chem.* **1975**, *40*, 812.  
b) Trost, B. M.; Hiroi, K.; Kurozumi, S. *J. Am. Chem. Soc.* **1975**, *97*, 438.
- <sup>10</sup> a) Bates, C. G.; Saejung, P.; Doherty, M. Q.; Venkataraman, D. *Org. Lett.* **2004**, *6*, 5005.  
b) Zheng, Y. F.; Du, X. F.; Bao, W. L. *Tetrahedron Lett.* **2006**, *47*, 1217.  
c) Ranu, B. C.; Chattopadhyay, K.; Banerjee, S. *J. Org. Chem.* **2006**, *71*, 423.
- <sup>11</sup> a) Carey, F. A.; Court, A. S. *J. Org. Chem.* **1972**, *37*, 939. b) Peterson, D. J. *J. Org. Chem.* **1968**, *33*, 780.

- <sup>12</sup> Posner, T. *Ber. Dtsch. Chem. Ges.* **1905**, *38*, 646.
- <sup>13</sup> Kondoh, A.; Takami, K.; Yorimitsu, H.; Oshima, K. *J. Org. Chem.* **2005**, *70*, 6468.
- <sup>14</sup> a) Bader, H.; Cross, L. C.; Heilbron, I.; Jones, E. R. H. *J. Chem. Soc.* **1949**, 619. b) Behringer, H. *Justus Liebigs Ann. Chem.* **1949**, *564*, 219.
- <sup>15</sup> Fessenden, R. W.; Schuler, R. H. *J. Chem. Phys.* **1963**, *39*, 2147.
- <sup>16</sup> V. R. Pallela, M. R. Mallireddigari, S. C. Cosenza, B. Akula, D. R. C. V. Subbaiah, E. P. Reddy, M. V. R. Reddy, *Org. Biomol. Chem.* **2013**, *11*, 1964-1977.
- <sup>17</sup> McDonald, J. W.; Corbin, J. L.; Newton, W. E. *Inorg. Chem.* **1976**, *15*, 2056.
- <sup>18</sup> Kuniyasu, H.; Ogawa, A.; Mizayaki, S. I.; Ryu, I.; Kambe, N.; Sonoda, N. *J. Am. Chem. Soc.* **1991**, *113*, 9796.
- <sup>19</sup> a) Kuniyasu, H.; Ogawa, A.; Sato, K.-I.; Ryu, I.; Kambe, N. Sonoda, N. *J. Am. Chem. Soc.* **1992**, *114*, 5902. b) Ogawa, A.; Ikeda, T.; Kimura, K.; Hirao, T. *J. Am. Chem. Soc.* **1999**, *121*, 5108.
- <sup>20</sup> Ogawa, A. *J. Organomet. Chem.* **2000**, *611*, 463.
- <sup>21</sup> Beletskaya, I. P.; Ananikov, V. P. *Chem. Rev.* **2011**, *111*, 1596–1636
- <sup>22</sup> Weiss, C. J.; Marks, T. J. *Dalton Trans.* **2010**, *39*, 6576–6588
- <sup>23</sup> Burling, S.; Leslie, D. F.; Messerle, B. A.; Khuong, Q. V.; Turner, P. *Dalton Trans.* **2003**, 4181.
- <sup>24</sup> a) Ananikov, V. P.; Malyshev, D. A.; Beletskaya, I. P.; Aleksandrov, G. G.; Eremenko, I. L. *Adv. Synth. Catal.* **2005**, *347*, 1993. b) Malyshev, D. A.; Scott, N. M.; Marion, N.; Stevens, E. D.; Ananikov, V. P.; Beletskaya, I. P., Nolan, S. P. *Organometallics* **2006**, *25*, 4462-4470.
- <sup>25</sup> Arisawa, M.; Yamaguchi, M. *Org. Lett.* **2001**, *3*, 763.

- <sup>26</sup> a) Cao, C.; Frasier, L. R.; Love, J. A. *J. Am. Chem. Soc.* **2005**, *127*, 17614. b) L. R. Fraser, J. Bird, Q. Wu, C. Cao, B. O. Patrick, J. A. Love. *Organometallics*, **2007**, *26*, 5602-5611. c) J. Yung, A. Sabarre, L. R. Fraser, B. O. Patrick, J. A. Love. *J. Org. Chem.* **2009**, *74*, 182-187.
- <sup>27</sup> Shoai, S.; Bichler, P.; Kang, B.; Buckley, H.; Love, J. A. *Organometallics* **2007**, *26*, 5778-5781
- <sup>28</sup> Misumi, Y.; Seino, H.; Mizobe, Y. *J. Organomet. Chem.* **2006**, *691*, 3157
- <sup>29</sup> Weiss, C. J.; Marks, T. J. *J. Am. Chem. Soc.* **2010**, *132*, 10533
- <sup>30</sup> Weiss, C. J.; Wobser, S. D.; Marks, T. J. *Organometallics* **2010**, *29*, 6308
- <sup>31</sup> a) A. Di Giuseppe, R. Castarlenas, J. J. Pérez-Torrente, M. Crucianelli, V. Polo, R. Sancho, F. J. Lahoz, L. A. Oro, *J. Am. Chem. Soc.* **2012**, *134*, 8171-8183. b) L. Palacios, M. J. Artigas, V. Polo, F. J. Lahoz, R. Castarlenas, J. J. Pérez-Torrente, L. A. Oro. *ACS Catal.* **2013**, *3*, 2910-2919.
- <sup>32</sup> Y. Yamamoto, X.-H. Han, J.-F. Ma, *Angew. Chem. Int. Ed.* **2000**, *39*, 1965-1968.
- <sup>33</sup> B. de Bruin, M. J. Boerakker, J. J. J. M. Donners, B. E. C. Christiaans, P. P. J. Schlebos, R. de Gelder, J. J. M. Smits, A. L. Spek, A. W. Gal. *Angew. Chem. Int. Ed.* **1997**, *36*, 2064.
- <sup>34</sup> a) B. de Bruin, M. J. Boerakker, R. de Gelder, J. M. M. smits, A. W. Gal. *Angew. Chem. Int. Ed.* **1999**, *38*, 219-222. b) B. de Bruin, M. J. Boerakker, J. A. W. Verhagen, R. de Gelder, J. M. M. Smits, A. W. Gal. *Chem. Eur. J.* **2000**, *6*, 298-312.
- <sup>35</sup> A. Dauth, J. A. Love, *Angew. Chem. Int. Ed.* **2010**, *49*, 9219-9224.
- <sup>36</sup> C. Aurisicchio, E. Baciocchi, M. F. Gerini, O. Lanzalunga. *Org Lett* **2007**, *9*, 1939-1942.
- <sup>37</sup> P. Zhao, C. Krug, J. F. Hartwig, *J. Am. Chem. Soc.* **2005**, *127*, 12066-12073.
- <sup>38</sup> P. Zhao, C. D. Incarvito, J. F. Hartwig, *J. Am. Chem. Soc.* **2006**, *128*, 9642-9643.

- <sup>39</sup> J. W. Tye, J. F. Hartwig, *J. Am. Chem. Soc.* **2009**, *131*, 14703-14712.
- <sup>40</sup> J. N. Harvey, *Organometallics*, **2001**, *20*, 4887.
- <sup>41</sup> S. Trofimenko. *J. Am. Chem. Soc.* **1966**, *88*, 1842-1844.
- <sup>42</sup> S. Trofimenko. *Chem. Rev.* **1993**, *93*, 943-980.
- <sup>43</sup> S. Trofimenko. *Prog. Inorg. Chem.* **1986**, *34*, 115-209.
- <sup>44</sup> K. Niedenzu, S. Trofimenko. *Top. Curr. Chem.* **1986**, *131*, 1-37.
- <sup>45</sup> Selected examples: a) C.A. Dodds, J. Reglinski, M. D. Spicer. *Chem. Eur. J.* **2006**, *12*, 931-939. b) A. F. Hill, M. K. Smith. *Organometallics* **2007**, *26*, 4688-4691. c) B. A. Greiner, N. M. Marshall, A. A. Narducci Sarjeant, C. C. McLauchlan. *Inorg. Chim. Acta* **2007**, *360*, 3132-3140.
- <sup>46</sup> Selected examples: a) B. Baird, A. V. Pawlikowski, J. Su, J. W. Wiench, M. Pruski, A. D. Sadow. *Inorg. Chem.* **2007**, *47*, 10208-10210. b) A. V. Pawlikowski, T. S. Gray, G. Schoendorff, B. Baird, A. Ellern, T. L. Windus, A. D. Sadow. *Inorg. Chim. Acta* **2009**, *362*, 4617-4525. c) K. Wu, D. Mukherjee, A. Ellern, A. D. Sadow, W. E. Geiger. *New J. Chem.* **2011**, *35*, 2169-2178. d) S. Xu, Y. Magoon, R. R. Reinig, B. M. Schmidt, A. Ellern, A. D. Sadow. *Organometallics* **2015**, *34*, 3508-3519.
- <sup>47</sup> Selected examples: a) B. E. Frauhiger, J. L. Templeton. *Organometallics* **2012**, *31*, 2770-2784. b) B. E. Frauhiger, P. S. White, J. L. Templeton. *Organometallics* **2012**, *31*, 225-237. c)
- <sup>48</sup> Selected examples: a) M. D. Spicer, J. Reglinski. *Eur. J. Inorg. Chem.* **2009**, 1553-1574. b) S. L. Kuan, W. K. Leong, L. Y. Goh, R. D. Webster. *J. Organomet. Chem.* **2006**, *691*, 907-915. c) C. Gengo, R. M. Silva, M. D. Smith, S. V. Lindeman, J. R. Gardinier. *Inorg. Chim. Acta* **2009**, *362*, 4127-4136.

- <sup>49</sup> Selected examples: a) R. J. Blagg, N. G. Connelly, M. F. Haddow, A. Hamilton, M. Lusi, G. Orpen, B. J. Ridgway. *Dalton Trans.* **2010**, 39, 11616-11627. b) M. Imran, B. Neumann, H.-G. Stammler, U. Monkowius, M. Ertl, N. W. Mitzel. *Dalton Trans.* **2013**, 42, 15785-15795.
- <sup>50</sup> S. Xu, W. C. Everett, A. Ellern, T. L. Windus, A. D. Sadow. *Dalton Trans.* **2014**, 43, 14638-14376.
- <sup>51</sup> Selected examples: a) H. Kopf, C. Pietraszuk, E. Hubner, N. Burzlaff. *Organometallics* **2006**, 25, 2533-2546. b) E. Hubner, N. V. Fisher, F. W. Heinemann, U. Mitra, V. Dremov, P. Muller, N. Burzlaff. *Eur. J. Inorg. Chem.* **2010**, 4100-4109. c) B. S. Hammes, B. S. Chohan, J. T. Hoffman, S. Einwachter, C. J. Carrano. *Inorg. Chem.* **2004**, 43, 7800-7806.
- <sup>52</sup> D. Adhikari, G. Zhao, F. Basuli, J. Tomaszewski, J. C. Huffman, D. J. Mindola. *Inorg. Chem.* **2006**, 45, 1604-1610.
- <sup>53</sup> A. Otero, J. Fernandez-Baeza, A. Antinolo, J. Tejada, A. Lara-Sanchez, L. F. Sanchez-Barba, I. Lopez-Solera, A. M. Rodriguez. *Inorg. Chem.* **2007**, 46, 1760-1770.
- <sup>54</sup> Selected examples: a) J. N. Smith, Z. Shirin, C. J. Carrano. *J. Am. Chem. Soc.* **2003**, 125, 868-869. b) V. V. Karambelkar, R. C. diTargiani, C. D. Incarvito, L. N. Zakharov, A. L. Rheingold, C. L. Stern, D. P. Goldberg. *Polyhedron* **2004**, 23, 471-480.
- <sup>55</sup> Selected examples: a) N. Masaaki, Y. Seki, T. Miyatake, Y. Ishikawa, K. Okamoto, K. Fujisawa. *Organometallics* **2004**, 23, 4335-4337. b) G. Paolucci, M. Bortoluzzi, M. Napoli, P. Longo, V. Bertolasi. *J. Mol. Catal. A: Chem.* **2010**, 317, 54-60. c) G. Alesso, V. Tabernerero, T. Cuenca. *J. Organomet. Chem.* **2012**, 717, 202-210. d) A. D. Asandei, I. W. Moran. *J. Polym. Sci. A Polym. Chem.* **2005**, 43, 6039-6047. e) K. Michiue, T. Oshiki, K. Takai, M. Mitani, T. Fujita. *Organometallics* **2009**, 28, 6450-6457. f) S. Milione, C.

Monetfusco, T. Cuenca, A. Grassi. *Chem. Commun.* **2003**, 1176-1177. g) C. Cuomo, S. Milione, A. Grassi. *Macromol. Rapid Commun* **2006**, 27, 611-618. h) A. Otero, J. Fernandez-Baeza, A. Antinolo, F. Carrillo-Hermosilla, J. Tejada, E. Diez-Barra, A. Lara-Sanchez, L. Sanchez\_barba, I. Lopez-Solera. *Organometallics* **2001**, 20, 2428-2430. i) S. Milione, V. Bertolasi, T. Cuenca, A. Grassi. *Organometallics* **2005**, 24, 4915-4925.

<sup>56</sup> Selected examples: a) M. A. Mairena, M. M. Diaz-Requejo, T. R. Belderrain, M. C. Nicasio, S. Trofimenko, P. J. Perez. *Organometallics* **2004**, 23, 253-256. b) S. Liang, M. P. Jensen. *Organometallics* **2012**, 31, 8055-8058. c) I. Arenas, M. A. Fuentes, E. Alvarez, Y. Diaz,\* , A. Caballero, S. Castillon, P. J. Perez. *Inorg. Chem.* **2014**, 53, 3991-3999.

<sup>57</sup> Selected examples: a) A. Garces, L. F. Sanchez-Barba, C. Alonso-Moreno, M. Fajardo, J. Fernandez-Baeza, A. Otero, A. Lara-Sanchez, I. Lopez-Solera, A. M. Rodriguez. *Inorg. Chem.* **2010**, 49, 2859-2871. b) A. Otero, J. Fernandez-Baeza, A. Antinolo, A. Lara-Sanchez, E. Martinez-Caballero, J. Tejada, L. F. Sanchez-Barba, C. Alonso-Moreno, I. Lopez-Solera. *Organometallics* **2008**, 27, 976-983. c) A. Otero, J. Fernandez-Baeza, L. F. Sanchez-Barba, J. Tejada, M. Honrado, A. Garces, A. Lara-Sanchez, A. M. Rodriguez. *Organometallics* **2012**, 31, 4191-4202. d) M. Honrado, A. Otero, J. Fernandez-Baeza, L. F. Fernandez-Baeza, L. F. Sanchez-Barba, A. Lara-Sanchez, J. Tejada, M. P. Carrion, J. Martinez-Ferrer, A. Garces, A. M. Rodriguez. *Organometallics* **2013**, 32, 3437-3440. e) M. Honrado, A. Otero, J. Fernandez-Baeza, L. F. Fernandez-Baeza, L. F. Sanchez-Barba, A. Garces, A. Lara-Sanchez, A. M. Rodriguez. *Organometallics* **2014**, 33, 1859-1866.

<sup>58</sup> Selected examples: a) L.L. Blosch, A.S. Gamble, J.M. Boncella. *J. Mol. Catal.* **1992**, 76, 229. b) W.M. Vaughan, K.A. Abboud, J.M. Boncella. *Organometallics* **1995**, 14, 1567. c) M.S.

- Sanford, L.M. Henling, R.H. Grubbs. *Organometallics* **1998**, *17*, 5384. d) U. Brand, M. Rombach, H. Vahrenkamp. *Chem. Commun.* **1998**, 2717.
- <sup>59</sup> M. Kumar, J. DePasquale, N. J. White, M. Zeller, E. T. Papish. *Organometallics* **2013**, *32*, 2135-2144.
- <sup>60</sup> L. D. Field, B. A. Messerle, K. Q. Vuong, P. Turner. *Dalton Trans.* **2009**, 3599-3614.
- <sup>61</sup> S. Burling, L. D. Field, B. A. Messerle, K. Q. Vuong, P. Turner. *Dalton Trans.* **2003**, 4181-4191.
- <sup>62</sup> K. Q. Vuong, C. M. Wong, M. Bhadbhade, B. A. Messerle. *Dalton Trans.* **2014**, *43*, 7540.
- <sup>63</sup> F. Alonso, I. P. Beletskaya, M. Yus. *Chem. Rev.* **2004**, *104*, 3079-3160.
- <sup>64</sup> R. Chinchilla, C. Najera. *Chem. Rev.* **2014**, *114*, 1783-1926.
- <sup>65</sup> X. Zeng. *Chem. Rev.* **2013**, *113*, 6864-6900.
- <sup>66</sup> J. C. Powers, J. L. Asgian, O. D. Ekici, K. E. James. *Chem. Rev.* **2002**, *102*, 4639-4750.
- <sup>67</sup> Selected examples: a) W. R. Roush, S. L. Gwaltney II, J. Cheng, K. A. Scheidt, J. H. McKerrrow, E. Hansell. *J. Am. Chem. Soc.* **1998**, *120*, 10994-10995. b) I. D. Kerr, J. H. Lee, C. J. Farady, R. Marion, M. Rickert, M. Sajid, K. C. Pandey, C. R. Caffrey, J. Legac, E. Hansell, J. H. McKerrrow, C. S. Craik, P. J. Rosenthal, L. S. Brinen. *J. Biol. Chem.* **2009**, *284*, 25697-25703.
- <sup>68</sup> J.-E. Backvall, A. Ericsson. *J. Org. Chem.* **1994**, *59*, 5850-5851.
- <sup>69</sup> T. Kondo, T.-A. Mitsudo. *Chem. Rev.* **2000**, *100*, 3205-3220.
- <sup>70</sup> V. R. Pallela, M. R. Mallireddigari, S. C. Cosenza, B. Akula, D. R. C. V. Subbaiah, E. P. Reddy, M. V. R. Reddy. *Org. Biomol. Chem.* **2013**, *11*, 1964-1977.
- <sup>71</sup> E. R. Kiemele, M. Wathier, P. Bichler, J. A. Love. *Org. Lett.* **2016**, *18*, 492-495.

- <sup>72</sup> H. Kuniyasu, A. Ogawa, K.-I. Sato, I. Ryu, N. Kambe, N. Sonoda. *J. Am. Chem. Soc.* **1992**, *114*, 5902-5903.
- <sup>73</sup> I. P. Beletskaya, V. P. Ananikov. *Chem. Rev.* **2011**, *111*, 1596-1636.
- <sup>74</sup> C. J. Wiess, T. J. Marks. *Dalton Trans.* **2010**, *39*, 6576-6588.
- <sup>75</sup> L. R. Fraser, J. Bird, Q. Wu, C. Cao, B. O. Patrick, J. A. Love. *Organometallics* **2007**, *26*, 5602-5611.
- <sup>76</sup> J. Yang, A. Sabarre, L. R. Fraser, B. O. Patrick, J. A. Love. *J. Org. Chem.* **2009**, *74*, 182-187.
- <sup>77</sup> Selected examples: a) C. J. Weiss, T. J. Marks. *J. Am. Chem. Soc.* **2010**, *132*, 10533-10546. b) L. Palacios, M. J. Artigas, V. Polo, F. J. Lahoz, R. Castarlenas, J. J. Perez-Torrente, L. A. Oro.
- <sup>78</sup> Y. Misumi, H. Seino, Y. Mizobe. *J. Organomet. Chem.* **2006**, *691*, 3157-3164.
- <sup>79</sup> H. Seino, T. Yoshikawa, M. Hidai, Y. Mizobe. *Dalton Trans.* **2004**, *21*, 3593-3600.
- <sup>80</sup> Selected reviews: a) T. E. Muller, K. C. Hultsch, M. Yus, F. Foubelo, M. Tada. *Chem. Rev.* **2008**, *108*, 3795-3892. b) T. E. Muller, M. Beller. *Chem. Rev.* **1998**, *98*, 675-703. c) F. Pohlki, S. Doye. *Chem. Soc. Rev.* **2003**, *32*, 104-114. d) R. Severin, S. Doye. *Chem. Soc. Rev.* **2007**, *36*, 1407-1420. e) I. Aillaud, J. Collin, J. Hannedouche, E. Schulz. *Dalton Trans.* **2007**, 5105-5118.
- <sup>81</sup> a) E. Bernoud, C. Lepori, M. Mellah, E. Schulz, J. Hannedouche. *Catal. Sci. Technol.* **2015**, *5*, 2017-2037. b) L. Huang, M. Arndt, K. Gooßen, H. Heydt, L. J. Gooßen. *Chem. Rev.* **2015**, *115*, 2596-2697.
- <sup>82</sup> V. Rodriguez-Ruiz, R. Carlino, S. Bezenine-Lafollee, R. Gil, D. Prim, E. Schulz, J. Hannedouche. *Dalton Trans.* **2015**, *44*, 12029-12059.

- <sup>83</sup> I. Bytschkov, S. Doye. *Eur. J. Org. Chem.* **2003**, 935-946.
- <sup>84</sup> a) G. A. Molander, J. A. C. Romero. *Chem. Rev.* **2002**, *102*, 2161-2185. b) S. Hong, T. J. Marks. *Acc. Chem. Res.* **2004**, *37*, 673-686.
- <sup>85</sup> a) J. J. Brunet, D. Neibecker, F. J. Niedercorn. *Mol. Catal.* **1989**, *49*, 235-259. b) A. M. Johns, N. Sakai, A. Ridder, J. F. Hartwig. *J. Am. Chem. Soc.* **2006**, *128*, 9306-9307.
- <sup>86</sup> K. C. Hultsch. *Adv. Synth. Catal.* **2005**, *347*, 367-391.
- <sup>87</sup> Y. Fukumoto, H. Asai, M. Shimizu, N. Chatani. *J. Am. Chem. Soc.* **2007**, *129*, 13792-13793.
- <sup>88</sup> a) Z. Zhang, D. C. Leitch, M. Lu, B. O. Patrick, L. L. Schafer. *Chem. Eur. J.* **2007**, *13*, 2012.  
b) Z. Zhang, L. L. Schafer. *Org. Lett.* **2003**, *5*, 4733.
- <sup>89</sup> V. Circu, M. A. Fernandes, L. Carlton. *Inorg. Chem.* **2002**, *41*, 3859-3865.
- <sup>90</sup> A. V. Pawlikowski, A. Ellern, A. D. Sadow. *Inorg. Chem.* **2009**, *48*, 8020-8029
- <sup>91</sup> J. F. Dunne, J. Su, A. Ellern, A. D. Sadow. *Organometallics* **2008**, *27*, 2399-2401
- <sup>92</sup> S. Hong, S. Tian, M. V. Metz, T. J. Marks. *J. Am. Chem. Soc.* **2007**, *129*, 4253-4271.
- <sup>93</sup> J. F. Dunne, D. B. Fulton, A. Ellern, A. D. Sadow. *J. Am. Chem. Soc.* **2010**, *132*, 17680-17683.
- <sup>94</sup> M. R. Gagne, T. J. Marks. *J. Am. Chem. Soc.* **1989**, *111*, 4108-4109.
- <sup>95</sup> S. Tobisch, *Chem.-Eur. J.* 2011, *17*, 14974-14986.
- <sup>96</sup> S. R. Neal, A. Ellern, A. D. Sadow. *J. Organomet. Chem.* **2011**, *696*, 228-234.
- <sup>97</sup> K. Manna, A. Ellern, A. D. Sadow. *Chem. Commun.* **2010**, *46*, 339-341.
- <sup>98</sup> K. Manna, W. C. Everett, G. Schoendorff, A. Ellern, T. L. Windus, A. D. Sadow. *J. Am. Chem. Soc.* **2013**, *135*, 7235-7250.
- <sup>99</sup> K. Manna, S. Xu, A. D. Sadow. *Angew. Chem. Int. Ed.* **2011**, *50*, 1865-1868.
- <sup>100</sup> K. Manna, M. L. Kruse, A. D. Sadow. *ACS Catal* **2011**, *1*, 1637-1642.

- <sup>101</sup> B. D. Stubbert, T. J. Marks. *J. Am. Chem. Soc.* **2007**, *129*, 6149-6167.
- <sup>102</sup> K. Manna, N. Eedugurala, A. D. Sadow. *J. Am. Chem. Soc.* **2015**, *137*, 425-435.
- <sup>103</sup> A. Otero, A. Lara-Sanchez, C. Najera, J. Fernandez-Baeza, I. Marquez-Segovia, J. A. Castro-Osma, J. Martinez, L. F. Sanchez-Barba, A. M. Rodriguez. *Organometallics* **2012**, *31*, 2244-2255.
- <sup>104</sup> A. Otero, J. Fernandez-Baeza, A. Antinolo, J. Tejada, A. Lara-Sanchez, L. Sanchez-Barba, A. M. Rodriguez, M. A. Maestro. *J. Am. Chem. Soc.* **2004**, *126*, 1330-1331.
- <sup>105</sup> R. Karmakar, P. Pahari, D. Mal. *Chem. Rev.* **2014**, *114*, 6213-6264.
- <sup>106</sup> M. Uchiyama, H. Ozawa, K. Takuma, Y. Matsumoto, M. Yonehara, K. Hiroya, T. Sakamoto. *Org. Lett.* **2006**, *8*, 5517-5520.
- <sup>107</sup> J. A. Goodwin, A. Aponick. *Chem Commun.* **2015**, *51*, 8730-8741.
- <sup>108</sup> B. Y.-W. Man, M. Bhadbhade, B. A. Messerle. *New J. Chem.*, **2011**, *35*, 1730-1739.
- <sup>109</sup> A. J. Hallett, K. M. Anderson, N. G. Connelly, M. F. Haddow. *Dalton Trans.* **2009**, 4181-4189.
- <sup>110</sup> C. J. Adams, N. G. Connelly, D. J. H. Emslie, O. D. Hayward, T. Manson, A. G. Orpen, P. H. Rieger. *Dalton Trans.* **2003**, 2835-2845.
- <sup>111</sup> B. Y.-W. Man, A. Knuhtsen, M. J. Page, B. A. Messerle. *Polyhedron*, **2013**, *61*, 248-252.
- <sup>112</sup> Selected examples: a) H. Inoue, Y. Nagaoka, K. Tomioka. *J. Org. Chem.* **2002**, *67*, 5864. b) F. Palacios, D. Aparicio, J. Garcia, E. Rodriguez, F. Fernandez-Acebes. *Tetrahedron* **2001**, *57*, 3131. c) R. K. Haynes, W. A. Loughlin, T. W. Hambley. *J. Org. Chem.* **1989**, *54*, 5162.

- <sup>113</sup> Selected examples: a) S. Ortial, H. C. Fisher, J.-L. Montchamp, *J. Org. Chem.* **2013**, *78*, 6599-6608. b) P. Ribierre, K. Bravo-Altamirano, M. I. Antczak, J. D. Hawkins, J.-L. Montchamp, *J. Org. Chem.* **2005**, *70*, 4064-4072.
- <sup>114</sup> L. Coudray, J.-L. Montchamp. *Eur. J. Org. Chem.* **2008**, 3601-3613.
- <sup>115</sup> D. Zhao, R. Wang. *Chem. Soc. Rev.* **2012**, *41*, 2095-2108.
- <sup>116</sup> S. V. Rooy, C. Cao, B. O. Patrick, A. Lam, J. A. Love. *Inorg. Chim. Acta* **2006**, *359*, 2918-2923.
- <sup>117</sup> C. Cao, L. R. Fraser, J. A. Love. *J. Am. Chem. Soc.* **2005**, *127*, 17614-17615.
- <sup>118</sup> C. Hansch, A. Leo, R. W. Taft. *Chem. Rev.* **1991**, *91*, 165-195.
- <sup>119</sup> L. P. Hammett. *J. Am. Chem. Soc.* **1937**, *59*, 96-103.
- <sup>120</sup> a) H. H. Jaffé. *Chem. Rev.* **1953**, *53*, 191-261. b) E. Berliner, M. C. Beckett, E. A. Blommers, B. Newman. *J. Am. Chem. Soc.*, **1952**, *74*, 4940-4944.
- <sup>121</sup> H. H. Jaffé. *Chem. Rev.* **1953**, *53*, 191-261.
- <sup>122</sup> C. Hansch, A. Leo, R. W. Taft. *Chem. Rev.* **1991**, *91*, 165-195.
- <sup>123</sup> R. W. Taft, I. C. Lewis. *J. Am. Chem. Soc.* **1958**, *80*, 2436-2443.
- <sup>124</sup> C. Hansch, A. Leo, R. W. Taft. *Chem. Rev.* **1991**, *91*, 165-195.
- <sup>125</sup> H. S. Gutowsky, D. W. McCall, B. R. McGarvey, L. H. Meyer. *J. Am. Chem. Soc.* **1952**, *74*, 4809-4817.
- <sup>126</sup> R. W. Taft. *J. Am. Chem. Soc.* **1957**, *79*, 1045-1049.
- <sup>127</sup> C. A. Grob, M. G. Schlageter. *Helv. Chim. Acta* **1976**, *59*, 264.
- <sup>128</sup> C. Hansch, A. Leo, R. W. Taft. *Chem. Rev.* **1991**, *91*, 165-195.

- <sup>129</sup> a) F. Rived, M. Rosés, E. Bosch. *Anal. Chim. Acta* **1998**, 374, 309-324. b) E. Bosch, F. Rived, M. Rosés, J. Sales, *J. Chem. Soc., Perkins Trans.*, **1999**, 2, 1953-1958.
- <sup>130</sup> a) D. D. Perrin, B. Dempsey, E. P. Seargeant. *pK<sub>A</sub> Prediction for Organic Acids and Bases*, Chapman and Hall, London, 1981. b) C. Hansch, A. Leo, D. Hoekman. *Exploring QSAR Hydrophobic, Electronic and Steric Constants*, ACS Professional Reference Book, American Chemical Society, Washington, DC, 1995.
- <sup>131</sup> a) W. P. Jencks, K. Salvesen. *J. Am. Chem. Soc.* **1971**, 93, 4433-4436. b) K. N. Dalby, W. P. Jencks. *J. Chem. Soc. Perkin Trans* **1997**, 2, 1555-1563. c) International Union of Pure and Applied Chemistry. *Ionisation Constants of Organic Acids in Aqueous Solution*, Pergamon Press, Oxford, New York, 1979.
- <sup>132</sup> Fenwick, A. *Public Health* 2012, 126, 233-236.
- <sup>133</sup> a) Teixeira, A. R.; Hecht, M. M.; Guimaro, M. C.; Sousa, A. O.; Nitz, N. *Clin. Microbiol. Rev.* **2011**, 24, 592-630. b) Kirchhoff, L. V. *N. Engl. J. Med.* **1993**, 329, 639-644.
- <sup>134</sup> Clayton, J. *Nature* **2010**, 465, S12-S15.
- <sup>135</sup> Schmunis, G. A.; Yadon, Z. E. *Acta Trop.* **2010**, 115, 14-21. b) Schmunis, G. A. *Mem. Inst. Oswaldo Cruz* **2007**, 102, 75-86.
- <sup>136</sup> J. R. Coura, S. L. de Castro, *Mem. Inst. Oswaldo Cruz*, **2002**, 97, 3-24.
- <sup>137</sup> a) Bern, C.; Montgomery, S. P.; Herwaldt, B. L.; Rassi, A., Jr; Marin-Neto, J. A.; Dantas, R. O.; Maguire, J. H.; Acquatella, H.; Morillo, C.; Kirchhoff, L. V.; Gilman, R. H.; Reyes, P. A.; Salvatella, R.; Moore, A. C. *JAMA* **2007**, 298, 2171-2181. b) Castro, J. A.; de Mecca, M. M.; Bartel, L. C. *Hum. Exp. Toxicol.* **2006**, 25, 471-479.

- <sup>138</sup> a) Gorla, N. B.; Ledesma, O. S.; Barbieri, G. P.; Larripa, I. B. *Mutat. Res.* **1989**, *224*, 263-267. b) Kaneshima, E. N.; Castro-Prado, Marialba A. *Mem. Inst. Oswaldo Cruz* **2005**, *100*, 325-330. c) Moraga, A. A.; Graf, U. *Mutagenesis* 1989, *4*, 105-110.
- <sup>139</sup> J. A. Urbina. *Acta Trop.* **2010**, *115*, 55-68.
- <sup>140</sup> a) H.-H. Otto and T. Schirmeister. *Chem. Rev.* **1997**, *97*, 133–171. b) Clayton, J. *Nature* **2010**, *465*, S12-S15. c) Leslie, M. *Science* **2011**, *333*, 933-935. d) McKerrow, J.; Doyle, P.; Engel, J.; Podust, L.; Robertson, S.; Ferreira, R.; Saxton, T.; Arkin, M.; Kerr, I.; Brinen, L.; Craik, C. *Mem. Inst. Oswaldo Cruz* **2009**, *104(Suppl. I)*, 263-269. e) Menezes, C.; Costa, G. C.; Gollob, K. J.; Dutra, W. O. *Drug Dev. Res.* **2011**, *72*, 471-479.
- <sup>141</sup> J. C. Powers,\* J. L. Asgian, O. D. Ekici, and K. E. James. *Chem. Rev.* **2002**, *102*, 4639–4750
- <sup>142</sup> a) Hanzlik, R. P.; Jacober, S. P.; Zygmunt, J. *Biochimica et Biophysica Acta (BBA) -General Subjects* **1991**, *1073*, 33-42. b) Hanzlik, R. P.; Zygmunt, J.; Moon, J. B. *Biochimica et Biophysica Acta (BBA) - General Subjects* **1990**, *1035*, 62-70. c) Li, Z.; Patil, G. S.; Golubski, Z. E.; Hori, H.; Tehrani, K.; Foreman, J. E.; Eveleth, D. D.; Bartus, R. T.; Powers, J. C. *J. Med. Chem.* **1993**, *36*, 3472-3480.
- <sup>143</sup> Eichhold, T. H.; Hookfin, E. B.; Taiwo, Y. O.; De, B.; Wehmeyer, K. R. *J. Pharm. Biomed. Anal.* **1997**, *16*, 459-467.
- <sup>144</sup> a) Simpkins, N. S. *Tetrahedron* **1990**, *46*, 6951-6984. b) Fuchs, P. L.; Braish, T. F. *Chem. Rev.* **1986**, *86*, 903-918.
- <sup>145</sup> J. T. Palmer, D. Rasnick, J. L. Klaus, D. Brömme *J. Med. Chem.* **1995**, *38*, 3193-3196.
- <sup>146</sup> a) Engel, J. C.; Doyle, P. S.; Hsieh, I.; McKerrow, J. H. *J. Exp. Med.* **1998**, *188*, 725-734. b) Jacobsen, W.; Christians, U.; Benet, L. Z. *Drug Metab. Dispos.* **2000**, *28*, 1343-1351.

- <sup>147</sup> Chen, Y. T.; Brinen, L. S.; Kerr, I. D.; Hansell, E.; Doyle, P. S.; McKerrow, J. H.; Roush, W. R. *PLoS Neglected Trop. Dis.* **2010**, *4*, e825.
- <sup>148</sup> J. A. Ellman, T. D. Owens, T. P. Tang, *Acc. Chem. Res.* **2002**, *35*, 984-995.
- <sup>149</sup> M. Wakayuma, J. A. Ellman, *J. Org. Chem.* **2009**, *74*, 2646-2650.
- <sup>150</sup> Reddick, J. J.; Cheng, J.; Roush, W. R. *Org. Lett.* **2003**, *5*, 1967-1970.
- <sup>151</sup> Hiemstra, H.; Wynberg, H. *J. Am. Chem. Soc.* **1981**, *103*, 417-430.
- <sup>152</sup> a) Bernardi, F.; Bottoni, A.; Rossi, I.; Robb, M. A. *J. Mol. Struct.* 1993, *300*, 157-169. b) Rosenberg, R. E. *J. Org. Chem.* 1998, *63*, 5562-5567
- <sup>153</sup> a) Bernadi, F.; Csizmadia, I. G.; Mangini, A.; Schlegel, H. B.; Whangbo, M.-H.; Wolfe, S. *J. Am. Chem. Soc.* **1975**, *97*, 2209-2218. b) Lehn, J.-M.; Wipff, G. *J. Am. Chem. Soc.* **1976**, *98*, 7498-7505. c) Borden, W. T.; Davidson, E. R.; Anderson, N. H.; Denniston, A. D.; Epiotis, N. D. *J. Am. Chem. Soc.* **1978**, *100*, 1604-1605. d) Bernadi, F.; Bottoni, A.; Venturini, A.; Mangini, A. *J. Am. Chem. Soc.* **1986**, *108*, 8171-8175.
- <sup>154</sup> W. R. Roush, S. L. Gwaltney II, J. Cheng, K. A. Scheidt, J. H. McKerrow, E. Hansell, *J. Am. Chem. Soc.* **1998**, *120*, 10994-10995.
- <sup>155</sup> (a) Bratz, M. ; Bullock, W.H. ; Overman, L. E. ; Takemoto, T. *J. Am. Chem. Soc.* **1995**, *117*, 5958-5966. (b) Pearson, W. H. ; Lee, I. Y. ; Mi, Y. ; Stoy, P. *J. Am. Chem. Soc.* **2001**, *123*, 6724-6725. (c) Pearson, W. H. ; Lee, I. Y. ; Mi, Y. ; Stoy, P. *J. Org. Chem.* **2004**, *69*, 9109-9122. (d) Mizuno, H. ; Domon, K. ; Masuya, K. ; Tanino, K. ; Kuwajima, I. *J. Org. Chem.* **1999**, *64*, 2648-2656.
- <sup>156</sup> a) J. Legros, J. R. Dehli, C. Bolm. *Adv. Synth. Catal.* **2005**, *347*, 19-31. b) J. M. Shin, Y. M. Cho, G. Sachs. *J. Am. Chem. Soc.* **2004**, *126*, 7800-7811.

- <sup>157</sup> Jacobsen, W.; Christians, U.; Benet, L. Z. *Drug Metab. Dispos.* **2000**, *28*, 1343-1351.
- <sup>158</sup> Ramana, M. V. *et al. J. Med. Chem.* Available ASAP.
- <sup>159</sup> (a) Bäckvall, Jan-E.; Ericsson, A. *J. Org. Chem.* **1994**, *59*, 5850-5851. (b) Barton, D. H. R.; Li, W.; Smith, J. A. *Tetrahedron Letters* **1998**, *39*, 7055-7058. (c) DesMarteau, D. D.; Petrov, V. A.; Montanari, V.; Pregnotato, M.; Resnati, G. *J. Org. Chem.* **1994**, *59*, 2762-2765. (d) Ali, M. H.; Bohnert, G. J. *Synthetic Communications* **1998**, *28*, 2983-2998. (e)
- <sup>160</sup> Selected publications: (a) Posner, T. *Ber. Dtsch. Chem. Ges.* **1905**, *38*, 646. (b) Kondoh, A.; Takami, K.; Yorimitsu, H.; Oshima, K. *J. Org. Chem.* **2005**, *70*, 6468. (c) Bader, H.; Cross, L. C.; Heilbron, I.; Jones, E. R. H. *J. Chem. Soc.* **1949**, 619. (d) Behringer, H. *Justus Liebigs Ann. Chem.* **1949**, *564*, 219.
- <sup>161</sup> (a) Hegedus, L. L.; McCabe, R. W. *Catalyst Poisoning*; Marcel Dekker; New York, 1984. (b) J. K. Dunleavy. *Platinum Metals Rev.* **2006**, *50*, 110.
- <sup>162</sup> a) Keim, W. *J. Organomet. Chem.* **1968**, *14*, 179–184. b) Barcelo, F. L.; Besteiro, J. C.; Lahuerta, P.; Foces-Foces, C.; Cano, F. H.; Martinez-Ripoll, M. *J. Organomet. Chem.* **1984**, *270*, 343–351. c) Knobler, C. B.; King, R. E., III.; Hawthorne, M. F. *Acta Crystallogr., Sect. C* **1986**, *C42*, 159–161. d) Barcelo, F.; Lahuerta, P.; Ubeda, M. A.; Foces-Foces, C.; Cano, F. H.; Marti´nez-Ripoll, M. *J. Organomet. Chem.* **1986**, *301*, 375–384. e) Barcelo, F.; Lahuerta, P.; Ubeda, M. A.; Cantarero, A.; Sanz, F. *J. Organomet. Chem.* **1986**, *309*, 199–208. f) Bianchini, C.; Masi, D.; Meli, A.; Peruzzini, M.; Zanolini, F. *J. Am. Chem. Soc.* **1988**, *110*, 6411–6423. g) Lahuerta, P.; Latorre, J.; Marti´nez-Manez, R.; Garcia-Granda, S.; Gomez-Beltran, F. *Inorg. Chim. Acta* **1990**, *168*, 149–152. h) Lahuerta, P.; Latorre, J.; Marti´nez-Manez, R.; Paya, J.; Tiripicchio, A.; Tiripicchio Camellini, M. *Inorg. Chim. Acta* **1993**, *209*, 177–186. (i)

- Bennett, M. A.; Bhargava, S. K.; Ke, M.; Willis, A. C. *J. Chem. Soc., Dalton Trans.* **2000**, 3537–3545. j) Y. Fukumoto, H. Asai, M. Shimizu, N. Chatani. *J. Am. Chem. Soc.* **2007**, *129*, 13792–13793. k) Cao, C.; Wang, T.; Patrick, B. O.; Love, J. A. *Organometallics* **2006**, *25*, 1321–1324.
- <sup>163</sup> F. Alonso, I. P. Beletskaya, M. Yus. *Chem. Rev.* **2004**, *104*, 3079–3159.
- <sup>164</sup> a) S. A. Svejda, M. Brookhart. *Organometallics* **1999**, *18*, 65–74. b) S. A. Svejda, L. K. Johnson, M. Brookhart. *J. Am. Chem. Soc.* **1999**, *121*, 10634–10635. c) J. W. Tye, J. F. Hartwig. *J. Am. Chem. Soc.* **2009**, *131*, 14703–14712.
- <sup>165</sup> (a) Kuniyasu, H.; Ogawa, A.; Sato, K.-I.; Ryu, I.; Kambe, N. Sonoda, N. *J. Am. Chem. Soc.* **1992**, *114*, 5902. (b) Ogawa, A.; Ikeda, T.; Kimura, K.; Hirao, T. *J. Am. Chem. Soc.* **1999**, *121*, 5108. (c) Malyshev, D. A.; Scott, N. M.; Marion, N.; Stevens, E. D.; Ananikov, V. P.; Beletskaya, I. P., Nolan, S. (d) Weiss, C. J.; Marks, T. J. *J. Am. Chem. Soc.* **2010**, *132*, 10533. (e) Weiss, C. J.; Wobser, S. D.; Marks, T. J. *Organometallics* **2010**, *29*, 6308
- <sup>166</sup> Misumi, Y.; Seino, H.; Mizobe, Y. *J. Organomet. Chem.* **2006**, *691*, 3157
- <sup>167</sup> a) A. Di Giuseppe, R. Castarlenas, J. J. Pérez-Torrente, M. Crucianelli, V. Polo, R. Sancho, F. J. Lahoz, L. A. Oro. *J. Am. Chem. Soc.* **2012**, *134*, 8171–8183. b) L. Palacios, M. J. Artigas, V. Polo, F. J. Lahoz, R. Castarlenas, J. J. Pérez-Torrente, L. A. Oro. *ACS Catal.* **2013**, *3*, 2910–2919.
- <sup>168</sup> a) H. Seino, T. Yoshikawa, M. Hidai, Y. Mizobe, *Dalton Trans.* **2004**, 3593. b) S. Nagao, H. Seino, M. Hidai, Y. Mizobe, *Dalton Trans.* **2005**, 3166.
- <sup>169</sup> Shiva Shoai. PhD. Dissertation, Univeristy of British Columbia, 2010.
- <sup>170</sup> Chris Tehennepe, B.Sc., University of British Columbia, 2012.

- <sup>171</sup> a) D. G. Blackmond. *Angew. Chem. Int. Ed.* **2005**, *44*, 4302-4320. b) J. S. Mathew, M. Klussmann, H. Iwamura, F. Valera, A. Futran, E. A. C. Emanuelsson, D. G. Blackmond. *J. Org. Chem.* **2006**, *71*, 4711-4722.
- <sup>172</sup> Parkin, G. *Acc. Chem. Res.* **2009**, *42*(2), 315.
- <sup>173</sup> Northcutt, T. O.; Wick, D. D.; Vetter, A. J.; Jones, W.D. *J. Am. Chem. Soc.* **2001**, *123*, 7257.
- <sup>174</sup> Hansch, C.; Leo, A.; Taft, R. W. *Chem. Rev.* **1991**, *97*, 165.
- <sup>175</sup> M. Gómez-Gallego, M. A. Sierra. *Chem. Rev.* **2011**, *111*, 4857-4963.
- <sup>176</sup> J. W. Tye, J. F. Hartwig, *J. Am. Chem. Soc.* **2009**, *131*, 14703-14712.
- <sup>177</sup> S. May, P. Reinsalu, J. Powell. *Inorg. Chem.* **1980**, *19*, 1582-1589.
- <sup>178</sup> B. Y.-W. Man, A. Knuhtsen, M. J. Page, B. A. Messerle. *Polyhedron*, **2013**, *61*, 248-252.
- <sup>179</sup> a) M. Gómez-Gallego, M. A. Sierra. *Chem. Rev.* **2011**, *111*, 4857-4963. b) G. Parkin. *Acc. Chem. Res.* **2009**, *42*, 315.
- <sup>180</sup> T. O. Northcutt, D. D. Wick, A. J. Vetter, W. D. Jones. *J. Am. Chem. Soc.* **2001**, *123*, 7257-7270.
- <sup>181</sup> a) D. D. Wick, K. A. Reynolds, W. D. Jones. *J. Am. Chem. Soc.* **1999**, *121*, 3974-3983. b) T. O. Northcutt, D. D. Wick, A. J. Vetter, W. D. Jones. *J. Am. Chem. Soc.* **2001**, *123*, 7257-7270. c) M. P. Jensen, D. D. Wick, S. Reinartz, P. S. White, J. L. Templeton, K. I. Goldberg. *J. Am. Chem. Soc.* **2003**, *125*, 8614-8624. d) W. D. Jones, E. T. Hessel. *J. Am. Chem. Soc.* **1992**, *114*, 6087-6095. e) M. Gómez-Gallego, M. A. Sierra. *Chem. Rev.* **2011**, *111*, 4857-4963. f) G. Parkin. *Acc. Chem. Res.* **2009**, *42*, 315.
- <sup>182</sup> a) T. O. Northcutt, D. D. Wick, A. J. Vetter, W. D. Jones. *J. Am. Chem. Soc.* **2001**, *123*, 7257-7270. b) W. D. Jones. *Acc. Chem. Res.* **2003**, *36*, 140.

- <sup>183</sup> W. D. Jones, *Acc. Chem. Res.* **2003**, *36*, 140-146.
- <sup>184</sup> a) T. O. Northcutt, D. D. Wick, A. J. Vetter, W. D. Jones. *J. Am. Chem. Soc.* **2001**, *123*, 7257-7270. b) W. D. Jones, F. J. Feher. *J. Am. Chem. Soc.* **1986**, *108*, 4814-4819.
- <sup>185</sup> W. D. Jones, E. T. Hessel. *J. Am. Chem. Soc.* **1992**, *114*, 6087-6095.
- <sup>186</sup> Cao, C.; Wang, T.; Patrick, B. O.; Love, J. A. *Organometallics* **2006**, *25*, 1321-1324.
- <sup>187</sup> a) Vetter, A. J.; Rieth, R. D.; Jones, W. D. *PNAS* **2007**, *104*, 6957. b) Y. Jiao, M. E. Evans, J. Morris, W. W. Brennessel, W. D. Jones. *J. Am. Chem. Soc.* **2013**, *135*, 6994-7004.
- <sup>188</sup> S. May, P. Reinsalu, J. Powell. *Inorg. Chem.* **1980**, *19*, 1582-1589.
- <sup>189</sup> D. D. Wick, W. D. Jones. *Inorg. Chem.* **1997**, *36*, 2723-2729.
- <sup>190</sup> U. E. Bucher, T. Lengweiler, D. Nanz, W. von Philipsborn, L. M. Venanzi. *Angew. Chem. Int. Ed.* **1990**, *29*, 548-549.
- <sup>191</sup> A. Albinati, U. E. Bucher, V. Gramlich, O. Renn, H. Rügger, L. M. Venanzi. *Inorg. Chim. Acta* **1999**, *284*, 191-204.
- <sup>192</sup> a) D. D. Wick, K. A. Reynolds, W. D. Jones. *J. Am. Chem. Soc.* **1999**, *121*, 3974-3983. b) T. O. Northcutt, D. D. Wick, A. J. Vetter, W. D. Jones. *J. Am. Chem. Soc.* **2001**, *123*, 7257-7270.
- <sup>193</sup> D. D. Wick, W. D. Jones. *Inorg. Chim. Acta* **2009**, *362*, 4416-4421.
- <sup>194</sup> C. K. Ghosh, W. A. G. Graham. *J. Am. Chem. Soc.* **1987**, *109*, 4726-4727.
- <sup>195</sup> a) P. E. Bloyce, J. Mascetti, A. J. Rest. *J. Organomet. Chem.* **1993**, *444*, 223-233. b) A. A. Purwoko, A. J. Lees. *Inorg. Chem.* **1995**, *34*, 424-425. c) A. J. Blake, M. W. George, M. B. Hall, J. McMaster, P. Portius, X. Z. Sun, M. Towrie, C. E. Webster, C. Wilson, S. D. Zarić. *Organometallics* **2008**, *27*, 189-201.

- <sup>196</sup> a) D. D. Wick, W. D. Jones. *Inorg. Chim. Acta.* **2009**, *362*, 4416-4421. b) T. Tanabe, M. E. Evans, W. W. Brennessel, W. D. Jones. *Organometallics* **2011**, *30*, 834-843.
- <sup>197</sup> E. T. Hessel, W. D. Jones. *Organometallics* **1992**, *11*, 1496-1505. b) D. D. Wick, W. D. Jones. *Organometallics* **1999**, 495-505. c) A. J. Vetter, R. D. Rieth, W. D. Jones. *Proc. Natl. Acad. Sci. U.S.A.* **2007**, *104*, 6957-6962. d) Y. Jiao, M. E. Evans, J. Morris, W. W. Brennessel, W. D. Jones. *J. Am. Chem. Soc.* **2013**, *135*, 6994-7004.
- <sup>198</sup> B. Procacci, Y. Jiao, M. E. Evans, W. D. Jones, R. N. Perutz, A. C. Whitwood. *J. Am. Chem. Soc.* **2015**, *137*, 1258-1272.
- <sup>199</sup> D. D. Wick, W. D. Jones. *Inorg. Chem.* **1997**, *36*, 2723-2729.
- <sup>200</sup> a) T. Tanabe, M. E. Evans, W. W. Brennessel, W. D. Jones. *Organometallics*, **2011**, 834-843. b) Y. Jiao, J. Morris, W. W. Brennessel, W. D. Jones. *J. Am. Chem. Soc.* **2013**, *135*, 16198-16212. c) Y. Jiao, W. W. Brennessel, W. D. Jones. *Organometallics* **2015**, *34*, 1552-1566. d) B. Procacci, Y. Jiao, M. E. Evans, W. D. Jones, R. N. Perutz, A. C. Whitwood. *J. Am. Chem. Soc.* **2015**, *137*, 1258-1272.
- <sup>201</sup> Correspondence with Dr. W. D. Jones of the University of Rochester and graduate student Jing Yuwen of the Jones group.
- <sup>202</sup> Y. Jiao, J. Morris, W. W. Brennessel, W. D. Jones. *J. Am. Chem. Soc.* **2013**, *135*, 16198-16212.
- <sup>203</sup> Y. Jiao, J. Morris, W. W. Brennessel, W. D. Jones. *J. Am. Chem. Soc.* **2013**, *135*, 16198-16212.
- <sup>204</sup> D. D. Wick, K. A. Reynolds, W. D. Jones. *J. Am. Chem. Soc.* **1999**, *121*, 3974-3983.

- <sup>205</sup> a) D. D. Wick, K. A. Reynolds, W. D. Jones. *J. Am. Chem. Soc.* **1999**, *121*, 3974-3983. b) T. O. Northcutt, D. D. Wick, A. J. Vetter, W. D. Jones. *J. Am. Chem. Soc.* **2001**, *123*, 7257-7270.
- <sup>206</sup> B. Procacci, Y. Jiao, M. E. Evans, W. D. Jones, R. N. Perutz, A. C. Whitwood. *J. Am. Chem. Soc.* **2015**, *137*, 1258-1272.
- <sup>207</sup> C. Cao, L. R. Fraser, J. A. Love. *J. Am. Chem. Soc.* **2005**, *127*, 17614-17615.
- <sup>208</sup> S. Shaoi, P. Bichler, B. Kang, H. Buckley, J. A. Love. *Organometallics* **2007**, *26*, 5778-5781.
- <sup>209</sup> a) Kuniyasu, H.; Ogawa, A.; Sato, K.-I.; Ryu, I.; Kambe, N. Sonoda, N. *J. Am. Chem. Soc.* **1992**, *114*, 5902. b) Ogawa, A. *J. Organomet. Chem.* **2000**, *611*, 463. c) Ananikov, V. P.; Malyshev, D. A.; Beletskaya, I. P.; Aleksandrov, G. G.; Eremenko, I. L. *Adv. Synth. Catal.* **2005**, *347*, 1993. d) Malyshev, D. A.; Scott, N. M.; Marion, N.; Stevens, E. D.; Ananikov, V. P.; Beletskaya, I. P., Nolan, S. P. *Organometallics* **2006**, *25*, 4462-4470. e) Misumi, Y.; Seino, H.; Mizobe, Y. *J. Organomet. Chem.* **2006**, *691*, 3157. f) Weiss, C. J.; Marks, T. J. *J. Am. Chem. Soc.* **2010**, *132*, 10533. g) Weiss, C. J.; Wobser, S. D.; Marks, T. J. *Organometallics* **2010**, *29*, 6308.
- <sup>210</sup> a) Ogawa, A.; Ikeda, T.; Kimura, K.; Hirao, T. *J. Am. Chem. Soc.* **1999**, *121*, 5108. b) Ogawa, A. *J. Organomet. Chem.* **2000**, *611*, 463. c) Shaoi, S.; Bichler, P.; Kang, B.; Buckley, H.; Love, J. A. *Organometallics* **2007**, *26*, 5778-5781. d) A. Di Giuseppe, R. Castarlenas, J. J. Pérez-Torrente, M. Crucianelli, V. Polo, R. Sancho, F. J. Lahoz, L. A. Oro, *J. Am. Chem. Soc.* **2012**, *134*, 8171-8183. e) L. Palacios, M. J. Artigas, V. Polo, F. J. Lahoz, R. Castarlenas, J. J. Pérez-Torrente, L. A. Oro. *ACS Catal.* **2013**, *3*, 2910-2919.
- <sup>211</sup> A. Ogawa, T. Ikeda, K. Kimura, T. Hirao. *J. Am. Chem. Soc.* **1999**, *121*, 5108-5114.
- <sup>212</sup> S. Van Rooy, C. Cao, B. O. Patrick, A. Lam, J. A. Love. *Inorg. Chim. Acta* **2006**, *359*, 2918-2923.

- <sup>213</sup> a) L. R. Fraser, J. Bird, Q. Wu, C. Cao, B. O. Patrick, J. A. Love. *Organometallics* **2007**, *26*, 5602-5611. b) Lauren R. Fraser, M.Sc. Dissertation, University of British Columbia, 2007.
- <sup>214</sup> S. Trofimenko. *Chem. Rev.* **1993**, *93*, 943-980.
- <sup>215</sup> a) M. G. Organ, M. Abdel-Hadi, S. Avola, N. Hadei, J. Nasielski, C. J. O'Brien, C. Valente. *Chem. Eur. J.* **2007**, *13*, 150-157. b) S. Çalimsiz, M. Sayah, D. Mallik, M. G. Organ. *Angew. Chem. Int. Ed.* **2010**, *49*, 2014-2017. c) L. Wu, E. Drinkel, F. Gaggia, S. Capolicchio, A. Linden, L. Falivene, L. Cavallo, R. Dorta. *Chem. Eur. J.* **2011**, *17*, 12886-12890. d) Q. Zhao, C. Li, C. H. Senanayake, W. Tang. *Chem. Eur. J.* **2013**, *19*, 2261-2265. e) G. Bastug, S. P. Nolan. *Organometallics* **2014**, *33*, 1253-1258.
- <sup>216</sup> D. E. Butler, H. A. DeWald. *J. Org. Chem.* **1975**, *40*, 1353-1355.
- <sup>217</sup> S. Trofimenko. *J. Am. Chem. Soc.* **1966**, *88*, 1842-1844.
- <sup>218</sup> J. F. Dunne, J. Su, A. Ellern, A. D. Sadow. *Organometallics* **2008**, *27*, 2399-2401
- <sup>219</sup> Cao, C.; Wang, T.; Patrick, B. O.; Love, J. A. *Organometallics* **2006**, *25*, 1321-1324.

# Appendix A. Sample Spectra and Concentration Plots for the Michael Addition of 2-phenethanethiol to Substituted Vinyl Sulfones

## A.1 Addition of 2-phenethanethiol to *para*-methoxy-substituted vinyl sulfone

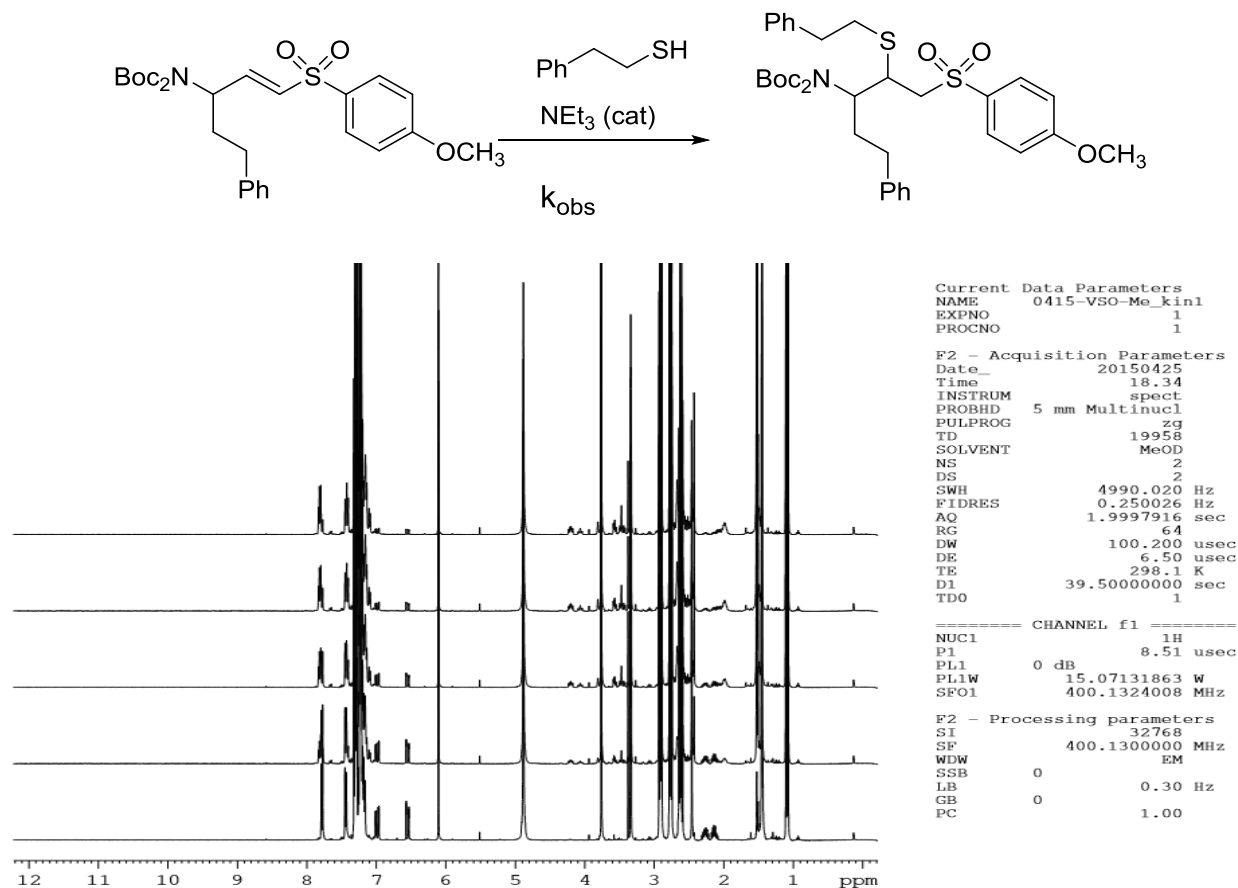
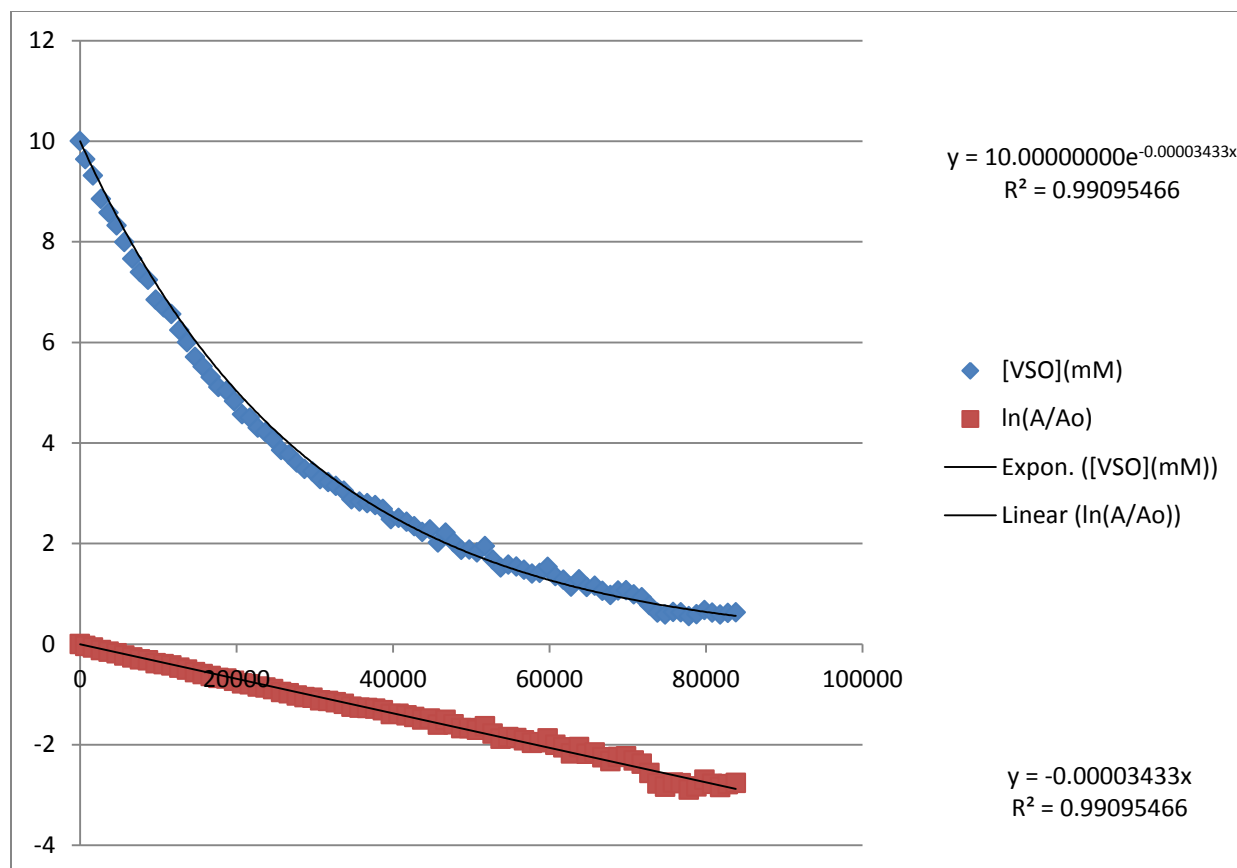


Figure A.1. <sup>1</sup>H NMR Spectra for the Addition of 2-phenethanethiol to *para*-methoxy-substituted vinyl sulfone.

Spectra were recorded, from bottom to top, at  $t = 15$  min, 5 hr 30 min, 11 hr, 16 hr 30 min, and 23 hr. Diagnostic vinylic resonances (7.0 ppm, 6.5 ppm) were integrated relative to the internal standard, trimethoxybenzene (6.1 ppm).



**Figure A.2. Time-course plot for disappearance of starting material for the addition of 2-phenethanethiol to *para*-methoxy-substituted vinyl sulfone.**

## A.2 Addition of 2-phenethanethiol to *para*-methyl-substituted vinyl sulfone

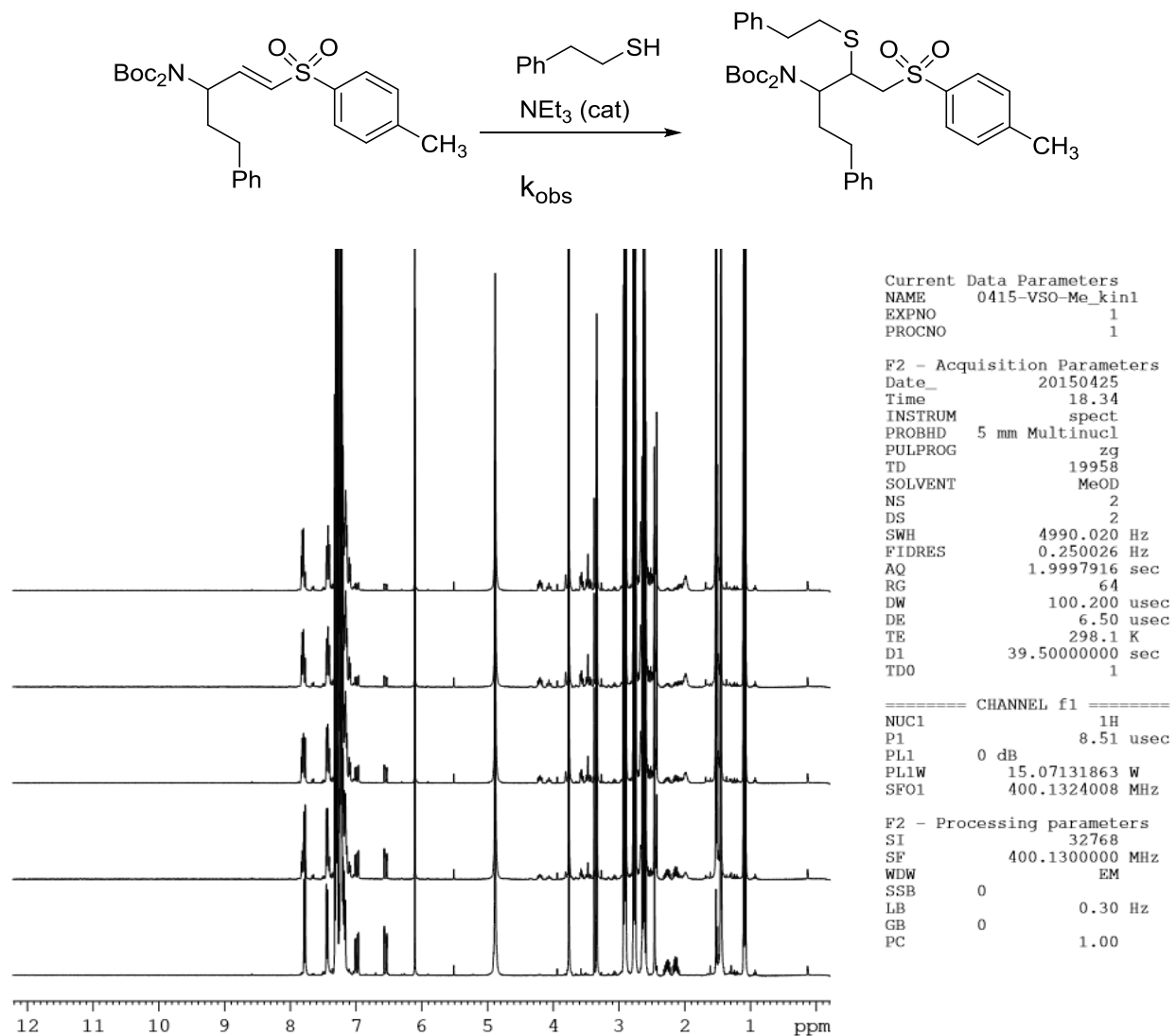


**Figure A.3.**  $^1\text{H}$  NMR Spectra for the Addition of 2-phenethanethiol to *para*-methyl-substituted vinyl sulfone

Spectra were recorded, from bottom to top, at  $t = 15$  min, 2 hr 45 min, 5 hr 30 min, 8 hr 15 min, and 11 hr. Diagnostic vinylic resonances (7.0 ppm, 6.5 ppm) were integrated relative to the internal standard, trimethoxybenzene (6.1 ppm).

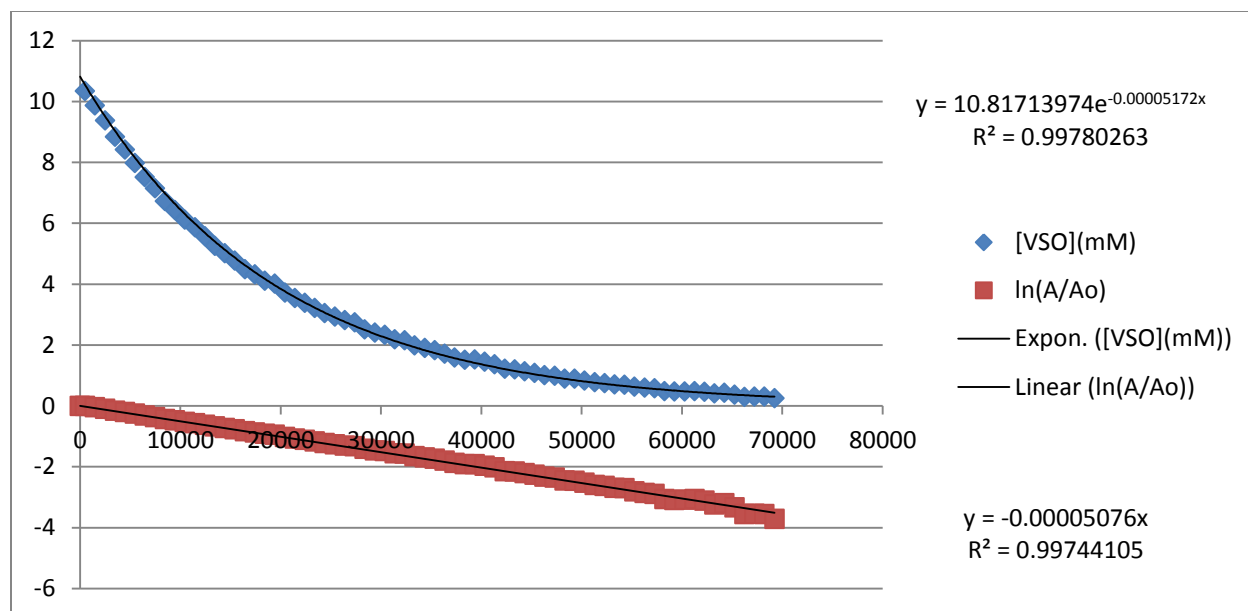


**Figure A.4.** Time-course plot for disappearance of starting material for the addition of 2-phenethanethiol to *para*-methyl-substituted vinyl sulfone.

### A.3 Addition of 2-phenethanethiol to parent vinyl sulfone

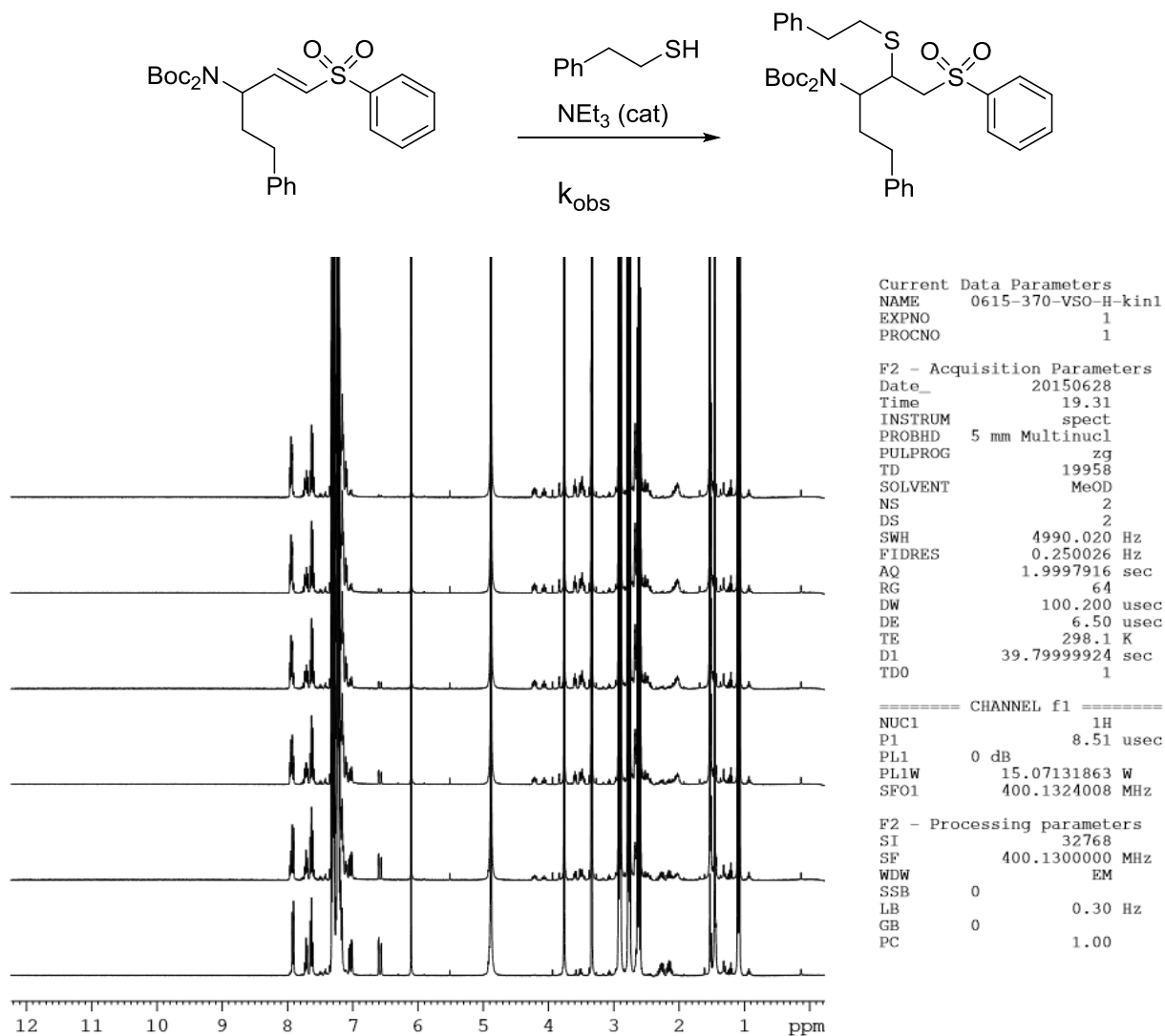


**Figure A.5.** <sup>1</sup>H NMR spectra for the addition of 2-phenethanethiol to parent vinyl sulfone.

Spectra were recorded, from bottom to top, at  $t = 15$  min, 1 hr 55 min, 3 hr 40 min, 5 hr 25 min, 7 hr 10 min, and 8 hr 55 min. Diagnostic vinylic resonance (6.6 ppm) was integrated relative to the internal standard, trimethoxybenzene (6.1 ppm).

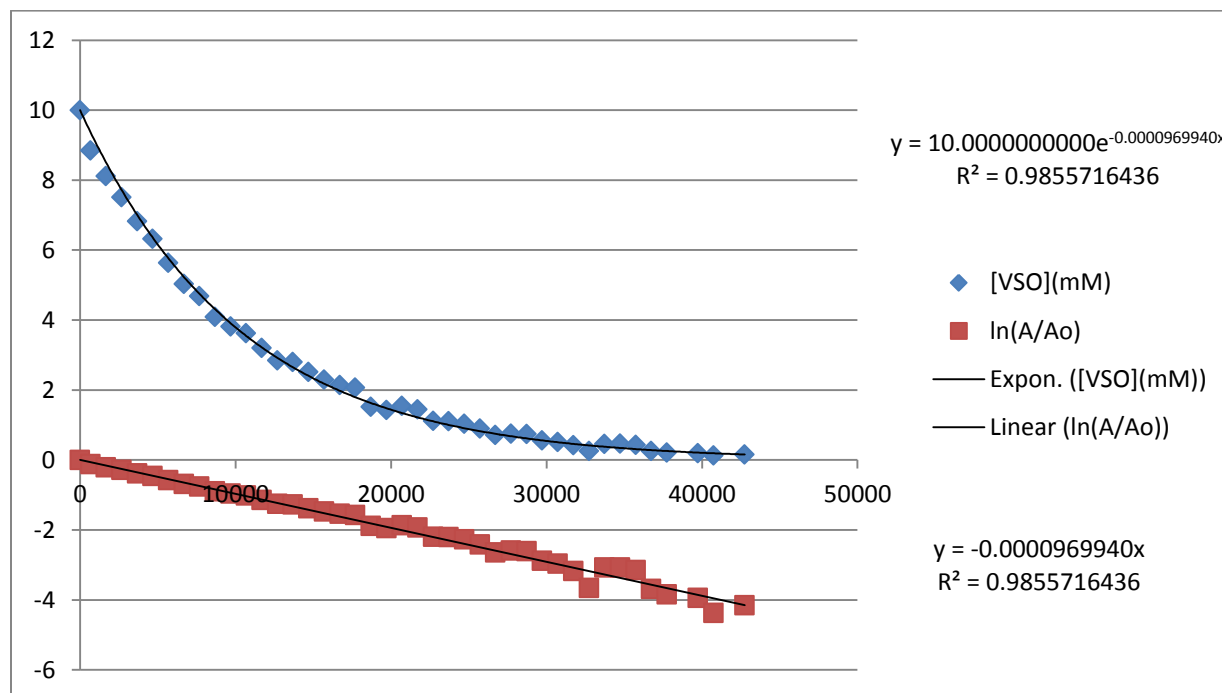


**Figure A.6. Time course plots of the disappearance of starting material for the addition of 2-phenethanethiol to parent vinyl sulfone.**

#### A.4 Addition of 2-phenethanethiol to *para*-chloro-substituted vinyl sulfone

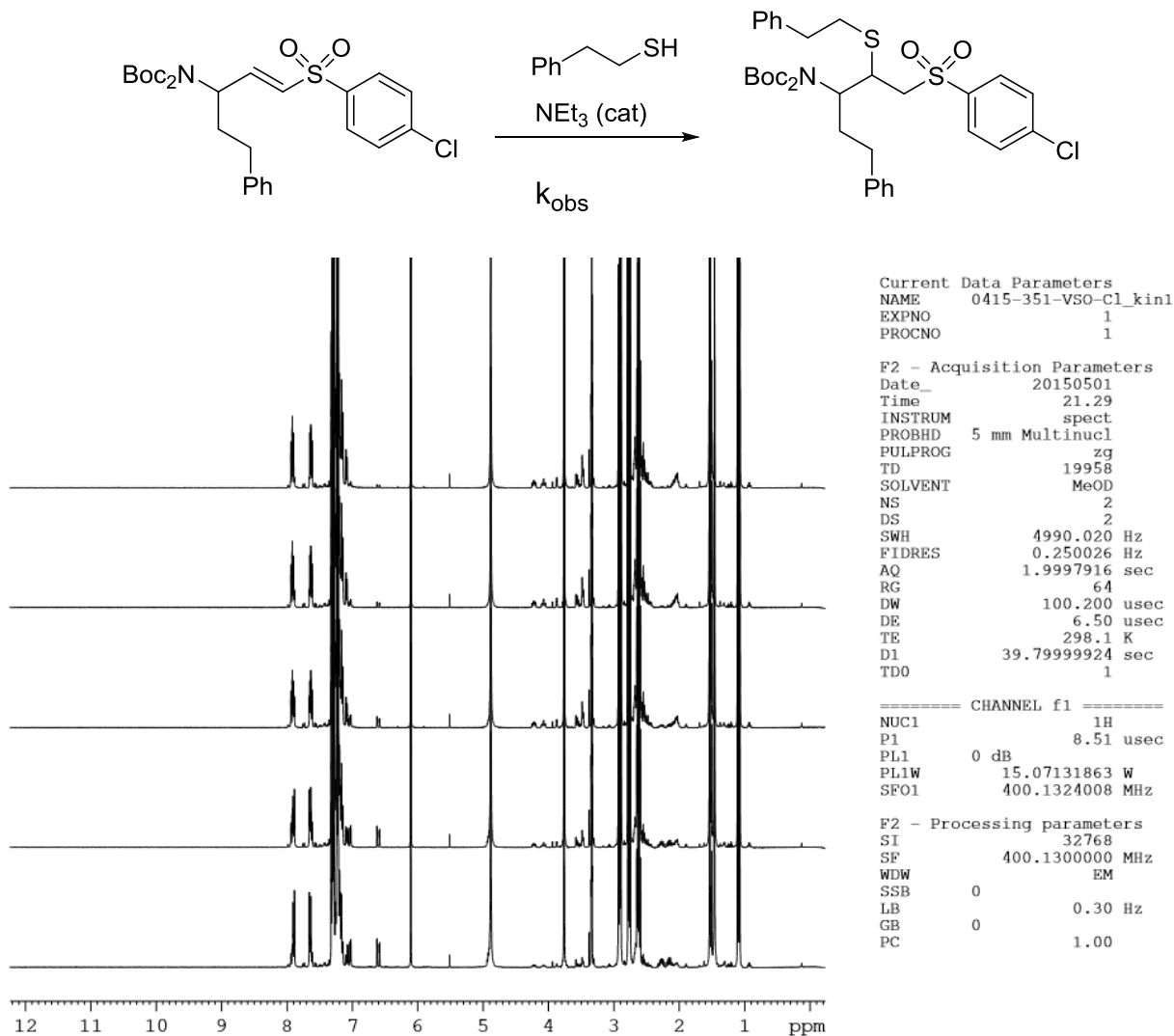


**Figure A.7.**  $^1\text{H}$  NMR spectra for the addition of 2-phenethanethiol to *para*-chloro-substituted vinyl sulfone.

Spectra were recorded, from bottom to top, at  $t = 15$  min, 30 min, 1 hr, 1 hr 15 min and 1 hr 30 min. Diagnostic vinylic resonance (6.6 ppm) was integrated relative to the internal standard, trimethoxybenzene (6.1 ppm).

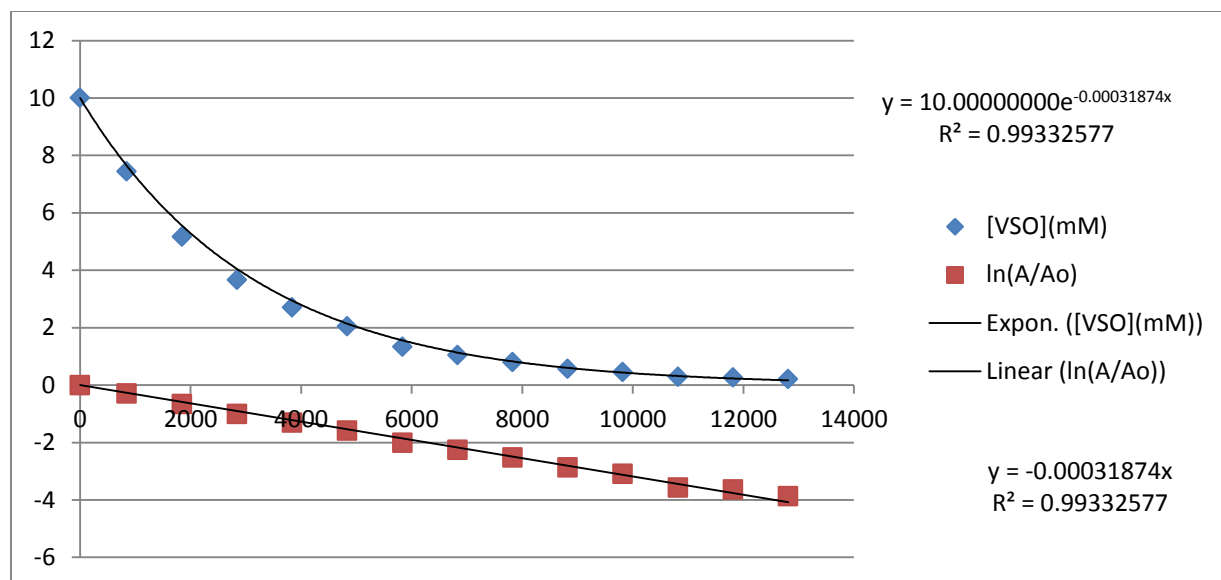


**Figure A.8. Time-course plots for the disappearance of starting material for the addition of 2-phenethanethiol to *para*-chloro-substituted vinyl sulfone.**

### A.5 Addition of 2-phenethanethiol to *para*-bromo-substituted vinyl sulfone

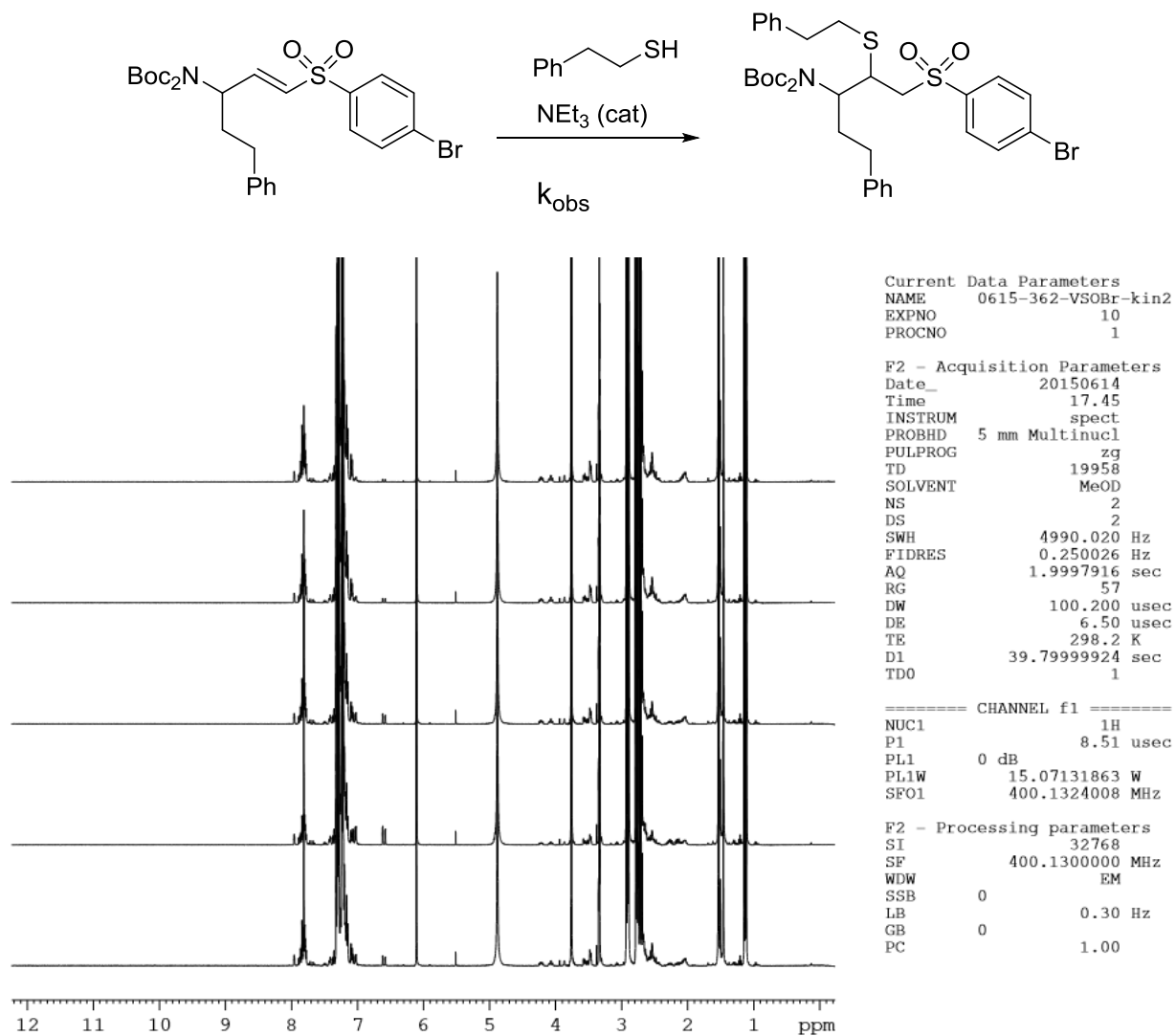


**Figure A.9.**  $^1\text{H}$  NMR spectra for the addition of 2-phenethanethiol to *para*-bromo-substituted vinyl sulfone.

Spectra were recorded, from bottom to top, at  $t = 15$  min, 1 hr 20 min, 2 hr 45 min, 4 hr 10 min, and 5 hr 35 min. Diagnostic vinylic resonance (6.6 ppm) was integrated relative to the internal standard, trimethoxybenzene (6.1 ppm).

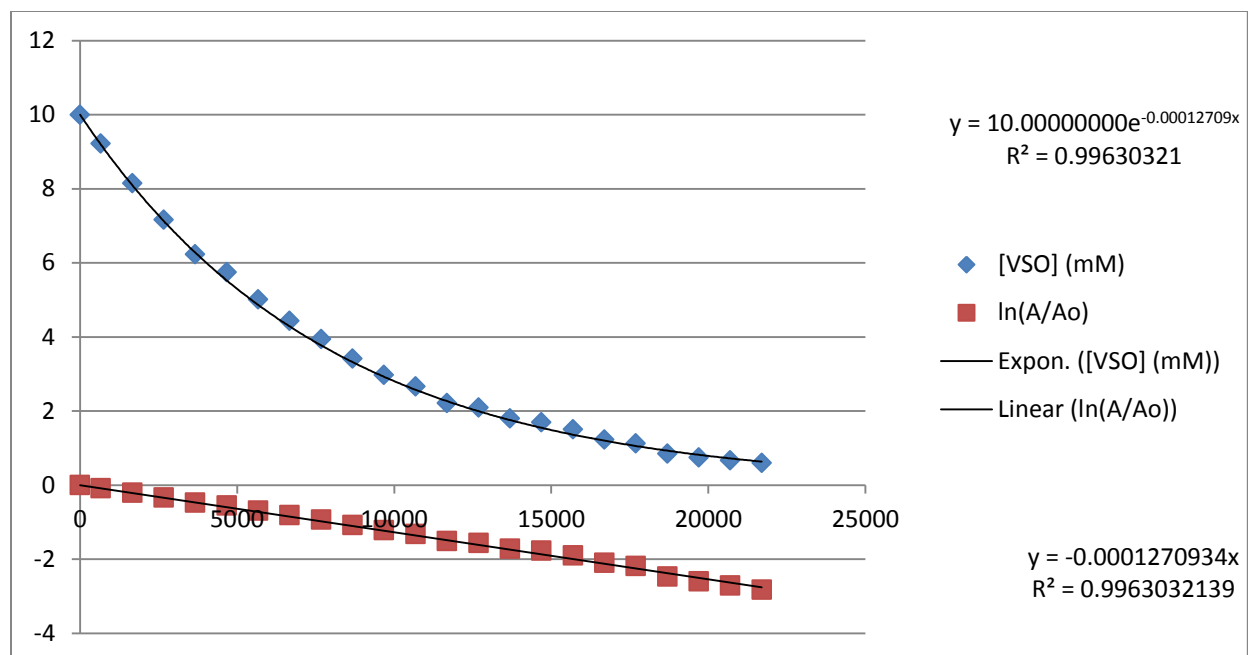


**Figure A.10.** Time-course plot for the disappearance of starting material for the addition of 2-phenethanethiol to *para*-bromo-substituted vinyl sulfone.

**A.6 Addition of 2-phenethanethiol to *para*-trifluoromethyl-substituted vinyl sulfone sulfone**

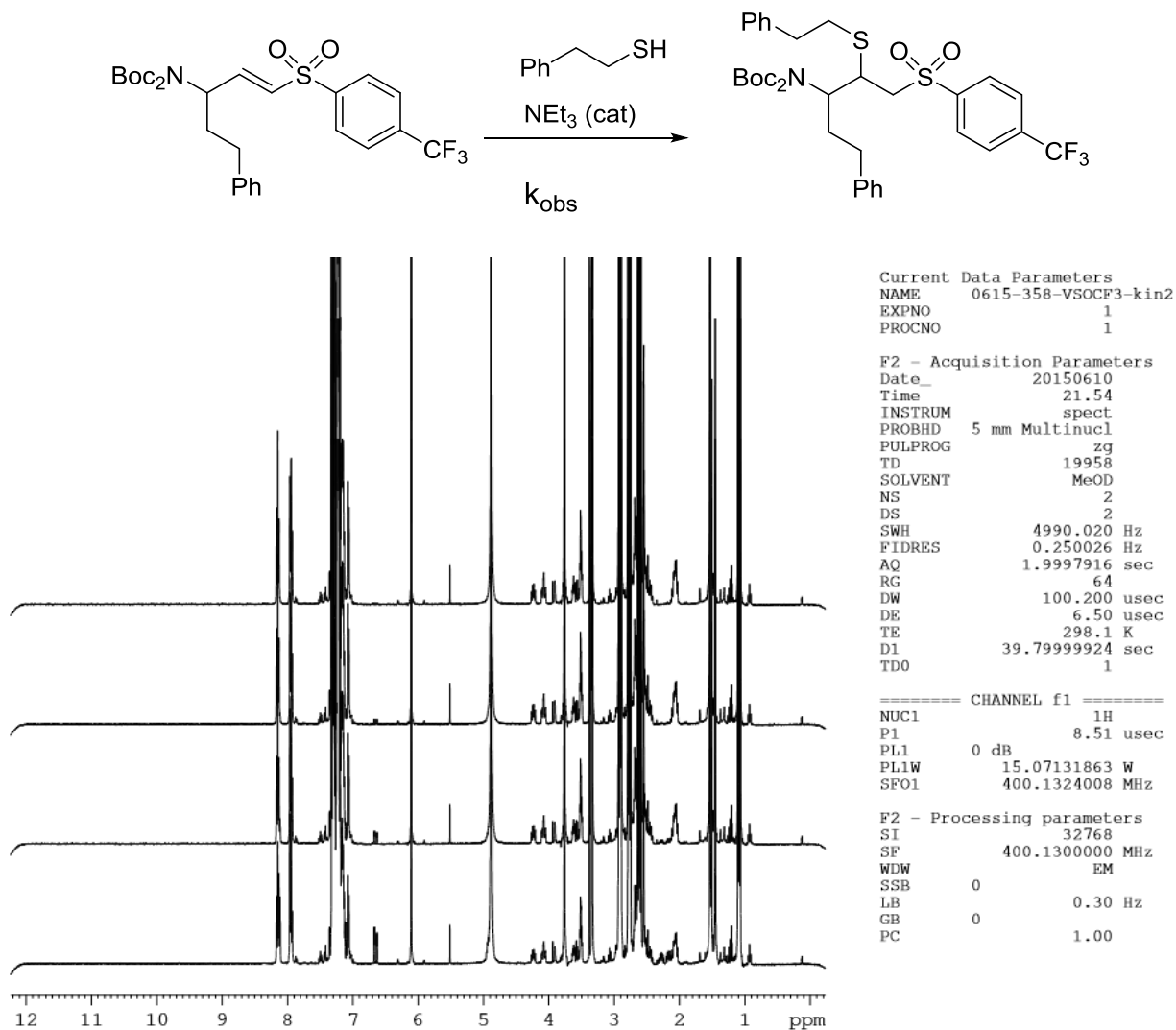


**Figure A.11.** <sup>1</sup>H NMR spectra for the addition of 2-phenethanethiol to *para*-trifluoromethyl-substituted vinyl sulfone.

Spectra were recorded, from bottom to top, at  $t = 15$  min, 30 min, 45 min, and 1 hr. Diagnostic vinylic resonance (6.7 ppm) was integrated relative to the internal standard, trimethoxybenzene (6.1 ppm).

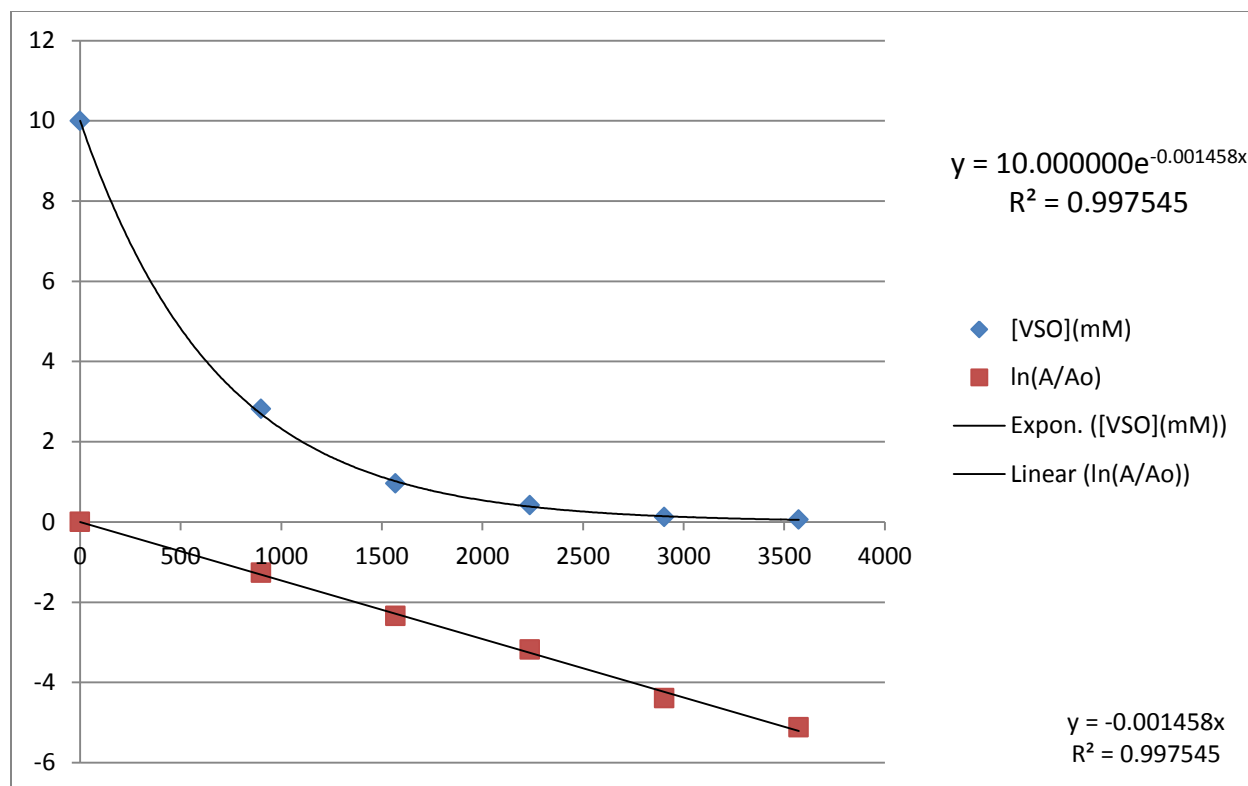


**Figure A.12.** Time-course plot for the disappearance of starting material for the addition of **2-phenethanethiol** to *para*-trifluoromethyl-substituted vinyl sulfone.

## Appendix B. Sample Spectra and Concentration Plots for Alkyne Hydrothiolation Catalyzed by $[\text{Tp}^*\text{Rh}(\text{PPh}_3)_2]$

### B.1 $[\text{Tp}^*\text{Rh}(\text{PPh}_3)_2]$ catalyzed hydrothiolation of phenylacetylene with *para*-methoxythiophenol

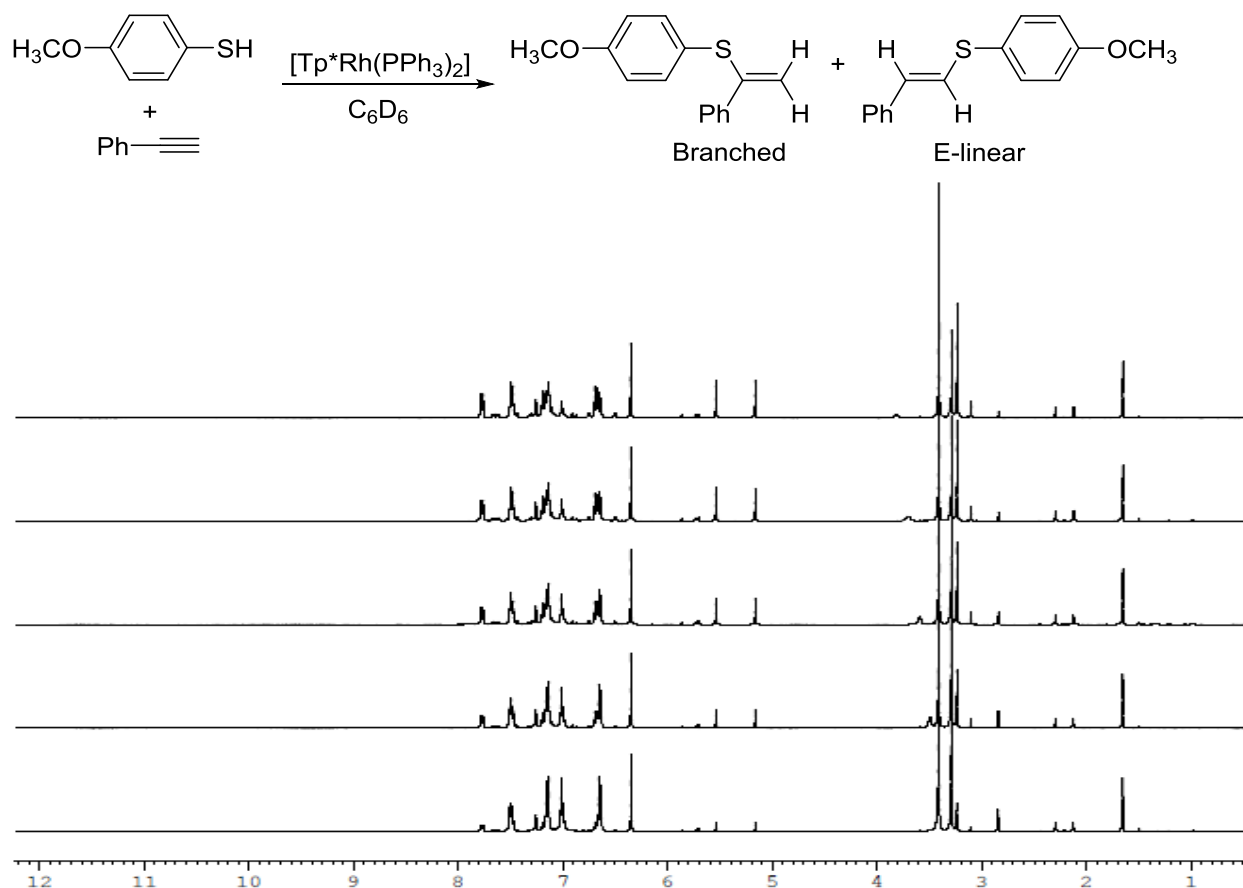
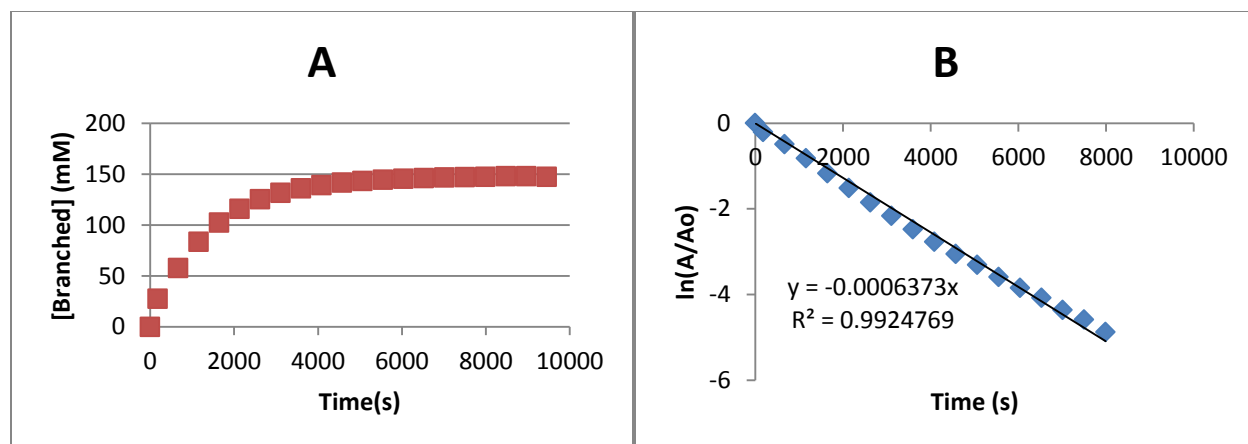


Figure B.1.  $^1\text{H}$  NMR spectra for the  $[\text{Tp}^*\text{Rh}(\text{PPh}_3)_2]$  catalyzed hydrothiolation of phenylacetylene with *para*-methoxythiophenol

Spectra were recorded, from bottom to top, at  $t = 3$  min, 11 min, 19 min, 27 min, and 35 min. Diagnostic vinyl sulfide peaks (5.2 ppm, 5.5 ppm) were integrated relative to internal standard, trimethoxybenzene (6.3 ppm).



**Figure B.2. Time-course plot (A) and natural log plot (B) for [Tp\*Rh(PPh<sub>3</sub>)<sub>2</sub>] catalyzed hydrothiolation of phenylacetylene with *para*-methoxythiophenol.**

Natural log plot was plotted according to the equation  $-kt = \ln \frac{[P]_{\infty} - [P]_t}{[P]_{\infty}}$

**B.2 [Tp\*Rh(PPh<sub>3</sub>)<sub>2</sub>] catalyzed hydrothiolation of phenylacetylene with *para*-methylthiophenol**

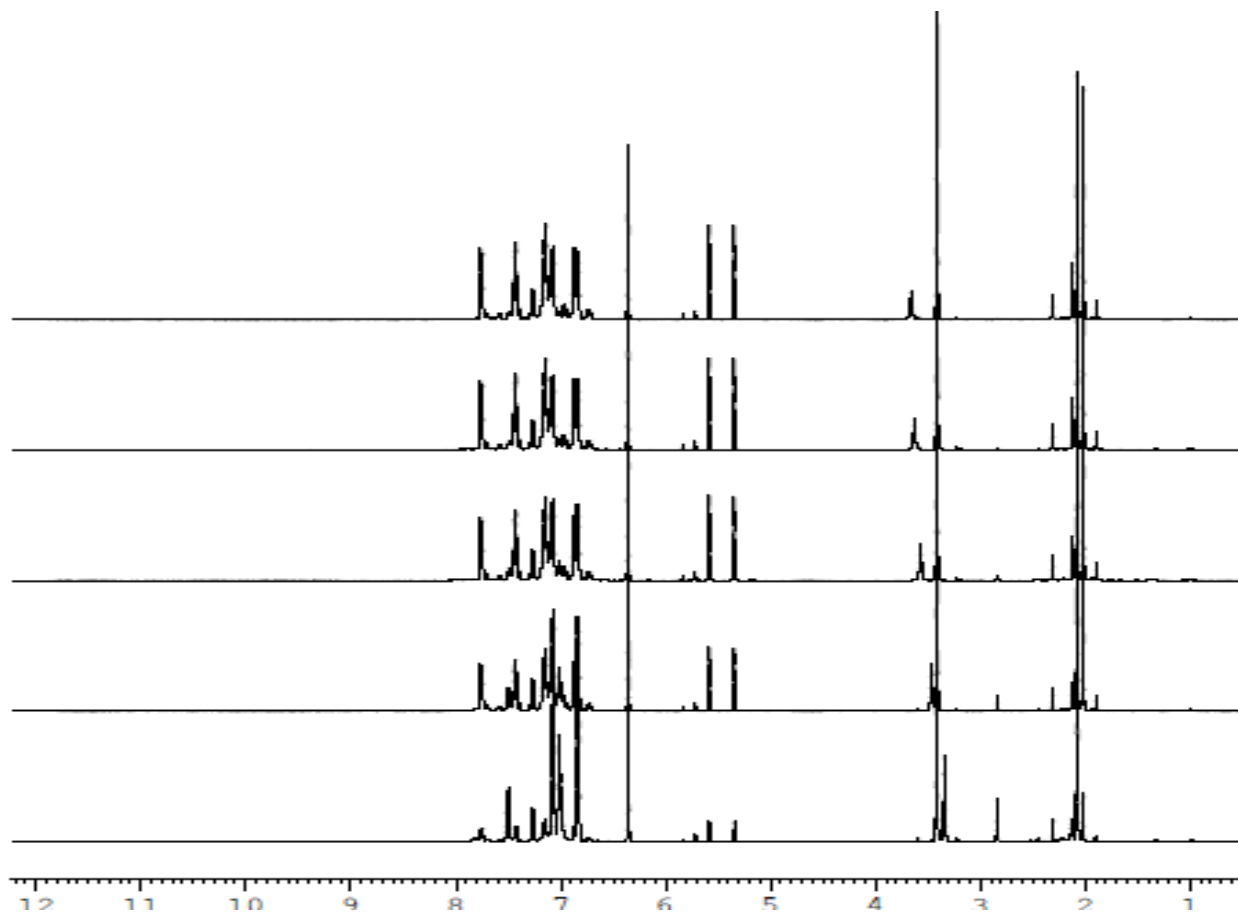
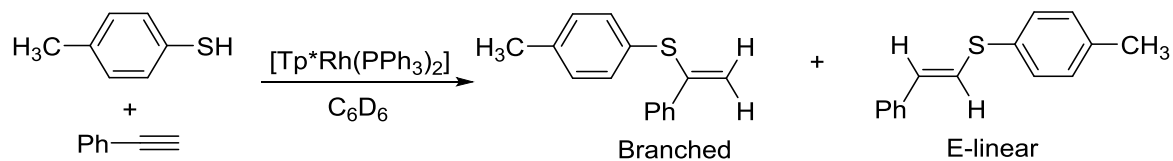


**Figure B.3.** <sup>1</sup>H NMR spectra for the [Tp\*Rh(PPh<sub>3</sub>)<sub>2</sub>] catalyzed hydrothiolation of phenylacetylene with *para*-methylthiophenol

Spectra were recorded, from bottom to top, at  $t = 5$  min, 24 min, 43 min, 62 min, and 81 min. Diagnostic vinyl sulfide peaks (5.3 ppm, 5.6 ppm) were integrated relative to internal standard, trimethoxybenzene (6.3 ppm).

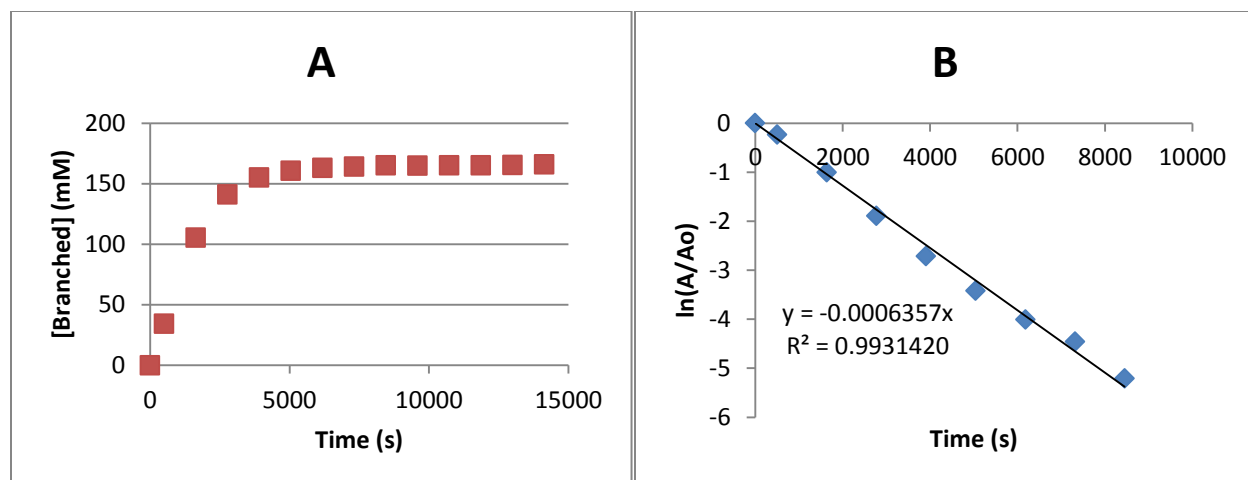


**Figure B.4. Time-course plot (A) and natural log plot (B) for [Tp\*Rh(PPh<sub>3</sub>)<sub>2</sub>] catalyzed hydrothiolation of phenylacetylene with *para*-methylthiophenol.**

Natural log plot was plotted according to the equation  $-kt = \ln \frac{[P]_{\infty} - [P]_t}{[P]_{\infty}}$

**B.3 [Tp\*Rh(PPh<sub>3</sub>)<sub>2</sub>] catalyzed hydrothiolation of phenylacetylene with *para*-(dimethylamino)thiophenol**

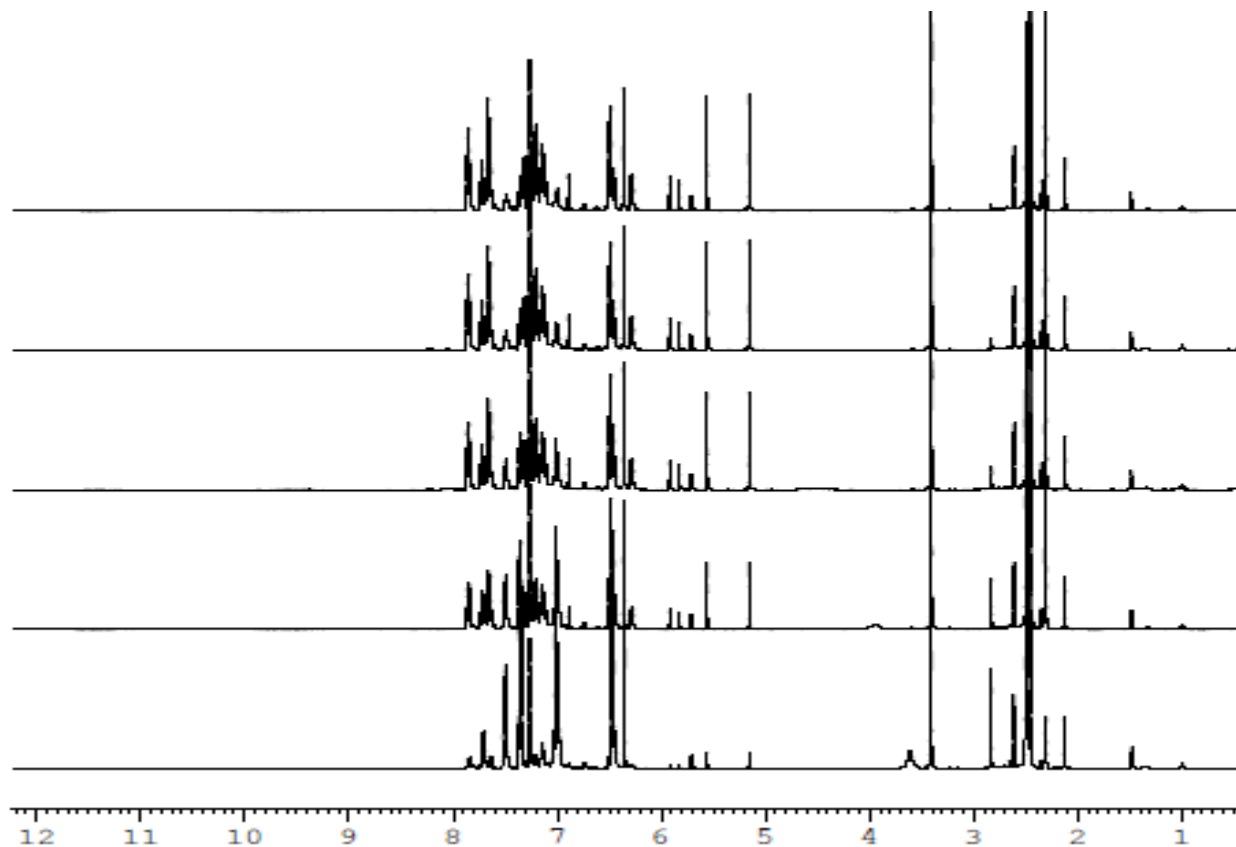
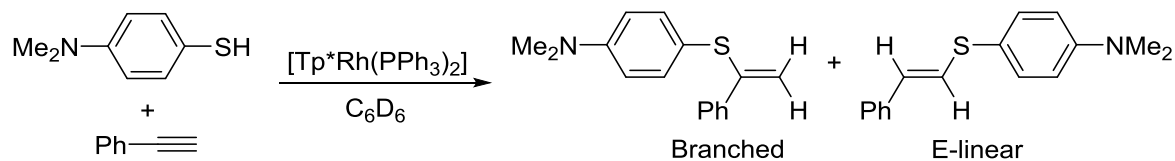


**Figure B.5. <sup>1</sup>H NMR spectra for the [Tp\*Rh(PPh<sub>3</sub>)<sub>2</sub>] catalyzed hydrothiolation of phenylacetylene with *para*-(dimethylamino)thiophenol**

Spectra were recorded, from bottom to top, at  $t = 5$  min, 24 min, 43 min, 62 min, and 81 min. Diagnostic vinyl sulfide peaks (5.2 ppm, 5.6 ppm) were integrated relative to internal standard, trimethoxybenzene (6.3 ppm).

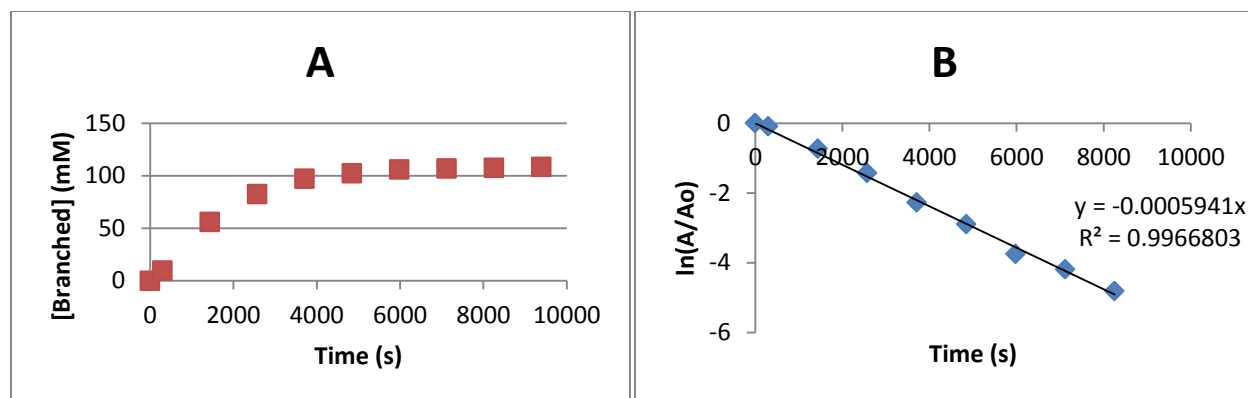


**Figure B.6. Time-course plot (A) and natural log plot (B) for [Tp\*Rh(PPh<sub>3</sub>)<sub>2</sub>] catalyzed hydrothiolation of phenylacetylene with *para*-(dimethylamino)thiophenol.**

Natural log plot was plotted according to the equation  $-kt = \ln \frac{[P]_{\infty} - [P]_t}{[P]_{\infty}}$

**B.4 [Tp\*Rh(PPh<sub>3</sub>)<sub>2</sub>] catalyzed hydrothiolation of phenylacetylene with *para*-(fluoro)thiophenol**

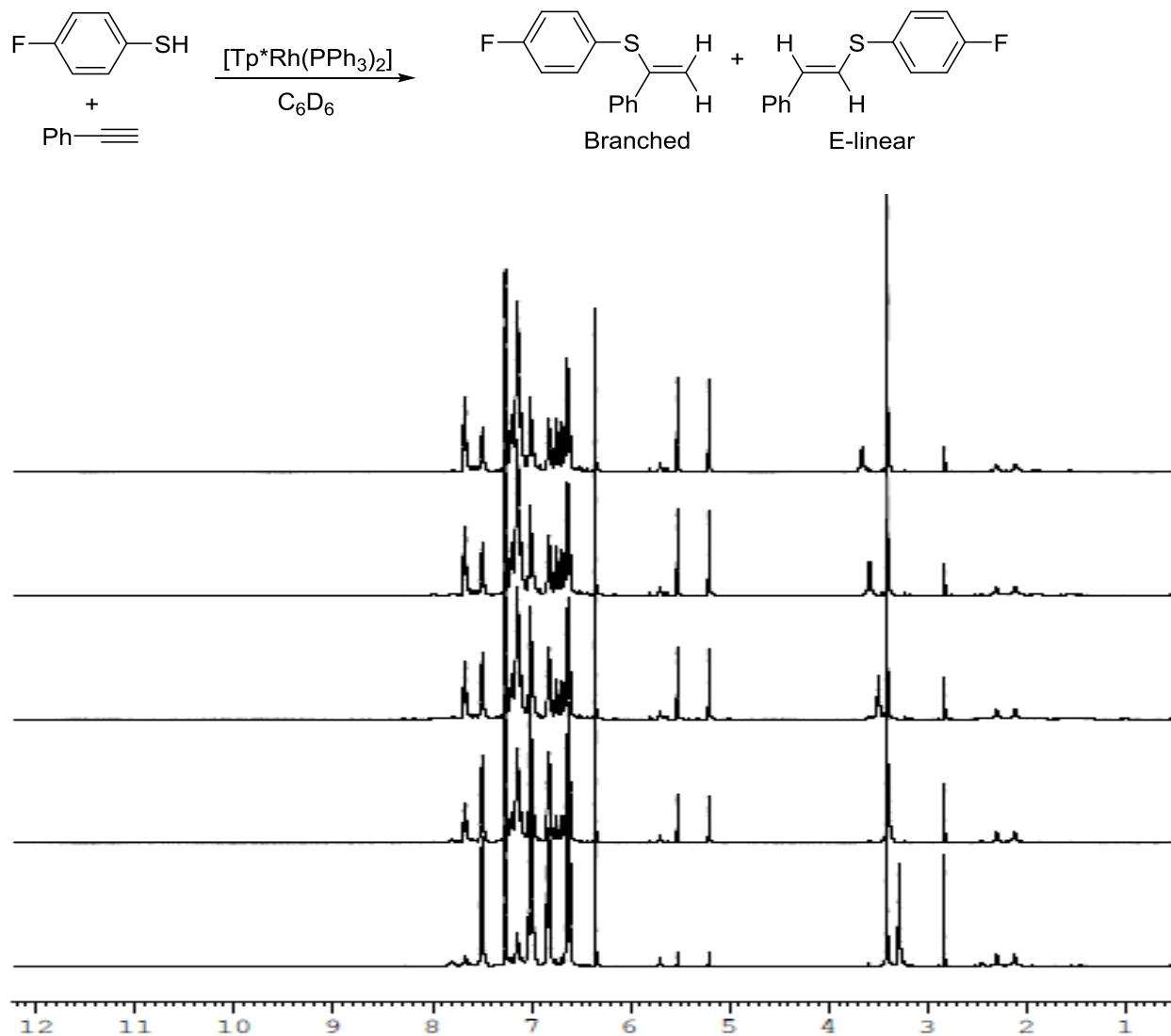


**Figure B.7.** <sup>1</sup>H NMR spectra for the [Tp\*Rh(PPh<sub>3</sub>)<sub>2</sub>] catalyzed hydrothiolation of phenylacetylene with *para*-(fluoro)thiophenol

Spectra were recorded, from bottom to top, at *t* = 5 min, 24 min, 43 min, 62 min, and 81 min. Diagnostic vinyl sulfide peaks (5.2 ppm, 5.6 ppm) were integrated relative to internal standard, trimethoxybenzene (6.3 ppm).

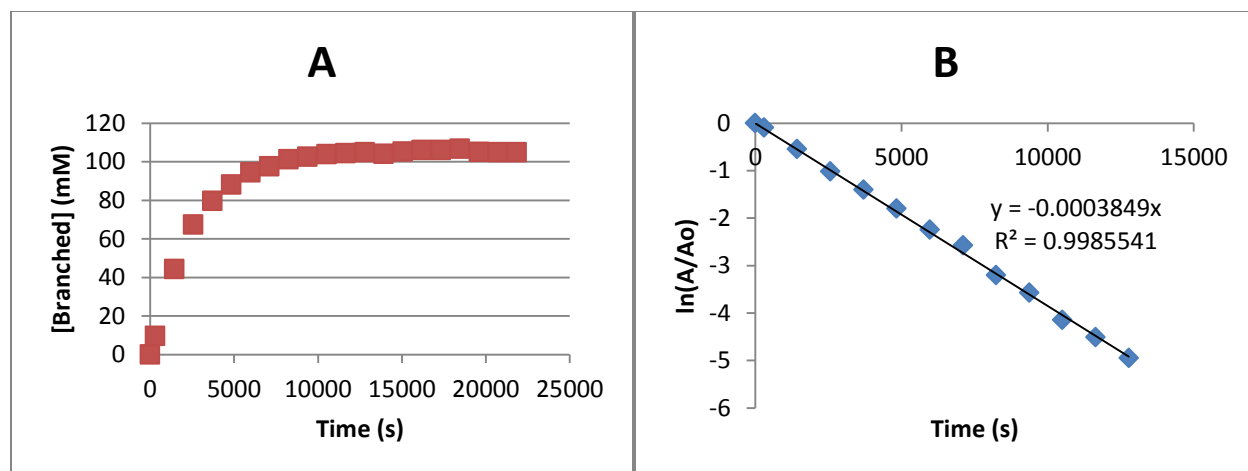


**Figure B.8. Time-course plot (A) and natural log plot (B) for [Tp\*Rh(PPh3)2] catalyzed hydrothiolation of phenylacetylene with *para*-(fluoro)thiophenol.**

Natural log plot was plotted according to the equation  $-kt = \ln \frac{[P]_{\infty} - [P]_t}{[P]_{\infty}}$

## B.5 [Tp\*Rh(PPh<sub>3</sub>)<sub>2</sub>] catalyzed hydrothiolation of phenylacetylene with thiophenol

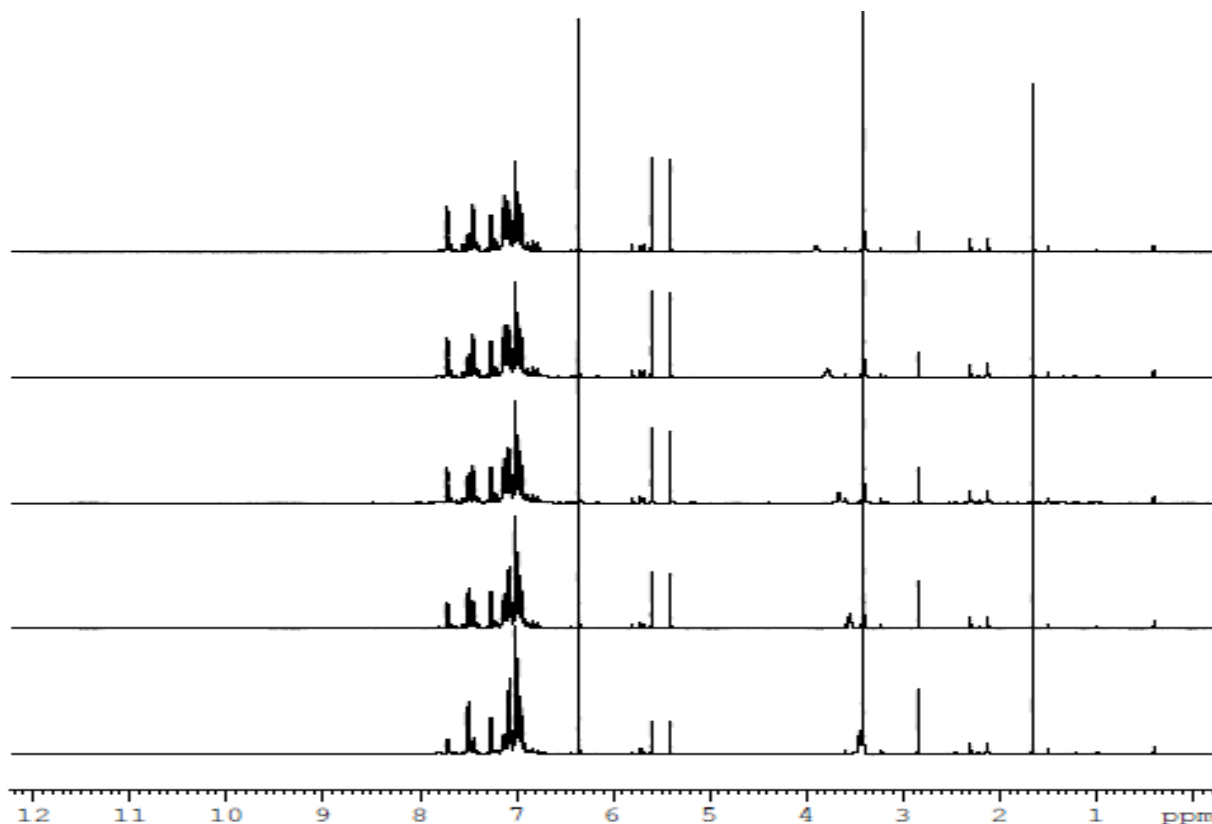
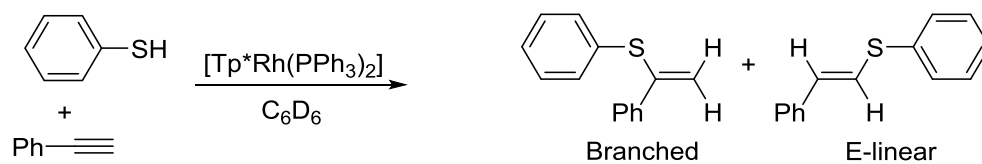


**Figure B.9.** <sup>1</sup>H NMR spectra for the [Tp\*Rh(PPh<sub>3</sub>)<sub>2</sub>] catalyzed hydrothiolation of phenylacetylene with thiophenol.

Spectra were recorded, from bottom to top, at  $t = 5$  min, 24 min, 43 min, 62 min, and 81 min. Diagnostic branched vinyl sulfide peaks (5.3 ppm, 5.6 ppm) and diagnostic *E*-linear vinyl sulfide peak (6.7 ppm) were integrated relative to internal standard, trimethoxybenzene (6.3 ppm).

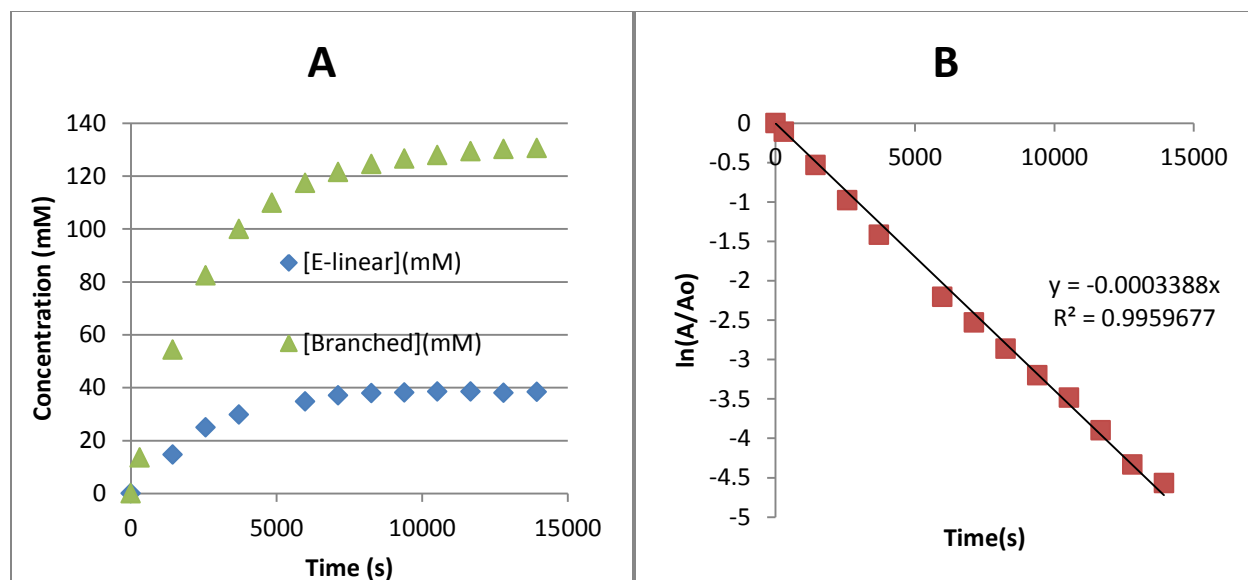


**Figure B.10. Time-course plot (A) and natural log plot (B) for [Tp\*Rh(PPh3)2] catalyzed hydrothiolation of phenylacetylene with thiophenol.**

Natural log plot was plotted according to the equation  $-kt = \ln \frac{[P]_{\infty} - [P]_t}{[P]_{\infty}}$

**B.6 [Tp\*Rh(PPh<sub>3</sub>)<sub>2</sub>] catalyzed hydrothiolation of phenylacetylene with *para*-(methylthio)thiophenol**

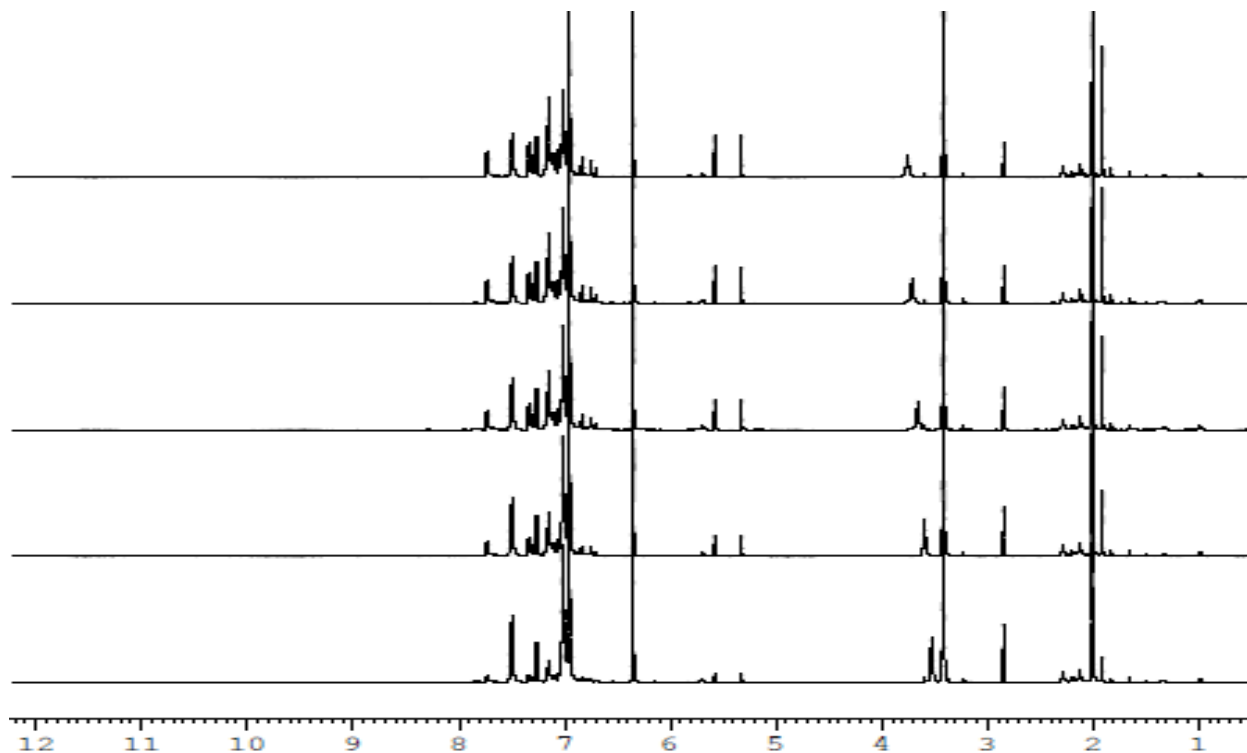
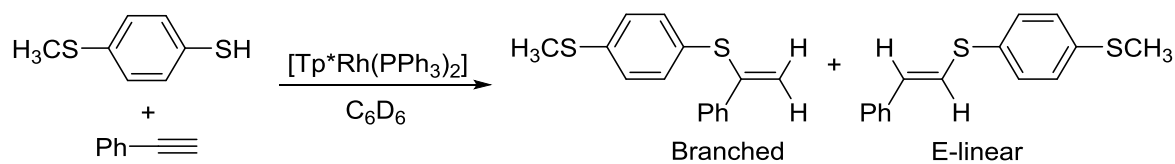


**Figure B.11.** <sup>1</sup>H NMR spectra for the [Tp\*Rh(PPh<sub>3</sub>)<sub>2</sub>] catalyzed hydrothiolation of phenylacetylene with *para*-(methylthio)thiophenol

Spectra were recorded, from bottom to top, at  $t = 5$  min, 24 min, 43 min, 62 min, and 81 min. Diagnostic branched vinyl sulfide peaks (5.3 ppm, 5.6 ppm) and diagnostic *E*-linear vinyl sulfide peak (6.7 ppm) were integrated relative to internal standard, trimethoxybenzene (6.3 ppm).

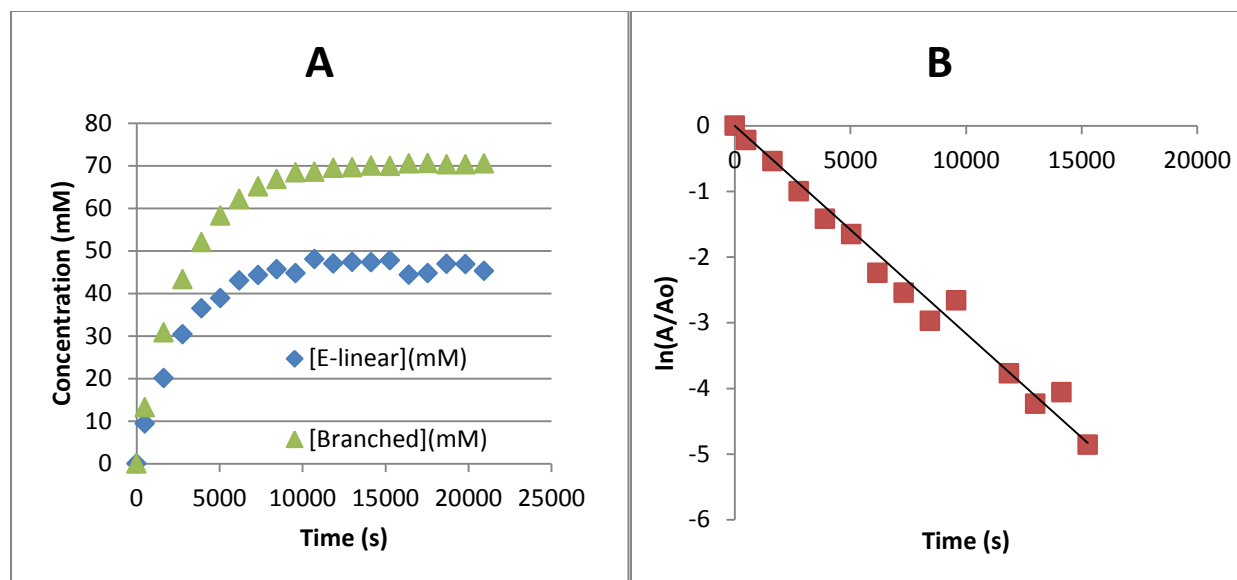


**Figure B.12.** Time-course plot (A) and natural log plot (B) for  $[\text{Tp}^*\text{Rh}(\text{PPh}_3)_2]$  catalyzed hydrothiolation of phenylacetylene with *para*-(methylthio)thiophenol.

Natural log plot was plotted according to the equation  $-kt = \ln \frac{[P]_\infty - [P]_t}{[P]_\infty}$

**B.7 [Tp\*Rh(PPh<sub>3</sub>)<sub>2</sub>] catalyzed hydrothiolation of phenylacetylene with *para*-(chloro)thiophenol**

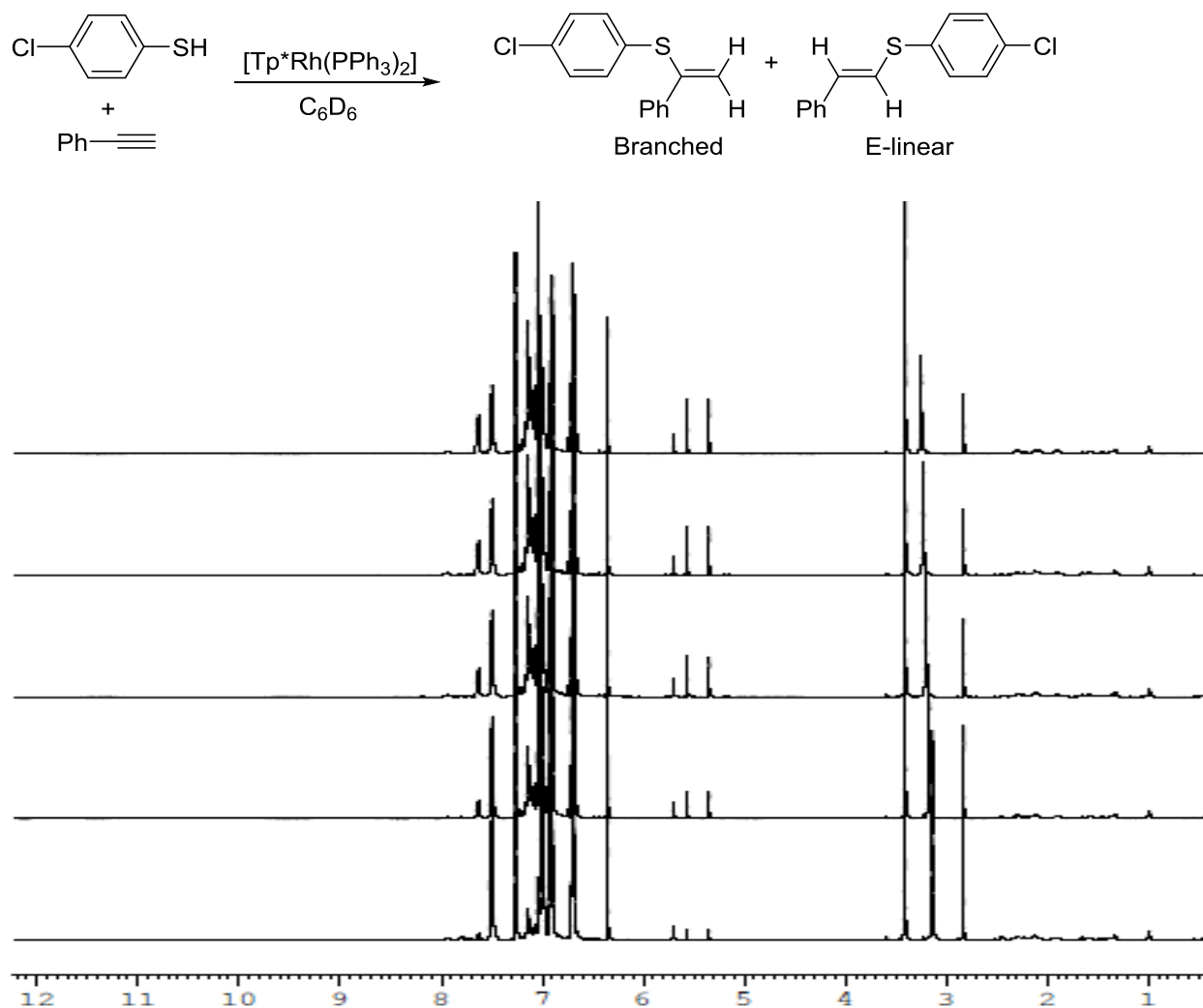


**Figure B.13.** <sup>1</sup>H NMR spectra for the [Tp\*Rh(PPh<sub>3</sub>)<sub>2</sub>] catalyzed hydrothiolation of phenylacetylene with *para*-(chloro)thiophenol.

Spectra were recorded, from bottom to top, at *t* = 5 min, 24 min, 43 min, 62 min, and 81 min. Diagnostic branched vinyl sulfide peaks (5.3 ppm, 5.6 ppm) and diagnostic E-linear vinyl sulfide peak (6.7 ppm) were integrated relative to internal standard, trimethoxybenzene (6.3 ppm).

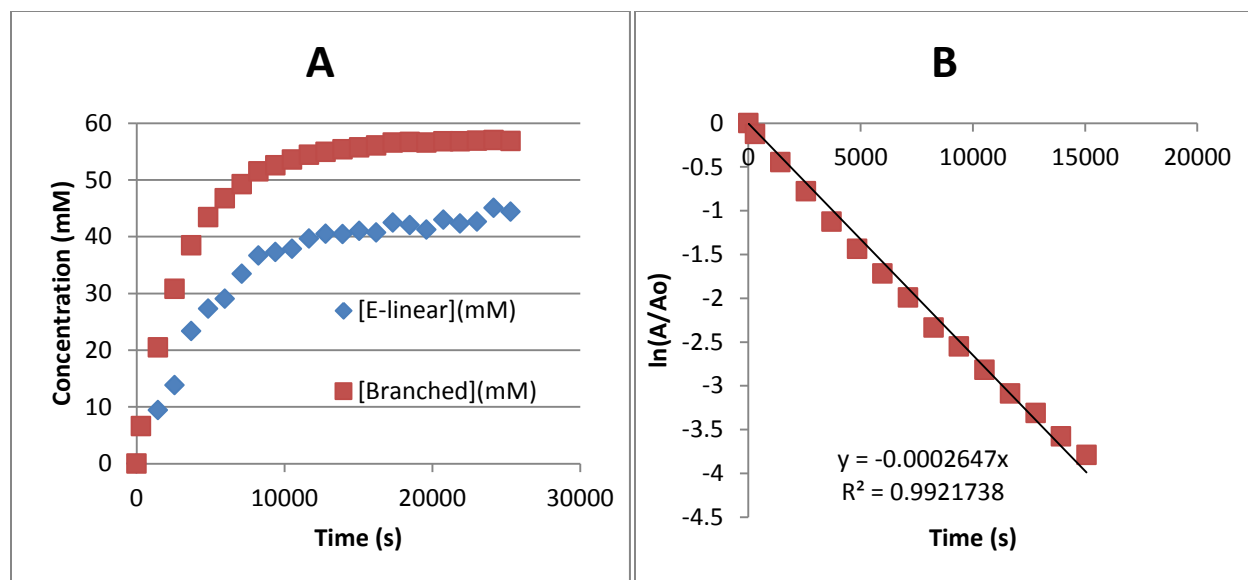


**Figure B.14.** Time-course plot (A) and natural log plot (B) for  $[\text{Tp}^*\text{Rh}(\text{PPh}_3)_2]$  catalyzed hydrothiolation of phenylacetylene with *para*-(chloro)thiophenol.

Natural log plot was plotted according to the equation  $-kt = \ln \frac{[P]_\infty - [P]_t}{[P]_\infty}$

**B.8 [Tp\*Rh(PPh<sub>3</sub>)<sub>2</sub>] catalyzed hydrothiolation of phenylacetylene with *para*-(bromo)thiophenol**

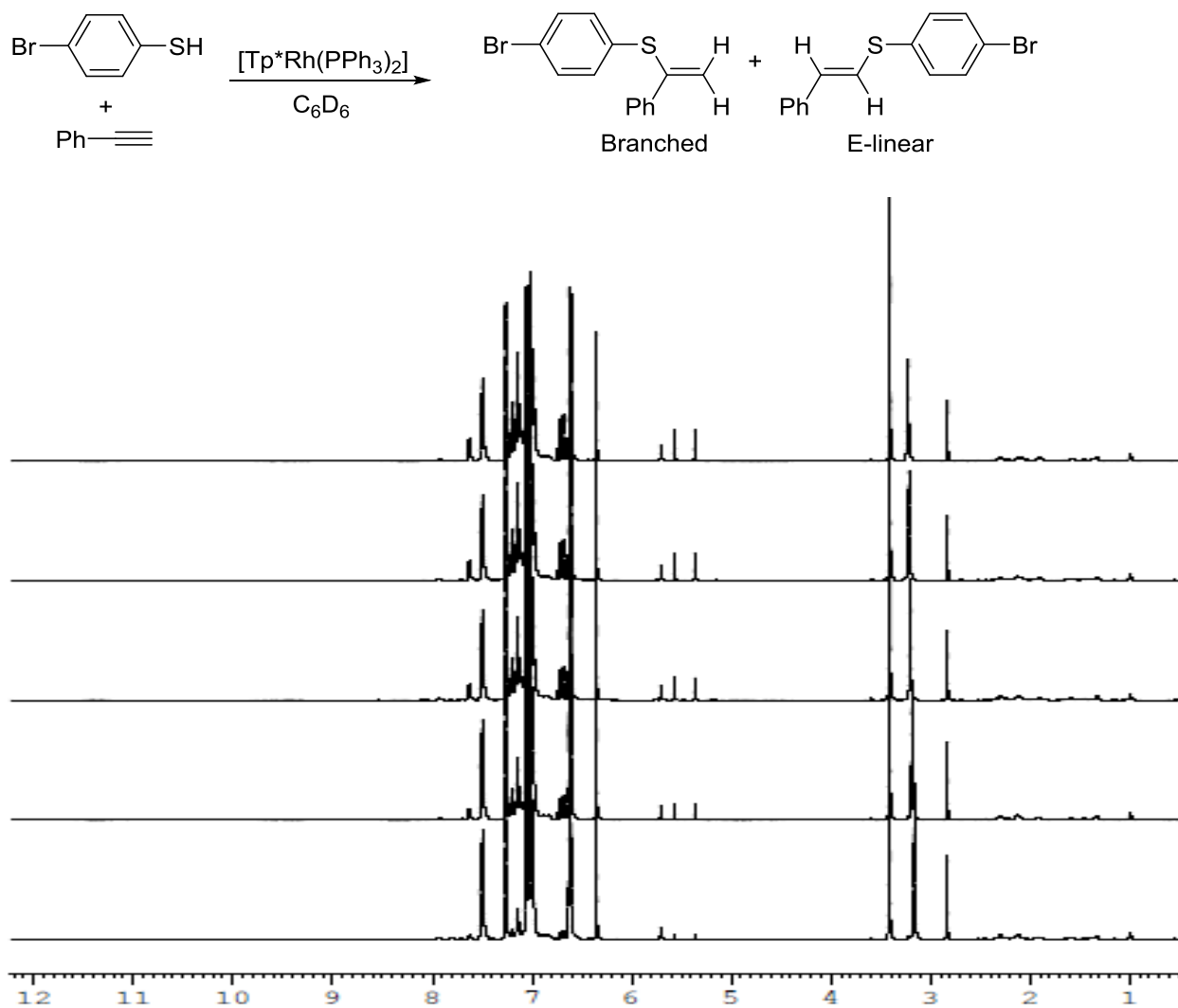


**Figure B.15.** <sup>1</sup>H NMR spectra for the [Tp\*Rh(PPh<sub>3</sub>)<sub>2</sub>] catalyzed hydrothiolation of phenylacetylene with *para*-(bromo)thiophenol

Spectra were recorded, from bottom to top, at *t* = 5 min, 24 min, 43 min, 62 min, and 81 min. Diagnostic branched vinyl sulfide peaks (5.3 ppm, 5.6 ppm) and diagnostic E-linear vinyl sulfide peak (6.7 ppm) were integrated relative to internal standard, trimethoxybenzene (6.3 ppm).

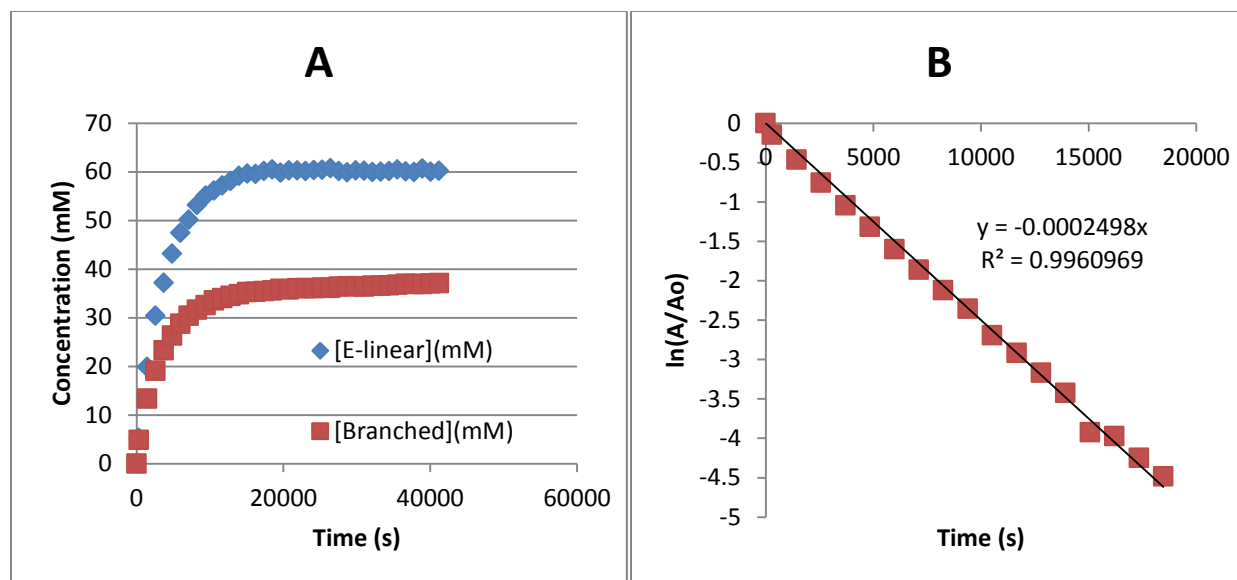


**Figure B.16.** Time-course plot (A) and natural log plot (B) for  $[\text{Tp}^*\text{Rh}(\text{PPh}_3)_2]$  catalyzed hydrothiolation of phenylacetylene with *para*-(bromo)thiophenol.

Natural log plot was plotted according to the equation  $-kt = \ln \frac{[P]_\infty - [P]_t}{[P]_\infty}$

**B.9 [Tp\*Rh(PPh<sub>3</sub>)<sub>2</sub>] catalyzed hydrothiolation of phenylacetylene with *para*-(trifluoromethoxy)thiophenol**

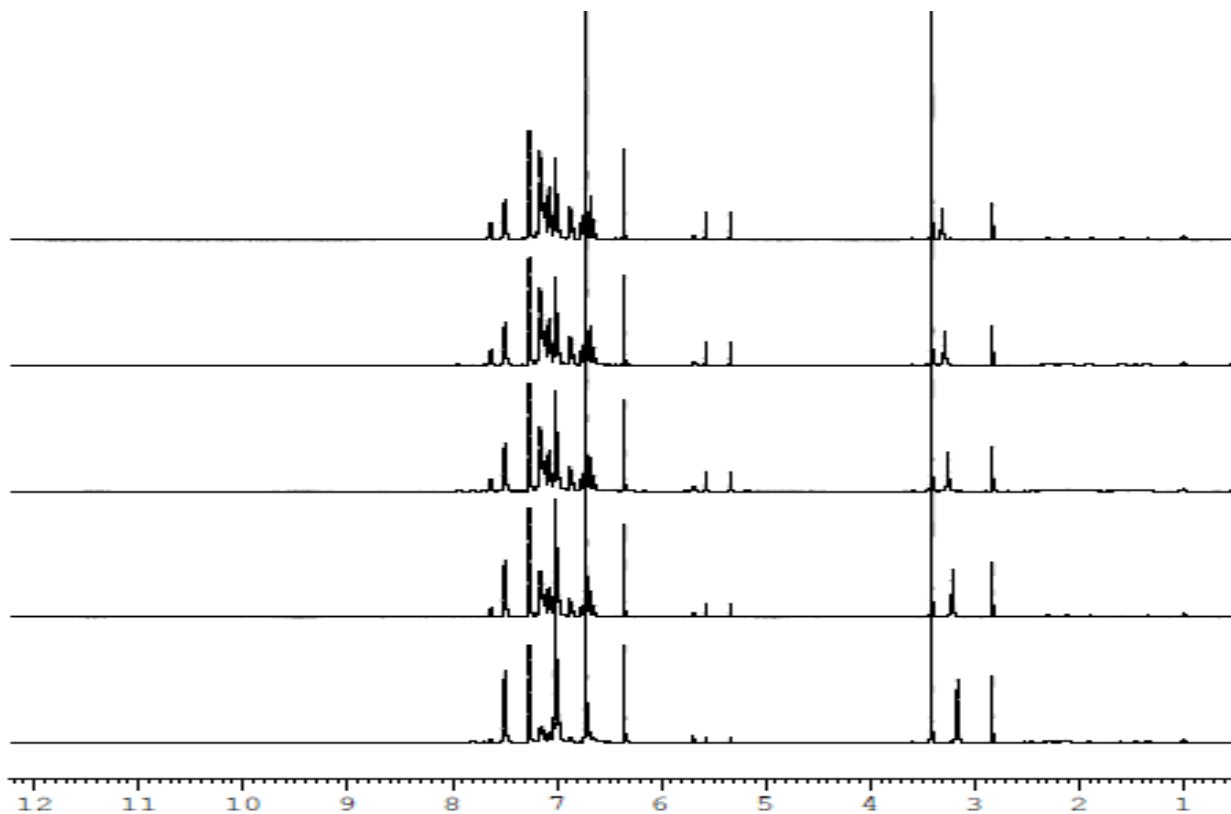
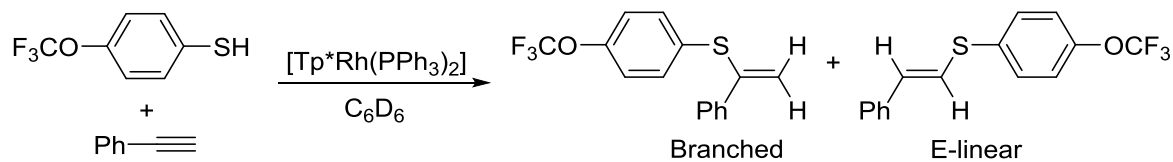


**Figure B.17. <sup>1</sup>H NMR spectra for the [Tp\*Rh(PPh<sub>3</sub>)<sub>2</sub>] catalyzed hydrothiolation of phenylacetylene with *para*-(trifluoromethoxy)thiophenol**

Spectra were recorded, from bottom to top, at  $t = 5$  min, 24 min, 43 min, 62 min, and 81 min. Diagnostic branched vinyl sulfide peaks (5.3 ppm, 5.6 ppm) and diagnostic E-linear vinyl sulfide peak (6.8 ppm) were integrated relative to internal standard, trimethoxybenzene (6.3 ppm).

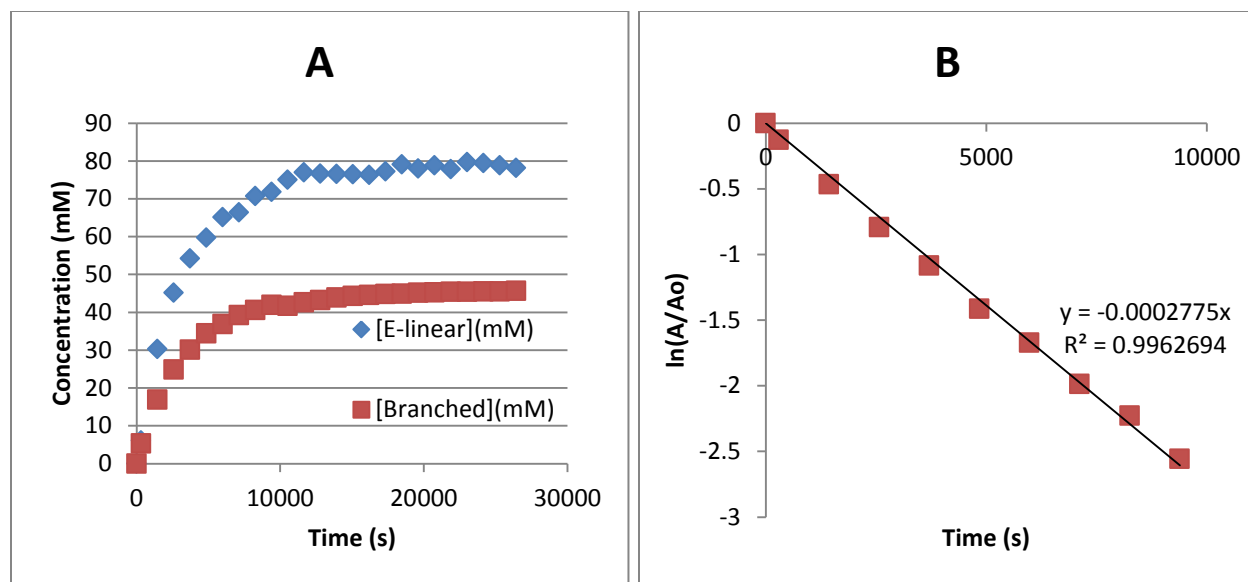


**Figure B.18. Time-course plot (A) and natural log plot (B) for [Tp\*Rh(PPh<sub>3</sub>)<sub>2</sub>] catalyzed hydrothiolation of phenylacetylene with *para*-(trifluoromethoxy)thiophenol.**

Natural log plot was plotted according to the equation  $-kt = \ln \frac{[P]_{\infty} - [P]_t}{[P]_{\infty}}$

**B.10 [Tp\*Rh(PPh<sub>3</sub>)<sub>2</sub>] catalyzed hydrothiolation of *para*-(methoxy)phenylacetylene with thiophenol**

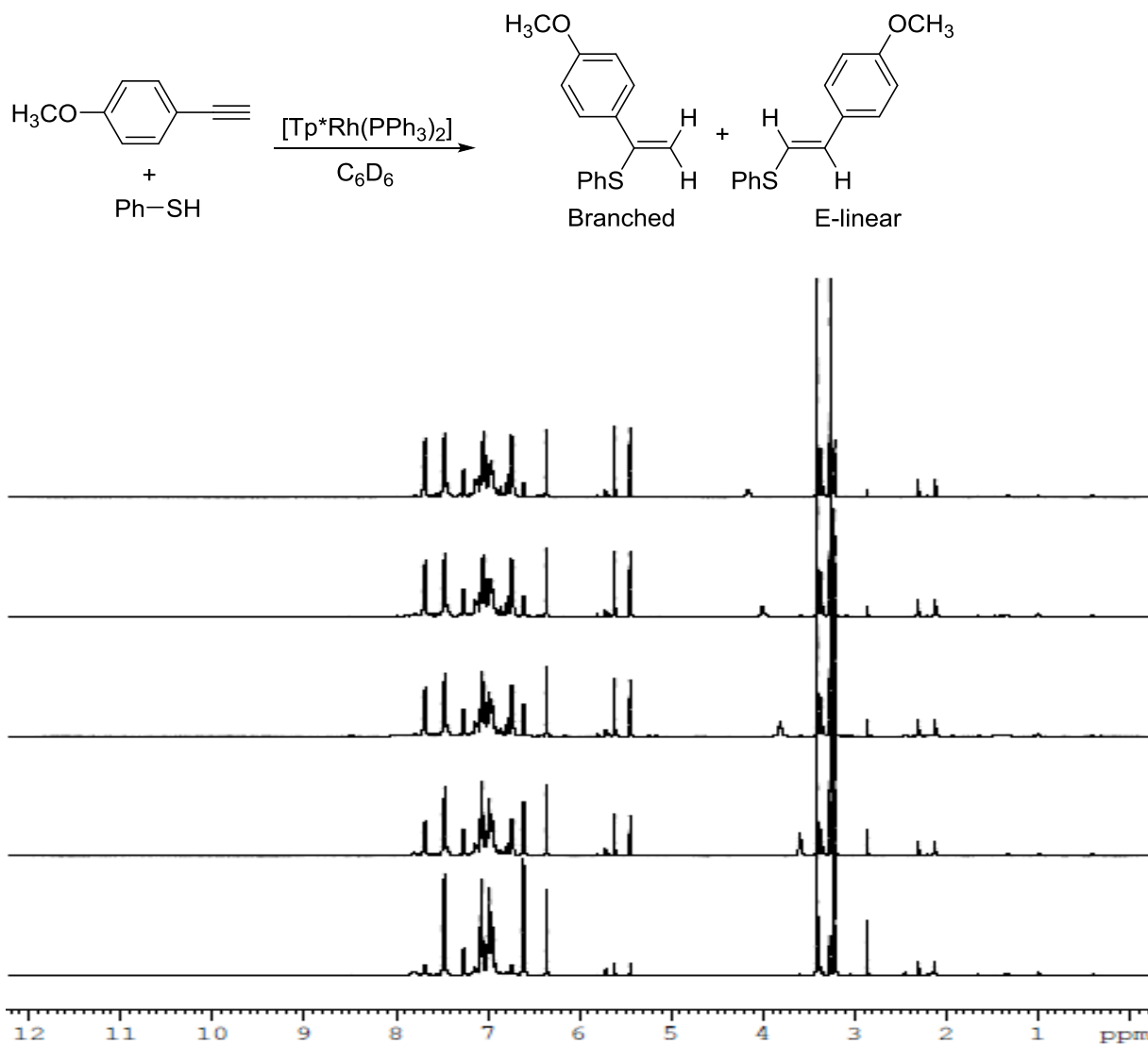


**Figure B.19.** <sup>1</sup>H NMR spectra for the [Tp\*Rh(PPh<sub>3</sub>)<sub>2</sub>] catalyzed hydrothiolation of *para*-(methoxy)phenylacetylene with thiophenol

Spectra were recorded, from bottom to top, at t = 5 min, 24 min, 43 min, 62 min, and 81 min. Diagnostic branched vinyl sulfide peaks (5.4 ppm, 5.6 ppm) were integrated relative to internal standard, trimethoxybenzene (6.3 ppm).

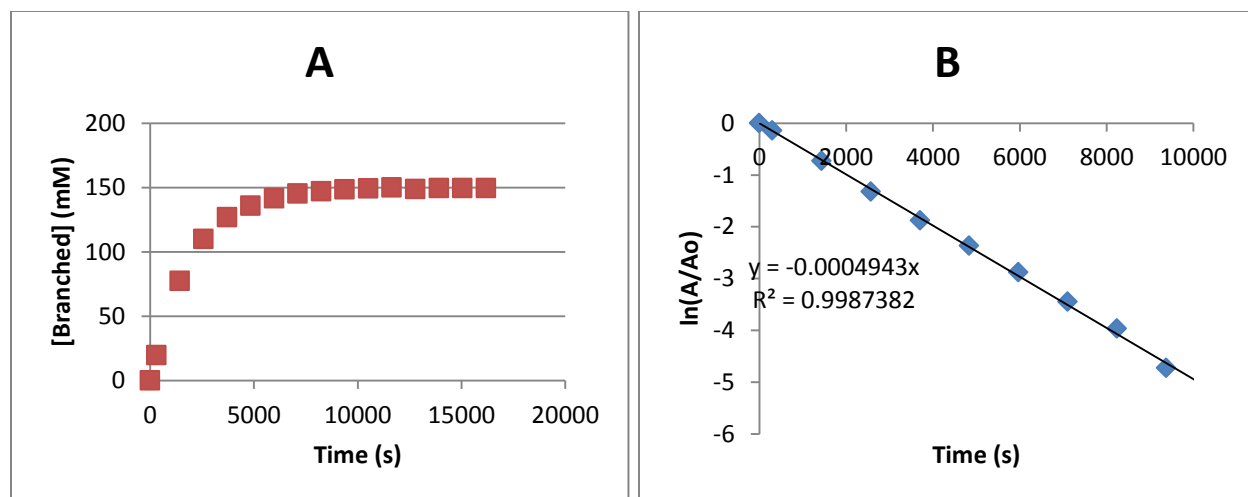


**Figure B.20. Time-course plot (A) and natural log plot (B) for [Tp\*Rh(PPh3)2] catalyzed hydrothiolation of *para*-(methoxy)phenylacetylene with thiophenol**

Natural log plot was plotted according to the equation  $-kt = \ln \frac{[P]_{\infty} - [P]_t}{[P]_{\infty}}$

**B.11 [Tp\*Rh(PPh<sub>3</sub>)<sub>2</sub>] catalyzed hydrothiolation of *para*-(methyl)phenylacetylene with thiophenol**

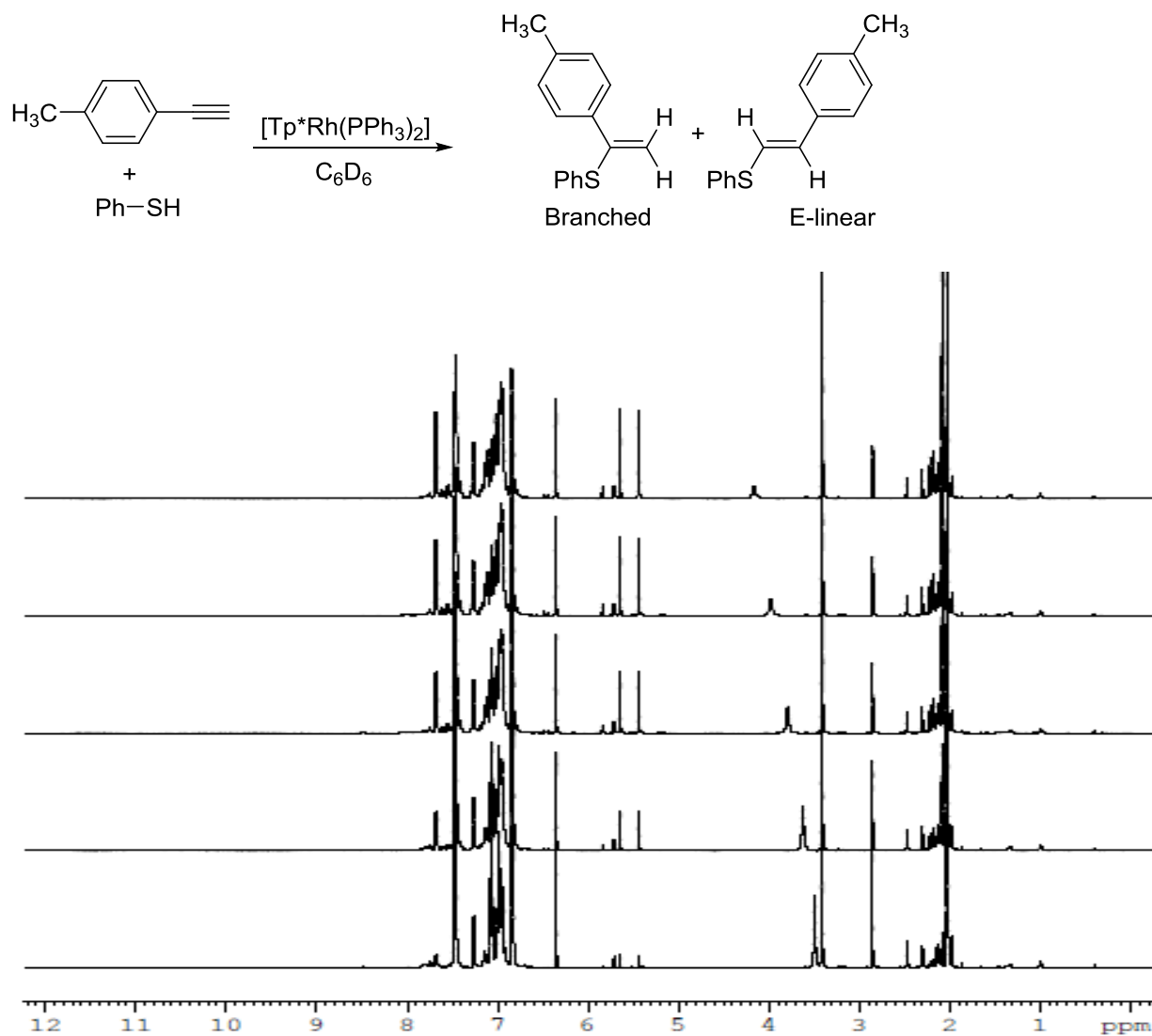


**Figure B.21.** <sup>1</sup>H NMR spectra for the [Tp\*Rh(PPh<sub>3</sub>)<sub>2</sub>] catalyzed hydrothiolation of *para*-(methyl)phenylacetylene with thiophenol

Spectra were recorded, from bottom to top, at  $t = 5$  min, 24 min, 43 min, 62 min, and 81 min. Diagnostic branched vinyl sulfide peaks (5.4 ppm, 5.6 ppm) were integrated relative to internal standard, trimethoxybenzene (6.3 ppm).

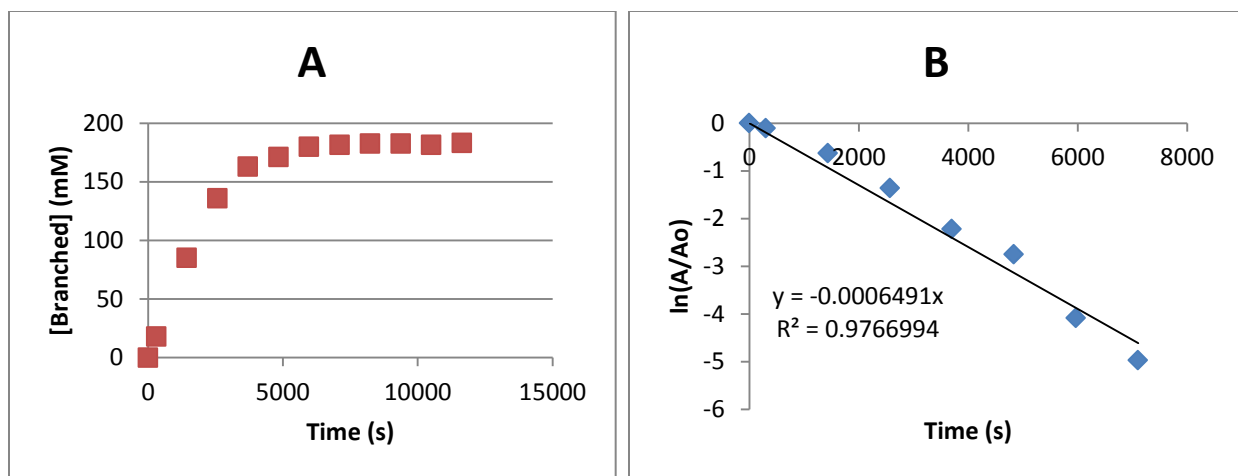


**Figure B.22. Time-course plot (A) and natural log plot (B) for [Tp\*Rh(PPh3)2] catalyzed hydrothiolation of *para*-(methyl)phenylacetylene with thiophenol**

Natural log plot was plotted according to the equation  $-kt = \ln \frac{[P]_{\infty} - [P]_t}{[P]_{\infty}}$

**B.12 [Tp\*Rh(PPh<sub>3</sub>)<sub>2</sub>] catalyzed hydrothiolation of *para*-(fluoro)phenylacetylene with thiophenol**

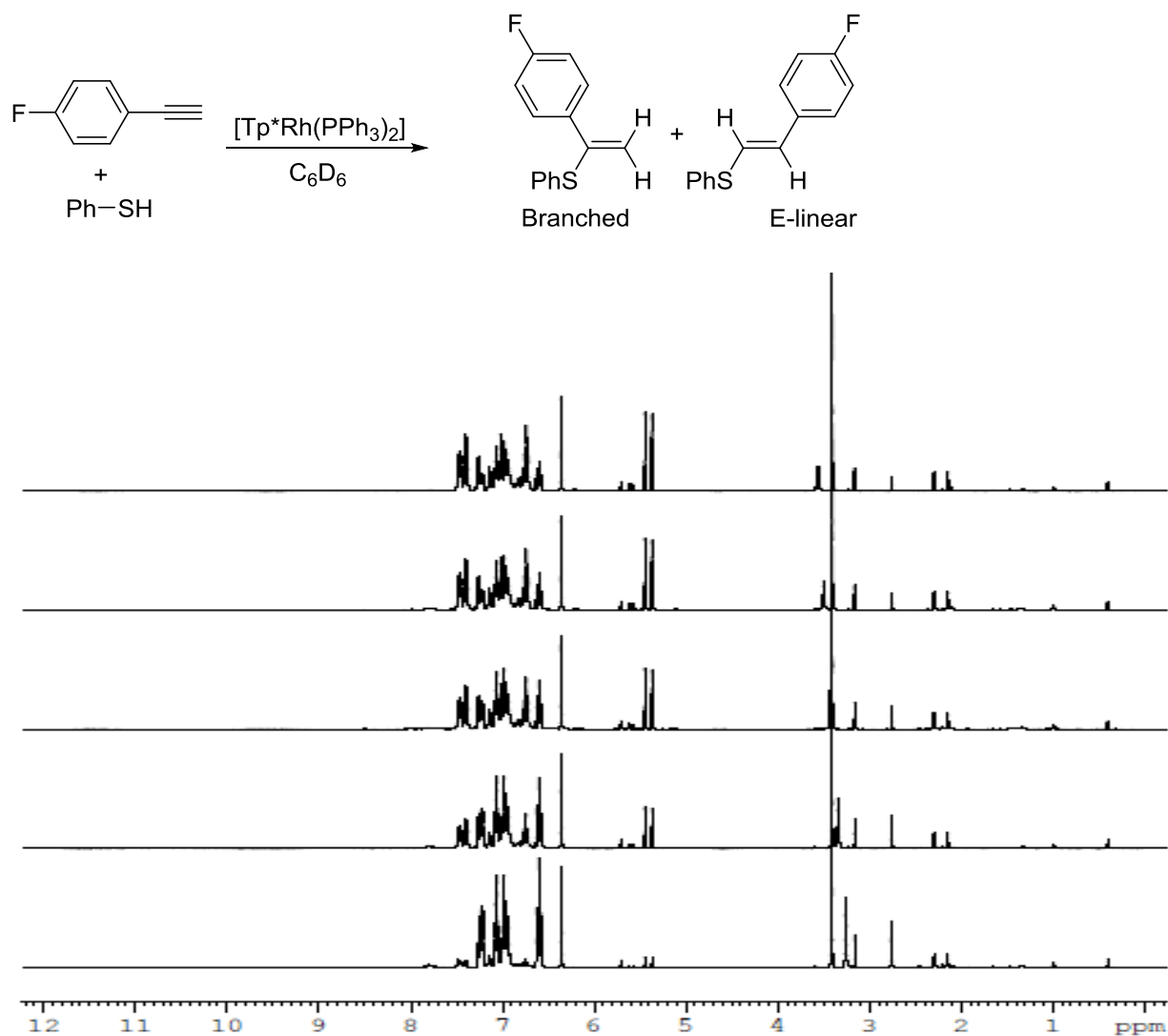


**Figure B.23. <sup>1</sup>H NMR spectra for the [Tp\*Rh(PPh<sub>3</sub>)<sub>2</sub>] catalyzed hydrothiolation of *para*-(fluoro)phenylacetylene with thiophenol**

Spectra were recorded, from bottom to top, at *t* = 5 min, 24 min, 43 min, 62 min, and 81 min. Diagnostic branched vinyl sulfide peaks (5.4 ppm, 5.5 ppm) were integrated relative to internal standard, trimethoxybenzene (6.3 ppm).

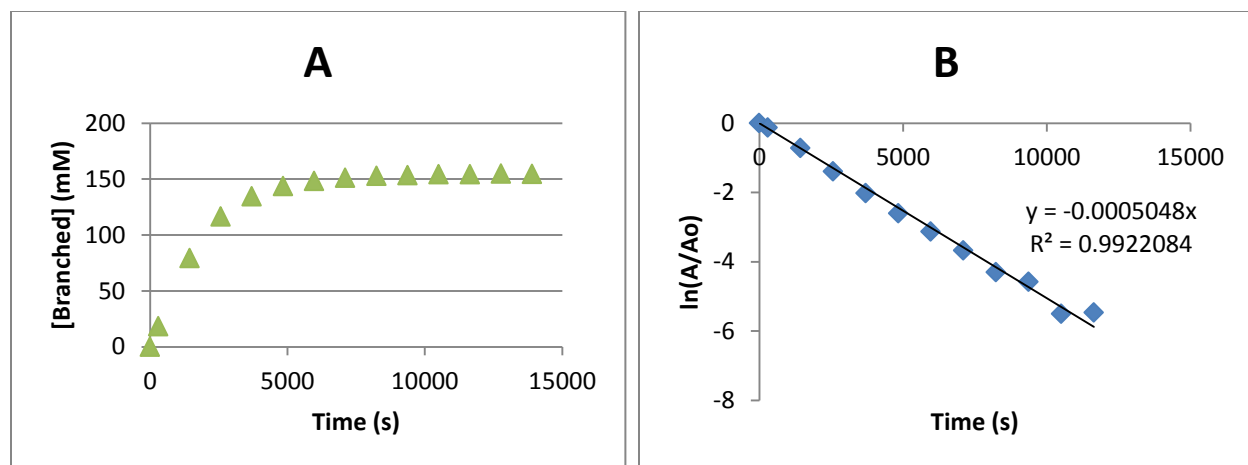


**Figure B.24. Time-course plot (A) and natural log plot (B) for [Tp\*Rh(PPh<sub>3</sub>)<sub>2</sub>] catalyzed hydrothiolation of *para*-(methyl)phenylacetylene with thiophenol**

Natural log plot was plotted according to the equation  $-kt = \ln \frac{[P]_{\infty} - [P]_t}{[P]_{\infty}}$

**B.13 [Tp\*Rh(PPh<sub>3</sub>)<sub>2</sub>] catalyzed hydrothiolation of *para*-(chloro)phenylacetylene with thiophenol**

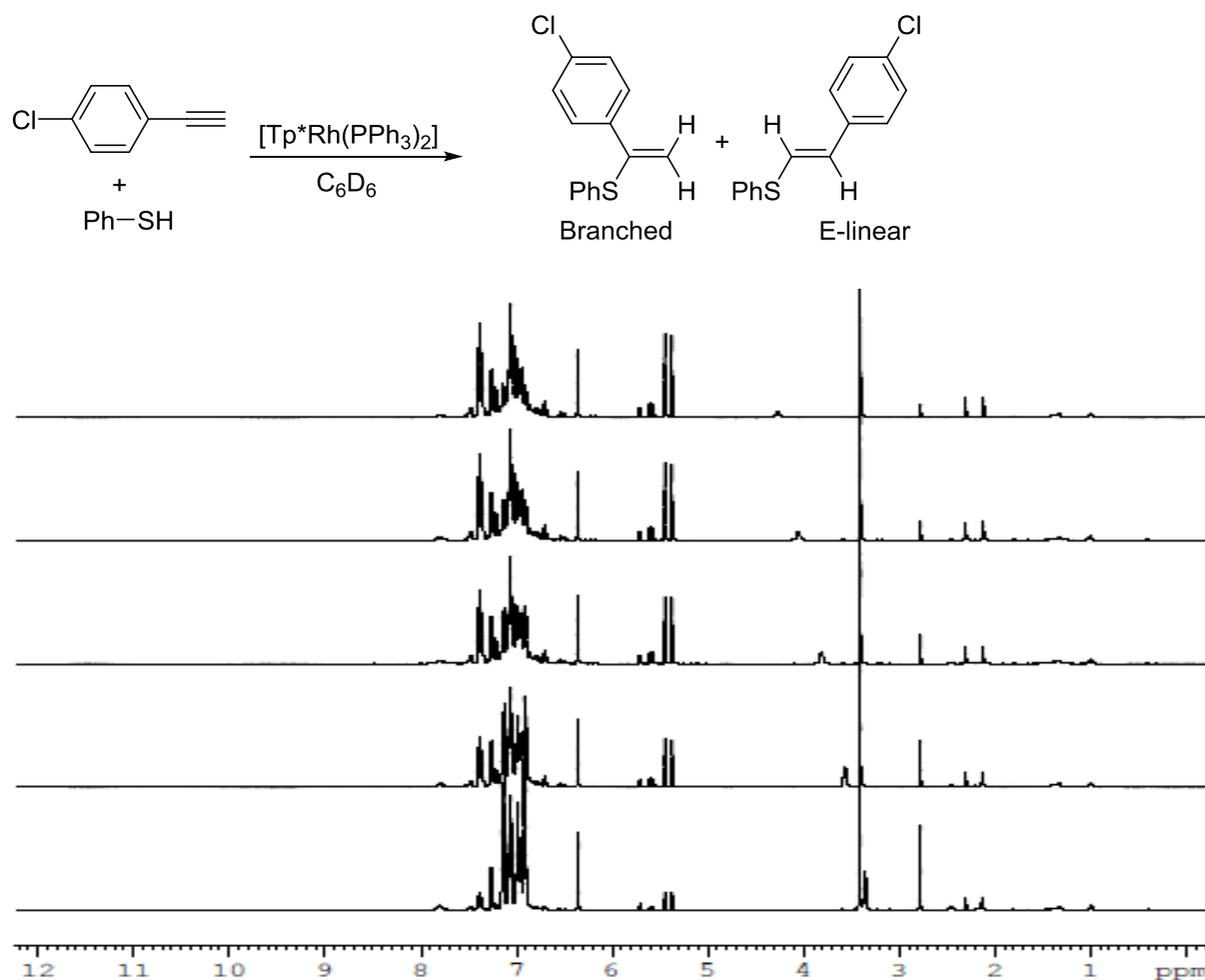


**Figure B.25. <sup>1</sup>H NMR spectra for the [Tp\*Rh(PPh<sub>3</sub>)<sub>2</sub>] catalyzed hydrothiolation of *para*-(chloro)phenylacetylene with thiophenol**

Spectra were recorded, from bottom to top, at  $t = 5$  min, 24 min, 43 min, 62 min, and 81 min. Diagnostic branched vinyl sulfide peaks (5.4 ppm, 5.5 ppm) were integrated relative to internal standard, trimethoxybenzene (6.3 ppm).

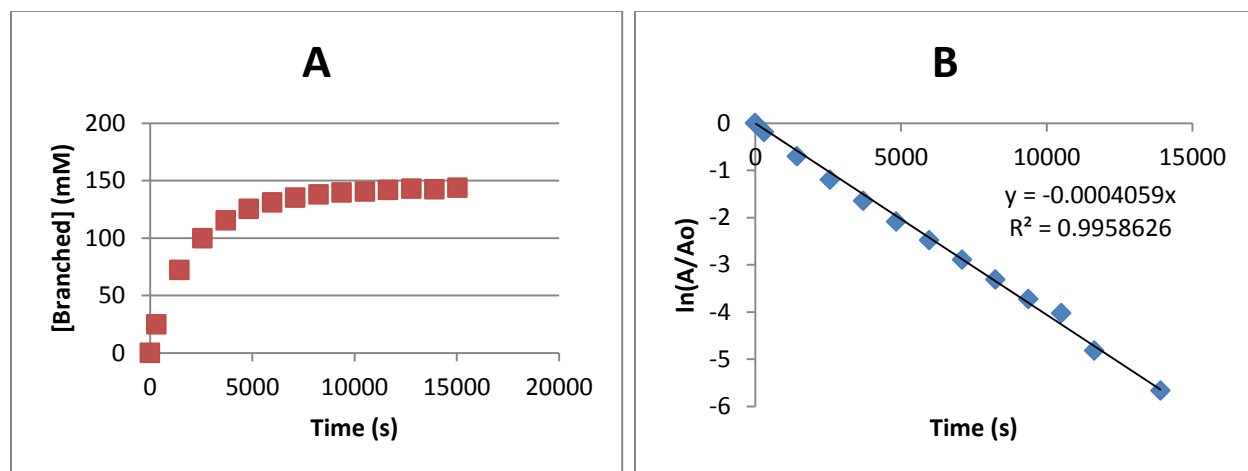


**Figure B.26. Time-course plot (A) and natural log plot (B) for [Tp\*Rh(PPh<sub>3</sub>)<sub>2</sub>] catalyzed hydrothiolation of *para*-(chloro)phenylacetylene with thiophenol**

Natural log plot was plotted according to the equation  $-kt = \ln \frac{[P]_{\infty} - [P]_t}{[P]_{\infty}}$

**B.14 [Tp\*Rh(PPh<sub>3</sub>)<sub>2</sub>] catalyzed hydrothiolation of *para*-(bromo)phenylacetylene with thiophenol**

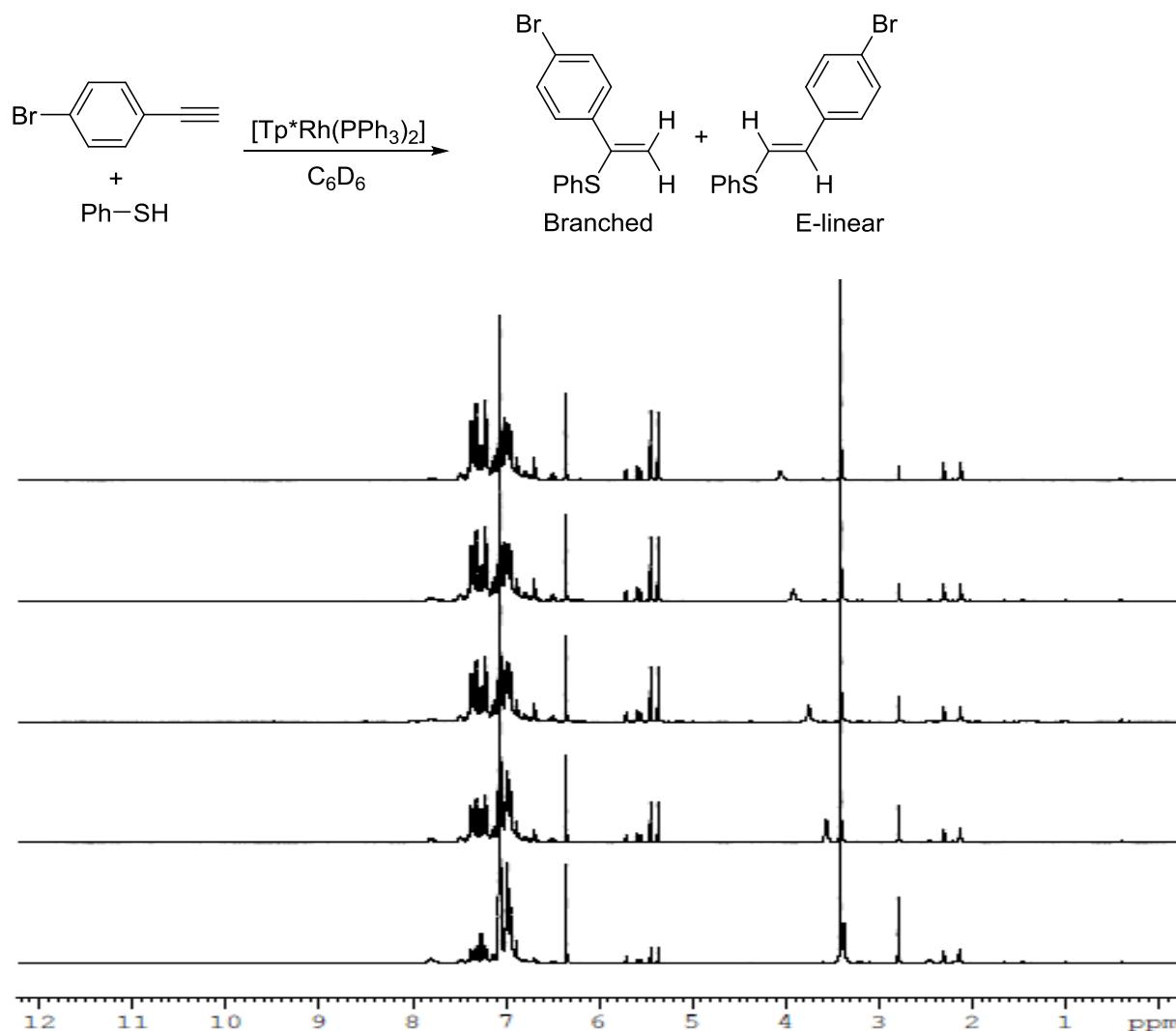


**Figure B.27.** <sup>1</sup>H NMR spectra for the [Tp\*Rh(PPh<sub>3</sub>)<sub>2</sub>] catalyzed hydrothiolation of *para*-(bromo)phenylacetylene with thiophenol

Spectra were recorded, from bottom to top, at *t* = 5 min, 24 min, 43 min, 62 min, and 81 min. Diagnostic branched vinyl sulfide peaks (5.4 ppm, 5.5 ppm) were integrated relative to internal standard, trimethoxybenzene (6.3 ppm).

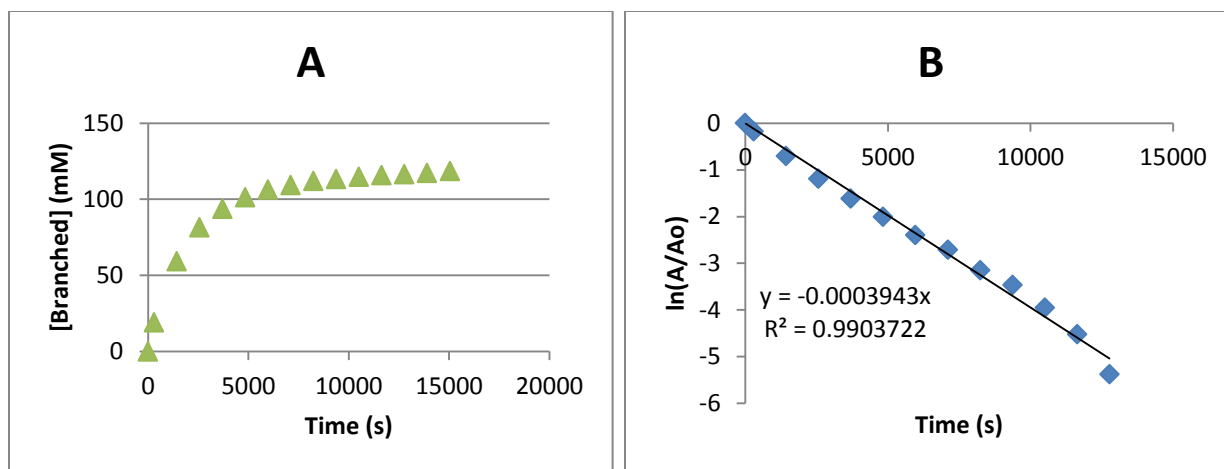


**Figure B.28. Time-course plot (A) and natural log plot (B) for [Tp\*Rh(PPh3)2] catalyzed hydrothiolation of *para*-(bromo)phenylacetylene with thiophenol.**

Natural log plot was plotted according to the equation  $-kt = \ln \frac{[P]_{\infty} - [P]_t}{[P]_{\infty}}$

**B.15 [Tp\*Rh(PPh<sub>3</sub>)<sub>2</sub>] catalyzed hydrothiolation of 3,5-dimethylphenylacetylene with thiophenol**

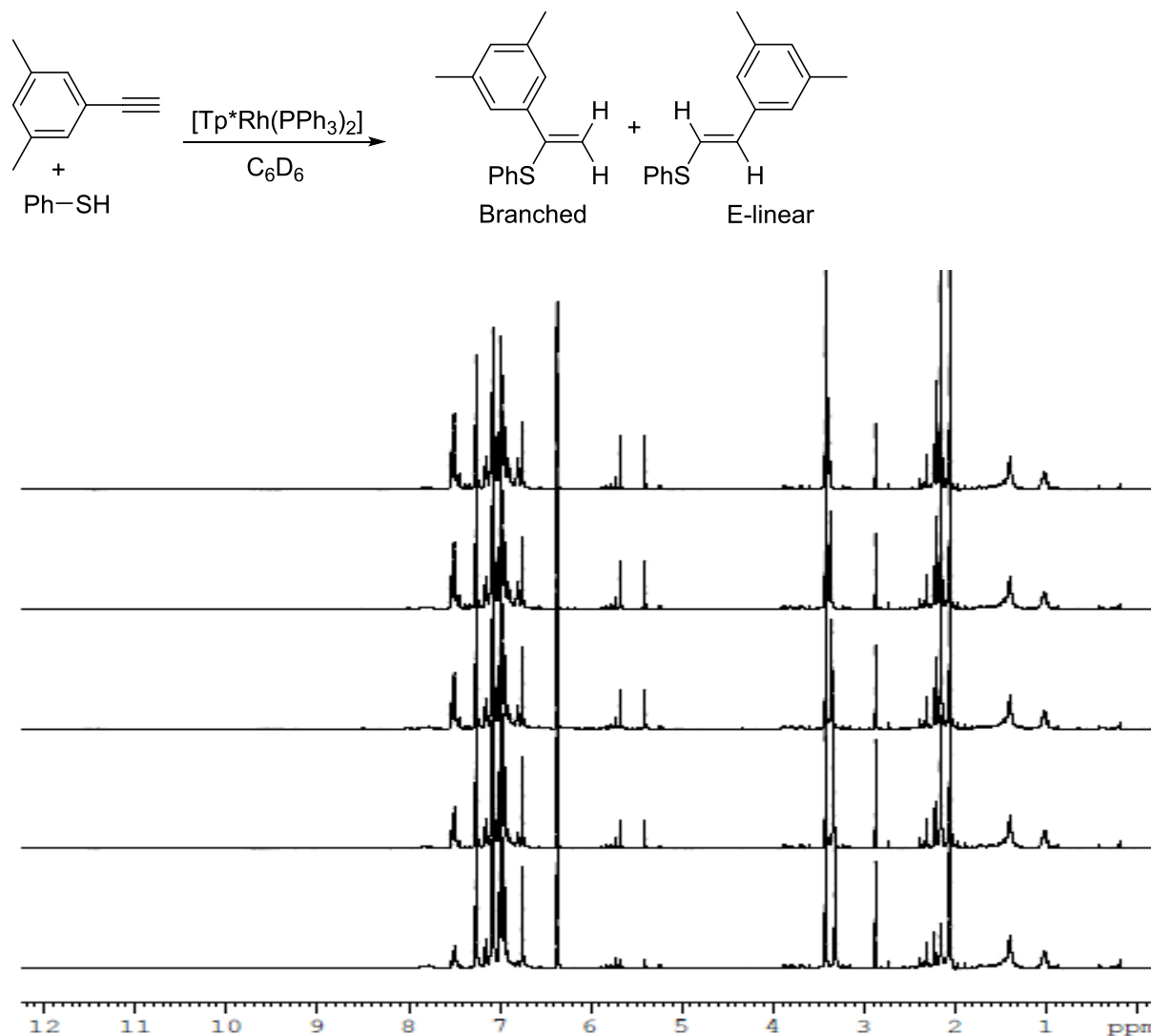


**Figure B.29.** <sup>1</sup>H NMR spectra for [Tp\*Rh(PPh<sub>3</sub>)<sub>2</sub>] catalyzed hydrothiolation of 3,5-dimethylphenylacetylene with thiophenol

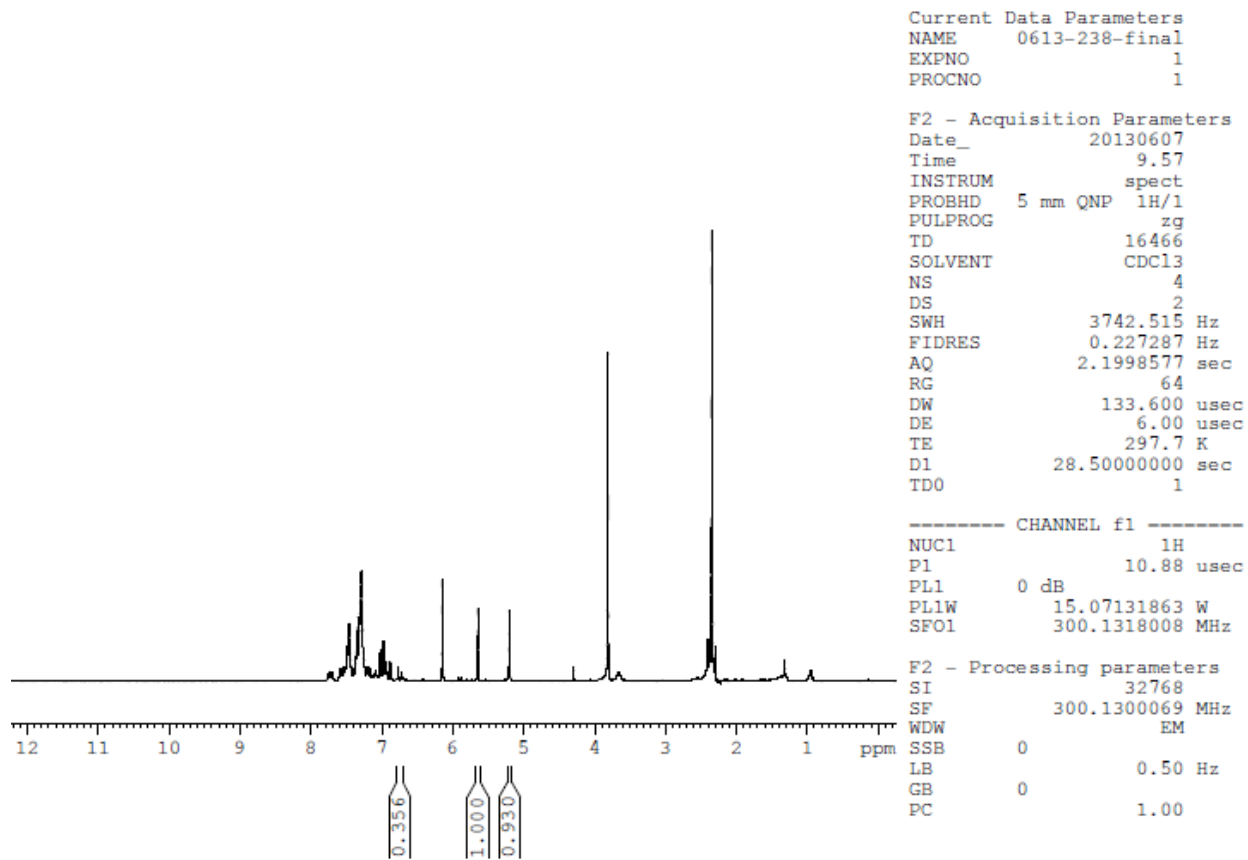


**Figure B.30. Final product ratio for [Tp\*Rh(PPh<sub>3</sub>)<sub>2</sub>] catalyzed hydrothiolation of 3,5-dimethylphenylacetylene with thiophenol**

**B.16** [Tp\*Rh(PPh<sub>3</sub>)<sub>2</sub>] catalyzed hydrothiolation of 3,5-di(*tert*-butyl)phenylacetylene with thiophenol

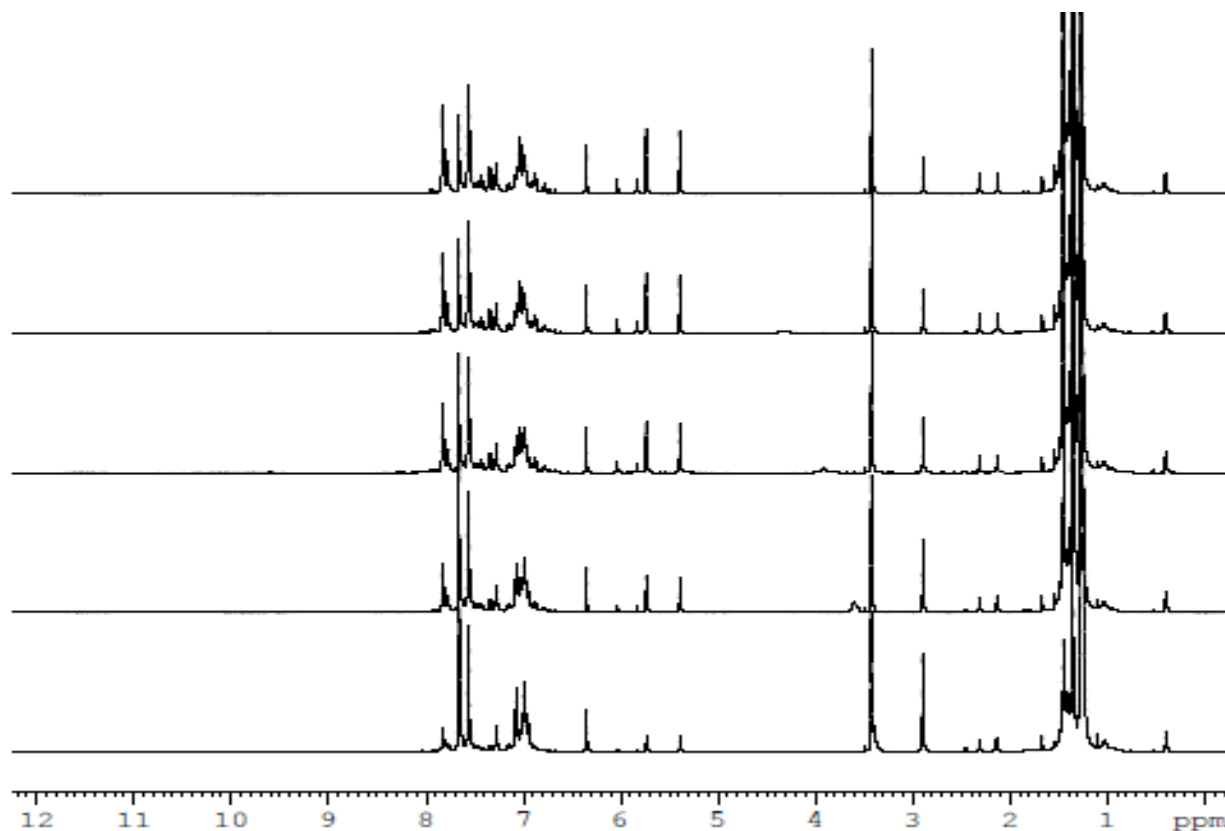
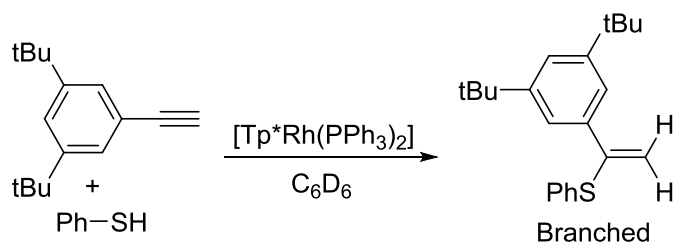


**Figure B.31.** <sup>1</sup>H NMR spectra for [Tp\*Rh(PPh<sub>3</sub>)<sub>2</sub>] catalyzed hydrothiolation of 3,5-di(*tert*-butyl)phenylacetylene with thiophenol

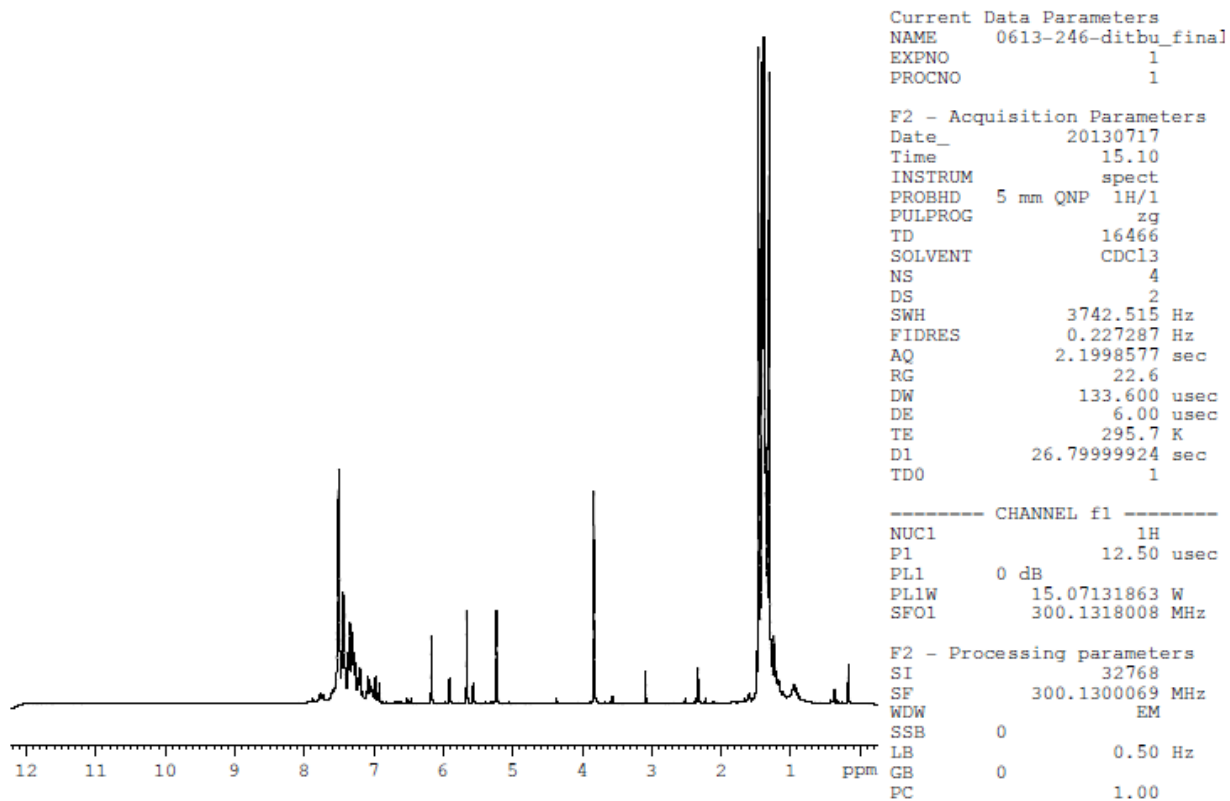


**Figure B.32. Final product ratio for [Tp\*Rh(PPh<sub>3</sub>)<sub>2</sub>] catalyzed hydrothiolation of 3,5-di(*tert*-butyl)phenylacetylene with thiophenol**

**B.17** [Tp\*Rh(PPh<sub>3</sub>)<sub>2</sub>] catalyzed hydrothiolation of 3,5-di(*tert*-butyl)phenylacetylene with *para*-(trifluoromethoxy)thiophenol

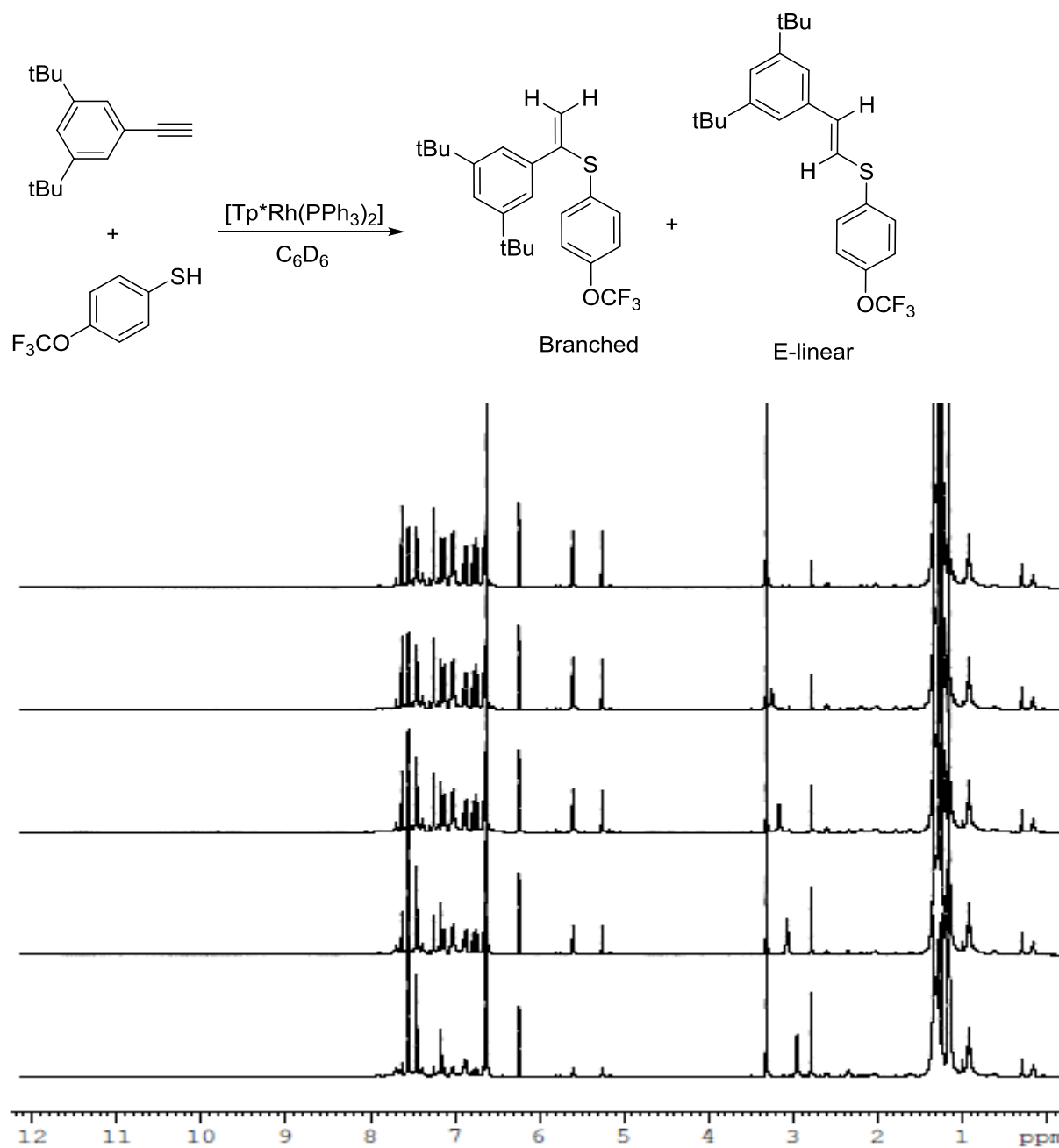


**Figure B.33.** <sup>1</sup>H NMR spectra for [Tp\*Rh(PPh<sub>3</sub>)<sub>2</sub>] catalyzed hydrothiolation of 3,5-di(*tert*-butyl)phenylacetylene with *para*-(trifluoromethoxy)thiophenol

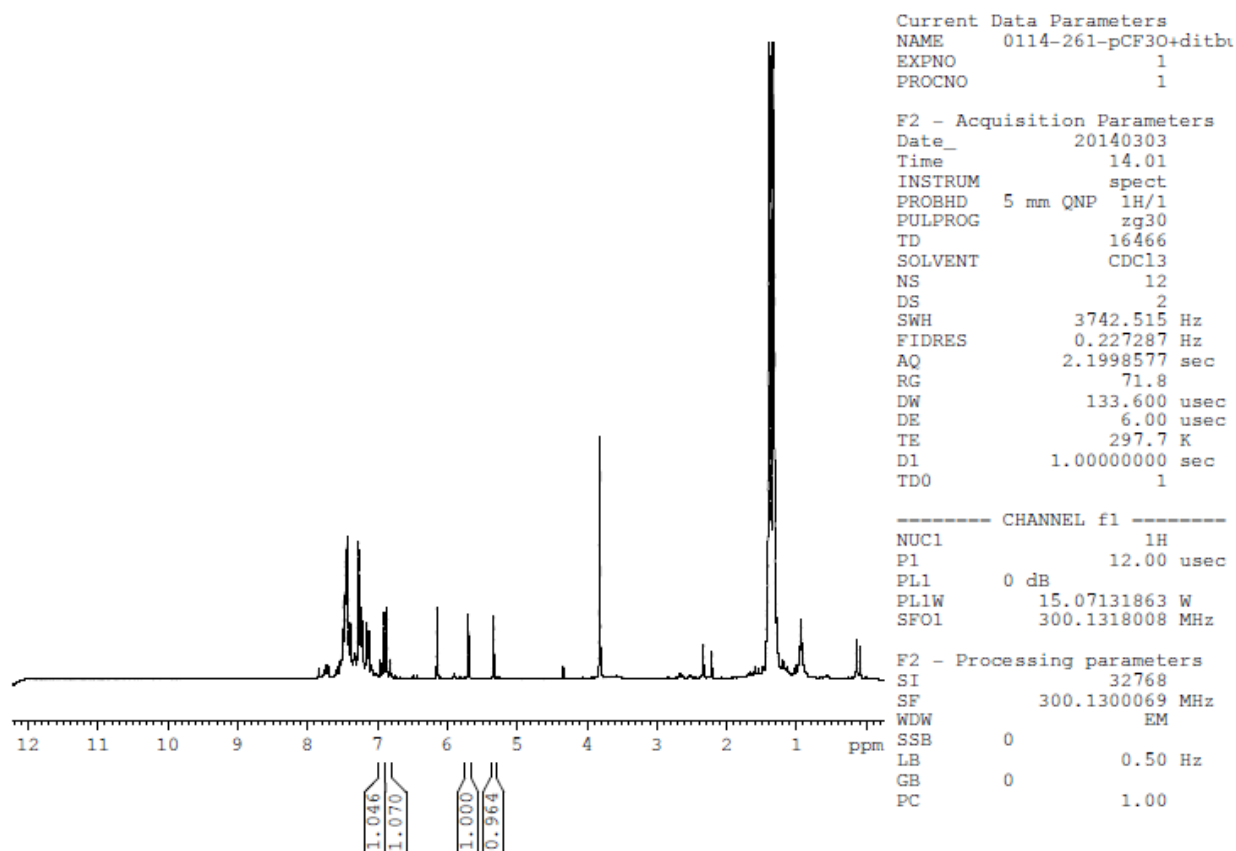


**Figure B.34. Final product ratio for [Tp\*Rh(PPh<sub>3</sub>)<sub>2</sub>] catalyzed hydrothiolation of 3,5-di(*tert*-butyl)phenylacetylene with *para*-(trifluoromethoxy)thiophenol**

**B.18 [Tp\*Rh(PPh<sub>3</sub>)<sub>2</sub>] catalyzed hydrothiolation of mesitylacetylene with thiophenol**

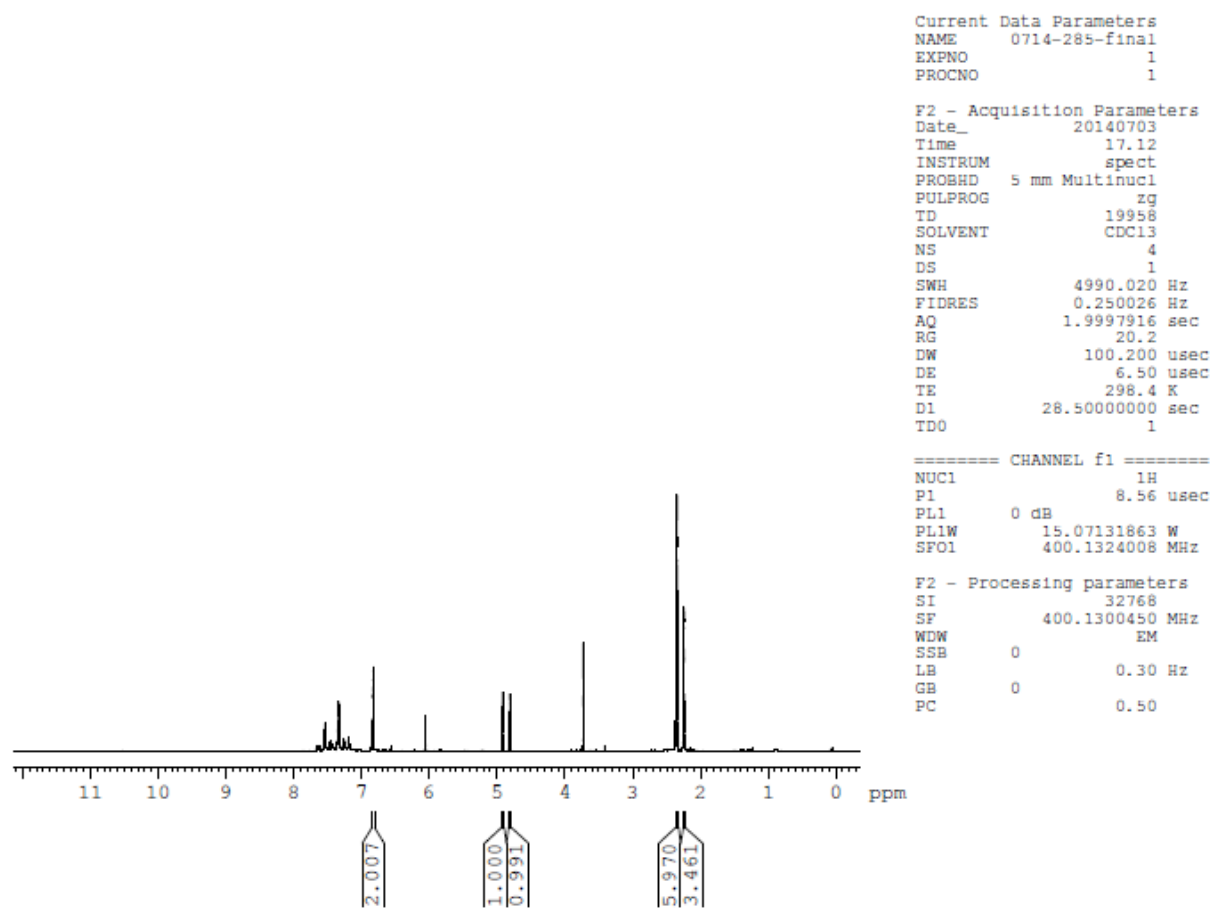
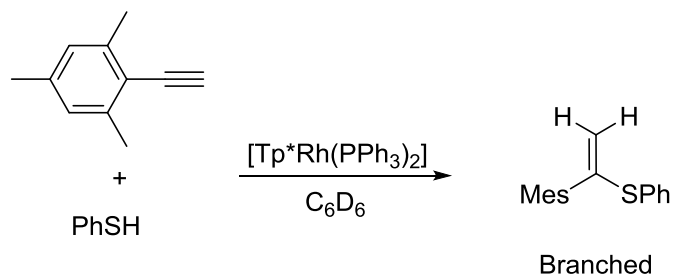


**Figure B.35. Final product ratio for [Tp\*Rh(PPh<sub>3</sub>)<sub>2</sub>] catalyzed hydrothiolation of mesitylacetylene with thiophenol**

**B.19 [Tp\*Rh(PPh<sub>3</sub>)<sub>2</sub>] catalyzed hydrothiolation of mesitylacetylene with *para*-(trifluoromethoxy)thiophenol**

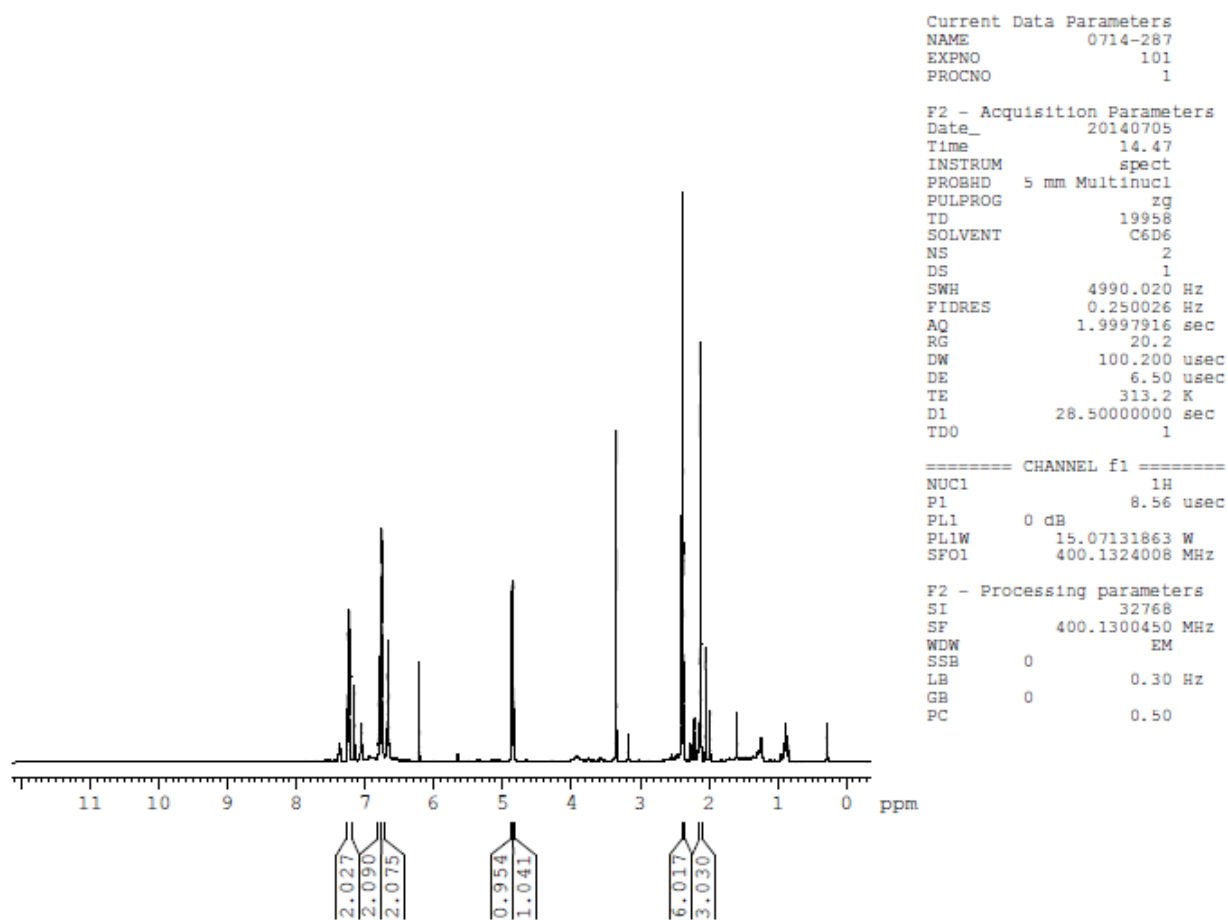
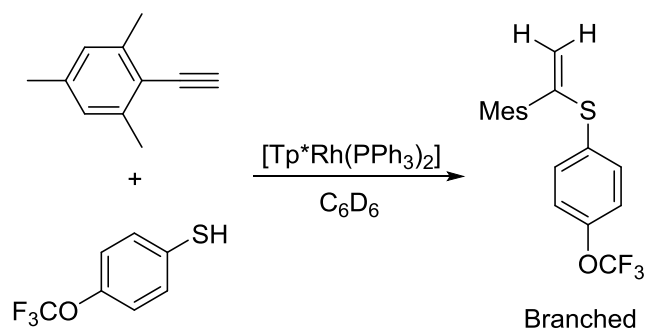


**Figure B.36. Final product ratio for [Tp\*Rh(PPh<sub>3</sub>)<sub>2</sub>] catalyzed hydrothiolation of mesitylacetylene with *para*-(trifluoromethoxy)thiophenol**

**B.20 [Tp\*Rh(PPh<sub>3</sub>)<sub>2</sub>] catalyzed hydrothiolation of *tert*-butylacetylene with thiophenol**

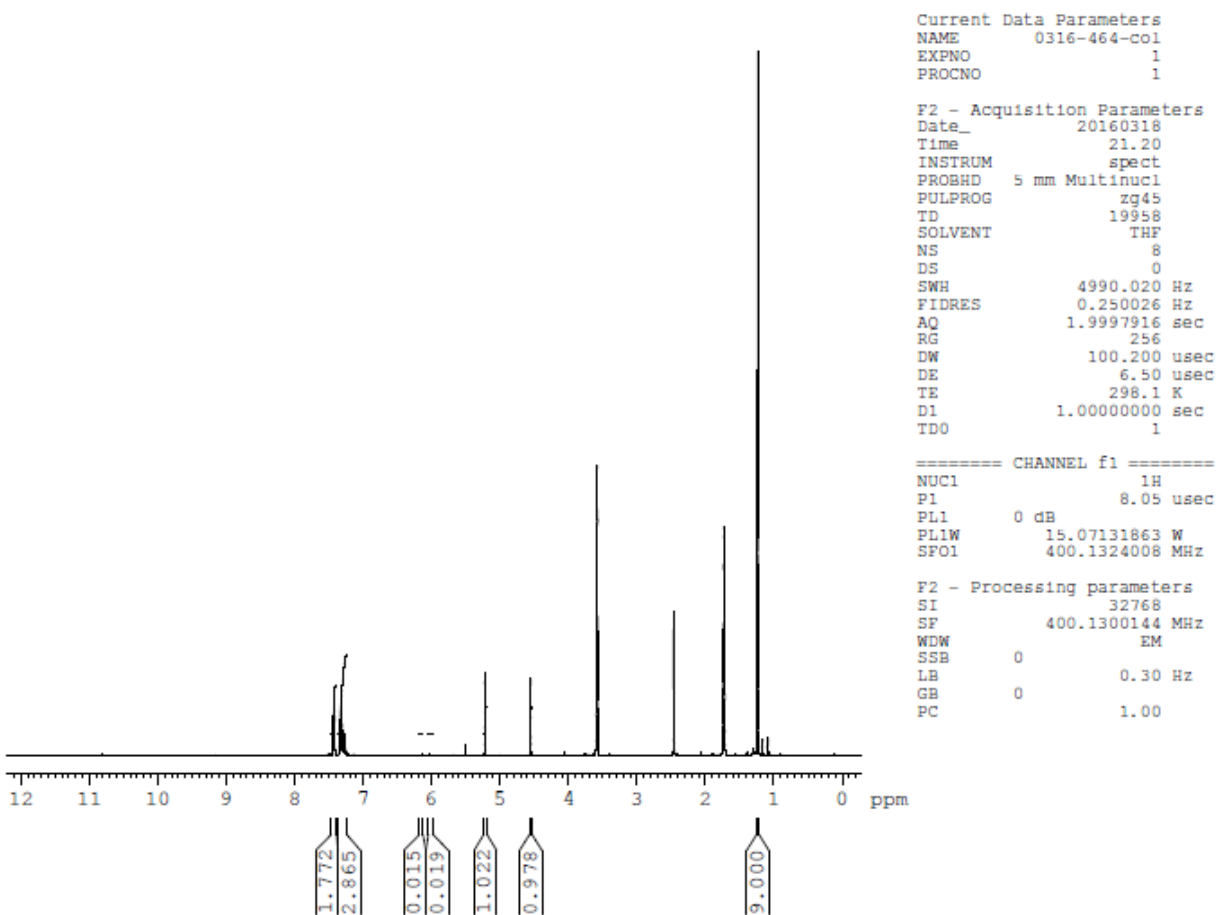
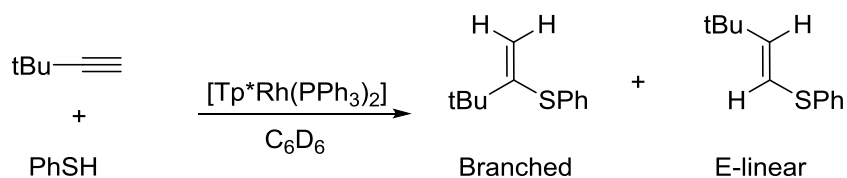


**Figure B.37. Final product ratio for [Tp\*Rh(PPh<sub>3</sub>)<sub>2</sub>] catalyzed hydrothiolation of *tert*-butylacetylene with thiophenol**

**B.21**  $[\text{Tp}^*\text{Rh}(\text{PPh}_3)_2]$  catalyzed hydrothiolation of *tert*-butylacetylene with *para*-(trifluoromethoxy)thiophenol

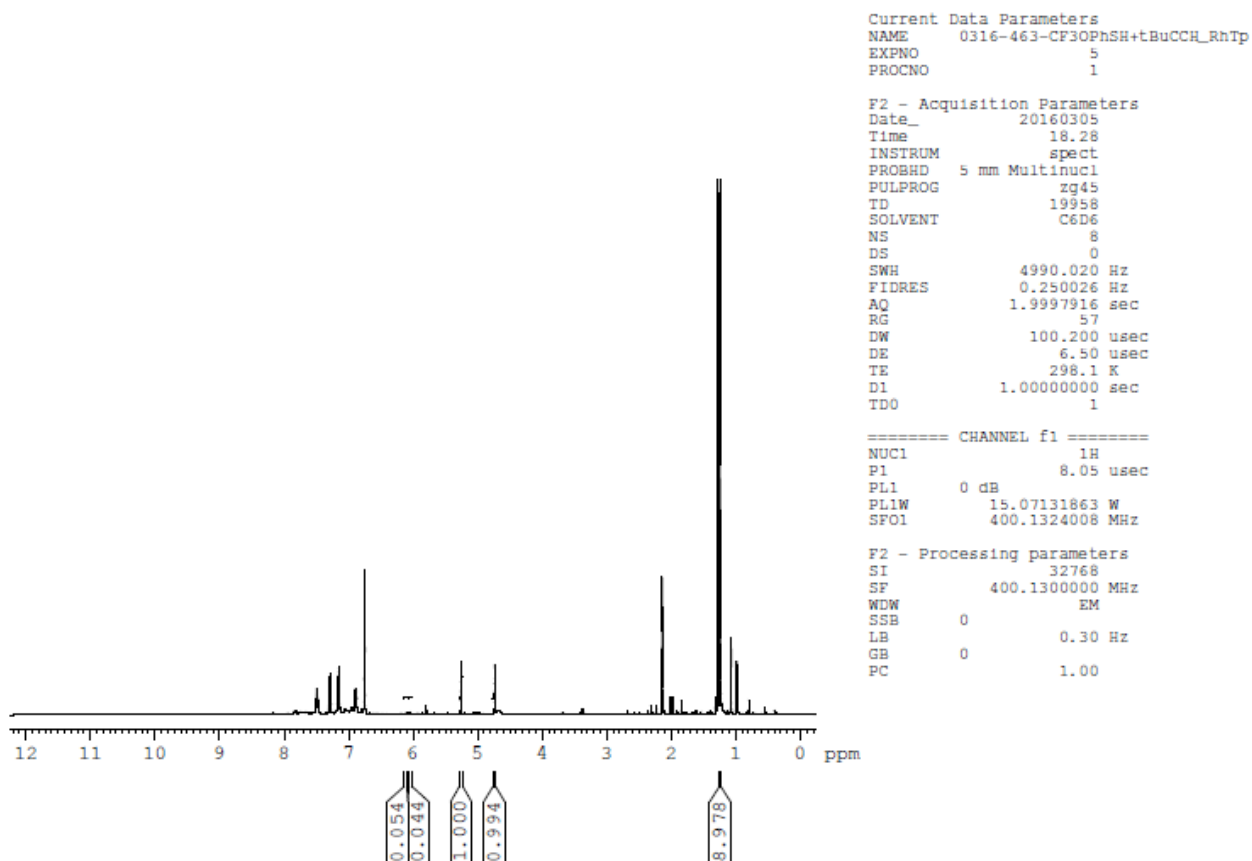
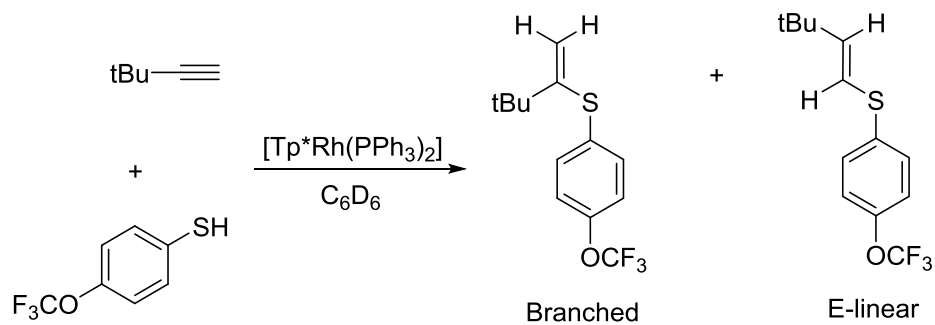


**Figure B.38.** Product ratio for  $[\text{Tp}^*\text{Rh}(\text{PPh}_3)_2]$  catalyzed hydrothiolation of *tert*-butylacetylene with *para*-(trifluoromethoxy)thiophenol

## Appendix C Characterization of Substituted Aldehydes and Alkynes

### C.1 Characterization of 3,5-dimethylphenylacetylene

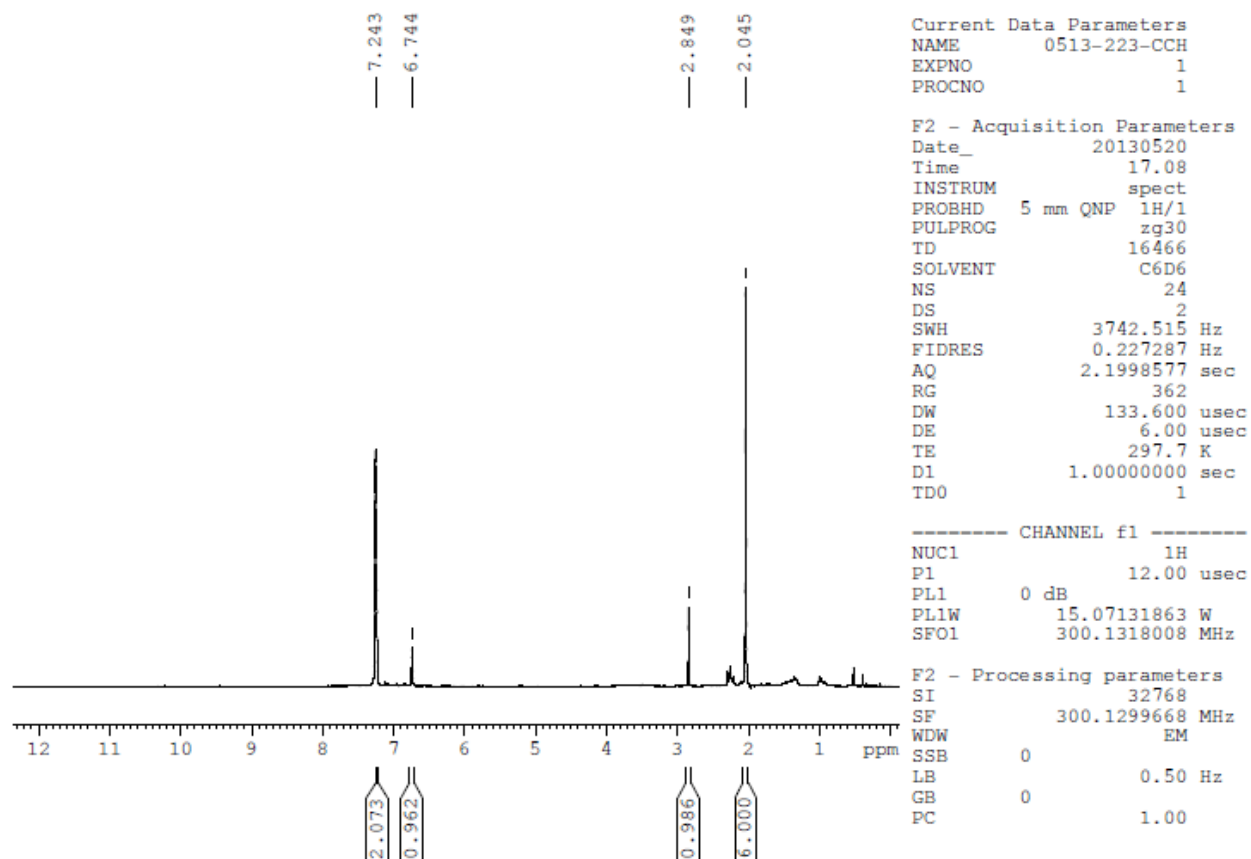


Figure C.1.  $^1\text{H}$  NMR spectrum ( $\text{C}_6\text{D}_6$ , 300 MHz) of 3,5-dimethylphenylacetylene

## C.2 Characterization of 3,5-di(*tert*-butyl)benzaldehyde.

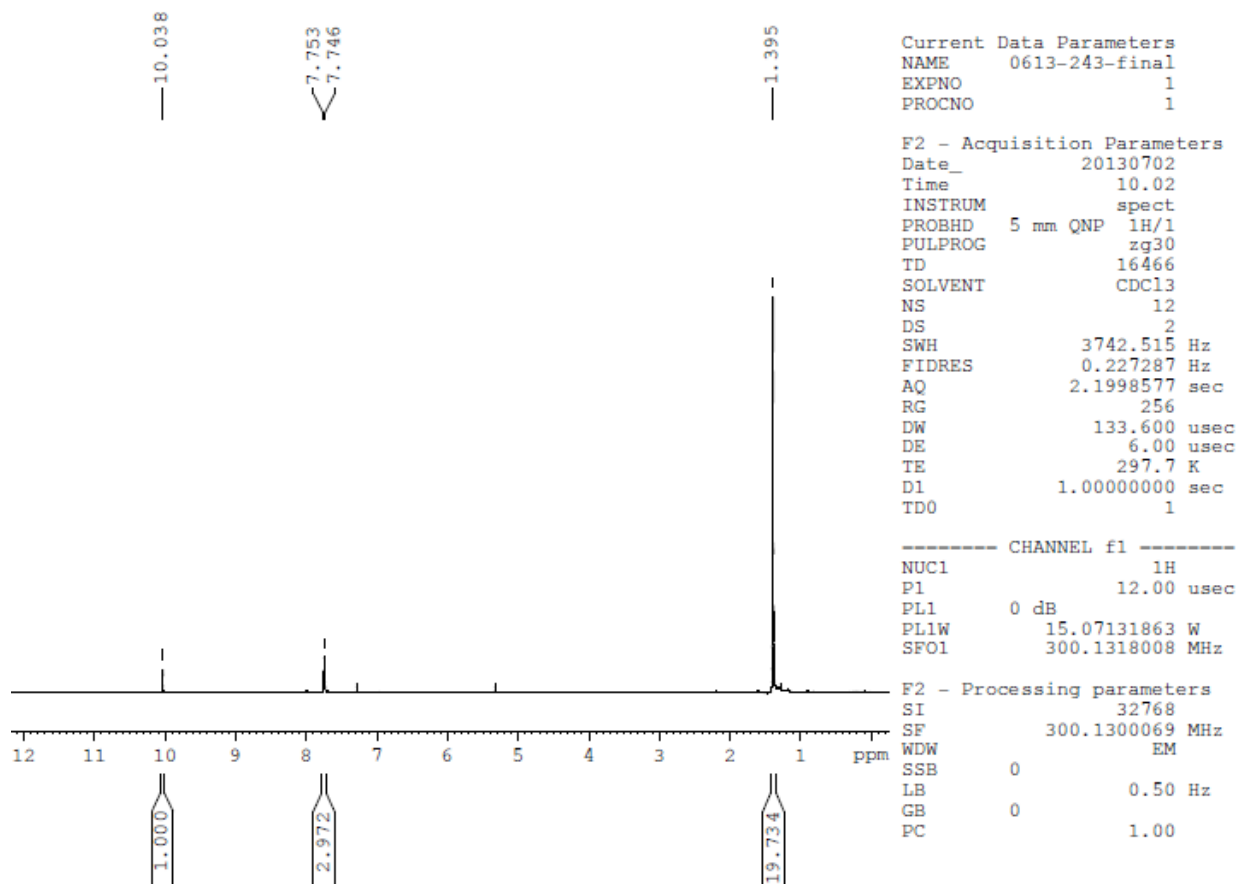


Figure C.2.  $^1\text{H}$  NMR spectrum ( $\text{CDCl}_3$ , 300 MHz) of 3,5-di(*tert*-butyl)benzaldehyde.

### C.3 Characterization of 3,5-di(*tert*-butyl)phenylacetylene.

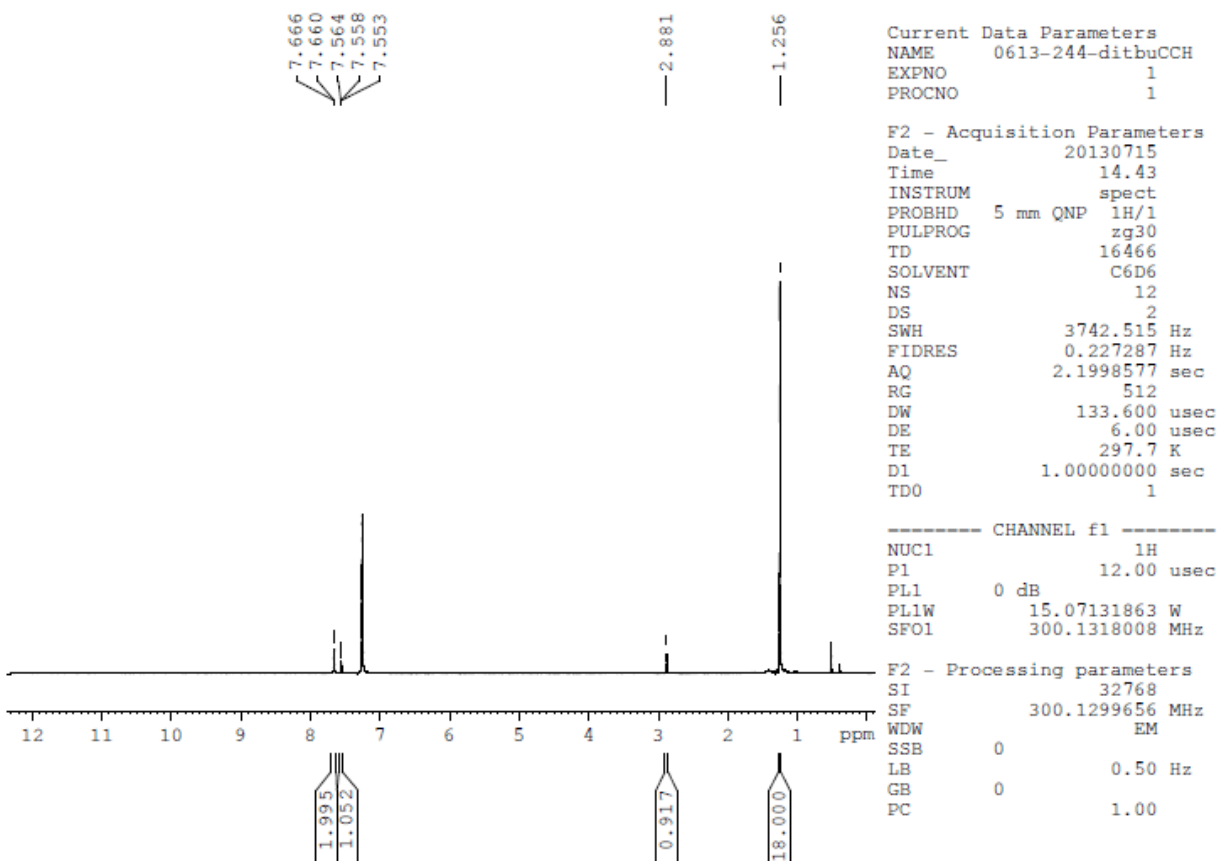


Figure C.3.  $^1\text{H}$  NMR spectrum ( $\text{C}_6\text{D}_6$ , 300 MHz) of 3,5-di(*tert*-butyl)phenylacetylene.

## C.4 Characterization of mesitylaldehyde.

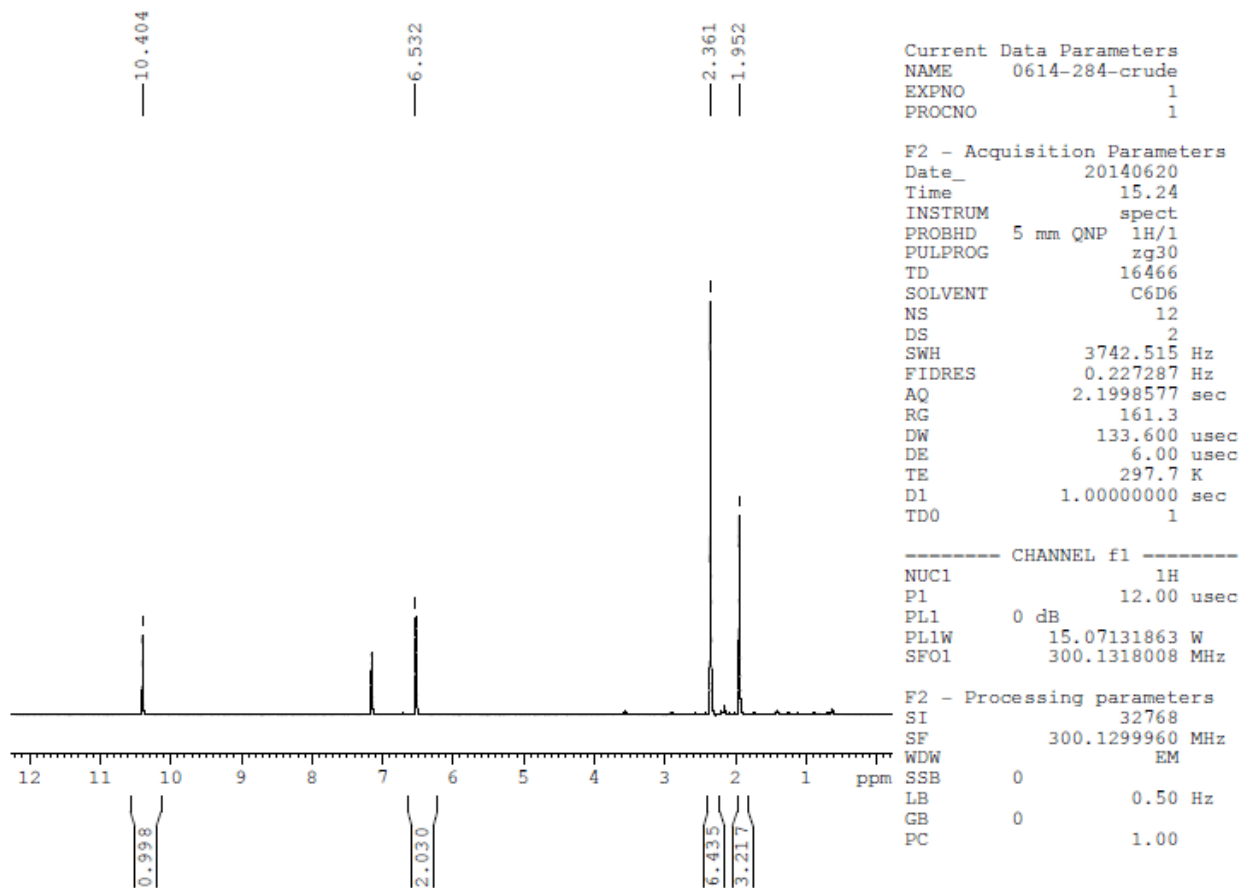


Figure C.4.  $^1\text{H}$  NMR spectrum ( $\text{C}_6\text{D}_6$ , 300 MHz) of mesitylaldehyde.

## C.5 Characterization of mesitylacetylene

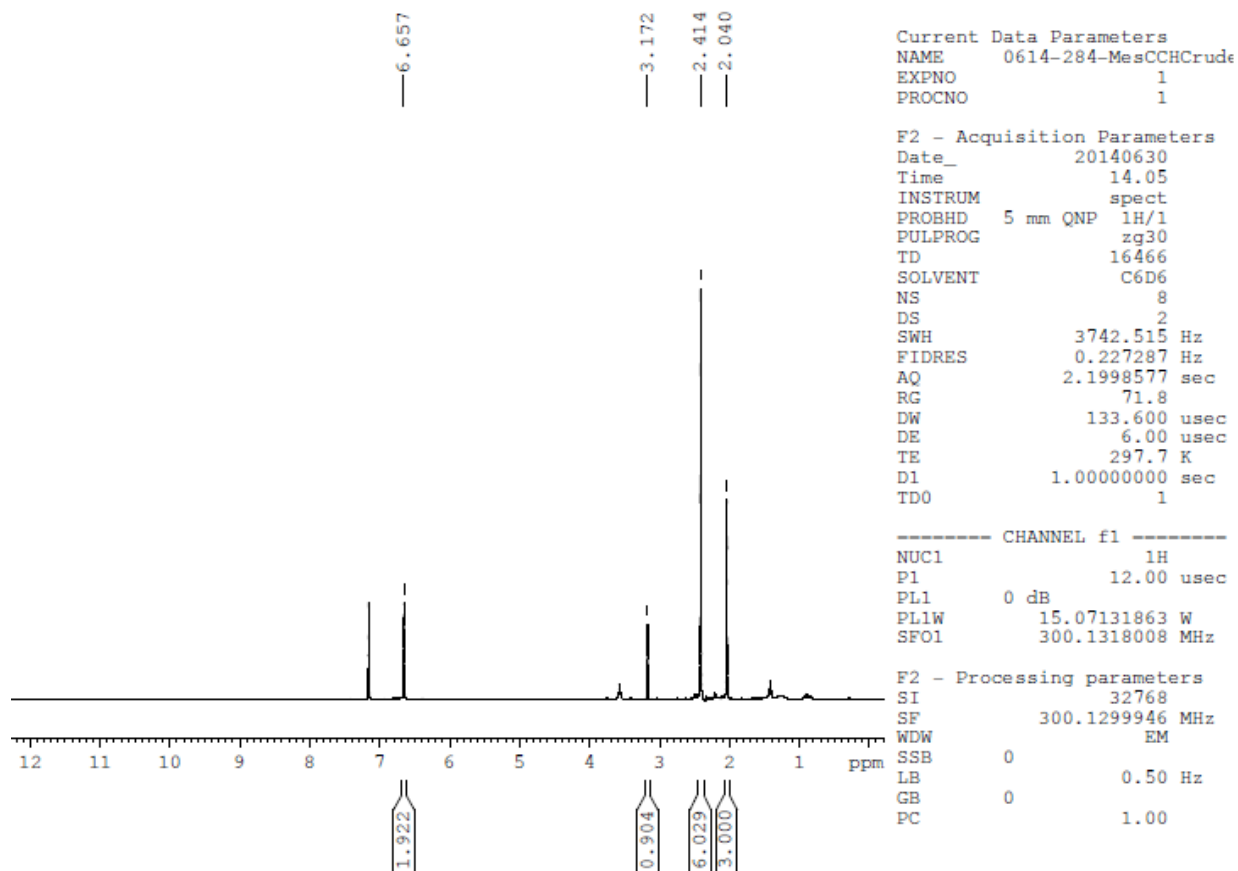


Figure C.5.  $^1\text{H}$  NMR spectrum ( $\text{C}_6\text{D}_6$ , 300 MHz) of mesitylacetylene.

## Appendix D Characterization of [Tp\*Rh<sup>III</sup>] Complexes

### D.1 Characterization of [Tp\*RhCl<sub>2</sub>(MeOH)]

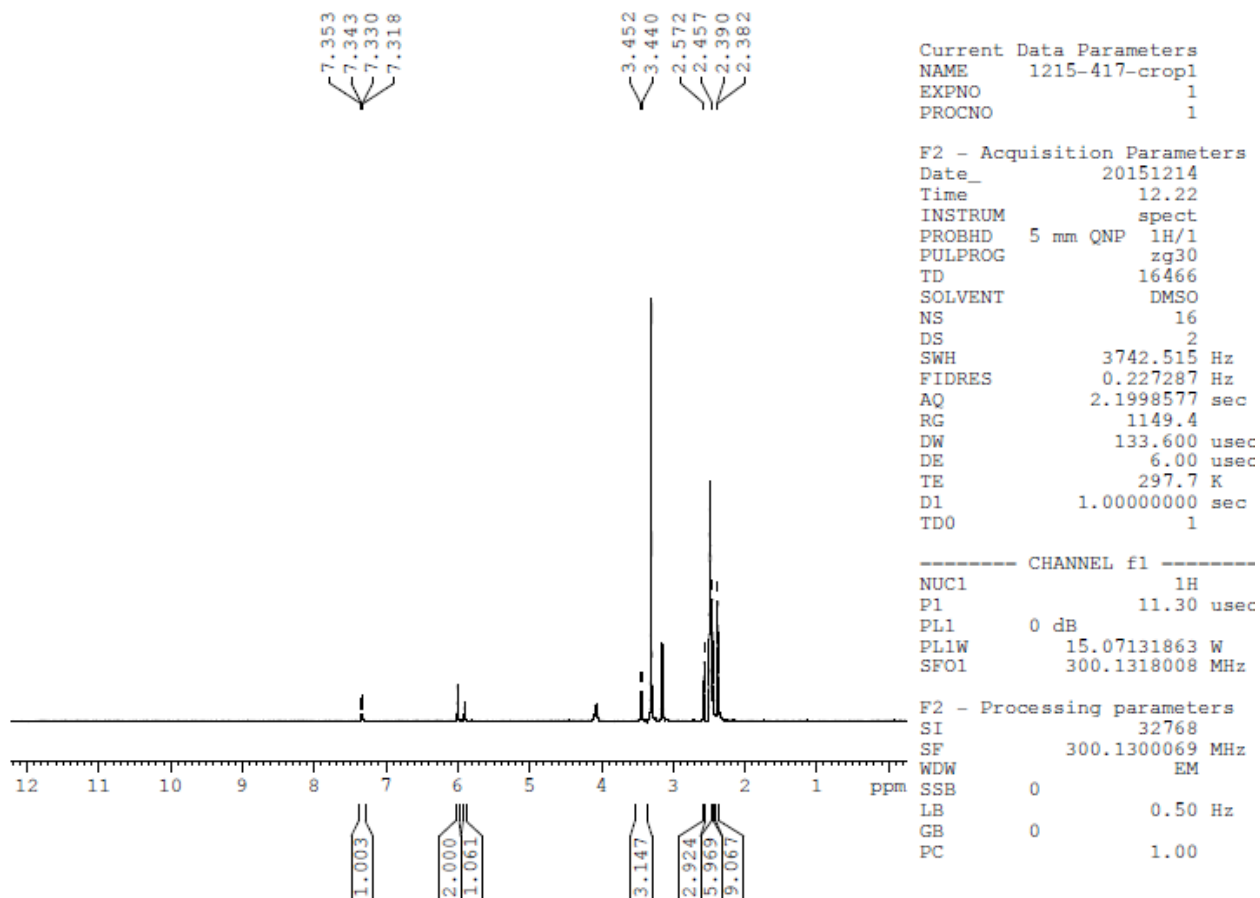


Figure D.1. <sup>1</sup>H NMR spectrum (DMSO-*d*<sub>6</sub>, 300 MHz) of [Tp\*RhCl<sub>2</sub>(MeOH)].

## D.2 Characterization of [Tp\*RhCl<sub>2</sub>(PPh<sub>3</sub>)]

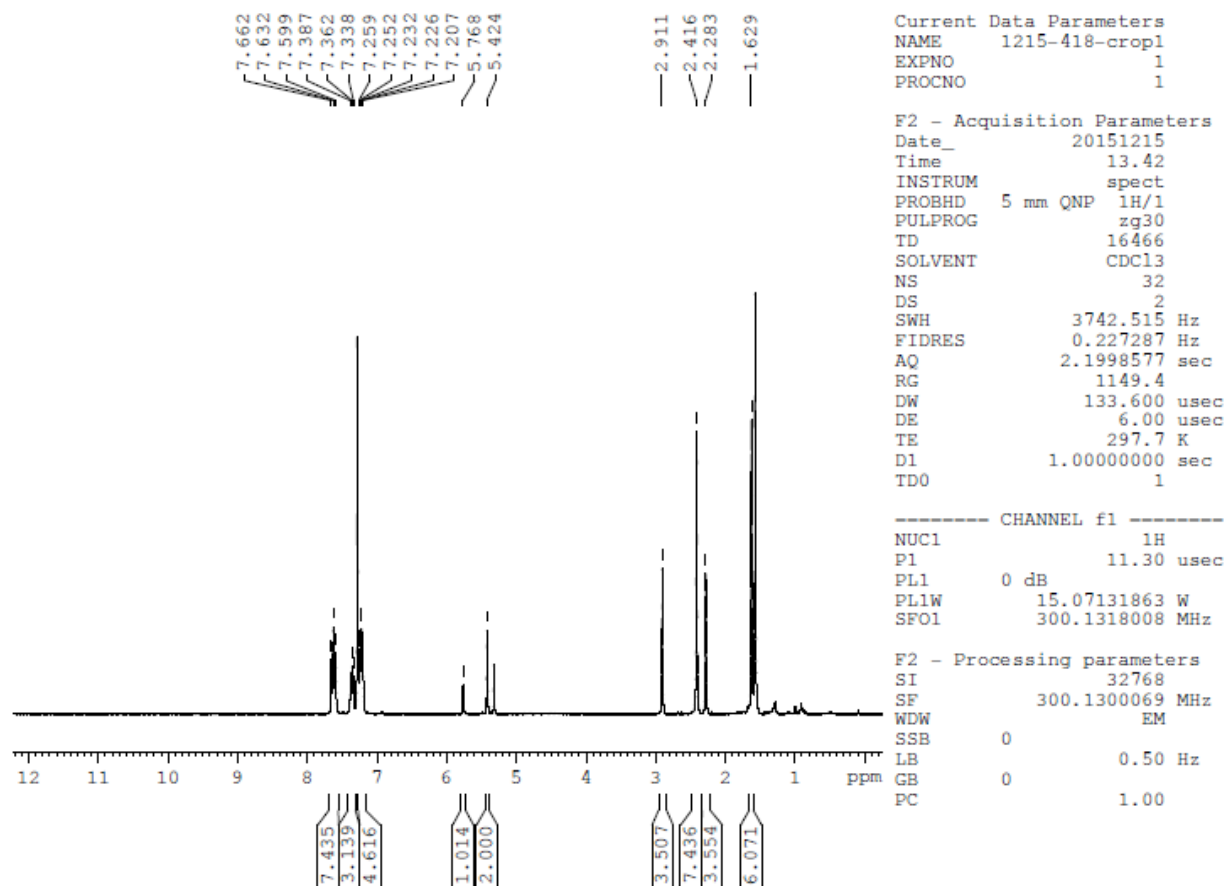


Figure D.2. <sup>1</sup>H NMR spectrum (CDCl<sub>3</sub>, 300 MHz) of [Tp\*RhCl<sub>2</sub>(PPh<sub>3</sub>)].

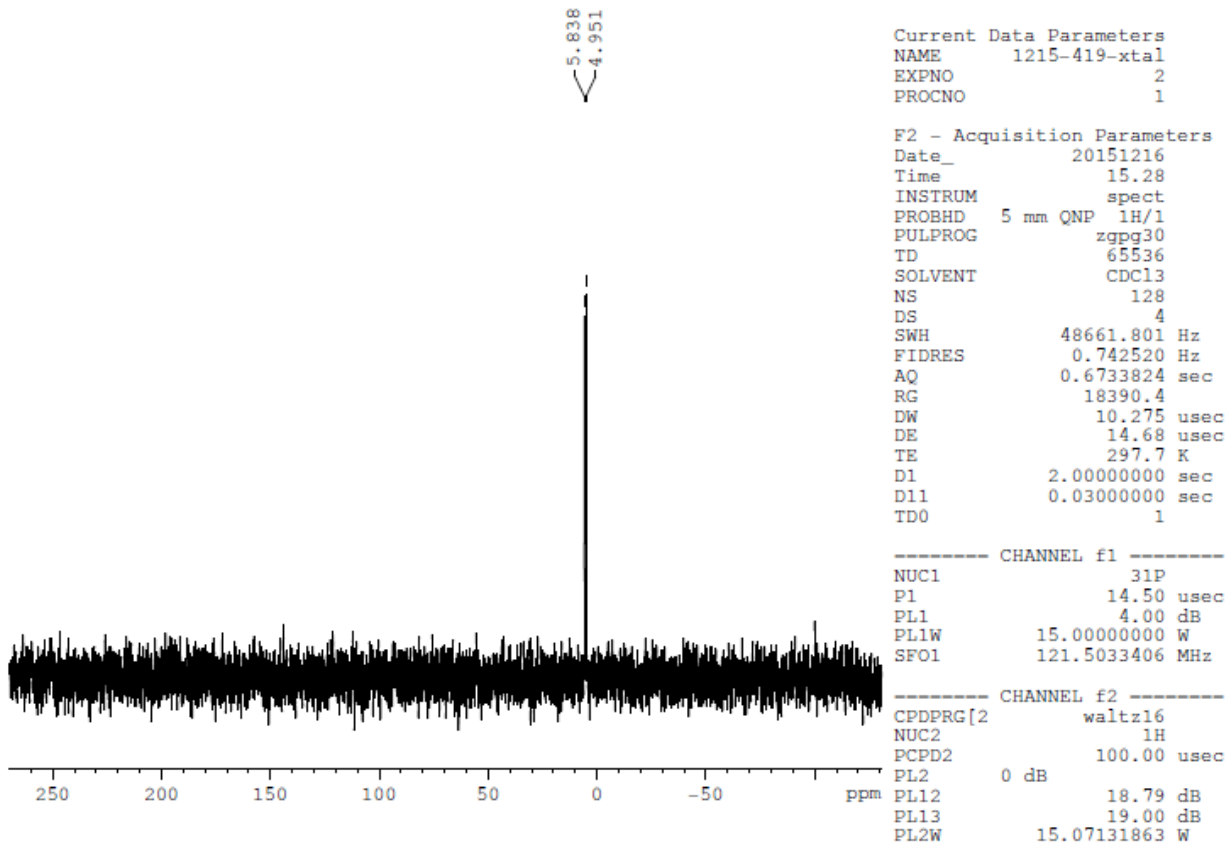


Figure D.3.  $^{31}\text{P}\{^1\text{H}\}$  NMR spectrum ( $\text{CDCl}_3$ , 300 MHz) of  $[\text{Tp}^*\text{RhCl}_2(\text{PPh}_3)]$ .

### D.3 Characterization of [Tp\*RhHCl(PPh<sub>3</sub>)]

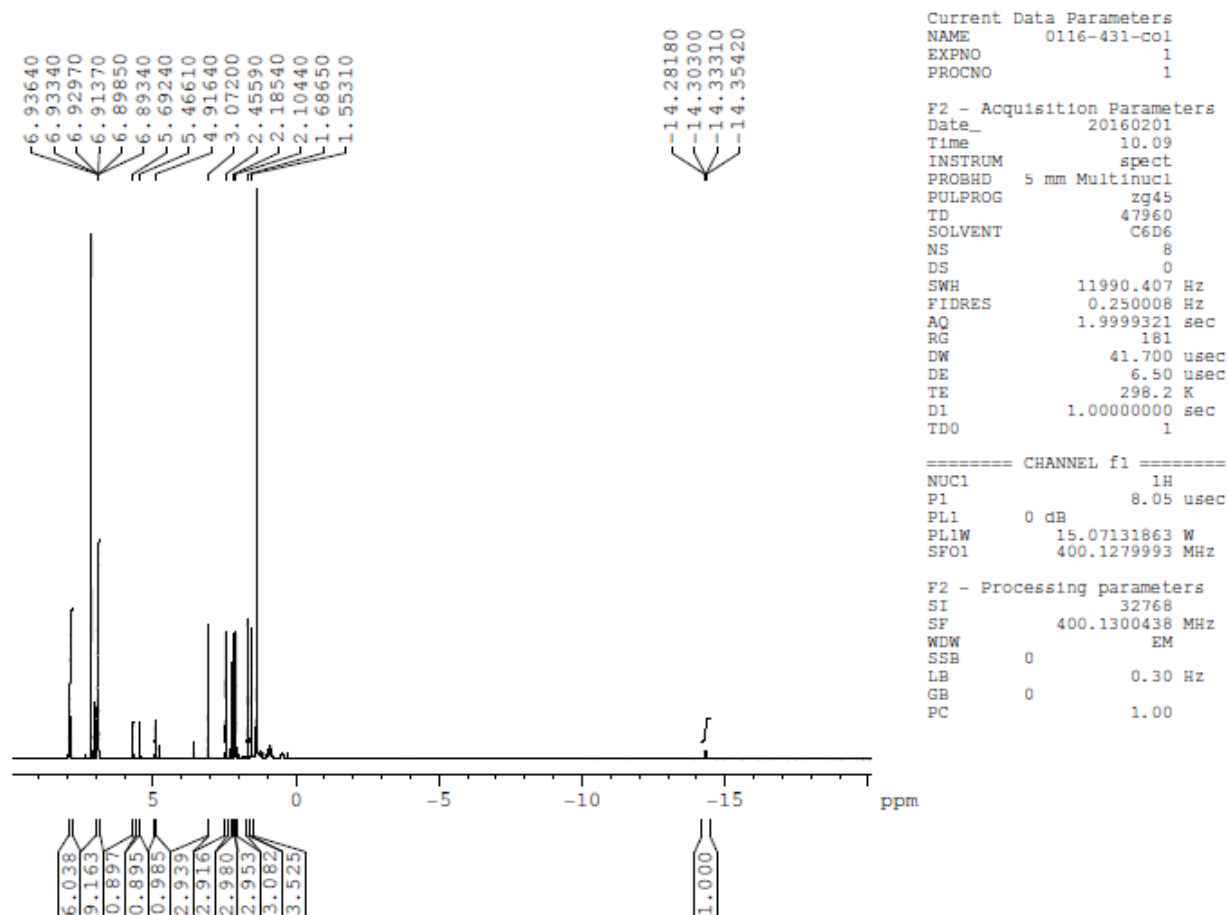


Figure D.4. <sup>1</sup>H NMR spectrum (C<sub>6</sub>D<sub>6</sub>, 400 Mhz) of [Tp\*RhHCl(PPh<sub>3</sub>)]

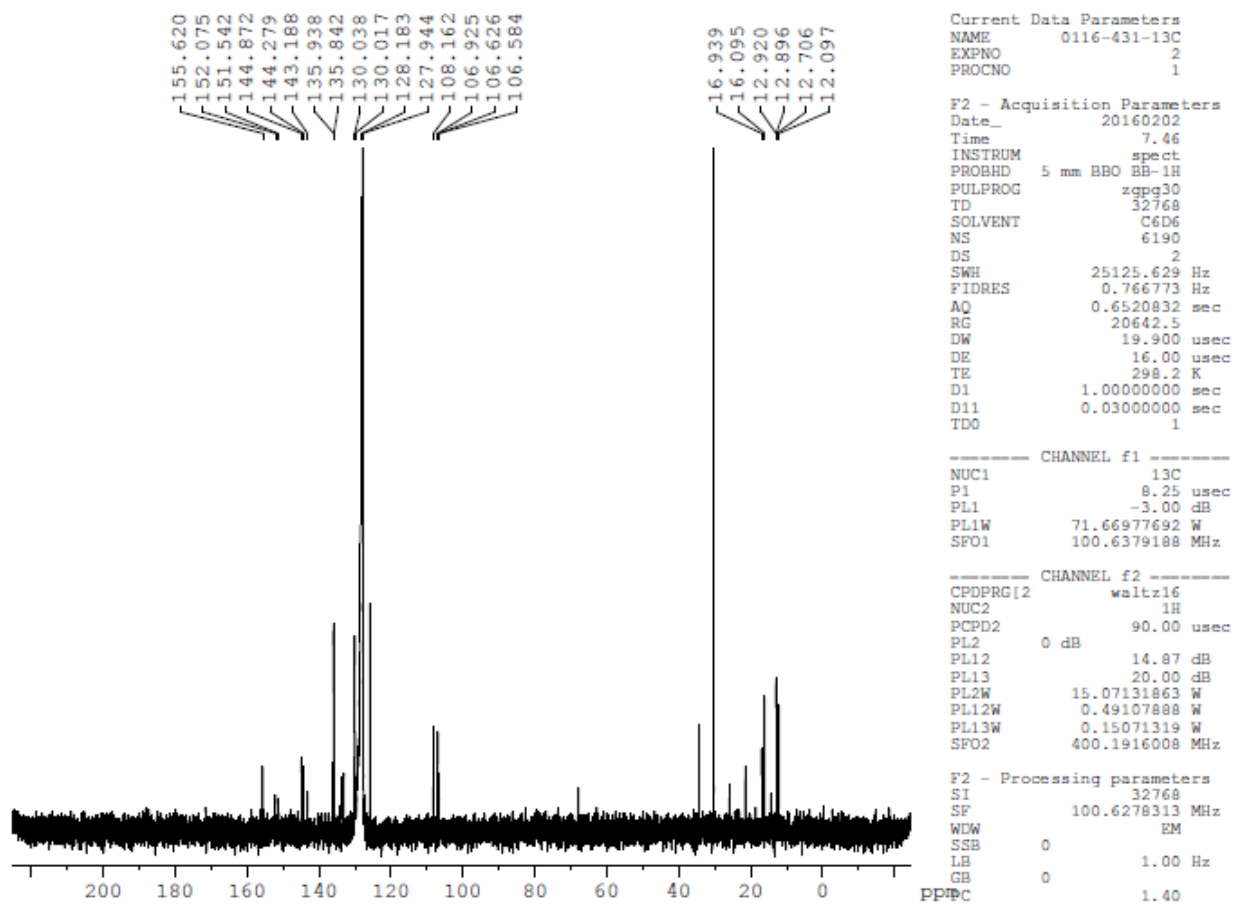


Figure D.5.  $^{13}\text{C}\{^1\text{H}\}$  NMR spectrum ( $\text{C}_6\text{D}_6$ , 100 Mhz) of  $[\text{Tp}^*\text{RhHCl}(\text{PPh}_3)]$

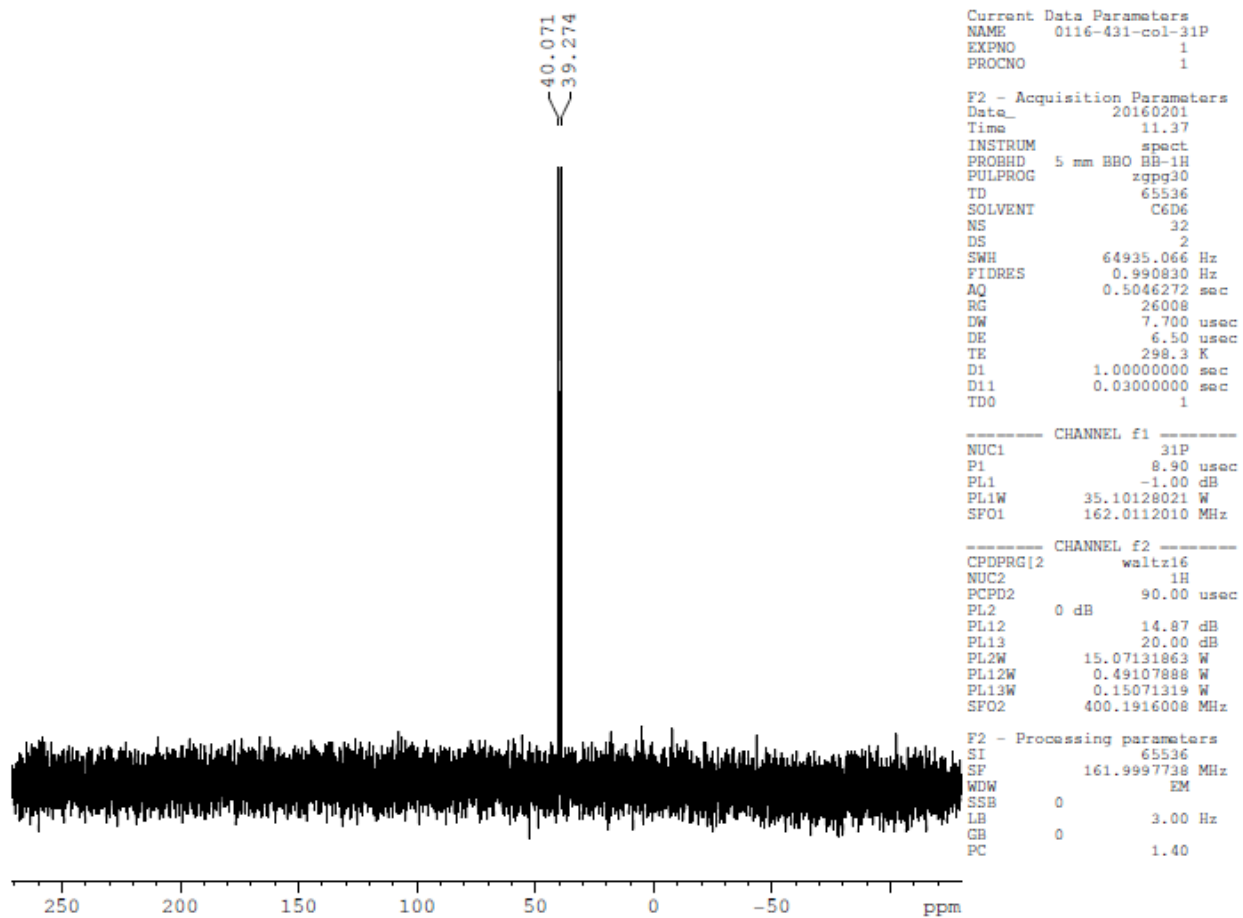


Figure D.6.  $^{31}\text{P}\{^1\text{H}\}$  NMR spectrum ( $\text{C}_6\text{D}_6$ , 162 Mhz) of  $[\text{Tp}^*\text{RhHCl}(\text{PPh}_3)]$

## D.4 Characterization of [Tp\*RhH<sub>2</sub>(PPh<sub>3</sub>)]

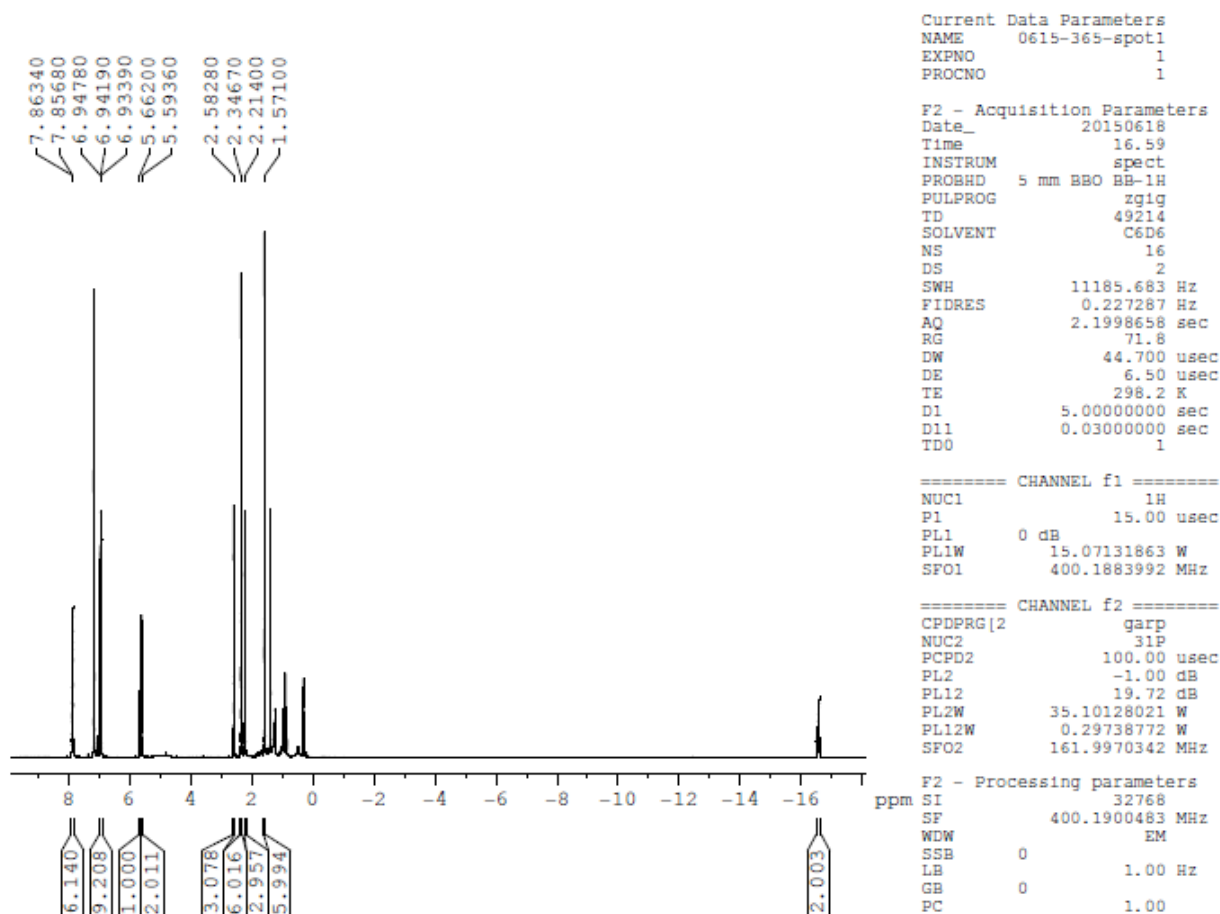


Figure D.7. <sup>1</sup>H NMR spectrum (C<sub>6</sub>D<sub>6</sub>, 400 Mhz) of [Tp\*RhH<sub>2</sub>(PPh<sub>3</sub>)]

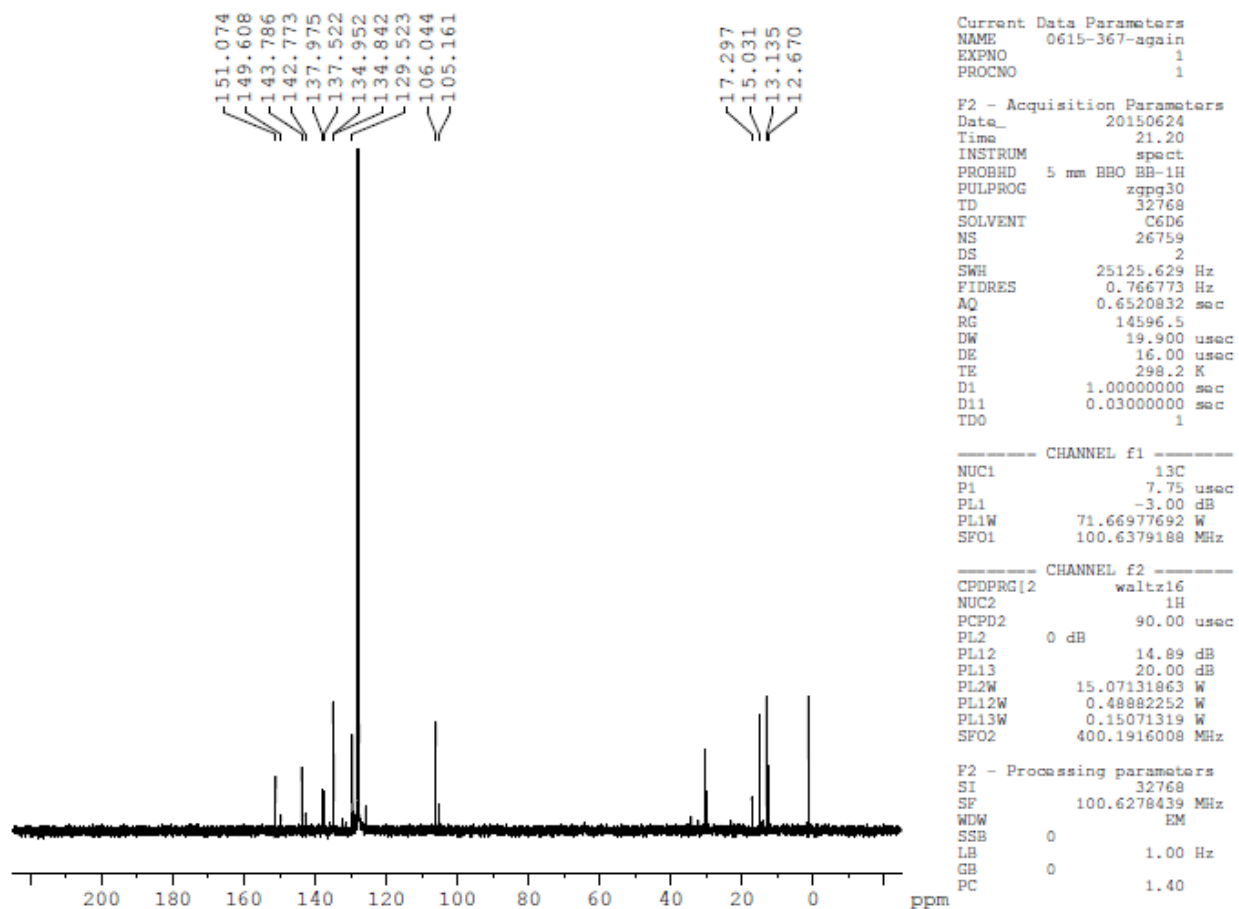


Figure D.8.  $^{13}\text{C}\{^1\text{H}\}$  NMR spectrum ( $\text{C}_6\text{D}_6$ , 100 Mhz) of  $[\text{Tp}^*\text{RhH}_2(\text{PPh}_3)]$

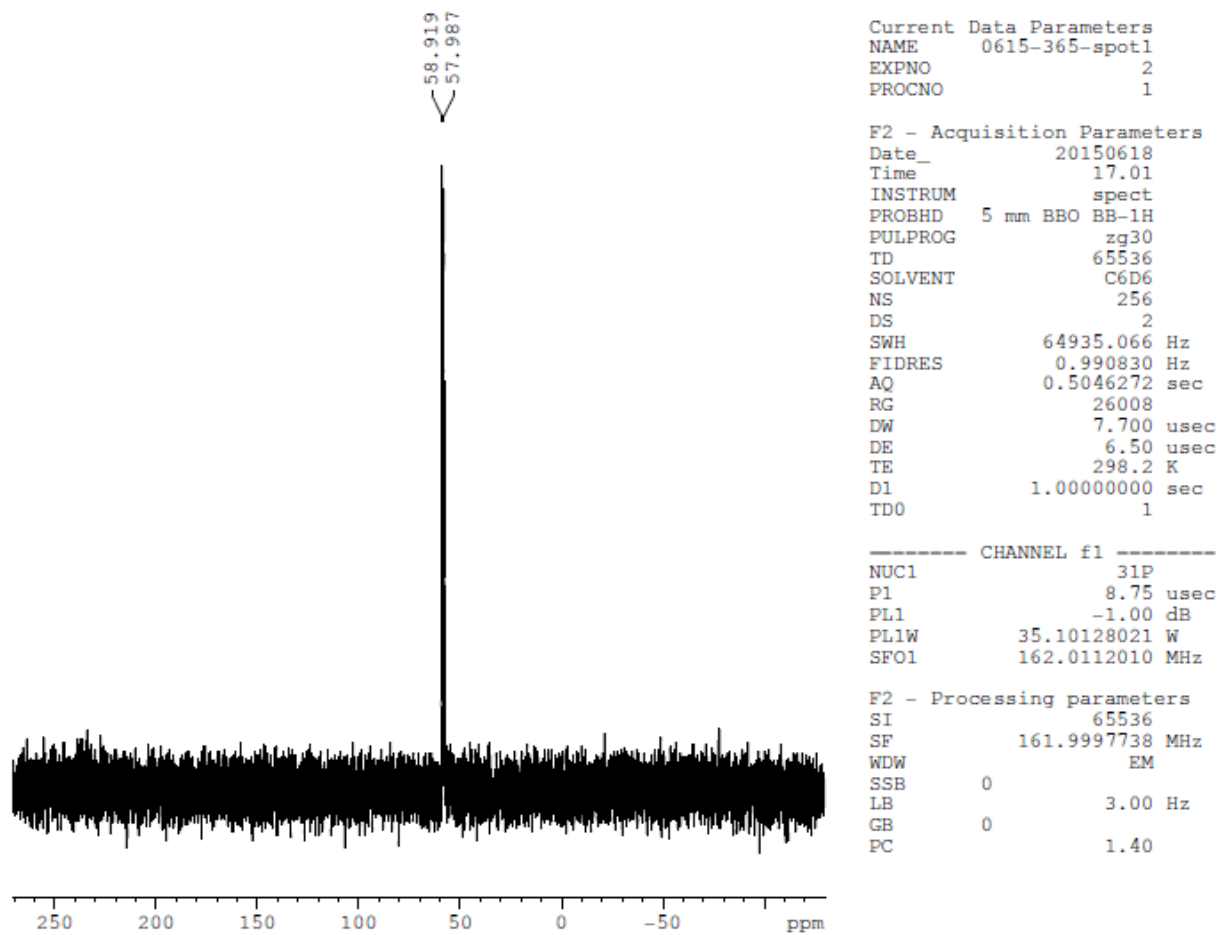


Figure D.9.  $^{31}\text{P}\{^1\text{H}\}$  NMR spectrum ( $\text{C}_6\text{D}_6$ , 162 Mhz) of  $[\text{Tp}^*\text{RhH}_2(\text{PPh}_3)]$

## D.5 Characterization of [Tp\*RhCl<sub>2</sub>(BnSH)]

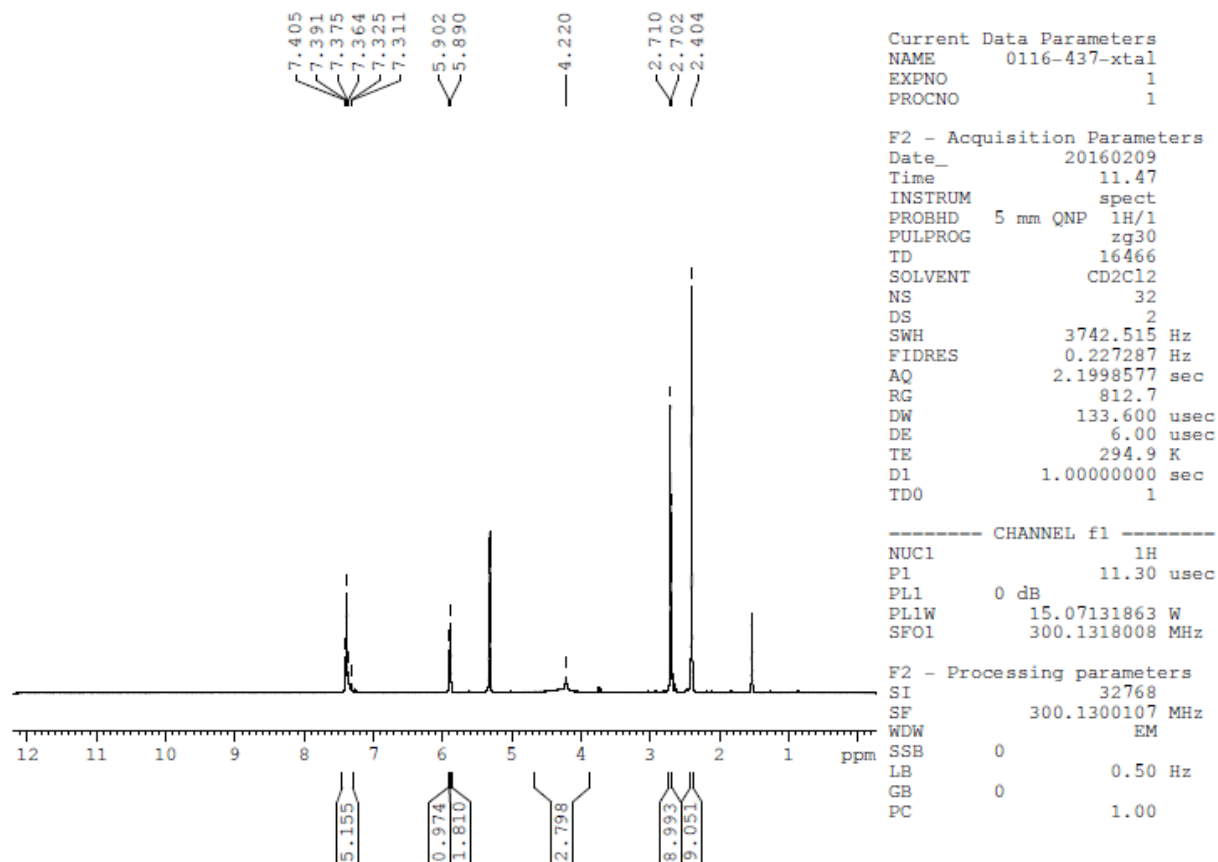


Figure D.10. <sup>1</sup>H NMR spectrum (CD<sub>2</sub>Cl<sub>2</sub>, 300 Mhz) of [Tp\*RhCl<sub>2</sub>(BnSH)]

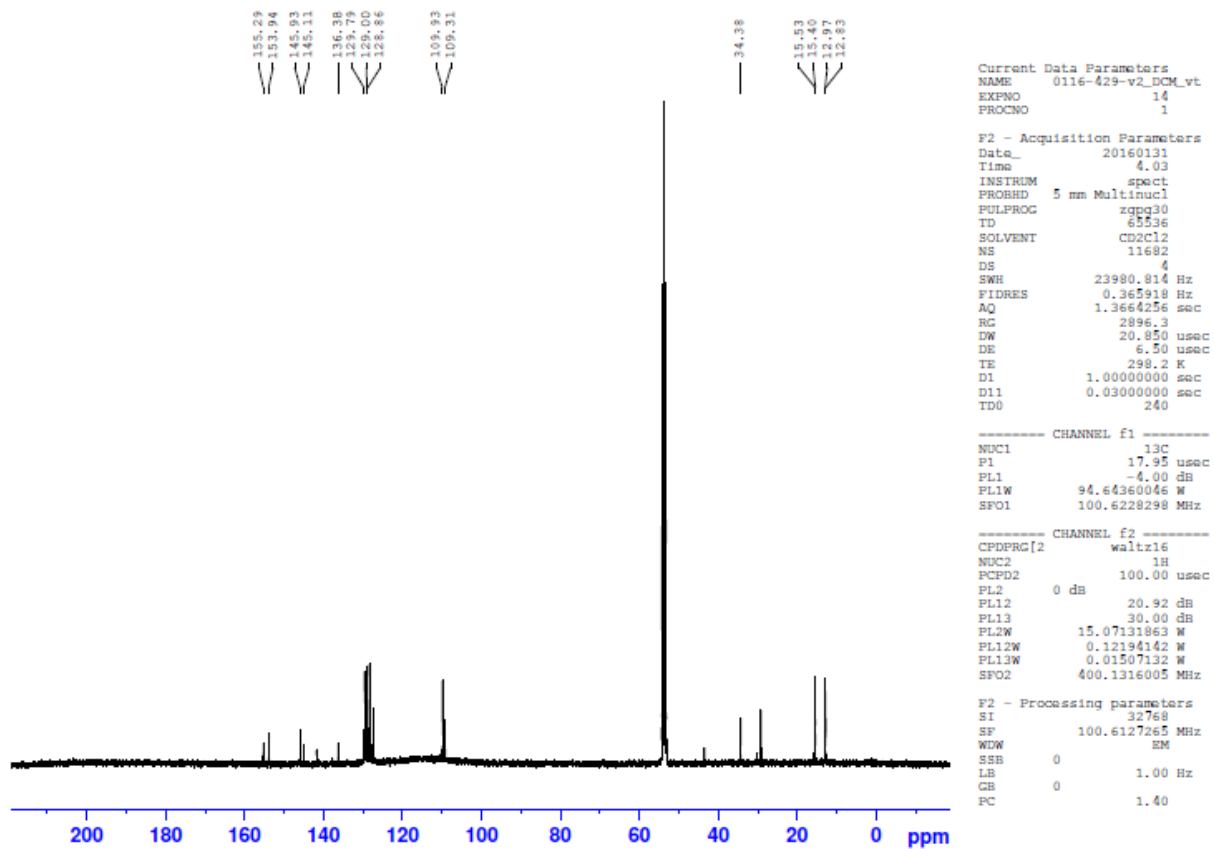


Figure D.11.  $^{13}\text{C}\{^1\text{H}\}$  NMR spectrum ( $\text{CD}_2\text{Cl}_2$ , 100 Mhz) of  $[\text{Tp}^*\text{RhCl}_2(\text{BnSH})]$

## D.6 Characterization of [Tp\*RhCl<sub>2</sub>(PEt<sub>3</sub>)]

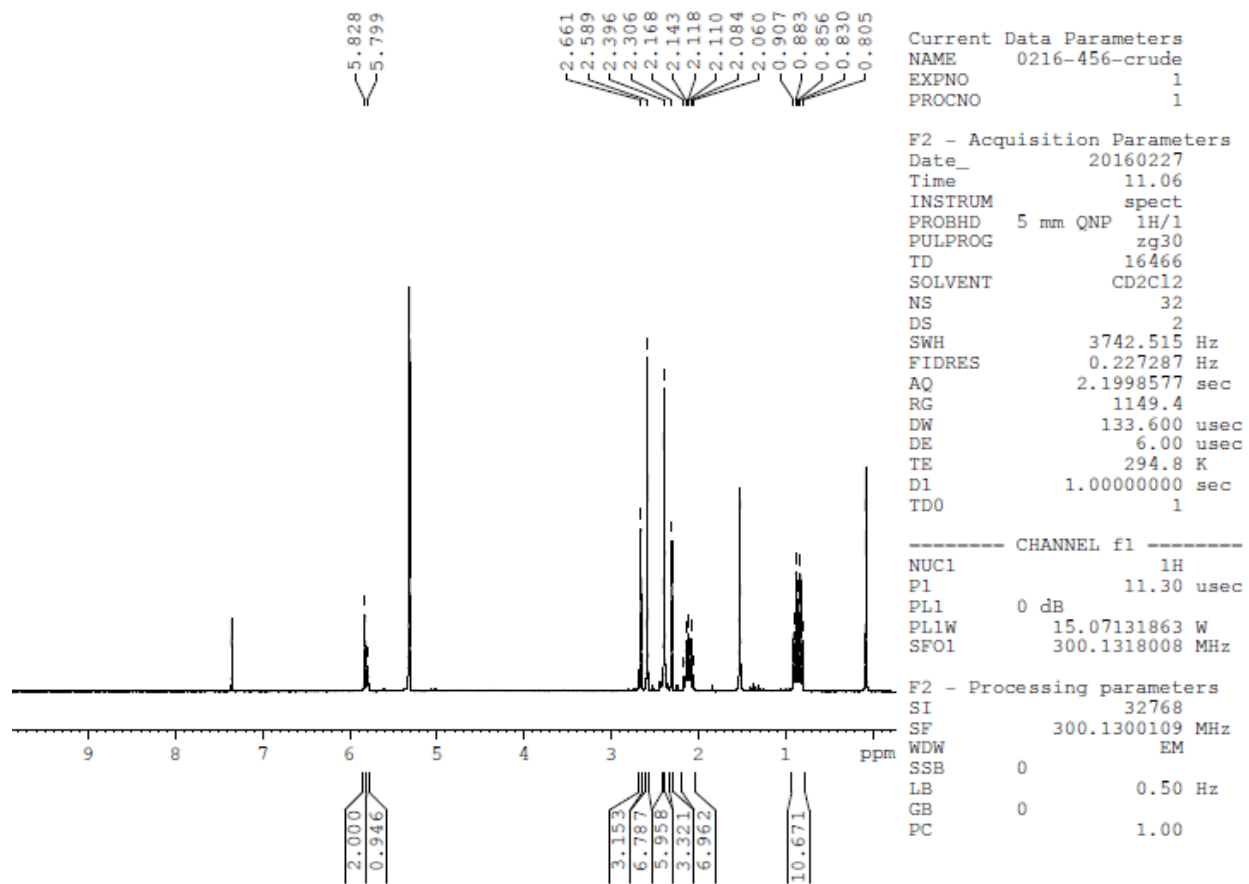


Figure D.12. <sup>1</sup>H NMR spectrum (CD<sub>2</sub>Cl<sub>2</sub>, 300 Mhz) of [Tp\*RhCl<sub>2</sub>(PEt<sub>3</sub>)]

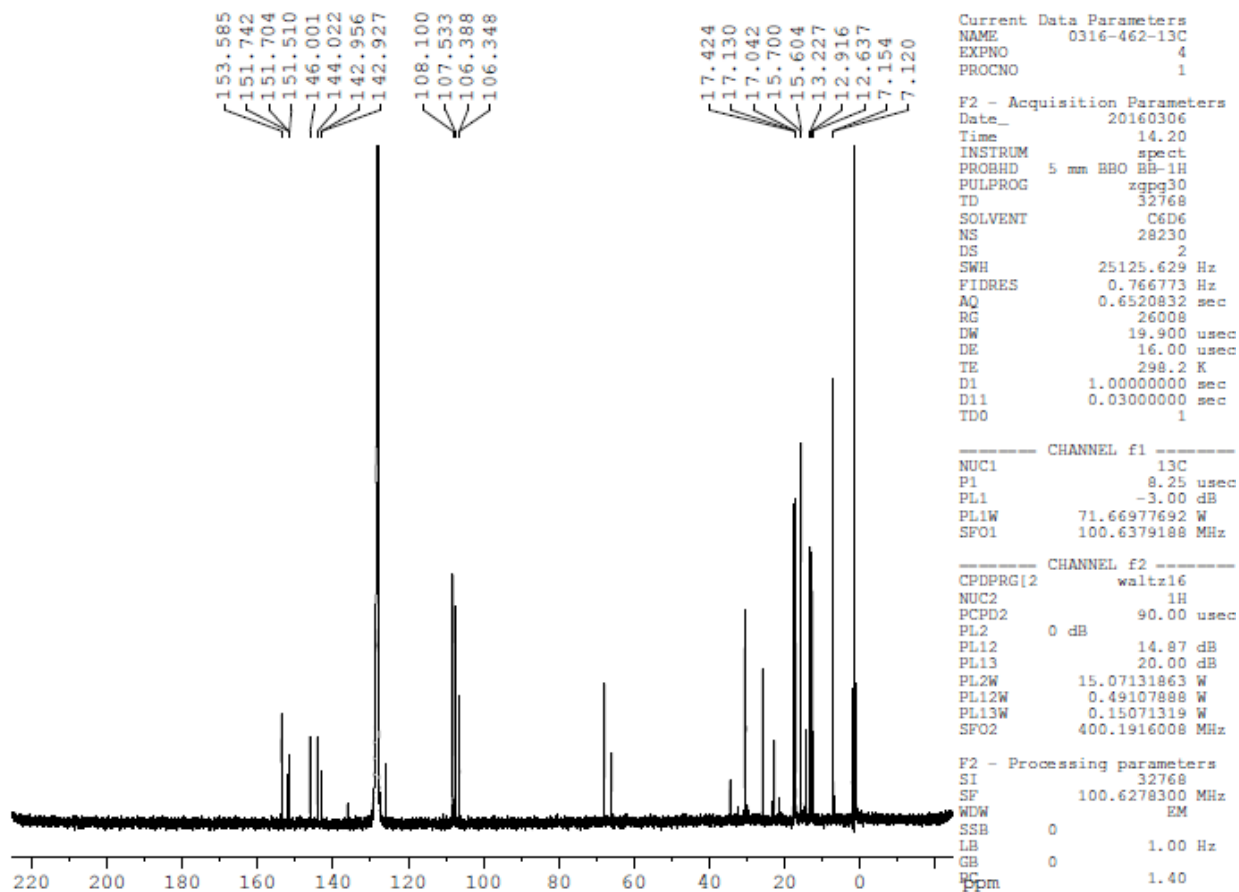


Figure D.13.  $^{13}\text{C}\{^1\text{H}\}$  NMR spectrum ( $\text{C}_6\text{D}_6$ , 100 Mhz) of  $[\text{Tp}^*\text{RhCl}_2(\text{PET}_3)]$

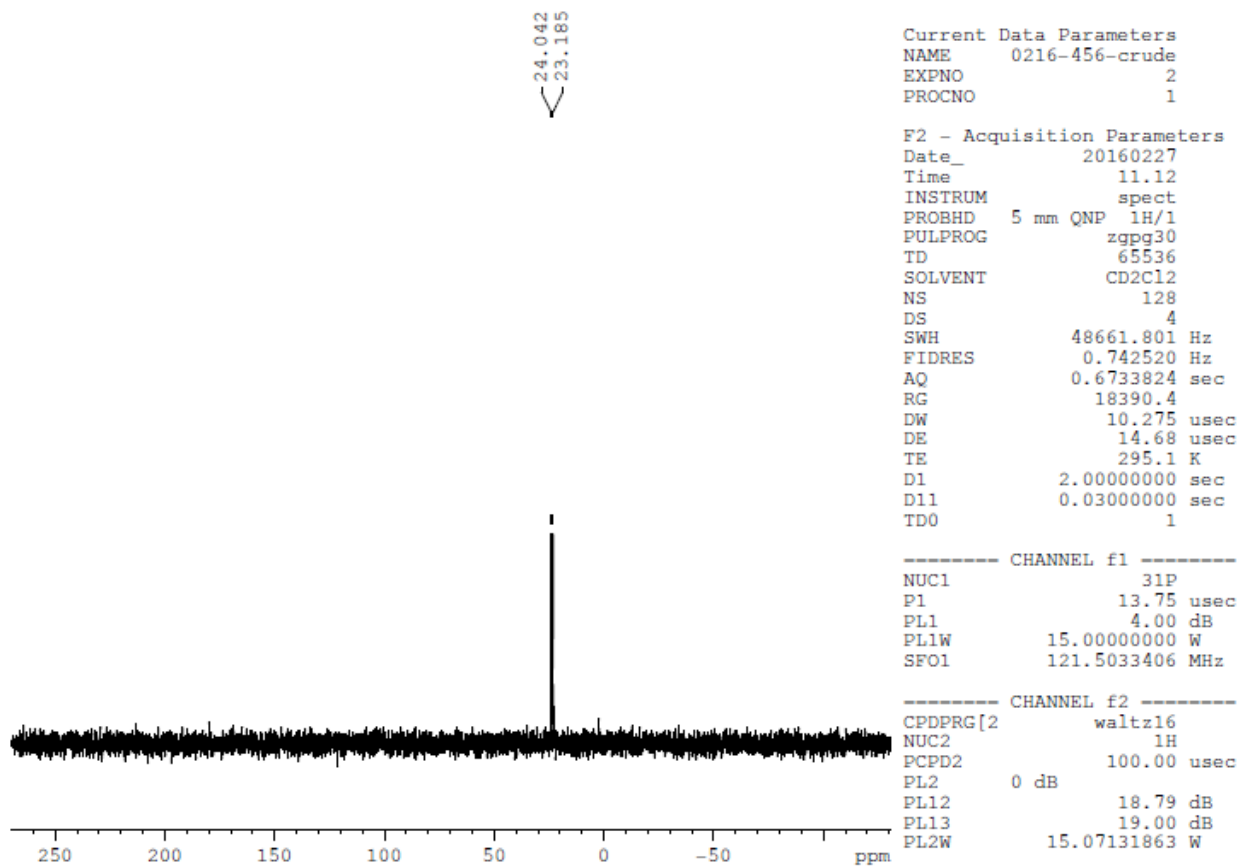


Figure D.14.  $^{31}\text{P}\{^1\text{H}\}$  NMR spectrum ( $\text{CD}_2\text{Cl}_2$ , 122 Mhz) of  $[\text{Tp}^*\text{RhCl}_2(\text{PEt}_3)]$

## D.7 Characterization of [Tp\*RhHCl(PEt<sub>3</sub>)]

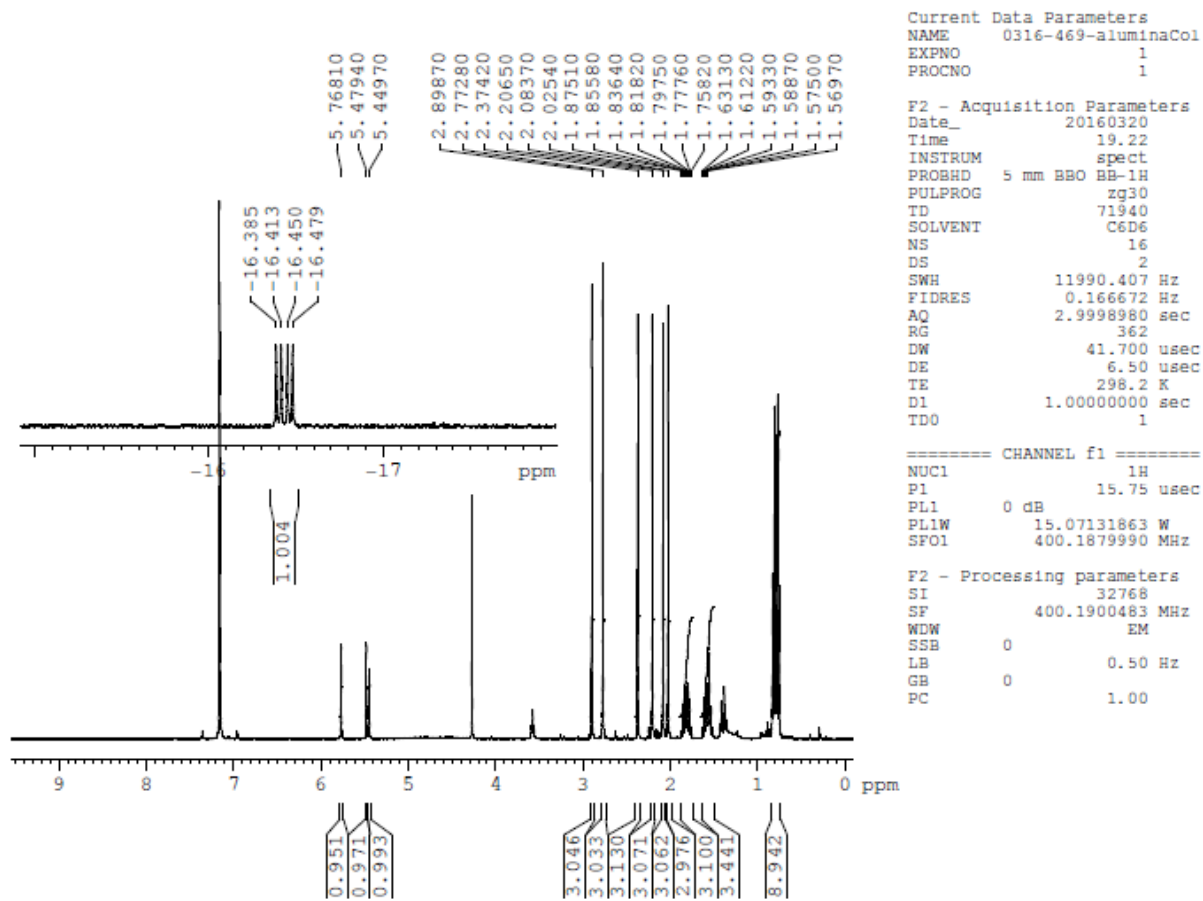


Figure D.15. <sup>1</sup>H NMR spectrum (C<sub>6</sub>D<sub>6</sub>, 400 Mhz) of [Tp\*RhHCl(PEt<sub>3</sub>)]

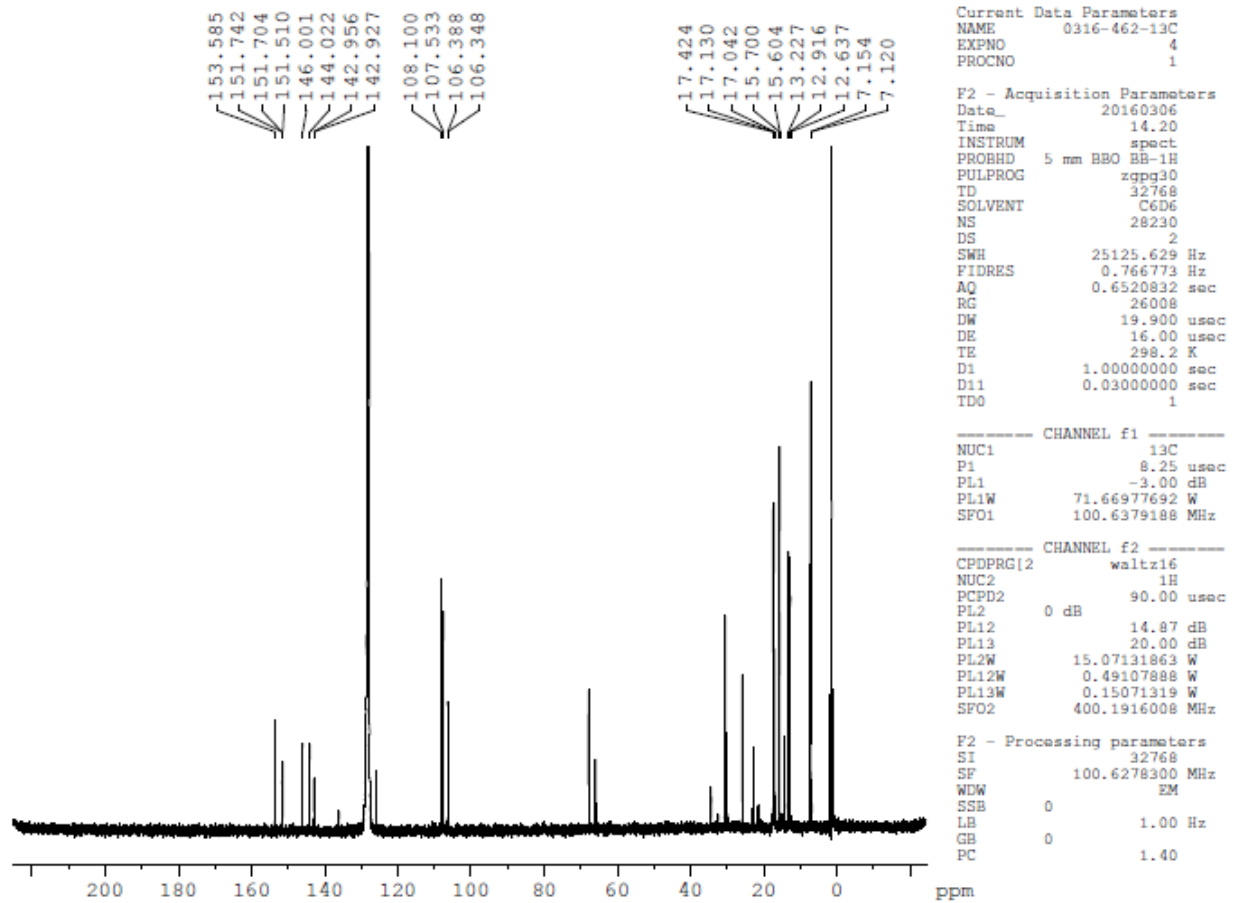


Figure D.16.  $^{13}\text{C}\{^1\text{H}\}$  NMR spectrum ( $\text{C}_6\text{D}_6$ , 100 MHz) of  $[\text{Tp}^*\text{RhHCl}(\text{PET}_3)]$

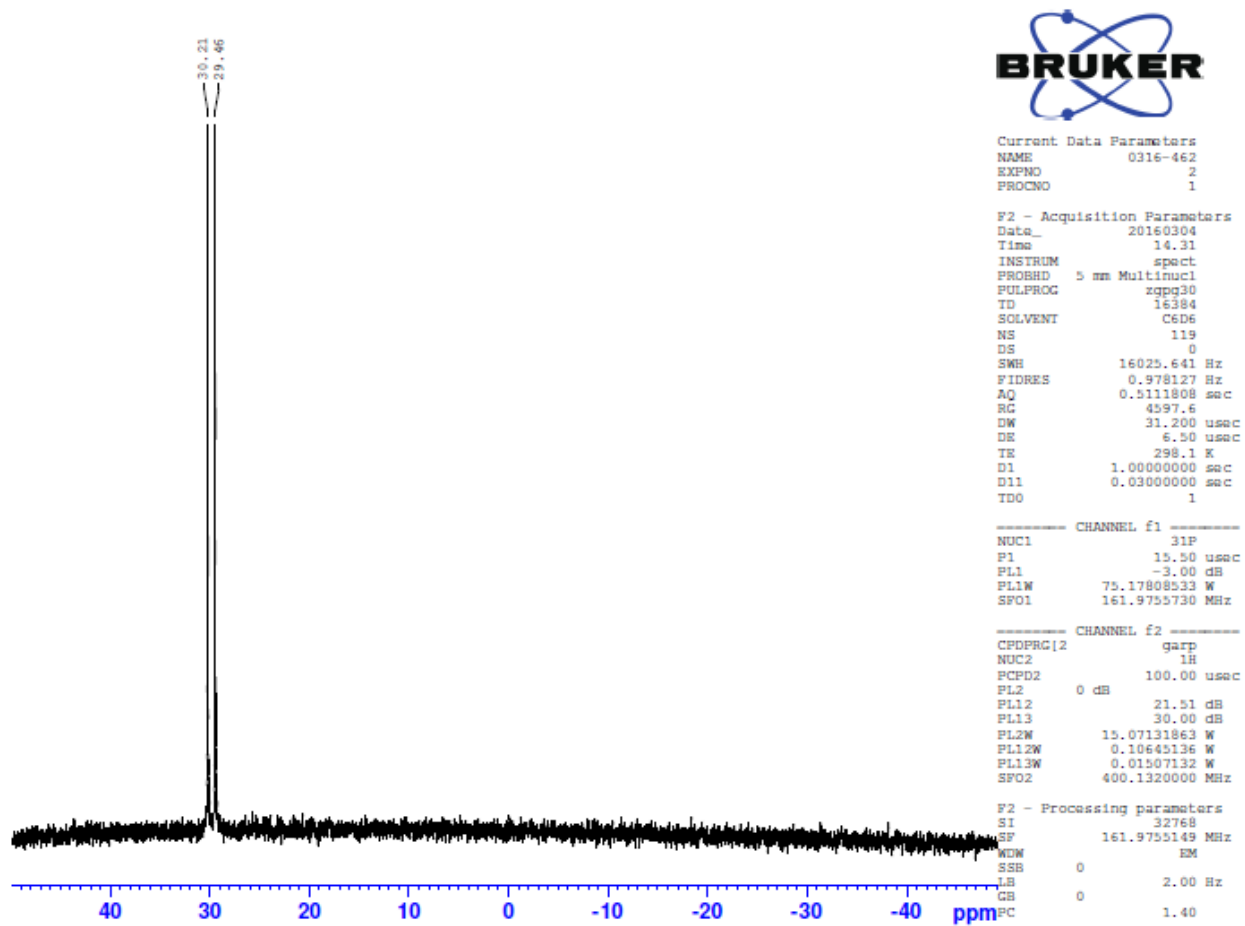


Figure D.17.  $^{31}\text{P}\{^1\text{H}\}$  NMR spectrum ( $\text{C}_6\text{D}_6$ , 162 Mhz) of  $[\text{Tp}^*\text{RhHCl}(\text{PEt}_3)]$

## D.8 Characterization of [Tp\*RhH(SBn)(PMe<sub>3</sub>)]

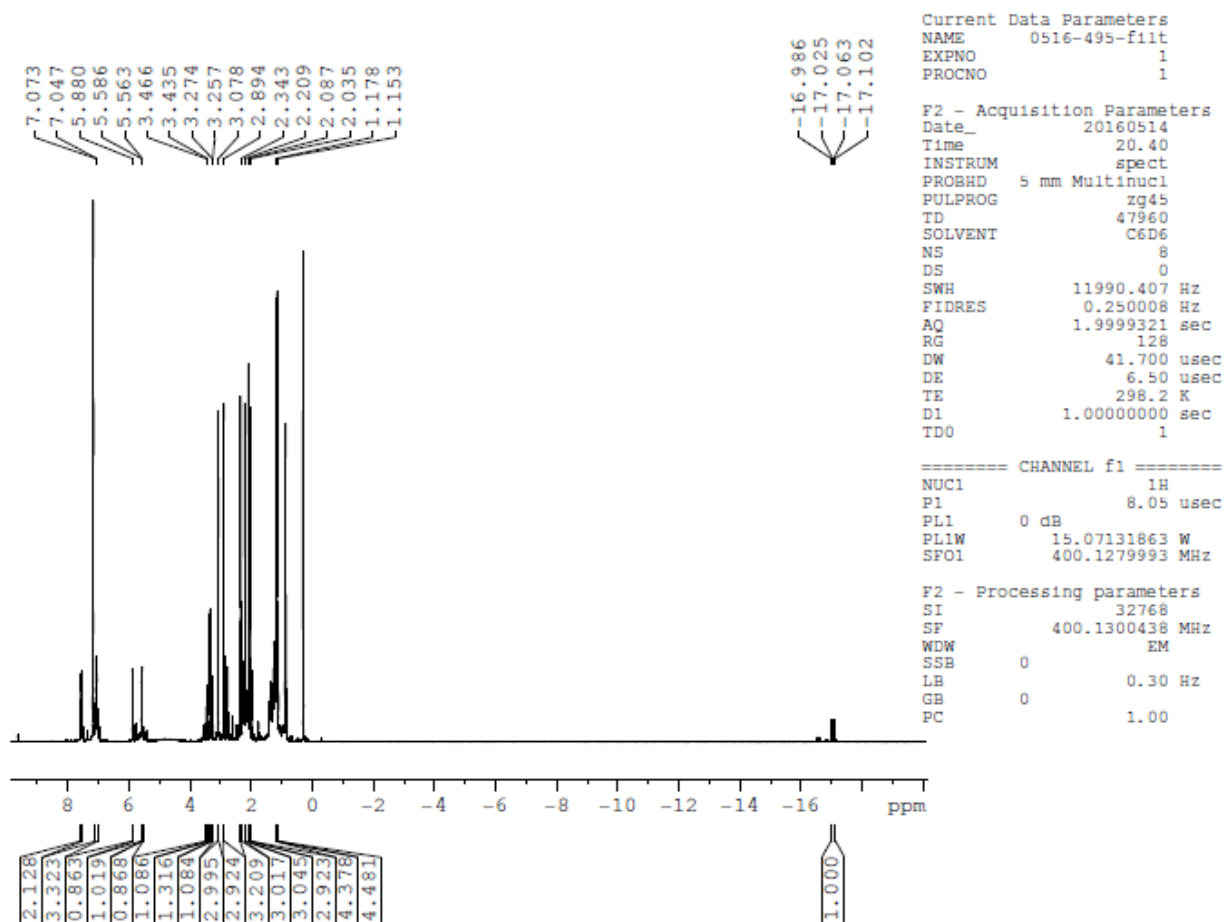


Figure D.18. <sup>1</sup>H NMR spectrum (C<sub>6</sub>D<sub>6</sub>, 400 Mhz) of [Tp\*RhH(SBn)(PMe<sub>3</sub>)]

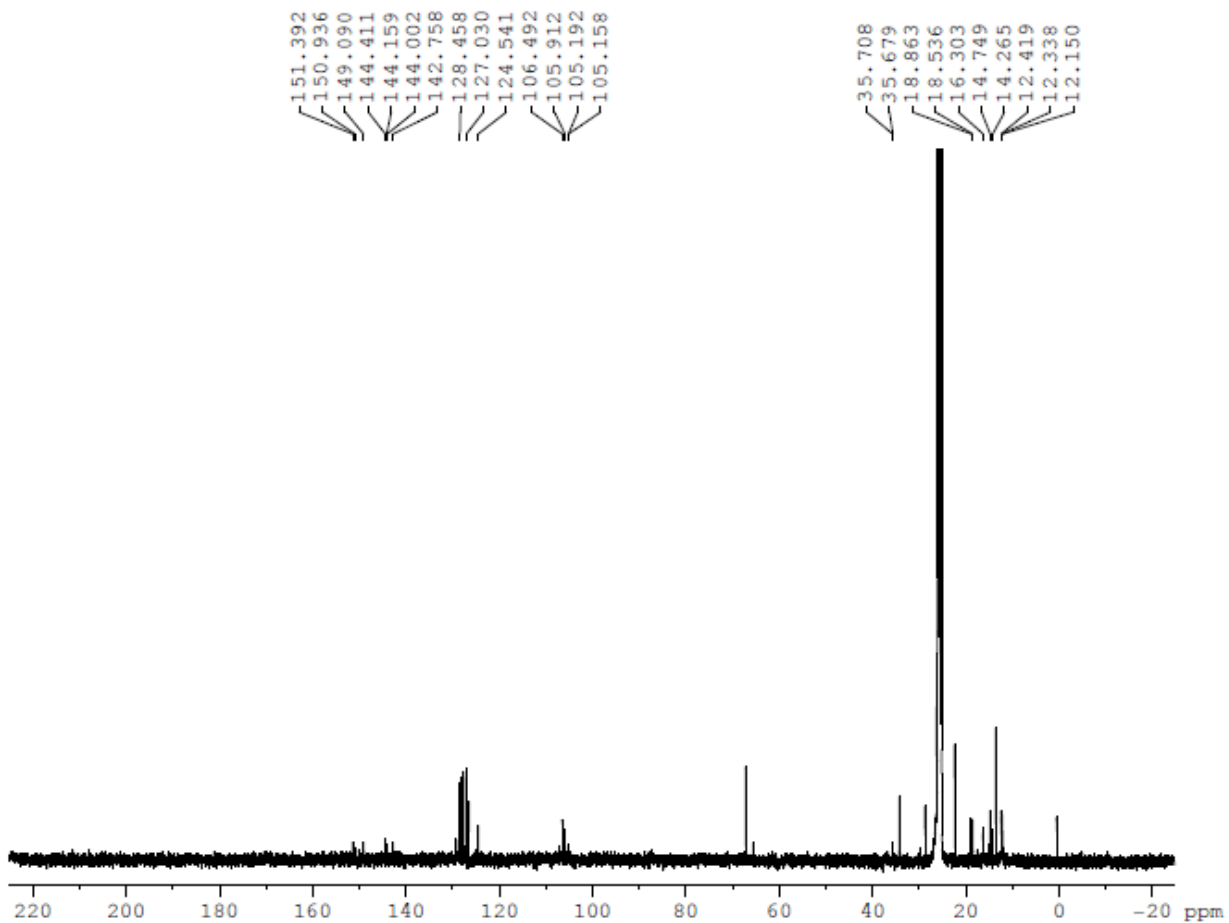


Figure D.19.  $^{13}\text{C}\{^1\text{H}\}$  NMR spectrum ( $\text{C}_6\text{D}_6$ , 100 Mhz) of  $[\text{Tp}^*\text{RhH}(\text{SBn})(\text{PMe}_3)]$

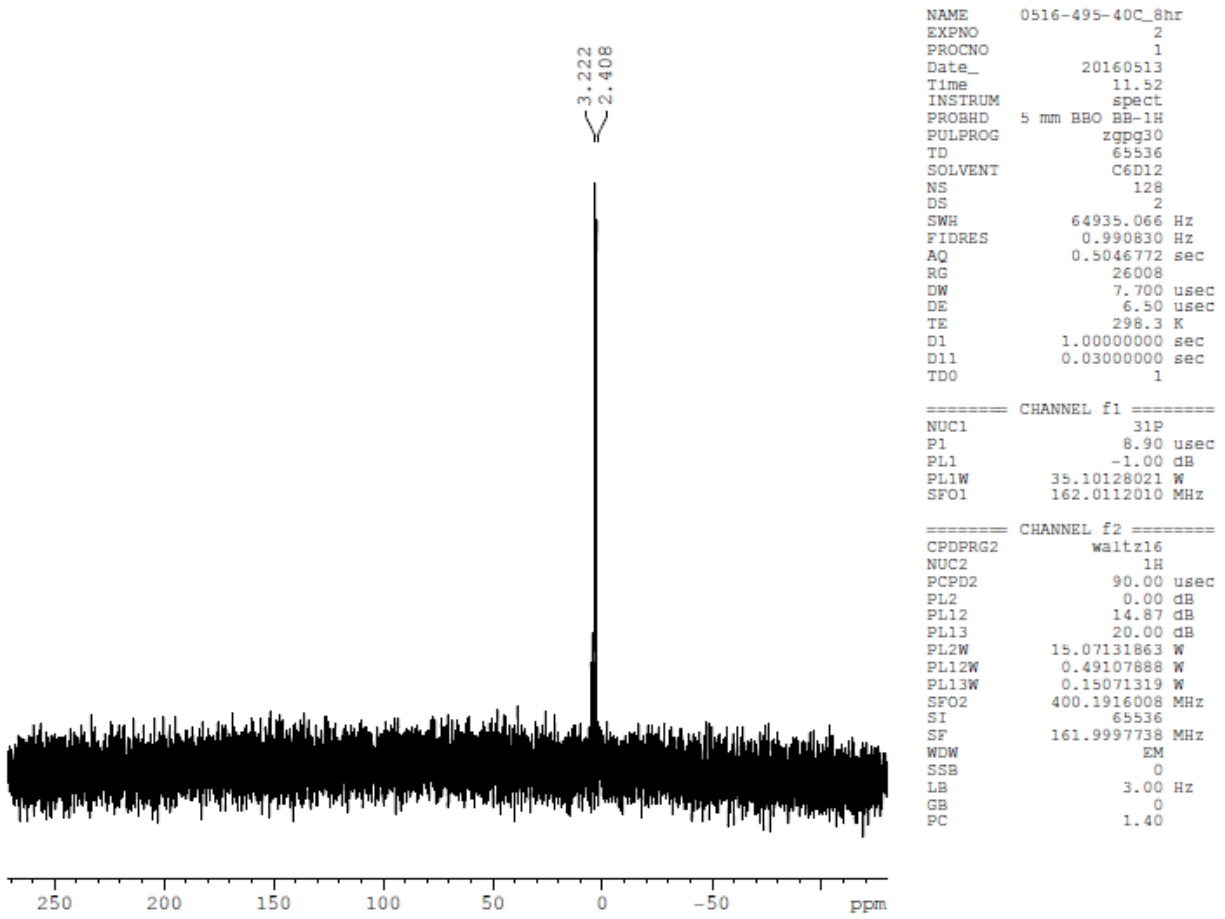


Figure D.20.  $^{31}\text{P}\{^1\text{H}\}$  NMR spectrum ( $\text{C}_6\text{D}_{12}$ , 162 Mhz) of  $[\text{Tp}^*\text{RhH}(\text{SBn})(\text{PMe}_3)]$

## D.9 Characterization of [Tp\*RhH(SEt)(PMe<sub>3</sub>)]

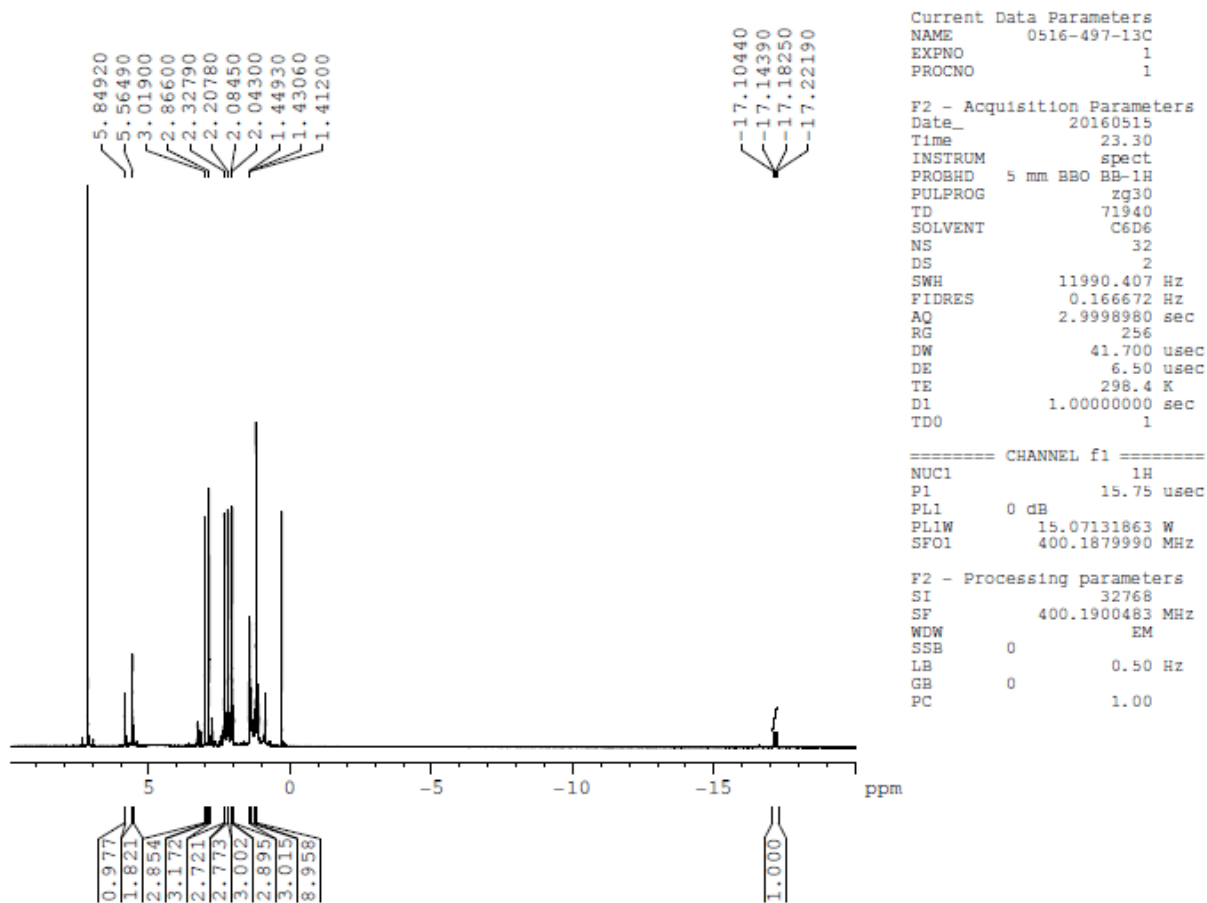


Figure D.21. <sup>1</sup>H NMR spectrum (C<sub>6</sub>D<sub>6</sub>, 400 Mhz) of [Tp\*RhH(SEt)(PMe<sub>3</sub>)]

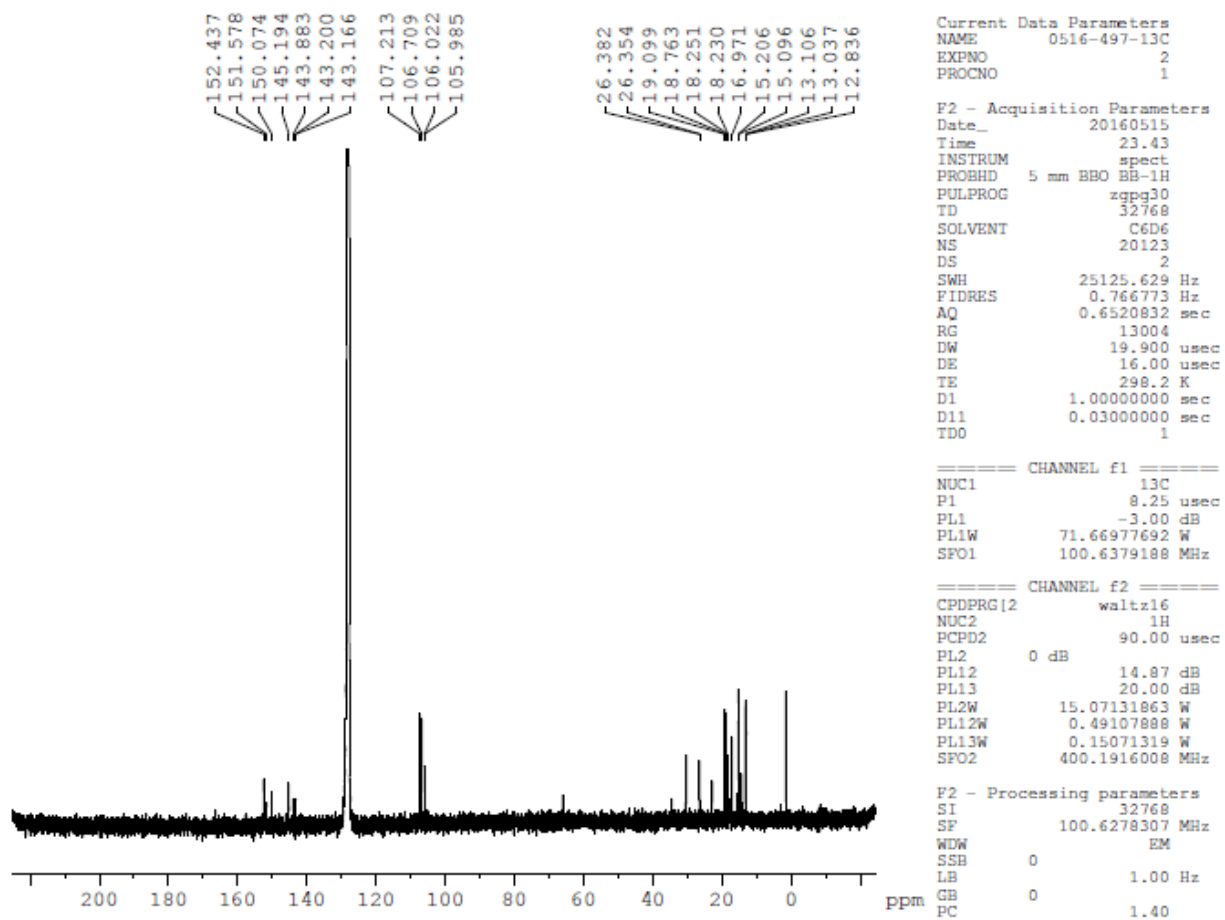


Figure D.22.  $^{13}\text{C}\{^1\text{H}\}$  NMR spectrum ( $\text{C}_6\text{D}_6$ , 101 Mhz) of  $[\text{Tp}^*\text{RhH}(\text{SET})(\text{PMe}_3)]$

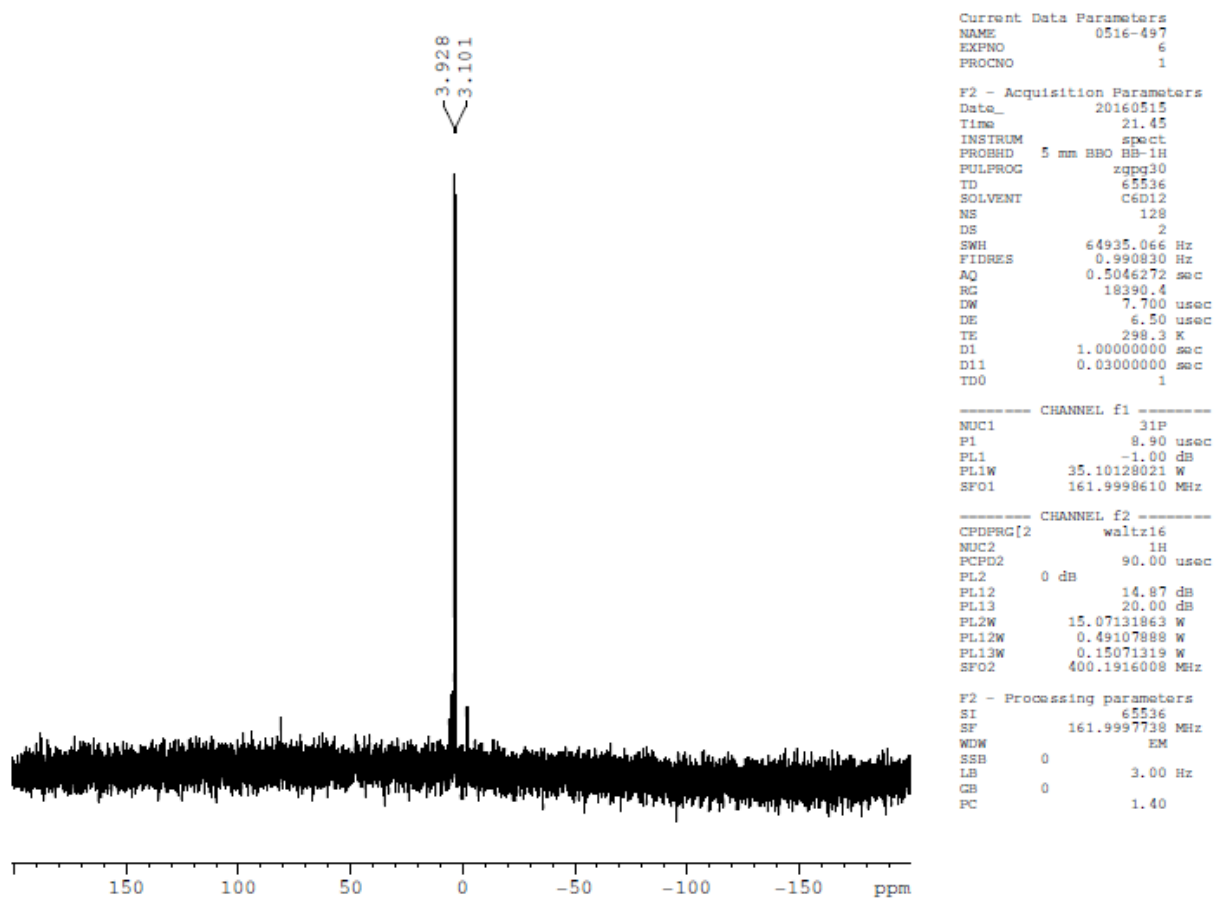


Figure D.23.  $^{31}\text{P}\{^1\text{H}\}$  NMR spectrum ( $\text{C}_6\text{D}_{12}$ , 162 Mhz) of  $[\text{Tp}^*\text{RhH}(\text{SET})(\text{PMe}_3)]$

## D.10 Characterization of [Tp\*RhH(SC<sub>6</sub>F<sub>5</sub>)(PMe<sub>3</sub>)]

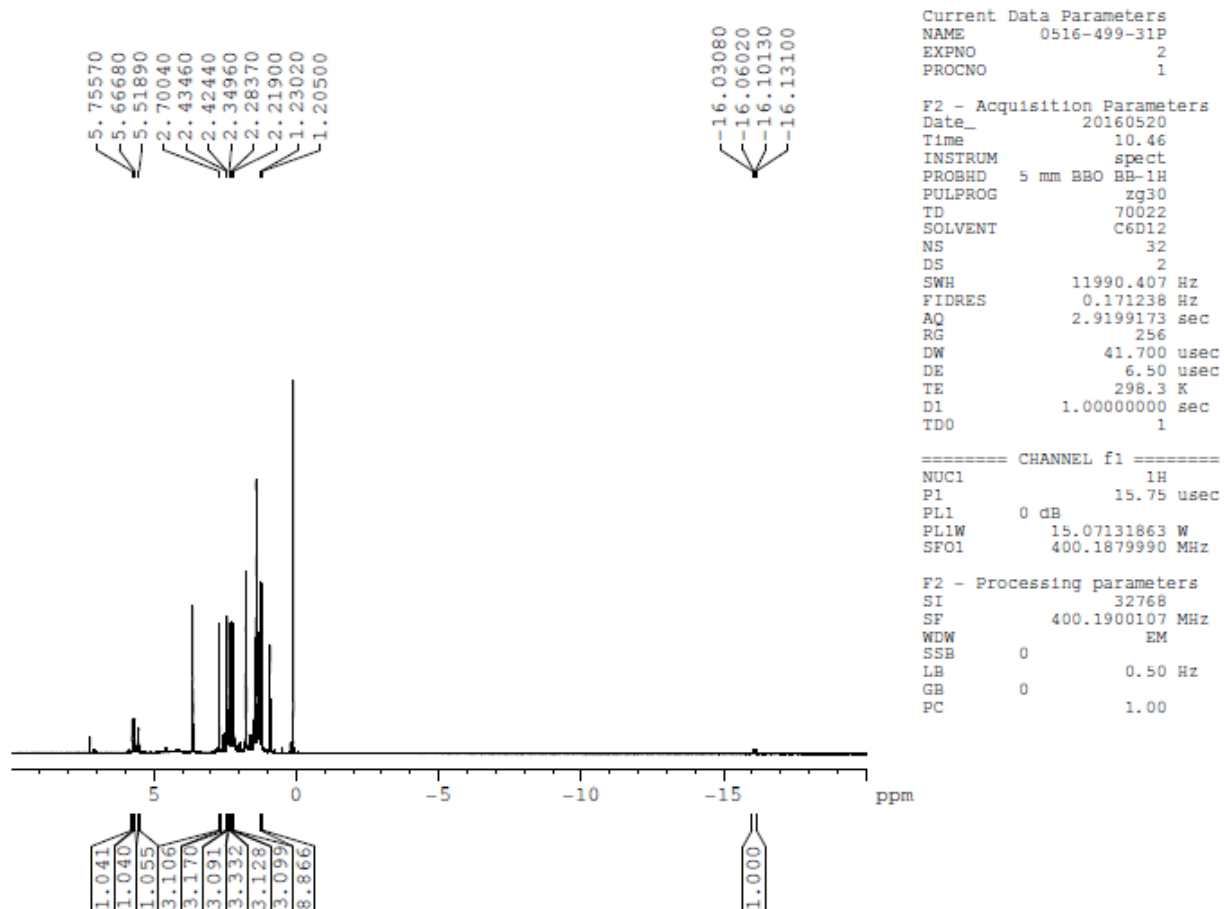


Figure D.24. <sup>1</sup>H NMR spectrum (C<sub>6</sub>D<sub>12</sub>, 400 Mhz) of [Tp\*RhH(SC<sub>6</sub>F<sub>5</sub>)(PMe<sub>3</sub>)]

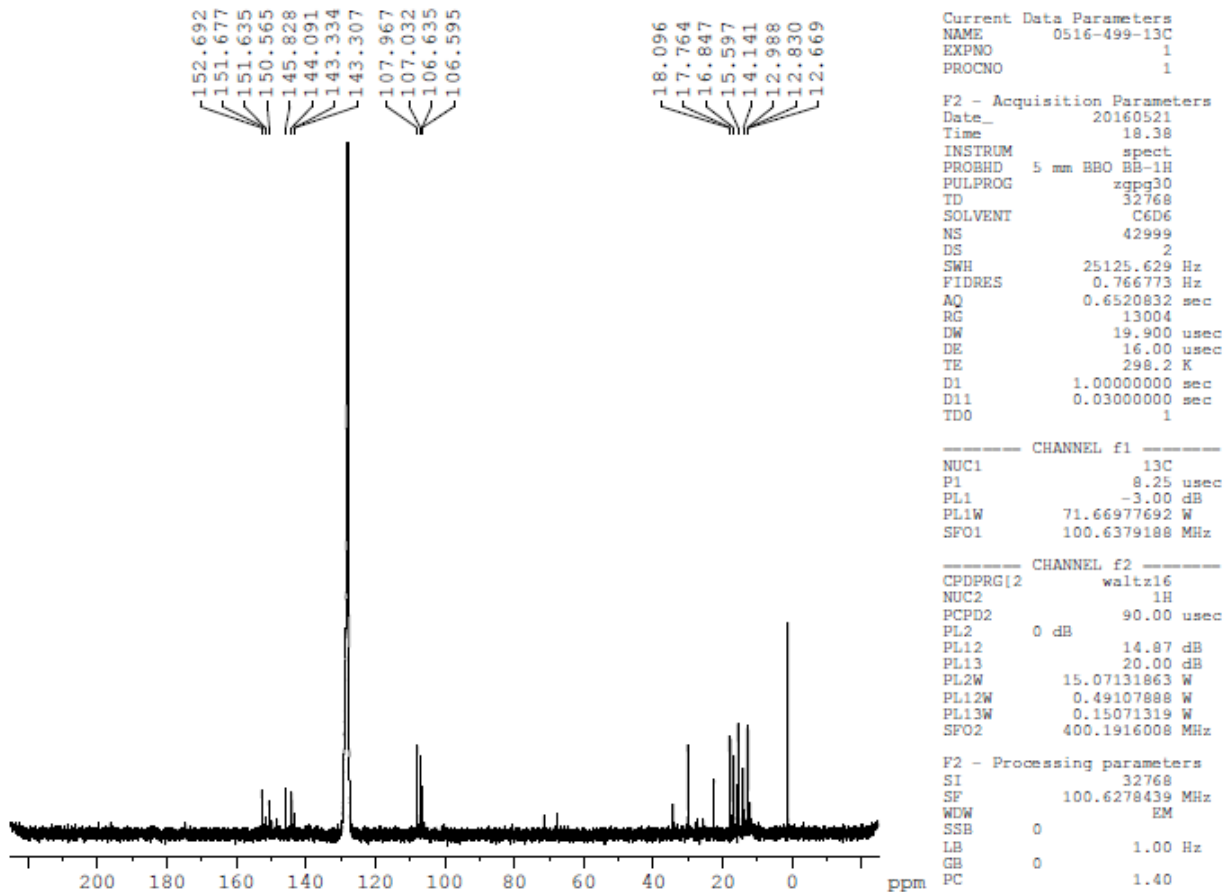


Figure D.25.  $^{13}\text{C}\{^1\text{H}\}$  NMR spectrum ( $\text{C}_6\text{D}_6$ , 101 Mhz) of  $[\text{Tp}^*\text{RhH}(\text{SC}_6\text{F}_5)(\text{PMe}_3)]$

$^{19}\text{F}$  referenced to  $\text{CFCl}_3$  at 0 ppm

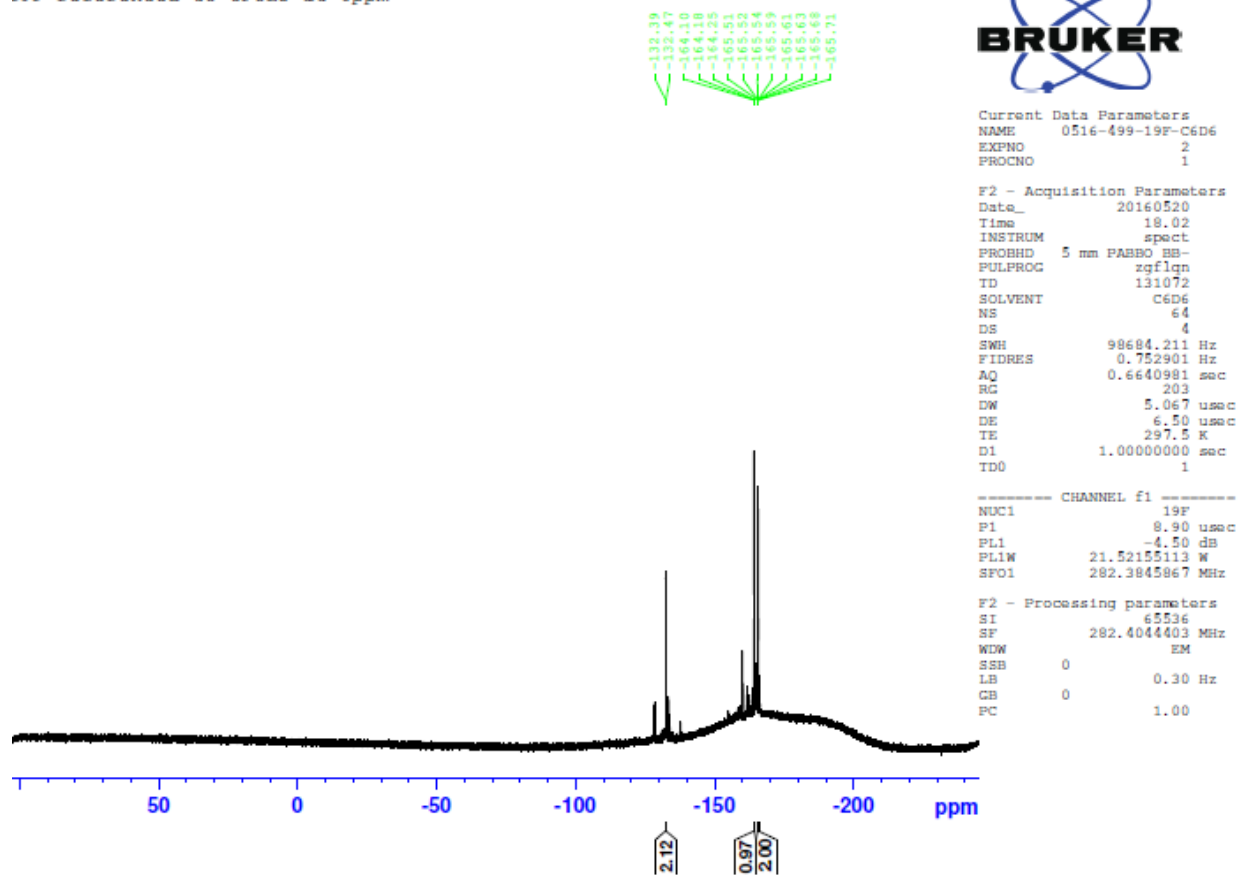


Figure D.26.  $^{19}\text{F}$  NMR spectrum ( $\text{C}_6\text{D}_6$ , 282 MHz) of  $[\text{Tp}^*\text{RhH}(\text{SC}_6\text{F}_5)(\text{PMe}_3)]$

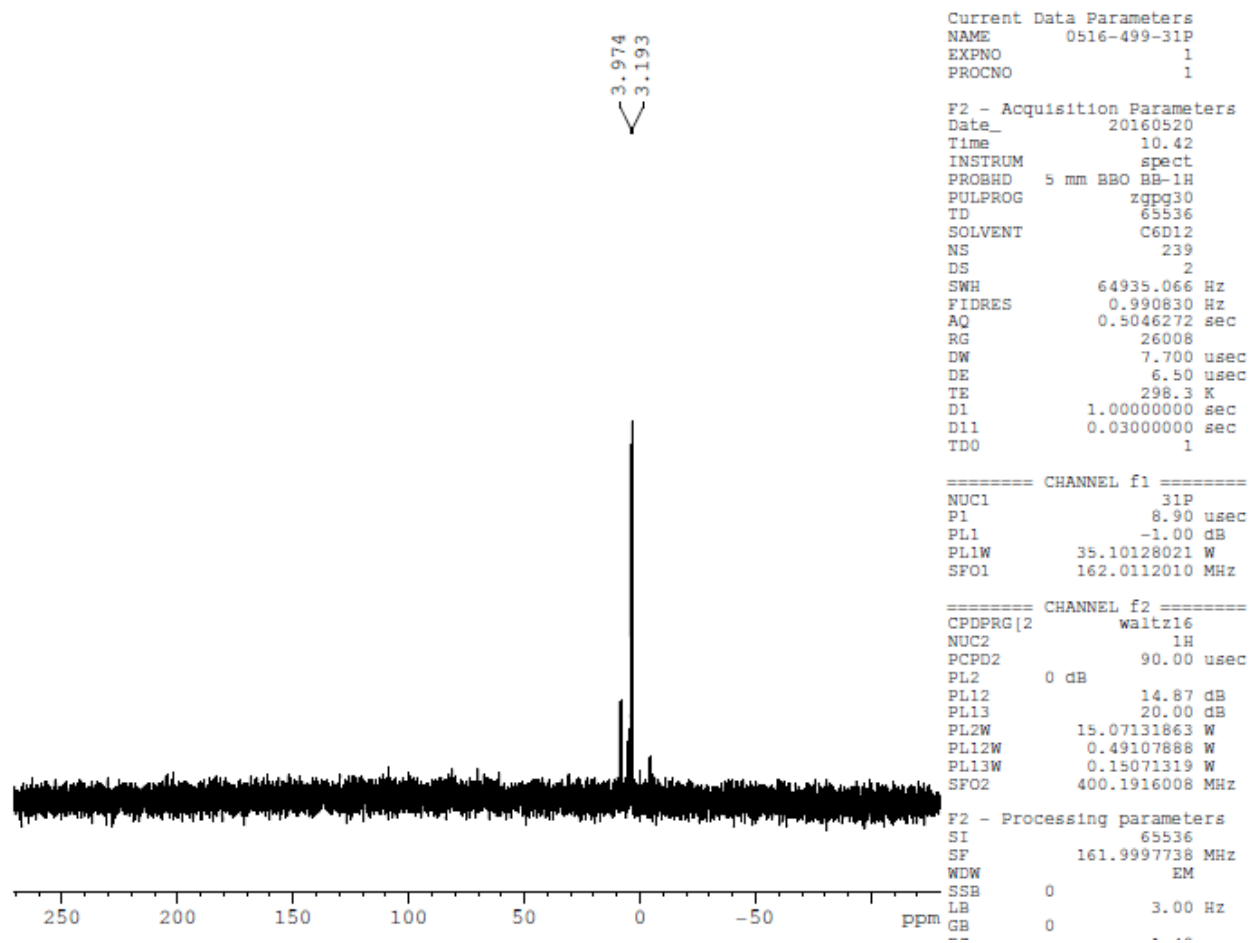


Figure D.27.  $^{31}\text{P}\{^1\text{H}\}$  NMR spectrum ( $\text{C}_6\text{D}_{12}$ , 162 Mhz) of  $[\text{Tp}^*\text{RhH}(\text{SC}_6\text{F}_5)(\text{PMe}_3)]$

## D.11 Characterization of [Tp\*RhH(SPh)(PMe<sub>3</sub>)]

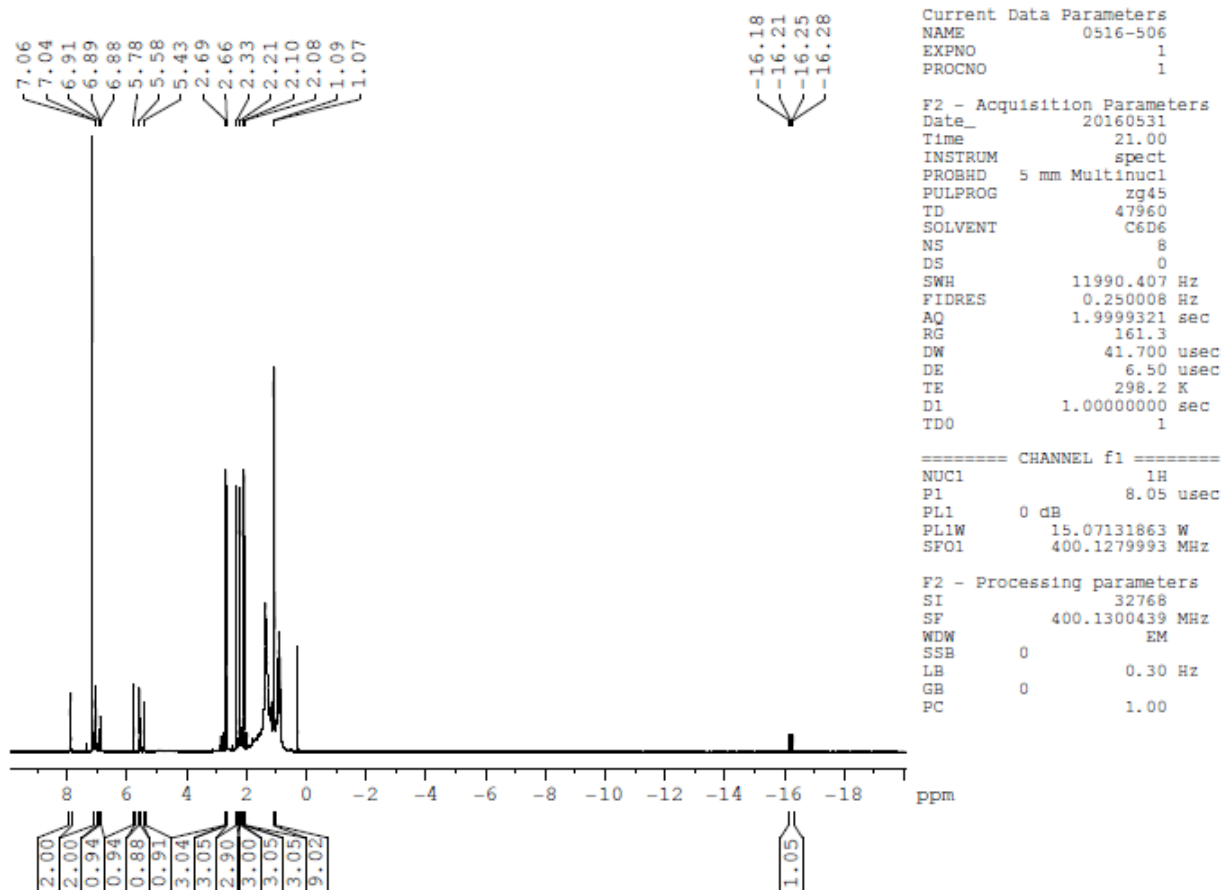


Figure D.28. <sup>1</sup>H NMR spectrum (C<sub>6</sub>D<sub>6</sub>, 400 Mhz) of [Tp\*RhH(SPh)(PMe<sub>3</sub>)]

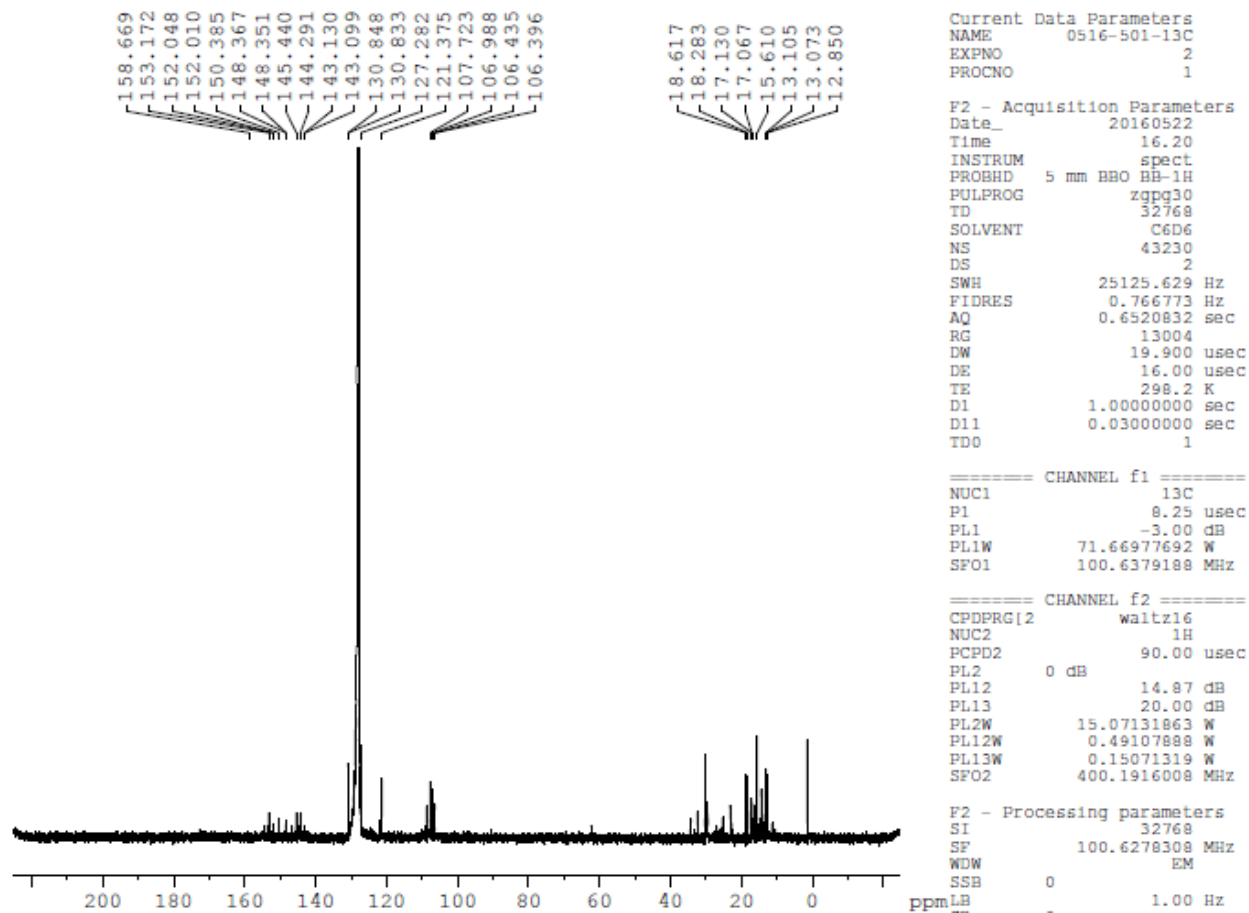


Figure D.29.  $^{13}\text{C}\{^1\text{H}\}$  NMR spectrum ( $\text{C}_6\text{D}_6$ , 101 Mhz) of  $[\text{Tp}^*\text{RhH}(\text{SPh})(\text{PMe}_3)]$

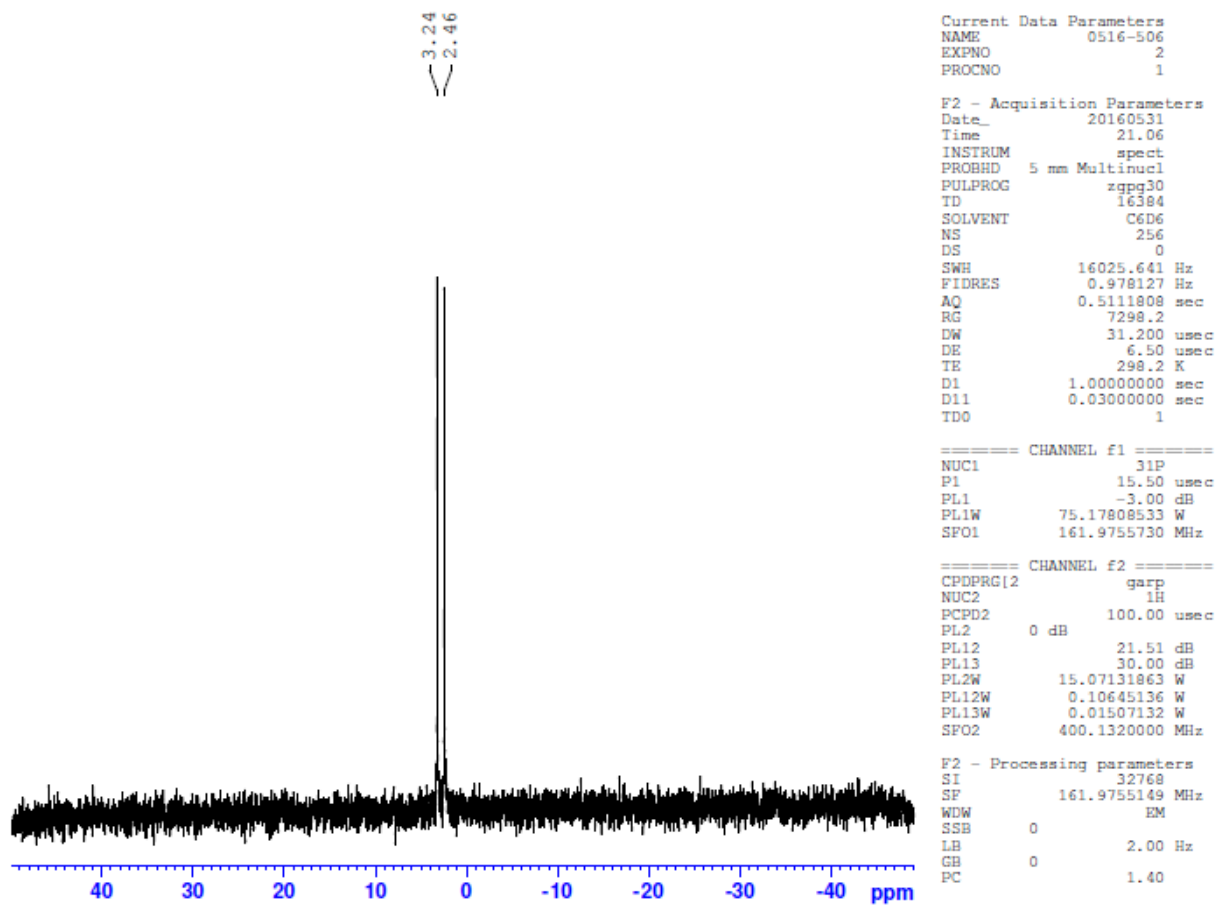


Figure D.30.  $^{31}\text{P}\{^1\text{H}\}$  NMR spectrum ( $\text{C}_6\text{D}_6$ , 162 Mhz) of  $[\text{Tp}^*\text{RhH}(\text{SPh})(\text{PMe}_3)]$

## Appendix E      Synthesis and Characterization of Substituted Pyrazoles

### E.1      Synthesis of 4-mesityl-1,3,5-trimethylpyrazole

In a glove box, Pd-PEPPSI-SIPr (13.6 mg, 0.020 mmol, 2 mol %) and LiCl (135.6 mg, 3.2 mmol, 3.2 equiv.) were weighed out and dissolved in dry THF (2 mL) and transferred to a Schlenk flask. On a Schlenk line, 4-bromo-1,3,5-trimethylpyrazole (189 mg, 1.0 mmol, 1.0 equiv) was added to the Schlenk flask under positive flow of nitrogen. 2.0 mL of a 1.0 M solution of MesMgBr in THF (2.0 mmol, 2.0 equiv) was then added all at once, and the solution was heated to 60 °C. After 24 h, 20 mL of a saturated Na<sub>3</sub>EDTA solution was added to the reaction mixture, and then extracted with 3 x 20 mL Et<sub>2</sub>O. The combined organic layers were washed with a saturated NaCl<sub>(aq)</sub> solution, and the solvent removed by rotary evaporation. The product was isolated by silica gel column chromatography using 4:1 hexanes : THF as eluent, yielding 4-mesityl-1,3,5-trimethylpyrazole (196 mg, 86%) as a colorless oil. <sup>1</sup>H NMR (CDCl<sub>3</sub>, 300 MHz) δ = 6.95 (s, 2H), 3.83 (s, 3H), 2.34 (s, 3H), 2.00 (s, 12H). Characterization matches literature data.

## E.2 Characterization of 4-mesityl-1,3,5-trimethylpyrazole

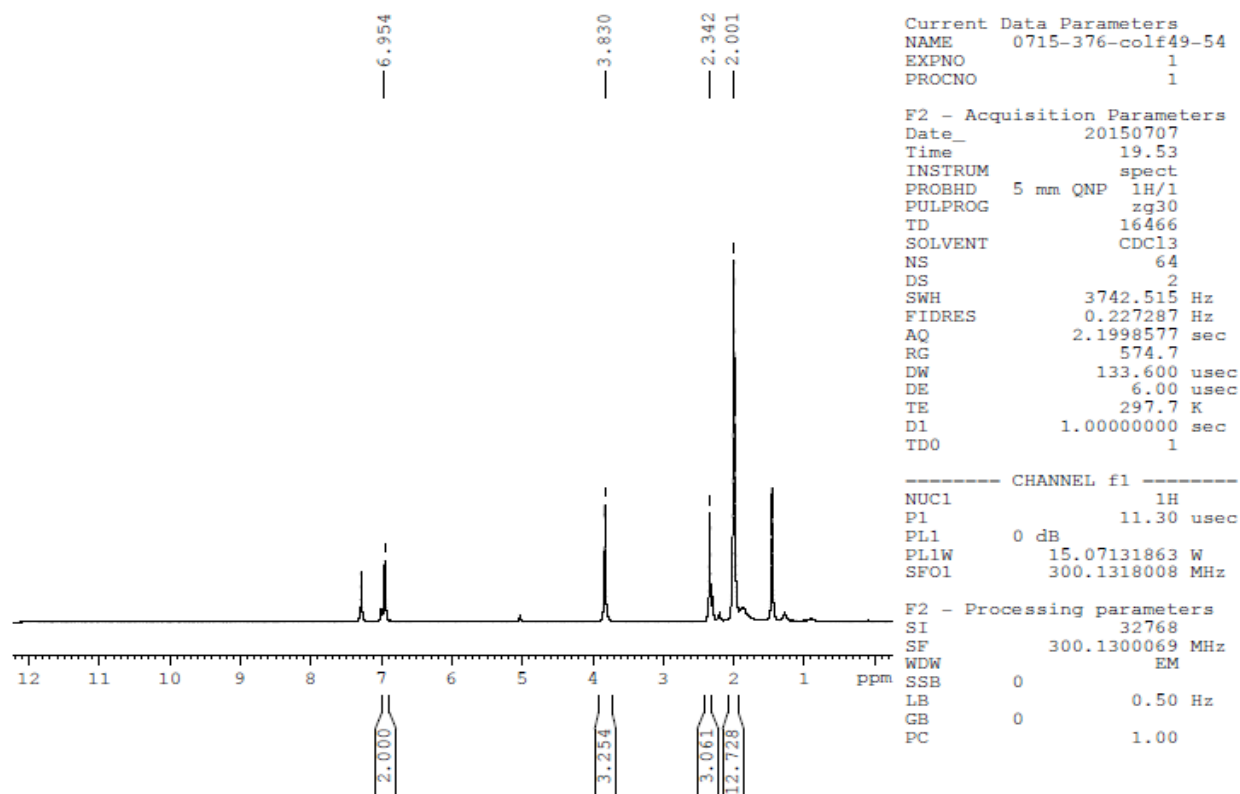


Figure E.1.  $^1\text{H}$  NMR spectrum ( $\text{CDCl}_3$ , 300 Mhz) of 4-mesityl-1,3,5-trimethylpyrazole

### E.3 Synthesis of 4-mesityl-3,5-dimethylpyrazole

4-mesityl-1,3,5-trimethylpyrazole (46.2 mg, 0.202 mmol) was added to a round bottom fitted with a stir bar. Pyridine (1.0 mL) and pyridine hydrochloride (939 mg) were added to the round bottom and a condenser attached. The solution was heated to 210 °C for 96 h. The solution was then quenched with saturated  $\text{NaHCO}_3(\text{aq})$  and extracted with toluene (3 x 20 mL). The solvent was removed under rotary evaporation to give 4-mesityl-3,5-dimethylpyrazole as a brown solid (8.2 mg) in 19% crude yield.  $^1\text{H}$  NMR ( $\text{CDCl}_3$ , 400 MHz)  $\delta$  = 6.94 (s, 2H), 2.33 (s, 3H), 2.04 (s, 6H), 1.98 (s, 6H).

### E.4 Characterization of 4-mesityl-3,5-dimethylpyrazole

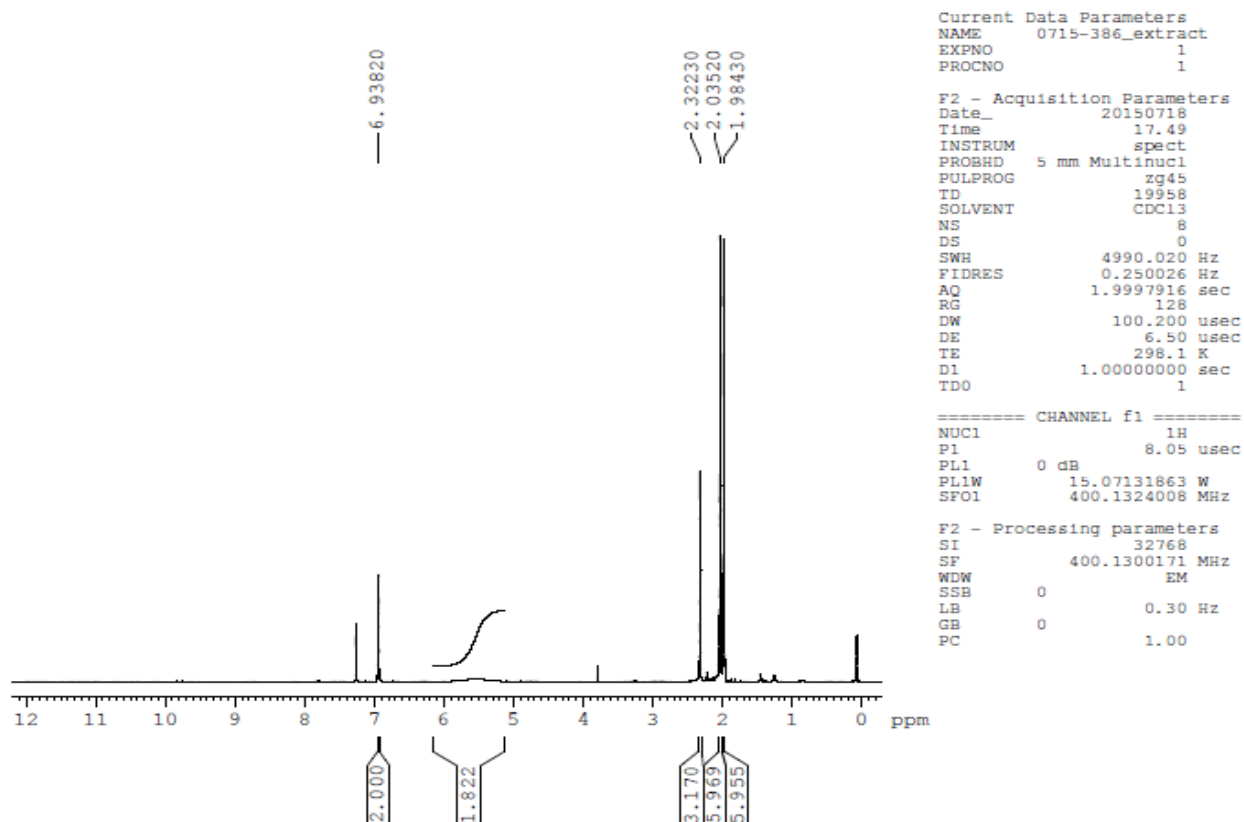


Figure E.2.  $^1\text{H}$  NMR spectrum ( $\text{CDCl}_3$ , 400 Mhz) of 4-mesityl-3,5-dimethylpyrazole

### E.5 Synthesis of *tert*-butyl 4-bromo-3,5-dimethylpyrazole-1-carboxylate

4-bromo-3,5-dimethylpyrazole (250.0 mg, 1.43 mmol, 1.0 equiv.) was dissolved in 25 mL of acetonitrile. To this solution was then added 4-dimethylaminopyridine (DMAP, 88.0 mg, 0.72 mmol, 0.5 equiv.), then di-*tert*-butyl dicarbonate (Boc<sub>2</sub>O, 623 mg, 2.86 mmol, 2.0 equiv.), then triethylamine (400 μL, 2.86 mmol, 2.0 equiv.). The solution was stirred at room temperature overnight, during which time the appearance of the solution changed from clear, colorless to clear, orange. The volatiles were then removed by rotary evaporation, and the product isolated by column chromatography (7:1 hexanes : ethylacetate as eluent) to give *tert*-butyl 4-bromo-3,5-dimethylpyrazole-1-carboxylate (339.1 mg, 86%) as a colorless liquid. <sup>1</sup>H NMR (CDCl<sub>3</sub>, 300 MHz) δ = 2.48 (s, 3H), 2.26 (s, 3H), 1.63 (s, 9H).

### E.6 Characterization of 1-boc-4-bromo-3,5-dimethylpyrazole

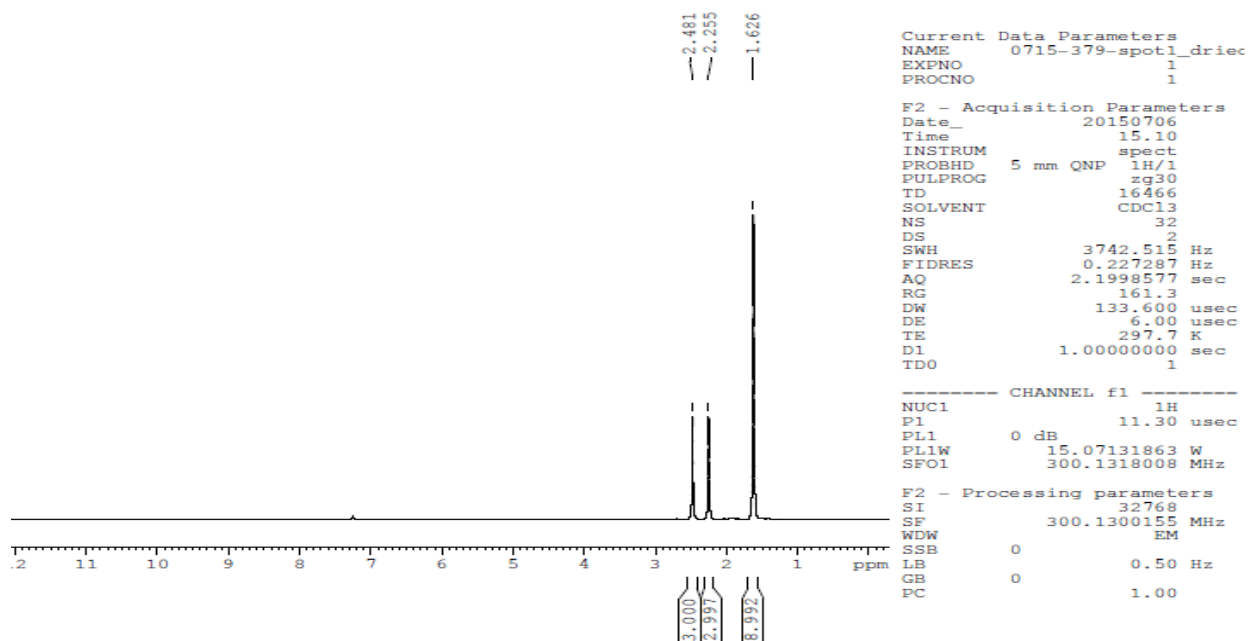


Figure E.3. <sup>1</sup>H NMR spectrum (CDCl<sub>3</sub>, 300 Mhz) of 1-boc-4-bromo-3,5-dimethylpyrazole

## E.7 Synthesis of 1-benzyl-4-bromo-3,5-dimethylpyrazole

4-bromo-3,5-dimethylpyrazole (751.4 mg, 4.293 mmol, 1.0 equiv.) was dissolved in 50 mL of acetonitrile. To this solution was then added benzylbromide (575  $\mu$ L, 4.83 mmol, 1.13 equiv.) and  $K_2CO_3$  (1.10 g, 7.96 mmol, 1.85 equiv.). The solution was then heated to reflux. After 14 h, the volatiles were removed by rotary evaporation, and the product isolated by column chromatography (7:1 hexanes : ethylacetate as eluent) to give 1-benzyl-4-bromo-3,5-dimethylpyrazole (853.5 mg, 75%) as a colorless oil.  $^1H$  NMR ( $CDCl_3$ , 300 MHz)  $\delta$  = 7.37-7.29 (m, 3H), 7.12-7.10 (m, 2H), 5.26 (s, 2H), 2.27 (s, 3H), 2.18 (s, 3H).

## E.8 Characterization of 1-benzyl-4-bromo-3,5-dimethylpyrazole

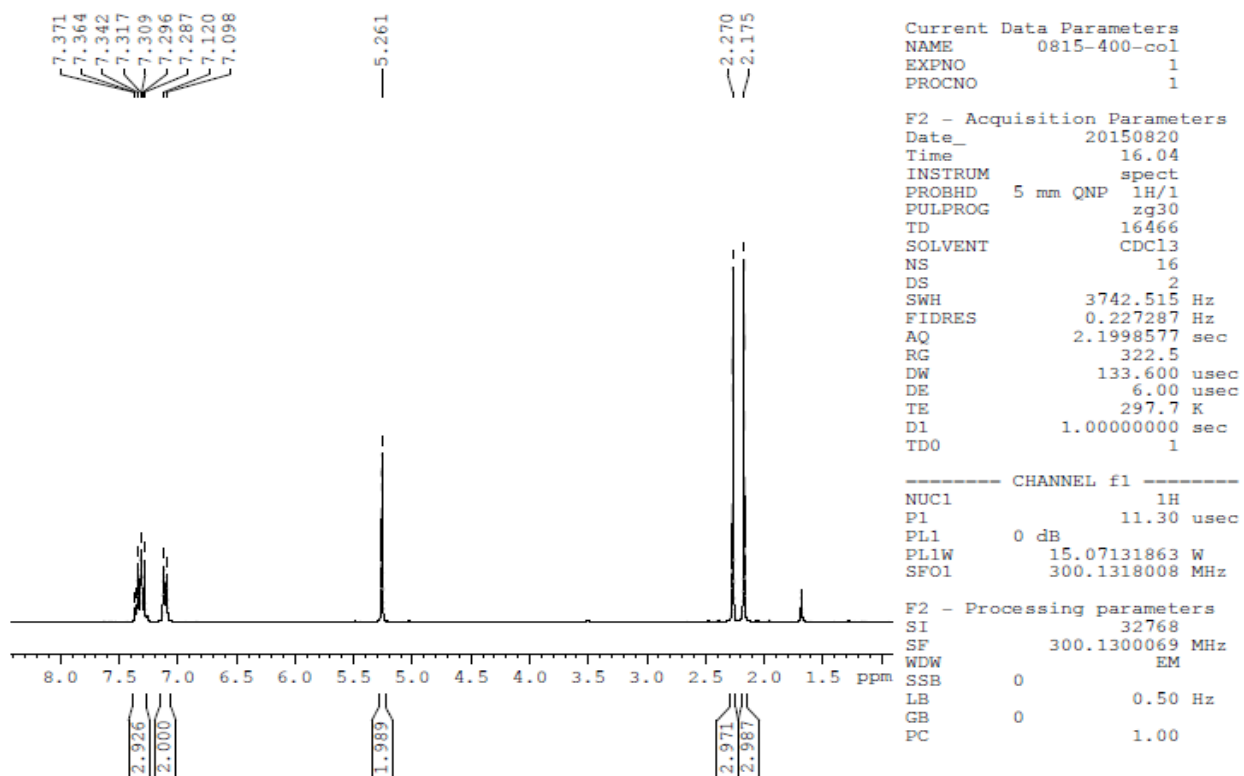
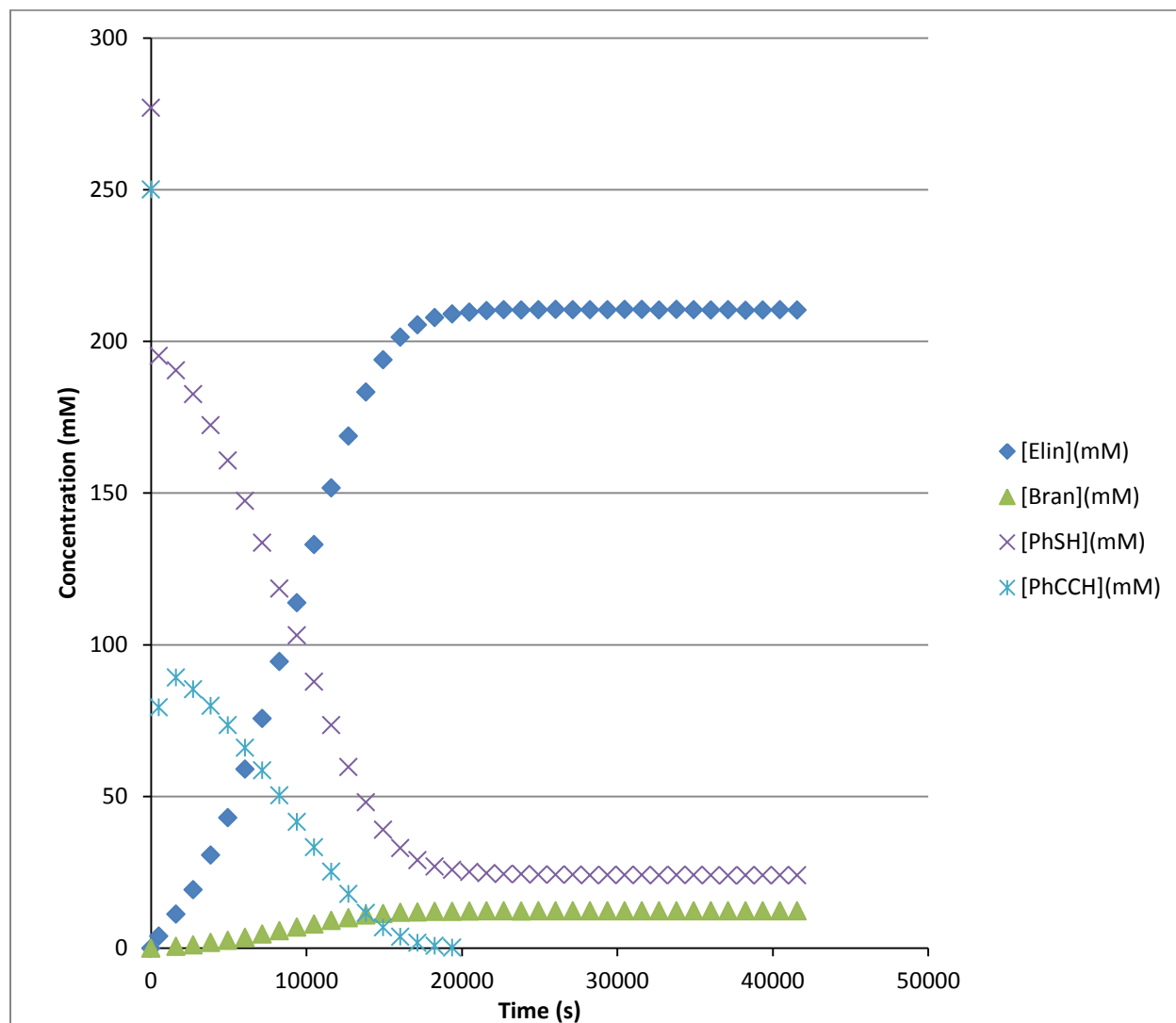
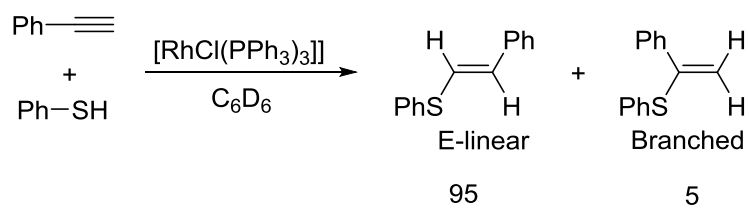


Figure E.4.  $^1H$  NMR spectrum ( $CDCl_3$ , 300 Mhz) of 1-benzyl-4-bromo-3,5-dimethylpyrazole

## Appendix F      Preliminary Mechanistic Studies of Alkyne Hydrothiolation Catalyzed by $[\text{RhCl}(\text{PPh}_3)_3]$

### F.1      Kinetic Profiles for Alkyne Hydrothiolation Catalyzed by $[\text{RhCl}(\text{PPh}_3)_3]$

Alkyne hydrothiolation catalyzed by  $[\text{RhCl}(\text{PPh}_3)_3]$  shows induction periods for both product formation and substrate consumption (Figure F.1). Whereas induction periods for product formation can usually be attributed to build up of an intermediate in the catalytic cycle, induction periods in the consumption of the substrate suggest that the induction periods are due to an off-cycle reaction or pre-equilibrium. The induction periods are dependent on the electronic nature of the thiol, with electron-rich thiols exhibiting shorter induction periods than electron-poor thiols (Figure F.2). The regioselectivity of the reaction is completely independent of the electronic nature of the thiol, producing a 95 : 5 ratio of *E*-linear : branched product for each aryl thiol examined.



**Figure F.1. Kinetic profile for the hydrothiolation of phenylacetylene with thiophenol catalyzed by  $[\text{RhCl}(\text{PPh}_3)_3]$ . 275 mM PhSH, 250 mM PhCCH, 7.50 mM  $[\text{RhCl}(\text{PPh}_3)_3]$ ,  $\text{CDCl}_3$ , 15 °C.**

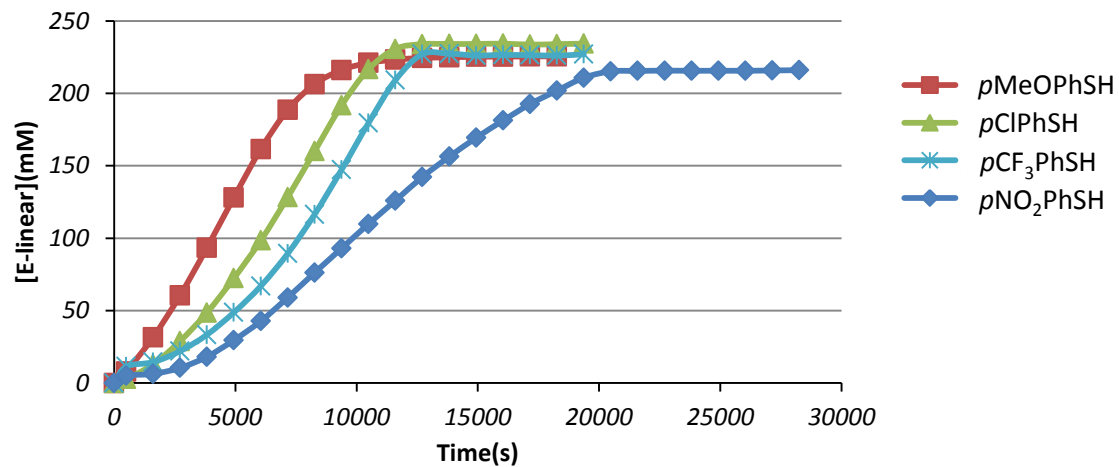


**Figure F.2. Time-course plots for the production of the *E*-linear vinyl sulfide products with substituted aryl thiols for the hydrothiolation of phenylacetylene catalyzed by [RhCl(PPh<sub>3</sub>)<sub>3</sub>].**